CRANFIELD INSTITUTE

OF TECHNOLOGY

SCHOOL OF PRODUCTION STUDIES

Ph.D. THESIS

TALIB NAJI TALIB

THE APPLICATION OF ELECTROLYTIC PHOTOETCHING AND PHOTOPOLISHING TO AISI 304 STAINLESS STEEL AND THE ELECTROLYTIC PHOTOETCHING OF AMORPHOUS COBALT ALLOY.

SUPERVISOR: DR. D. M. ALLEN

JANUARY 1986

ProQuest Number: 10820991

All rights reserved

INFORMATION TO ALL USERS
The quality of this reproduction is dependent upon the quality of the copy submitted.

In the unlikely event that the author did not send a complete manuscript
and there are missing pages, these will be noted. Also, if material had to be removed,
a note will indicate the deletion.

ProQuest 10820991

Published by ProQuest LLC (2019). Copyright of the Dissertation is held by Cranfield University.

All rights reserved.
This work is protected against unauthorized copying under Title 17, United States Code
Microform Edition © ProQuest LLC.

ProQuest LLC.
789 East Eisenhower Parkway
P.O. Box 1346
Ann Arbor, MI 48106 – 1346

SUMMARY

The results presented cover broad aspects of a quantitative investigation into the elecrolytic etching and polishing of metals and alloys through photographically produced dielectric stencils (Photoresists).

A study of the potential field generated between a cathode and relatively smaller anode sites as those defined by a dielectric stencil was carried out. Numerical, analytical and graphical methods yielded answers to the factors determining lateral dissolution (undercut) at the anode/stencil interface.

A quasi steady state numerical model simulating the transient behavior of the partially masked electrodes undergoing dissolution was obtained.

AISI 304 stainless steel was electrolytically photoetched in 10% w/w HCl electrolyte. The optimised process parameters were utilised for quantifying the effects of galvanostatic etching of the anode as that defined by a relatively narrow adherent resist stencil.

Stainless steel was also utilised in investigating electrolytic photopolishing. A polishing electrolyte (orthophosphoric acid - glycerol) was modified by the addition of a surfactant which yielded surface texture values of 70nm (Ra) and high levels of specular reflectance. These results were used in the production of features upon the metal surface through photographically produced precision stencils. The process was applied to the production of edge filters requiring high quality surface textures in precision recesses.

Some of the new amorphous material exhibited high resistance to dissolution in commercially used spray etching formulations. One of these materials is a cobalt based alloy produced by chill block spinning. This material was also investigated and electro etched in 10% w/w HCl solution. Although passivity was not overcome, by selecting suitable operating parameters the successful electro photoetching of precision magnetic recording head laminations was achieved. Similarly, a polycrystalline nickel based alloy also exhibiting passivity in commercially used etchants was successfully etched in the above electrolyte.

ACKNOWLEDGMENTS

I wish to express my profound gratitude to my Supervisor Dr. D.M. Allen for his consistent advice, guidance and support during this investigation.

I would like to thank my wife Nadia for her patience and support throughout.

I also wish to thank the following for their assistance:

Dr. D.F. Horne

Mr. M. Kaciniel

Dr. A. Chryssafis

Dr. J.E. Strutt

Dr. G.F. Prentice

Mr. I. Routledge

Mr. P.J. Gillbanks

Mr. L. Atkins

TO MY WIFE AND CHILDREN,
NAJI, YASAMIN, NAMEER &
RULA.

LIST OF CONTENTS

1.0 INTRODUCTION 1

1.1 GENERAL 1

1.2 PHOTORESISTS 2

1.2.1 Application of photoresists to substrates
1.2.2 Exposure of photoresist

1.3 PHOTOCHEMICAL MACHINING 4

1.4 ELECTROCHEMICAL CORROSION 4

1.4.1 Iron in hydrochloric acid
1.4.2 Cell thermodynamics

1.5 THE CONVENTIONAL METAL REMOVAL PROCESS IN P.C.M. 8

1.6 ELECTROLYTIC DISSOLUTION IN P.C.M. 9

1.6.1 Electrolytic photoetching (e.p.e.)
1.6.2 Electrolytic photopolishing (e.p.p.)

1.7 LITERATURE SEARCH 11

1.7.2 The computer search
1.7.3 The manual search
1.7.4 The industrial search

1.8 LITERATURE REVIEW 12

1.8.1 The photochemical machining
1.8.2 The etching system

1.9 PREVIOUS REVIEWS 21

1.9.1 Relevant Books

1.10 SUMMARY OF MATHEMATICAL METHODS 22

1.10.1 Choice of Method

1.11 FINITE DIFFERENCE METHOD 23

1.12 THE OBJECTIVES OF THE INVESTIGATION 24

2.0 FIELD ANALYSIS 26

2.1 GENERAL 26

2.2 A TWO DIMENSIONAL ANALYTICAL SOLUTION FOR THE ELECTROLYTIC ETCHING OF A THIN LINE THROUGH AN ADHERENT STENCIL. 27

2.3 GRAPHICAL METHOD 31

2.3.1 Principles of graphic plotting.

2.4 FIELD PLOTTING 32

2.4.1 Plot one
2.4.2 Plot two
2.4.3 Plot three
2.4.4 Plot four

2.5 THE EFFECT OF DIFFERING LINE WIDTHS ON THE DEPTH OF ETCH 35

2.6 NUMERICAL MODEL 36

2.6.1 Cell Description
2.6.2 The Program Structure
2.6.3 Model Details
2.6.4 The New Boundary

2.7 COMPUTATIONAL METHOD 44

3.0 PROCEDURES, MATERIALS AND EQUIPMENT. 45

3.1 GENERAL 45

3.2 ARTWORK PREPARATION 45

3.3 PHOTOGRAPHIC REPRODUCTION 46

3.3.1 Photographic materials
3.3.2 The photographic work

3.4 THE SUBSTRATE MATERIAL SELECTION 48

3.4.1 AISI 304 Stainless Steel
3.4.2 Recovac
3.4.3 Vitrovac 6025

3.5 SURFACE PREPARATION PRIOR TO PHOTORESIST COATING 49

3.5.1 The surface preparation of AISI 304 stainless steel.
3.5.2 Surface preparation for Recovac
3.5.3 Surface preparation for Vitrovac 6025

3.6 THE PHOTORESISTS 50

3.7 APPLICATION OF THE PHOTORESIST 51

3.7.1 Application of liquid resists
3.7.2 Applications of dry film resist

3.8 EXPOSURE OF PHOTORESIST 52

3.9 PHOTORESIST DEVELOPMENT 53

3.10 HEAT TREATMENT OF THE PHOTORESIST 53

3.11 THE ELECTROLYTE 54

3.11.1 Selected electrolytes

3.12 THE EQUIPMENT AND INSTRUMENTATION 55

3.12.1 Equipment for polarization measurement
3.12.2 Electro-etching/polishing equipment
3.12.3 Metrology
3.12.4 The analysis of the results

4.0 THE ELECTROLYTIC ETCHING OF AISI 304 STAINLESS STEEL. 57

4.1 GENERAL 57

4.2 PASSIVATION 58

4.3 POLARIZATION 59

4.4 THE POTENTIOSTAT AND MEASUREMENT CELL 59

4.5 POTENTIOSTATIC OR GALVANOSTATIC ETCHING 61

4.6 POLARIZATION MEASUREMENTS FOR AISI 304 STAINLESS STEEL IN 10% (w/w) HCl ACID SOLUTION. 62

4.6.1 Experimental details
4.6.2 The Results
4.6.3 Selection of the galvanostatic operating conditions

4.7 GALVANOSTATIC ETCHING 65

4.7.1 Experimental details
4.7.2 Geometric profile results
4.7.3 Mass of metal removed
4.7.4 Surface Texture Results

4.8 ANODE SURFACE BLACKING 68

4.9 RECOMMENDED PARAMETERS FOR ELECTROETCHING 69

5.0 NUMERICAL AND EXPERIMENTAL ASSESSMENT OF E.P.E. PARAMETERS. 70

5.1 THE RESOLUTION CHART 71

5.1.1 Experimental procedures
5.1.2 The undercut of the resist
5.1.3 Depth of etch results
5.1.4 Etch factors

5.2 DOUBLE SIDED ETCHING 79

5.2.1 Experimental details
5.2.2 Profile development results

5.3 NUMERICAL RESULTS 82

5.3.1 Single line width simulation
5.3.2 Simulated resist damage
5.3.3 Electro photoforming (epf)

5.4 SIMULATED CHART 85

5.4.1 Results of the numerical chart
5.4.2 Analysis of chart results

6.0 THE ELECTROLYTIC PHOTOPOLISHING E.P.P. OF AISI 304 STAINLESS STEEL 90

6.1 ELECTROLYTIC POLISHING 90

6.2 THE ELECTROLYTE 91

6.3 THE SURFACE TEXTURE MEASUREMENT OF ELECTRO-POLISHED AISI 304 STAINLESS STEEL. 92

6.3.1 Sample preparation
6.3.2 The electrolytic polishing cell
6.3.3 The electrolytic polishing procedure
6.3.4 The surface texture measurement and results.

6.4 THE MODIFIED ELECTROLYTE 95

6.4.1 The surface texture with the modified electrolyte.
6.4.2 The metal removal rate

6.5 QUANTIFYING THE E.P.P. PARAMETERS 96

6.5.1 The experimental procedure
6.5.2 The undercut measurement
6.5.3 The depth of polish
6.5.4 The etch factor
6.5.5 The cross-sectional profile of the electro-polished lines

6.6 THE APPLICATION OF E.P.P. IN THE PRODUCTION OF AN EDGE FILTER 100

6.6.1 Strategy of edge filter production
6.6.2. Details for the edge filter production

7.0 THE ELECTROLYTIC PHOTOETCHING OF OTHERWISE DIFFICULT TO ETCH MATERIALS. 103

7.1 AMORPHOUS METALS 104

7.2 THE ELECTROLYTIC PHOTOETCHING OF 'VITROVAC 6025' 105

7.2.1 Procedures and experimental details.
7.2.2 Polarization measurements

7.3 PRODUCTION OF MAGNETIC RECORDING HEAD LAMINATIONS. 107

7.3.1 Laboratory method
7.3.2 The continious flow processing of Vitrovac 6025

7.4 THE ELECTROLYTIC PHOTOETCHING OF 'RECOVAC' 109

7.4.1 Polarization measurement
7.4.2 Galvanostatic etching of Recovac

8.0 REMARKS AND CONCLUSIONS 112

REFERENCES 123
BIBLIOGRAPHY 128
APPENDICES 132
FIGURES 220

LIST OF APPENDICES

A	Literature search.	132
B	Two dimensional analysis of the current density distribution.	135
C	Field plotting equipment.	139
D	Manufacturers/suppliers of equipment and materials.	140
E	Co-ordinatograph and scribing tools.	143
F	The reduction camera	144
G	Development procedure for exposed high resolution plates Kodak type 1A.	145
H	Registration for double-sided mask.	147
I	AISI 304 Stainless Steel.	148
J	Specifications for Recovac.	149
K	Specifications for Vitrovac 6025.	152
L	Measurement of viscosity & resist thickness.	154
M	Development of the photoresists.	155
N	Preliminary tests for selecting electrolytes for working stainless steels.	156
O	Design of Galvanostat.	158
P	Measurement of surface roughness.	160
Q	The computer and softwear.	161
R	The potentiodynamic results.	164
S	The geometric profile produced by galvanostatic etching.	185
T	Photomicrographs of the stainless steel sections produced by e.p.e.	197
U	An application for e.p.e. in the production of steel rulers.	208
V	Specifications and processing of Shipley AZ.340 photoresist.	211
W	Preliminary tests for etching Vitrovac and Recovac with ferric chloride.	212
X	Fluxgate magnetometers.	213
Y	Method of measuring the recording head laminations.	215
Z	Proposed continuous photochemical machining of amorphous alloys.	217

LIST OF FIGURES

FIG.	TITLE	
1.1	Schematic illustrating the exposure and development of negative working photoresist.	220
1.2	Schematic illustrating the exposure and development of a positive working photoresist.	221
1.3	A photoetched aluminium drum and phototool.	222
1.4	Magnification of a phototool for the production of camera shutter blades made from spring steel, courtesy of Allen et at.	223
1.5	A commercial photoresist classifications; from lecture notes at C.I.T.	224
1.6	Dipcoating machine used for the work.	225
1.7	Dry film photoresist lamination machine.	226
1.8	A typical p.c.m. process flow chart.	227
1.9	Standard oxidation-reduction potentials.	228
1.10	Schematic diagram of a conventional spray etching system.	229
2.1	Calculated current density distribution results and plot.	230
2.2	The effect of changes in the value of the angle on the equation for current density distribution for the solution of case 2.	231
2.3	The effect of changes in the value of the angle on the equation for current density distribution for the solution of case 2.	232
2.4	The principle of graphical field plotting.	233
2.5	Plot of the potential field and the current density distribution for the initial boundary conditions obtained by using a graphical method.	234
2.6	Calculations for the initial current density distribution by the graphical method.	235
2.7	Measurements and plot of the current density distribution obtained by a graphical method.	236
2.8	Plot of the calculated and measured initial current density distribution.	237
2.9	Plot of the potential field and current density distribution for the case when etching has taken place and the metal removed distribution being determined by the initial boundary conditions.	238
2.10	Potential field plot for two adjacent and parallel lines of a width ratio of 3:2.	239
2.11	Potential field plot for two adjacent and parallel lines of a width ratio of 2:1.	240
2.12	Plot of the relationship between etched line width and depth of etch at the centre of the etched line for two adjacent and parallel lines.	241
2.13	Schematic of the numerical cell.	242
2.14	Program flow chart.	243
2.15	Node potential calculations.	244
3.1	The coordinatograph.	245

3.2	Schematic illustrating the dimension compensation for straight edge results.	246
3.3	The photographic reduction camera.	247
3.4	The mercury vapour UV exposure unit and frame.	248
3.5	The 'Littlejohn' double sided exposure unit.	249
4.1	Schematic polarization diagram of a passivating system.	250
4.2	a) The effect of concentration on the corrosion of iron in HCl. b) The influence of chlorides on anodic polarization.	251
4.3	Schematic polarization plots for passivating systems.	252
4.4	Schematic of a polarization measurement cell.	253
4.5	Schematic of the principle of a potentiostat in a potentiodynamic set-up.	254
4.6	Dimensions matrix for the tool used for the polarization measurements and the preliminary etching tests.	255
4.7	Schematic layout of the cell and equipment used for potentiodynamic polarization measurements.	256
4.8	Photograph illustrating the cell component parts.	257
4.9	Photograph illustrating the component parts of the measuring cell in position.	258
4.10	Photograph illustrating the cell in position in the water bath and fume cabinet.	259
4.11	Some of the instrumentation utilised for carrying out the potentiodynamic measurements.	260
4.12	The average anodic polarization plot for AISI 304 stainless steel in 10% (w/w) HCl at 15°C.	261
4.13	The average anodic polarization plot for AISI 304 stainless steel in 10% (w/w) HCl at 20°C.	262
4.14	The average anodic polarization plot for AISI 304 stainless steel in 10% (w/w) HCl at 25°C.	263
4.15	The average anodic polarization plot for AISI 304 stainless steel in 10% (w/w) HCl at 30°C.	264
4.16	Anodic polarization diagrams for AISI stainless steel in 10% (w/w) HCl.	265
4.17	Current density standard deviation versus anode potential.	266
4.18	The percentage standard deviation of current density versus anode potential at 15°C.	267
4.19	The percentage standard deviation of current density versus anode potential at 20°C.	268
4.20	The percentage standard deviation of current density versus anode potential at 25°C.	269
4.21	The percentage standard deviation of current density versus anode potential at 30°C.	270
4.22	Profiles produced by e.p.e. at a range of current densities together with time of etch (t,min.), peak-to-valley measurement (PV, µm) and surface texture (Ra, µm). The matrix corresponds to the position of the apertures in the resist stencil on the stainless steel anode.	271

4.23	Stylised current density distribution obtained in electrolytic photoetching.	272
4.24	The mass of AISI 304 stainless steel removed under galvanostatic etching in 5 minutes.	273
4.25	The mass of AISI 304 stainless steel removed under galvanostatic etching in 10 minutes.	274
4.26	The mass of AISI 304 stainless steel removed under galvanostatic etching in 15 minutes.	275
4.27	The mass of AISI 304 stainless steel removed under galvanostatic etching in 20 minutes.	276
4.28	Calculation of the coefficient of the variable (time) for the general equation of mass of metal removed.	277
4.29	The mass of metal removed versus current density for AISI 304 stainless steel in 10% (w/w) HCl at 25°C.	278
4.30	The surface texture and peak-to-valley versus current density results for e.p.e. AISI 304 stainless steel for 5 minutes in 10% (w/w) HCl.	279
4.31	The surface texture and peak-to-valley versus current density results for e.p.e. AISI 304 stainless steel for 10 minutes in 10% (w/w) HCl.	280
4.32	The surface texture and peak-to-valley versus current density results for e.p.e. AISI 304 stainless steel for 15 minutes in 10% (w/w) HCl.	281
4.33	The surface texture and peak-to-valley versus current density results for e.p.e. AISI 304 stainless steel for 20 minutes in 10% (w/w) HCl.	282
4.34	Photomicrograph of a potentiostatic etching of a 10 x 10 mm aperture at -250 mV (v. SCE) in 10% (w/w) HCl acid solution.	283
5.1a	Dimensions of the resolution etch chart illustrating four of the six line widths on the chart, 1.6, 0.8, 0.4, 0.2, 0.1, and 0.05 mm.	284
5.1b	Photograph of the resolution etch chart (not to scale).	285
5.2	Double sided exposure frame.	286
5.3	Schematic diagram of the etching jig made from acrylic.	287
5.4	Results and plot of the undercut of the resist layer versus etched line width for AISI 304 stainless steel in 10% (w/w) HCl at 25°C in 3 minutes.	288
5.5	Results and plot of the undercut of the resist layer versus etched line width for AISI 304 stainless steel in 10% (w/w) HCl at 25°C in 6 minutes.	289
5.6	Results and plot of the undercut of the resist layer versus etched line width for AISI 304 stainless steel in 10% (w/w) HCl at 25°C in 9 minutes.	290

5.7	Results and plot of the undercut of the resist layer versus etched line width for AISI 304 stainless steel in 10% (w/w) HCl at 25°C in 12 minutes.	291
5.8	Results and plot of the undercut of the resist layer versus etched line width for AISI 304 stainless steel in 10% (w/w) HCl at 25°C in 15 minutes.	292
5.9	Calculation for the regression coefficient 'a' of the general equation for undercut.	293
5.10	Calculation for the regression coefficient 'b' of the general equation for undercut.	294
5.11	The depth of etch versus etched line width in 3 minutes.	295
5.12	The depth of etch versus etched line width in 6 minutes.	296
5.13	The depth of etch versus etched line width in 9 minutes.	297
5.14	The depth of etch versus etched line width in 12 minutes.	298
5.15	The depth of etch versus etched line width in 15 minutes.	299
5.16	The depth of etch versus original line width.	300
5.17	Results and plot of the depth of etch versus etch duration for an original line width of 50 µm.	301
5.18	Results and plot of the depth of etch versus etch duration for an original line width of 100 µm.	302
5.19	Results and plot of the depth of etch versus etch duration for an original line width of 200 µm.	303
5.20	Results and plot of the depth of etch versus etch duration for an original line width of 400 µm.	304
5.21	Results and plot of the depth of etch versus etch duration for an original line width of 800 µm.	305
5.22	Results and plot of the depth of etch versus etch duration for an original line width of 1600 µm.	306
5.23	Analysis of variance for linear regression applied to the depth of etch experimental data.	307
5.24	The correlation coefficient 'a' from the equations for depth of etch versus etch durations plotted versus original line width.	308
5.25	The correlation coefficient 'b' from the equations for depth of etch versus etch durations plotted versus original line width.	309
5.26	The etch factor versus etched line width for an etch duration of 3 minutes.	310
5.27	The etch factor versus etched line width for an etch duration of 6 minutes.	311
5.28	The etch factor versus etched line width for an etch duration of 9 minutes.	312
5.29	The etch factor versus etched line width for an etch duration of 12 minutes.	313
5.30	The etch factor versus etched line width for an etch duration of 15 minutes.	314

5.31	The general etch factor trend in terms of line width and etch duration.	315
5.32	Three dimensional plot of the pooled experimental data illustrating etch factor in terms of etch duration and original line width.	316
5.33	Dimensions for the double sided tool artwork.	317
5.34	Schematic diagram of the galvanostatic double-sided etching cell and instrumentation.	318
5.35	Photomicrograph (X100) of the surface of the resist when double-sided etching. a) t = 6 minutes, b) t = 8 minutes.	319
5.36	Photomicrograph (X100) of the surface of the resist when double-sided etching. c) t = 10 minutes, d) t = 12 minutes.	320
5.37	Photomicrograph (X100) of the surface of the resist when double-sided etching. e) t = 14 minutes.	321
5.38	The undercut versus etch duration for double-sided etching.	322
5.39	Photomicrographs (X100) of the cross-sections of the double-sided results; Print mag. = X96.7	323
5.40	The average cross-sectional profile for double-sided etching; t = 6 mins.	324
5.41	The average cross-sectional profile for double-sided etching; t = 8 mins.	325
5.42	The average cross-sectional profile for double-sided etching; t = 10 mins.	326
5.43	The average cross-sectional profile for double-sided etching; t = 12 mins.	327
5.44	The average cros-sectional profile for double-sided etching; t = 14 mins.	328
5.45	Plot of the average cross-sectional profiles in double-sided etching; a = 6, b = 8, c = 10, d=12, e = 14 minutes.	329
5.46	Numerical simulation of a centrally positioned insulator (dimension 100μm).	330
5.47	Numerical simulation of a centrally positioned insulator (dimension 150μm).	331
5.48	Numerical simulation of a centrally positioned insulator (dimension 200μm).	332
5.49	Numerical simulation of a centrally positioned insulator (dimension 250μm).	333
5.50	Numerical simulation of a centrally positioned insulator (dimension 300μm).	334
5.51	Numerical simulation of a centrally positioned insulator (dimension 350μm).	335
5.52	Key and results of the splicing in modeling the etched chart.	336
5.53	Numerical simulation of resist failure (pin hole).	337
5.54	Numerical simulation of dissolution of dissimilar features 50,600 μm wide.	338
5.55	Numerical simulation illustrating electro-forming of dissimilar features 50,600μm.	339

5.56 Numerical simulation of electro-forming illustrating resist over-plating. 340
5.58 Numerical simulation of resolution chart (minor cell A). 341
5.59 Numerical simulation of resolution chart (minor cell B). 342
5.60 Numerical simulation of resolution chart (minor cell C). 343
5.61 Numerical simulation of resolution chart 344 (minor cell D).
5.62 Undercut for 50 µm line in cell 'A'. 345
5.63 Undercut for 100 µm line in cell 'A'. 346
5.64 Undercut for 100 µm line in cell 'B'. 347
5.65 Undercut for 200 µm line in cell 'C'. 348
5.66 Undercut for 200 µm line in cell 'B'. 349
5.67 Undercut for 400 µm line in cell 'C'. 350
5.68 Undercut vs. max./centre depth for 50 um line in cell 'A'. 351
5.69 Undercut vs. max. depth for 100 µm line in cell 'A'. 352
5.70 Undercut vs. max. depth for 100 µm line in cell 'B'. 353
5.71 Undercut vs. max. depth for 200 µm line in cell 'B'. 354
5.72 Undercut vs. max. depth for 200 µm line in cell 'C'. 355
5.73 Undercut vs. max. depth for 400 µm line in cell 'C'. 356
5.74 Rates of lateral to normal attack vs. maximum depth. 357
5.75 Rates of lateral to normal attack vs. centre depth. 358
5.76 Predicted average maximum depth of etch of chart. 359
5.77 Predicted feature centre depth of etch of chart. 360
5.78 Plots of the theoretical and practical depth of etch. 361
5.79 Predicted undercut vs. line width. 362
5.80 Plots of the theoretical and experimental undercut. 363
6.1 The relationship between specular reflectance and current density and electrolyte temperature, from 'Uhlig' (Ref. 61). 364
6.2 Schematic diagram of the polishing jig fabricated from acrylic sheet 6.35 mm thick. 365
6.3 Schematic diagram of the electrolytic cell utilised for double sided electrolytic polishing. 366
6.4 Plot of the surface texture of the electro-polished AISI 304 stainless steel versus current density in 5 minutes. 367
6.5 Plot of the surface texture of the electro-polished AISI 304 stainless steel versus current density in 10 minutes. 368
6.6 Plot of the surface texture of the electro-polished AISI 304 stainless steel versus current density in 15 minutes. 369
6.7 Plot of the surface texture of the electro-polished AISI 304 stainless steel versus current density in 20 minutes. 370
6.8 Plot of the surface texture of the electro-polished AISI 304 stainless steel versus current density in 25 minutes. 371

6.9	The surface texture of electro-polished AISI 304 stainless steel for current densities of 2.5, 5, 7.5, 10 and 12.5 A/dm^2.	372
6.10	AOV of the results for the surface texture versus current density for the modified electropolishing solution, etch duration was 15 minutes.	373
6.11	AOV of the results for the metal removal rate versus the current density when electropolishing AISI 304 stainless steel with the modified electrolyte.	374
6.12	Method and results for the profile measurement of the electro photopolished results.	375
6.13	AOV of the results for the resist undercut versus the original line width in e.p.p. AISI 304 stainless steel.	376
6.14	Photomicrograph of the electro photopolished chart, magnification = x 23.2.	377
6.15	Photomicrograph of the electro photopolished chart, magnification = x 23.2.	378
6.16	Photomicrographs of the sections of the electro photopolished resolution chart.	379
6.17	Photomicrographs of the sections of the electro photopolished resolution chart.	380
6.18	Photomicrographs of the sections of the electro photopolished resolution chart.	381
6.19	AOV of the results for the maximum depth of polish (c) of the 'W' profile versus the original line width.	382
6.20	The depth of polish measured at the centre versus original line width for line numbers 4, 5 & 6.	383
6.21	AOV of the results for the etch factor versus original line width in e.p.p., where the etch factor was calculated using the maximum depth of polish.	384
6.22	AOV of the results for the etch factor versus original line width in e.p.p. where the etch factor was calculated using the depth of polish at the centre of the line.	385
6.23	Plots of the etch factor as calculated for the depth of polish at the centre of the line and for the maximum depth.	386
6.24	Plots of the sectional profiles of the electro photopolished stainless steel for differing original line widths.	387
6.25	Edge filter patented by the Swedish company Aktiebolaget Separator in 1927.	388
6.26	Dimensions of the edge filter produced by e.p.e.	389
6.27	Strategy of edge filter production.	390
6.28	The e.p.p. tool for producing the edge filter (magnification x 4.7).	391

6.29 Photomicrograph of a section of the electro photopolished edge filter. (Magnification = x 25). 392

7.1 Exploded view of the Vitrovac sample holder. 393

7.2 Schematic diagram of the equipment and instrumentation used in the potentiodynamic polarization measurement for Vitrovac 6025. 394

7.3 Potentiodynamic polarization measurement for 'Vitrovac 6025' in 10% w/w HCl solution at 15°C. 395

7.4 Potentiodynamic polarization measurement for 'Vitrovac 6025' in 10% w/w HCl solution at 20°C. 396

7.5 Potentiodynamic polarization measurement for 'Vitrovac 6025' in 10% w/w HCl solution at 25°C. 397

7.6 Potentiodynamic polarization measurement for 'Vitrovac 6025' in 10% w/w HCl solution at 30°C. 398

7.7 Plot of the maximum active zone current density versus electrolyte temperature for Vitrovac 6025 in 10% w/w HCl. 399

7.8 Potentiodynamic polarization measurements of Vitrovac 6025 in 10% (w/w) HCl solution. 400

7.9 Drawing of the recording head lamination. 401

7.10 The measured distribution of the dimension ($1.4 \pm^{0.03}_{0.00}$ mm) of a sample of ten etched frets. 402

7.11 Photograph illustrating part of a fret produced by e.p.e. 403

7.12 Photomicrograph of partly electroetched Vitrovac 6025. 404

7.13 Potentiodynamic polarization measurement for 'Recovac' in 10% w/w HCl solution at 10 , 20 and 25 °C. 405

7.14 The depth of etch of 'Recovac' versus etch duration at J = 25 A/dm^2. 406

7.15 The depth of etch of 'Recovac' versus etch duration at J = 50 A/dm^2. 407

7.16 The depth of etch of 'Recovac' versus etch duration at J = 100 A/dm^2. 408

NOTATIONS

A	Stencil line width or original line width.
AOV	Analysis of variance.
B	Etched line width measured at metal surface.
C.I.T.	Cranfield Institute of Technology.
CURVE	Curve fitting & analysis of variance program.
c	Concentration (mol/cm).
D	Depth or Weighting factor.
DE	Depth of etch.
DPLOT	Data plotting program.
	adjacent features.
E	Electric field
e.f.	Etch factor
e.p.e.	Electro photoetching.
e.p.p.	Electro photopolishing.
F	Faraday, 96500 C
FPLOT	Function plotting program.
H,h	Distance
I	Current.
J	Current density
J_o	Exchange current density.
L	Half line width (A/2).
l	Mean length of current tube element.
M	Atomic weight (g/mol).
m	Mass of metal removed.
n	Number or number of electrons participating in an electrode reaction.
PV	Peak to valley.
p	Density.
p.c.m.	Photochemical machining.
R	Resistance.
R_a	Centre line average.
R_{max}	Peak to valley.
SCE	Saturated calomel electrode.
SOR	Successive overrelaxation
Q	Charge
R	Gas constant
T	Temperature.
t	Time.
U	Undercut.
U_d	Undercut in double-sided work.
V	Electrode potential.
v/v	Volume by volume ratio.
W	Mean width of current tube element.
w/w	Weight by weight ratio.
w/v	Weight by volume ratio.
w.r.t.	With respect to.

X,Y	Cartesian coordinates.
z	Equivalents/mol

SUBSCRIPTS

j	Index of point on the surface
lim	Limiting
n	Normal
p	Polish
s	Surface
x	Abscissa component.
y	Ordinate component

SUPERSCRIPTS

r	Iteration number in potential loop.
s	Time step number.

GREEK NOMENCLATURE

α	Angle the anode recedes by at the resist interface.
β	Fraction of distance between grid points
∇^2	Laplace operator.
γ	Exponent of concentration dependence
η	Overpotential (V)
θ	Angle between normal to electrode surface and Y axis (rad)
σ	Electrolyte conductivity
ρ	Density (g/cm^3)
ϕ	Potential (V)
ϕ_o	Surface potential (V)
ω	Overrelaxation parameter

1.0 INTRODUCTION

1.1 GENERAL

The most common role of photochemical machining (p.c.m.) is the manufacturing of precision components from metalic foils with the aid of photography and chemistry. Components made by this process have applications in today's most sophisticated technologies [1].

Photochemical machining (p.c.m.) was not possible until the invention of photography and its association with the lithographic printing process in the 19th century. In 1852 William Fox Talbot obtained the British Patent No.565 for devising a method of producing patterns in copper. He used ultra violet (UV) light to expose a sensitised dichromate gelatin coating to produce a stencil through which he etched the copper [2]. Copper laminates are still etched today using a modification of Fox Talbot's process.

Technological advances in the second half of this century initiated p.c.m. Now this recently emerged industry is assuming an important and ever increasing role in manufacturing. In certain applications p.c.m. is replacing traditional processes such as stamping and engraving. Stamping has been the means of producing components from sheet or foil materials. Such products may now be produced using p.c.m. whereby the designer is offered unique properties and opportunities such as:

i. Greater design freedom, as there are relatively less restrictions. Shapes or profiles of intricate designs may be produced, which under certain circumstances may not be possible by other manufacturing techniques such as stamping. In principle any shape that can be drawn may be reproduced.

ii. Short design-to-finished product times, this is mainly due to the short lead time required in tool preparation.

iii. Low tooling cost, at least one to two orders of magnitude lower than those required by comparable press tooling.

iv. The ability to work difficult materials, not being impaired by their mechanical properties.

v. Stress free components due to the lack of mechanical working of the substrate and hence unaffected material properties.

vi. No subsequent finishing operations such as de-burring are required.

vii. Accurate, precise and reproducable results are all features of the process.

viii. No tool wear 'as such' when compared to mechanical metal working processes. The tool in p.c.m. is used for imaging and hence does not wear as conventional tools

would, where the metal removal is carried out by the tool itself.

ix. Design changes are easily implemented. This is due mainly to the factors pointed out in (ii), (iii) above and the ability to modify the artwork under certain circumstances.

Photochemical machining may be defined as a manufacturing process for the working of metals and non-metals with the aid of photography and chemistry. Precision parts may be produced by generating a photoresist stencil on the surface of a material, and chemically etching away the exposed areas of material defined by the stencil [3].

The photoresist mask is formed by applying a photo sensitive resist coating on the surface of the base material. Then by imaging the photoresist photographically and after suitable resist development, the desired patterns are reproduced as a photoresist stencil. Chemical or electrochemical etching, or any other surface finishing such as plating is preceded by the selective masking of the base material (Fig. 1.1&2).

Substrates or base materials may not necessarily be metallic or flat. Glasses, ceramics, plastics or any suitable material may be processed. Objects that are not flat such as a photoetched aluminium drum (Fig. 1.3) are also produced using p.c.m., although the majority of components produced by the process are flat (Fig. 1.4).

1.2 PHOTORESISTS

The essential requirement from a photoresist is the ability to form uniform adherent coats which are highly resistant to chemical or physical attack during processing. The name 'photoresist' is descriptive of a material which is imaged photographically.

Photoresists in p.c.m. are generally available either as a dry film or as a liquid. Their processing and handling procedures differ slightly and each resist has advantages and disadvantages over the other. Once either photoresist has been applied, the subsequent processing steps are essentially the same. Figure 1.5 is a chart illustrating a commercial photoresist classification.

1.2.1 Application of photoresists to substrates

a) Liquid resists

There are several methods for applying liquid resists [4]. The choice of which will depend upon the product, process, type of resist etc. and the following are some of those methods:

i. Dip Coating - probably the most commonly used method which is carried out by the controlled withdrawal of the substrate through the meniscus of the resist (Fig. 1.6). "Wedging" may occur due to

the difference in thickness of coat between the top and bottom of the substrate. Dipping will also result in double sided coating.

ii. Flowing - This is where the photoresist is poured on one side of a horizontal plate. This is subsequently tilted at a suitable angle to allow the resist to flow over the surface. The excess resist is then drained.

iii. Whirling - The resist is poured onto a substrate which is subsequently rotated at a relatively low speed (100s of revs./min.). This spreads a 'pool' and whirls off the excess.

iv. Spinning - This is high speed whirling (1000s revs./min.) used on small substrates such as circular scales and silicon slices.

v. Spraying - Equipment such as spray guns or 'aerosols' are used in applying the photoresist. The resist is usually of low viscosity, as required for spraying.

vi. Roller coating - In batch production high viscosity resists are processed using specialised rollercoating machinery.

vii. Curtain coating - A flow production method where the component is passed through a thin film of resist forming a 'curtain'. This is produced by the resist passing through a horizontal slit or over an edge and falling due to gravity.

b) Dry film

Dry film resists are laminated onto the substrate by means of heated rollers (Fig. 1.7). The polythene layer of the triple sandwich structure is removed revealing the resist layer just prior to it being adhered to the surface of the substrate. Adhesion is by means of the temperature and pressure regulated rollers. Double sided coating is carried out by simultaneously duplicating the above process for the other side of the substrate by using another resist roll and heated roller.

1.2.2 Exposure of photoresist

Photoresists are exposed through a mask to ultra violet (UV) light. The duration of exposure is dependent upon the intensity and the distance of the UV radiation source from mask/substrate. Vacuum is applied between the mask and the substrate so as to insure good contact. The emulsion of the mask is usually in contact with the resist layer. This is all carried out under yellow safe light conditions.

1.3 PHOTOCHEMICAL MACHINING

This is a multistage process [5] requiring careful and precise planning and execution of the work at each of the process stages. A typical p.c.m. process chart is illustrated in figure 1.8 and is summarised as follows:

1- Artwork preparation.
2- Photographic reproductions.
3- Metal selection.
4- Surface preparation for the resist coating.
5- Resist coating.
6- Pre-baking (where applicable).
7- Registration of masks (double sided work).
8- Exposure of photoresist coating.
9- Development of exposed photoresist coating.
10- Post-baking the resist image (where applicable).
11- Etching process.
12- Photoresist removal (if required).
13- Inspection.

Some of the above process stages are cumulatively dependent, such as stages 4 to 6 and 8 to 10. Therefore errors are cumulative and hence great care must be taken in the preparation of those stages. This is obviously time consuming but is essential for achieving high batch yields of substrates suitable for etching.

1.4 ELECTROCHEMICAL CORROSION

Most metals exist in their natural state as compounds (oxides, sulfides, etc.). This is their thermodynamically stable state. These are extracted from the ground to produce the metals we use. Unless we have substantially changed the metal (e.g. by alloying), the thermodynamics will not have changed. When we expose this metal to a natural environment, it will revert to its natural state by forming compounds, this is known as 'corrosion'.

There are also metals such as gold that exist in nature as a pure element and have excellent corrosion resistance in natural environments.

Thermodynamics similar to the above example apply to corrosion in all media. Corrosion is only possible if its products are more stable than the reactants, but not all thermodynamically possible reactions take place.

1.4.1 Iron in hydrochloric acid

Iron is the most commonly used industrial metal and hence shall be used to illustrate the theory of electrochemical corrosion. Iron reacts vigorously in hydrochloric acid, hydrogen is evolved and the iron goes completely into solution. The reaction being:

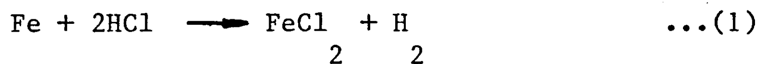

$$Fe + 2HCl \longrightarrow FeCl_2 + H_2 \qquad ...(1)$$

The solution in the above reaction is ionised, it contains positively and negatively charged ions. The hydrochloric acid contains hydrogen ions (H^+) and chloride ions (Cl^-). Likewise, ferrous chloride in solution can be considered as iron ions (Fe^{++}) and chloride ions (Cl^-).

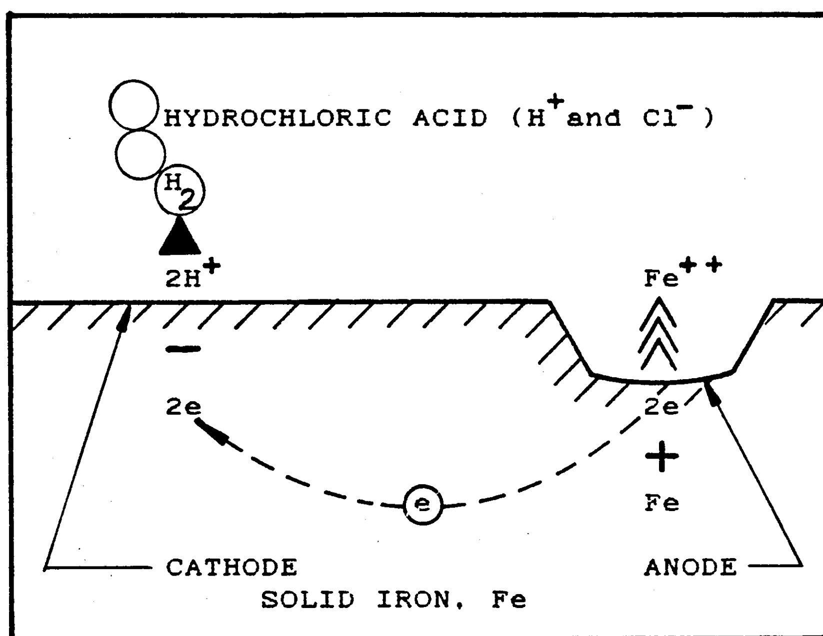

Corrosion of iron in hydrochloric acid.

Hence, Eq. (1) can be written as:

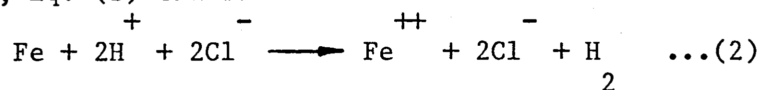

$$Fe + 2H^+ + 2Cl^- \longrightarrow Fe^{++} + 2Cl^- + H_2 \qquad ...(2)$$

Iron has been converted to ion and by definition, the iron is said to have been oxidized. On the other hand, the hydrogen ions have gained an electron and again by definition, they have been reduced. The overall reaction can be considered as two separate ones:

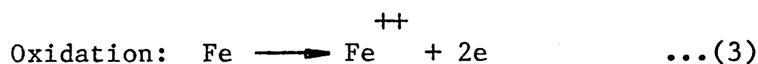

$$\text{Oxidation:} \quad Fe \longrightarrow Fe^{++} + 2e \qquad ...(3)$$

$$\text{Reduction:} \quad 2H^+ + 2e \longrightarrow H_2 \qquad ...(4)$$

The mechanism of this example is illustrated in the figure above.

These reactions both take place on the metal surface. The areas where oxidation occurs are defined as "anodes", and those where reduction takes place are "cathodes". An electrical potential exists between the anode and cathode areas. The electrons produced in Eq.(3) flow through the metal to the cathode areas to take part in the reaction of Eq.(4). Hydrogen ions in the vicinity of the anode areas are not needed there, and under the influence of potential difference they flow to the cathode to sustain the reduction reaction.

The faster the solid is converted to iron ions (i.e. the greater the corrosion), the larger is the current flowing in the "cell".

Many such cells occur on a corroding metal surface. Anode and cathode sites can switch roles so that uniform corrosion can take place. The two reactions of Eq.(3) and Eq.(4) must occur at the same rate to conserve the electrical neutrality of the metal. If either reaction stops then the other must similarly stop.

Other metals or alloys and corrodants (etchants) combinations do not differ greatly from the above. In all cases of electrochemical corrosion, the anodic reaction consists of oxidation of the solid metal to its ions in solution:

$$M \longrightarrow M^{+n} + ne$$

When an alloy corrodes, several anodic reactions may take place simultaneously. For example the anodic reactions of an aluminium-copper alloy might be:

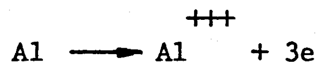

$$Al \longrightarrow Al^{+++} + 3e$$

$$Cu \longrightarrow Cu^{++} + 2e$$

Therefore, the possible anodic reactions in a system are relatively easy to predict. With cathodic reactions, there are more possibilities. Various types of reactions can occur such as:

i. Hydrogen evolution in acid solution.

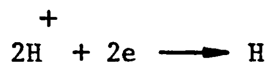

$$2H^{+} + 2e \longrightarrow H_2$$

ii. Oxygen reduction in acid solution

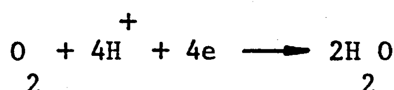

$$O_2 + 4H^{+} + 4e \longrightarrow 2H_2O$$

iii. Oxygen reduction in neutral or alkaline solutions.

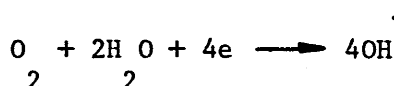

$$O_2 + 2H_2O + 4e \longrightarrow 4OH^{-}$$

iv. Metal ion reduction.

$$M^{+++} + e \longrightarrow M^{++}$$

v. Metal plating.

$$M^{+} + e \longrightarrow M$$

Hydrogen evolution and oxygen reduction are the most common cathodic reactions. Different cathodic reactions can occur simultaneously.

1.4.2 Cell thermodynamics

The driving force that causes the current to flow through the solution is the electrical-potential difference. Some metals corrode in certain environments while others do not. The laws of thermodynamics state that for a reaction to proceed, it must have a negative free-energy change (ΔG). For electrochemical reactions:

$$\Delta G = - n.F.E. \qquad ...(5)$$

where n is the number of electrons involved in the reaction, F is Faraday's constant,and E is the cell potential. For the reaction to be feasible(G is negative), the cell potential E must be positive.

To understand the cell potential, first we must consider the separate anode and cathode reactions. If a solid piece of iron is placed in a solution containing iron ions, a potential difference, $E[Fe/Fe^{++}]$, exists beween the iron atoms in the solid and the iron ions in the solution. This potential can be measured by connecting a voltmeter to an inert reference electrode placed in the solution. This is just an equilibrium potential that exists between a metal and its ions in solution. This is called a "half-cell potential" because it is for an electrode that can form half of a corrosion cell (i.e. the anode). Similarly, a half-cell potential exists for the cathode reaction. A measured half cell potential depends on the concentration of ions in solution. If metal ions are present in the amount of 1 gram-atom/l. (i.e. unit activity), the half-cell potential is called a "Standard Half-Cell Potential", and if this is known, then the half-cell potential at any concentration can be calculated.

By convention, the hydrogen reaction:

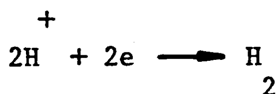

$$2H^{+} + 2e \longrightarrow H_2$$

is assigned a standard half-cell potential of zero volts. All other half-cell potentials are measured relative to that of hydrogen. A list of such potentials is in figure 1.9. These are also oxidation-reduction potentials (redox potentials) because they represent oxidation or reduction depending upon the direction.

The cell potential E used in the free-energy change equation, Eq.(5), is defined as the potential difference between the cathode and the anode half-cells. For the example of iron in acid solutions:

$$E = E[H^{+}/H_{2}] - E[Fe/Fe^{++}]$$

$$E = 0 - (-0.440) = + 0.440\ V$$

Since E is positive, ΔG in Eq.(5) is negative, hence the reaction is feasible.

1.5 THE CONVENTIONAL METAL REMOVAL PROCESS IN P.C.M.

Substrate materials are conventionally etched by spraying chemical etchants through the resist stencil (Fig. 1.10).

The etching of metals or alloys such as copper, steels including stainless steel is successfully carried out in industry. Etchants such as aqueous ferric chloride ($FeCl_3$) are commonly used in p.c.m. and spraying is the preferred method of application. Specially constructed machinery, with etchant temperature control are used for this process. The advantages of spray etching over other methods such as dipping the material into the etchant, are the relatively greater metal removal in the direction of the spray and the rapid dispersal of the exhausted etchant from the metal surface. This yields a rapid,uniform metal removal and minimises sidewards etching [6].

When the movement of a corrodant over the metal surface increases the rate of attack, this may in general be classified as an erosion corrosion. This type of corrosion thrives on high velocity conditions, turbulance and impingement. The role of the erosion may be attributed to the removal of protective surface films such as previously formed oxide films or adherent process by-products. The attack exhibits a directional pattern related to the path taken by the corrodant as it impinges the metal surface.

The main reactions that take place when ferric chloride is in contact with stainless steel are:

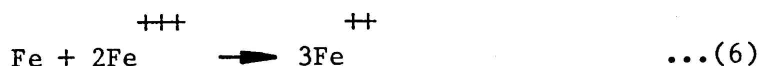

$$Fe + 2Fe^{+++} \rightarrow 3Fe^{++} \quad ...(6)$$

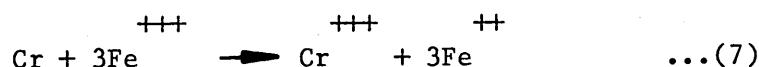

$$Cr + 3Fe^{+++} \rightarrow Cr^{+++} + 3Fe^{++} \quad ...(7)$$

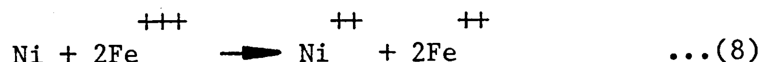

$$Ni + 2Fe^{+++} \rightarrow Ni^{++} + 2Fe^{++} \quad ...(8)$$

The cell potential 'E' for the above reactions Eqs. (6), (7) and (8) are +1.21V, +1.51V and +1.02 respectively at temperature of 25° C [7].

Although ferric chloride is not as toxic, hazardous and expensive as other possible etchants, disposal of exhausted solutions is a problem. Some of the larger p.c.m. manufacturers are now using recycling plant [8].

1.6 ELECTROLYTIC DISSOLUTION IN P.C.M.

Electrochemical corrosion takes place during chemical spray etching, where anodic and cathodic reactions occur on the metal surface being worked. This process may be accelerated by introducing an external potential between the cathode and anode. Although this is not practical or possible to implement on a metal surface, the work piece is made the anode, and an external cathode is introduced in the cell. A potential is applied between the two electrodes, and in general if the cell is assumed to be purely resistive the current flowing through the cell is proportional to the applied potential (Ohm's law). The metal rate dissolution is proportional to the charge (I.t), this is based on Faraday's first law.

Therefore, it is suggested that an electrochemical cell similar to the above be utilised in the metal removal in p.c.m. The mechanism of metal removal under such conditions and the resultant surface textures and process features had not been fully investigated.

The surface textures produced by electrolytic etching were not predicted to be similar to those produced by their counterpart conventional spray etching as the type of metal dissolution is a function of imposed electrolytic parameters.

Under certain conditions high degrees of anodic surface polish may be achieved, this is a particular case of anodic dissolution. Hence the electrolytic metal removal as applied to p.c.m. shall be classified into two fields as follows:

1- Electrolytic photoetching (e.p.e.).

2- Electrolytic photopolishing (e.p.p.).

1.6.1 Electrolytic photoetching (e.p.e.).

The electrolytic metal removal system has been discussed previously, and has been researched extensively by many workers. Nevertheless, the application of the process to p.c.m. has not been covered satisfactorily.

The pre-etching preparation stages of the work piece is identical to that of conventional p.c.m., the exception being the 'masking off' of the exposed anode areas not to be etched. This is important as areas unaccounted for when calculating the current density 'J' will reduce the metal removal rate and possibly change the metal removal characteristics.

$$J = I/A$$

Where, 'I' is the current and 'A' is the anode area.

A constant current etching mode is preferred where possible. This is due to the metal removal rate being proportional to the current and hence the depth of etch would theoretically be predictable by measuring the duration of etch. Galvanostatic (constant current) etching under certain circumstances was not possible, this is mainly due to substrate passivation, as unpredictable etching may occur under such conditions. Potentiostatic etching may overcome this by maintaining the anode potential at a fixed value and hence controlling the dissolution characteristics.

The use of two cathodes on either side of the substrate provided means for double-sided etching. This may be achieved by using two cathodes and where a centrally mounted anode is etched on both sides simultaneously. By ensuring that the anode/cathodes separations are equal on both sides, then the metal removal rate should also be equal.

Controlling the electrolyte temperature is essential, and electrolyte agitation under certain conditions should be limited, in particular when electro-polishing.

1.6.2 Electrolytic photopolishing (e.p.p.).

Anodic dissolution may increase or decrease the macro and/or micro-surface roughness of a metal surface. Furthermore a decrease in either or both surface roughness does not necessarily accompany a polishing effect.

On a microscopic scale a metal surface is complex where small irregularities are superimposed on the larger macroscopic contours and in order to produce a flat surface both these irregularities must be removed [9]. Therefore the function of the polishing process must be:

i. "Smoothing" by elimination of large-scale irregularities (greater than 25 µm).
ii. "Brightening" by removing all smaller irregularities (typically 0.25 µm).

Etching may cause smoothing but the surface retains a dull matt finish. Electropolishing differs as it combines both of the above capabilities. Brightening is difficult to determine quantitatively. The apparent brightness of a surface depends on the ratio of specular to diffused reflection.

The formation of a relatively thick viscous layer of reaction products around the anode surface is believed [10] to control the smoothing action, and similarly the formation of a thin film on the surface of the anode controls the brightening action.

Polishing is a particular case of anodic dissolution, the mechanism of which has not been investigated in sufficient detail. Therefore empirical methods of investigation are used to achieve optimum working conditions as predicting these conditions may be difficult.

Electrolytic polishing is not a new industrial process it has been used extensively since the early parts of this century [11]. Further applications have been in the field of metallurgy, where it is used in the preparation of samples for examination. Therefore extensive practical details are available on electrolyte formulations and methodology for a wide range of metals and alloys.

It has been suggested that for certain applications, selectively polishing areas of the surface of a metallic substrate through the precision of a photographically produced stencil may have some applications. This process will be referred to as electrolytic photopolishing (e.p.p.). At the beginning of this investigation no information on the application of electro-polishing to photographically produced adherent resist stencils was found and hence was also selected for investigation.

1.7 LITERATURE SEARCH

The subjects of p.c.m. and electrolytic or electrochemical metal removal individually have been researched extensively, especially in the case of the latter. The application of an electrolytic metal removal process to p.c.m. was used by a United Kingdom company [12], it is believed that it has since ceased trading. Hence no detailed information was available on their application of the process. It is also believed [13] that other commercial concerns are involved in researching the field, but when asked for details of their process and applications they declined any information. This was typical, as traditionally this industry tends to guard its methods jealously and hence the limited availability of quantitative data on the process.

A search was carried out for general information relating to the subjects above and in particular the combination of the two fields of p.c.m. and electrolytic metal dissolution. This search was carried out by the following methods:

A) Computer
B) Manual
C) Industrial

1.7.2 The computer search

Computer searches were carried out using the 'on-line Lockheed dialogue system' which is a retrieval service available at the library of C.I.T. The information was retrieved by feeding in key words which are relevant to the subject in question. The computer search can be divided chronologically into three parts, and is described in Appendix A.

1.7.3 The manual search

An extensive manual search for published work and subject related literature was carried out. This covered the subjects of p.c.m. in general, electrolytic etching and electrolytic polishing of steels. It also included the application of the latter two to the former. Other fields were also searched including the preparation and corrosion behaviour of amorphous materials. The sources for the search are also listed in Appendix A.

The London patent office was visited where an extensive search was carried out for applications for electrolytic metal removal systems in p.c.m.

1.7.4 The industrial search

There are a number of UK companies using p.c.m. as a manufacturing process. Some of those companies (App. A) were contacted and inquiries were made about the application of electrolytic metal removal systems if those were utilised in their manufacturing or research work. The results in general were negative, although there were indications that some of those companies were working in this area.

1.8 LITERATURE REVIEW

1.8.1 The photochemical machining

A series of five papers by Allen et al titled "Quantitative examination of photofabricated profiles" [2,6,14,15,16] were the guidelines for the experimental methodology of this work. These were as follows:

Part 1: Design of experiment [2]:

In this paper the origins of the process were explained as a brief historical review of the process. The sequential steps of the p.c.m. process were described in detail and methods for quantifying the process capability were presented, an example was the etch factor, this was defined as

$$e.f. = D / 0.5(B - A)$$

where, (U) = 0.5(B - A)
= The resist undercut
and D = The depth of etch

Metal surface impingement by the sprayed etchant was described explaining the effects of turbulent flow on the lifting of the resist layer. Further it illustrated the 'U' shaped sectional profile as it develops with depth of etch.

Part 2: Photoetched profiles in stainless steels [14]:

Hard rolled AISI 302 stainless steel was photoetched utilising two etchants both being aqueous ferric chloride:

A: 40.3 Be' strength (s.g. 1.385) with $< 0.3\%$ w/w free HCl.
B: Same as 'A' but with 0.4% w/w free HCl.

and two different photoresists. The resist stencil was produced utilising a 'Sayce' resolution chart in a modified form [17]. The relationship between the depth of etch and etch duration was not linear and the rate of etching decreased with time and depth. Depth of etch on the other hand increased with etched line width for lines between 0.073 and 0.88mm. A linear relation was recorded for the growth in line width versus etch duration. Etch factors of the order of 2:1 were recorded for the wider lines (0.47 & 0.88mm) and remained constant for up to 80% of the metal thickness (0.25mm). A reduction of etch factors was recorded with smaller line widths. With etchant 'B' reduced etch factors were recorded throughout. Etching was at 52 C, and the etchant was sprayed on. Metal removal rates in the order of 20μm/minute were reported.

Part 3: Measurement of etch factor [15]:
This paper deals with the methods of measuring the etched slot width and the depth of etch. The calibration and use of a microscope graticule is described and a 'direct measurement' of the the resist undercut is also described. The mean etch factor is obtained using the average undercut and depth of etch. The depth of etch may be established by one of three methods, the first being the use of differential focusing with microscope, the second is the measurement of the cross section of the etched line and the third is the depth measurement with the aid of a surface texture measuring instrument (Talysurf 4).

Part 4: Photoetched profiles in mild steel [16]:

The results presented in this paper are qualitatively similar to those for stainless steel, it was concluded that the etch factor is not a unique number dependent only on the metal and etching system. It was a function of original line width and depth of etch.

The experimental results illustrated that for original line widths of >0.2mm, the mean maximum depth of etch was constant for etch durations up to 3 minutes. For an etch duration of 4 minutes the

above was valid for line widths >0.3mm. In general the rate of etching decreased markedly as for stainless steel at line width <0.2mm.

In general good etch factors are explained in terms of preferential attack of the metal surface at the points of impact of the etchant spray particles. It is said that the energy dissipation from the vertical impact of the particles is able to penetrate the chemical agent at the bottom of the etched slot, whereas tangential impact is insufficient to produce etching on the side-walls. Further particles may likewise purge the boundary layer at the bottom of the slot relatively more effectively.

Part 5: Effect of stencil integrity on etch factors [6]:

This work was related to the adherence and mechanical strength of the resist stencil and its relation to the resultant quality of etching. It related the resist properties to the adherence on the substrate surface and the mechanical properties and the resistance to the impingement by the spray etching action to the physical dimensions of the resist layer. Conversion coatings "passivation" were discussed and the role of nitric acid in this passivation process. Here it was reported to increase the thickness of a hydrated amorphous oxide layer already present at the surface. Further it is suggested that conversion coatings reduce the lateral etching of the side-walls (undercut) both by improving the stencil adhesion and, due to the existence of a surface layer, the material etched more slowly than the bulk metal.

The properties of two liquid photoresists used in photoetching of stainless steels were investigated by Allen et al [18]. Two methods for measurement of the photoresist coating thickness were reported, both were by water displacement resulting in specific gravity values of 1.36 and 1.11 for resists 'A' and 'B' respectively. The weight of resist per unit area and coating thickness were plotted versus the viscosity of the resists measured in zahn.seconds. The resolution expected from a photoresist layer is related to its thickness and the minimum line width should be at least 3 to 5 times that value.

The effects and benefits of a pre-bake stage were also discussed for resist 'B', and also its unsuitability for resist 'A' where "heat fogging" was reported. Resist 'A' was found to be stiff and hard whereas 'B' was relatively elastic and rubbery and hence can withstand the applied forces during spray etching better than the former.

Resist 'B' is believed to be similar to the liquid negative resist used for this work.

The preparation of p.c.m. specimens for microscopic examination was described by Allen et al [19]. Recommendations are made for specimen cleaning, potting and sectioning for microscopic examination. Useful practical details were for all preparatory

stages. Further recommendations were made on the abrasion and polishing for the specimen edge retention.

1.8.2 The etching system

i. Chemical etching

The conventional etching mechanism was investigated in detail by Allen et al [20], it has been shown that when spray etching AISI 304 stainless steel, surface texture values (Ra) varying between 9 and 0.35μm are obtained for changes in the etching temperatures ,{$FeCl_3$} and {HCl} when spray etching with an aqueous ferric chloride-hydrochloric acid system. Ra values in the order of 0.35μm may be achieved at an etching temperature of 50°C with a solution of 41.8 to 44.3 Baume′ strength and containing 0.27-0.43% w/w free HCl.

ii. Electrolytic etching

Relatively few suitable etching electrolytes were found, some of these were mainly intended for application in electrochemical machining (ECM). These included solutions of sodium chloride and sodium nitrate [21,22,23,24]. The current densities used for metal removal in ECM are typically two orders of magnitude greater than what was considered suitable for electrolytic photoetching. ECM exhibits a rapid and extremely vigorous anodic reaction and considered not suitable for applications in conjunction with resist stencils.

The Kodak application data P-91 [25] described an electrolyte and recommended it for the etching of stainless steels in general. This was a 10% w/w hydrochloric acid solution. Information on optimum anodic potentials, current densities and operating temperatures were not published and no further references were disclosed. The company was contacted for further details but none were recieved.

Pospelov et al [26], described the fabrication of perforated metallic light attenuators by foil etching through a resist. Chemical or electrochemical dissolution was suggested, and steels were etched using the latter. No comparisons between the two methods were presented.

iii. Electrolytic polishing

An analysis of the current density/voltage relationship provides a basis for understanding the anodic processes accompanying the electrolytic polishing of metals. For most electropolishing processes, the ′V(cell) versus J′ curves have similar shapes. The data presented by Jacquet [27] contains a typical electropolishing curve, for the case of copper immersed in orthophosphoric acid solutions (600 g./l). Based on these experiments, Jacquet assumed that a certain relationship exists between the formation of a coloured layer, as produced by the anodic dissolution by-products in the electrolyte, and the polishing effect. He further suggested

that the process should be maintained at constant voltage between 1.6 & 1.8V rather than a constant current density, as it is not necessary to calculate the total surface area of the sample to be polished with this mode.

Batashev [28] suggested that it is not possible to control the electropolishing process solely on the basis of voltage or current density measurements, because of the effect of distance between the anode and cathode, the electrolyte concentration, the temperature and rate of agitation, and the size and shape of the polishing bath.

The applied cell voltage V is a function of the anode, cathode potentials, voltage drop in the electrolyte (IR1) and the voltage drops in the conductors and contacts (IR2). Therefore:

$$V = [\ E(anode) - E\ (cathode)\ ] + IR1 + IR2\ .$$

Where, f(V) may be expressed in terms of ΔE, R1 and R2. Similarly, f(R1) is expressed in terms of on the electrolyte concentration, anode and cathode surfaces, arrangement of electrodes in the cell, and the shape and size of the cell. Therefore, control by the applied cell voltage as used by Jacquet might not always correspond to the optimum polishing conditions. According to Batashev, the electropolishing process could be controlled by quantifying the anode potential versus a high-quality result. This could be achieved through the use of a special non-polarizing reference electrode. The use of such an electrode does not require a measurement of the surface area of samples to be polished.

According to Shchigolev [10], and on other works [29,30,31] the evolution of oxygen does not take place on a clean metal surface but on oxide regions with special electrical characteristics. Further the electrochemical oxidation of the metal may take place at anode potentials below the oxygen-evolution potential. The formation of adsorbed oxygen films is thermodynamically favoured over the formation of separate-phase oxide layers.

Works by Jacquet [27,32,33], on the electropolishing of copper in phosphoric acid solutions, proposed a simple mechanism for the electrolytic polishing process. He suggested that when a current passes through the cell, a liquid layer of anodic dissolution by-products is formed on the surface of the anode. Where this layer has relatively higher viscosity and a greater electrical resistivity. The thickness of this layer on a rough surface differs from site to site, in crevices the thickness is greater than on projections. Therefore, due to the non-uniform "insulation" of the anode, the current density is also non-uniform. Hence on projections the current density is higher than in crevices and therefore dissolve more rapidly resulting in surface-smoothing.

Elmore [34] suggested that the main factor affecting the electropolishing performance is related to the diffusion of anodic dissolution by-products from the anode surface to the bulk of the

electrolyte. Since the concentration gradient of the dissolution by-products on projections of the surface texture is greater than in crevices, the dissolution rate of projections is also greater.

Jacquet attributes the smoothing of rough surfaces to differences in the degree of "insulation" of peaks and crevices. While Elmore believes that the effect is associated with differences in the concentration gradients of metal ions.

According to Baumann and Ginsberg [34] and for purely geometrical considerations, surface smoothing should occur as a result of preferential dissolution of peaks. When there is no surface film a non-uniform current distribution is observed. The electric field in an electrolyte has a higher intensity at corners, edges and peaks on the electrode. A thermodynamic analysis would also indicate a greater probability of dissolution at peaks, since at such sites the work required for transfer from the solid to an ionized state is smaller.

Edwards [36] was critical of the diffusion theory of Elmore. Where in addition he assumed that the electropolishing processes are controlled by the diffusion of "acceptors" to the anode surface. It is suggested that in the electropolishing of copper in phosphoric acid solutions, the PO_4^{3-} ions serve as the "acceptor" and bind the dissolved copper. Electropolishing begins with the establishment of a critical "acceptor" concentration on the anode surface, and its rate is determined by the rate of diffusion of the "acceptor" to the anode. Edwards assumes differences between the acceptor-concentration gradients on peaks and those in crevices. Whereas, Elmore assumes a difference in the ionic concentrations between those sites.

Wagner [37], carried out a mathematical analysis of smoothing that occurs during electropolishing. The theory assumes that the diffusion of one reactant , called the "acceptor", is the controlling factor in electropolishing. The current density plateau associated with polishing [32,33] is explained that the "limiting current density corresponds to a maximum concentration gradient when practically all the acceptor approaching the anode readily reacts with the metal ions, and thus the acceptor concentration at the anode is much lower than the bulk concentration". Wagner modelled the surface texture as sine wave profile. The validity of Wagners' theory was investigated by Hojka et al [38] when electropolishing tantalum and the results reported were consistent with the analysis.

Similar to Baumann et al [34], Levin [39] believes that surface smoothing during electropolishing may be attributed to the concentration of electric field lines on peaks in a rough surface. This then leads to a change in the surface tension of films at the peaks resulting in the film break-down and the dissolution of those peaks. Similar work was carried out by Edwards [40], where he investigated the the electropolishing of copper in phosphoric acid. He also treated the smoothing action of the process in terms of

current density distribution using graphical methods for determining the potential field in the electrolyte.

Shchigolev [10], when discussing the work by Popilov et al [41], suggested that electropolishing produces the best results with deep drawn or stamped articles. The poorest results with cast articles. Better electropolish results are obtained with metal or alloy surfaces that are homogeneous physically. The duration of electropolishing depends on a number of factors, including the initial surface state of the articles to be polished, the nature of the metal and electrolyte and the operating conditions. Electropolishing times in excess of the optimum may markedly impair the surface quality. As a rule, the electropolishing time should decrease with increasing current density or with decreasing initial roughness of the surface. The effectiveness of the electropolishing process depends on the initial roughness of the surface to be polished.

Further, Shchigolev recommends that before electropolishing, the surfaces must be degreased and cleaned with organic solvents (benzene, dichloroethane, etc.) or by chemical or electrolytic etching in suitable solutions. Further, during electropolishing under steady-state conditions, the anodic reaction products accumulate on the surface of the polished metal. In many cases, natural diffusion and convection processes cannot remove these products from the anode surface into the bulk of the electrolyte, and this may interfere with the electropolishing process. In such cases the electrolyte must be stirred. Shchigolev also suggested that stirring prevents local heating of the surface and assists in maintaining a uniform temperature within the electrolyte. Stirring is used in cases in which the anode is coated with sparingly soluble films, or when it is necessary to remove bubbles adhering to the surface. In the case of the former the agitation increases the rate of dissolution of the anodic film while in the case of the latter, forced circulation removes gas bubbles from the electrode surface and thus prevents pitting or formation of band patterns.

Alkire et al. [42] using the relatively recently developed finite element method, predicted the electrode shape change of a flat cathode embedded in one wall of a rectangular cell. They computed profiles over a range of cell dimensions and polarization parameters.

Alkire and Mirarefi [43] solved the tertiary current distribution in a tubular reactor with the aid of Green's functions, which they derived in terms of an infinite series involving Bessel functions.

In dealing with moving boundary problem Fitz-Gerald and McGeough [44] first applied a linear perturbation to calculate a reduction in small-scale roughness when calculating the effect of increasing the overpotential on machining times, depth and smoothing. Using a similar approach in a following publication [45] they investigated cathode design in ECM to produce specific irregularities upon the

anode.

Trofimov and Ivanov [46] calculated the primary current distribution on a plane electrode partially covering one wall of a rectangular cell using the straightlines method devised by Soviet mathematicians.

Baraboshkin et al. [47] computed the current distribution on a linearly polarized sinusoidal electrode using the above method. They pointed out the limitations of the method when curved boundaries are encountered.

Nilson and Tsuei [48] used the inverse Cauchy method to determine steady-state workpiece geometries in an electrochemical machining process. By treating the spatial coordinates as the dependent variables, they transformed the problem into a rectangular domain where a solution by the finite-difference method was achieved.

Caban and Chapman [49] applied orthogonal collocation to the current distribution on a disk below the limiting current. They showed how rapid simulation of the experimental system could be used to facilitate analysis of kinetic data.

Glarum [50] applied the variational approach to the disk electrode problem. As an illustration of the method, he derived a simple analytical expression when the overpotential is linear. He further [51] calculated the current distribution on a flat strip electrode with linear polarization.

Plane parallel electrodes embedded in insulating walls have been used in mass transport studies and find application in industrial eletrolytic cells. Because of the importance of this system, a great deal of effort has been devoted to describing the current distribution for a large number of variations in geometry and polarization characteristics.

Wagner [52] considered the case of parallel electrodes where the electrode separation was much greater than the electrode width, and the walls perpendicular to the electrodes were far removed. Using conformal mapping, he calculated the primary current distribution and the secondary distribution with a linear polarization approximation.

The effects of the side walls on the primary current distribution were calculated by Hine et al. [53]. They found a more uniform current distribution as the walls were moved closer to the electrodes.

In a series of three papers, Yoshida and Koseki [54] considered unequal electrode lengths as well as interaction with insulating walls perpendicular to the electrodes. By varying the system dimensions and polarization parameters, they determined the combination of parameters that gave the most uniform current distribution. Results of current distribution calculations derived

from potential mapping and copper deposition experiments, which show qualitative agreement with the simulated results, are also presented.

Tafel kinetics was incorporated in the treatment by Gnusin et al. [55]. They used integral methods to derive an expression for the current distribution when the counterelectrode and perpendicular insulating walls were far removed.

Tobias and Wijsman [56] studied the effect of electrode resistance in a rectangular cell. They determined the current distribution for a wide range of linear polarization parameters.

Parrish and Newman [57] calculated the tertiary current distribution for planar electrodes in a channel with laminar flow. The current and concentration distributions as a function of the polarization parameters were presented.
In a subsequent article Parrish and Newman [58] extended their methods to examine the effects of electrode width-to-separation ratios.

Viswanathan and Chin [59] studied the current distribution on a continuous, moving sheet electrode in a rectangular cell. The primary and secondary current distributions are uniform in this system, and they determined that operation below 78% of the limiting current also yields a uniform distribution.

Sides and Tobias [60] used tangent sphere coordinates to derive an expression for the primary current distribution around a nonconducting sphere on a plane electrode. From their analysis they predicted the resistance due to a sparse collection of bubbles on an electrode and calculated the minimum resistance caused by a denser collection of bubbles.

Alkire and Lu investigated the effect of gas evolution on the current distribution in a vertical cell. They empirically ascertained the current distribution by depositing copper while evolving hydrogen and compared these results with their model[61]. They used the finite element method to predict the shape change of an initially flat polarized cathode in a rectangular cell. Some gain in computational efficiency and the ability to follow an irregular geometry appear to be the main advantages of this method.

Sunu and Burrows [62] recently modeled the current and potential distribution by the finite-difference method with aim of optemising grid design in lead acid batteries.

Dean and Brown [63] Investigated the terriary current distribution of electro deposition through polymeric masks.

Allen and Gillbanks [64] reported a method of producing specimen holders used in secondary ion mass spectrometry from tantalum by electrolytic photoetching.

Klokov et al [65] recently produced an expression for metal dissolution in conjuction with surface dielectric masks using conformal mapping; limiting current density was assumed over the entire surface.

1.9 PREVIOUS REVIEWS

General surveys covering different aspects of the current distribution problem have been published and a selection is summarized as follows:

1. Kronsbein [66] presented a historical review of current distribution problems which were traced back to the early 19th century, with emphasis on metal distributions in plating processes.

2. Shchigolev [10] carried out an extensive review of literature related to both theoretical and practical aspects of electropolishing.

3. Kardos [67] reviewed the literature on micro-profile current distribution where practical aspects of plating were discussed.

4. Fleck et al. [68] summarized the analytical techniques that had been applied to current distribution problems, presented a range of cell geometries that previously had been solved analytically.

5. Russelot [69] presented a summary of the principles governing current distribution and included analog methods used in obtaining potential maps.

6.Newman [70,71,72] in a series of publications described fundamental principles governing mass transport and current distribution in an electrolytic cell. He reviewed mathematical methods used in solving current distribution problems outlining methods and applicability of the techniques such as perturbation. Further he explained mass transport, fluid flow, and kinetics and their affect on the current distribution.

7. Ibl [73,74] discussed the general characteristics of primary, secondary, and tertiary current distributions. In a later review he expanded in terms of analytical and numerical solutions of current distribution problems.

8. Prentice and Tobias [75] more recently carried out an exhaustive general review of work relating to all facets of this subject, covering analytical and practical aspects of solving current distribution problems.

1.9.1 Relevant Books

Three books on electrochemical machining were found to be of general use in this investigation and are as follows:

1. Electrochemical Machining [21].
2. Principles of Electrochemical Machining [76].
3. Practice and Theory of Electrochemical Machining [77].

1.10 SUMMARY OF MATHEMATICAL METHODS

The primary current distribution problem requires a solution of Laplace's equation for the potential field and current density is proportional to the gradient of the potential at conducting boundaries.

A relatively small part of available field analysis literature is directly relevant to the evaluation of current distribution in electrochemical systems. The number of electrode geometries and cell configurations for which analytical field solutions can be readily obtained are relatively small. This is due to complex geometries and nonlinear boundary conditions associated with electrochemical systems.

Primary and secondary current distribution problems have been solved by analytical techniques such as:

1. Superposition.
2. Method of images.
3. Series solutions.
4. Integral equations.
5. Conformal mapping.

Other methods also used in developing expression for electrochemical systems in general are:

1. Green's functions
2. Perturbation
3. Straightlines
4. Coordinate inversion
8. Orthogonal collocation
6. Variational methods
7. Finite elements
8. Finite-difference.

The latter two methods have become more popular recently.

1.10.1 Choice Of Method

The availability of high speed digital computers facilitates economic numerical solutions of current distribution problems without the need to simplify geometries and boundary conditions to such an extent where there is little resemblence between the mathematical simulation and electrolytic systems.

Few direct comparisons between the finite element and finite difference methods have been performed. Hohl and Hamilton [78]

used both of those methods to calculate one-dimensional, transient, diffusion profiles for which analytical solutions are available. They showed that the average error was least for the finite-difference method coupled with relatively better computational efficiency.

Gresho et al. [79] used the finite element method and showed that it was less sensitivite to successive grid refinement. They solved one-dimensional and a two-dimensional advection-diffusion equation. For both cases they found that the linear finite element method gave more accurate results than those of higher order finite-difference methods.

The advantages of using one method over another are not easily defined. The choice of method is largely depend on factors such as:

1. Accuracy
2. Ease of programming
3. Computer storage
4. Simulation cost

In general the square elements in the finite-difference method offer ease of manipulation and computation for the user, whereas the triangular elements of the finite element method offer the advantage of following an irregular boundary more accurately which may be an advantage under certain circumstances.

1.11 FINITE-DIFFERENCE METHOD

In the finite-difference method the differential equations are approximated by their difference formulations. The domain is generally divided into rectilinear elements. Approximation of the field variable must then be made at a curved boundary. While a large number of iterations may be required to solve a current distribution problem, the computer time per iteration is generally small. The finite-difference method is easy to implement, and square elements, which are frequently employed, are ideally suited for computer manipulation.

Klingert et al. [80] outlined a procedure for calculating the primary and secondary current distributions by the finite-difference method.

Fleck et al. [68] presented a general computer program for solving current distribution problems by the finite-difference method. They incorporated an arbitrary polarization expression in their model. They simplified the simulation by approximating the normal current density as the projection of the current density vector onto one of the axes of the coordinate system. They studied the computational parameters and considered features such as increasing the size of the computational molecule, changing the order of computation, and varying the overrelaxation parameter 'w'.

Prentice [81] used finite-difference techniques to simulate plating for several cell geometries. The dissolution of high amplitude-to-wavelength profiles was simulated, and the results were used to show the range of validity for Wagner's approximate solution. He developed an algorithm to overcome the instabilities associated with the nonlinear boundary conditions of the secondary and tertiary current distributions. By weighting the surface potential at each iteration as a function of the average change in current density, the Wagner number, and several other variables, converged solutions were obtained for all reasonable values of the physical and polarization parameters. A general computer program was presented for the calculation of the primary and secondary current distribution simulations in two-dimensional systems. For certain types of geometries, mass transport effects can also be simulated.

1.12 THE OBJECTIVES OF THE INVESTIGATION

When the application of electrolytic metal removal systems to p.c.m. was selected for investigation, no specific industrial requirement was known. Initially it was believed that this process might yield improved etch factors and greater depths of etch than those of its counterpart (conventional spray eching). A limited analytical investigation aimed at determining the current density was carried out, resulting in a normalised primary current density over electro etched features.

The primary objectives of this work were to generate empirical data for e.p.e. and e.p.p. to facilitate so that comparisons with conventional p.c.m. and whereby such practical results would be useful to the industry as very little information exists on the subject. Although later in the work it was believed neccessary to investigate the process further by analytical and computational methods. The latter is thought to be the most comprehensive and practical when simulating e.p.e. and e.p.p. Further, a variant of the model is illustrated to be capable of simulating electro photoforming (e.p.f). this is a process whereby material is electroplated on the substrate with the presence of an adherent stencil.

It has been shown that some information exists on the conventional photoetching of stainless steels, consequently this was the material selected for investigation. The type of stainless steel used was AISI 304 being the same as that used by Allen et al [20]. It became apparent from early stages of the work that this stainless steel exhibited non-uniform etching with the recommended etching electrolyte [25]. This necessitated investigating the corrosion behaviour so that a better understanding was achieved.

Numerical simulation of the transient behaviour of solid electrodes featuring surface dielectric layers undergoing either deposition or dissolution by a quasi steady state model was achieved.

This may account for:

1. Ohmic drop.
2. Charge transfer overpotential.
3. Mass transport limitations.

The finite difference method, coupled with successive overrelaxation (SOR), was used for solving the potential field.

An algorithm previously devised [81] to overcome the computational instabilities associated with the calculations of the secondary and tertiary current distributions was implemented.

Further into the investigation, the feasibility of applying e.p.e. and e.p.p. as a manufacturing process was apparent. A number of opportunities in the form of industrial requirements were presented for investigation. A solution was required to overcome the problems exhibited by two materials with high resistance to etching under normal industrial conditions and with commercially used etchants in p.c.m. [20]. The materials that were presented as being difficult to etch were 'Vitrovac 6025' and 'Recovac' produced by Vacuumschmelze [82].

The work presented here forms a broad investigation into the physical aspects of electrolytic photopolishing and etching. This in preference to a narrow investigation dealing only with a small area of the subject is believed to be of greater contribution at present as the process is still at an infant stage.

Part of this work was published as three independent papers in 'Precision Engineering' [83,84,85].

2.0 FIELD ANALYSIS

2.1 GENERAL

A region is a field if it is concerned with a manifestation of energy. It is a region of space 'empty, or occupied by a solid, liquid, or gaseous medium' in which certain physical states occur.

When the conditions of a field, notably its boundary configurations, make a direct analysis difficult or impossible, a solution in general may be found by graphical or numerical or experimental means.

Etch bands are boundaries of varying widths positioned around components or features to be etched out in p.c.m., e.p.e. and e.p.p. These are as named, areas of substrate material generally surrounding the etched feature. These areas may also be included within the component such as holes or slots and as illustrated in figure 1.4. In conventional (p.c.m.) spray etching, the cross sectional profile of the etched band as defined by the resist stencil is broadly of a 'U' shape [2]. The etch profile in general retains this 'U' section throughout the etching period. This is not the case for e.p.e. or e.p.p., where the profile of the etch is dictated primarily by the current density distribution upon the anode surface.

The primary current density is the case where the surface overpotentials are neglected altogether and the electrolyte in the proximity of the electrode is taken to be of equipotential thus defining the classical problem in mathematical physics. At electrode edges the current density is always infinite or zero with the exception of the case where the electrode is perpendicular to an insulator.

For a flat cathode parallel to a flat substrate with a relatively narrow etch band (anode) as defined by a resist stencil, the current density distribution is determined by the geometry of the cell boundaries. Prior to etching these boundary conditions are geometrically simple, but as etching takes place, the anode profile develops a relatively complex form. Hence the cell boundaries are dynamic and a function of a number of variables.

Complete analytical solutions may, if the system is not geometrically very simple, be difficult or impossible [86]. Due to the predicted non-uniform current distribution on the anode surface, the boundary condition will change from a relatively simple flat anode to a resultant function of the initial current distribution.

Therefore a simplified analytical solution is obtained to satisfy the initial conditions, this is then followed by a graphical method to illustrate the resultant changes in boundary conditions.

to illustrate the resultant changes in boundary conditions.

2.2 A two dimension analytical solution for the electrolytic etching of a thin line through an adherent stencil.

CASE 1:-
The figure below represents a narrow slot generated by a photoresist stencil when etching a line. The dimension (-L to +L) is that of the line width. The resist layer is assumed to be very thin and hence presented level with the anode surface.

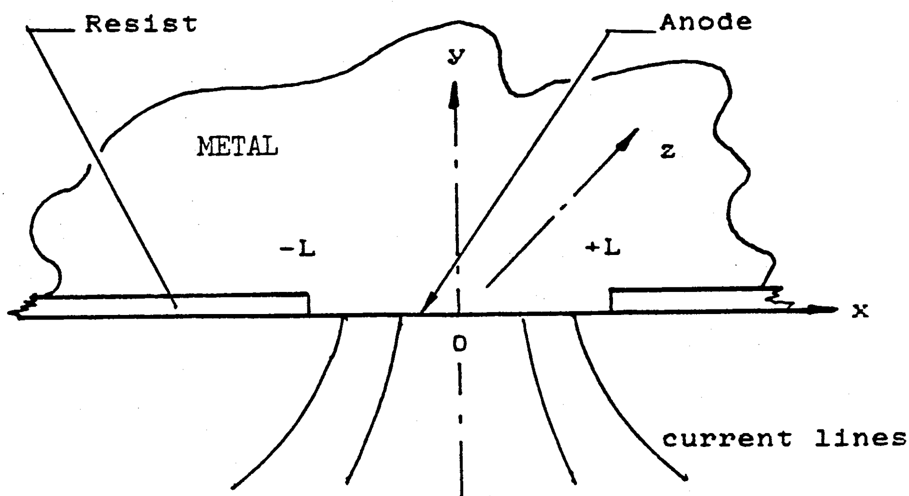

assumptions:

i. A constant potential between the anode and cathode.

ii. The anode/cathode are parallel and symmetrical about the centre.

iii. The resist thickness is assumed to be infinitely small (typically < 1/1000 of the anode/cathode gap).

iv. The total width of the anode and cathode substrates is >> than the line width.

v. No metal removal has taken place and the anode is flat (i.e. t = 0).

If,

$$\frac{d^2\phi}{dx^2} + \frac{d^2\phi}{dy^2} = 0 \quad \text{at} \quad y < 0$$

and,

$$\phi = \text{const.} \quad \text{on} \quad y = 0, \quad -L < x < +L$$

$$\frac{d\,\phi}{d\,y} = 0 \quad \text{on} \quad y = 0, \quad x > L$$

From Morse & Feshbach [87] and Lamb [88], for fluid flow through a slit, the expression is modified such:

$$E_y = -\left[\frac{d\,\phi}{d\,y}\right]_{y=0} = B\,(L^2 - x^2)^{-0.5}$$

The constant 'B' can be related to the total current passing per unit length in the 'z' direction. Let this be 'I', then on $y = 0$, $x < L$.

The current density,

$$J_y = -\left[\sigma . E_y\right]_{y=0} = \sigma . B\,(L^2 - x^2)^{-0.5} \qquad .....(9)$$

where,

E_y = Electric field (E = -grad V).

and,

σ = Conductivity of the medium.

as,

$$\int J_y\, dx = I$$

Therefore 'B' is calculated (App.B) in terms of 'I':

$$B = I.\,(\sigma . \pi)^{-1}$$

CASE 2:-
The result in case 1 only indicates that potentialy greater etching will take place close to the edges. It does not include what might occur under the resist stencil close to the resist edge (x=L).

Consider what occurs after initial etching has taken place, at the edges close to the resist. This problem is simplified in the figure below. When etching takes place due to the conditions of case 1, the anode surface recedes to a lower level. Hence an angle is generated and the undercut of the resist layer may be attributed to the following:

RESIST
METAL BULK
y
r
θ
α
x
$\frac{\partial \phi}{\partial \theta} = 0$
$\phi = C$
ANODE

If

$\nabla^2 \phi = 0$ for $-\alpha < \theta < 0$

$\phi = C$ on $\theta = 0$

$\frac{\partial \Phi}{\partial \theta} = 0$ on $\theta = -\alpha$

C = CONSTANT

The mathematical operation given by:

$$\nabla^2 \phi = \frac{\partial^2 \phi}{\partial x^2} + \frac{\partial^2 \phi}{\partial y^2} + \frac{\partial^2 \phi}{\partial z^2}$$

is labelled by the symbol ∇ which is called the Laplace operator. The result of the operation on the function ϕ is called the Laplacian. One immediate consequence of the definition is that the scalar function $\phi(x, y, z)$ can have no maxima or minima in the region where $\nabla^2 \phi = 0$. Further when we have a family of equipotential surfaces then a vector field 'F' can be represented in terms of the scalar field ϕ [87]. Due to axial symmetry, the 'z' component is not used.

Then from Appendix B we have the solution:

$$\phi = C - r^{\frac{\pi}{2\alpha}} \sin(\frac{\pi}{2\alpha}\theta)$$

This represents the potential at the corner between conductor and insulator. The current density on the anode ($\theta = 0$, $0<r<\infty$) is:

$$J_y = \sigma E_y = -\sigma\left[\frac{\partial\phi}{r\partial\theta}\right]_{\theta=0} = \frac{\sigma\pi}{2\alpha} r^{(\frac{\pi}{2\alpha}-1)} \quad \ldots.(10)$$

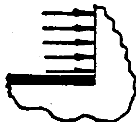

i. If $\alpha = \frac{\pi}{2}$, then $J_y = \frac{\sigma\pi}{2\alpha}$ = constant

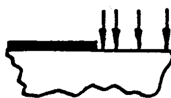

ii. If $\alpha = \pi$, then $J_y = \frac{\sigma\pi}{2\alpha} \cdot \frac{1}{r^{\frac{1}{2}}}$

$J_y \rightarrow \infty$ as, $\frac{1}{r^{\frac{1}{2}}}$

This is as for case 1 near the resist edge.

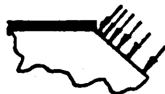

iii. If $\alpha > \pi$, then $J_y = \frac{\sigma\pi}{2\alpha}\left[r^{1-\frac{\pi}{2\alpha}}\right]^{-1}$

$J_y \rightarrow \infty$ as, $\left[r^{1-\frac{\pi}{2\alpha}}\right]^{-1}$

Therefore the current density will tend towards ∞ for (iii) above faster than for (ii). Further, as the angle α increases, the

higher the rate at which $J_y \to \infty$ at the edge. This seems to indicate that high undercutting of the photoresist layer will occur.

The results for both cases one and two are plotted by substituting values for 'X' (1 to 10 units), and the result 'Y' ,representing a current density factor is plotted in figure 2.1. Similarly for case two, four plots were made illustrating the effect in figures 2.2 and 2.3 of changes in the distribution factor due to the angle α.

2.3 GRAPHICAL METHOD.

When a potential exists between two electrodes (cathode/anode) in an electrolytic cell, a potential gradient exists between them. The current is orthogonal to the equipotential lines. The example in the figure below illustrates this.

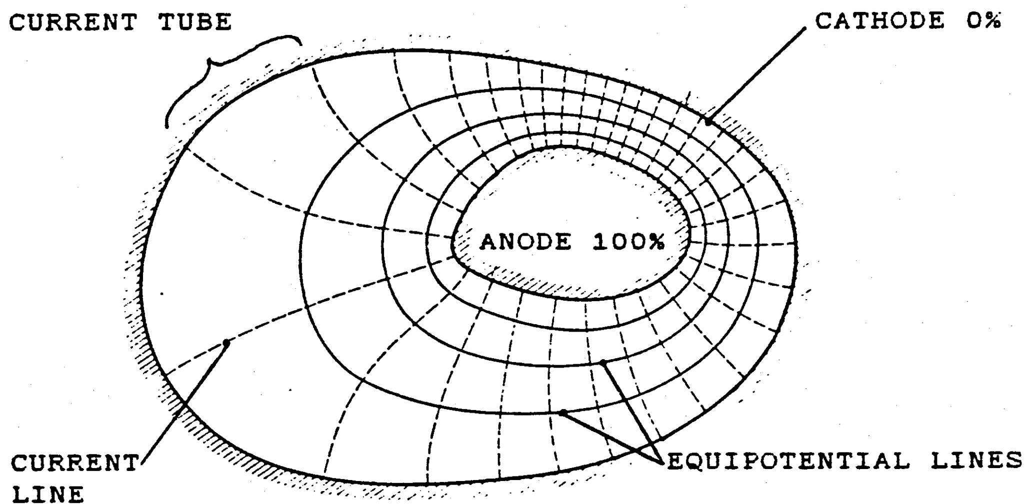

It can be seen that between the anode and cathode boundaries of the plot any intermediate potential may be selected for constructing an equipotential line, and any set of lines normal to the equipotentials will indicate the correct direction of current. When successive equipotential lines are close together the potential gradient is high. The current lines are drawn in such a way that they cross the equipotential lines to give 'squares' of curved sides and these are called curvilinear squares. Hence the concentration of flow lines can be directly related to the current density. The properties of field can be obtained approximately by observing the sizes of the curvilinear squares.

The graphical method is fundamentally a trial-and-error process for drawing traces of current lines and equipotential lines on a representative plane.

It is believed to be an important method for determining a two dimentional steady state field with complex boundaries. The reason being is a solution may be achieved more rapidly than other method in the event that no numerical or analytical model exists. Neverless, it is laborious and certainly if multiple exprimentaion is needed then other methods such numercal should be used.

2.3.1 Principles of graphic plotting.

Although three-dimensional cases with axial symmetry can be tackled, this method is really useful only for fields in two dimensions with a homogeneous media.

The plane marked out in figure 2.4 with a field plot, represents the field structure for the volume made by the depth 'D' between two parallel planes. the equipotential and current lines are drawn such that the mean length 'l' of a current tube between successive equipotential planes and the mean width 'W' between the current planes are related throughout the plot by:

$$l \;/\; W.D \;=\; \text{constant.}$$

As 'D' is constant and the medium is homogeneous, therefore :

$$l \;/\; W \;=\; \text{constant.}$$

Plotting is greatly simplified if 'l' is made to equal 'W' in which all mesh areas between pairs of equipotential and current lines become curvilinear squares. The potential difference across any curvilinear square is the same as that across any other. Hence, the potential gradient and the current density vary inversely to the size of the curvilinear square. The field energy contained in the volume formed by the square and unit depth below it is a constant for all curvilinear squares.

2.4 FIELD PLOTTING.

A series of field plots were carried out utilising the equipment and materials detailed in Appendix C. These plots were carried out on large sheets of conductive carbon sheet and subsequently reduced for presentation.

The anode and cathode are made conductive by applying a silver conductive paint to these areas. A series of electrical connections are made between the positive terminal on the field plotting instrument and the anode (conductive coat). The separation between those connections along the length of the anode were such that at any intermediate point between those connections a potential variation greater than 1/1000 was not allowed. The cathode was similarly connected to the negative terminal of the field plotter.

The field plotter was then switched on and allowed to stabilise for 30 minutes. The field was divided into ten equipotential lines,

this by selecting the required potential as percentage of the total potential between the cathode and anode. This was carried out by adjusting the ten turn vernier control potentiometer on the instrument to the desired potential. The probe was passed from cathode to anode along and in contact with the conductive paper. When a null is detected by the instrument as the potential on the field equals that set, a high voltage is fed back through the probe onto the plot causing a spark to cross the gap between the probe and paper.This suitably marks the plot at the position corresponding to the set potential. The procedure above is repeated at suitable intervals along the plot to facilitate the drawing of the particular potential line. This method is repeated for all required potentials.

2.4.1 Plot one.

This plot is illustrated in figure 2.5, the purpose of which was to establish the initial current density distribution upon the anode surface.

As the potential field is symmetrical about the centre of the anode, it is not necessary to carry out a full plot of the line. This gave greater magnification within the constraints of the available material and practical working conditions.

The dimensions of the plot are given in figure 2.5 and the boundary between the two halves of the cell is achieved by cutting the conductive paper. The method and results for the measurement of the current density distribution from the field plot are presented in figure 2.6. The results are subsequently plotted in figure 2.7.

From this result it can clearly be seen that the current density increases along the anode face as the value of 'x' increases. At the proximity of the resist layer, 'J' tends towards a high value. Further the result from the analytical solution in figure 2.3 are compared with graphical result in figure 2.7 and represented on the same plot (Fig. 2.8). This clearly illustrates good correlation.

2.4.2 Plot two.

This is a potential field and current density distribution plot illustrating
the secondary effect of the initial theoretical metal removal profile. The aim was to illustrate graphically the current density concentration at the proximity of the resist layer previously described in 'case 2'.

The geometric profile of the anode was drawn according to the profile determined by the equation in figure 2.1, the profile was plotted such that at $x = 0$, $J_y = 0$ i.e. at the stage where no etching has taken place at the centre of the etched line (Fig. 2.9).

The theoretical result tends to infinity as the value of 'x' approaches 'L', this is not practical or possible due to either the dimensional limitations of field plotting, or the results of actual etching. It is known that although relatively greater metal removal takes place at the edges of the resist, it is of a finite value. Hence a small angle was introduced replacing the vertical edge generated by the theoretical result, thus limiting the depth of etch to a finite value at the proximity of the resist edge by preventing the value of 'x' reaching that of 'L'.

A qualitative result for the secondary predicted current density distribution is obtained. It can be seen that the highest current density is again at the proximity of the resist edge. The current lines are orthogonal to the anode surface of the anode indicating the direction of metal dissolution. Due to the relatively small rectilinear squares near the resist edge, a high undercut of the resist must be expected. Further in support of the argument in the previous paragraph, it can be seen that the lowest current density value along the anode surface is at the 'V' shaped length. As relatively greater etching takes place close to the resist edges producing a 'W' profile with a peak at the centre and two troughs on either side and due to preferential dissolution taking place at the former as has previously been discussed, hence an equilibrium state will be reached.

Although the equation (10) is a limited solution for predicting the etched profile in terms of current density distribution, it is by no means a general solution. The actual depth of etch taking place at the proximity of the resist would probably be determined or limited by other process factors not accounted for by the equation. These may include the type of metal dissolution taking place, the throwing power of the electrolye, the physical orientation of the anode with respect to the cell and the dynamic composition of the electrolyte whether it is local or general.

2.4.3 Plot three.

When etching parallel lines, the current density distribution upon the individual line and in general for all the anodic areas, is determined by the profile of the potential gradient between the cathode and the anodes. This in turn is a function of the boundary conditions.

The potential field is simulated in a reduced form, and is illustrated in the plot itself (Fig. 2.10). This, a simulation of two parallel lines with width/resist stencil ratios of 3:2:2, corresponding to the following dimensions, and from left to right:

i. The first line, 300mm wide and only half of the line was drawn similar to plots one and two.

ii. The resist layer, separating the two lines was 200mm wide.

iii. The second line, again and as for the first line this

represents a line width of 200mm.

This yielded an interesting result, where the potential gradient existing between the anodes and cathode as revealed by the plotting of the equipotential lines was found to be symmetrical about a centre of the resist layer dimension dividing the plot normal to the resist surface and as indicated by r1 or r2. Due to this potential field symmetry about the centre of the resist, the current density distribution about this dividing line will also be symmetrical.

Hence a predicted similar metal removal profile at the resist edges closest to the centre of symmetry for adjacent lines.

2.4.4 Plot four.

The purpose for producing this potential field plot was to check the result obtained in section 2.4.3. This by variations in the geometry of the plot. The plot is illustrated in figure 2.11 where ratios of 8:3:4 were used and corresponding to:

i. The first line width of 400mm.

ii. The resist layer dimension of 150mm separating the lines.

iii. The second line width of 200mm.

Qualitatively the result was identical to that of plot 3, where symmetry in the potential field plot was noted about a position dividing the centre of the resist. This supports the remarks made in the previous section.

2.5 The effect of differing line widths on the depth of etch.

When electrolytically etching two unequal features such as two parallel lines of differing widths, it can be seen from plots 3&4 in figures 2.10 and 2.11, that the equipotential gradients are symmetrical about the dotted lines which divide the resist dimension separating the simulation of the two etched lines. Therefore the current distribution on the narrow line between x=0 and x=1 is the same as that on the portion of the wider line marked between x=(L-1) and x=L.

Hence, the current density Jy at the centre of the wider line is lower value than that at the centre of the narrow line. This is based on the following:

from equation (9), at x = 0

$$J_y = B(L^2 - x^2)^{-0.5}$$

$$J_y = B.L^{-1}$$

where, B = constant.

The depth of etch at centre is proportional to the current density, hence the difference in depth of etch between two parallel lines in terms of their width is:

$$J_{y,(L1-L2)} = B\ (L1^{-1} - L2^{-1})$$

This relationship is graphically illustrated in figure 2.12 by substituting:

$$L1 = 1;\ L2 = 2,3,4,..10;\ B = 1$$

Corresponding to the line width ratios of 1:2 to 1:10.

Newman [71] using the method of separation of variables and Fourier series has described the primary current distribution on a disc electrode of radius R embedded in an infinite insulating plane as:

$$i_n / i_{avg} = 0.5\ [1- (r/R)^2]^{-0.5}$$

The similarity between this expression and that of Eq.9 is clear.

2.6 NUMERICAL MODEL

2.6.1 CELL DESCRIPTION

i.The Geometry:
A rectangular cell described by cartesian coordinates with a maximum mesh array of (100jx100i) was used. Geometric aspects that are not user specified are two vertical insulating walls normal to the electrode surfaces, the electrodes that are initially flat and parallel and an auxiliary electrode fixed at the origin. The latter does not physically respond to current density variations on its surface.

Specified geometric parameters are:

1. Inter-electrode gap.
2. Cell width.
3. Dimensions of fine grid.
4. Dimensions of coarse grid.
5. The position of simulated dielectric layer.

The interface between the two grids may be selected to give the

maximum possible grid density at the proximity of the working electrode. The cell height is the constraining factor as the maximum electrode gap is a function of the mesh size.

The cell width is the product of the coarse grid dimensions and the number of columns defined giving a good cell width range but the resolution is restricted by the array dimension 'j'.

The working electrode can be masked by introducing a parallel insulating layer at the proximity of its surface. The dimensions of this insulator (Fig.2.13) are defined in units of 'j' main grid and 'i' fine grid giving control on position and width of the layer w.r.t. the cell width. The thickness of the layer is equal to the dimension of the fine grid.

The sharp discontinuity at the simulated electrode/dielectric interface is an area where very high potential gradients exist, this was previously discussed in this chapter where the primary current density tends to infinity at this point. Solution convergence was not possible due to instabilities caused by the high order fields.

A routine was devised to overcome this by generating an approximate initial boundary (WE) movement causing the undercutting of the insulator. This has the effect of reducing the high current densities at the interface zone and in turn achieving convergence in following boundaries. The approximate solution was achieved by lifting the insulator above the working electrode by '-2i' typically in the order of 10-20μm and proceeding to generate the approximate solution using a charge value typically 20% of that utilised in following time intervals. At the second time interval the insulator is returned to the normal required position to proceed with the solution. The approximate is seen in all the results as the first boundary which is illustrated further on.

ii. Kinetics and Mass Transport

In a general electrochemical system the potential distribution and concentration distributions of all reacting species must be known before the current distribution can be determined.

Calculation of the concentration distributions depends in turn on the local hydrodynamic conditions.

The local reaction rate of each species also depends on the polarization due to kinetic and mass transport limitations.

If gas is evolved at an electrode, the bubbles tend to increase the local mass transport rate, but since they are less conductive than the electrolyte, the bubbles tend to increase the cell resistance.

A general two-dimensional model which takes into account hydrodynamic variations, polarization, ohmic drop, mass transport limitations, simultaneous electrode reactions, and gas evolution

would be extremely complicated and is thought not to exist.

The developed model is a quasi steady state simulation of a transient problem which is suitable for two-dimensional and axisymmetric cells featuring a dielectric surface stencil and accounts for:

1. Electrode polarization.
2. Ohmic drop.
3. Mass transport limitations.

Mass transport limitations are approximated [81] by a concentration overpotential expression, which is valid if an excess of supporting electrolyte is assumed where conductivity variations in the diffusion layer and the diffusion potential may be neglected.

The hydrodynamics must be sufficiently well defined so that an effective mass transport boundary layer thickness can be estimated at any position over the investigated electrode.

The charge transfer overpotential may be calculated by an arbitrary kinetic expression. This by separately treating the bulk electrolyte from the diffusion layer. Current density in the bulk may be determined by Ohm's law and as diffusion layers are relatively thin, hence the local current density entering the layer from the bulk is assumed to equal that entering the electrode.

Surface potential may be calculated from the appropriate overpotential expression and one of the following may be selected:

1. No polarization (primary current distribution).
2. Constant polarization.
3. Linear polarization.
4. Tafel polarization.

The solution of the current distribution on the working electrode is obtained by iterating over the process controlling equations.

2.6.2 THE PROGRAM STRUCTURE

Structure of the 'Fortran' program is outlined in a flow chart (Fig. 2.14) where the basic procedure in calculating successive profiles is illustrated. Two programs were produced, the first simulates an anodic working electrode and hence dissolution (electro-photoetching) and the second is a cathodic working electrode (electro photoforming 'e.p.f.'). Although the latter was outside the scope of this investigation, it was thought worth implementing as work is currently being carried out in this field and no numerical model simulating this process is believed to exist.

2.6.3 MODEL DETAILS

It is assumed that the bulk electrolyte is homogeneous due to sufficient stirring such that no concentration gradients exist. Hence a Laplacian field applies (Eq.11).

$$\nabla^2 \phi = 0 \qquad \text{....(11)}$$

A method outlined in Lapidus [89] is used to approximate the potential at nodes adjacent to the surface. This is illustrated in figure 2.15. For node points in the bulk (ie h1=h2=h3=h4) the expression is reduced to a basic five point molecule.

$$4\phi_{j,i} = \phi_{j-1,i} + \phi_{j,i+1} + \phi_{j+1,i} + \phi_{j,i-1}$$

The surface insulator is a variant of this where the potential on either side of the insulator is assumed to be equal and the surface charge is negligable. A schematic of the dielectric layer is illustrated in figure 2.13. If the origonal electrode surface is at row'i' then the potential on the bottom row of the insulator (i-2) is described by:

$$3\phi_{j,i} = \phi_{j-1,i} + \phi_{j+1,i} + \phi_{j,i-1}$$

as,

$$\phi_{j,i} = \phi_{j,i+1}$$

Analogously ,the top row (i-1) of the insulator:

$$3\phi_{j,i} = \phi_{j-1,i} + \phi_{j,i+1} + \phi_{j+1,i}$$

as,

$$\phi_{j,i} = \phi_{j,i-1}$$

A three point numerical differentiation formula is used to calculate the current density at each surface node. The components of the field in the 'X' and 'Y' directions are initially

calculated by obtaining expression for both components of the field by expanding the node potentials (ϕ) using a Taylor series about the potential at which the gradient is to be established.

For example by expanding the potential P at nodes j,i-1 and j,i-2 in figure 2.13 about that of node j,i gives an expression of the 'Y' component of the field.

$$E_y = \frac{1}{h}\left(\frac{1}{2}\phi_c - 2\phi_b + \frac{3}{2}\phi_a\right)$$

if the distance (β) between 'b' and 'a' is smaller than that between 'b' and 'c' (h) which is the usual case at the proximity of a surface.

$$E_y = \frac{1}{h}\left[\frac{\beta(\phi_c - \phi_b)}{1+\beta} - \frac{(1+\beta)}{\beta}(\phi_b - \phi_a)\right]$$

Analogously, a similar expression can be obtained for the 'X' component of the field.

The electric field normal to the surface is calculated from the projections of the X and Y components on the normal as illustrated in figure 2.13.

$$E_n = E_x \sin\theta + E_y \cos\theta \qquad \ldots.(12)$$

At the boundaries the normal current density is proportional to the potential gradient. The current density at the surface is the product of the conductivity and the field.

$$J_n = \sigma . E_n \qquad \ldots.(13)$$

This approximation for the current density at the r th iteration is substituted in the Butler-Volmer equation to get an estimate of the overpotential. The equation describes the dependence of surface potential on current density.

$$J_n = J_o \left[e^{(Pa)\eta_s} - e^{-(Pc)\eta_s} \right] \qquad \ldots.(14)$$

where,

$$(Pa) = \frac{\alpha a.F}{RT}$$

$$(Pc) = \frac{\alpha c.F}{RT}$$

The exchange current density may be a function of the surface ion concentration

$$J_o = J_{ob} \left[\frac{c}{c_b}\right]^{\gamma} \qquad \ldots.(15)$$

If linear concentration gradients are assumed

$$J_o = J_{ob} \left[1 - \frac{J}{J_{lim.}}\right]^{\gamma} \qquad \ldots.(16)$$

The surface overpotential appears in a transcendental expression, and an explicit solution cannot be obtained. The Newton method is most efficient for obtaining this overpotential.

A function 'G' is defined such that the overpotential at the r th iteration is the solution for the specified current density and hence from Eq.4:

$$G^{(r)} = J_n^{(r)} - J$$

and

$$\frac{dG^{(r)}}{d\eta} = J_o \left[(Pa).e^{(Pa)\eta^{(r)}} + (Pc).e^{-(Pc)\eta^{(r)}} \right]$$

The value of the overpotential must be initially guessed and an improved estimate is obtained from:

$$\eta^{(r+1)} = \eta^{(r)} - \frac{G^{(r)}}{G'^{(r)}}$$

The result is then re-substituted in the defining equation and the iterations proceed until the value of 'G' is less than a user specified convergence criterion.

Alternatively, if the entire profile is in the Tafel or linear region, the overpotential can be obtained explicitly.

The concentration overpotential calculated explicitly from (Eq.17). Where in well-supported electrolyte, the concentration overpotential can be approximated [81] by:

$$n_c = \frac{RT}{nF} \ln \left[1 - \frac{J}{J_{lim.}}\right] \qquad \text{....(17)}$$

The total overpotential (η) is the sum of the surface and concentration overpotentials and hence the anodic surface potential can be calculated from (Eq 18).

$$\phi_o = V - \eta \qquad \text{....(18)}$$

A weighting parameter (D) ranging between zero and one was used in obtaining a new estimate of the surface potential.

$$D = \frac{\phi_o^{(r+1)} - \phi_o^{(r-1)}}{\phi_o^{(r)} - \phi_o^{(r-1)}} \qquad \text{....(19)}$$

The surface potentials are checked for convergence before the weighting is performed. If the surface potentials meet the convergence criterion, the weighting factor is then reduced on successive iterations until the normalized change in current density between iterations also meets the specified error.

2.6.4 The New Boundary

Integrating the normal current density over the electrode surface results in the current value which is in turn used for calculating the time step.

$$\Delta t = Q.I^{-1}$$

The distance the boundary moves is proportional to the product of the normal current density and time, hence the normal distance the surface moves at any j th node along the boundary is described by Eq.20.

$$H_n\Big|_j = \frac{M}{zFp} J_n\Big|_j . \Delta t \qquad \ldots.(20)$$

The new coordinates of the jth surface point for an anodic working electrode are calculated by:

$$X_j^{(s)} = X_j^{(s-1)} + H_n\Big|_j \sin \theta_j \qquad \ldots.(21)$$

$$Y_j^{(s)} = Y_j^{(s-1)} + H_n\Big|_j \cos \theta_j \qquad \ldots.(22)$$

After Ahlberg [90], interpolating polynomials of the cubic spline are used to interpolate back to the original abscissa coordinates:

$$X_j^{(s-1)}$$

If the profiles tend toward discontinuous behaviour such as sharp points or cusps, optional least squares smoothing may at this stage be optionally performed on the new coordinates:

$$X_j^{(s)} \text{ and } Y_j^{(s)}$$

The piecewise cubic polynomials that uniquely specify the curve

have the following properties:

1. The polynomials on either side of each surface node intersect at that node.
2. The first and second derivatives are continuous at each node.

2.7 Computational Method

The finite difference method, coupled with SOR, is used to calculate the potential distribution in the bulk. Fleck's [68] results showed that an overrelaxation parameter 'w=1.8-2.0' produced the optimum computational efficiency and 'w=1.85' has more recently been recommended. The optimising algorithm for 'D' [81] was incorporated as the advantage in terms of computational time is believed significant.

The size of the time step influences the shape of the final profile. The error in the quasi-steady state approximation should decrease as the number of time steps for a given amount of charge passed is increased. The boundary ordinates must be interpolated back to the original abscissa coordinates at each time step. Therefore, there is an optimum number of time steps, beyond which the cumulative interpolation error overshadows the accuracy achieved in reducing the quasi-steady state error.

At each time step the normal to the surface is determined from a numerical differentiation of the surface coordinates. The error associated with the differentiation process decreases as the grid interval is reduced.

The current densities at the electrode surface and the derivatives of the surface coordinates are two quantities that can be determined more accurately by reducing the mesh size. Determining the accuracy of the current densities a priori is not possible, but it will approach values where further reduction in mesh size will not have a significant affect on the results.

If the profile tends toward unstable behaviour such as in primary distribution and near the resist edge, least squares smoothing may be performed to reduce the instability.

In specifying the maximum root-mean-square (rms) error in the polynomial curve with respect to the generated coordinates, a polynomial equation of an appropriate degree can be determined. As the rms error specification is increased, the degree of the polynomial is reduced, along with the accuracy of the solution. A sufficiently small rms specification will force the polynomial curve to pass near each point, and hence little smoothing. Therefore it is recommended that for this type of simulation the smoothing routine is by-passed.

3.0 PROCEDURES, MATERIALS AND EQUIPMENT.

3.1 GENERAL

The preparation stages prior to the electrolytic etching or polishing of all the sample materials are essentially similar. Hence the pre-etch sample preparation will be discussed in this chapter and where differences may arise, these will be described with further detail in their relevant chapters. The suppliers of materials and equipment used throughout this work are listed in Appendix D.

The p.c.m. equipment required for the pre-etching stages of workpiece preparation was already available prior to starting the work. Yet the majority of the equipment utilised for the electrochemical aspects of the work had to be either purchased or made. This chapter is divided into the following areas:

- i. Phototool preparation.
- ii. Investigated materials.
- iii. Metal surface cleaning.
- iv. Photoresists & coating
- v. Exposure & development of resists.
- vi. The experimental equipment.
- vi. Metrology & Analysis.

3.2 ARTWORK PREPARATION

The material selected for making the artwork was chosen taking the following points into consideration:

- i. The ability to be readily photographed and give results with suitable density and contrast.
- ii. Dimensional stability to changes in humidity and temperature.
- iii. Toughness and resistance to tear and abrasion.
- iv. Surface smoothness and its acceptance of tape or ink.

Environmental changes such as temperature and relative humidity may vary the artwork dimension. Changes due to temperature variation can be readily minimised by controlling the laboratory environment. The conditions where the artwork was prepared were ideal as the laboratory where the work was carried out is air-conditioned. The temperature is controlled to 20°C $\pm$0.5 and a 45% relative humidity (RH).

'Rubylith' was the material used throughout for producing the art work . This is a polyester based material of low moisture absorption and hence minimising the resultant swelling or contraction.

Artworks were all prepared on a co-ordinatograph type 'ARISTO' (Appendix E) with a rotary table (Fig. 3.1). This is a high precision 'X' and 'Y' co-ordinate plotting machine, capable of locating a point with precision of ±0.02 mm. Special tools were used for cutting the red coloured strippable layer which is laminated on the polyester base material. The tools applied sufficient cutting pressure to cut the red layer in a uniform and precise manner. Hence negligible distortion of the film.

Close tolerances on the final product are achieved by dimensional modifications and compensation carried out to the artwork.

The p.c.m. process features necessitating compensation in the artwork are as follows:

i. Etch factors
ii. Etch bands
iii. Straight-edge profile
iv. Stencil size reduction

i. Etch factor as previously defined in section 1.8.1 is the ratio of depth of etch to the undercut. Etch factors may vary due to differences between the lateral and depth of etching rates caused by process factors including feature dimensions and materials worked. Therefore the required dimensions are achieved by artwork modification.

ii. Etch bands (Fig. 1.4) are used to ensure uniform break-through on all etch areas [14]. In general these are usually the same dimension as the features to be etched e.g. holes etc. But there is also a relationship between line widths and etch factors which should be taken into consideration.

iii. When double sided etching, 'cusps' as illustrated in the figure 3.2 are produced in p.c.m. If a straight edge profile is required etching must be continued to achieve this and hence a dimensional compensation is necessary (Fig. 3.2).

iv. Stencil-size reduction was noted and may be attributed to the hardening of the resist layer in the area of direct exposure during resist development.

3.3 PHOTOGRAPHIC REPRODUCTION

Maximum performance is essential at all the stages in the photography of the original artwork in order to achieve sharp, dense and precise transparencies. The photographic system must provide accurate line widths, clear areas which are perfectly transparent with no veiling, opaque areas which are absolutely opaque void of any pin holes and finally dimensional stability.

3.3.1 Photographic materials

High resolution photographic plate (H.R.P.) type 1A supplied by 'Kodak' was used throughout in the preparation of the masters. This is negative working, very high contrast, orthochromatic reproduction plate of high density and low fog level [91].

Working masks or sub-master were produced using Kodak high resolution photographic film (H.R.F.) type 'SO 343'. This has a 0.178 mm Ester base, It is capable of resolving >2000 lines per millimetre [92].

3.3.2 The photographic work

A 1st. Reduction type Camera (Type 1503 by David W. Mann Co.) was used. It is illustrated in figure 3.3 and described in Appendix F. The photographic reduction throughout the bulk of the work was 20:1. Reduction ratios are controlled by the distance between the screen and the lens, this distance was set utilising a previously prepared calibration chart. The results were further checked using the microscope/graticule on the camera system by measuring a reduced image dimension on the focal plane.

Back illumination of the screen is a feature of the camera system, where the artwork is sandwiched by a transparent blanket of thin polyester sheet placed over the screen. This was used to retain the vacuum generated between the screen and the polyester sheet itself. The result is the elimination of the air and the flat retention of the artwork. This is necessary to achieve sharp definition.

Fluorescent tube light, green in colour illuminated the screen and this is regulated to less than 5% variation in intensity of illumination.

The sharpest image formation was placed at or just below the image surface. This was achieved by using an exposed dummy plate featuring lines on the emulsion surface and inserted in to the plate holder with this surface facing towards the screen. Therefore the lines take up the position of the H.R.P. emulsion surface. The camera viewing microscope was made to focus on the features of this surface. Similarly, the image reduced from the screen and positioned centrally on the plate was then brought to focus on the same plane. The correct image size was obtained by using the built-in vernier of the microscope to measure the image size dimensions directly of the image plane. Recommendations and procedures are detailed by Allen et al [93].

The first reduction of the artwork upon H.R.P. is the master. An exposure time of 25 seconds and a development time of 2.5 minutes were obtained experimentally giving the desired density. The unexposed H.R.P. (63.5 x 63.5mm) were inserted into the holder with the emulsion side facing the screen. The screen is then illuminated and the plate is given an exposure of 25 seconds through the

shutter which is positioned in front of the lens. The plate is then developed using the developing materials and procedures laid out in Appendix G and was carried out under red safe light conditions. After suitable drying, contact printing is used to transfer the image on the master to a photographic film. This was carried out in a wooden frame with a flat-glass window measuring 110 x 115 mm, a padded wooden backing plate and rubber foam sandwich between them. The master and film are placed between the glass and the foam with emulsion to emulsion contact. The master was placed closest to the frame window and a sheet of white paper was placed between the foam and the film. Contact pressure was by means of two cross bars locating the back wooden plate. The emulsion was exposed by placing the frame vertically with the window facing a 275 watt photo-flood lamp two metres from the frame. This was then developed similar to the H.R.P. and when a positive image was required, reversal developing procedures were utilised and also detailed in Appendix G.

The 'mask' which is the photographic pattern produced by contact printing from a master is the working tool from which images are cast upon the photoresist layer. Thus the master is safe from wear or damage. This type of mask is suitable for single-sided imaging and for double-sided work, a double sided mask should be produced with both sides in accurate register [94] with the photographic emulsions in contact with each other. The procedures and equipment are outlined in Appendix H.

3.4 THE SUBSTRATE MATERIAL SELECTION

Important factors for the selection of materials for p.c.m. may include:

1- The manner in which the metal has been rolled or formed.
2- The grain size and structure.
3- The ability of the material to be worked chemically without the need for using hazardous and socially unacceptable etchants.

A further consideration is the mechanical condition which the material is available in i.e. the degree of flatness, the freedom of the surface from scratches or inclusions sustained during rolling or otherwise. Finally, the suitability of the metal for the end product application is obviously the most important factor.

As previously stated in chapter one, due to the availability of information on the p.c.m. performance of AISI 304 stainless steel, it was therefore selected for investigation. Due to the lack of sufficient information on electrolytic photo-milling in general, it is believed that direct comparisons between performance parameters of conventional p.c.m. and e.p.e. or e.p.p. would yield useful results.

Later in the work, further materials were investigated and was mainly due to industrial interest. These materials were required by the particular concerns due to their physical properties. The properties and the material specifications are discussed further in their relevant chapters. The two materials were:

1- 'Recovac' a polycrystalline nickel base alloy.
2- 'Vitrovac 6025' an amorphous cobalt based alloy.

Hence, the three materials investigated differed physically, chemically and mechanically. The trade names used to describe alloys 1 & 2 above and hereinafter are those of their supplier (Vacuumschmelze [82]).

3.4.1 AISI 304 Stainless Steel

Stainless steels in general have wide and ever increasing applications in and out of industry. This is an austinetic stainless steel of low carbon content. The material was supplied in the annealed state. The specifications and details of the AISI 304 stainless steel as used are detailed in Appendix I.

3.4.2 Recovac

It is a high-permeability nickel-iron alloy similar to Mumetal, which, through special additives, exhibits significantly higher resistance to wear. Details of the specification of Recovac are in Appendix J.

3.4.3 Vitrovac 6025

This is an amorphous soft magnetic alloy based on Co. The alloy exhibits potentially favourable magnetic and mechanical properties.

Detailed specifications of Vitrovac 6025 are in Appendix K.

3.5 SURFACE PREPARATION PRIOR TO PHOTORESIST COATING

Incomplete surface preparation would often result in photoresist failure, therefore proper cleaning and surface treatment ensures good photoresist adhesion. The latter is critically important for successfully achieving clearly defined and mechanically durable stencils. Thus preventing the lifting of the resist as may be caused by the turbulent flow generated when spray etching and alternatively as by the effect of vigorous agitation of the electrolyte during e.p.p. or e.p.e. The latter two occurring often with gas being generated at the surface of the anode, this all at elevated and wide inter-process differentials in temperature.

3.5.1 The surface preparation of AISI 304 stainless steel.

All samples used throughout the experimental work were prepared using the following sequence:

a) Degreasing the sample by swabbing both sides with acetone.
b) Using an aqueous acid solution (CD/70 20% v/v solution) acting as a cleaner deoxidizer. This by suspending the samples in the solution with the aid of stainless steel clips for 15 minutes.
c) Rinsing thoroughly in running water until a uniform layer of water is observed on both sides of the sample and this was then followed by a further rinse with distilled water.
e) Immediate drying the substrate using oil free and dry compressed air. Thus preventing drying marks on the surface.
f) Heating the substrate in an oven at 90 degrees C for 20 minutes to completely dry it.

3.5.2 Surface preparation for Recovac

The surface of Recovac was prepared in a similar manner to that of the stainless steel. It only differed in (b) above where a 2% w/v solution of Quadralene is used rather than CD/70. This removed the possibility of changing the characteristics of the metal surface. Quadralene is detergent whereas CD/70 is also a de-oxidizer.

3.5.3 Surface preparation for Vitrovac 6025

This material was prepared as Recovac but due to its amorphous structure which is relatively less stable, there is a risk of re-crystallization at prolonged high temperature treatments. The drying temperature was therefore restricted to 80 degrees C for 10 minutes only. Although the re-crystallization temperature was considerably higher (500 $^{\circ}$C), this material is sensitive to heat treatment and thus this risk was reduced. Vitrovac (as supplied on a spool) was inherently clean and extensive swabbing with acetone was not necessary.

3.6 THE PHOTORESISTS

In p.c.m. in general, negative working resists are preferred to positive working resists when etching metals [2]. The positive resists operate on photosolubilization and hence the stencil consists of an unaltered resin. Alternatively, negative resists consist of resins which are insolubilized by photochemical cross-linking. Hence the latter is generally more durable.

Three types of resists were used throughout the work, these were selected due to their availability and suitability for the proposed applications. The resists used were as follows:

1. Thiokol 'Laminar AM', this is a dry film negative working resist and post lamination measured thickness of 26um.
2. Hunt 'WayCoat SC180', this is a negative working liquid resist applied in a layer thickness typically 3μm dry.
3. Shipley 'AZ 340', this also is a liquid resist but this is positive working.

The use of the latter was restricted to a possible industrial application and is described in its relevant chapter (6).

The characteristics of a dry film photoresist are uniform and homogeneous coatings. The limitation of this type of resist is its' availability in relatively large thicknesses only and hence achieving relatively lower resolution when compared to liquid resists. As a general rule the resolution is 3-5 times the thickness of the resist.

The advantage of using a liquid photoresist is that the thickness of the coating may be controlled down to small values e.g. 1μm or less. The factors governing the coating thickness when dip coating are the viscosity and the withdrawal rate [18].

3.7 APPLICATION OF THE PHOTORESIST

The measurement of the viscosity and the dry coating thickness of the photoresists is described in Appendix L. Generally substrates were kept and handled with great care prior to the resist coating and in particular the samples that were destined for coating with liquid photoresist. This was to ensure that the surfaces were free from particles such as dust which is believed to be a major contributor to localised coating failure. In e.p.e. or e.p.p. a resultant pin hole is more likely to occur than with conventional p.c.m., and for this reason, all liquid resists must be protected and kept free from contamination.

Due to the greater relative thickness of the dry film resist (typically one order of magnitude), and its homogeneous composition, none of the above mentioned problems were encountered in its use.

3.7.1 Application of liquid resists

The method used for both types of liquid resist was the controlled dip coating method. This ensures a relatively uniform and continuous film of photoresist. The equipment used is illustrated in figure 1.6, where the substrate is suspended at the top of the structure and the photoresist tank is raised to the material to be coated. Raising the tank is carried out with aid of a hydraulic jack, the sample is thus submerged in the resist to the required

level and the tank is allowed to drop at a controlled rate governed by the hydraulic variable control valve.

Drawbacks of this method of coating were slight wedging of the resist thickness between the top and the bottom of sample and the possibility of contamination during any of stages of the process by air blown particles.

3.7.2 Applications of dry film resist

The substrates were pre-warmed prior to being laminated and this was by laminating immediately after the drying stages so that the sample did not act as a heat sink. The laminator illustrated in figure 1.7 was used for this work. Using two resist rolls simultaneously, both sides of the metal surface were coated in the same pass. The laminator removes the polythene protective layer prior to adhering the resist to the metal surface by a combination of pressure and heat by the rollers. Laminating was carried out under yellow safe light conditions.

3.8 EXPOSURE OF PHOTORESIST

The three resists used are sensitive to ultra violet (UV) radiation. Two exposure units were utilised and are as follows:

1- A high pressure mercury vapour short arc source (Metax type Hg 201) was used for the higher resolution work, this required a power supply producing 4 amps. @ 46volts. The unit and exposure frame is illustrated in figure 3.4.

2- A 'Littlejohn' double-sided exposure unit utilising two banks of fluorescent illumination. This featured an inbuilt timer and vacuum pump and is illustrated in figure 3.5.

In both apparatus vacuum was used to ensure complete contact between the mask and the resist layer thus reducing light scattering and diffraction effects. The exposure duration is a function of the UV source intensity and the UV transmission quality of the mask and exposure frame components.

A 'Kodak' T-14 density scale was used to determine correct exposure time for each resist, this featuring 14 steps with a uniform increase in optical density of 0.15 from one step to the next. The correct exposure time was determined by exposing the photoresist to the UV source through the chart. Then after suitable development of the photoresist, an acceptable exposure time occurred when step 7 was partially developed away with the first 6 steps completely insoluble to the developer [95].

When exposing thick substrates the sharpness of the imaged pattern in the stencil may be adversely effected by poor contact between the mask and the photoresist. This may be due to the stiffness of the sample and its lack of flexure to the force exerted by the

vacuum, hence possibly leaving a small gap between the two surfaces due to the non-flatness of the metal substrate. This may be overcome by making the mask marginally smaller than the sample.

The removal of the protective polyester layer of dry film resist prior to exposure yielded improved results as this brought the emulsion of the mask closer and in contact with the resist layer. The use of 'beeswax' on the resist prevented adhesion between the mask and the resist layer.

3.9 PHOTORESIST DEVELOPMENT

Post exposure development of each of the resists differed from the others, the development process of the liquid negative working resist such as Waycoat SC 180, is a process in which the unexposed monomer is dissolved in the developer and subsequently washed during rinsing. This is carried out in yellow safe light. The polymeric stencils produced were examined under a microscope to inspect the sharpness of the resist layer edges and to ensure that the stencil size was correct.

The dry film resist was developed utilising specialised developing equipment featuring spray developing techniques. Processing times were in the order of 75 seconds and at temperatures of 30°C, this was followed by a thorough rinse in clean water. Properly developed stencils produced no unexposed resist residues.

Appendix M describes the procedures for developing 'Waycoat SC180' and 'Laminar AM'.

3.10 HEAT TREATMENT OF THE PHOTORESIST

The requirement for heat treatment of resist layer varies and is dependent on the type of resist being used. Liquid resists in general required both a pre-exposure and a post-development baking, whereas the dry film resist did not require a pre-exposure treatment and the post-development baking is seldom used [4].

Pre-baking the liquid resist coated substrates is necessary in order to remove residual solvents in the resist layer. Retention of these solvents reduces the photosensitivity and the response of the resist layer to U.V. radiation. However, pre-baking time and temperature are critical as overheating degrades the image quality by spill over into the clear areas which are to be etched (-ve resist) [18]. A temperature of 90°C for a duration of 10 minutes was found to be suitable for the 'Waycoat SC180' resist and this was reduced when amorphous substrates were used.

Post baking the stencil was found to increase the durability of the photoresist during etching. With liquid resists it also evaporated the residual solvents from the developing stage which could result in premature failure.

For 'Waycoat SC 180' a post-bake of 15 minutes at 120°C was used.

A Post-bake of the dryfilm resist was carried out at 80°C for 15 minutes and the resist image showed increased durability during prolonged etching periods.

3.11 THE ELECTROLYTE

A range of potentially suitable electrolytes was investigated in a series of preliminary tests. Published formulations were selected for working stainless steels and for application in e.p.e. or e.p.p. There is a wide selection of electrolytes suitable for electropolishing a wide range of metals and alloys [9,10]. Hence basic requirements were set to reduce the choice available and this was based on the following considerations:

i. Non toxicity.
ii. Unconditionally non-volatile
iii. Cost effective.

Satisfying the above requirements, would in general favour the adoption of this process by industry.

A number of sources when searching for suitable electrolytes were used [9,10,25,26], these were intended for a wide range of applications ranging metal finishing such as polishing for decorative work to the preparation of metallurgical samples for microscopic inspection.

Selected electrolytes were investigated and further eliminated in preliminary experimental results as summarized in Appendix N and due to their unsuitability for e.p.e or e.p.p. Reasons for elimination were mainly due to their attack upon the resist stencil and/or poor metal removal performance.

3.11.1 Selected electrolytes

As the investigation may be divided into two fields, e.p.e. and e.p.p., two electrolytes were selected for those applications and are as follows:

1. e.p.e. Hydrochloric acid solution diluted 3:1 by volume (36% w/w HCl) as
recommended by Kodak [25] for the electrolytic etching of steels.

2. e.p.p. Orthophosphoric acid in glycerol a recommended elecropolishing solution by Tegart [9] for stainless steels. The formulation being:

i. 300 ml orthophosphoric acid
ii. 530 ml glycerol
iii. 90 ml water

3.12 THE EQUIPMENT AND INSTRUMENTATION.

The equipment used throughout may be subdivided into four groups as follows:

i. Polarization
ii. Etching.
iii. Metrology
iv. Analysis of results

3.12.1 Equipment for polarization measurement

Polarization measurements were carried out initially with aid of a 'Chemical Electronics 703A' potentiostat, this was used in conjunction with a 'LDU 1' linear sweep generator for carrying out potentiodynamic measurements. These first were kindly lent by Dr. J. E. Strutt. Later in the work, the same type of measurements were carried out with a 'Thompson Ministat 7amp' potentiostat and a 'DRG 16' digital linear sweep generator was used.

A 'Lloyd type PL 50' 'X-Y' recorder was used for recording the potentiodynamic polarization measurements on A4 size paper. The instrument was used in conjunction with the two potentiostat systems described above.

Calomel reference electrodes 'K.I.M. type 1370' were used for the measurement of the anode potential via a KCl/Agar salt bridge made as follows:

a) 12g KCl + 8g Agar + 200 ml distilled water.

b) Heated until relatively viscous.

c) Poured into a flexible tube with a suitably formed glass measuring tip attached to the end of it.

3.12.2 Electro-etching/polishing equipment

The majority of the work was carried out under galvanostatic conditions. A commercial constant current source with the required performance could not be located, hence a suitable design was made and built, this is detailed in Appendix O. The unit was found to be extremely stable and performed reliably throughout.

The potential and current measurements were made with aid of digital multimeters. Two 'Sinclair DM 450' 4.5 digit units were used for the calibration of the 'X-Y' recorder scales and the continuous monitoring of the process. The main advantage of using this type of instrumentation is the accuracy, resolution, and high impedance. A disadvantage was their unsuitability to rapidly fluctuating measurements, hence complementary analogue meters were used in those conditions.

3.12.3 Metrology

Geometric profiles were measured with the aid of a 'Talysurf 3' suitably modified with an extension to the stylus arm, thus reducing the magnification of the instrument to read the profile of a feature rather than its surface textures. The profile was determined by producing traces of the surfaces for further analysis this by levelling the sample to give the same reading on both extremes of the stylus run.

Measurement of the surface texture was with the aid of a 'Talysurf 4'. Two methods were used to quantify the surface roughness and are as follows:

i. The center line average (Ra).
ii. The peak-to-valley (R max.).

The above (i & ii) are further described in Appendix P.

A 'Vickers M41 Photo Plan' microscope with an extensive range of accessories including a polaroid camera, a 35mm camera, a range of objectives and graticules was used extensively throughout the work.

A 'Micro 2000 digital micrometer' was used for metal and resist thickness measurements. This was a 0-25mm 'Moore & Wright' with a display resolution of 1μm.

The mass of metal removed was determined with the aid of a 'Oertling' beam balance by measuring the mass of the substrate before and after electrolytic dissolution.

3.12.4 The analysis of the results

The experimental results were analysed with the aid of a 'Hewlett Packard HP 85' computer utilising a curve fitting program (CURVE), function fitting program (FPLOT) and data plotting program (DPLOT). These are further detailed in Appendix Q.

4.0 THE ELECTROLYTIC ETCHING OF AISI 304 STAINLESS STEEL.

4.1 GENERAL

A decision was made to use a 10% w/w hydrochloric acid solution [25] as an electrolyte for e.p.e. of stainless steel. This was based in part on the results obtained from the preliminary electrolyte suitability tests (App. N) in the initial stages of the work .

Further preliminary tests were carried out on the electrolytic etching of AISI 304 stainless steel in a 10% w/w HCl acid solution. These covered an electrolyte temperature range between 15 and 25°C. Results were inconsistent and unpredictable, differences were noted in surface textures and mass of metal removed in tests where the same etching parameters were applied. Surface pitting occurred in certain tests whereas in previous runs uniform types of dissolution took place. This work was carried out under galvanostatic conditions where the cell potential was monitored using a chart recorder. It was noted that under certain conditions, mainly at the lower part of the temperature range investigated, step changes in the potential occurred during the etching. The cell potential changed from a high level to a lower one. Unsuccessful attempts were made to repeat those results in a consistent manner. Further when a potential change occurred, the time of the event within the etch duration could not be predicted or repeated.

It was assumed that the steel was passivating under the applied conditions and the information obtained from the above reference was incomplete. The recommendation [25] of etching at 6 volts with no information on electrode separation, anode current density, or anode potential was not sufficient. Further there were no details on the performance with changes in etching temperatures. No further details could be obtained from Kodak, and in the general search carried out no specific information was found.

As AISI 304 stainless steel exhibited a tendency to passivate in the selected etching environment, it was necessary to carry out polarization measurements to facilitate a better understanding of the metal surface behaviour under the applied conditions.

A polarization diagram of a typical passivating system is illustrated in figure 4.1. Under galvanostatic etching and at current densities in the proximity of (J a,b,c), any of three etching mechanisms may take place whose anode potentials are Ea, Eb, and Ec. At Ea, lying in the active zone, etching would be uniform whereas at Ec, pitting and intergranular attack may occur. Eb lies in the transition zone between the active and passive zones, where the anode is unlikely to remain at Eb due to its instability, although at this potential pitting would be expected.

Electrochemical process variables influence the rate of corrosion through one or both of the anodic or cathodic reactions. The main cathodic reaction for iron corroding in dilute inorganic acid is:

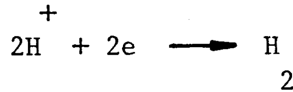

$$2H^{+} + 2e \longrightarrow H_2$$

Hence the greater the availability of hydrogen ions, the faster the cathodic reaction will be, and this in turn permits a greater rate of anodic dissolution. This is the case throughout the concentration range for hydrochloric acid.

The anodic reaction is effected by the presence of chloride ions and chlorides are particularly effective in destroying passivity in materials such as stainless steels by decreasing the potential range at which the stainless steel exhibits passivity.

The effect of concentration of hydrochloric acid upon the corrosion rate and the effect of chloride ion increase are graphically illustrated in figures 4.2a and 4.2b, respectively.

An increase in temperature generally increases the rate of corrosion. There are few exceptions and these are usually due to a decrease in the oxygen content of the solution as temperature is raised. Oxygen is required to depolarize the cathodic reaction and in turn increase the anodic reaction and hence a relatively greater metal dissolution.

4.2 PASSIVATION

A metal is said to be passive in a certain environment if it exhibits a relatively low corrosion rate, when thermodynamically it is expected to corrode rapidly. Usually passivity can be overcome and a more rapid corrosion takes place by changes in the environmental conditions. Hence a metal that is passive in one environment will not necessarily be passive in another. Passivity is the result of a continuous reaction between a metal and its environment. Corrosion continues to take place even when a metal is in its passive state, though relatively at a very low rate. The results of passivity may be readily measured, and this measurement may provide a useful tool for evaluating, and possibly developing either alloys for corrosion resistance or as in this work where it may be used in developing an environment whereby passivity is avoided or possibly eliminated to facilitate suitable metal dissolution. The progress of corrosion reactions is dependent upon polarization at the anode and cathode. Although passivity is a property of the anode, and shows up on the anodic polarization curve, achieving it is also much dependent upon the cathodic reactions.

A reliable way to reduce the possibility of passivity is to change the anodic polarization behaviour, this is illustrated in figure 4.3. These are typical anodic polarization measurements for a

system that exhibits passivity. The modifications shown may be achieved by changes such as temperature, composition and concentration of the environment (electrolyte).

4.3 POLARIZATION

Polarization is defined as a change in the potential of an electrode as current flows to and from it. The degree of polarization increases as the rate of corrosion decreases.

There are basically three reasons for polarization and are as follows:

i. Activation
ii. Concentration
iii. IR-drop

Activation polarization is the result of a slow step in an electrode reaction at the cathode or anode. This can be illustrated in the following example, where hydrogen evolves at the cathode. The reaction might be considered as:

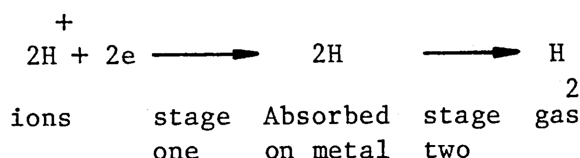

$$2H^{+} + 2e \longrightarrow 2H \longrightarrow H_2$$

ions — stage one — Absorbed on metal — stage two — gas

Stage one occurs rapidly, whereas stage two is relatively slower and hence the rate controlling step.

Concentration polarization is the slowing down of the reaction due to an insufficiency of a desired species, or an excess of an unwanted species at the electrode surfaces. It is dependent on the diffusion rates, and may be reduced by stirring the electrolyte.

An IR-drop is a potential drop that is equal to that across the electrolyte (reacting at the electrodes). It can also include any corrosion by-products such as surface films.

4.4 THE POTENTIOSTAT AND MEASUREMENT CELL

A metal that is freely corroding develops a potential between itself and its ions in solution. This potential can be changed with the aid of an external circuit, which in turn changes the degree of corrosion of the metal.

Guidelines have been drawn for polarization measurements from the ASTM [96,97,98,99,100] series of publications in the field. These guidelines, where possible, were used in carrying out the

experimental work. The suggested guidelines included the following preparation steps:

1. The metal is cleaned and installed in the cell.

2. It is then allowed to reach its natural corroding state which may take several minutes or hours.

3. The external circuit is used to change the potential in the positive direction (noble) by a fixed amount. It is allowed to remain at this level for a period of time sufficient for conditions to reach equilibrium.

4. A measurement of the current flow in the external circuit is then made.

5. The two procedures above are repeated until the desired potential range is covered.

This technique is termed potentiostatic polarization measurement. An alternative method is to continuously change the potential at a slow rate [101] (to ensure equilibrium) in the noble direction (+ve) and record the current value continuously and preferably simultaneously plotting it versus the swept potential. This technique is known as potentiodynamic polarization measurement [96].

The potentiostat is an instrument that is used in the external circuit to hold a desired potential constant, or change it in a particular desired way. This external circuit is schematically illustrated in figure 4.4. A potentiostat may perform other functions, but it is most frequently associated with the determination of the anodic polarization behaviour.

The principle of the potentiostat is illustrated in figure 4.5. This is a schematic diagram of the major internal functional parts. The anode potential is measured at the working electrode with aid of a salt bridge this in turn isolates the saturated calomel electrode (SCE) from the electrolyte and acts as a buffer. The SCE is positioned in the reference cell, this for the purpose of this work consisted of a saturated solution of KCl. The operational amplifier A1 is connected as voltage follower with a characteristic high impedance. This is necessary so that the measurement circuit does not electrically load the working cell. This part of the circuit is the feed-back path of the system.

A linear sweep generator is an instrument capable of producing a voltage ramp versus time with floating output. In general such instruments are capable of producing different user defined functions. The output is used to drive the potentiostat and the X-Y recorder ('Y' axis) simultaneously. A2 is the front end amplifier where the demand signal is applied. It is a differential input arrangement being driven by either or both the sweep generator or the potential set on the reference potentiometer.

The forward loop consists of A3 operating as a comparitor and the power amplifier (PA) which is driven by A3 and is the part of the system that supplies the current to the cell. The counting resistor acts as a shunt and the voltage drop across it is proportional to the current flowing into the cell. This is then suitably amplified and used to drive the 'X' axis of the recorder.

A positive/negative supply is used for the system, with the zero line strapped to earth. It can be seen from figure 4.5 that the working electrode can be made anodic or cathodic with respect to the auxiliary electrode, and with the aid of the sweep generator it can be moved from one to the other without interruption. If a sinosoidal or any other function with respect to time is introduced in place of the linear sweep, this can be reproduced onto the working electrode (W.E.) and the centre about which this oscillation occurs can be made anodic or cathodic or at 0 volts (v. SCE).

A potentiostat is essentially a precision dual rail power supply with the electrolytic cell being part of the feed-back loop. This ensures potential stability at the feed-back take off point (i.e. working electrode surface).

4.5 POTENTIOSTATIC OR GALVANOSTATIC ETCHING

Potentiostatic or galvanostatic modes of electrolytic etching may be employed. The difference between constant voltage and what is termed potentiostatic is that where the internal components of the cell are not included in the feed-back circuit of the power supply and the power supply looks at the cell as a single load, this is what is termed 'constant voltage'. Alternatively, where a reference electrode is utilised to measure and maintain the anode potential constant, is termed potentiostatic etching. Hence the position of the feed-back determines the convention and terminology. Due to the complexity of positioning reference electrodes as required by potentiostatic etching, it may be considered not practical for industrial applications. Under certain circumstances a constant cell voltage may achieve the required results.

The alternative, galvanostatic etching, control of the metal removal rate is readily achievable as the mass of metal removed is proportional to the charge (Faraday's law). For materials that exhibit no passivity, galvanostatic etching is relatively simple to implement, yet with passivating materials such as stainless steels difficulties may occur at current densities in the region of Ja,b,c (Fig. 4.1) causing the inconsistencies in results. The general aims were to achieve an extension to the active zone and/or eliminate passivity by environmental modifications such as temperature and electrolyte concentration.

Although, as previously illustrated, improved dissolution is achieved with an increase in concentration of the HCl solution, it is believed that higher levels of electrolyte concentration than

the suggested (10% w/w) was unsuitable for industrial applications. This is due to both practical and 'health and safety' reasons.

The effects of increasing the electrolyte temperature were investigated and anodic polarization diagrams for the proposed system yielded results indicating favourable operating conditions, without resorting to increased electrolyte concentrations.

4.6 POLARIZATION MEASUREMENTS FOR AISI 304 STAINLESS STEEL IN 10% (w/w) HCl ACID SOLUTION.

4.6.1 EXPERIMENTAL DETAILS

Details of the equipment and materials used throughout the experimental work are listed in Appendix D.

The current density calculations would be greatly simplified by using a fixed anode area for all measurements. This was achieved by producing a photoresist stencil defining the anode areas on the sample surface, and by repeating this a number of times per sample plate would not only maximise the yield, but also reduce the possibility of the effects of sample variations. This method saved time due to the large number of samples required and the time required to prepare the sample for measurement or etching. The stainless steel material used throughout these results was of the same batch and all the handling and cutting was carried out simultaneously.

Flat square pieces of AISI 304 stainless steel 51 mm X 1.63 mm thick were cut from a large sheet. These in turn were carefully cleaned by a swab and with acetone. The degreased samples were then suspended in a CD/70 solution (1:5 distilled water) for a period of 10 minutes. The samples were then rinsed in tap water thoroughly and this was followed by a final rinse in distilled water. Oil free and filtered compressed air was used to remove and dry the water surface film. Care was taken throughout to ensure that the sample surfaces were not touched at all times. Sample handling was with the aid of protective gloves by applying pressure to the sample edges.

Further drying was necessary and was carried out in an oven at 90° C. This served a secondary purpose, where the samples were removed from the oven and immediately laminated on both sides with the dry flim photoresist, thus reducing the possibility of poor resist adhesion to the steel due to temperature differentials between the laminator heated rollers and the samples. The greater the sample mass, the higher is the chilling factor and is therefore relatively proportional to the sample thickness. 'Laminar AM' was the photoresist used throughout this series of work.

A double sided mask was prepared without photographic reduction. It was made by producing a 3 x 3 matrix of 10 mm square cut-outs in 'Rubylith' the matrix dimensions are in figure 4.6. The

coordinatograph was used for producing the master directly. Due to the instrument's cutting accuracy of ± 0.02 mm, this would give a maximum possible anode area error of 0.5%. The two sides of the mask were produced by contact printing onto HR film (SO-343) and developed normally as described in Appendix G. The two sides of the mask were registered (not essential) and stapled together using suitable thickness spacers marginally >1.63mm (metal thickness).

The coated stainless steel samples were then exposed to UV light through the double-sided mask. This was carried out in a vacuum exposure system made by 'Littlejohn'. Prior to placing the sample between the two sides of the mask, the photoresist protective polyester layer is removed and the surface of the resist is carefully coated with a thin layer of beeswax. The advantage of this was to reduce the distance between the emulsion of the mask and the surface of the photoresist, in turn improving the resolution of the process. The wax prevents the resist from adhering to the mask under the force generated by the vacuum.

Spray developing equipment is utilised for processing the exposed samples and a development time of 60 seconds was found to be sufficient at developer temperature of 35° C. The developer composition is in Appendix M. Samples were then washed in water and dried.

The resist stencil pattern allows the same sample plate to be measured or electroetched 18 times under different etching conditions. Electrical insulation tape (PVC type) was found to be the most suitable temporary maskant for the protection of apertures which were not involved in a particular test.

The electrical interconnections between the instrumentation and cell which were utilised in the potentiodynamic measurements are schematically illustrated in figure 4.7. The working electrode (anode) and the auxiliary or secondary electrode (cathode) were mounted vertically in a glass cell. The cell in turn was partially immersed in a temperature controlled water bath. A paddle stirrer was used to gently agitate the electrolyte to ensure constant temperature. Figure 4.8 is a photograph illustrating the cell components in detail and includes from left to right the stirrer, cathode, salt bridge, anode, and SCE. At the top of the photograph is the glass tank and below it is plastic photographic plate holder which was used for holding the cathode and anode vertically and parallel to each other and at a fixed distance of 150mm. The salt bridge consisted of two parts, the glass section with the measurement tip and the flexible section. The composition of the bridge is in section 3.12.1. The above described cell components are assembled together and illustrated in figure 4.9 which is a close-up photograph of the assembly. Figure 4.10 is another photograph illustrating the complete cell in position in the water bath and the fume cabinet. Some of the instrumentation is illustrated in figure 4.11 which includes a potentiostat (type 703A), linear sweep generator (type LSU 1) and the X-Y recorder.

Two digital multimeters (Sinclair DM450) were used to monitor the

current and the anode potential (v.SCE) and calibrate the 'X' and 'Y' scales on the recorder.

4.6.2 The Results

A series of potentiodynamic measurements were repeated 18 times at an electrolyte temperature of 15°C and 9 times for each of 20, 25, and 30°C. The polarization measurements were produced by sweeping the anode potential at a rate of 150 mV/minute from -0.4V to + 1.0V (v. SCE). A greater number of tests were carried out at 15°C due to the system passivating at this temperature.

Photographic reductions of the potentiodynamic traces, results of the measurements made from those traces and the mean and standard deviation of current density versus anode potential results are illustrated and tabulated in Appendix R. Direct measurements were made from the traces between -0.3V and +1.0V at intervals of 100mV. Those are the tabulated results from which the mean and standard deviation of current density versus anode potential were calculated, this for each of the temperatures investigated. The mean polarization curve and the standard deviation band for the temperatures 15, 20, 25, and 30°C are plotted in figures 4.12, 4.13, 4.14 & 4.15 respectively.

The calculated mean polarization results for all investigated temperatures are plotted in figure 4.16 simultaneously, where the effect of the electrolyte temperature increase is clearly illustrated. Similarly the standard deviation in current density versus anode potential is plotted in figure 4.17 for the four temperatures investigated.

4.6.3 SELECTION OF THE GALVANOSTATIC OPERATING CONDITIONS.

Increasing the electrolyte temperature has been shown (Fig. 4.16) to reduce the tendency of the material to passivate. It also has the effect of pushing the anodic polarization curve to the high current density zone of the plot, thus resulting in an increase in the current density values in the active zone and hence an increase in the metal removal rates in an area where the type of dissolution is uniform.

The potentiodynamic results illustrate that AISI 304 stainless steel passivated in 10% w/w HCl at 15°C at an anode potential value between -100 and -50mV (v. SCE) (Fig. 4.12). Although passivation of the anode surface at 20°C is apparently eliminated (Fig. 4.13), nevertheless, due to the inherently high values of standard deviation in current density (Fig. 4.17), only the probability of passivation is reduced by increasing the temperature.

Calculating the percentage of standard deviation in current density measurements per current density and plotting this versus the anode potential gives a better indication of the level of deviation in current density. This was carried out on the experimental results

for the temperatures 15, 20, 25, and 30°C and are tabulated and plotted in figures 4.18, 4.19, 4.20 & 4.21 respectively. The results for 15 °C and at an anode potential of 200mV (v. SCE) produced a 96% level. This was due to the current density value being low during passivation, rather than a particularly high deviation in current density value. Arguably these results illustrate the passivation potential value more clearly. Further it can be seen that between 400mV to 500mV a drop in the percentage ratio occurs, and corresponds to the higher values of current density of the transpassive zone and its associated intergranular attack.

The polarization slopes at the active zone for electrolyte temperatures of 20, 25, and 30°C as illustrated in figures 4.12, 4.13, and 4.14 respectively, change to greater values at certain anode potentials where the mechanism of metal removal differ and to feature a less uniform type of dissolution. Those potentials and the corresponding current densities are tabulated below.

Temperature°C	20	25	30
Anode potential mV (v.SCE)	+100	0	-100
Current density A/dm^2	57	84	87

Therefore from the results in the table, no major advantage is achieved by etching at 30°C in preference to 25°C as the difference in maximum useable current density is small yet the evolution of HCl gas from the solution noticeable. At 20°C the current density is 68% of that at 25°C and therefore significant.

Hence, for galvanostatic etching, increasing the electrolyte temperature to 20 °C prevents passivation. Further it is not necessary to exceed 25°C to achieve this. At 30°C the evolution of HCl gas was noticeable and necessitates the use of a fume cabinet, whereas only marginal gains in terms of an increase in the active zone current density range.

4.7 GALVANOSTATIC ETCHING

AISI 304 stainless steel was etched using galvanostatic (constant current) etching based on the recommendations in section 4.6.3 above.

4.7.1 EXPERIMENTAL DETAILS

Details of the equipment and materials used throughout the experimental work are listed in Appendix D.

Galvanostatic etching was carried out utilising the same type of

workpiece preparation and identical photoresist stencil as that used for the polarization work and as described in 4.6.1. The etching cell was also the same as that used for the polarization measurements and the differences were as follows:

i. A power supply was used as an alternative to the potentiostat.
ii. No requirements for the reference electrode, sweep generator and 'X-Y' recorder.

A suitable constant current source was not available, this necessitated the design and building of such an instrument. The specifications, circuit, and details are in Appendix O.

Temperature control was again with aid of a water bath controlling the cell to 25°C with a tolerance of better than ±0.5°C. The workpiece (anode) and the cathode (Pb) were mounted vertically with a 150mm separation. The electrolyte used was 10% w/w HCl acid solution. Each of the apertures were etched individually and while the others were masked off during a test, all other exposed areas such as metal edges were similarly protected using PVC insulation tape. The varied process parameters were:

i. The current density, this was in the range of 10 to 90 A/dm^2 in steps of 10 A/dm^2.
ii. The etch duration, this was in the range of 5 to 20 minutes and in steps of 5 minutes.

The mass of metal removed was established by weighing the workpiece before and after each test, ensuring that the samples were suitably dry prior to carrying out the measurements.

4.7.2 GEOMETRIC PROFILE RESULTS

The geometric profile is defined as that produced by the depth of etch produced by the electrolytic dissolution across the face of the etched aperture.

This was measured utilising a modified surface texture measuring instrument with an extended stylus arm. The purpose of this was to reduce the magnification. The stylus arm was 120mm long, and gave a suitable range of magnification when attached to a 'Talysurf 3' surface measuring instrument.

The measurement sweeps were carried out normally to the vertical etching orientation and across the centre of the aperture. It was necessary to strip the resist stencil prior to carrying out the measurements. Samples were adjusted with respect to stylus so that readings at the beginning of the trace were equal to those at the end of the run. Measurements were made starting from the unetched portion previously under the resist stencil and ending at its counter position on the opposite side of the aperture.

The results presented in Appendix S include all the relevant details and magnifications for each of the profile measurements. Due to the use of differing magnifications, manual measurements were made from all the traces so that the profiles may be compared easily. Dimensional measurements were made direct from the traces at intervals of 10mm (Horizontal magnification X 20) working from the centre of the trace and in both directions. The depths of etch were calculated utilising the appropriate magnification. Included in Appendix S are the result of these calculations and where they are tabulated and plotted. The plotting was made with the aid of 'DPLOT' and this yielded maximum effect to the trend in geometric profile. This by only plotting between the minimum and maximum points of the individual profile.

The etched profile results are replotted in figure 4.22, where their position in the figure matrix corresponds to the actual etching position in the 3 X 3 array of apertures on the workpiece. Each position in the array represents a current density value used and each of the profiles presented within corresponds to one of the investigated etch durations. Further and superimposed upon the profiles are the surface texture measurements, these will be discussed in the following section.

The result matrix illustrates that although the aperture is a relatively large feature (10 X 10mm) when compared to etch bands (e.g. 0.2mm) in p.c.m., the 'W' shaped profile predicted in chapter two can be clearly seen. The undercut of the resist stencil was not quantified at this stage of the work. Hence the profile has an imposed cutoff of the dimension of the aperture (i.e. 10mm). Relatively better profile symmetry was noted in the central column. It can be seen that the adjacent columns on either side contained profile results which are asymmetric about their centres. Generally deeper etching on the side closest to the matrix centre were recorded and may be attributed to the aperture misalignment with respect to the parallel cathode area. This is illustrated schematically in figure 4.23.

There is a general trend that with increased depths of etch, the 'W' profile tended towards a 'U' profile. The latter is not achieved because of the high aperture width to depth of etch ratio. Hence for narrower lines and as the depth of etch increases the two troughs of the 'W' profile were predicted to blend to form 'U' shape.

4.7.3 MASS OF METAL REMOVED

The results for the mass of metal removed are tabulated and plotted in figures 4.24, 25, 26 & 27 for the etch durations of 5, 10, 15, and 20 minutes. Linear regression was used as this produced the best fits to the experimental results and were also plotted in the above mentioned figures using 'CURVE'.

From the individual equations obtained for all the above etch durations a general equation may be extracted. The mass of metal removed (m)=0 @ t=0, therefore the intercepts for all four equations (YHAT) in the above mentioned figures are not used. The coefficients of the variable term are plotted versus the etch duration (t) as illustrated in figure 4.28. where a further analysis of variance was carried out also yielding a linear fit. Hence the following empirical equation (22) for the mass of metal removed in terms of current density and etch duration for AISI 304 stainless steel in 10% w/w HCl at $25^{o}C$:

$$m = J\,(0.15\,t + 0.16) \qquad \ldots\ldots(22)$$

Where 'm' is the mass of metal removed (mg), 't' is etch duration (mins.), and 'J' is the current density (A/dm^2). The experimental results are further plotted simultaneously in figure 4.29 for all four durations.

4.7.4 SURFACE TEXTURE RESULTS

A 'Talysurf 4' was used to measure the surface texture of the etched apertures. The 'Ra' of the surface was measured and repeated four times using a sample cut off length of 0.8mm which corresponds to the 'K' setting on the instrument.

The peak-to-valley (PV) measurements are also established by direct measurement from the trace produced by the instrument. This was by measuring the difference between the highest peak and the lowest valley about the centre of the trace.

The 'Ra' and 'peak-to-valley' (PV) results for each etch duration are tabulated and plotted in the same figure. Figures 4.30, 31, 32, & 33 are the results for the etch durations 5, 10, 15, and 20 minutes respectively.

The 'Ra' values at t = 10mins. for J = 80 and 90 A/dm^2 and similarly at t = 15 and 20mins. for J = 90 A/dm^2 are not presented. This was due to these values exceeding the maximum scale of 10um on the measuring instrument.

It can be seen in all the results a similar trend is exhibited, relatively low surface texture values in the order of 1um Ra and 10μm (PV) were recorded for current densities <60-70 A/dm^2. A rapid deterioration of surface textures occurred at higher current densities. This is due to intergranular attack, non uniform dissolution and vertical striations produced by the dissolution by-products streaming down the face of the aperture.

4.8 ANODE SURFACE BLACKING

Surface blacking of the anode was noted at current densities <20 A/dm^2 . At J>20 A/dm^2 the black layer began to break down starting

at the stencil edges and working inwards towards the centre of the aperture. This may be attributed to the relatively higher densities at the stencil/metal interface as illustrated in figure 4.34. Maximum blackness density was achieved at the current density at which the surface layer began to breakup. The degree of blacking is dependent upon the duration of etch and hence it is a function of the charge (I.t) at anode potentials <-250mV (v. SCE).

The black layer was easily removed by rubbing whilst still wet and it was wax like. When the anode is washed in cold tap water and allowed to dry at room temperatures, this black adhered strongly to the underlying steel. No analysis was carried out on the composition of this layer but it is thought to be an iron hydroxide initially which further oxidizes in air to form this adherent oxide layer. It is not a passive layer, as illustrated in the profile results of figure 4.22 at current densities of 10 and 20 A/dm^2.

4.9 RECOMMENDED PARAMETERS FOR ELECTROETCHING

Uniform dissolution of AISI 304 stainless steel can be achieved under galvanostatic etching if the electrolyte and its temperature are selected to prevent passivation of the steel surface.

Uniform galvanostatic etching in 10% HCl at 25°C was carried out at $J<60$ A/dm^2, this being the upper limit of uniform surface textures. Etching and surface blacking was noted at $J<20$ A/dm^2 with breakup of the black surface layer commencing at the resist stencil edges at $J>20$ A/dm^2.

The Ra was shown to increase with current density in the range $20<J<60$ A/dm^2 with typical results being in the range 0.25 to 2μm. At a current density of 50 A/dm^2, a recommended relatively safe current density, Ra values of 1.1 to 1.34μm were recorded. An etch rate of 10μm/minute is expected under such working conditions.

The Anode/Cathode orientation effects the current density distribution and consequently the metal removal profile. Hence care should be taken to orientate the anode with respect to the cathode so that no adverse etching results may occur and as a general rule, symmetry is recommended.

5.0 NUMERICAL AND EXPERIMENTAL ASSESSMENT OF E.P.E. PARAMETERS.

The photoetching parameters in p.c.m. have in the past been quantified in terms of the depth of etch and the photoresist undercut, the latter being caused by metal removal taking place under the resist stencil [15]. The relationship between the two values, the depth of etch to undercut ratio is termed the etch factor (e.f.) and is another form of quantifying the process. Hence a good etching result, is that where the undercut value is small relative to the depth of etch. This is indicated by a high etch factor value. There is no reason why the same methodology could not be applied to e.p.e. or e.p.p although the mechanisms of dissolution are obviously different.

In pcm the overall depth of etch is determined by etchant spray pattern uniformity over the entire surface of the substrate. The etchant impingement density is essentially the uniformity determining factor and therefore mechanically controlled.

A model simulating the micro current density defined here as the current density over an individual surface feature was achieved. It was applied throughout this work to simulate constant overpotential conditions.

Due to computational limitations in terms of cost and resources the program featured a maximum grid array of 100x100 nodes.

The replacement of the electrolyte continuum by a square mesh results in a finite error of the potential values. Determining the accuracy of the simulation a priori is not possible. Accuracy is controlled by a number of factors one of which is the mesh size. Guidelines on error criteria for similar modeling have been proposed [81], whereby for grid spacing the current density change between successive surface nodes should be <15%. The recommendation was obtained from work carried out on a smooth function (sin) where the change in current density between nodes is relatively small. Due to the rapid change in the current density at the proximity of the insulator edge this recommendation was found to be too stringent. Therefore the maximum available resolution was used over a maximum cell width of 0.5mm (ie 5μm grid).

Initial experiments were carried out testing the effect of increasing the mesh size to 10μm which resulted in a profile change <1%. Based on this, 5μm was used almost exclusively throughout the work. Although for one test the resolution was reduced to 10μm to simulate a cell 0.8mm wide.

The size of the steady state steps was determined by the specified charge. The charge per time step was controlled to achieve boundary

movements not in excess of 10μm and typically of the order of 5μm. The reason being is to strike a balance between the solution accuracy by reducing the steady state time interval and the errors introduced by interpolating back to the original abscissa at each profile.

The size of the time step has an effect on the shape of the final profile. The error in the quasi-steady state approximation should decrease with an increase in the number of time steps for a given charge. As the boundary ordinates must be interpolated back to the original abscissa coordinates at each time step a cumulative error is introduced.

Further restriction was the simulated depth of etch, where convergence was not achieved at depths typically in excess of 60μm. It also was dependent on the feature dimension, greater difficulties were encountered with narrow features.

A method for assessing the accuracy of the model was by comparing the anodic and cathodic current values. These were in the order of 0.5% at the final boundaries.

By reducing the grid spacing, convergence criterion, and time step interval, a more accurate solution is likely to be obtained. The disadvantage in arbitrarily reducing grid spacing and time step interval is that the execution time in the computer increases.

The optional smoothing was not used as this generated profile errors due to the accuracy limits of the computer (VAX 11/782) working in single precision. The polynomial fitted exceeded the computational resources.

The smoothing routine functions by fitting a polynomial equation to the boundary points where the RMS error is user specified. This treats the entire surface of the substrate as a single entity. Therefore areas shielded by the insulater (dielectric) were also disturbed.

5.1 THE RESOLUTION CHART

i. PRACTICAL CHART

A resolution test chart was utilised in the past for quantifying the p.c.m. parameters [2]. This was a variant of resolution chart by Sayce [17]. The use of this chart provided a series of graded parallel lines, the form of which was convenient for section cutting of sample for inspection. This type of chart was found to be unsuitable for electrolytic photoetching. The reason being that this type of chart utilises a fixed relationship between the line gap and the line width adjacent to it. Hence as the lines become smaller, the distance separating them also decreases. In initial tests, no adverse results were encountered in using this chart provided that the depth of etch was limited. If further etching was

carried out, this resulted in blending of the narrower lines and subsequently in the lifting of the photoresist layer.

In chapter 2 the field plotting results have shown that the potential gradient is symmetrical about the centre of the resist layer separating two anodic areas of unequal width. This indicated that the current density distributions upon the anodes at the proximity of the resist edges are similar. Therefore based on this result it may be assumed that the value of the undercut of the resist layer between adjacent lines are also equal. This assuming that the current density distribution does not change after etching has taken place.

Therefore another chart was produced, where a fixed line separation was used. In addition a simpler linear relationship between adjacent lines was utilised. The range of line widths investigated were between 0.050mm and 1.6mm and details of the chart are illustrated in figure 5.1a and 5.1b where it can be seen that the interline relationship described by the equation below was implemented.

$$L_{(n)} = 2 \times L_{(n-1)} \qquad \text{where, } n = \text{line number}, \; L = \text{line width}$$

ii. SIMULATED CHART

The micro distribution has been previously defined. The macro current distribution is that over the entire substrate surface (i.e. including the resist) and subsequently determined by the size and distribution of the features upon the investigated surface.

Most practical applications are for non uniform etching patterns, and generally the most commonly required metal removal.

The practical requirement in general is a combination of patterns of different sizes and distribution over a substrate surface. Taking a single feature in isolation for investigation is of relatively little practical use. On the other hand taking a practical application for analysis is of little contribution to further work. A system for quantifying the effects of the macro distribution upon that of the micro distribution is desirable. Hence a chart is a logical approach.

The simulation of an entire chart is not practical as the resolution (100x100) decreases with increased cell size. Therefore to overcome this restriction it is proposed that a series of cells are spliced together to generate a 'quasi-chart'. This determined the design of the 'element cell' used in this work.

The model features axial symmetry about the centres of two etched features on the same substrate, separated by an insulated surface.

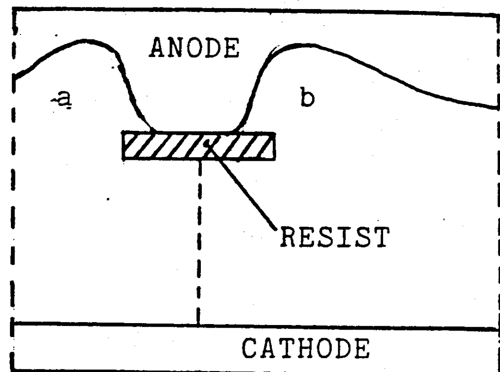

The position and size of the insulator is user specified, therefore the features 'a' and 'b' above are selected by determining the start and finish of the insulator [f(j)]. The feature centre depth is measured for a given run and a chart may be approximated by splicing two or more cells together, for example splicing half feature 'a' of cell one to 'b' of cell. By arranging equal depths of the spliced features, the other two features on both cells may be quantified. In this method it is assumed that the field potential on either side of the normal at the centre of feature is not equal. The graphical results of the potential field of two adjacent features indicate that there is potential symmetry about the centre of the insulator dimension. The applied method is obviously an approximate approach for solving large cell configurations and there is potential for improving the model which will be discussed later.

5.1.1 EXPERIMENTAL PROCEDURES

The material used was again AISI 304 stainless steel (App.I). The sample plates were also the same as those used previously and of the same batch (i.e. 52mm square X 1.63mm thick).

Degreasing was by acetone swabbing. This was followed by suspension in a CD/70 (1:5) solution for 10 minutes. The samples were then thoroughly washed in cold tap water, and also followed by a further rinse in distilled water. These are then dried using filtered and oil free air and then further dried in an oven at a temperature of 80°C for 20 minutes. The samples were then allowed to cool down to room temperature.

The photoresist used for coating those samples was 'Waycoat SC180' (App. L). This a liquid negative working resist, was thinned with xylene to achieve a viscosity of 60 zahn sec. [18]. The ratio was approximately 70% v/v resist to 30% v/v xylene. Viscosity was measured using a No.1 Seta zahn cup viscometer.

Samples were coated on both sides using the dip-coating method, this by withdrawing the sample vertically at a controlled rate through the meniscus of the photoresist [18]. The withdrawal rate used for all the samples was 100mm/minute. This yielded a dried resist thickness of 3μm as measured by digital micrometer. The

coated samples were allowed to air dry for a minimum period of 30 minutes prior to pre-baking in an oven temperature of 90°C for ten minutes. Residual solvents were expelled by the first stage and hardening of the resist layer and an improved adhesion by the second.

The exposure of the resist layer was with the aid of a high pressure mercury vapour UV light source as described in chapter 3 and illustrated in figure 3.4. The mask was made marginally smaller than the sample plate so as to prevent the emulsion from lifting off the resist when vacuum contact force was applied. The emulsion side of the mask was put in contact with the resist layer and mounted in the vacuum frame illustrated in figure 5.2. After establishing the correct exposure time of 45 seconds, using a Kodak T14 density scale [95], both sides of the resist were exposed. The reverse side was also processed to protect it during electroetching.

Development of the exposed resist was by immersing the sample into a solution of 60% xylene and 40% white spirit for a duration of 30 seconds. This caused the unexposed areas to dissolve in to the developer leaving an adherent polymerized stencil, and this is washed immediately in cold running tap water. The sample is then dried by the gentle application of filtered and oil free compressed air. Prior to post baking at 120°C for 15 minutes, all samples were inspected for faults.

The sample edges were protected using PVC tape to ensure the correct current density upon the surface. A sample retainer was built from acrylic sheet using a suitable cement, the dimensional details are given in figure 5.3. This was built to facilitate double sided etching, although for this application a single cathode was used facing the apertures on the anode face. The instrumentation and power source were as used previously in chapter 4 for the galvanostatic etching.

The electrolyte was 10% w/w HCl acid solution and this was brought to the working temperature of 25°C with the aid of a hot plate. A magnetic follower was used to briskly agitate the electrolyte.

The recommended galvanostatic etching conditions (chapter 4) were used and the current value setting on the galvanostat was calculated on the basis of a current density of $50A/dm^2$. The total area of the anode defined by the stencil was $78.75mm^2$. This required a cell current of 394mA to achieve the current density. It must be noted that as the etched profile develops the value of the current density decreases due to the increase in anode area.

5.1.2 THE UNDER CUT OF THE RESIST

A direct measurement of the resist undercut was used [15]. This is a method whereby the undercut is measured directly using a microscope and graticule. The advantages of this method are, reliable evaluations of undercut, and in addition the undercut may

be measured at any point along the etched line. The undercuts were measured and calculated by the following method:

U = 0.5 (B - A)

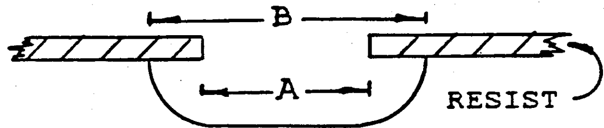

where A = The stencil line width
B = The etched slot width
U = The resist undercut

Three magnifications were used, and gave the following graticule calibration results:

Magnification	Scale Division (μm)	Measured Line Width (mm)
x 40	22	1.6 and 0.8
x 100	9.3	0.4, 0.2, and 0.1
x 400	2.4	0.5

The dimension 'A' was found to be essentially the same as that of the opaque portion of the mask. This is mainly due to the rejection of substandard workpieces. The dimension 'B' was recorded by sweeping along each line of the chart for the maximum reading.

The samples were etched at current value of 394mA with the aid of the galvanostat (App. O). This value was monitored throughout the tests with a Sinclair DM450 digital multimeter. No deviation from this setting was detected.

A range of etching durations between 3 and 15 minutes and in increments of 3 minutes were used. The samples were then carefully washed in cold tap water taking care not to damage the resist. This was followed by a similarly careful drying operation using clean compressed air at a low flow rate. Undercut measurements were then made on the microscope.

The calculated undercut results are tabulated in figure 5.4 to 5.8, corresponding to the etch durations of 3, 6, 9, 12, and 15 minutes.

The analysis of variance (AOV) of the results were carried out with aid of the'HP85A' computer and the curve fitting program (CURVE) (App. Q). A power curve yielded the best fit for the undercut data. The result of the analysis and the plot for each group of data is also presented in its relevant figure. In general the undercut trend tended to increase with a decrease in line width for all etch durations. A general empirical equation for undercut in terms of original line width and etch duration was derived. This from the

experimental results, by deriving the two equations for the coefficients of the power fits versus etch duration in figures 5.4 to 5.8. The AOV for this is illustrated in figures 5.9 and 5.10 respectively. The following is the general equation for undercut for an AISI 304 stainless steel/HCl system:

Undercut,

$$U = 79.887\, t^{0.181} \cdot A^{(0.007t-0.133)}$$

where,

A (µm) = Stencil line width
t (mins.) = Etch duration in minutes.

5.1.3 DEPTH OF ETCH RESULTS

The results for the depth of etch were obtained by cross sectioning the same samples used for the undercut measurements. The samples were first stripped from the resist stencil layer, this with the aid of 'Hunt Microstrip'. The excess metal adjacent and parallel to the lines was cut off. The samples were then cleaned and degreased with acetone and this was followed by further submersion in an aqueous CD/70 (1:5) solution for 10 minutes. These were then washed in tap water and then dried using filtered and oil free compressed air.

The embedding media was a thermosetting optically clear casting resin. An Araldite system of MY753 plasticized liquid epoxy resin and HY953 hardener with a ratio of 100 parts to 18.3 parts by weight respectively was used, as recommended [19].

The 'Metaserv' moulds were waxed with 'bees wax' and samples were retained in the mould in a vertical orientation with the aid of two stainless steel plates (150µm thick) suitably bent at an angle of 90 degrees. These strips of supporting metal were mounted on either side of the sample plate with the two extremes of the 'L' shape in contact with sample as illustrated in the figure below.

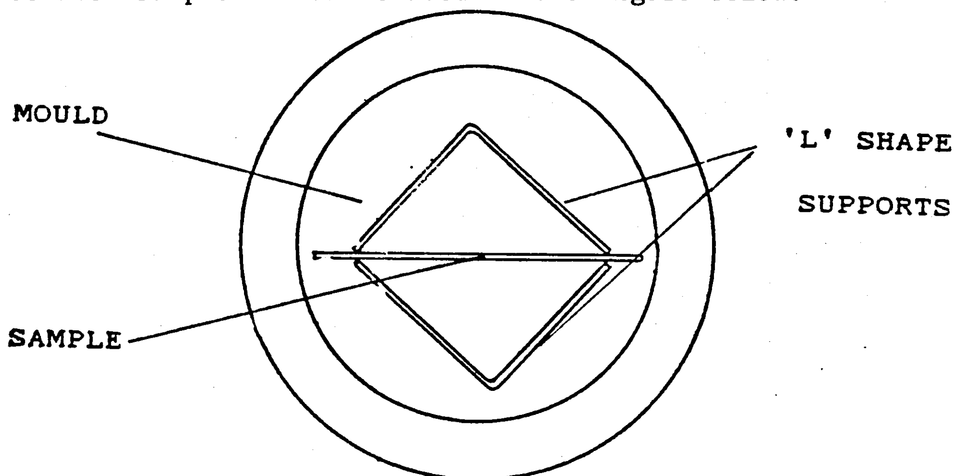

The assembly was installed in the two parts of the polythene moulds (40mm dia. x 25mm deep) and in situ in a vacuum desiccator. The

mixed potting components were poured carefully into the mould, ensuring that the plates were not disturbed. Vacuum was applied to the desiccator to remove the air bubbles entrapped by the mixing of the resin. Limiting of the duration of the vacuum application was used to prevent excessive surface frothing. This was then left for a period of 24 hours at 20°C to allow the resin to fully cure. The mouldings were then removed from the moulds and prepared for sectioning.

The mouldings were put in the chuck of a 'Metaserv' cut-off machine and sliced into two halves orthogonally to the etched lines. This was followed by polishing of the specimen surfaces to be inspected, and as recommended [19] for the preparation of samples for microscopic examination.

The sectional profiles of the range of etched line widths were photomicrographed using a 35mm camera attachment on the Vickers M41 Photoplan microscope. Those results are illustrated in Appendix T. Estimation of the depth of etch method was used [15] for quantifying the depth dimension from the cross-sections of the results. This by direct measurements with the aid of the graticule previously calibrated in 5.1.2.

The measured results were those of the depth dimension at the centre of the etched line. Those are tabulated and plotted (using 'DPLOT' App. Q) in figures 5.11 to 5.15 which correspond to the etch durations of 3 to 15 minutes in steps of 3 minutes respectively. Further the results were re-plotted manually and simultaneously for the five etching durations as presented in figure 5.16, giving a graphical illustration of the data.

The results confirm the predicted relationship (Chapter 2) between the depth of etch at the centre of the feature and the original line width. Although it is believed that other process features are also superimposed on the results, an apparent optimum depth of etch for all etch durations exists for an original line width of between 100µm and 300µm. It is also apparent that the depth of etch for line width values smaller than those where the peak depth occurred at, tended towards a very low value and have a large gradient. This result, for original line width values greater than 200µm, agrees qualitatively with the predicted trend of chapter 2 for the differences in depth of etch at the centre between two adjacent and parallel lines.

The existence of a maximum in the results for depth of etch versus line width may be attributed to the physical restriction on the electrochemical reaction caused by the relatively small features defined by the resist stencil. This in general is noted for line widths smaller than 200µm. Replenishment of the electrolyte in the etched feature is believed to be restricted, and hence the decrease in metal dissolution due to the stifling of the electrochemical reaction caused by localised concentration polarization in the affected anodic areas.

Hence features smaller than 200μm are not recommended due to the high sensitivity of depth of etch to variations in original line widths.

An empirical equation describing the depth of etch in terms of original line width and etch duration was obtained from the experimental data. Using the curve fitting program ('CURVE' App. Q), linear correlation produced in general marginally higher coefficients of determination values (R SQUARE), indicating a better fit than those obtained for a power relation. The analysis of variance (AOV) and data plots are illustrated in figures 5.17 to 5.22 corresponding to the data for the depth of etch versus the etch duration for the original line widths of 50, 100, 200, 400, 800, and 1600μm respectively. From those results it can be seen that power fits were selected. A table of AOV results (Fig. 5.23), illustrates the relatively higher coefficients of determination values obtained when linear regression is applied. Nevertheless, power fits were used because at t = 0, DE = 0. Whereas for linear regression high intercept values were recorded.

The correlation coefficients 'a' and 'b' for a general power equation describing the depth of etch in terms of original line width and etch duration are calculated in figures 5.24 and 5.25 respectively. These were obtained by plotting the relevant coefficient from the equations in figures 5.17 to 5.22, versus the line width. Hence the general empirical equation:

$$DE = 117.4A^{-0.33} \cdot t^{(0.13\ \ln.A-0.07)}$$

where, A = Original line width (μm).
t = Etch duration (mins.)
and DE = Depth of etch at the line centre (μm).

5.1.4 ETCH FACTORS

The etch factor is defined as the ratio between the depth of etch and the resist undercut [15]. The results of depth of etch and photoresist undercut measured in sections 5.1.2 and 5.1.3 were utilised for calculating the etch factor results (e.f.). The etch factors values versus original etched line width are tabulated and plotted in figures 5.26 to 5.30 for the etch durations of 3 to 15 minutes respectively and in steps of 3 minutes.

The results were calculated as:

$$e.f. = \frac{\text{measured depth of etch (at centre)}}{\text{measured photoresist undercut}}$$

From these results and on first inspection, the trend is similar to that of the depth of etch measurements, where a maximum exists in

the line width range of between 50 and 300μm. A general increase in the etch factor with etch duration was noted. This is illustrated numerically and graphically in figures 5.31 and 5.32 respectively, where the matrix of etch factor results were obtained by substituting values equal to those used experimentally back into the ratio of empirical equations for depth of etch and undercut. This was not intended as a method for obtaining an expression for etch factor but merely as a method of pooling the experimental data to illustrate the general trend for etch factor in terms of original line width and etch duration. Figure 5.32 is a three dimensional plot illustrating the increase in etch factors with increase in etch duration and simultaneously the effects of line widths upon the result. The results were obtained from the following expression for etch factor:

$$e.f. = f(A,t)/F(A,t)$$

where, $f(A,t)$ = The derived equation for depth of etch.

and, $F(A,t)$ = The derived equation for undercut.

5.2 DOUBLE SIDED ETCHING

The production of components from metal foils is usually carried out by double-sided etching, this with the aid of a registered pair of photo-tools. The aims of this investigation were to quantify the double-sided etching performance of e.p.e. of AISI 304 stainless steel.

In the work carried out in this section a double-sided tool was utilised for the production of three parallel 220μm wide lines in a material thickness of 150μm. The art work for this had been previously prepared by Mr. I.Routledge and Dr. G.W.W.Stevens and used by Mr. K.K.Cheung [102] for his work. This tool was initially designed for a reduction 20:1 to produce a line width of 250μm. The reason for selecting this width is based on the results of the previous section.

The reduction camera was suitably adjusted to produce a reduction of 22.73 from the original art work. This gave the required line width of 220μm. The dimensions of the tool are given in figure 5.33.

5.2.1 EXPERIMENTAL DETAILS

Strips of AISI 304 stainless steel (App. I) 30 x 70mm and 150μm thick were cut from a larger sheet. These were degreased, washed, dried, and coated with 'Waycoat SC180' negative working resist and the sample plates were processed in general in a similar manner to that in section 5.1.1. The exposure stage differed slightly due to the type of tool where the component was positioned in the tool prior to mounting in the exposure frame. Exposure duration was

found to be the same as that for single sided etching, and was made on both sides of the sample.

The current value at which the galvanostat was set, was calculated from the previously recommended current density of $50A/dm^2$. The total area of the features on both sides of the sample to be etched was calculated, as follows:

Features	No.off	Dimensions (mm)	Area (mm^2)
Reg. marks	12	1.056 x 1.056	13.382
small squares	16	0.22 x 0.22	0.774
lines	6	15 x 0.22	19.800

The total area = 33.956 mm^2

Hence to achieve an anode current density of $50A/dm^2$, a current value of 170 mA was set at the galvanostat.

Exposure of the photoresist layer was with the aid of high pressure mercury vapour light source. The vacuum frame previously used for the exposure of the resolution chart was also used for this application. This ensured the necessary good emulsion to photoresist contact (Fig. 5.2). The photoresist coated metal was sandwiched between the mask pair, and both sides were exposed without removing the vacuum, thus eliminating the possibility of misregistration that could occur otherwise.

The exposure time was again determined with the aid of the Kodak T14 density scale. The correct exposure time of 45 seconds per side was used.

The resist development was similar to that of section 5.1.1 with the added precaution of ensuring that the developer was in contact with both sides evenly.
After suitable washing, drying and post baking the sample edges were protected with PVC insulating tape.

Etching was carried out vertically in a glass beaker with a 10% w/w HCl solution. The samples were mounted in an acrylic jig (Fig. 5.3) and in turn partially submerged in the electrolyte. A double cathode arrangement was used and lead (Pb) sheet (1mm thick) was the cathode material. In figure 5.34, a schematic diagram of the cell, the equipment, and instrumentation can be seen. Etching was carried out at a temperature of 25°C and this was controlled by a thermostatic hot-plate incorporating a magnetic follower.

The samples were etched for 6, 8, 10, 12, and 14 minutes. After etching, each of the samples was carefully washed in water and dried. The undercut on all of the samples was then measured on the microscope with the aid of the graticule. Figures 5.35 to 5.37 contain photomicrographs of the etched results corresponding to the

etch durations of 6 to 14 minutes and labelled 'a' to 'e' respectively. Measurements were made on all three lines and the maximum undercut in each line was recorded. The average result for each group of three readings was then used in the plot illustrated in figure 5.38 for undercut versus etch duration in double-sided etching.

5.2.2 PROFILE DEVELOPMENT RESULTS

The current density distribution differs in the 'post break-through' to that for 'non-break-through' etching and this is reflected in the sectional profiles of double-sided etching.

The samples were sectioned and prepared for microscopic examination in a similar manner to that of section 5.1.3. Sections were photomicrographed using the microscope 35mm camera attachment. The graticule was also photographed as a measurement reference. The negatives of the results were then projected with the aid of a photographic enlarger on to a 1mm grid screen (A3 size graph paper). The profile measurement was by centralising the projected image on a cross marked in the middle of the sheet (screen) thus dividing the image into four sections. The quarter profile in each section was then measured, the average profile was calculated by taking depth measurements at suitable intervals and summing the values for each point and dividing this by four. The measured cross-sections are illustrated in figure 5.39.

The average results are tabulated and plotted in figures 5.40 to 5.44 corresponding to the etch durations of 6, 8, 10, 12, and 14 respectively. The number of measurements taken along the profile varied between the sections and this was dependent upon the quality and length of the profile. The results were replotted manually in figure 5.45 illustrating the development of the double-sided etched profile with etch duration. It can be seen that the 'W' profile exists in the 6 minute result (a) only. The section thereon is that of a 'U' shape. At this depth of etch surface break-through occurs at the centre of the etched line, and if a thinner material was used (e.g. $<40\mu m$), break-through would have taken place at two different points along the profile. Hence the type of break-through is a function of the line width and thickness of the material. From the same result and for profiles 'c' and 'd' it can be seen that the metal recedes rapidly in the resist edge direction, the average rate being in the order of $40\mu m$/minute. This may be attributed to the relatively high current density on the tip of the profile as generated by break-through.

A graphical illustration of the actual undercut value and its development with etch duration is also illustrated in figure 5.45, illustrating that for short etch durations poor etch factors should be expected for this alloy/electrolyte combination.

The electroblacking feature of the HCl/stainless steel system may find an industrial application. The e.p.e. of precision steel

rulers as used in engineering may be possible on a commercial basis. Etching can be followed by electroblacking at a lower current density producing the desired contrast between the scale features and the reflective metallic background. A limited investigation was carried out in this area and the results are presented in Appendix U.

5.3 NUMERICAL RESULTS

In the practical work it was assumed that the surface of the feature was etched at approximately the middle of the active zone range. This was based on the results of the polarization measurements. These measurements characterised the overall anode area investigated, and hence it does not strictly describe the dissolution mechanisms taking place across the etched feature surface.

Modeling with one type of current density dependent polarization in preferance to another can only be an over-simplification and in the extreme be misleading. Further investigation into the mass transport, concentration effects and diffusion layer properties and dimensions within the feature and at the sub-resist level is required.

The model at present treats the area above a finite diffusion layer thickness as bulk electrolyte. It does not take into account the resultant effects of electrolyte entrapment between the metal surface and resist layer after undercut has taken place and its subsequent effect on concentration in this zone. Therefore for this work a constant polarization was assumed throughout. The general cell specifications were:-

Temperature	$25^{\circ}C$
Electrolyte conductivity	$0.035\ \Omega^{-1}$
Constant polarization (A)	130 mV
Interelectrode gap	5 mm
Overrelaxation parameter (w)	1.85
convergence criterion	10^{-5} to 10^{-4}
calculated atomic weight	55.14 (Alloy)
Density	7.913 gms/cm^3
Calculated valency	1.97 (Alloy)
Efficiency	100%
coulombs per time step	Variable
Anode potential	5 volts
Cathode potential	0 volts
Max. field iterations	2000

5.3.1 Single line width simulation.

A series of qualitative results are presented in this section to illustrate the effects of maintaining a constant charge value in a

symmetrical cell of fixed width but varying insulator dimension. A cell 500µm wide was simulated, featuring a fine mesh of 5µm. Hence, the total number of cell columns equals 100.

A series of graphical results illustrating the solution were directly plotted by the program. These are presented as figures 5.46 to 5.51 and correspond to the insulator/feature dimensions as tabulated below:

		Insulator			feature
Plot No.	Figure No.	start row	finish row	dimension (µm)	size (µm)
1.	5.46	41	61	100	200
2.	5.47	36	66	150	175
3.	5.48	31	71	200	150
4.	5.49	26	76	250	125
5.	5.50	21	81	300	100
6.	5.51	16	86	350	75

The dimension of the insulator is graphically represented on the secondary abscissa in each plot to illustrate the position of the insulater w.r.t. the surface.

Results obtained clearly illustrate the charactaristic 'W' profile as it develops with time or depth. Other feature dimensions such as the undercut can clearly be seen. On inspection, the results illustrate that with increased depth or reduced feature width the profile will tend towards 'U' section.

In this series of results the total charge was constant. The number of coulombs per time step was 1.5. Undercut was measured directly from the graphical results (i.e. point of profile interception of the origin) and the accuracy is restricted by the array resolution of the 100 columns. This gives a measured accuracy of +-2.5µm as the limit of this method. Measured undercut results for the above plots are as follows:

Plot No.	1	2	3	4	5	6	units
Undercut	*	48.9	50	52.1	54.2	58.3	µm
Depth max.	28	33	38	44	51	#	µm
e.f. max.		0.67	0.76	0.84	0.94		
Depth cent.	22	24	27	32	40	#	µm
e.f. cent.		0.49	0.54	0.61	0.74		
Delta e.f.		0.18	0.22	0.23	0.2		

* The undercut cannot be measured as feature blending occurs (i.e. the undercut>half the insulator).

The depth results of the last profile were not tabulated as the required number of profiles (10) was not met due to solution divergence during the calculation of the tenth profile with 2000 iterations. This result was presented as such to illustrate a limitation encountered prior to resorting to parameter modifications such as the convergence criteria.

The results presented above illustrate qualitative similarities with the practical results previously discussed.

Investigating the difference in results between the maximum feature depth and that at the centre as expressed by 'Delta e.f.', a maximum value exists (plot 4). This is the maximum depth differential point beyond which the sectional profile tends towards that of a 'U' shape with increased depth.

5.3.2 Simulated resist damage.

A problem encountered in general p.c.m. work is the non homogeneity of the resist layer possibly due to inclusions and in particular with liquid photoresists. Probably due to the small size of the break down sights, the label "pin-hole" is used. During the experimental work it was clear that the problem becomes relatively more acute with electrolytic etching and the damage level is far greater than that encountered in conventional chemical spray etching.

An experiment was set to test this by simulating an arbitrary pinhole in the insulator. The smallest dimension possible was that of one fine grid size (5µm) being equivalent to a pin hole of 10µm. For comparison this was simulated adjacent to a feature 220µm wide. The insulator dimension is hence 380µm as the cell utilised was 500µm wide.

An arbitrary charge of one coulomb was used with similar conditions to those of section 5.3.1. The result is presented in figure 5.53 illustrating that the pin-hole on the LHS of the diagram etched to a depth of 54µm while the centre depth of the feature on the RHS is 42µm and the maximum depth of the same feature is 56µm.

This result is not strictly an accurate representation of pin-hole effects and should be taken as an indication of the effects of primary current density on small features. In practice such depth ratios are not common due to the concentration limits within the pin-hole imposed by the physical restriction of the resist hole size. As the model does not take this into account, the media in the pin-hole is assumed to be bulk electrolyte. Neverless, from this result and at the initial stages of the dissolution, the damage is probably caused by a similar mechanism to that simulated.

5.3.3 Electro photoforming (epf)

This is a related subject to e.p.e. and e.p.p., where metal is electrolytically deposited on the areas of the substrate defined by a photoresist stencil.

Although this subject is outside the scope of this work a modification to the program allows the simulation of e.p.f. and a sample is therefore presented in figure 5.54 and 5.55 illustrating cells 500μm wide and with defined features of 50 and 600μm (total width). Retaining identical conditions for both plots the first was electro etched and the second was electroformed. A further simulated e.p.f. result is presented in figure 5.56 with an insulater 100μm wide positioned at the centre of the cell. The number of boundaries generated in this case was increased until the simulated resist was over-plated.

No attempt was made to quantify these results they are merely presented to illustrate the flexibility of the model and perhaps stimulate interest in further work in this area.

5.4 SIMULATED CHART

The geometry of the practical chart was simulated by numerical quasi-chart. Due to constraints imposed by the specified dimensions of the computer model which in turn were determined by the allocated computational resources, the simulation of an entire chart with suitable resolution as a single entity was not feasible. Hence a method was utilised for quantifying the effect on the feature current density when approximating continuum of a chart. This was by splicing together minor cells similar to those described previously in section 5.3.1.

A maximum cell width of 500μm with a resolution of 5μm was utilised. The upper dimensional simulated line widths in a minor cell were 200 and 400μm separated by a 200μm insulator (resist). The minimum simulated line width was 50μm. The reasons for the latter limit are the problems encountered and described earlier (#) in section 5.3.1, this coupled with discrepancies in excess of 2% between the calculated anodic and cathodic currents for features <50μm prevent further reductions of the line width.

Increasing the fine grid size to 10μm facilitates the inclusion of the 800μm line to extend the simulated range. Only the depth results were utilised from this simulation as increasing the mesh size exhibited a significant dimensional error of resist undercut.

The charge per time interval was set to achieve a small step of 5 to 10μm to satisfy the guidelines [81] for a steady state solution, whereas at the same time provide a method of finally controlling the depth at the centre of the feature. The latter is coarsly set by specifying the total number of time steps. Depths at feature centres are measured at the extremes of the minor cell i.e. at columns 1 and 'j last'.

Hence the simulated line widths are:-

Cell feature	A a b	B a b	C a b	D a b	units left right
Lines Tot.width	50-100 275	100-200 350	200-400 500	400-800 800	(µm) (µm)

The two central cells 'B and C' contained the pivot points. Where the pivot is the value of the feature centre depth at 'a of B' and 'b of C' (i.e. the two 200µm features). The centre depth at each of these features in both cells was set to an experimentally derived value (34µm). This was a depth value achieved in an etch duration of three minutes. The cell set up is schematically represented in figure 5.52.

The principle of this technique is to assume axial symmetry of the potential field about the normal at the centre of the insulator. This appears to be a valid assumption for a minor cell individually (e.g. A or B etc.) and is supported by the results of the graphical plots of chapter two. Therefore, the profile in each feature is determined by the potential field of the minor cell and is independent of that in the adjacent minor cell. This obviously is an approximation, but the depth of etch at the centre of each feature is arranged to be equal in value to that of the adjacent cell when two cells are spliced. The results for depths and undercut are quantified by working outwards from the pivot points in both directions. The mean of the maximum depths of adjacent minor cells is assumed to be the representative result.

Hence, the assumption may be summarised as the current density on any half side of a feature is independant of that on the other half and each side is determined by its corresponding potential field.

5.4.1 Results of the numerical chart.

As above, when two cells are spliced (e.g. A and B), the centre depths of feature 'b' in cell'A' is arranged to equal that of its counter half of cell B(a). From cell 'A' the maximum depth of etch in features 'a' and 'b' may be then measured in addition to the centre depth of feature 'a'. The latter may then be utilised for setting the following cell in the chain.

From the overall result, numerical and graphical data is obtained. The numerical data for each cell was further analysed and this shall be discussed in the following section. The graphical representation of moving boundaries are plotted from the program utilising a computer library routine 'GINOGRAF' and the results are illustrated in figures 5.58 to 5.61 corresponding to cells 'A' to 'B' respectively.

5.4.2 Analysis of chart results

Similar to previously discussed results, the development of the 'W' profile into a 'U' sectional profile may be clearly seen. The profiles of the 50μm line in cell'A' are of a 'U' section throughout. In the same cell and for the 100μm line it can be seen that due to the relatively small difference between the centre depth and the maximum depth coupled with the main slope of the profile the section will move from a 'W' to a 'U' with a suitable increase in depth. From this it may be concluded that feature width to depth ratio is one of the profile determining factors. Another could be the mechanism of dissolution taking place inside the feature.

The resolution restriction is the main cause of the high measurement tolerance when directly measuring the undercut from the profile or data. An improved method for quantifying the value of undercut is by fitting a suitable function to a section of the etched profile and from which the undercut may be calculated. The selected profile length for this purpose is that directly under the insulator.

A cubic polynomial yielded the most suitable fit and the number of coordinates used depended on the profile depth and ranged between 8 to 14. A sample of the undercut results is illustrated in figures 5.62 to 5.67. The results presented are those of the final profiles of all features (cells A to D). The same method was also applied to when calculating the undercut values of the intermediate profiles.

Undercut results for each time interval and all surface features of the four cells were plotted versus the maximum depth at the relevant time interval.

A power function was then fitted to each group of results as illustrated in figures 5.68 to 5.73. The first derivative of each equation was obtained and those equations are also presented in the figures above. The latter operations were similarly repeated with the exception of using the centre depth rather than the maximum depth.

The derivatives dU/dDm related to the maximum depth group of data are plotted against the depth of etch in figure 5.74. Similarly in figure 5.75, results of the derivative dU/dDc from the centre depth group of data are plotted against relative depths.

Results in the last two figures illustrate how the rate of lateral to normal dissolution decreases with depth of etch. At approximately 10μm depth in both results, a value of one indicates that the lateral to normal dissolution rates are equal. It may be concluded that improved etch factors will be achieved for depths >10μm. It can be seen that for depths of etch in the order of 100μm the normal dissolution is approximately three times greater

than that of the lateral. Further, with greater depths of etch the repeatability in terms of feature lateral dimension should improve due to the reduced lateral rates. Based on these results, the process should be more applicable to deep etching provided no other constraints exist.

The relationship between the maximum depths of etch and the chart line widths were investigated. The average maximum depth for this purpose is taken as the mean of the two maximum depths measured at the interface of two spliced cells (e.g. line 100µm in cells A and B). The depths at the 50µm end of the quasi-chart is equal to the centre depth value ('U'section). The maximum depth at the other extreme of the chart (800µm line) is the last in the chain and hence not averaged. These results are plotted in figure 5.76 and from which the following equation is obtained:

$$D_{m\ av.} = 186\ A^{-0.238}$$

where, $D_{m\ av.}$ = Maximum average depth (µm)

A = Chart feature dimension (µm)

The relationship between the centre depths of etch and the chart line widths was similarly investigated. The depth results at the centre of the features versus the chart line widths are presented in figure 5.77 from which the following equation is obtained:

$$D_c = 284.76\ A^{-0.35}$$

where, D_c = Centre depth (µm)

The above two functions are simultaneously re-plotted in figure 5.78 with the experimental etching results for an etch duration of three minutes. Good correlation exists between the experimental data and that of the numerically derived equations for both methods of quantifying the depth of etch.

The undercut relationship with chart line width was also analysed and the resultant relationship is illustrated in figure 5.79 from which the following equation is obtained:

$$U = 94.3\ A^{-9.35}$$

where U = Undercut (µm)

The undercut equation above is replotted in figure 5.80 simultaneously with that of the empirical equation for undercut and the experimental results for electrolytically etching the chart in a duration of 3 minutes.

There is a qualitative similarity between all the results but the experimental result was lower than both the empirical and in particular the theoretical result. This is probably due to the entrapment of process by-products under the resist thus limiting the reactions in this zone. This was not simulated in the model. The same reasoning may be applied to the practical depth of etch results as illustrated in figure 5.78 where it can be seen that a limiting effect is taking place at the narrow line widths. The profile turns towards the origin rather than feature high values similar to those exhibited by the theoretical results.

6.0 THE ELECTROLYTIC PHOTOPOLISHING E.P.P. OF AISI 304 STAINLESS STEEL

Photopolishing may be defined as the selective smoothing and brightening of a metallic surface through a photographically produced resist stencil. Electro photopolishing (e.p.p.) differs only in that it specifies the mechanism by which the metal dissolution takes place. It is where the substrate is made anodic in an electrolytic polishing cell and the areas exposed to the electrolyte and the process are defined by a photographically produced resist stencil.

At the initial stages of the work industrial applications were not known for a system where electro photopolishing (e.p.p.) was required. It was thought that possible applications may arise where a high quality surface texture, and/or a relatively higher degree of specular reflection on selected areas of the substrate may be required. This is not possible in conventional p.c.m. where industrially used etchants such as aqueous ferric chloride are used. Although there are other chemical etchants that may be used for such an application, it is believed that with electro-polishing and due to its inherent smoothing capability, better and more controllable results may be achieved.

Suggested applications for this process might be in the field of control engineering where the production of linear or circular reflective gratings could be utilised in the feed back elements of motion control systems. Although no industrial requirements were known initially, further into the work certain industrial specifications necessitated the use of e.p.p., whereby the surface smoothing features of the process were utilised.

6.1 ELECTROLYTIC POLISHING

The discovery of electro-polishing may be attributed to Shpital'skii [11] in 1910. In 1930 Jaquet [103] published his first work on the electro-polishing of copper and nickel, and subsequently carried out a systematic study of many polishing baths, on the properties of electro-polished surfaces and the theory of the process.

Since Jaquet's initial publications, further explanations of the mechanisms of the process have been developed by a number of workers in the field, and various theories for electro-polishing have been suggested [34,37,40,104,105]. These explained the preferential dissolution of raised areas of the anode in terms of the properties of the layer of electrolyte in immediate contact with the anode. Procedure in most cases has been to determine certain properties of this layer and then to consider the likely effect on uneveness of the surface and whether the observed

properties could contribute to a levelling effect. Wagner [37] derived an analytical expression for an ideal electro-polishing process. This with other empirically derived equations by other workers provided extensive research in the field. A graphical method was used by Edwards [40], where field plotting techniques were utilised to explain the smoothing action caused by the high potential gradients at the proximity of peaks rather than valleys. Hence a resultant higher relative current density on the former. Further, he carried out an experimental study to determine the behaviour in a polishing solution of peaks and recesses on the anode surface.

The general interest shown by many workers in this field was possibly due in part to industrial requirements. An alternative manufacturing process that may successfully replace the labour intensive and costly mechanical polishing of metallic products was always sought after and was possibly one of the aims of the research. Electro-polishing is also used in laboratory work for the preparation of metallurgical samples for microscopic examination.

The metal or alloy to be electro-polished forms the anode in an electrolytic cell and the irregularities upon its surface are removed by the dissolution process in such a way that surface smoothing and brightening take place. This is a particular phenomena of anodic dissolution and is dependent upon the applied electrolytic cell conditions such as the electrolyte formulation, temperature, and anodic current density.

The microscopic inspection of a mechanically generated metal surface reveals a surface topography consisting of a series of hills and valleys. The ratio and frequency of those features is directly related to the manufacturing method of that particular surface. On macroscopic irregularities are superimposed smaller microscopic features. Both those irregularities must be removed resulting in smooth and brightened surfaces. Hence, smoothing is achieved by the removal of the larger scale irregularities which are typically greater than 25 μm and brightening is by the removal of the smaller irregularities down to 250 nm [9].

6.2 THE ELECTROLYTE

Due to the extensive work published, a range of electrolyte formulations suitable for the electro-polishing of a wide range of materials were available. The works by Tegart [9] and Shchigolev [10] contained information on formulations and operating conditions for the electro-polishing of stainless steels in general. Hence due to the availability of suitable formulations, it was considered unnecessary to further diverge into the design of electrolytes for the electro-polishing of AISI 304 stainless steel. A number of suggested formulations from the two sources above were investigated, and tests were carried out utilising those electrolytes. Electro-polishing was carried out through a square

aperture (20x20mm) defined by a photoresist stencil. The photoresists used for this work were, 'Waycoat SC180' negative working liquid resist, 'Laminar AM' negative working dry film resist, and 'Shipley AZ 340' positive working liquid resist (App. V). A series of tests were carried out on all three photoresists and using the recommended operating conditions as layed out in the above publications. The electrolyte selection was based on the following:

- i. Good polishing performance.
- ii. No adverse reaction with photoresists.
- iii. Unconditionally non volatile.
- iv. Relatively low cost.
- v. Simplicity and ease of preparation and handling.
- vi. Non toxic.

The results of those tests are outlined in Appendix N. and from this preliminary work a formulation as recommended by Tegart [9] was selected, this being :-

1. 300 ml orthophosphoric acid
2. 530 ml glycerine (sp. gr. 1.26)
3. 90 ml water

This electrolyte yielded an excellent surface brightening performance and did not react adversely with the photoresists tested. This formulation was initially referred to by Uhlig [105], where data concerning the degree of brightening rather than surface smoothing of 18-8 stainless steel were presented. The published data included the percentage of specular reflection in terms of the electrolyte temperature and current density. These relationships are illustrated in figure 6.1 where the percentage specular reflectance is plotted versus the temperature and the current density (J) simultaneously. These results clearly illustrate why Tegart recommended the electro-polishing parameters of $110^{\circ}C \pm 5^{\circ}C$, and a current density of $7.8\ A/dm^2$. He further recommended a polishing duration of 15 minutes. It must be noted that surface smoothing does not necessarily accompany high specular reflectance, as the latter can exist on rough surfaces with high Ra values. Insufficient data was available on the smoothing performance of this system and this necessitated part of the following experimental work.

6.3 THE SURFACE TEXTURE MEASUREMENT OF ELECTRO-POLISHED AISI 304 STAINLESS STEEL.

The surface texture of the AISI 304 stainless steel was measured using a 'Talysurf 4'. The material was measured prior to polishing and this resulted in surface values of 0.1 μm (Ra).

6.3.1 Sample preparation

Samples of stainless steel 1.63mm thick were cut into '51x51mm' squares. These were then degreased and cleaned by swabbing with acetone and followed by an immersion in a CD/70 (1:5 solution) for 10 minutes in an identical manner to that described in Chapter 4. The substrates were coated with 'Laminar AM' dry film photoresist, this with the aid of a laminating machine. Samples were then exposed to an ultra violet light source (Littlejohn) through a registered phototool. The tool was produced directly on the co-ordinatograph by cutting a square aperture (20 mm sq.). From this, and by contact printing a registered double-sided tool was made. The two sides of the tool were assembled using a 1.6mm cardboard spacer, and stapled together to produce approximate registration. This was sufficiently accurate for the required application. Samples were exposed through the above prepared tool to the UV light source on both sides simultaneously. This was followed by suitable developing in the spray developing machine as described in section 4.6.1. After drying the exposed samples' edges were protected using asphaltum 'Washout', this was in preference to P.V.C. insulation tape as the latter lost its adhesion properties and was softened by the elevated operating temperatures.

6.3.2 The electrolytic polishing cell

During electro-polishing, a suitably made acrylic jig was utilised to hold the samples vertically, the dimensions of this are in figure 6.2. This was mounted in a beaker, and a double cathode arrangement was used for polishing the sample on both sides simultaneously. The separation between the cathodes and the anode was 30 mm. The cathode material was also AISI 304 stainless steel of the same dimensions as that of the sample plate. Agitation of the electrolyte was with the aid of a magnetic follower. The set up is illustrated in figure 6.3.

The electrolyte was poured into the beaker, this was very viscous at ambient temperatures. The temperature of the solution was brought up to 110°C, and maintained at this temperature using the thermostatic hotplate. Polish durations of 5, 10, 15, 20 and 25 minutes were investigated and the current densities were varied for each of the temperatures in the range of 2.5, 5, 7.5, 10 and 12.5 A/dm^2. The cell current was calculated as follows:-

$$I = J \times Area$$

The total area = (20 x 20 x 2) mm sq. = 0.08 dm^2

From this the cell current corresponding to each required current density was calculated and the results are as follows:-

$J(A/dm^2)$	2.5	5.0	7.5	10.0	12.5
I(mA)	200	400	600	800	1000

6.3.3 The electrolytic polishing procedure

The samples were mounted in the jig between the two cathodes. Polishing was carried out in durations of 5, 10, 15, 20, and 15 minutes at the above calculated cell current values. The required current value was set on the galvanostat and monitored with the aid of a 'Sinclair DM450' digital multimeter.

Throughout the tests, the anode surface was observed and the formation of a viscous layer was noted on the surface. This layer was green in colour and was noted to be forming on the face of the anode and streaming past it towards the bottom of the beaker. Due to the agitation of the electrolyte, the solution became green in colour rapidly. In general gas bubbles formed on the anode surface but at $J = 2.5\ A/dm^2$ gas bubbles were not visible. As the current density was increased the gas evolution also increased. The total area of the anode was masked by a layer of apparently adherent or stationary gas bubbles. Electrolyte agitation had a small effect on these stationary bubbles. In general with increased current densities, an increase in the volume of gas, size of bubble and dislodgement of the surface adherent gas bubbles was noted. At current densities greater than $10\ A/dm^2$ rapid gas evolution was noted and the observation of the gas formation upon the anode was not possible. Surface brightening was noted to improve with increased current density and etch duration and hence is related to the charge for a given anode area.

6.3.4 The surface texture measurement and results.

A 'Talysurf 4' was used throughout for the surface texture measurements. The centre line average (Ra) was the standard method used in quantifying the quality of the surface. Two orthogonally related measurements were made on each sample and the mean of the two results was used. Prior to polishing, the surface textures of the samples were measured and Ra values of 0.1µm were recorded.

Surface texture measurements were made for all polish durations and for all the current densities investigated. The Ra values are plotted versus current density, and are illustrated in figures 6.4 to 6.8, corresponding to the polishing durations of 5 to 25 minutes in increments of 5 minutes respectively.
The plot of the Ra results illustrated that in general a deterioration in surface smoothness had taken place although the surface was notably brighter. The surface texture reached Ra values greater than three times that of the original surface value i.e. for the 25 minutes polish duration. A trend of increased surface roughness over a wide range of current densities was noted with increased polish durations.

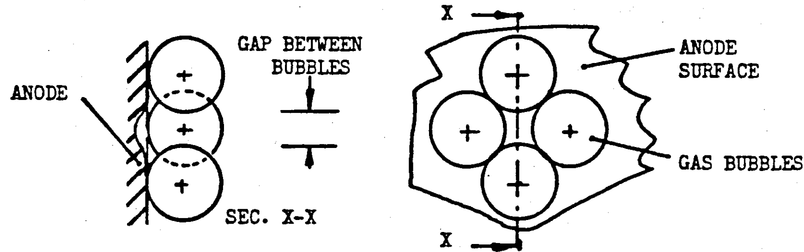

The surface roughness increase may be attributed to the formation of gas bubbles on the anode surface. Those act as dielectric spherical shields on the surface resulting in a non uniform current distribution upon the anode. This results in relatively greater metal being removed at the anode areas directly exposed to the cathode rather than those shielded by the bubbles. This effect is schematically illustrated in the text figure on the previous page.

The Ra values for all the results are plotted in figure 6.9 versus polish duration, and from this plot it can be seen that at J = 5 & 7.5 A/dm^2 the Ra values were high throughout the range of polish durations. This may be attributed to the stationary gas bubbles not being dislodged from the surface. At J = 10 A/dm^2 as gas bubble movement is greater, a relatively better result was achieved. The best surface texture results were at 12.5 A/dm^2, where an improvement on the original surface was recorded. This was also equal to or less than the original surface Ra value throughout the polishing durations investigated.

This result indicates that the recommended current density by Tegart [9] was low and probably the degree of specular reflectance only was the base by which electro-polishing was assessed by. Therefore the electrolyte as recommended should be used at J = 12.5 A/dm^2 rather than J = 7.8 A/dm^2.

6.4 THE MODIFIED ELECTROLYTE

A modification to the formulation was made to encourage bubble evolution from the anode. To this end a surfactant or wetting agent, 'Kodak Photo-Flo', was added to the original electrolyte which aided the formation of much smaller bubbles and hence reduced the duration in which the bubble was in the surface of the anode. This resulted in relatively less localised shielding of the anode.

An additive volume of 3 ml was found to be sufficient for achieving the desired effect. A greater volume of 'Photo-Flo' was found to cause excessive frothing on the surface of the electrolyte and caused an overflow of the cell in prolonged polishing durations. Further no advantage in surface texture was detected with greater ratios of additive.

6.4.1 The surface texture with the modified electrolyte.

Samples were polished similarly to those of section 6.3, but with the modified electrolyte. Where the resist stencil was prepared in an identical manner and the electro-polishing cell set-up was also the same. A 15 minute duration was used for the electro-polishing of the substrates, and a relatively wider current density range was investigated. Current density values between 0 and 35 A/dm^2 were used and from the results, surface texture measurements were made. Those results are illustrated in figure 6.10, where it can be seen that Ra values between 0.065 and 0.07μm were typical within the investigated current density range.

6.4.2 The metal removal rate

The metal removal rate was calculated by weighing the samples prior and post electro-polishing. The average depth of polish was calculated using the density value for AISI 304 stainless steel (7913.12 Kg/m^3) as follows:

$$\text{The depth of polish} = (m1-m2)\, p^{-1} . \text{Area}^{-1} \quad (dm^3)$$

where, m1 = mass of the sample before polishing (Kg).
m2 = mass of the sample after polishing (Kg).
p = 7.91312 Kg/dm^3 (density for AISI 304).
Area = 0.08 dm^2, total anode area.

The average metal removal rate was calculated by dividing the depth of polish above (for each polish duration) by the polish duration. This was found to be directly proportional to current density (Fig. 6.11), and therefore a wide range of accurate depths of etch could be obtained with a smooth finish by choosing the appropriate polishing time for a selected current density. The results of the AOV illustrate the linear relationship between the metal removal rate and the current density and as described by the following equation:

$$\text{metal removal rate} = 0.032J - 0.035$$

where, the metal removal rate is in $\mu m/min$.
and J = The current density (A/dm^2)

The intercept value of '0.035' is due to experimental error, and at J=0, the metal removal rate should also =0. This value is approximately 10% of the total metal removal rate at J=15 A/dm^2 and is smaller for higher current densities. For J is small (i.e. at the proximity of zero) the error becomes more significant.

6.5 QUANTIFYING THE E.P.P. PARAMETERS

This section is concerned with the e.p.p. aspects of the process, these include:

1. Etch factor
2. Depth of polish
3. Undercut

The relationship between the above and the resist stencil line width is also investigated.

6.5.1 The experimental procedure

A similar phototool to that utilised for quantifying the e.p.e. parameters as described in chapter 5 and illustrated in figures 5.1a & b was utilised for this work, this featured the same line separation. The photoresist used for coating the samples was 'Thiokol Laminar AM'. The samples were prepared and coated as described in section 4.6.1. Exposure to UV radiation was with the high pressure mercury light source described in 5.1.1. The exposure duration was determined using a Kodak T-14 density scale and 40 seconds yielded the optimum results. The removal of the polyester protective layer on the resist layer prior to exposure was found to be essential to achieve the required resolution.

Development of the photoresist was as described in section 4.6.1 and this was followed by a water rinse and dried prior to the sample edges being protected. Asphalt paint was used to prevent the electro-polishing of areas other than those defined by the photoresist stencil.

The sample was mounted in the jig (Fig. 6.2) utilising a single cathode arrangement. The stainless steel cathode was mounted facing the stencil aperture.

A current density of 20 A/dm^2 was used, this previously was shown to produce smooth surfaces over a wide current density range. An electro-polish duration of 30 minutes was used to achieve average depth in the order of 30µm this based on the average metal removal rate of 1µm/minute. The cell current of 158 mA was calculated from the total anode area of 78.75 mm^2. The galvanostat was accordingly set and the sample was then polished in the modified electrolyte and under the same general operating conditions as those utilised in quantifying the surface textures.

After polishing, the samples were removed and carefully washed in warm water to remove the viscous electrolyte from the surface. This was followed by careful drying with filtered and oil free compressed air, without causing damage to the resist stencil.

6.5.2 The undercut measurement

As previously described in 5.1.2, the undercut was directly measured with the microscope graticule. The results measurements are tabulated in figure 6.12 and the undercut is plotted versus the original stencil line width in figure 6.13. It can be seen that the

relationship was linear and as described by the following equation:

$$U_p = 139.025 - 0.04 A$$

Where 'U_p' is the undercut in e.p.p. (μm)
and 'A' is the original line width (μm).

This equation was the best fit for the experimental data using the curve fitting program (CURVE). The result illustrates that the undercut increases as the line width decreases but at A=0 then UC must =0. Hence the equation is only valid for the line widths investigated.

Although the undercut was found to be relatively high, the quality in terms of linearity and parallelism of the polished edges were good. The results illustrated in figures 6.14 and 6.15 are 'plan view' photomicrographs of the electro photopolished lines, with the resist stencil removed. Those also illustrate the high quality of the surface and the 'W' profile.

6.5.3 The depth of polish

The depth of polish was measured from the cross-section of the sample. Sectioning was carried out as previously described in section 5.1.3. The Vickers M41 microscope in conjunction with the previously calibrated graticule were used for those measurements.

Like the results obtained with e.p.e. a characteristic 'W' profile was recorded as illustrated in figures 6.16, 6.17 and 6.18. These are sectional photomicrographs of the electro-polished lines. From those results it can be seen that three readings for the depth of polish can be made, the first being the depth as measured at the centre of the lines as previously used in e.p.e. and the other two are of the maximum depth of polish as measured between the original metal surface and the two troughs of the 'W' profile. The mean of the two maximum readings for each line was calculated and the results are also tabulated in figure 6.12. The maximum average depth of polish is plotted versus original line width in figure 6.19 and the relation is described by the following equation:

Maximum depth of polish =

$$Dp_{max.} = 9.813 A^{0.272} \quad (\mu m)$$

where, A = The original line width (μm)

It can be seen that the two methods (maximum depth & depth at centre) for assessing the depth of polish have equal values for line numbers 1, 2, and 3 in figure 6.12. Therefore only the depth of polish values as measured at the centre of the lines numbered 4, 5, and 6 were used in plotting the curve 'depth of polish at the

centre versus the original line width' in figure 6.20. For line width exceeding 470μm, this is described by the equation as follows:

Depth of polish at the centre =

$$Dp_{centre} = 99.602\ A^{-0.123} \qquad (\mu m)$$

where, A = Original line width (μm)

This indicates that two depths of polish curves intercept at an original line width of approximately 310μm. Therefore it is assumed that the two troughs of the 'W' profile merge to form a 'U' profile at original line width smaller than 310μm.

The reduction in depth of polish at the centre with increased original line width supports the predicted trend of chapter 2 but only for original line widths greater than 310μm.

6.5.4 The etch factor

The etch factor in general was found to be relatively low when compared to e.p.e. This was mainly due to the high values of resist undercut.

The etch factor may be calculated in two forms and as follows:

1- The maximum etch factor.

$$e.f._{max.} = \frac{\text{max. depth of polish}}{\text{resist undercut}}$$

2- The etch factor using the depth of polish as measured at the centre of the line.

$$e.f._{centre} = \frac{\text{depth of polish at the centre}}{\text{resist undercut}}$$

The etch factors 1 and 2 above are plotted in figures 6.21 and 6.22 respectively. The two results were also plotted simultaneously in figure 6.23.

6.5.5 The cross-sectional profile of the electro-polished lines

The electro-polished sample was stripped from the resist and prepared for potting and sectioning as described in chapter 5 where an identical procedure was employed.

The sectional profiles were measured by the projection method in the same manner as that described in section 5.2.2. Photomicrographs of the line sections numbered 1 to 6 are illustrated in figures 6.16, 6.17 and 6.18.

Measurements were made from the projected image from the negatives of the above results, and a series of dimensional readings were made about the centre of the polished lines. The mean depth along the profile was obtained by averaging values corresponding to equal distances about the centre of the line.

The average profile results for all six line widths are simultaneously presented in figure 6.24. This result graphically illustrates the transition from a 'W' to a 'U' profile with a decreased line width.

6.6 THE APPLICATION OF E.P.P. IN THE PRODUCTION OF AN EDGE FILTER

When thin metal annulae with radial channels recessed into the surface are stacked together in register to form a hollow, perforated cylinder, the assembly is known as an edge filter. Fluids are filtered by passing them from the outside to the centre, whence they may be dispensed. Chemically milled edge filters (Fig. 6.25) in brass and aluminium were patented in 1927 by the Swedish company Aktiebolaget Separator [106] and used in internal combustion engine lubrication systems.

Current industrial requirements now demand that the depth of the etched channels should be extremely uniform (typically 9.5 + 0.5 um) and that the resultant surface finish on a substrate such as AISI 304 stainless steel is smooth with Ra $\leqslant$ 0.08µm.

Unfortunately, although the complex geometry of a modern filter (Fig. 6.26) is readily achieved using conventional photochemical machining (pcm) technique, previous work [107] has shown that spray etching of this stainless steel with pcm standard etchant of aqueous ferric chloride-hydrochloric acid will produce a minimum Ra of 0.35 µm . Hence alternatively, electrolytic photoetching (e.p.p.) is suggested.

The possibility of producing edge filters, of the type described, by photoetching has been investigated. Two metal removal processes were used in manufacturing the final product. Firstly, the slow, electrolytic photopolishing technique was used to produce polished recesses on the metal surface, and secondly a faster, standard spray etching method was used for the 'chemical blanking' of the annulus.

6.6.1 Strategy of edge filter production

The production of the edge filter as dimensioned in figure 6.26,

required two separate operations to be carried out. These being on the stainless steel sheet from which the edge filter is manufactured. The strategy of the edge filter production is summarised in figure 6.27. The polished recessed surface (Ra $\leqslant$ 0.08 μm) needs to be polished relatively slowly so that the depth of polish can be controlled to the required precision (± 0.5 μm). After polishing, the resist stencil needs to be removed completely so that the sheet can be re-coated with photoresist in preparation for a second etching through the metal.

A positive-working photoresist (Shipley AZ 340; App.V) was favoured for the first coating because it is completely soluble in solvents such as acetone and methyl ethyl ketone, and thus easily stripped from the sheet. It is required that the annulus is etched out, rather than stamped out, to prevent burr formation on its edges. This operation may be carried out at a typical etch rate of 20 μm/min by spray-etching with aqueous ferric chloride-hydrochloric acid through a resilient stencil made from a negative-working photoresist (Waycoat SC180). Stencils made from positive-working photoresists tend to chip at the edges and produce an inferior product when undercut exceeds 0.02 mm.

6.6.2. Details for the edge filter production

A phototool was produced conventionally by photo-reduction from the prepared artwork (X 20 mag.). This in turn was cut-out using the co-ordinatograph as detailed in chapter 3. This work preparation was carried out by Dr. D. M. Allen. The principles and methodology of photo-reduction and the preparation of the registered double-sided phototool for use with positive photoresist are detailed in chapter 3. A magnification of this phototool is illustrated in figure 6.28 where the registration marks are also featured.

The required material, 50μm thick AISI 304 stainless steel material was not available at the time this work was carried out. A material with a thickness of 208μm was used for this application. Although it was not to the required dimension as outlined in the drawing, nevertheless, it is believed that the thickness of the material is not a contributory factor to the process.

Samples, 208μm thick were cut to 40 x 20 mm and carefully degreased by swabbing with acetone. This was followed by an immersion in a CD/70 (1:5) solution for 10 minutes and then thoroughly washed in cold running water. The substrate was dried with filtered and oil free compressed air and further heated to 90°C in an oven for 15 minutes. The samples were dip-coated in Shipley AZ 340 photoresist utilising an extraction rate of 150mm/minute. These were then dried for 15 minutes at 65°C.

The samples were exposed to UV radiation for a period of 65 seconds per side utilising the same exposure unit and vacuum frame described in section 5.1.1. The exposure was determined using the Kodak T-14 density chart.

Development of the photoresist was with a Shipley AZ 303 developer diluted with water in the ratio of 1:4 respectively and for a duration of 2.5 minutes. This was followed by a water wash and then dried with clean compressed air. A post-bake at 60°C for 10 minutes followed.

The total area of the sample was 0.16 dm^2. The area of the filter features were 0.011437 dm^2. Hence the total polish area is 0.14856 dm^2. Therefore for current density of 16.718 A/dm^2, the cell current should be 2.484 Amps based on the average metal removal rate (Fig. 6.11), this current density should yield a metal removal rate of 0.5µm/minute and hence a total polish duration of 20 minutes was required. The samples were electro-polished at the above current density and the thickness of the metal at the centre of the annulus features was measured as 188µm with the digital micrometer. The surface texture value was also measured at the same position and this was 0.07µm (Ra).

The positive resist stencil was then removed with acetone and the polished samples were cleaned and prepared again for coating with photoresist. The samples were suitably dried and pre-baked. These were then coated with 'Waycoat SC 180' (viscosity of 60 zahn seconds) negative working resist by dip-coating and extracting at rate of 100mm/minute. The samples were allowed to air dry for one hour prior to pre-baking at 80°C for 10 minutes.

A further phototool was prepared to produce a protective stencil on the annulae during the chemical blanking operation. Hence a registered pair of tools with a transparent annulae with an inner diameter of 12.5mm and an outer diameter of 18mm was produced. It also contained registration marks identical in size and position with respect to the annulae to those of the polishing tool. The purpose of the latter was to assist in the accurate registration of the blanking tool over the previously polished annulae. The exposure and development of this resist is described in section 5.1.1.

Chemical blanking was carried out by spray etching with aqueous ferric chloride-hydrochloric acid at 45°C, this took 10 minutes at an average metal removal rate of approximately 20µm/minutes. The photomicrograph in figure 6.29 illustrates a section of the electrolytically photopolished edge filter. The small dark spots on the surface are possibly inclusions in the metal surface.

7.0 THE ELECTROLYTIC PHOTOETCHING OF DIFFICULT TO ETCH MATERIALS.

In industry the majority of p.c.m. etching is carried out by spray etching the substrate material with an aqueous ferric chloride-hydrochloric acid etchant. Manufacturers prefer this system due to its technical and commercial effectiveness, it is arguably the most successful method for the processing of a wide range of materials. Unfortunately, it does not suit all materials, and unsuccessful results are obtained with some of the new alloys being produced. This is due to these materials exhibiting high degrees of passivity in the commercially used etching environments as used with other materials [20].

New alloys are constantly being developed. In the field of magnetism some of those alloys have generated wide industrial interests. There is a large requirement for the production of precision components from the foils of such materials. Applications may include motor stators, relay parts, magnetic recording head laminations, and specialised transformer cores.

This part of the work was instigated in part by industrial requirements [108,109]. Two dissimilar materials were presented by two independent companies as being 'difficult to etch'. The term 'difficult to etch' may be defined as the high resistance to etching of a material by conventionally used formulations such as those used in the pcm industry.

Preliminary tests were made on both alloys to investigate the validity of the claims that the two materials were difficult to etch with aqueous ferric chloride. The results obtained confirmed the received information (App. W).

The first enquiry was made by Magnetic Components Ltd. [108] regarding a suitable method for the etching of a high permeability polycrystalline nickel based alloy with the trade name of 'Recovac' (App. J).

Similarly, 'Vitrovac 6025' was suggested for investigation by EMI Central Research Laboratories [109]. This is a cobalt based amorphous structured alloy, also of relatively high permeability (App. K).

The intended final product application being the same for both materials was only a coincidence, namely magnetic recording head laminations. A further coincidence was that both materials were produced by the same manufacturer. In addition to this application, 'Vitrovac 6025' was also to be utilised in fluxgate magnetometers (App. X), in the form of annulae laminations for a toroid transformer. Where the latter may be utilised as part of an

extremely low level magnetic field detection system.

Materials for magnetic heads based on the principle of induction require high initial permeability, adequate saturation, high electrical resistivity, high mechanical hardness, wear resistance and zero magnetostriction [110]. Some amorphous alloys, such as Vitrovac 6025, are suited for the application as magnetic recording heads as they satisfy the unique combination of magnetic and mechanical requirements.

7.1 AMORPHOUS METALS

Work carried out in 1959 at the California Institute of Technology yielded a novel gold-silicon alloy with an amorphous structure [111]. This discovery initiated extensive research into the production of new metal-metalloid amorphous alloys of approximate composition T80 M20. Where T80 represents 80 atomic per cent of one or more transition metals such as iron, nickel and cobalt, and M20 represents 20 atomic per cent of one or more of the metalloid (glass-former) elements such as boron, carbon, silicon and phosphorus.

The alloys may be produced by methods such as sputtering and vapour deposition but chill block melt spinning (rapid cooling at 10 K/s from the melt) is the method employed for the bulk production of ribbons and wires [112]. Maximum ribbon width is in excess of 300 mm for some alloys, but the usual widths encountered are an order of magnitude smaller.

Amorphous metal alloys, also known as metallic glasses, were found to exhibit unique magnetic, chemical, electrical and mechanical properties which stimulated further work into their applications. In the past, only polycrystalline alloys were used for magnetic applications, and amorphous materials are a relatively new alternative.

Metal-metalloid based amorphous magnetic alloys suitable as soft magnetic materials [110] may be grouped as follows:

i. Iron base alloys featuring high saturation polarization and excellent soft magnetic properties.

ii. Iron - nickel alloys with intermediate saturation polarization and good soft magnetic properties.

iii. Cobalt base alloys with near-zero magnetostriction and excellent soft magnetic properties combined with a unique insensitivity to mechanical stress.

The amorphous structure is thermodynamically unstable, however, it exhibits a chemical homogeneous nature because of the lack of defects which may act as chemically active sites such as grain boundaries, twins and any other lattice faults in crystalline

structures. It also exhibits no compositional heterogeneity such as precipitates, segregates or other compositional fluctuations. Therefore, in general, the local corrosion susceptibility of an amorphous metal is expected to be lower than its crystalline counterpart. However, amorphous metals consist of complicated constituents previously unknown in crystalline materials, in particular when high metalloid ratios exist.

The majority of the research carried out in the field of amorphous metals is concerned with both:

1. The production and formulation of the alloys.

2. Investigations into the mechanical, magnetic and corrosion properties of such alloys.

The latter is broadly relevant to this work and the literature search yielded publications mainly related to the magnetic properties and corrosion behaviour of different amorphous alloys in particular environments. Generally this type of work was orientated towards the corrosion resistance rather than methods of improving dissolution which would have been more relevant to the production of components from such materials by p.c.m. methods.

No quantitative data on the photoetching of glassy alloys is known. Consequently the purpose of the following work was to initially detect the passivation characteristics of Vitrovac 6025 and then successfully etch it through a resist stencil.

7.2 THE ELECTROLYTIC PHOTOETCHING OF 'VITROVAC 6025'

Vitrovac 6025 {atomic percentage [Co(66) Fe(4) Mo(2) Si(16) B(12)]} is a cobalt-based amorphous alloy which has generated industrial interest due to its excellent magnetic properties coupled with its wear resistance (App. K). It does, however, also exhibit great resistance to stamping, only 10000 stampings produced from a high quality, expensive press tool [109,113].

It exhibits a high resistance to etching with ferric chloride at concentrations and temperatures used commercially for etching other metals [20]. Although it may be etched at temperatures in excess of 55°C, considerable undercutting of the resist stencil may result [113].

7.2.1 Procedures and experimental details.

With the ultimate aim of applying a suitable process for the working of 'Vitrovac 6025' in industry, an electrolyte of 10% w/w hydrochloric acid solution was selected for the electrolytic photoetching of this material. As previously for the etching of stainless steels, this was thought to be of low enough concentration to cause minimal 'health and safety' risks and is

also relatively inexpensive.

7.2.2 Polarization measurements

Potentiodynamic polarization measurements [96,99] were carried out on Vitrovac 6025 in 10% w/w HCl to establish the most suitable etching parameters. Due to the relatively high current densities required in achieving acceptable metal removal rates, the thickness of the available ribbon (35 μm) was insufficient to establish a continuous potentiodynamic polarization measurement. To achieve equilibrium a slow anode potential sweep rate was required and hence the requirment for a greater material thickness to complete the measurement. This necessitated the stacking of the material and retaining this stack under suitable pressure to maintain electrical contact between the layers. Further due to the material being thin and unsupported in an agitated electrolyte, the small movements of the anode (Vitrovac) with respect to the reference electrode would have a marked influence on results, more so at the higher current densities.

To overcome these problems a cylindrical retainer was made to locate a suitable stack of circular samples cut from the ribbon. An exploded view of this Jig is illustrated in figure 7.1. This features an aperture defining a fixed sample area ($71.2mm^2$) and hence the current density calculation may readily be calculated, also reducing the possibility of errors caused by area differences between tests. The illustrated method of sample retention has the advantage of keeping the material flat and taut in the stirred electrolyte. A Spring loaded brass contact ensures minimal electrical contact resistance between the samples. The design incorporates an 'O' ring seal to prevent electrolyte contaminating the electrical contact, spring and cable.

A schematic diagram (Fig. 7.2) illustrates the measuring cell and instrumentation used with the sample holder mounted at approximately 45 degrees. This allows any gasses formed on the surface of the anode to escape freely towards the surface of the electrolyte and the reaction by-products to stream downwards to the bottom of the beaker, thereby encouraging the dispersion of any dissolution retarding layers between the amorphous alloy surface and the electrolyte bulk. Homogeneity of the solution was aided by stirring the electrolyte using a magnetic follower.

A salt bridge/probe (Agar + KCl), as described in chapter 4 was used for measuring the anode potential. The measuring point of the reference probe was located as close as possible to the anode surface. Anode potential was measured via the bridge by a saturated calomel electrode (SCE) located in a saturated solution of KCl. The cell was powered by a potentiostat which, in turn, was controlled by a linear sweep generator. Current was measured with the aid of a counting resistor and was directly plotted against anode potential on a 'X-Y' recorder. The current scale on the plotter was calibrated with aid of a digital multimeter 'B' (Fig.

7.2). Similarly the anode potential scale was also calibrated and monitored by 'C'.

The electrolyte temperature was thermostatically controlled and measurements were made in the range 15-30°C in steps of 5 °C. The results are illustrated in figures 7.3 to 7.6 respectively, where the anode potential for each of the measurements was swept from -0.5 to 3.5 V (v. SCE) at the rate of 6.67 mV/s. Results obtained illustrate that anodic passivation occurred at all temperatures tested for anode potentials in the region of 1.1 V (v. SCE). By increasing the electrolyte temperature, the anode current density increased for any potential value at the active zone. Hence for the potential 1.1 V (v. SCE), the following current densities were obtained:

Electrolyte Temperature	°C	15	20	25	30
Anode Current Density	A/dm^2	102.8	121.4	134.3	144.3

The table above is plotted in figure 7.7 of the maximum useable current densities versus electrolyte temperature and under potentiostatic etching conditions. 'Maximum usable current density' refers to the active zones' maximum current density and above which non-uniform dissolution would take place. The following equation describes the above relationship

$$\text{Maximum active zone } J = 59.91 \ln T - 58.9 \qquad (A/dm^2)$$

Where, T = The electrolyte temperature °C

Under galvanostatic etching the active zone's current density values are considerably lower and current densities greater than 25 A/dm^2 are not recommended, for at such values etching may occur at any of two or more anode potentials in the passive and transpassive zones leading to unpredictable results (Fig. 7.8). In these regions unpredictable metal removal rates and surface textures result. Therefore when electrolytically photoetching Vitrovac 6025 in 10% HCl under constant current conditions, it is recommended that current densities should be less than 25 A/dm^2. There is also no major advantage in increasing the temperature of the solution beyond 20°C at such current densities.

7.3 PRODUCTION OF MAGNETIC RECORDING HEAD LAMINATIONS.

Electrolytic photoetching of 'Vitrovac 6025' requires the same photoresist processing stages as those described in previous chapters. The photoresist used was Waycoat SC 180 at a viscosity of 60 zahn-seconds.

7.3.1 Laboratory method

Vitrovac 6025 was cut from the ribbon as supplied (on a spool) to 20 mm wide by 90 mm long strips. These were carefully cleaned by swabbing with acetone although arguably this was unnecessary due to the clean condition of the material as supplied. This is probably due to its method of manufacture and the minimal processing and handling post the casting stage of the alloy.

The strips were then dipcoated in the photoresist and an extraction rate of 85 mm/min was used. These were air dried for 60 minutes and then pre-baked at 80°C for 5 minutes. Low temperature and duration were used to prevent heat treating the alloy.

Phototooling was by photographic reduction from a 'Rubylith' artwork, this was then 'stepped and repeated' to produce a fret of laminations (3 rows x 4 columns). Further, locating holes as required by the stacking jigs used during the bonding of the laminations were added. The artwork and mask were made by Dr. D. M. Allen and Mr. I. Routledge from the drawing in figure 7.9. In the design of the artwork an estimated etch factor of one was allowed for.

Exposure to a UV source was through a double sided registered phototool and an exposure duration of 35 seconds was found to be sufficient. The exposure procedure and equipment were as those in section 5.1.1 where the production of the resist resolution chart stencils is described.

After suitable resist development and post-baking at 80°C for 10 minutes, the samples were electrolytically etched under constant current conditions. A metal removal rate of 5 μm/min was achieved for a current density of 25 A/dm^2.

Etching was carried out vertically and on both sides simultaneously with the workpiece (anode) equidistant between two cathodes at 20° C. This was with the jig in Figure 5.5 suitably modified to compensate for the relatively narrow anode.

Sixty frets were produced with dimensional results within the tolerances required and as specified in figure 7.9. The figure below is 1:1 silhouette of an etched fret.

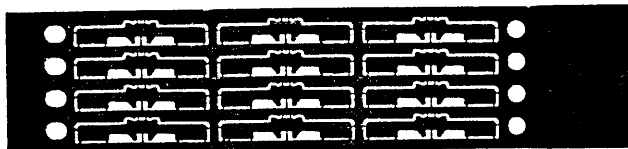

As the workpieces were etched in a vertical position a slight etch wedging was noted, i.e. greater metal removal rate at the top of the workpiece. The dimension of $1.4^{+0.03}_{-0.00}$ mm was measured as described on all the laminations in a sample of ten frets and the method of measurement and results are tabulated in Appendix Y, where the rows were averaged and as plotted in figure 7.10. Wedging is clearly illustrated and may be attributed to the effect of process by-products streaming down the face of the anode, retarding the etching of features at the bottom of the sheet. Figure 7.11 is a photograph illustrating part of a fret etched by this method.

A transparent residual film was observed at the etch bands after metal dissolution had taken place. This after drying was noted to shrink and crack. It is brittle and may be totally removed by a small impact. It is believed to be the metalloid or glass forming matrix of the alloy and consisted of the silicon and boron. A partially etched through sample was photomicrographed illustrating residue seen in the lighter areas of figure 7.12. The leaching out of the metallic components from the alloy appears to have taken place.

7.3.2 The continuous flow processing of Vitrovac 6025

Amorphous materials produced by chill block melt spinning in general lend themselves to continuous or flow processing either with p.c.m. or e.p.e. This is due to the physical dimensions and mechanical properties of the material. A proposed method for processing Vitrovac 6025 in particular and other alloys in general is described in Appendix Z.

7.4 THE ELECTROLYTIC PHOTOETCHING OF 'RECOVAC'

This is a high permeability nickel-iron alloy, it is similar to 'Mumetal' but exhibits relatively higher resistance to wear and in the order of 7 to 10 times greater. Further it has enhanced hardness (App. J) when compared with normal high-permeability alloys.

Difficulties have been encountered by pcm manufacturers when etching 'Recovac'. It is claimed to have exhibited high resistance to etching by aqueous ferric chloride, although it was etched in hydrofluoric acid (HF) of unspecified concentration [108]. Due to the problems associated with HF in terms of handling and 'health and safety', the quoted cost of production was six times greater than those for other high permeability alloys.

The aim of the following work was to investigate the feasibility of electrolytically etching Recovac as was achieved previously with Vitrovac 6025. The electrolyte used was again the same as that used in the major part of this work (HCl) and for the same reasons.

7.4.1 Polarization measurement

Potentiodynamic measurements were carried out on Recovac in a 10% w/w HCl acid solution. The sample material obtained had a measured thickness of 130μm.

The method for the polarization measurement was the same as that described in chapter 4 for AISI 304 stainless steel.

The substrate cleaning was slightly different, where 'Quadralene' rather than CD/70 was used as the latter was found to stain the surface and hence was not used. 'Quadralene' is a detergent based cleaning agent.

Laminar AM photoresist was laminated on to the substrate and subsequently exposed to the phototool producing a '3x3' matrix of 10mm apertures. These apertures were protected with PVC tape and only the one under test was exposed to the electrolyte.

An identical cell and instrumentation setup as that for stainless steel was used. The electrolyte temperatures investigated were, 10, 20, and 25°C.

The anode potential was swept between -0.5 and 2.5V (v. SCE) at a rate of 1 mV/sec. The results were simultaneously plotted on the same sheet and are illustrated in figure 7.13. This result was different from all previous measurements, the relationship was almost linear throughout for all three temperatures. Slight passivation was recorded on all traces and the effect of temperature increase was to raise the passivation potential and achieving maximum active zone current densities of 54, 90,115 A/dm^2 corresponding to electrolyte temperatures of 10, 20, 25 °C respectively.

Hence, for galvanostatic etching at ambient temperatures, the current density should not exceed 90 A/dm^2 and preferably lower to allow a safety margin.

7.4.2 Galvanostatic etching of Recovac

Similar samples as used in the section above were also used for the following tests. The '10 x 10mm' apertures were etched under constant current conditions, the cell was as used previously and etching was at 20 °C in a 10 % HCl w/w acid solution.

The thickness of the sample was measured before and after each test with a 'Micro-2000' digital micrometer. Etching durations of 2.5, 5, 7.5 and 10 minutes were used and were limited due to the available thickness of the material (130μm). Three current densities were used and were 25, 50 ,100 A/dm^2, and requiring cell currents of 250, 500, 1000 mA.

The surface results for the following current density were:

J (A/dm^2)	25	50	100
Ra (μm)	0.7	0.35	1.0

The original surface texture was 0.1μm, hence all measured results were degradations of that. Nevertheless at all the current densities, uniform dissolution took place resulting in a smooth dull grey coloured surface. During etching , a black layer was noted to form on the surface but this broke up during the etch and its dissipation from the surface was assisted by the electrolyte agitation. The depth of etch results versus the etch durations are plotted in figures 7.14, 7.15 & 7.16 corresponding to the current densities of 25, 50 and 100 A/dm^2.

Recovac etched readily in 10% HCl and the best results were at 50 A/dm^2 where a metal removal rate of approximately 9μm/minute was achieved.

8.0 REMARKS AND CONCLUSIONS

The metal dissolution profiles produced when spray etching a metallic substrate through resist stencils are characterised by 'U' cross-sections. Alternatively when electro-etching a similar feature, 'W' sections have been recorded. The sectional profiles produced by e.p.e. or e.p.p. are influenced by the physiochemical aspects of the process. The geometric profile of the dissolution is a function of the current density.

The investigated processes are unlike conventional p.c.m. where metal dissolution is essentially mechanically controlled by etchant spray density, electrolytic systems are dependent on the cell boundary conditions and the localised electrochemical systems of dissolution.

In general for electrochemical dissolution, predicting the material removal distribution (profile) is difficult but for the simplest of geometries. Resultant surface profiles are a function of the normal current density on the surface. In the majority of cases the surface current density and the resultant profiles are determined by non-linear boundary conditions.

Methods used in this work for calculating the potential field and determining moving boundary problems are summarised as follows:

1. Experimental methods

This is achieved by carrying out experimental work and generating data from which empirical equations may be derived. This is without doubt the most accurate and descriptive method. Unfortunately, it is laborious and singular i.e. the data accumulated is only applicable to similar problems.

2. Analogue methods

By simulating the potential and current distribution graphically using conductive media. This method is less laborious than the above but only primary current distributions may be simulated by measuring the potential values in the field. Recently this technique has been almost totally superseded by computational methods. Nevertheless, it is the quickest method for determining a two or three dimensional field with complex boundary conditions, and its usefulness is defined by these conditions.

3. Numerical method

Solving the potential field may be achieved by a number of numerical methods, the most popular of these are the finite-difference and the finite element methods. This is not a complex mathematical method and in particular for Laplacian fields.

In recent years this has become the most popular and effective way for solving complex transient problems such as those encountered with electrolytic systems. The reason being, the availability of high speed digital computers.

4. Analytical methods

A number of methods exist and are summarised in chapter two. Analytically modelling transient problems in general is difficult and relatively few examples exist. Simplifying assumptions must be made in order to achieve a solution. Although this is applicable to other methods, due to the complexity of electrochemical systems a risk exists whereby the model has little resemblance to the process.

The initial aims of this work were to quantify experimentally the process capabilities of an electrolytic metal dissolution system and evaluate it as a manufacturing process in p.c.m.
At the beginning of the work directly related information on the subjects of electrolytic photoetching was very limited and rudimentary. Since then, this has not changed a great deal.

During the work it was found necessary to quantify the current density on a metal surface feature defined by an adherent dielectric layer (photoresist) by other means than those obtained experimentally. This was due to relatively high observed lateral dissolution under the dielectric layer (undercut).

Initially three methods were utilised, the first two were analytical and the latter graphical.

Using cartesian coordinates the primary current density over a surface feature was described by a simple relationship originating from hydrodynamics (Eq.9). At a later stage this was tested for validity against results by the graphical method and good correlation was exhibited (Fig.2.8). Recently a similar expression was found for a rotating disk electrode embedded in an insulating wall. Equation 9 although shown to be valid for primary current density did not describe fully why rapid undercut occurs. This is due to the equation describing the normal current density at t=0 and hence a near orthogonal to the required relationship.

Using polar coordinates, a relationship was derived (Eq.10) for the primary current density as a function of the dissolution angle and the distance from the resist edge. When this relationship was tested at a dissolution angle= α i.e. the same condition as for equation 9 the same result was obtained. It was further tested at different angles of dissolution to confirm its validity.

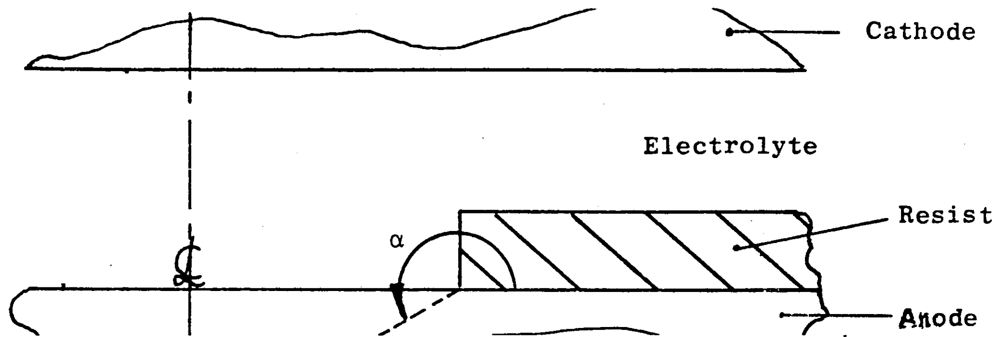

The results from this equation when plotted for a range of dissolution angles (Figs2.2 & 2.3) illustrate that at the proximity of the dielectric/metal interface the primary current density tended towards infinity at a greater rate with increased values of dissolution angle. The important feature of this equation is that it describes the lateral undercut as schematically illustrated above.

The graphical method provided important and rapid results regarding the primary current distrbution on a micro scale (i.e. over a single feature) and on a macro scale (i.e. multiple features). The latter and for a two feature cell, potential field symmetry about a normal at the centre of the dielectric surface (Fig.2.10 & 2.11) was noted. This was the result the numerical chart was based upon.

The result of equation 10 is important, as undercut is believed to be described for the first time in terms of these parameters. This is a steady state result and for ease of solution it does not take into account the moving boundary. The assumption is that the angle of dissolution remains fixed at a point about the dielectric/metal interface. This is not strictly accurate but provides an explanation to why high values of undercut occur.

A two dimensional numerical simulation of the transient behaviour of the anode undergoing dissolution with the presence of a dielectric surface layer was developed. A method for overcoming the solution divergence due to the initial high field values at the proximity of the insulator/electrode interface was introduced. This was by generating an initial approximate electrode boundary.

The moving boundary was simulated by a quasi steady state solution and the model may take into account electrode polarization. In this work, constant polarization was considered. Concentration and homogeneity within the etched features as defined by narrow dielecric aperture, are believed to significantly effect the resultant profile. Prior to specifying a density dependent polarization, an understanding of the inner feature mass transport parameters is required. Applying general assumptions in this case may therefore be misleading due to the physical small dimensions of the features whereby diffusion layer dimensions become significant. This could be an interesting area for further investigation and would yield useful results.

Another related area for possible further work is the variant of this program which is capable of simulating electro photoforming as demonstrated in figures 5.54 & 5.57 where in the latter the over plating of a very thin resist layer was simulated.

The results obtained from the model may be divided into two sections:

a) Results demonstrating cells with adjacent, equal and parallel features as those in figures 5.46 to 5.51 in which the boundary movement with etch time is recorded. The centrally positioned insulator is varied in dimension. The overall charge was constant in all results. It can be seen that for an insulator dimension of 100μm (Fig. 5.46) the undercut value is approximately equal to half the insulator size (50μm). Hence for depths of this order of magnitude the insulator dimension is insufficient. This demonstrates why a 200μm feature separation was used in the experimental work. This value was determined experimentally when the resolution chart used for this work was developed. Results illustrate process resolution as determined by the undercut phenomina. In general feature separation should be >200μm.

From the same group of results, the transition from a 'W' cross section to that of a 'U' appears to be a function of feature depth to width ratios. The profile changes to that of a 'U' as this ratio increases and by inspection this is >1.

b) The second series of results were those for the quasi-chart. This is a numerically simulated resolution chart made by the splicing of minor cells which in turn are modeled by the program. The method was developed to overcome resolution problems imposed by the maximum dimensions of the mesh array in dimensionally large simulations and the methodology is detailed in chapter 5.

The test carried out was aimed at simulating the experimental conditions when electrolytically etching AISI 304 stainless steel. An etch duration of three minutes was simulated, the minor cells are illustrated in figures 5.58 to 5.60 and from those results the lateral to normal etch rates versus depth of etch were derived and plotted in figures 5.74 & 5.75 corresponding to results calculated for maximum feature depth and centre depth respectively.

Depth of etch, versus line width are simultaneously plotted with the experimental values in figure 5.78 featuring good correlation for both the maximum and centre depth results for line widths >200um. Below this value the experimental values dropped rapidly. This may be due to non replenishment of the electrolyte in the narrow features thus causing limiting effects.

Undercut versus the feature width was simultaneously plotted (Fig. 5.80) with experimental results and those calculated from the empirical equation derived from the pooled experimental results. A good qualitative similarity exists between the results but the theoretical undercut was greater than those obtained experimentally. This may also be attributed to the entrapped electrolyte under the resist layer not being replenished.

THE EXPERIMENTAL WORK

Hydrochloric acid (10% w/w) was utilised as an e.p.e. electrolyte due to its suitability for working stainless steels [25], and in part due to the lack of quantitative data on its performance in this role specifically and on the field in general.

Although AISI 304 stainless steels passivated in this environment at 15 ^{o}C, passivity was reduced by increasing the electrolyte temperature >20°C. Due to the predictable uniform metal dissolution of the active zone, it was selected as the most suitable operating area for e.p.e. The maximum usable current density for galvanostatic etching within the active zone was sought. From the polarizaton results (Fig. 4.16) and for temperatures of 20, 25 and 30° C the maximum (active zone) current densities were J = 57, 85 and 87 A/dm^{2} respectively. Hence an operating temperature of 25°C was selected due to the marginal benefits by exceeding this.

Galvanostatic etching was carried out at 25 ^{o}C where a current density range between 10 and 90A/dm^{2} was investigated. The criteria by which the usability was assessed was the dissolution uniformity as measured in terms of surface texture and anode profile. At J<60-70 A/dm^{2} , surface texture values in the order 1μm (Ra) and 10μm (PV) were recorded. A rapid deterioration in the surface textures takes place at J>70 A/dm^{2}. A current density of 50 A/dm^{2} is recommended for etching under such conditions as this allows for a buffer density of 10 A/dm^{2}.

An empirical equation (11) for the mass of metal removed was obtained, and from which an average metal removal rate of 10um/minute for J = 50 A/dm^{2} was calculated.

The general profile produced when etching these results through 10 x 10 mm aperture yielded the predicted 'W' shape section caused by the 'interface' effects. Two other features were recorded and are as follows:

a) The form of the profile is also related to the anode cathode relationship. Hence care must be taken if uniform dissolution across etched features is required. Symmetry of the cathode w.r.t. the etched feature is suggested.

b) Surface blacking of AISI 304 steel at J < 20 A/dm^{2} or alternatively at anode potentials <-250 mV (v.SCE). A dense black layer was achieved under these conditions and at 25°C. This layer became adherent to the underlying steel after rinsing and drying at room temperatures.

E.P.E. OF STAINLESS STEEL

A resolution type mask was utilised for quantifying the p.c.m. parameters of the electrolytic etching system. This chart featured a series of parallel lines of varying widths ranging from 50 μm to 1.6mm. It was used for imaging single-sided stencils on the -ve

working liquid resist 'Waycoat'. Etching was at $J=50\ A/dm^2$ and the depth of etch and photoresist undercut were measured.

The etch duration in addition to the differing line width were the variables from which the e.p.e. performance was assessed in terms of undercut (U), depth of etch (DE) and the etch factor (e.f.).
A decay in the undercut absolute value was recorded with increased line widths, and for lines >200 μm the relative differences in undercut values were small. The relationship is described by the general empirical equation:

$$U = 80\ t^{0.18} . A^{(0.007t-0.13)} \qquad (\mu m)$$

where A = Stencil line width (μm)
and t = Etch duration (mins)

The depth of etch at the centre of the etched feature is also described in the equation in terms of the above variables as follows:

$$DE = 117.4\ A^{-0.33} . t^{(0.13ln.A-0.07)} \qquad (\mu m)$$

Based on the results in section 2.5, the depth of etch at the centre of two adjacent features increases as the relative line width decreases and as described by the equation:

$$\frac{J}{(L_1 - L_2)} = \sigma B(L_1^{-1} - L_2^{-1}) \qquad (A/dm^2)$$

Where ∇J above is the relative difference between current densities at the centre of the two adjacent features. This again is based on a reduced model assuming primary current density conditions.

The experimental results illustrate that for line widths >200μm a qualitative similarity existed whereby the relative depth of etch at the centre decreased with increased line widths. The validity of this ceases for line widths <200μm where the opposite to the predicted result occured as the depth of etch values tended towards zero rapidly. The reason for this is believed to be caused by the mechanical restrictions imposed by the narrower line widths thus stifling the anodic reactions. Hence a peak depth of etch result for line widths between 100 and 300μm (Fig. 5.16). For A<200μm the dissolution rate decreased rapidly as illustrated by a high gradient. Hence small deviations in A at values<100μm would yield a large range in depth of etch. Therefore improved repeatability would be expected when etching at A>200μm.

The three dimensional plot for etch factors versus line width and etch durations (Fig. 5.32), illustrate clearly that etch factors increased with etch duration and feature width in general. Etch factor values for single sided etching were influenced by stencil line widths and durations of etch. Measured values ranged between 0.726 and 1.203.

A registered double-sided phototool featuring line widths of 220um was used to electrolytically etch the stainless steel on both sides simultaneously, this at the operating conditions preveously described. Uniform etching was achieved on both sides using a symmetrical dual cathode arrangement.

The undercut was measured and its relationship with the duration of etch (mins.) is described by:-

$$U_d = 12.4\, t^{0.76} \quad (\mu m) \qquad \text{(Fig. 5.38)}$$

Prior to break-through the sectional profile of the double-sided etched feature developed from 'W' to a 'U' profile with increased etch durations. After break-through the cusp receded rapidly. The sectional results in figure 5.45 illustrate clearly the decaying undercut rate versus etch duration. Before break-through an etch factor of 0.91 is achieved.

E.P.P. OF STAINLESS STEEL

Electro photopolishing of AISI 304 in an orthophosphoric acid system yielded different metal removal characteristics in terms of dissolution rates and surface texture. The recommended polishing solution [9] produced high specular reflectance, at the recommended current density of 7.8 A/dm^2. Polishing by definition is a combination of smoothing and brightening. The operating conditions as suggested yielded relatively poor smoothing results as the initial surface texture was 0.1 μm (Ra) and with electro polish at a duration range 0-25 minutes. Maximum Ra values were recorded at J=2.5-10 A/dm^2 and at t=25 minutes, these were in the range 3.2-3.4 μm (Ra). This is over 3 times the value of the original surface and may be attributed to the formation of adherent gas bubbles on the surface. These were relatively large and are believed to act as dielectric shields causing a poor distribution of 'J'. When dispersion of the gas off the surface of the anode was encouraged by the addition of a surfactant (Photo-Flo), the Ra values achieved were considerably improved over a wide range of current densities and in the order of 70nm (Ra). The metal removal rate described by the empirical solution:

$$R_p = 0.032\, J - 0.035 \quad (\mu m/min) \qquad \text{(Fig. 6.11)}$$

where, J is in A/dm^2

In electrolytic photopolising the steel through a resolution chart the result yielded (Fig. 6.13) a undercut relation of:

$$U_p = 139 - 0.04\, A \quad (\mu m) \qquad \text{(Fig. 6.13)}$$

where, A = Stencil line width in (um).

E.P.E. OF NON-FERROUS ALLOYS

Two 'difficult to etch' materials were investigated for procesing by e.p.e. These exhibited passivity to etching with commercially used solutions of ferric chloride - hydrochloric acid.

'Vitrovac 6025' an amorphous cobolt based alloy was tested with a 10% w/w HCl solution. Polarization results illustrated that it passivated in temperatures of 15, 20, 25 and 30°C. Increasing the electrolyte temperatures did not remove passivity but moved the diagram towards the high current density region. The maximum active zone value for J was described in figure 7.7 where the relationship between the latter and increasing the temperatures is described by:

$$J_{max.} = 60 \ln T - 59 \qquad (A/dm^2)$$

where, T is in ^{o}C.

This result is only suitable for potentiostatic etching due to the galvanostatic etching complications associated with a passivating system where a possibility of etching in more that one anode potential zone exists. Hence for galvanostatic etching reduced metal dissolution rates are tolerated. The polarization diagram in Fig. 7.8 illustrates this, and as the electrolyte temperature is increased, the passive current density also increases. Therefore 25°C was used for carrying out the etching work and similar to stainless steel only marginal gains were made in increasing the temperature to 30°C. If potentiostatic etch is used at 25°C then an anode potential of 1.08 V (v.SCE) may be used, this is estimated to yield three times the metal removal rate as that achieved by galvanostatic etching. Hence an e.p.e. system for working Vitrovac utilising a 10% w/w HCl solution lends itself towards potentiostatic etching if maximum metal removal rate is required. If this is not critical then galvanostatic etching may be used successfully where $J < 25$ A/dm^2 (i.e. anode potentials< 100 mV (v. SCE)).

The second material that exhibited passivity to etching in ferric chloride - hydrochloric acid was a nickel based polycrystalline alloy (Recovac).

This material exhibited slight passivity when electroetched in 10% w/w HCl. It produced uniform dissolution and current densities in the order of 115 A/dm^2 at 25°C may be achieved under galvanostatic conditions, but at 20°C this value drops to $J<90$ A/dm^2. Ra values of 0.35 were recorded at $J = 50$ A/dm^2. This material electroetched far more readily than the stainless steel.

RECOMMENDATIONS FOR FURTHER WORK

1. The optimising of the numerical quasi-chart by improved splicing with a relatively more rigorous method. This by including a depth dependent function describing the potential at the cell interface boundaries. This in turn may be utilised in the calculation of the adjacent cell by introducing potential values at the interface for etch time interval rather than assuming an insulated boundary.

2.Investigating the micro mass transport within an etched feature so that the correct type of polarization may be applied.

3. Simulating electro photoforming e.p.f. utilising the model developed in this work as a tool for quantifying the process parameters.

CONCLUDING REMARKS

Due to the lack of detailed information on the subject of electrolytic dissolution in p.c.m., a broad investigation was carried out to facilitate a better overall understanding of the process features and limitations. Throughout this work, the process suitability as a manufacturing alternative was always one of the aims and when industrial requirements were presented the problems were tackled.

A methodology is proposed and demonstrated for quantifying experimentally or theoretically the process capabilities of the e.p.e. or e.p.p. Based on the principle of masking the electrode with a non uniform but regular pattern of features, the the resultant distortions of the potential field upon the surface current densities and the feature profiles may then be quantified by either mathematical or experimental methods.

A computer program was developed to simulate the electrode boundary movement with the presence of a feature defining surface dielectric layer. It is hoped that this will be utilised in simulating experimental situations that normally take days to set up in a few minutes. Thus increasing the yield and understanding of the process.

The results of this investigation may answer some of the questions related to the role this process may play in the general field of photochemical machining. First, the process must be classified according to is application. These may fall into two categories, determined by the type of dissolution taking place as follows

I. Electrolytic etching.
II. Electrolytic metal finishing.

I. Electrolytic etching

The application field for electrolytic etching is termed 'electrolytic photoetching'(e.p.e.). This is the area where metal removal rate is one of the main factors by which the process capability may be quantified, in terms of this and other process factors related to photoetching, e.p.e. may be quantified. These aspects include:

a) Metal dissolution rates.
b) Surface textures.
c) Etch factors.

Therefore, e.p.e. may be directly compared with the conventional etching systems currently being used by the industry. When doing so for AISI 304 stainless steel, a material readily etched in aqueous ferric chloride systems, the results obtained for etching this material in 10% w/w HCl electrolyte were comparatively poor. It has been shown [20] that spray etching this particular alloy with $FeCl_3$- HCl - H_2O at stengths in the order of 34 to 40 Be', metal removal rates in the order of 20μm/min. are achieved. Surface textures as low as 0.35μm (Ra) were also reported. This compared favourably with electrolytic dissolution rates of 10μm/min. and Ra values of 1μm. Further, the high lateral dissolution characteristic of the process results in relatively low etch factors in the order of 0.7 to 1.2 were recorded, whereas etch factors between 1.5 and 3 have been reported when spray etching steel for the same depths of etch. This is further compounded by the minimum inter-feature resolution obtained from the numerical results of 100μm determined at early stages in etching and hence poorer results with shallow etching although for deep etching improved etch factors are predicted from e.p.e. Nevertheless, based on the obtained results it must be concluded that materials that are readily etched by conventional methods should not be tackled by this process unless a particular electrolyte/material combination would yield relatively improved results. This was not the case for AISI 304 in 10% HCl.

The electrolytic photoetching of materials such as 'Recovac' and 'Vitrovac 6025' proved very successful and in particular the case of the latter material where it exhibited high resistance to etching with commercially used etchants. It is a material reportedly difficult to mechanically process (e.g. stamping) yet it electro-etched readily and precision components were successfully produced using a 10% HCl w/w electrolyte. It is believed that this process could play an important role in the production of components from such relatively new materials. A 'continuous processing' method of electo-etching amorphous ribbons such as 'Vitrovac 6025' was proposed and requires further investigation.

II. Electrolytic metal finishing

The second classification, that of metal finishing, is where the properties of the electrolytic reaction determined by cell conditions results in surface quality such as blacking or polishing. Hence 'electrolytic photopolishing' (e.p.p.) falls within this category. This is a field where conventional spray etching systems do not compare as the anodic surface treatment in general is a characteristic of electrolytic dissolution. It has been demonstrated that electro photopolishing (e.p.p.) is a viable process as used in th production of edge filters whereby high quality surface textures in the order of 70nm (Ra) were achieved in AISI 304 stainless steel in conjunction with a photoresist stencil. Further the surface blacking of the same material in 10% HCl at anode potentials <-250 mV (v. SCE) were utilised successfully in improving the contrast on steel measuring scales such as rulers.

In conclusion, it is believed that the role of e.p.e. or e.p.p. compliments the existing chemical spray etching techiques as a further process that may be utilised in the general field of p.c.m. rather than being an alternative process.

LIST OF REFERENCES

1. E.A. Szukalski & W.M. Lehrer, An update on applying photo chemical machining, Design engineering conference, NEC, session 6b, paper 4, 1981.
2. D.M. Allen, D.F. Horne and G.W.W. Stevens, Quantitative examination of photofabricated profiles part 1: Design of experiment, The journal of photographic science, Vol. 25, No.6, Nov./Dec. 1977, pp.250-253.
3. D.M. Allen, Photoetched precision devices and components, Design engineering conference, NEC, session 6b, paper 3, 1981.
4. W.S. De Forest, "Photoresists: Materials and processes", McGraw Hill, 1975.
5. D.M. Allen, Design and production of small hole profiles in thin materials, C.M.E., March 1981, pp.37-40.
6. D.M. Allen, D.F. Horne, S. Masum and G.W.W. Stevens, Quantitative examination of photofabricated profiles part 5: Effect of stencil integrity on etch factor and the deep etching of stainless steel, The journal of photographic science, Vol. 28, No.3, 1980, pp.140-144.
7. A.J. Hegarty, An investigation into variations in etched profiles and surface finishes, MSc. Thesis, 1980, CIT, Bedford.
8. P.M. Wible, Regeneration of etchants, The photo chemical machining institute journal, No.6, 1981, pp.7-11.
9. W.G. Tegart McG., "The electrolytic and chemical polishing of metals in research and industry", Pergamon, 2nd Ed. Revised, 1959.
10. P.V. Shchigolev, "Electrolytic and chemical polishing of metals", Freund publishing house, 1970, Holon.
11. E.I. Shpitalskii, Versahren der oberflachen von metallen galvanischen metallniedershlagen ein a glanzend poliertes assehen zu gaben, German Patent No. 225873, 1910.
12. Salfret Ltd., The story of Salfret, 53 Gt. Suffolk St. London SE1.
13. Private communication.
14. D.M. Allen, D.F. Horne and G.W.W. Stevens, Quantitative examination of photofabricated profiles part 2: Photoetched profiles in stainless steel, The journal of photographic science,Vol. 26, No.1, Jan./Feb. 1978, pp.72-76.
15. D.M. Allen, D.F. Horne and G.W.W. Stevens, Quantitative examination of photofabricated profiles part 3: Measurment of etch factor, The journal of photographic science,Vol. 26, No.6, Nov./Dec. 1978, pp.242-245.
16. D.M. Allen, D.F. Horne and G.W.W. Stevens, Quantitative examination of photofabricated profiles part 4: Photoetched profiles in mild steel, The journal of photographic science,Vol. 27, No.4, Jul./Aug. 1979, pp.181-184.
17. G.W.W. Stevens,"Sayce" test chart of modified design, The journal of photographic science, Vol. 25, No.1, Jan./Feb. 1977, p.211.
18. D.M. Allen, D.F. Horne and G.W.W. Stevens, Properties of liquid photoresists used in the photoetching of stainless steel, The journal of photographic science,Vol. 25, No.6, Nov./Dec. 1977, pp.250-253.
19. D.M. Allen, D.F. Horne and G.W.W. Stevens, Preparation of specimens for microscopic examination of edge profiles, Journal of microscopy, Vol. 111, Pt 2, Nov. 1977, pp.203-210.
20. D.M. Allen, A.J. Hegarty and D.F. Horne, Surface textures of annealed AISI 304 stainless steel etched by aqueous ferric chloride-hydrochloric acid solutions, Transactions of the institute of metal finishing, Vol. 59, 1981, pp.25-32.
21. A.E. Debarr and D.A. Oliver, "Electrochemical Machining", Macdonald London 1968.
22. Technical file No.9, "Electrochemical Machining", Engineering, Vol.214, No.9, Sept. 1974.
23. C.H. Wick, Electrical and chemical machining methods, Machinery and

production engineering, 11 Feb. 1970.
24. J.F. Wilson, "Practice and theory of electrochemical machining", Wiley-Interscience, 1971.
25. Application Data For Kodak Photosensitive Resists (Kodak Publication No. P-91, Eastman Kodak Co., NY, 14650, USA. Dec. 1966.
26. B.A. Pospelov, Ye.M. Ostashinsaya & T.I. Solov′yeva, The Fabrication of Perforated Metalic Light Attenuators and Other Similar Items by Foil Etching, Sov. Jnl. Opt. Tech.(USA), Vol. 40, 1973, p138.
27. P.A. Jacquet, Electrolytic polishing of metalic surfaces, Metal Finishing, Parts I to V, Vol. 47, Nos. 5,6,7,9 & 10, 1949, pp.48-54, 58-64, 60-70 & 68-73; Parts VI & VII, Vol. 48, Nos. 1 & 2, 1950, pp.56-62 & 55-60.
28. K.P. Batashev, Metallurgiya Tsventnyh Metallove, Metallurgizdat, 1951, p.152.
29. G.S. Vozdvizhensii, Gas evolution on electrode surface, DAN SSSR, 59, 1948, p. 1587.
30. N.D. Tomashov, Theory of metal corrosion, Metallurgizdat, 1952.
31. N.D. Tomashov, Formation of separate-phase oxide layers on electrodes, DAN SSSR, 88, 1953, p.1923.
32. P.A. Jacquet, Electrolytic method for obtaining bright copper surfaces, Nature, 135, 1935, p.1076.
33. P.A. Jacquet, Electolytic polishing of copper, lead, tin, and their alloys and its application to metallography, Bull. soc. chem., Vol 3, 1936, pp.705-723.
34. W.C. Elmore, Electrolytic Polishing Part I, Journal of Applied Physics, Vol. 10, 1939, p. 796; W.C. Elmore, Electrolytic Polishing Part II, Journal of Applied Physics, Vol. 11, 1940, p.403.
35. F. Bauman, H. Ginsberg, Untersuchungen uber den glanzmechanismus an oberflachen von aluminium und aluminiumlegierungen, Aluminium (BRD), Vol. 32, No. 11, 1956, pp.706-711.
36. J. Edwards, The mechanism of electropolishing of copper in phosphoric acid solutions, Journal of the Electrochemical Soc., 100, No. 7, 1953, p.187. and No. 8, 1953, p.223.
37. C. Wagner, Contribution to the theory of electropolishing, J. Electrochemical Soc., Vol 101, May 1954, p.225.
38. H.M. Hojka, M. Zamin & M.K. Murthy, On the validity of Wagner′s theory of electropolishing, Vol. 126, No. 5, J. Electrochemical Soc., May 1979, p.795.
39. L.I. Levin, Trudy Ural′skogo instituta im. irova, No. 27, Metallurgizdat, 1947.
40. J. Edwards, The mechanism of electropolishing of copper, in phosphoric acid solutions: The Mechanism of Smoothing, J. of the Electrochemical Soc., Vol. 100, 1953, pp.223c-230c.
41. L.Ya. Popilov, Technology of electropolishing metals, Mashgiz, Moscow, 1953.
42. R. Alkire, T. Bergh, and R.L. Sani, Predicting electrode shape change with use of finite element methods, Journal Electrochemical Soc., Vol. 125, 1978, p.1981.
43. R. Alkire and A.A. Mirarefi, The current distribution within tubular electrodes under laminar flow, Journal Electrochemical Soc., Vol. 120, No.11, 1973, pp.1507-1515.
44. J.M. Fitz-Gerald and J.A. McGeough, Mathematical theory of electrochemical machining; 1- Anodic smoothing, J. Inst. Maths. Applics., Vol. 5, 1969, pp.387-408.
45. J.M. Fitz-Gerald, J.A. McGeough, and L. McL.Marsh, 2- Anodic shaping, J. Inst. Maths. Applics., Vol. 5, 1969, pp.409-421.
46. A.N. Trofimov and V.T. Ivanov, Distribution of current density on the cathode in the electrodeposition of metals in an ultrasonic field,

Soviet Electrochem., Vol. 1, 1965, p.186.
47. A.N. Baraboshkin, V.T. Ivanov, and G.A. Kondrateva, Microdistribution of current during the passivation of a cathode surface by electroactive substances, Soviet Electrochem.,Vol. 11, 1974, p. 741.
48. R.H. Nilson and Y.G. Tsuei, Trans., Film cooling by oblique slot injection in high-speed laminar flow, ASME, Vol. 98, 1976, p.54.
49. R. Caban and T.W. Chapman, Statistical analysis of electrode kinetics measurements, Journal Electrochemical Soc., Vol. 124, 1977, p.1371.
50. S.H. Glarum, Variational approximations to current distribution problems; 1- Rotating disk electrode, Journal Electrochemical Soc., Vol. 124, 1977, p.518.
51. S.H. Glarum, Variational approximations to current distribution problems; 2- Rectilinear electrodes & baffles, Journal Electrochemical Soc., Vol. 125, 1978, p.84.
52. C. Wagner, Theoretical analysis of the current density distribution in electrolytic cells, Journal Electrochemical Soc., Vol. 98, 1951, pp.116-128.
53. F. Hine, S. Yoshizawa, and S. Okada, The effect of the walls of electrolytic cells on the current density, Journal Electrochemical Soc., Vol. 103, 1956, p.186.
54. T. Yoshida and K Koseki, Extended equation of current distribution in rectangular cells, Journal Electrochem Soc. Japan., Vol. 35, 1967, p.24; K. Koseki, Y. Hashimoto, and T. Yoshida, A new approach to current distribution in rectangular cells, Journal Electrochemical Soc., Vol. 35, 1967, p.88; K. Koseki,Extended equation for current distribution in rectangular cells, Journal Electrochemical Soc., Vol. 36, No.4, 1968, pp. 226-236.
55. N.P. Gnusin, N.P. Poddubnyi, E.I. Rudenko, and A.G. Fomiev, Current distribution on a strip cathode with the polarization curve expressed by the Tafel equation, Soviet Electrochem., Vol. 1, 1965, p.391.
56. C.W. Tobias and R. Wijsman, Theory of the effect of electrode resistance on c.d. distribution in electrolytic cells, Journal Electrochemical Soc., Vol. 100, 1953, p.459.
57. W.R. Parrish and J. Newman, Numerical solution of coupled ordinary differential equations, Journal Electrochemical Soc., Vol. 116, 1969, p.169.
58. W.R. Parrish and J. Newman, Current distribution on plane parallel electrodes in channel flow, Journal Electrochemical Soc., Vol. 117, 1970, p.43.
59. K. Viswanathan and D.T. Chin, Current distribution on a continuous moving sheet electrode, Journal Electrochemical Soc., Vol. 124, 1977, p.709.
60. P.J. Sides and C.W. Tobias, Primary potential and current distribution around a bubble on an electrode, Journal Electrochemical Soc., Vol. 127, 1980, p.288.
61. R. Alkire and P. Lu, Effect of hydrogen on current distribution during electro-deposition at vertical electrodes, Journal Electrochemical Soc., Vol. 126, 1979, p.2118.
62. W.G. Sunu and B.W. Burrows, Mathematical model for design of battery electrodes, Journal of the Electrochemical Soc., Vol. 131, 1984, p.1.
63. W.M. Deen and R.A. Brown, Mass transfer analysis of electrodeposition through polymeric masks, Journal Electrochemical Soc., Vol. 131, 6, 1984, p.1251.
64. D.M. Allen and P.J. Gillbanks, Manufacture of some SIMS components from tantalum foils by electrolytic photoetching, Precision Engineering, Vol 7, No.2, April 1985, pp.105-109.

65. V.V. Klokov, Z.B. Sadykov, R.M. Khairutdinov and T.V. Shishkina, Electrochemical milling of surfaces with an applied photoresist, Elektronnaya Obrabotka Materialov, No. 1, 1984, pp.10-14. (Translation received November 1985).
66. J. Kronsbein, Current and metal distribution in electrodeposition, Plating, Vol. 37, 1950, p.857.
67. O. Kardos, Current distribution on microprofiles, Plating & surface finishing, Vol. 61, 129, 229, 1974, p.316.
68. R.N. Fleck, D.N. Hanson, and C.W. Tobias, "Numerical evaluation of current distribution in electrical systems", Lawrence Radiation Laboratory, Berkeley, CA, (UCRL-11612), Sept. 1964.
69. R.H. Russelot, "Repartition du potential et du courant dans les electrolytes", Dunod, Paris , 1959.
70. J. Newman, Engineering desighn of electrochemical systems, Industrial Eng. & Chem., Vol. 60, 4, 1968, pp.12-27.
71. J. Newman, in "Electroanalytical Chemistry", Vol. 6, A.J. Bard, Editor, p. 187, Marcel Dekker, Inc., New York, 1973.
72. J. Newman, "Electrochemical Systems", Prentice-Hall, Inc., Englewood Cliffs, NJ, 1973.
73. N. Ibl, Current distribution in electrolysis, Oberflache Surface, Vol. 16, 1975, pp.23-32.
74. N. Ibl, in "Comprehensive Treatise of Electrochemistry", Vol. 3, Plenum Press, New York.
75. G.A. Prentice and C.W. Tobias, Survey of numerical methods & solutions for current distribution problems, Journal of the Electrochemical Soc., 129, 1982, pp.72-78.
76. J.A. McGeough, "Principles of Electrochemical Machining", Chapman and Hall, 1974.
77. J.F. Wilson, "Practice and Theory of Electrochemical Machining", John Wiley, 1971.
78. J.H. Hohl and P.J. Hamilton, Errors in calculation of pre-deposition diffustion profiles by iterative numerical methods, Journal Electrochemical Soc., Vol. 124, 1977, p.1912.
79. P.M. Gresho, R.L. Lee, and R.L. Sani, "Finite Elements in Fluids", Vol. 3, p. 335, John Wiley & Sons, Inc., New York, 1977.
80. J.A. Klingert, S. Lynn, and C.W. Tobias, Evaluation of current distribution in electrode systems by high speed digital computers, Electrochim. Acta, Vol. 9, 1964, pp.297-311.
81. G.A. Prentice , PhD. Dissertation, "Modeling of changing electrode profiles", University of California, Berkeley, 1981.
82. Vacuumschmelze GmbH, Gruner Weg 37, D-6450 Hanau-1, FDR.
83. D.M. Allen, T.N. Talib & D.F. Horne, Surface textures and process characteristcs of the electrolytic photoetching of annealed AISI 304 stainless steel in hydrochloric acid, Precision Engineering, April 1983, p.51.
84. D.M. Allen, T.N. Talib, Manufacturing of stainless steel edge filters: an application of electrolytic photopolishing, Precision Engineering, April 1983, p.57.
85. D.M. Allen, T.N. Talib, Electrolytic photoetching of Vitrovac 6025 for the production of magnetic recording heads, Precision Engineering, July 1984, p.125.
86. D. Vitkovitch, "Field Analysis", Van Nostrand, 1966.
87. P.M. Morse, and H Feshback, "Methods Of Theoretical Physics", Part ii:Chapters 9 to 13, McGraw-Hill.
88. H. Lamb, "Hydrodynamics", 6th Ed., C.U.P., 1975.
89. L. Lapidus, "Digital Computation for Chemical Engineering", McGraw-Hill, NY, 1962.

90. A.J. Ahlberg, E.N. Nilson and J.L. Walsh, "The theory of splines and their applications", Accademic Press, NY, 1967.
91. Kodak High Resolution Plate, Eastman Kodak Co., 1974, Pamphlet No. P-47.
92. Kodak High Resolution Film (Thick Ester Base), Eastman Kodak Co., Pamphlet No. P-183.
93. D.M. Allen, D.F. Horne and G.W.W. Stevens, Focusing of precision cameras for photofabrication mask making, The journal of photographic science,Vol. 28, No.3, Mar./Apr. 1980, pp.136-139.
94. D.M. Allen, D.F. Horne and G.W.W. Stevens, Evaluating the registration of mirror-image photoresist stencils, J. Photogr. Sci. 28, Sept./Oct. 1980, p.87.
95. G.W.W. Stevens, Photographic materials and processes used for microelectronics, The Production Engineer, Nov. 1974, pp.437-445.
96. "Recommended practice for standard reference method for making potentiostatic and potentiodynamic anodic polarization measurements", ASTM G5-69, American Soc. Testing Mater., Philadelphia.
97. "Conventions applicable to electrochemical measurents", ASTM G3-74, American Soc. Testing Mater., Philadelphia.
98. "Preparing, cleaning, and evaluating corrosion test specimens", ASTM G1-72, American Soc. Testing Mater., Philadelphia.
99. "Conducting potentiodynamic polarization resistance measurments", ASTM G59-78, American Soc. Testing Mater., Philadelphia.
100. "Conducting cyclic potetiodynamic polarisation measurements for localized corrosion", ASTM G61-78, American Soc. Testing Mater., Philadelphia.
101. F. Mansfield & M. Kendig, Concerning the choice of scan rate in polarization measurment, Corrosion, NACE, Vol. 37, No. 9, Sept., 1981, p.545.
102. K.K. Cheung, Production of precision slot profiles by photoetching and electroforming, Cranfield Inst. of Tech., MSc Thesis, 1980-81.
103. H. Figour & P.A. Jacquet (Le Material Telephonique), Persectionnements aux traitements electrolytiques des metaux, French Pat. 707526, 1930. .
104. P.A. Jacquet, The mechanism of electrolytic polishing of copper, C. R. Acad. Sci. (Paris), Vol. 202, 1936, pp.402.
105. H.H. Uhlig, Electrolytic polishing of stainless steels, Trans. Electrochemical Soc., 1940, p.78.
106. British Pat. 244,111: Improvements in and connected with edge filters Assigned to Aktiebolaget Separator, accepted March 4th 1927.
107. D.M. Allen, D.F. Horne, H.G. Lee and G.W.W.Stevens, Production of spring steel camera shutter blades by photoetching, Precision engineering 1, 1, 1979, pp.25-28.
108. Private communication from Magnetic Components Ltd., Chertsey, Surrey.
109. Private communication from Thorn EMI Central Research Laboratories, Hayes, Middlesex.
110. H. Warlimont and R. Boll, Applications of amorphous soft magnetic materials, R & D Devision, Vacuumschmelze GmbH, D-6450 Hanau, FRG.
111. W. Klement, R.H. Willens and P. Duwez, Non-crystalline structure in solidified gold-silicon alloys. Nature, Vol. 187, 1960, p.869.
112. C. Grand and R. MacKim, Materials with a magnetic future, New Sci., 94(1308), 1982, pp.637-640.
113. A. Honig, Instructions for processing of amorphous metals. Tech. Note Vacuumschmelze GmbH, 1981.

BIBLIOGRAPHY

NO. AUTHOR, TITLE, PUBLISHER, Vol., no., date

1. D.F. Horne, Photomasks, Scales and Gratings, Adam Hilger Ltd., Bristol, 1983.
2. T. Harris, Chemical Milling, Oxford series on advance manufacturing, 1976.
3. F.A. Lowenheim, Electroplating- Fundamentals of Surface Finishing, McGraw Hill, 1978.
4. J. Murdoch, Barnes J.A., Statistics; Problems and Solutions, The Macmillan Press Ltd., 1977.
5. R.A. Higgins, Engineering Metallurgy, The English Universities Press Ltd., 1970.
6. L.F. Adams, Engineering Measurements and Instrumentation, The English Universities Press Ltd., 1975.
7. P. Balta and E. Balta, Introduction to the Physical Chemistry of the Vitreous State, Abacus Press, 1976.
8. S. Wernick, Electrolytic Polishing and Bright Plating of Metals, Alvin Redman Limited, 1948.
9. Blum W. & Hogaboom G.R., Principles of Electroplating and Electroforming, McGraw-Hill Book Company, 1949.
10. J.F. Wilson, Practice and Theory of Electrochemical Machining, John Wiley & Sons Inc., 1971.
11. H.J.S. Sand, Electrochemistry and Electrochemical Analysis, Blackie & Son Ltd., 1945.
12. J.A. Von Fraunhofer, Basic Metal Finishing, Paul Elek (Scientific Books) Ltd., 1976.
13. J.A. Von Fraunhofer, Instrumentation in Metal Finishing, Paul Elek (Scientific Books) Ltd., 1975.
14. H.G. Lee, Photoetching study for making thin spring steel shutter blades, MSc. Thesis, September 1978.
15. G. Lundstrom, An investigation of fluidic element fabrication techniques, specially chemical milling of stainless steel. Cranfield Fluidics Conference, 17-20 March, 1970. Coventry. Paper D2.
16. S. Masum, Photofabrication by Etching: An analysis of etching thick gauge stainless steel. Cranfield, MSc Thesis, 1979.
17. F.A. Cotton, Wilkinson N.G., Advanced Inorganic Chemistry: a comprehensive test., 3rd Edition, New York, Wiley Intersciene, 1972.
18. L. Colombier, J. Hochmann, Stainless and Heat Resisting Steels. Edward Arnold Ltd. London 1967.
19. D. Prenguber, J.B. Mohler, Chemically Milled Finishes and what to expect on various metals and alloys, The Boeing Co., Machine Design, pp133-140.
20. H.A. Liebhafsky, A.E. Newkirk, Corrosion of Stainless Steel

in Ferric Chloride Solution. Corrosion - National Association of Corrosion Engineers, Vol.12, pp. 92-98.
21. J. Parr, A. Hanson, An Introduction to Stainless Steel, American Society for Metals, Chapman and Hall Ltd.
22. Photofabrication methods with Kodak photosensitive resists, Eastman Kodak Company, P-246, 1971.
23. G.O Okamoto, Passive film of 18/8 stainless steel structure and its function, Corrosion Sciene, Vol. 13, 1973, pp 471-439.
24. C.R. Arnold, E.G. Bishop, Hill J.H., Photofabrication of perforated electrodes for a liquid metal ion source. Scientific Administration Division, AERE Harwell, UK, January 1977.
25. J. Kratz, To stamp or to etch - how to choose Electronic Packaging and Production Vol. 8, Feb. 1972, PP. 58-64.
26. K.G. Budinski, Photofabrication of metal parts, Mechanical Engineering, Nov. 1971, PP. 19-21.
27. K. Sikandar, An investigation into the quantification of artwork compensation for producing etched right angle corners in sheet metal by photofabrication, Cranfield, MSc Thesis, 1978.
28. J. Woolman and R.A. Mottram, The Mechanical and Physical Properties of the British Standard EN Steels. Vol. 3, EN 40 - EN 363, Pergamon Press, 1969.
29. S.M. Faris and T.K. Gustafson, Novel microfabrication process,J. Vac. Sci.Technol., Vol. 12, No. 6, Nov/Dec. 1975.
30. M.B. Holland, Electrical Machining - whatever happened to it?, CME, May 1979.
31. R.J. Schaefer and J.A. Blodgett, Holographic Study of Electropolishing, JNL. Electrochemical Soc. USA, Vol. 123, 1976, pp. 1701-1705.
32. D.M. Allen, D.F. Horne, I.A. Routledge, and G.W.W. Stevens, Photoetching of narrow deep slots for stylus wear standards, Precision Engineering, 2 (4), 1980, pp. 177-182.
34. Horne D.F., Dividing, Ruling and Mask Making, Chap. 6.8, Adam Hilger, London 1974.
35. D.M. Allen, D.F. Horne and I.A. Routledge, Radial grating master making, Precision Engineering, 3 (4), 1981.
36. D.M. Allen, D.F. Horne, and I.A. Routledge and G.W.W. Stevens, "High depth to width ratio profiles in (110) silicon produced by anisotropic photoetching. J. Photogr. Sci. 29 (6), 1981.
37. D.M. Allen, Anisotropic etching microtechnology, Precision Engineering, 3 (3), 1981, PP. 161-166
38. D.F. Horne, Recent advances in graticule and mask making, Optica Acta, Vol. 20, No. 12, 1973, PP. 939-957.
39. D.F. Horne, Optical scales, reticles, gratings, masks, and standards, Applied Optics/Vol 20, No. 23, 1 Dec. 1981.
40. D.F. Horne, Manufacturing techniques for making precision circular scales, Precision Engineering, 1980.
41. G. Bellows, Chemical Manufacturing - Production with Chemistry, Machinability Data Center Publication No. MDC 77-102, Feburary 1977.
42. B.R. Delamere, Manufacture of silicon electroforming mandrels by anisotropic etching, Cranfield Inst. of Tech. MSc Thesis, September 1980.

43. A.J. Hegarty, An investigation into variations in etched profile and surface finishes, Cranfield Inst. of Tech. MSc Thesis, September 1980.
44. A.R McCombie, Determination of the optimum etchant and glass specification for chrome-on-glass graticule production, Cranfield Inst. of Tech. MSc. Thesis, September 1981.
45. D.M. Allen, Electrolytic photoetching, The Photo Chemical Machining Institute J., Summer 1982.
46. D.R. Johnson, Photo chemical machining - a viable alternative to stamping, N.E.C., Session 6b, Paper 1, Oct. 1981.
47. C. Poplaski, Unusual photo chemical machined parts, N.E.C., Session 6b, Paper 1, Oct. 1981.
48. D.M. Allen, Photoetched precision devices and components, N.E.C., Session 6b, Paper 1, Oct. 1981.
49. Ugo Betocci, Applications of a lownoise potentiostat in electrochemical measurment, J. Electrochemical Soc. Electrochemical science and technology, September 1980.
50. A.J. Dowell, The alternating curret etching of aluminiumm lithogrphic sheet, Trans. of the Inst. of metal finishing, Vol. 57, 1979, pp.138-144.
51. L. Eyges, Classical Electromagnetical Field.
52. J. Jeans, Electricity And Magnetism, C.U.P., 1946.
53. D.M. Allen, D.F. Horne and G.W.W. Stevens, Production of high resolution photoetched stainless steel plaques, The journal of photographic science,Vol. 28, No.1, Jan./Feb. 1980.
54. D.M. Allen, Photochemical Machining, Electronic Production, September 1982, pp. 113-117.
55. T. Tsuru, S.X. Zhang, and R.M. Latanision, Corrosion Resistance of Microcrystalline alloys, 4th Int. Conf. on Rapidly Quenched Metals, Japan, Aug. 1981.
56. K. Kobayashi, K. Asami, and K. Hashimoto, Spontaneously passivating amorphous iron-base alloys in hydrochloric acids of various concentrations and temperatures, 4th Int. Conf. on Rapidly Quenched Metals, Japan, Aug. 1981, PP. 24-28.
57. M.T. Thomas and D.R.Baer, Corrosion layers formed on Metglass 2826A analysed by AES and XPS,4th Int. Conf. on Rapidly Quenched Metals, Japan, Aug. 1981, PP. 24-28
58. R.M. Latanision, et al., Corrosion resistance, Proc. 3rd Int. Conf. on Mechanical Behaviour of Materials - Cambridge, Aug 1979, PP. 20-24.
59. T. Masumoto and K. Hashimoto, Corrosion properties of amorphous metals, Journal De Physique, 41, 1980.
60. C. Grant and R. McKim, Materials with a magnetic future, New Scientist, 3 June 1982.
61. K.J. Overshott, Amorphous ribbon materials and their possibilities, Electronics & Power, May 1979.
62. D.R. Baer, and M.T. Thomas, Chemistry of corrosion layers on amorphous FENiCrPB alloys, J. Vac Sci. Technol, 18(3), April 1981.
63. R.B. Diegle and M.D. Merz, Corrosion Behaviour of Glassy Chromium-Containing Alloys Prepared by Sputtering, J. Electrochem. Soc. Vol 127, No. 9, Sept. 1980.
64. K. Kobayashi, K. Hashimoto, and T. Masumoto, Spontaneously Passivating Amorphous Fe-Cr-Mo-Metalloid Alloys in 6 HCl at Room

Temperature and 80°C., Sci Rep. R.I.T.U., As9 No.2, 1981.
65. T. Hryniewicz, The solution of electropolishing problems in some particular cases, Surface Technology, 8, 1979.
66. H.P.E. Helle, G.H.M. Beek, and J. TH. Ligtelijn, Numerical determination of potential distributions and current densities in multi-electrode systems, National Assoc. of Corrosion Engineers, Vol 37, No. 9, September 1981.
67. D.R. Gabe, Electropolishing of mild steel in phosphoric and perchloric acid containing electrolytes, Corrosion Science, Vol 13, 1973.
68. Norio Sato, Kiyokatsu Kudo, and Tetsuji Noda, Constant Voltage Electropolishing for Iron and Nickel, NACE,Vol 30, No. 7, July 1974.

APPENDIX A

LITERATURE SEARCH

1. THE COMPUTER SEARCH

i. The initial search, this was carried out at the early stages of the work and was relatively broad. The aims were to cover most of the 'key words' possible for the proposed area of research.

SET	WORD/S	SET	WORD/S
1	Electrochemical etch	2	Electrochemical polish
3	Electrolytic etch	4	Electrolytic polish
5	Electroetch	6	Electro etch
7	Electropolish	8	Electro polish
9	Photofabricate	10	Steel
11	Metal	12	Alloy

The search strategy was as follows:

a) 1 or 2 or 3 or 4 or 5 or 6 or 7 or 8
b) 10 or 11 or 12
c) (a) AND (b)

This search was carried out on 7/2/1980 the data bases that were searched were as follows:

INSPEC	1969 to search date
Chemical Abstracts	1972 to search date
Claims/US Patents	1978 to search date

ii. The departmental search, this was structured by Dr. D. M. Allen to cover in general the area of interest and work in the field of p.c.m. within the department. This is carried out monthly using the SDI Dialogue (Selected dessemination of information). The data files are INSPEC and COMPENDEX.

SET	WORD/S	SET	WORD/S
1	Photoetching	2	Photofabrication
3	Chemical milling	4	etch factor
5	Anisotropic etch	6	Anisotropic etching
7	Electrochemical	8	Mask
9	Jets	10	Nozzle
11	Etch	12	Photoresist
13	Ink jet nozzel	14	Ink jet printing

The search strategy is as follows:

a) 1 OR 2 OR 3 OR 4 OR 5 OR 6 OR 12 OR 13 OR 14
b) (11) AND (10 OR 9 OR 8 OR 7)

iii. The final search, this was made prior to the final draft of the thesis, the aim of which was to carry out a specific search on the subjects of this work.

SET	WORD/S	SET	WORD/S
1	Cobalt alloy	2	Amorphous
3	Metallic glass	4	Stainless steel
5	Nickel alloy	6	Photoetching
7	Photofabrication	8	Photochemical
9	Machining	10	Milling
11	Etching	12	PCM
13	Chemical	14	Electro
15	Electrolytic	16	Electrochemical
17	Chemical polishing	18	Electrolytic polishing

The search strategy was as follows:

a) 1 AND (2 OR 3)
b) 6 OR 7 OR 8 AND (9 OR 10) OR 12
c) 13 OR 14 OR 15 OR 16
d) 9 OR 10
e) c AND b
f) c AND d

This search was carried out on the 27/9/1984 the data bases that were searched were as follows:

INSPEC	1969 to search date
Chemical Abstracts	1972 to search date
Claims/US Patents	1978 to search date
COMPENDEX, Eng. Index	1970 to search date
METADEX, Metals	1966 to search date

2. THE MANUAL SEARCH

An extensive manual search at the CIT library for pubished work and subject related literature was carried out. This was initially a general search, and later became more specific. The main sources covered by the search were:

1. Journal of Electrochemical Society
2. Engineering Index
3. International Journal Production Research
4. Precision Engineering
5. Journal of the Institute of Corrosion Science and Technology, Corrosion Science.
6. The Journal Photo Chemical Institute.
7. The Journal of Science and Engineering, Corrosion, NACE.
8. The Institute of Mechanical Engineers Proceedings.

3. UK PHOTOETCHING COMPANIES

a. Grainge & Hodder Ltd., Birmingham.
b. Graticules Ltd., Tonbridge.
c. Micro-cut, Northampton.
d. Microponent Developments Ltd., Birmingham.
e. Photofabrication (Services) Ltd., Huntington.
f. Photo-Planar Ltd., Walton-on-Thames.
g. Syncronol Industries Ltd., Camberley.
h. Tecan Components Ltd. Waymoth.

APPENDIX B

TWO DIMENSIONAL ANALYSIS OF THE CURRENT DENSITY DITRIBUTION

The following is a two dimensional solution to the Laplacian field satisfying the defined boundary conditions when narrow lines are etched electrolytically through a resist stencil. This is presented in two stages, the first of which satisfies the initial boundary conditions before any metal removal takes place using cartesian co-ordinates. The second involves a reduced problem to satisfy the conditions close to the resist edge after the metal recedes generating an angle between the surface of the resist and the new metal surface, using polar coordinates.

CASE 1

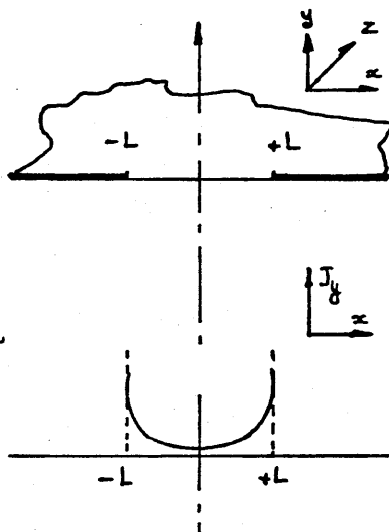

If $\dfrac{\partial^2 \phi}{\partial x^2} + \dfrac{\partial^2 \phi}{\partial y^2} = 0$ for $y < 0$

and ϕ = constant on $y = 0$, $-L < x < +L$

$\dfrac{\partial \phi}{\partial y} = 0$ on $y = 0, \; |x| > L$

From Morse & Feshbach (1) and Lamb (2), for flow through an aperture or slit:

$$- \left[\frac{\partial \phi}{\partial y} \right] = \frac{B}{\sqrt{L^2 - x^2}}$$

Where 'B' is a constant and can be related to the total current (I) passing per unit length in the 'z' direction.

on $y = 0$, $|x| < L$

Then on

$$J_y = \sigma Ey = - \sigma \left[\frac{\partial \phi}{\partial y} \right]_{y = 0} = \frac{\sigma B}{\sqrt{L^2 - x^2}}$$

But,

$$\text{But} \quad I = \int_{-L}^{+L} J_y \; dx$$

'B' can be found in terms of 'J' using the standard integral result:

$$\int_{+1}^{+1} \frac{1}{\sqrt{1 - s^2}} ds = \mathrm{Sin}^{-1}(s)$$

and

$$I = \int_{-1}^{+1} \frac{B}{\sqrt{L^2 - x^2}}$$

By substituting
$$x = Ls$$
then
$$dx = L\, ds$$

$$I = \int_{-1}^{+1} \frac{\sigma B\, ds}{\sqrt{1 - s^2}} = \sigma B \left[\mathrm{Sin}^{-1}(s) \right]_{-1}^{+1}$$

$$I = \sigma A \left[\frac{\pi}{2} + \frac{\pi}{2} \right] = \sigma B \pi$$

Hence,
$$B = \frac{I}{c\pi}$$

and
$$J_y = \frac{I}{\pi \sqrt{L^2 - x^2}} \qquad \text{.............(1)}$$

CASE 2

When etching takes place and the surface of the anode recedes, the boundary conditions change from those of case 1 and a solution for Laplace's equation given the following boundary conditions and at the proximity of the resist is as follows:

$$\nabla^2 \phi = 0 \quad \text{for} \quad -\alpha < \theta < 0$$

$$\phi = C \quad \text{on} \quad \theta = 0$$

$$\frac{\partial \phi}{\partial \theta} = 0 \quad \text{on} \quad \theta = -\alpha$$

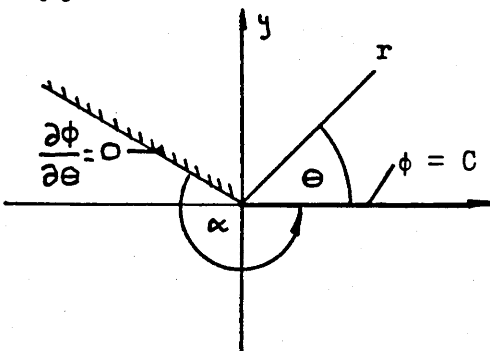

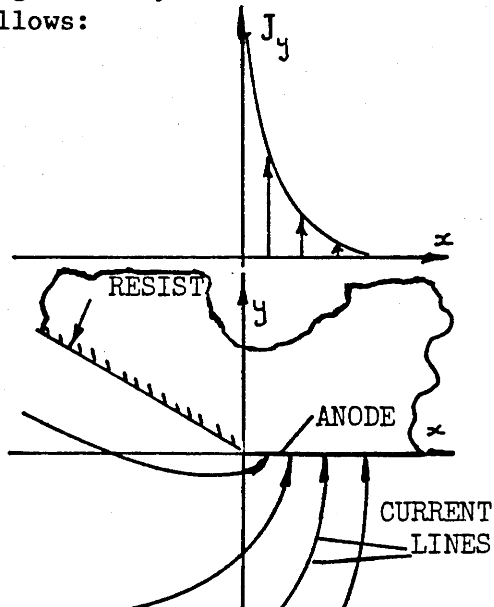

From Eyges (3) a two solution to Laplace's equation is shown to be of this form:

$$\phi\,(r\,,\theta\,) = R\,(r)\;\;F\,(\theta)$$

The function $F\,(\theta)$ is either of the form,

$$\text{Cos}\,n\,\theta, \quad \text{or} \quad \text{Sin}\,n\theta$$

and $R\,(r)$ is of the form r^n

where 'n' is integer.

Similarly Jeans (4) shows that a general form of the solution in three dimensional spherical polar coordinates and using Jeans' notation, is of the form:

$$V = R.S$$

and again $R = f\,(r)$ only,

and $S = f\,(\,\theta,\phi\,)$ only.

For spherical polar coordinates,

$$\frac{\partial}{\partial r}\left(r^2\,\frac{\partial V}{\partial r}\right) + \frac{1}{\text{Sin}\,\theta}\,\frac{\partial}{\partial\theta}\left(\text{Sin}\,\theta\,\frac{\partial V}{\partial\theta}\right) + \frac{1}{\text{Sin}^2\theta}\,\frac{\partial^2 V}{\partial\phi^2} = 0$$

A reduced equation for r and θ for a two dimensional solution is:

$$\frac{1}{r}\,\frac{\partial}{\partial r}\left(\,r\,\frac{\partial V}{\partial r}\,\right) + \frac{\partial^2 V}{r^2\,\partial\theta^2} = 0$$

The solution to this equation is of the form:

$$r^n\,\text{Sin}\,n\,\theta\;, \quad \text{or} \quad r^n\,\text{Cos}\,n\,\theta$$

The value of 'n' needs to be such that the expression for potential 'V' fits the boundary conditions.

If the boundary comprises of two rigid walls at any angle α, then 'n' is of the form:

$$\left(\frac{\pi}{\alpha}\right) \quad \text{(Lamb)}$$

By inspection, a solution of the equation for the given boundary conditions may be obtained.

Using the same notation as in case 1, the solution will be of the

following form:

$$\phi\ (r\ ,\ \theta) = C - r^{n} \operatorname{Sin} n\ \theta \qquad \text{...........(2)}$$

and,

$$\frac{\partial\phi}{\partial\theta} = n\ r^{n} \operatorname{Cos} n\ \theta \qquad \text{...........(3)}$$

Where

$$n = f\ (\tfrac{\pi}{\alpha})$$

For the boundary conditions: $\phi = C$ at $\theta = 0$

$$\frac{\partial\phi}{\partial\theta} = 0 \quad \text{at} \quad \theta = -\alpha$$

hence at , $\theta = 0$,

from equ. 2,

$$\phi\ (r,\theta\ ) = C$$

and at , $\theta = -\alpha$,

from equ. 3,

$$\frac{\partial\phi}{\partial\theta} = 0 = n\ r^{n} \operatorname{Cos}\ (\ -\alpha^{n}) \ .$$

if

$$\operatorname{Cos}\ (\ -\alpha n) = 0$$

hence

$$-\alpha n = \frac{\pi}{2}$$

Therefore,

$$n = -\frac{\pi}{2\alpha} \quad \text{or} \quad \frac{\pi}{2\alpha}$$

$$\phi\ (r\ ,\theta\ ) = C - r^{\frac{\pi}{2\alpha}} \operatorname{Sin}\ (\ \frac{\pi}{2\alpha}\theta\ ) \longleftarrow$$

REFERENCES

1. P. M. Morse, and H Feshback, Methods Of Theoretical Physics Part ii:Chapters 9 to 13, McGraw-Hill.
2. H. Lamb, Hydrodynamics, 6th Ed., C.U.P., 1975.
3. L. Eyges, Classical Electromagnetical Field,
4. J. Jeans, Electricity And Magnetism, C.U.P., 1946.

APPENDIX C

FIELD PLOTTING EQUIPMENT

1. Field Plotter type GRADUATE 6000 with automatic detection and marking.

2. Plotting paper type Anaplot 18" wide.

3. Silver conductived paint.

The figure below is a view of the control panel of the field plotter.

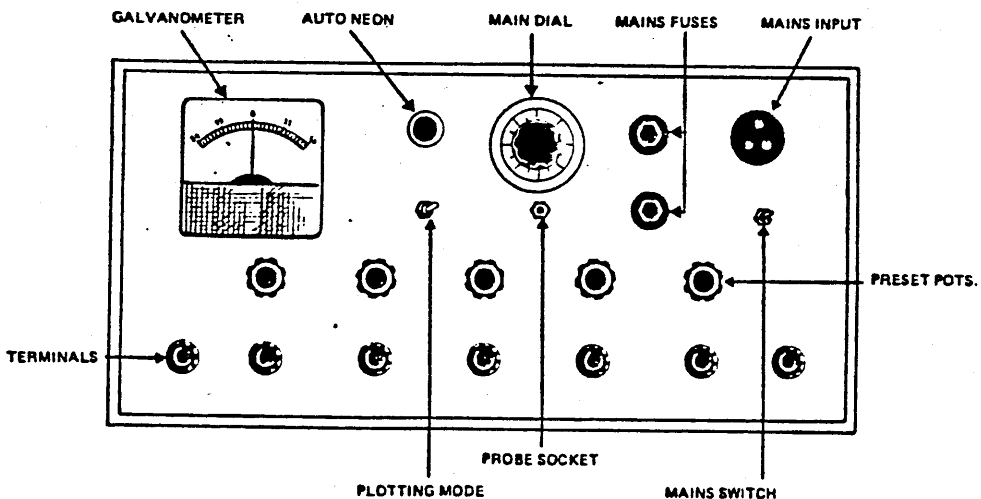

Supplied by:

Sensitised Coatings Ltd.

King's Lynn, Norfolk

APPENDIX D

MANUFACTURERS/SUPPLIERS OF EQUIPMENT AND MATERIALS

A. MANUFACTURERS OF EQUIPMENT

No.	Equipment	Manufacturer
1.	Co-ordinatograph	Aristo-erke Denver Pape Kg, D-2000 Hamburg 50, P.O.B. 500380 West Germany
2.	Reduction camera	David W. Mann Co. (GCA Corporation) Burlington Massachusetts, USA
1.	Dip Coating machine	Cotswold Proces Dipping Equipment Ltd. 164 Slad Road Stroud Gloucestershire, GL5 1RF
3.	Ultra violet exposure unit	Rank Taylor Hobson P.O. Box 36 Guthlaxton Street Leicester LE2 OSP
4.	U.V. exposure unit	Littlejohn Circuit Equipment Ltd. Great Park Street Wellingborough Northants, U.K.
5.	Dry film laminator	ditto
6.	Dry film development spray tank	ditto
7.	Spray etching tank	Procirc Co., Ltd West Haddon England
8.	Metaserv cut-off machine	Metallurgical Services Laboratories Ltd. Reliant Works Brockham Betchworth Surrey RH3 7HW
9.	Metaserv grinder & polisher	Ditto
10.	Metaserv moulds etc.	Ditto
11.	Power supply	Weir Electronics Ltd. Durban Road Bognor Regis Sussex PO22 9RW
12.	Oven	A.Gallenkamp & Co. Ltd. Christopher Street London EC2P 2ER

13.	Hotplate/Stirrer	Ditto
14.	Ammeter & votmeter	Griffin & George Ltd. 285 Ealing Road Alperton Wembley HA0 1HJ
15.	Beam balance	Oertling Ltd. Orpington Kent BR5 2HA
16.	Micrometer (0-25mm) Micro 2000	More & Wright (Sheffield) Ltd. Sheffield, England
17.	Talysurf 3 & 4 measuring instrument	Rank Taylor Hobson P.O. Box 36 Guthlaxton Street Leicester LE OSP
18.	Vickers M41 Photo Plan microscope	Vickers Instruments (Vickers Ltd.) Breakfield Coulsdon Surrey CR3 2UP
19.	Protocol film registration punch	Protocol Registratio systems North Bridge Road Berkhamstead, Herts HP41EJ, UK
20.	Sinclair DM 450	Sinclair Electronics Cambridge
21.	Thompson Potentiostat Ministat 7amp	H. B. Thompson & Ass. Cherwel Sq. West Moor, Newcastle Upon Tyne
22.	Linear Sweep Gen. Type DRG 16	Ditto
23.	Calomel Ref. Electrode Type 1370	Kent Industrial Measurment Ltd. EIL Instrements Chertsey, Surrey
24.	Potentiostat Type 703A	Chemical Electronics (Britley) Ltd. Britley
25.	Linear sweep Gen. Type LSU 1	Ditto
26.	Lloyd PL 50 X-Y Recorder	J J Lloyd Inst. Ltd. Brook Av., Warsash Southampton

MATERIALS

1.	CD/70 Cleaner/ De-oxidiser	Robertson Chemicals Diss, Norfolk

2.	Quadralene cleaner	Quadralene Chemicals Ltd Liversage Works Bateman Street Derby DE 3 8JL
3.	Photographic materials a) HR Plates Type 1A b) HR Film Type SO-343 c) Kodak D8 developer d) Kodak Rapid Fix e) Photo-Flo 600	Kodak Ltd. P.O. Box 66 Hemel Hempstead Herts. HP1 1JU
4.	Resin MY753 Hardener HY596	Ciba-Geigy Plastics and Additives Co. Duxford, Cambridge CB2 4QA
5.	Beeswax	Trylon Ltd. Wollaston, Northhants.
6.	Shipley AZ-340 photoresist	Shipley Europe Ltd. Humber Avenue Coventry
7.	Shipley AZ developer AZ-303	Ditto
8.	Laminar AM dry film Photoresist	Thiokol Chemicals Ltd. Longley Lane Wythenshawe, Manchester
9.	Developing agents KB 1A & KB 1B	Ditto
10.	Waycoat SC180	Hunt Chemicals Ltd. Grovelands Indus. Est. Longford Rd. Coventry
11.	Asphaltum 'Washout'	Howson-Algraph Ring Rd. Seacroft, Leeds

APPENDIX E

CO-ORDINATOGRAPH AND SCRIBING TOOLS

The ARISTO co-ordinatograph model 4438/1 is equipped with rotary table and permits drafting in rectangular co-ordinates, and polar co-ordinates. The drafting surface is ground transparent plate glass, uniformly illuminated from beneath. The rotary table is positioned by means of a slow motion srew. The measuring dials for the orthogonal system embody verniers reading to 0.0127 mm. Some of the specifications for the ARISTO co-ordinatograph used are as follows:

Circle Division 360°

Working area 800mm dia or 850 x 850 mm

Plotting accuracy ± 0.02 mm

The graduations on the rails are figured by interchangeable numeration tapes. The position of the origin (zero point) of the co-ordinate system can be freely chosen. This being so because the numeration tapes can be shifted by winding on the spools. The recording dials are turned by the meshed pinion, allowing the index mark of the carriage to be brought to any desired graduation on the measuring scale. The various working instruments (tools) are accommodated in the socket of the ordinate carriage. During the work two types of tools were used and as follows:

i. The cutting and scribing tool '7600' slides on a support roller and this is provided with an adjustable built-in spring system to control the tool-bit pressure. It ensures constant cutting and scribing depth. Line width achieved by this tool is 0.1 mm.

ii. The small circle cutting device '7731' incorporates similar basic features to the '7600'. Additionally, it has an accuracy of ±0.015 mm while scribing small circles. It can scribe up to 10.00 mm radius circles. It was found that the radii setting mechanism resulted in a constant error of 0.18 mm. This was allowed for in the final artwork.

APPENDIX F

THE REDUCTION CAMERA

A 1st Reduction type Camera (Type 1503 by David W. Mann Co.) featuring:

1- A screen using green transmitted light.

2-Vacuum screen and pump.

3- Fitted with a Carl Zeiss S-Planar f1.4 60mm lens (No.4330836).

4- Plate holders 50.8 x 50.8mm & 63.5 x 63.5mm.

The camera was designed to give a reduction of between 13:1 and 25:1. The reduction used throughout the bulk of the work was 20:1. The reduction ratio being controlled by the distance between the screen and the lens was set utilising a previously prepared reduction calibration chart. The results were further checked using the micoscope on the camera.

Back illumination of the screen is a feature of the camera system where a transparent blanket of thin polyester sheet was placed over the screen. This was used to retain the vacuum generated between the screen and the polyester sheet. This causes the elimination of the air and the flat retention of the artwork. This is necessary to achieve sharp definition.

Fluorescent tube light, green in colour illuminated the screen and this is regulated to less than 5% variation in intensity of illumination.

Made By: David W. Mann Co.
GCA corporation
Burlington
Massachusetts, USA

APPENDIX G

DEVELOPMENT PROCEDURE FOR EXPOSED HIGH RESOLUTION PLATES KODAK TYPE 1A

The development of exposed photographic plates was carried out under safe-light by processing in the following materials and sequences:

	Solution	Time
1.	Kodak D8 developer	2.5 minutes
2.	Cold running water	quick rinse
3.	Kodak Rapid Fixer (1+3) Solution	3 mins
4	Filtered cold running water	5 min
5.	Kodak Photo-Flo 600 Solution (1+600)	20 seconds

Exposed plates were immersed into the Kodak D8 developer (1) with the emulsion surface upwards in order to prevent scratches during agitation and to ensure good development. The plates were then given a rinse in cold running water before immersing it in the Kodak Rapid Fixer. Solution (3). The plate was then given a good rinse, for 5 minutes, under filtered cold running water. This was essential to produce a clear transparent background. To prevent drying marks, it is necessary to dip the plate in Kodak photo-flo 600 solution which helps remove the water off the surface of the plate uniformly during drying.

MAKING A MASK BY REVERSAL DEVELOPMENT

Reversal development processing technique was used to obtain a mask as a duplicate of the master. The procedure in making such a mask is as follows:

1. Operation	Solution	Time (mins)
2. Develop	Kodak D8	3.0
3. Wash	Cold running water	1.0
4. Bleach	R21a (1 + 9)	2.0
5. Wash	Cold running water	0.5
6. Clear	Na_2SO_3 (10% w/v)	0.5
7. Re-expose (room light)	Na_2SO_3 (solution)	0.5
8. Re-develop	Kodak D8	2.0
9. Quick rinse	Cold running water	-
10. Fix	Kodak Rapid Fixer (1 + 3) v/v solution	1
11. Wash	Cold running water	5.0
12. Dip	Photo-flo 600 (1 + 600) v/v solution	0.25

NOTE:

1. A fresh sodium sulphite (Na_2SO_3) solution is prepared for every mask.
2. The developing process is carried out at $20^{\circ}C$ room temperature.
3. Bleach R21a should be prepared by the following procedure:

(a) dissolve 12.5 gm of potassium dichromate in 200 ml of distilled water;
(b) add 12.5 ml of concentrated sulphuric acid very gradually and with constant stirring to keep the solution temperature down. Mixing should be done in fume chamber;

(c) top up to 250 ml with distilled water;

(d) the bleach used was diluted in the ratio of (1+9) by volume.

APPENDIX H

REGISTRATION FOR DOUBLE-SIDED MASK

A double-sided mask must be accurately registered to ensure correct alignment while etching from both sides. The masks were made from Kodak SO-343 film.

REGISTRATION EQUIPMENT

A 'Protocol Film Registration Punch' produces two holes simultaneously. A round and a rectangular hole are punched into the film. The round hole controls the registration where a Protocol ground round pin where (interference fit of 0.025mm) is placed. The rectangular hole, houses a rectangular pin thus preventing lateral movement.

Making a mirror image mask

The first mask was made from the master plate onto a SO-343 film. This mask was placed on the registration punch with emulsion side up and the two holes were then punched simultaneously. A suitable size unexposed SO-343 film was then punched in the same way as previously, but with the emulsion side down. The latter operation was carried out under red safe light. It was then placed in contact with the pre-punched mask with the register pins fitting in their respective holes in both parts of film. The unexposed film was then contact printed with an exposure period and method as that used for the first mask. It was then suitably developed producing mirror image and registered double-sided mask. Registration of the two parts of the masks was checked with aid of the microscope. Spacers equal to the thickness of the {metal + resist} were punched in a similar manner and spaced according to the required thickness between the two parts of the phototool.

Equipment Supplied By:

Protocol Registration Systems
North Bridge road, Berkhamstead, Herts.

APPENDIX I

AISI 304 STAINLESS STEEL

This is a readily available, low carbon content, steel which is produced in a range of standard thicknesses. This stainless steel was manufactured to AISI 304 specification. It is an austenitic steel, supplied in this particular case in the annealed form. Annealed steel has two advantages over its' cold rolled counterpart. The first is that any hardness produced by the cold working is removed and the second is that precipitated carbides at the grain boundaries are redissolved into the matrix.

MATERIAL SPECIFICATIONS

i. Material: Stainless steel AISI 304
BS 1449/1972: Part 4

ii. Heat treatment: Annealed

iii. Chemical composition (304 S16)

Element	Maximum (%)
chromium	19.00
nickel	11.00
manganese	2.00
silicon	1.00
sulphur	0.30
carbon	0.06
phosphorous	0.045

iv. Hardness: 500-600 HV

v. Surface finish: Softened and descaled with an Ra value of 0.1 μm.

vi. Supplier:

Knight Strip Metals Ltd
Cranborne Road
Potters Bar
Herts. EN6 3JL (UK)

APPENDIX J

SPECIFICATIONS FOR RECOVAC

COMPOSITION:

Ni	Mo	Cu	Ti	Nb	Fe
76.5%	4%	4%	2%	3%	balance

STRUCTURE: Polycrystalline

SUPPLIED BY:

Vacuumschmelze GmbH
Gruner Weg 37,D-6450 Hanau-1
Federal Republic of Germany.

1. Introduction

Recovac is a high-permeability nickel-iron alloy similar to MUMETAL, which through special additives, exhibits significantly higher resistance to wear and enhanced hardness when compared with normal high-permeability alloys. This material is thus particularly suitable for the manufacture of wear-resistant magnetic heads for tape recorders and magnetic-tape information-storage devices.

Until now, only the NiFe alloys, including the aluminium-iron have been used for these purposes. However, in comparison Recovac has a resistance to wear which is higher by a factor of 7-10 accompanied by only slightly lower permeability. In comparison with an aluminium-iron alloy the resistance to wear is about the same, but the initial permeability of Recovac is higher by a factor of 5. Additionally, Recovac has the advantage where it can be cold-worked.

Apart from use in the technique of magnetic head manufacture, Recovac is suited for applications where a material which is highly resistant to wear and exhibits high values of permeability is required, e.g. relay components.

2. Forms of supply

Recovac is usually available in the form of cold-rolled strip or preannealed strip capable of being deep-drawn. It can also be supplied heat-treated. Table 1 gives the ranges of strip sizes.

Table 1: Strip thicknesses and widths for Recovac

Strip thicknesses (mm)	Maximum strip width (mm)
0.25...1.0	140
0.1...0.2	120
0.05	100
0.025	100

3. Magnetic properties

Table 2 shows the magnetic properties of Recovac after optimal final annealing. Fig. 1 shows the induction-field strength curves at 50 Hz for tapewound cores.

Table 2: Average values for the magnetic properties for Recovac of various strip thicknesses after optimal final annealing.

Properties			Thickness of strip		
			0.1mm	0.05mm	0.025mm
Coercivity	Hc	mA/cm	15	20	30
Permeability at 4 mA/cm, 50Hz	$\mu 4$		40000	30000	20000
Maximum (50 Hz) permeability	μmax		100000	80000	50000
Induction at 1 A/cm	B1	T	0.45	0.44	0.43
Saturation induction	B	T		about 0.5	
Curie temperature	Tc	°C		280	
Specific electrical resistivity		$\frac{\Omega.mm}{m}$		0.9	
Loss in magnetic hysteresis	P				
at 0.3 T/50 Hz		W/Kg	0.01	0.015	0.02
at 0.3 T/1 kHz		W/Kg	0.6	0.6	0.6
at 0.2 T/20 kHz		WKg	30	12	8

4. Mechanical properties

The mechanical properties are less dependent on the strip thickness than the magnetic properties. The values given in Table 3 are average values for strip from 0.1 to 1 mm thickness.

Table 3:

Average values for the mechanical properties of Recovac for the following conditions: cold rolled, pre-annealed and ready heat-treated.
Strip thickness: 0.1 to 1 mm.

Properties		Condition		
		hard (cold rolled)	pre-annealed	ready heat-treated
Vickers hardness		400	170-200	230
Yield point	N/mm^2	1370	360	540
Breaking point	N/mm^2	1400	800	1000
Elongation	%	0.5	33	25
E-modulus	N/mm^2		190000-200000	

Appendix K

SPECIFICATIONS FOR VITROVAC 6025

COMPOSITION:

Co	Fe	Mo	Si	B
66%	4%	2%	16%	12%

STRUCTURE: Amorphous

SUPPLIED BY:

Vacuumschmelze GmbH,
Gruner Weg 37, D-6450 Hanau-1,
Federal Republic of Germany

(i) Characteristics of the alloy:

An amorphous soft magnetic Co-based alloy. With suitable heat treatments, tape-wound cores exhibiting square hysteresis loops (Z) or flat loops (F) are achieved. As the alloy is largely free of magnetostriction it shows favourable magnetic properties even without heat treatment (6025 X). Ribbons are available in widths of 3, 10, 15 and 20 mm and in thicknesses of 0.025 to 0.04 mm.

(ii) Magnetic properties of tape-wound cores (typical values):

Material Heat treatment for	6025 X	6025 F F loop	6025 Z Z loop
Permeability $\mu 4$, dc	10000	250000	700000
Permeability $\mu 4$, 50 Hz	10000	150000	150000
Permeability μmax, dc	100000	300000	1000000
Coercivity dc, mA/cm	8-15	3	3
Remanence ratio Br/Bm	0.05-0.3*		>0.8
Total loss (B=0.2 T; f=20 KHz)W/Kg	15	6	10
Saturation induction, T		0.55	
Curie temperature, °C		250	
Saturation		<0.3 x 10	

*Approximate and adjustable by heat treatment

(iii) Physical and mechanical properties (typical values):

Properties (as cast; without additional heat teatment)	
Density, g/cm^3	7.7
Electrical resistivity, mm^2/m	1.35(=135 $\mu\Omega$cm)
Temperature coefficient of resistance (0-200° C), K^{-1}	1-2 x 10^{-4}
Thermal expansion coefficient, 10^{-7} /K	125
Vickers hardness, (HV_{02})	1000
Tensile strength, N/mm^2	1500-2000
Young's modulus, kN/mm^2	approx 150
Bending fatigue limit (10^7 load cycles), N/mm^2	±700
Minimum bending radius without deformation, mm	2
Upper application temperature, °C	80
Crystallization temperature, °C	approx. 500

APPENDIX L

MEASUREMENT OF VISCOSITY & RESIST THICKNESS

1. Measurement of resist viscosity.

The Hunt Waycoat SC180 had an initial viscosity of 60 Zahn second. During use the resist vicosity increases owing to evaporation.

The photoresist viscosity was measured with the aid of a Zahn cup, this is a viscosity cup with a small orifice at the bottom. Measurements were carried out under yellow safe light. Xylene was the solvent used for reducing the viscosity of the Waycoat SC180 photoresist. This was by adding the xylene to the resist in a glass beaker, the zahn cup was then immersed and filled to the rim of the cup and then gently withdrawn vertically. The time taken for the photoresist to flow through the orifice until the first interruption in the continuous flow was then recorded. Adjustments by the addition of controlled amounts of xylene were made until a duration of 60 seconds was achieved and hence a viscosity of 60 zahn seconds

2. Direct measurement of resist thickness.

The resist thickness was measured by a direct method with the aid of a digital micrometer 'Micro 2000' (0-25mm) with a display resolution of 0.001mm. Measurements were carried out by measuring the thickness of the substrate before and then after coating. The difference was then divided by two giving the mean thickness per reading. This operation was repeated ten times and from the results an average final result was used, this as follows:

a) Dry film resist (Laminar AM) was 26μm thick.

b) Liquid resist (Waycoat SC180 @ 60 zahn sec.) coated with an extraction rate of 100mm/min. was 3μm thick.

APPENDIX M

DEVELOPMENT OF THE PHOTORESISTS

A. Development procedure for the dry film resist.

The Laminar AM resist is developed in a spray tank. The composition of its developer is as follows:

1. Solution A (KB1A - an alkaline mixture)
2. Solution B (KB1B - an organic solvent)

Twenty four litres of water is mixed with one litre of solution A and 250 ml of solution B .

The developing machine featured a temperature control system and a developing duration timer. The samples were suspended in the developing tank by means of stainless steel clips and the developer sprayed on to both sides of the exposed resist simultaneously. After development, the substrate is washed thorughly.

Materials were supplied by Thiokol Photochemicals Ltd. Longley Lane, Manchester, M22 4SY.

B. Development procedure for liquid photoresist.

The exposed photoresist coatings made with Hunt 'Waycoat SC180' were developed by dissolving the unexposed areas of the coating with the following:

i. Xylene 60%
ii. White spirit 40%

The substrate is immersed in the above solution for two minutes, during which it is turned over after the first minute to ensure equal development on both sides. After development it was rinsed in cold running water to wash away the unexposed areas of the resist. Cold running water is used to avoid any adverse effects in subsequent stages.

APPENDIX N

PRELIMINARY TESTS FOR SELECTING ELECTROYTES FOR WORKING STAINLESS STEELS

The recommended electrolytes for electro etching and polishing of stainless steels.The first group was from Shchigolev main text reference [10].

			Anodic c.d. (A/dm^2)	Temp. ($^{\circ}C$)	Time (mins.)
A-	H_3PO_4	42%	20-80	90-140	8-15
	Glycerol				
	H_2O	11%			
B-	H_3PO_4	40-45	40-70	70-80	5-15
	H_2SO_4	37-34			
	CrO_3	3-4			
	H_2O	20-17	(Cathode Pb)		
C-	H_3PO_4	65	5-25	40-70	
	H_2SO_4	15			
	CrO_3	5			
	Glycerol	12			
	H_2O	3	(Cathode Pb)		
D-	H_2SO_4	11	40-60	40-80	2-5
	CrO_3	35-50g			
			(25-30 volts)(Pb)		
E-	H_2SO_4	50	30-100	80-90	3-10
	Glycerol	40			
	H_2O		(Cathode Pb)		
F-	H_2SO_4	15-20%	5-50	43-54	5-10
	H_3PO_4	63-67%			
	H_2O	13-22%	(Cathode Pb)		
G-	Citric acid	50-70%	10-20	45-125	5-10
	H_2SO_4	15-20%			
	H_2O	25-30	(Cathode Pb)		

The following was from "The fabrication of perforated metallic light attenuators and other similar items by a foil etching." by B.A. Pospelov, Ye. M. Ostashinskaya & T.I. Solouyeva. Main text reference [26].

			Anodic c.d. (A/dm^2)	Temp. ($^{\circ}C$)	Time (mins.)
H-	Fe SO_4	100g/l	4-8	20	-

$.7H_2O$

NaCl	200g/l
CH_3COOH glac.	40g/l

The following are from Tegart, main text reference [9].

			Anodic c.d. (A/dm)	Temp. (C)	Time (mins.)
I-	H_2SO_4	110ml	8-55 or (6-8V)	50-125	1-3
	Citric Acid	600g			
	Methyl Alco.	250ml	(Cathode S.S)		
J-	H_3PO_4	300ml	7.8110 +5	15	
	Glycerol	530ml	(Cathode S.S)		
	H_2O	90ml			
K-	H_2SO_4	125ml	7.8-22.5	82-88	5-10
	H_3PO_4	650ml	or		
	H_2O	225ml	(8-15V)		

The following was from the Kodak publication, main text reference [25]

L-	HCl(37%)	1 vol.	Etching at 6 volts
	H_2O	3 vol.	

PROCEDURES

Small amounts of electrolytes A to L were prepared and tested according to the recomendations published with AISI 304 stainless steel coated with the following photoresists:

a) Laminar AM dry film resist (26μm thick).
b) Waycoat SC180 liquid resist where the viscosity was 60 zahn sec. and a coating extraction rate of 100mm/minute were used.

The recomended modes of etching were used mode and each current/ voltage setting was at the middle of the recommended range.

Remarks

1- All electrolytes containing CrO_3 caused damage to the resist B,C & D.
2- Good polishing results were obtained with electrolytes A & J.
3- Electrolytes F & K caused excessive pin holes & damage to resist.
4- Electrolyte L produced good results with a matt finish.
5- Electrolyte G produced good polished results.
6- Electrolyte H produced Vitrical Striations & a poor surface.
7- Electrolyte I solidified below 50° Approx.

APPENDIX O

DESIGN OF GALVANOSTAT

1- SPECIFICATIONS

1. 4 Amps. Continuous Rating
2. Current Stability <0.2%
3. Ripple Content 0.1%
4. Maximum Voltage 0-30 volts

The design is illustrated in the attached figure and consists of the following components.

2- COMPONENTS

i. Semiconductors:

D1 Bridge Rectifier 15A + Heat sink
D2 ditto 5A
TR1,2 2N3055 (plastic package) + Heat sink
TR3 2N3053 + Heat sink

IC2	7805	+5V	Voltage Regulator (1.5A)
IC3	7824	+24V	Voltage Regulator (1.5A)
IC4	7908	-8V	Voltage Regulator (1.5A)
IC1	MC1436	Operational Amplifier by Motorola	

ii. Capacitors:

C1,2	1000 μF,	63V	electrolytic
C3	10,000 μF,	63V	electrolytic
C4	1000 μF,	25V	electrolytic
C5,6,7	10 nF		ceramic
C8,9	100 nF		ceramic

iii. Variable Resistors (ohms):

VR1 10K Trim. pot.
VR2 1K 10 turn pot.

iv. Resistors (ohms):

R1	0.33
R2	1
R3	10
R4	100
R5	1K

The two 0.5 output resistors are 10 watts each.

v. Others:

Switch: . 5 way single pole
Transformer: 150 VA, 240V:24V & 20-0-20V

3- OPERATION

- VR1 Is the null adjustment for IC1. This is set to give OV output at '6' when inputs '3' and '2' are grounded.
- VR2 Current output control.
- SW The circuit may supply currents from 100 μA to 3A in 5 overlapping ranges.

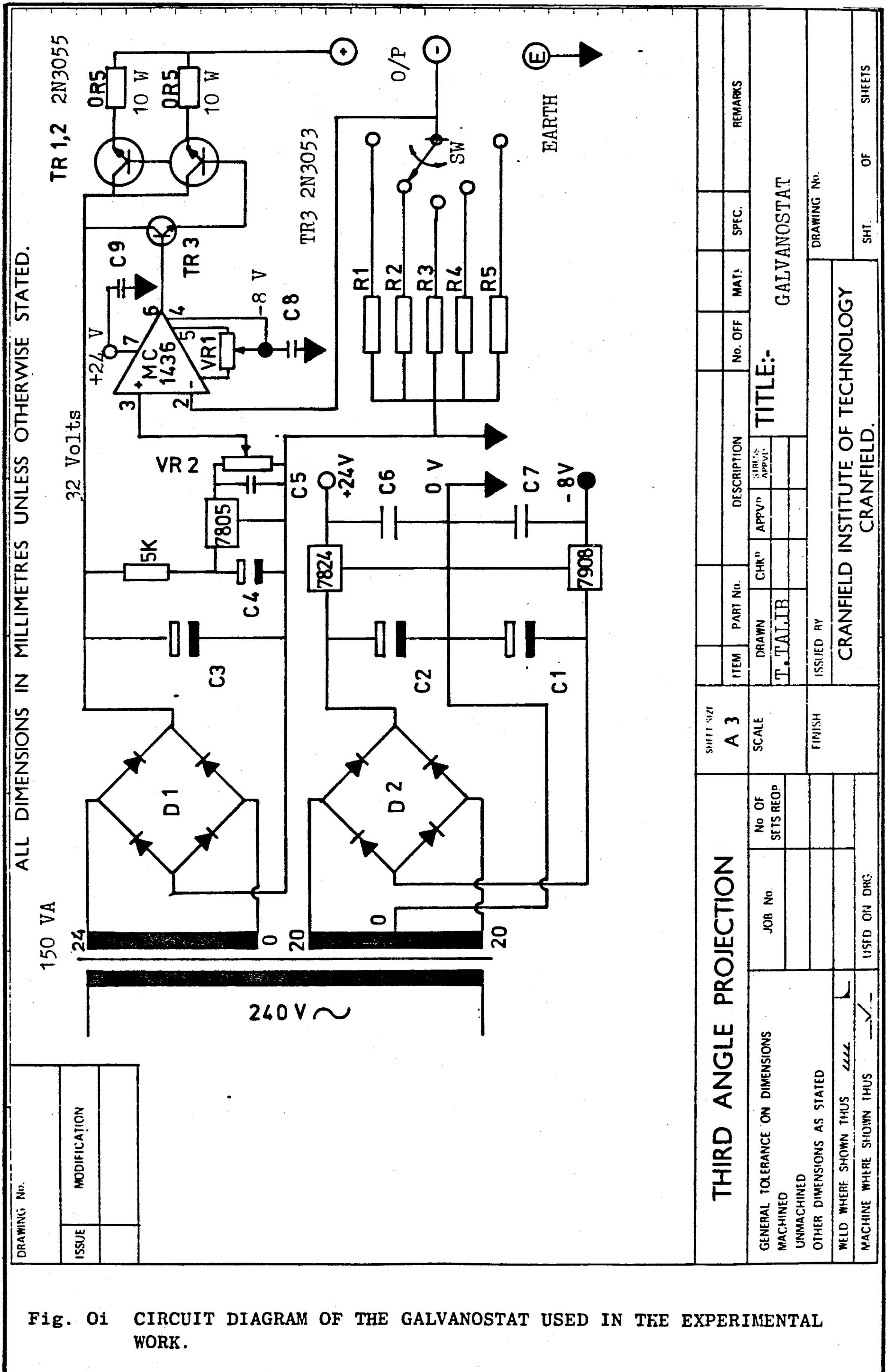

Fig. Oi CIRCUIT DIAGRAM OF THE GALVANOSTAT USED IN THE EXPERIMENTAL WORK.

APPENDIX P

MEASUREMENT OF SURFACE ROUGHNESS

The centre line average (Ra) value is the arithmetical average value of the surface value of the departures of the profile both above and below its' centre line over the prescribed sampling length (Ref.)

$$Ra = \frac{1}{L}\int_{0}^{L} y \, dx$$

where, L = sample length

The Peak-to-Valley (R max) is as its' name implies, the distance between the highest peak and the lowest valley over the sample length (Ref.)

Trace recordings and Ra values were obtained by use of a Talysurf 4 measuring instrument. The Ra values obtained were influenced by the sample flatness. Surface texture values were obtained by taking a series of traces as described in the main text as this depended on the particular feature being measured. In general three measurements were made and were in 'x', 'y', and at 45 degrees to either of the first two measurements. Hence, an average Ra value was obtained for all directions. On the instrument a 'K' cut-off length was selected for all results. When taking repeated traces across the surface care was taken to avoid previous stylus tracks which may influence the resultant values.

The peak-to-valley was determined from the surface trace produced by the machine, this by measuring the the maximum and minimum deflectons about the centre of the trace.

REFERENCE:

A. J. T. Scarr, Metrology and Precision Engineering, McGraw-Hill, London.

APPENDIX Q

THE COMPUTER AND SOFTWEAR

The computer used throughout the experimental work for the analysis and plotting of the results was a 'Hewlett Packard' type HP 85A.

Three programs were used in the work and these are part of the standard softwear pack supplied with the machine. The programs used are as follows:

1. Auto data plot (DPLOT).
2. Auto function plot (FPLOT).
3. Curve fitting (CURVE).

1. Auto data plot

This program automatically sets up scaling factors and plots a user entered set of paired data. Data can be either entered from the keyboard or from a data file. The data set can contain up to 200 data points.

After data has been entered, it can then be printed, edited, and ploted. In the plot specification, the scale factors can selected automatically. The X-axis labels can either be vertical or horizontal and in general tic and lable spacing can also be selected. Further user defined labels can also be included and a grid may be drawn.

2. Auto function plot

This program will automatically set up the scaling factors and plot a user defined function. The function is stored as single or multi-line function starting at line 5000 before running the program. Up to 25 points of singularity can be entered which will be checked and skipped before calling the function. A table of values can also be printed on request.

3. Curve fitting

This program can be used to fit data to:

i. Straight lines (linear regression); $y = a - bx$

ii. Exponential curves; $y = ae^{bx}$ $(a>0)$.

iii. Logarithmic curves; $y = a + b \ln x$.

iv. Power curves; $y = ax^{b}$ $(a>0)$.

The type of curve fit is specified after data is entere. Any curve can be specified by pressing the desired key. Data is entered from the keyboard, but can then be stored on tape. the program will accept a maximum of 200 data pairs. The entered data can also be tabulated. Once the curve fit has been selected, the regression values will be calculated. The coefficent of determination, r^2,

indicates the quality of fit achived by the regression. Values of r^2 close to 1.00 indicate a better fit than values close to zero. The regression coefficents, a and b, define the curve generated, according to the equations above. After the analysis of variance has been calculated and printed, plotting the regression line over the data may be carried out. Projections can also be made based on the curve fit. The analysis of the variance which is printed for each regresion type prints the following values:

a) Degrees of freedom (DF).
b) Sum of squares (SS).
c) Mean sum (MS).
c) F-ratio (F).
d) r^2 (R SQUARE).

The value of the F-ratio is set to 999.9 if it is greater than 999.9. Therefore if the r^2 value is close or equal to 1, the value of the F-ratio is printed as 999.9. The method of calculating the coefficients a and b and also r^2 are in illustriated in the figures Qi attached to this appendix.

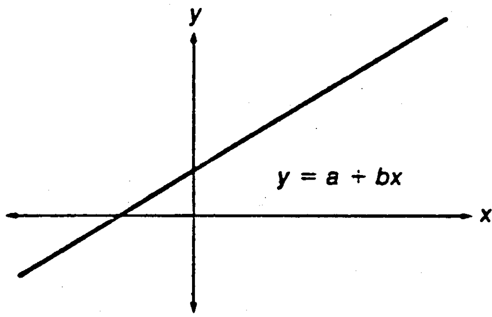

$$b = \frac{\Sigma x_i y_i - \frac{\Sigma x_i \Sigma y_i}{n}}{\Sigma x_i^2 - \frac{(\Sigma x_i)^2}{n}}$$

$$a = \left[\frac{\Sigma y_i}{n} - b\,\frac{\Sigma x_i}{n}\right]$$

$$r^2 = \frac{\left[\Sigma x_i y_i - \frac{\Sigma x_i \Sigma y_i}{n}\right]^2}{\left[\Sigma x_i^2 - \frac{(\Sigma x_i)^2}{n}\right]\left[\Sigma y_i^2 - \frac{(\Sigma y_i)^2}{n}\right]}$$

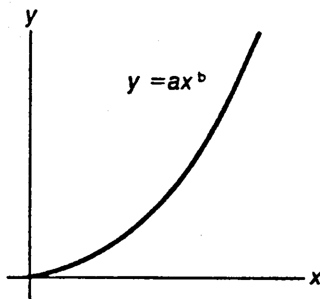

$$b = \frac{\Sigma(\ln x_i)(\ln y_i) - \frac{(\Sigma \ln x_i)(\Sigma \ln y_i)}{n}}{\Sigma(\ln x_i)^2 - \frac{(\Sigma \ln x_i)^2}{n}}$$

$$a = \exp\left[\frac{\Sigma \ln y_i}{n} - b\,\frac{\Sigma \ln x_i}{n}\right]$$

$$r^2 = \frac{\left[\Sigma(\ln x_i)(\ln y_i) - \frac{(\Sigma \ln x_i)(\Sigma \ln y_i)}{n}\right]^2}{\left[\Sigma(\ln x_i)^2 - \frac{(\Sigma \ln x_i)^2}{n}\right]\left[\Sigma(\ln y_i)^2 - \frac{(\Sigma \ln y_i)^2}{n}\right]}$$

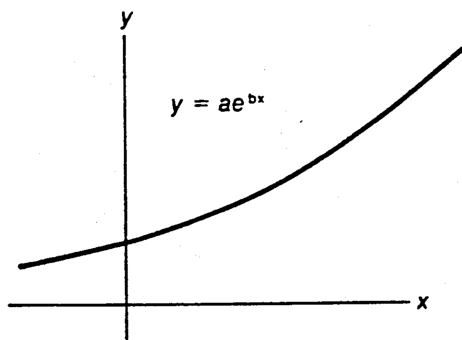

$$b = \frac{\Sigma x_i \ln y_i - \frac{1}{n}(\Sigma x_i)(\Sigma \ln y_i)}{\Sigma x_i^2 - \frac{1}{n}(\Sigma x_i)^2}$$

$$a = \exp\left[\frac{\Sigma \ln y_i}{n} - b\,\frac{\Sigma x_i}{n}\right]$$

$$r^2 = \frac{\left[\Sigma x_i \ln y_i - \frac{1}{n}\Sigma x_i \Sigma \ln y_i\right]^2}{\left[\Sigma x_i^2 - \frac{(\Sigma x_i)^2}{n}\right]\left[\Sigma(\ln y_i)^2 - \frac{(\Sigma \ln y_i)^2}{n}\right]}$$

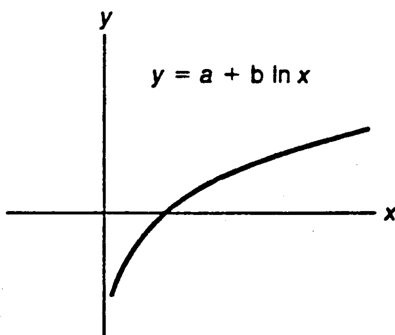

$$b = \frac{\Sigma y_i \ln x_i - \frac{1}{n}\Sigma \ln x_i \Sigma y_i}{\Sigma(\ln x_i)^2 - \frac{1}{n}(\Sigma \ln x_i)^2}$$

$$a = \frac{1}{n}(\Sigma y_i - b\,\Sigma \ln x_i)$$

$$r^2 = \frac{\left[\Sigma y_i \ln x_i - \frac{1}{n}\Sigma \ln x_i \Sigma y_i\right]^2}{\left[\Sigma(\ln x_i)^2 - \frac{1}{n}(\Sigma \ln x_i)^2\right]\left[\Sigma y_i^2 - \frac{1}{n}(\Sigma y_i)^2\right]}$$

Fig.Q

APPENDIX R

THE POTENTIODYNAMIC RESULTS

This appendix contains all the results of the potentiodynamic measurements carried out on AISI 304 stainless steel in 10 HCl w/w at electrolyte temperatures of 15, 20, 25, 30°C. The results may be located as follows:

i. Measurements carried out at 15°C are coded A1 to A18 in figures R1 to R6.

ii. Measurements carried out at 20°C are coded B1 to B9 in figures R7 to R9.

iii. Measurements carried out at 25°C are coded C1 to C9 in figures R10 to R12.

iv. Measurements carried out at 30°C are coded D1 to D9 in figures R13 to R15.

The current density was measured directly from each result at anode potential intervals of 100mv (v.SCE). The mean and standard deviation for each potential measurement was calculated using a 'Texas Instrument SR-51A' calculator. This was repeated for all four electrolyte temperatures.

The percentage ratio of standard deviation per current density was also calculated as follows:

$$\text{The \% ratio of s.d.} = \frac{\text{s.d.}}{J} \times 100$$

The results are tabulated in figures R16 & R17 for 15°C, and in figures R18, R19 & R20 for electrolyte temperatures of 20, 25 & 30 C° respectively.

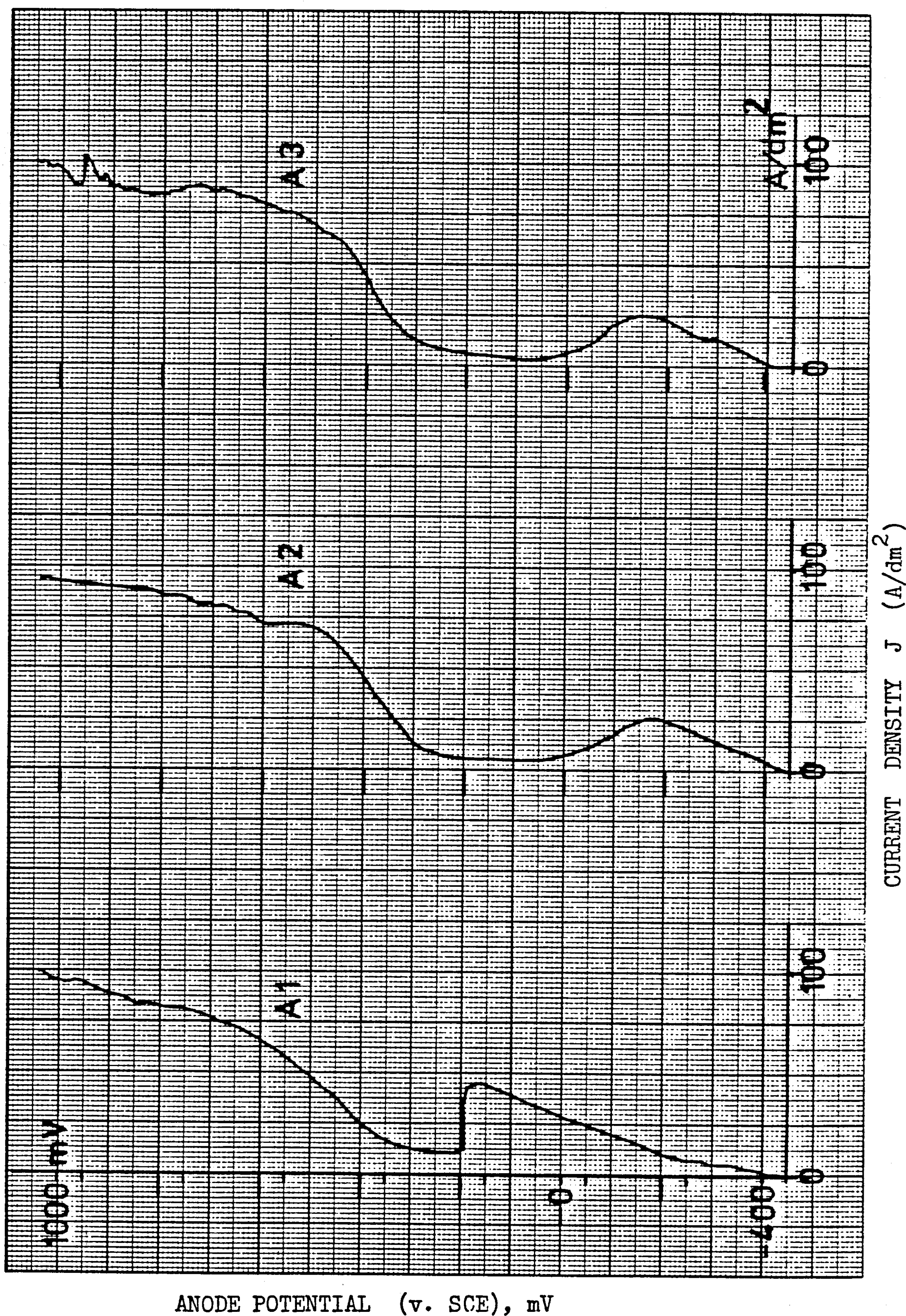

Fig. R1 POTENTIODYNAMIC POLARIZATION MEASUREMENTS FOR AISI 304 STAINLESS STEEL IN 10% (w/w) HCl SOLUTION.
TEMP. = 15°C

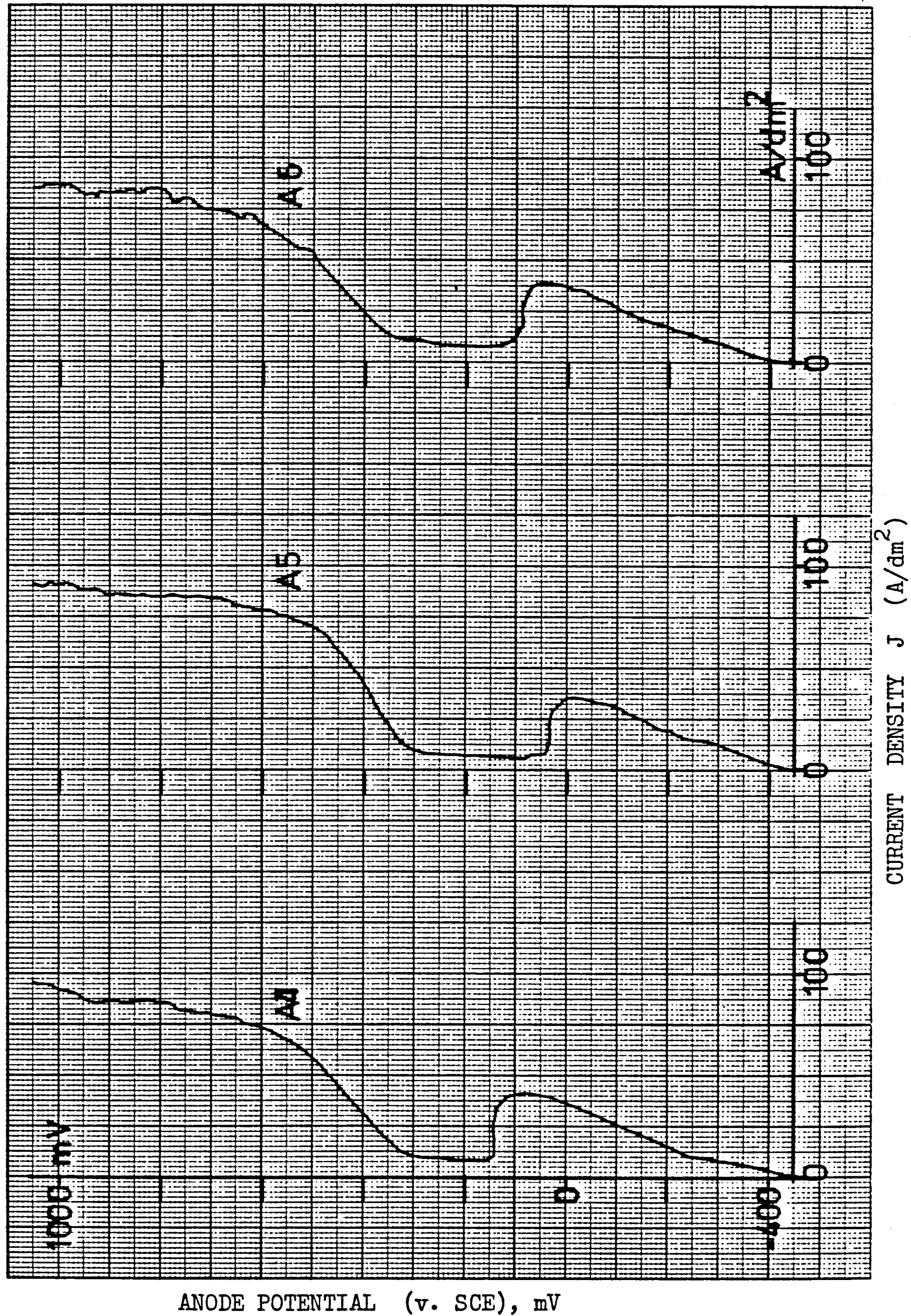

Fig. R2 POTENTIODYNAMIC POLARIZATION MEASUREMENTS FOR AISI 304 STAINLESS STEEL IN 10% (w/w) HCl SOLUTION.
TEMP. = 15°C

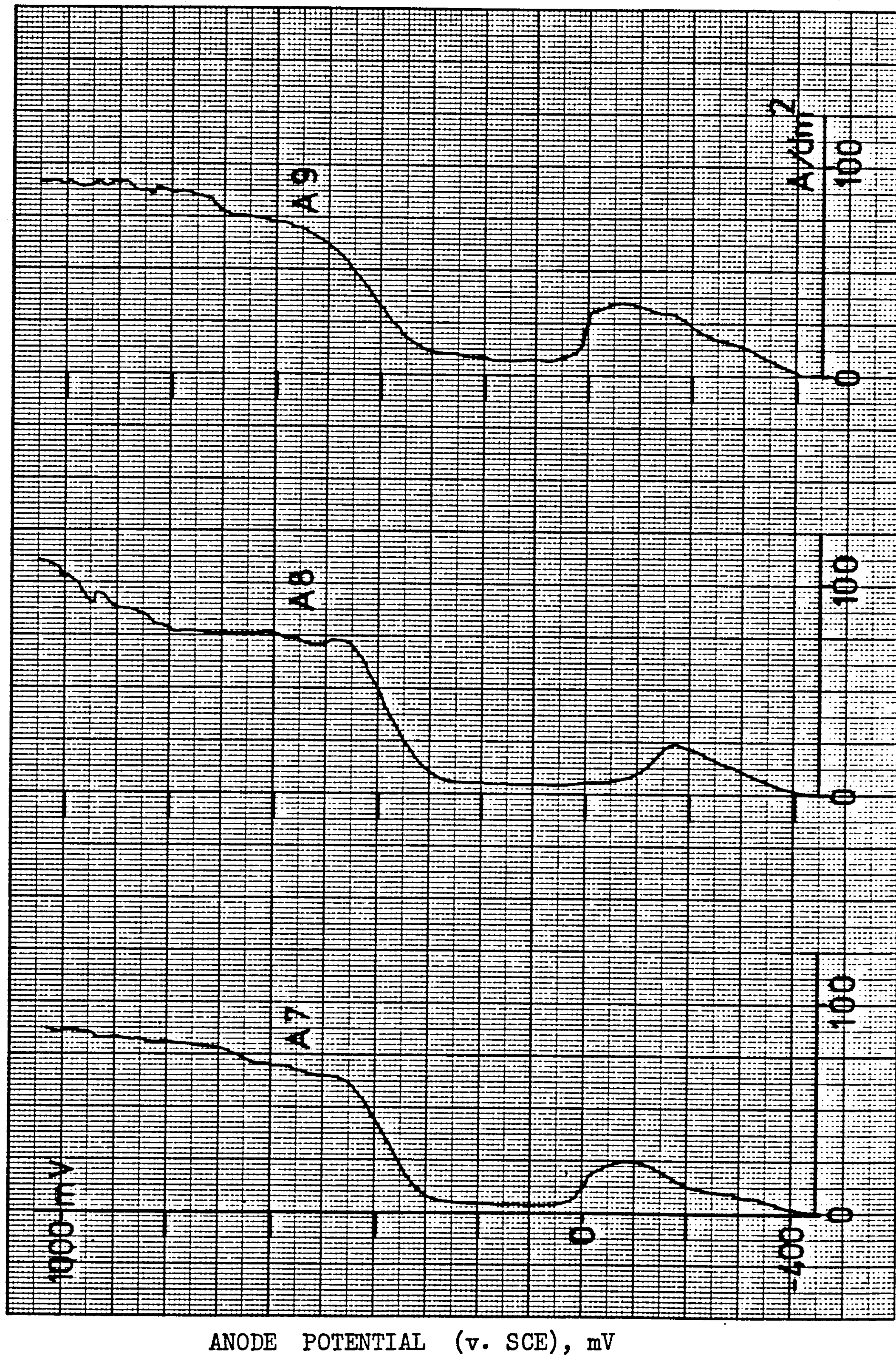

Fig. R3 POTENTIODYNAMIC POLARIZATION MEASUREMENTS FOR AISI 304 STAINLESS STEEL IN 10% (w/w) HCl SOLUTION.
TEMP. = 15°C

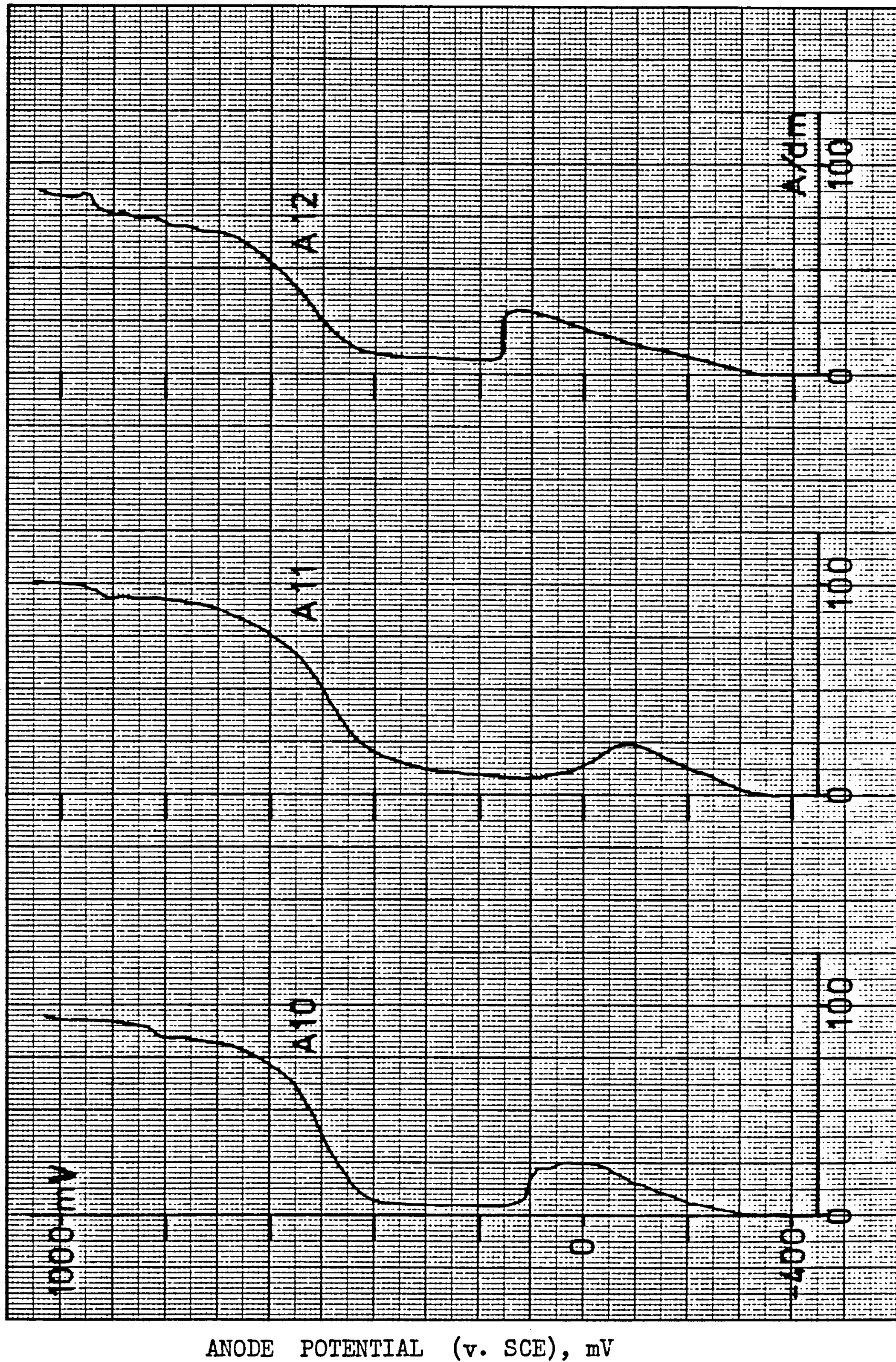

Fig. R4 POTENTIODYNAMIC POLARIZATION MEASUREMENTS FOR AISI 304 STAINLESS STEEL IN 10% (w/w) HCl SOLUTION.
TEMP. = 15°C

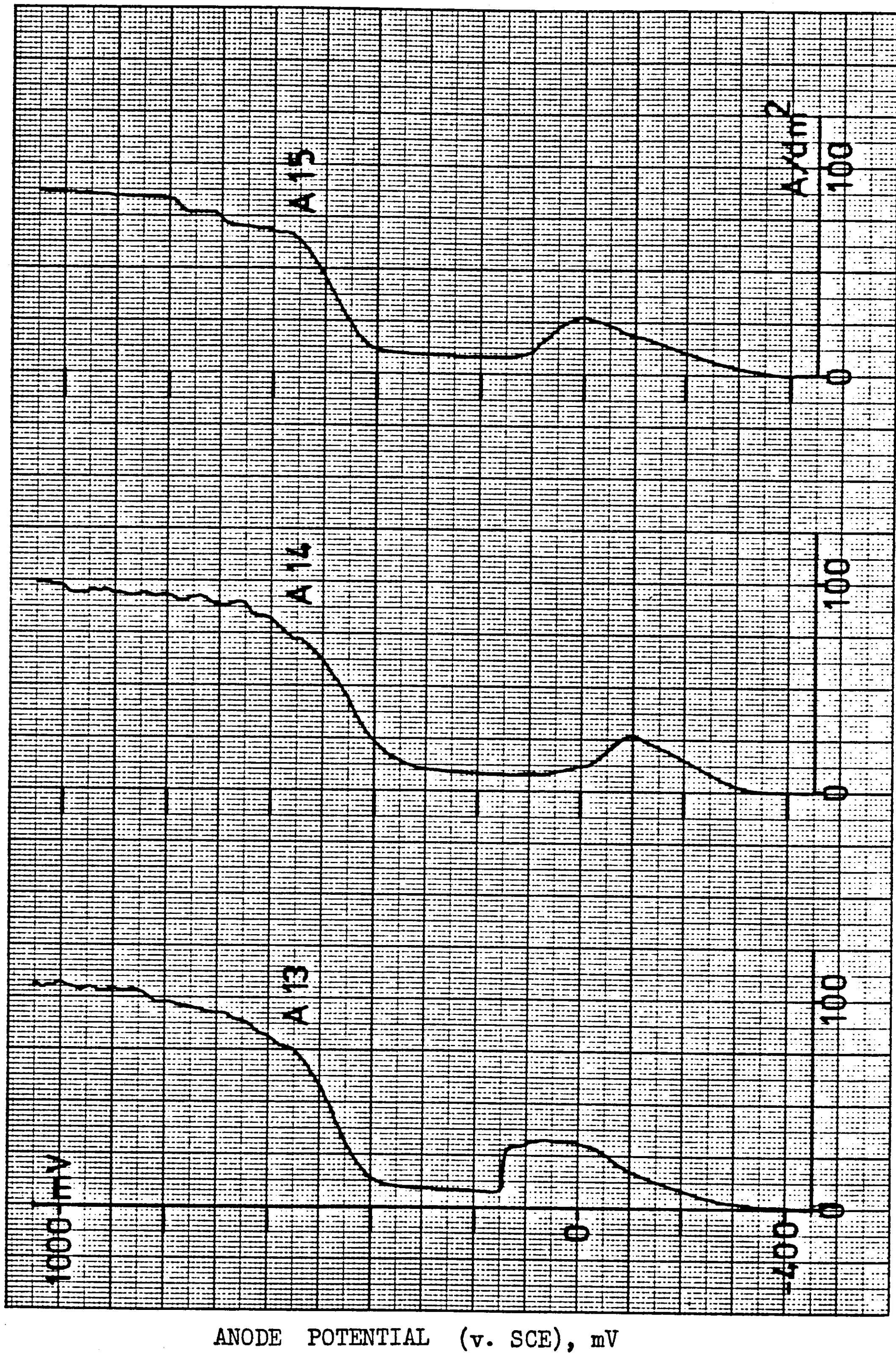

Fig. R5 POTENTIODYNAMIC POLARIZATION MEASUREMENTS FOR AISI 304 STAINLESS STEEL IN 10% (w/w) HCl SOLUTION.
TEMP. = 15°C

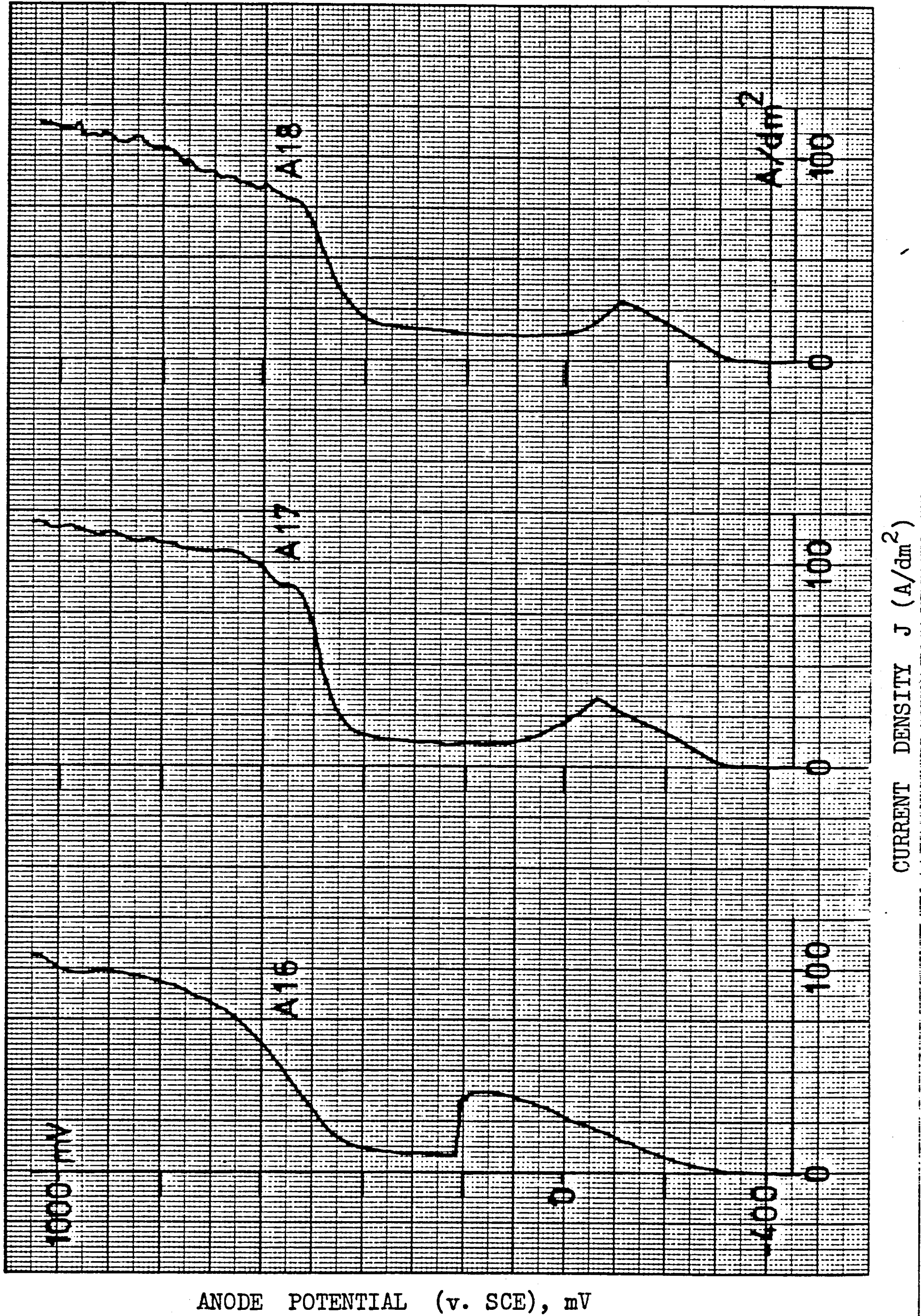

Fig. R6 POTENTIODYNAMIC POLARIZATION MEASUREMENTS FOR AISI 304 STAINLESS STEEL IN 10% (w/w) HCl SOLUTION.
TEMP. = 15°C

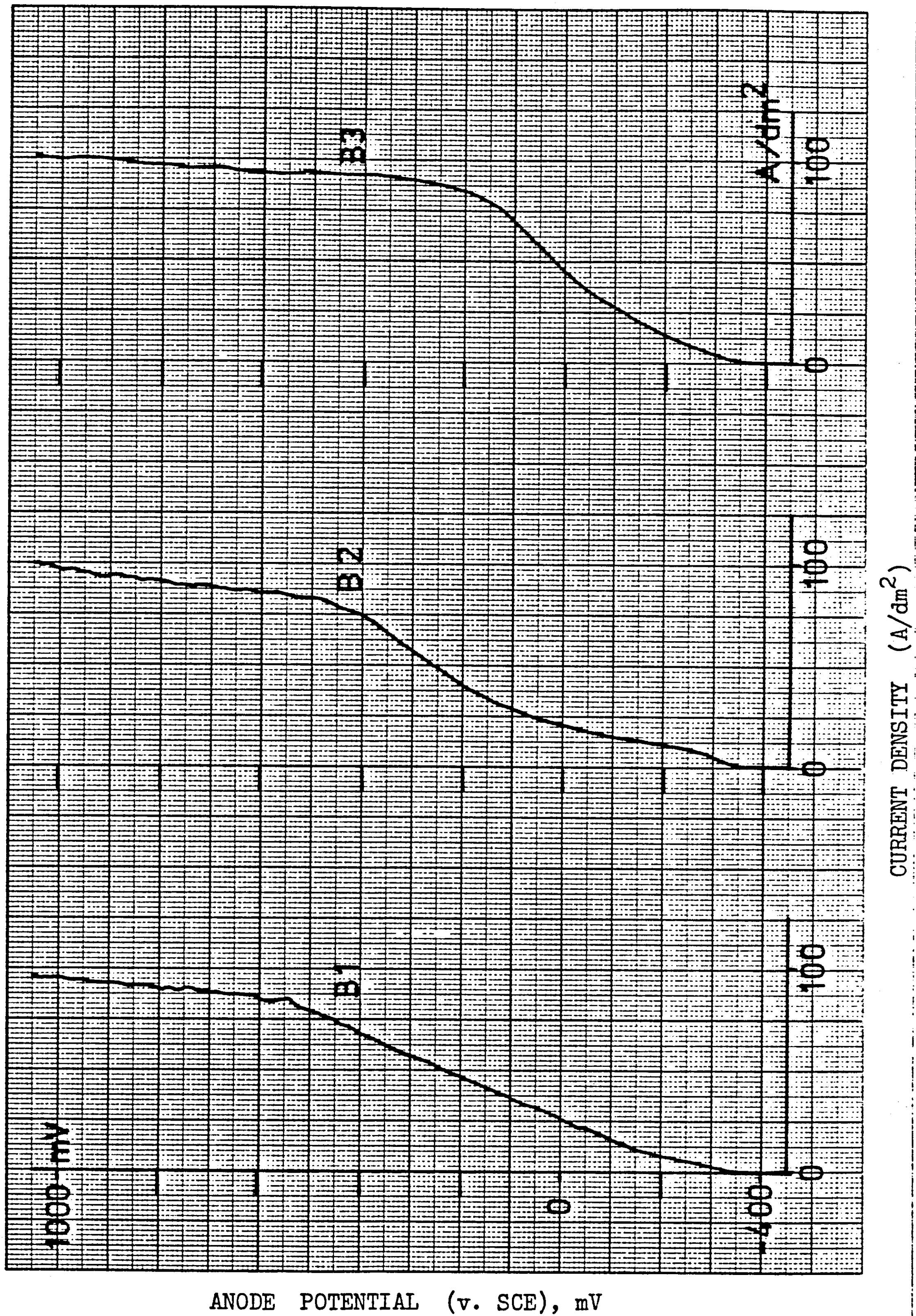

Fig. R7 POTENTIODYNAMIC POLARIZATION MEASUREMENTS FOR AISI 304 STAINLESS STEEL IN 10% (w/w) HCl SOLUTION.
TEMP. = 20°C

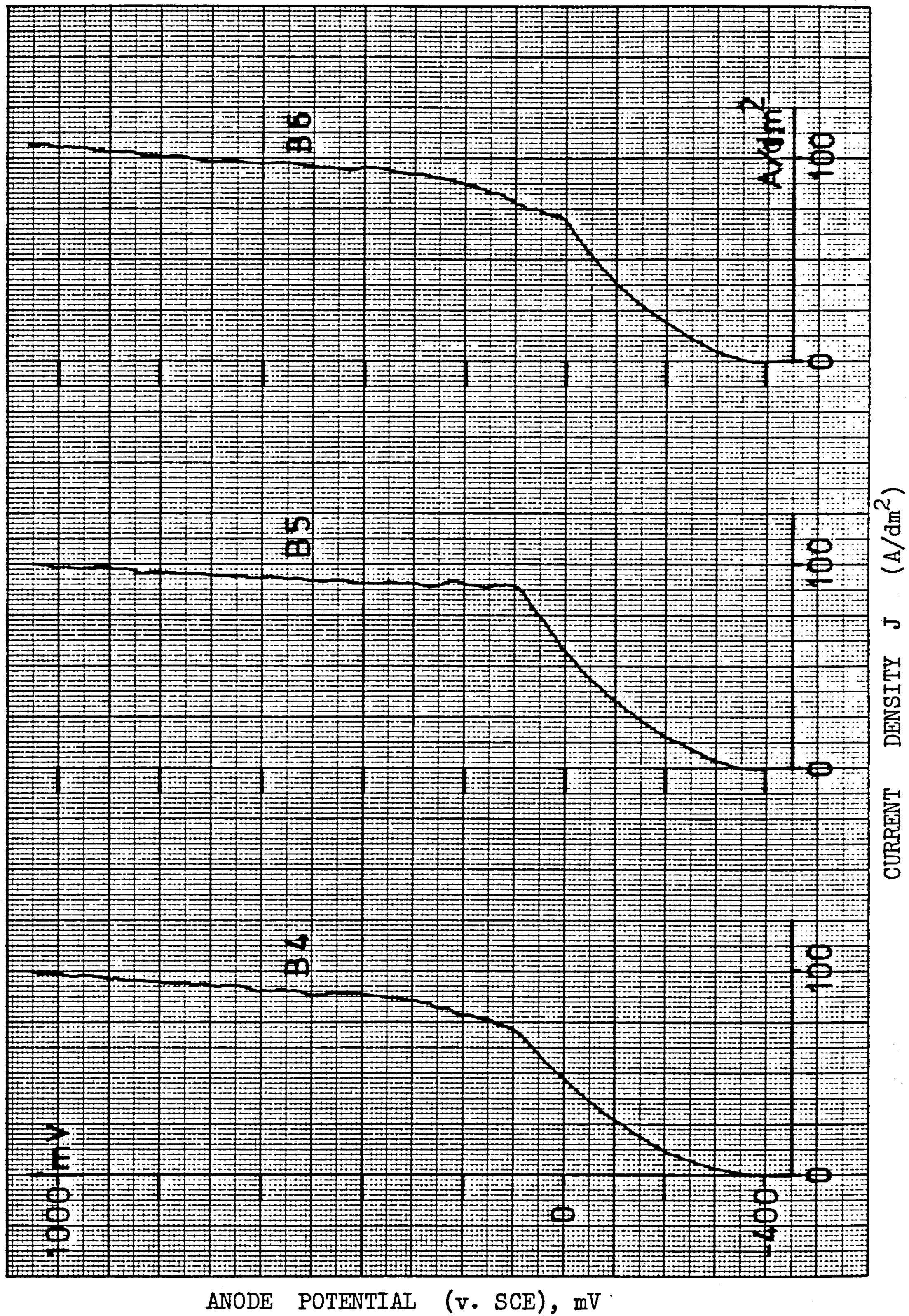

Fig. R8 POTENTIODYNAMIC POLARIZATION MEASUREMENTS FOR AISI 304 STAINLESS STEEL IN 10% (w/w) HCl SOLUTION.
TEMP. = 20°C

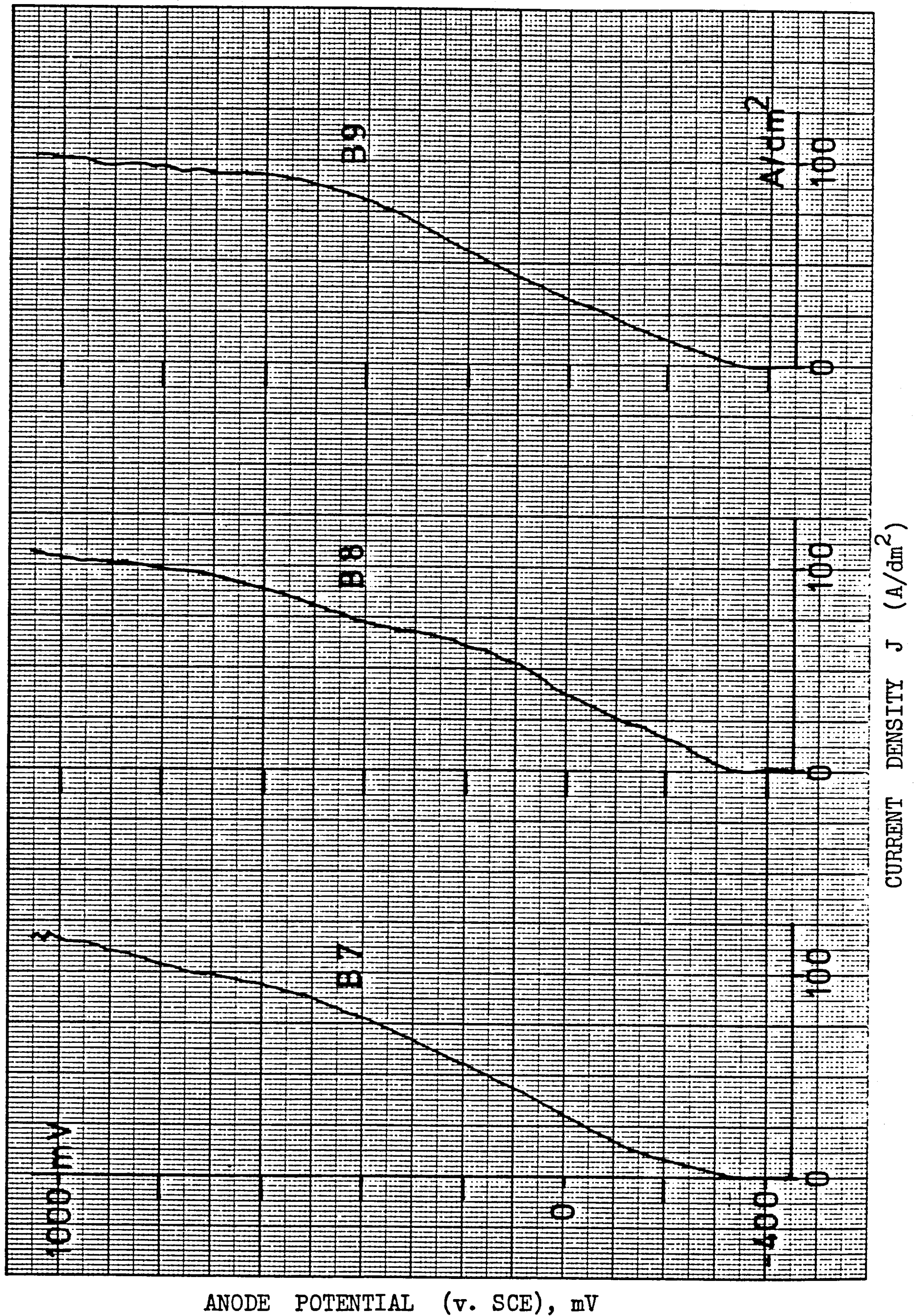

Fig. R9 POTENTIODYNAMIC POLARIZATION MEASUREMENTS FOR AISI 304 STAINLESS STEEL IN 10% (w/w) HCl SOLUTION.
TEMP. = 20°C

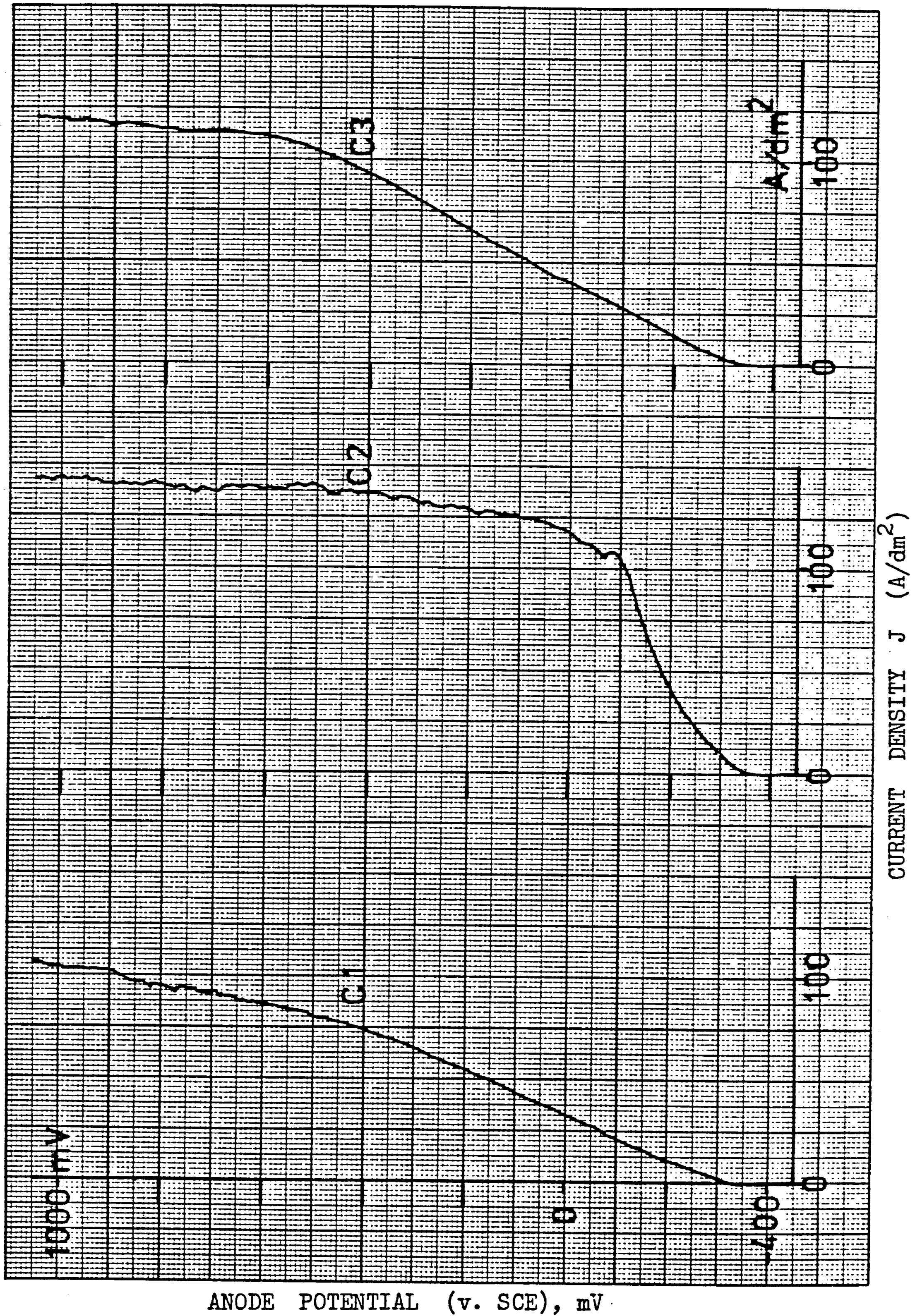

Fig. R10 POTENTIODYNAMIC POLARIZATION MEASUREMENTS FOR AISI 304 STAINLESS STEEL IN 10% (w/w) HCl SOLUTION.
TEMP. = 25°C

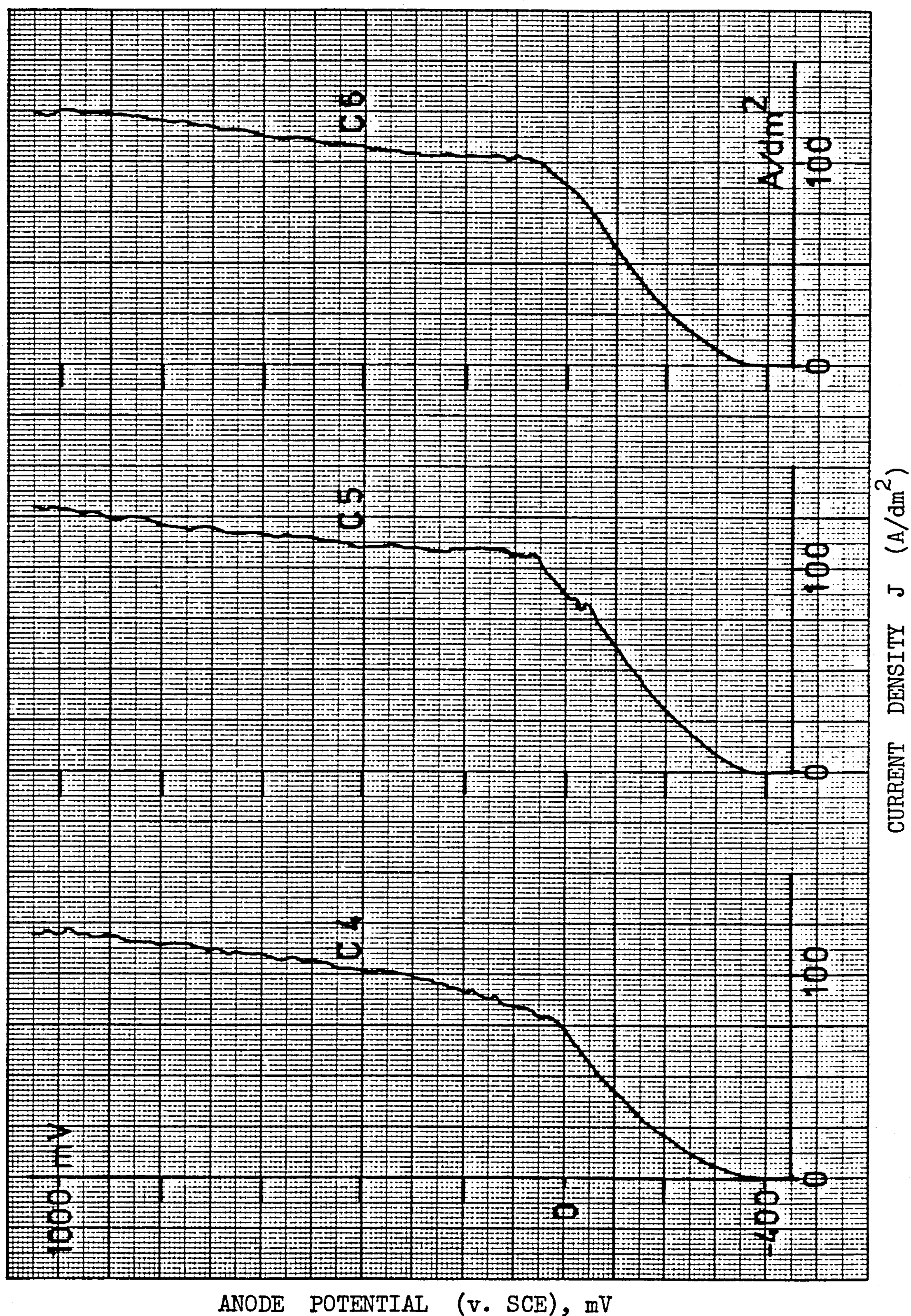

Fig. R11 POTENTIODYNAMIC POLARIZATION MEASUREMENTS FOR AISI 304 STAINLESS STEEL IN 10% (w/w) HCl SOLUTION.
TEMP. = 25°C

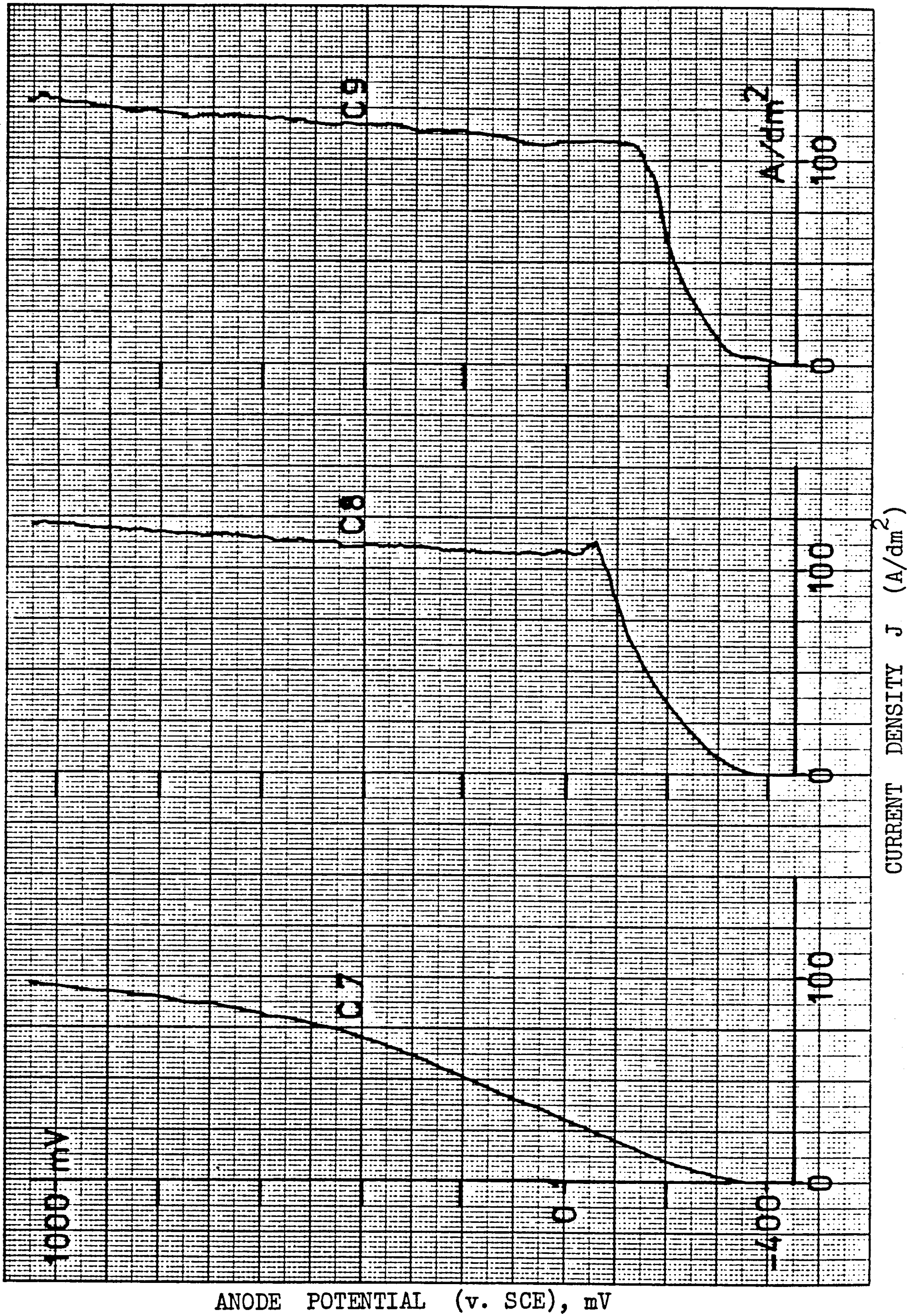

Fig. R12 POTENTIODYNAMIC POLARIZATION MEASUREMENTS FOR AISI 304 STAINLESS STEEL IN 10% (w/w) HCl SOLUTION.
TEMP. = 25°C

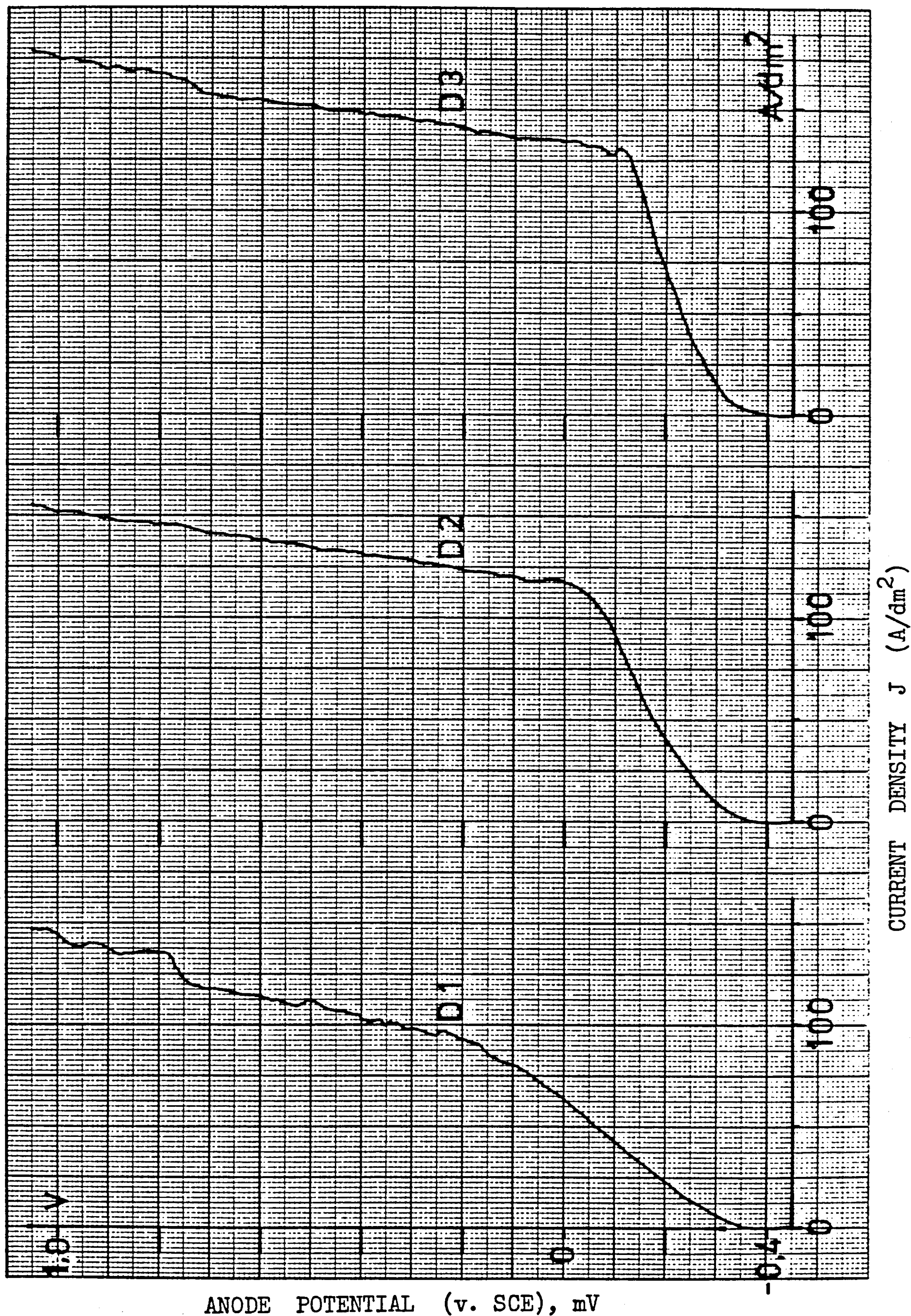

Fig. R13 POTENTIODYNAMIC POLARIZATION MEASUREMENTS FOR AISI 304 STAINLESS STEEL IN 10% (w/w) HCl SOLUTION.
TEMP. = 30°C

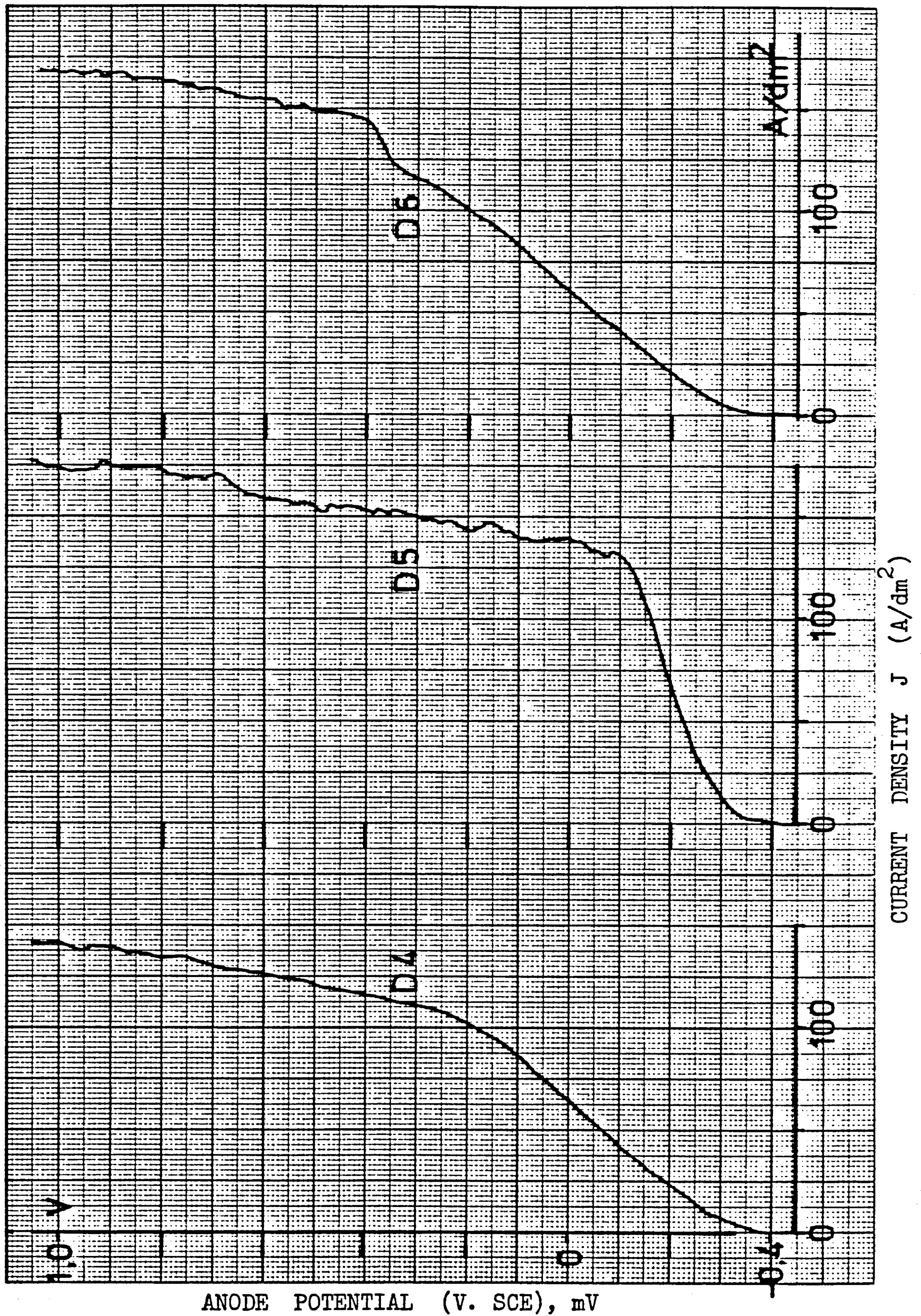

Fig. R14 POTENTIODYNAMIC POLARIZATION MEASUREMENTS FOR AISI 304 STAINLESS STEEL IN 10% (w/w) HCl SOLUTION.
TEMP. = 30°C

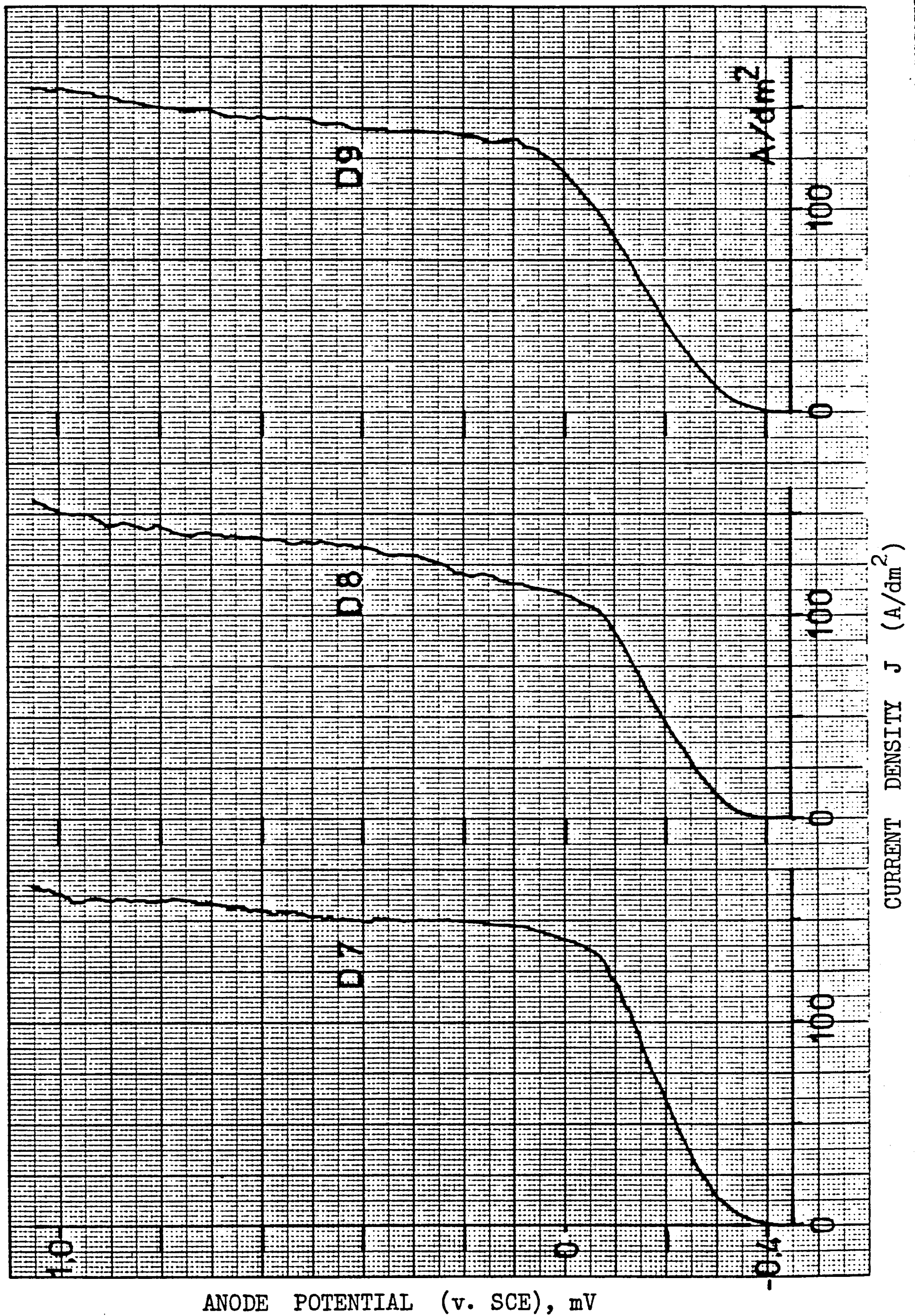

Fig. R15 POTENTIODYNAMIC POLARIZATION MEASUREMENTS FOR AISI 304 STAINLESS STEEL IN 10% (w/w) HCl SOLUTION.
TEMP. = 30°C

Anode Potential x 10^2 mV (v SCE)	Current Density J (A/dm^2)								
Test No. →	A1	A2	A3	A4	A5	A6	A7	A8	A9
-3	2.5	2.5	2.5	2.5	2.5	2.5	2.5	2.5	2.5
-2	5.0	10.0	12.5	10.0	10.0	10.0	7.5	12.5	12.5
-1	10.0	20.0	22.5	17.5	17.5	16.3	12.5	22.5	25.0
0	20.0	22.5	20.0	25.0	27.5	25.0	22.5	7.5	32.5
+1	30.0	10.0	5.0	35.0	35.0	37.5	7.5	5.0	12.5
+2	40.0	5.0	5.0	40.0	5.0	12.5	5.0	5.0	7.5
+3	8.8	5.0	7.5	7.5	5.0	7.5	5.0	5.0	7.5
+4	10.0	7.5	12.5	10.0	10.0	10.0	10.0	12.5	12.5
+5	27.5	30.0	30.0	30.0	37.5	25.0	50.0	50.0	37.5
+6	50.0	62.5	70.0	57.5	70.0	50.0	65.0	72.5	75.0
+7	65.0	70.0	80.0	70.0	77.5	67.5	70.0	75.0	75.0
+8	77.5	80.0	85.0	77.5	82.5	75.0	77.5	75.0	80.0
+9	82.5	85.0	85.0	85.0	85.0	80.0	80.0	80.0	87.5
+10	90.0	90.0	90.0	87.5	87.5	85.0	82.5	90.0	90.0

Fig.R16 THE RESULTS OF THE POLARIZATION MEASUREMENTS FOR AISI 304 STAINLESS STEEL IN 10% (w/w) HCl AT 15°C.

Anode Potential x 10^2 mV (v SCE)	Current Density J (A/dm^2)										Average Current Density $\bar{J}$ (A/dm^2)	Standard Deviation in $\bar{J}$ s.d. (A/dm^2)	Percentage ratio of Standard Deviation in Current Density for Current Density s.d./$\bar{J}$ %
	Test No. →	A10	A11	A12	A13	A14	A15	A16	A17	A18			
-3		2.5	2.5	2.5	2.5	2.5	2.5	2.5	2.5	2.5	2.5	0	0
-2		7.5	12.5	10.0	10.0	15.0	10.0	10.0	17.5	17.5	11.1	3.23	29.0
-1		15.0	22.5	15.0	20.0	25.0	17.5	17.5	27.5	27.5	19.5	5.0	27.0
0		25.0	12.5	22.5	30.0	12.5	27.5	27.5	17.5	12.5	21.68	6.75	31.0
+1		12.5	7.5	30.0	27.5	7.5	10.0	37.5	12.5	12.5	18.60	12.25	66.0
+2		5.0	10.0	7.5	7.5	8.8	8.8	7.5	10.0	12.5	11.25	10.75	96.0
+3		5.0	12.5	7.5	8.8	12.5	8.8	7.5	10.0	15.0	8.13	2.88	35.0
+4		7.5	22.5	8.8	12.5	25.0	12.5	7.5	12.5	20.0	12.43	5.0	40.0
+5		37.5	50.0	27.5	60.0	62.5	47.5	32.5	75.0	65.0	43.88	14.70	34.0
+6		72.5	75.0	52.5	82.5	82.5	67.5	65.0	100.0	82.5	69.13	13.25	19.0
+7		80.0	87.5	67.5	90.0	87.5	75.0	82.5	105.0	90.0	78.60	10.38	13.0
+8		82.5	90.0	72.5	97.5	92.5	82.5	92.5	107.5	102.5	85.0	10.0	11.0
+9		90.0	92.5	75.0	102.5	95.0	85.0	97.5	112.5	107.5	88.50	10.0	11.0
+10		92.5	100.0	85.0	105.0	97.5	85.0	100.0	115.0	112.5	93.75	9.75	10.0

Fig.R17 THE RESULTS OF THE POLARIZATION MEASUREMENTS FOR AISI 304 STAINLESS STEEL IN 10% (w/w) HCl AT 15°C.

Anode Potential x 10^2 mV (v SCE)	Current Density J (A/dm^2)										Average Current Density $\bar{J}$ (A/dm^2)	Standard Deviation in $\bar{J}$ s.d. (A/dm^2)	Percentage ratio of Standard Deviation in Current Density for Current Density s.d./$\bar{J}$ %
	Test No: →	B1	B2	B3	B4	B5	B6	B7	B8	B9			
-3		2.5	2.5	2.5	3.75	5.0	5.0	2.5	2.5	5.0	3.48	1.21	35.0
-2		7.5	7.5	12.5	7.5	15.0	20.0	10.0	12.5	15.0	11.18	4.29	38.0
-1		15.0	12.5	25.0	27.5	35.0	40.0	20.0	25.0	25.0	25.0	8.75	35.0
0		25.0	22.5	42.5	47.5	60.0	72.5	32.5	37.5	32.5	43.44	15.75	36.0
+1		35.0	27.5	67.5	72.5	87.5	80.0	45.0	52.5	45.0	56.95	20.83	37.0
+2		45.0	40.0	82.5	80.0	90.0	85.0	57.5	60.0	55.0	66.10	18.55	28.0
+3		55.0	57.5	87.5	85.0	90.0	92.5	67.5	65.0	70.0	74.45	14.50	19.0
+4		67.5	72.5	90.0	87.5	90.0	95.0	77.5	72.5	85.0	81.95	9.65	12.0
+5		77.5	82.5	91.3	87.5	92.5	95.0	87.5	80.0	87.5	86.80	5.83	7.0
+6		85.0	85.0	92.5	90.0	93.8	97.5	95.0	87.5	90.0	90.70	4.38	5.0
+7		85.0	85.0	95.0	92.5	95.0	100.0	97.5	92.5	92.5	92.78	5.08	5.0
+8		90.0	90.0	96.3	95.0	97.5	100.0	102.5	97.5	95.5	95.98	4.13	4.0
+9		92.5	92.5	98.8	97.5	97.5	102.5	110.0	100.0	97.5	98.75	5.53	6.0
+10		95.0	97.5	100.0	98.8	98.8	105.5	112.5	102.5	100.0	101.1	5.13	5.0

Fig.R18 THE RESULTS OF THE POLARIZATION MEASUREMENTS FOR AISI 304 STAINLESS STEEL IN 10% (w/w) HCl at 20°C.

Anode Potential x 10^2 mV (v SCE)	Current Density J (A/dm^2)										Average Current Density $\bar{J}$ (A/dm^2)	Standard Deviation in $\bar{J}$ s.d. (A/dm^2)	Percentage ratio of Standard Deviation in Current Density for Current Density s.d./$\bar{J}$ %
	Test No. → C1	C2	C3	C4	C5	C6	C7	C8	C9				
-3	2.5	7.5	7.5	6.3	10.0	7.5	10.0	7.5	8.8		7.5	2.25	30.0
-2	10.0	25.0	27.5	32.5	30.0	25.0	45.0	32.5	32.5		29.68	9.26	31.0
-1	17.5	45.0	60.0	42.5	62.5	55.0	95.0	77.5	75.0		58.88	22.75	39.0
0	27.5	75.0	92.5	72.5	87.5	87.5	112.5	97.5	102.5		83.88	24.5	29.0
+1	37.5	92.5	105.0	82.5	107.5	102.5	112.5	97.5	103.8		93.5	22.75	24.0
+2	47.5	100.0	102.5	92.5	110.0	102.5	115.0	100.0	105.0		97.23	19.7	20.0
+3	56.3	105.0	106.3	97.5	112.5	105.0	117.5	103.8	107.5		101.25	17.75	18.0
+4	67.5	105.0	110.0	100.0	112.5	107.5	118.8	107.5	110.0		104.25	14.75	14.0
+5	78.8	108.8	113.8	105.0	115.0	110.0	117.5	112.5	112.5		108.33	11.63	11.0
+6	87.5	108.8	117.5	107.5	117.5	112.5	122.5	115.0	115.0		111.5	10.0	9.0
+7	95.0	110.0	120.0	112.5	120.0	115.0	123.8	117.5	118.8		114.7	8.5	7.0
+8	100.0	113.8	122.5	113.8	122.5	118.8	125.0	120.0	121.3		117.5	7.5	6.0
+9	105.0	115.0	125.0	117.5	125.0	122.5	127.5	125.0	125.0		120.75	7.18	6.0
+10	110.0	117.5	130.0	120.0	130.0	125.0	127.5	130.0	127.5		124.18	6.98	6.0

Fig. R19 THE RESULTS OF THE POLARIZATION MEASUREMENTS FOR AISI 304 STAINLESS STEEL IN 10% (w/w) HCl AT 25°C.

Anode Potential x 10^2 mV (v SCE)	Current Density J (A/dm^2)											Average Current Density $\bar{J}$ (A/dm^2)	Standard Deviation in $\bar{J}$ s.d. (A/dm^2)	Percentage ratio of Standard Deviation in Current Density for Current Density s.d./$\bar{J}$ %
	Test No. →	D1	D2	D3	D4	D5	D6	D7	D8	D9				
-3		7.5	10.0	15.0	7.5	12.5	7.5	12.5	10.0	12.5		10.55	2.75	26.0
-2		25.0	42.5	37.5	25.0	75.0	22.5	60.0	47.5	45.0		42.23	17.43	41.0
-1		42.5	95.0	130.0	45.0	130.0	42.5	117.5	90.0	87.5		86.68	36.1	42.0
0		75.0	117.5	135.0	65.0	137.5	75.0	140.0	100.0	115.0		103.88	32.9	32.0
+1		80.0	120.0	137.5	87.5	140.0	85.0	142.5	112.5	132.5		115.25	25.25	22.0
+2		95.0	125.0	142.5	102.5	142.5	102.5	145.0	127.5	133.8		124.0	19.35	16.0
+3		100.0	125.0	145.0	110.0	150.0	117.5	147.5	132.5	136.3		128.18	16.3	13.0
+4		105.0	132.5	150.0	115.0	152.5	145.0	150.0	133.75	137.5		135.7	16.45	12.0
+5		112.5	135.0	152.5	120.0	155.0	150.0	150.0	135.0	140.0		138.88	14.9	11.0
+6		115.0	140.0	152.5	125.0	160.0	155.0	152.5	135.0	142.5		141.95	14.93	11.0
+7		120.0	142.5	158.75	130.0	167.5	160.0	155.0	137.5	146.3		146.38	15.48	11.0
+8		135.0	147.5	167.5	135.0	172.5	162.5	155.0	140.0	148.75		151.5	13.33	9.0
+9		137.5	150.0	170.0	137.5	175.0	167.5	157.5	142.5	152.5		154.45	13.9	9.0
+10		142.5	152.5	175.0	142.5	175.0	167.5	162.5	165.0	157.5		158.33	12.55	8.0

Fig.R20 THE RESULTS OF THE POLARIZATION MEASUREMENTS FOR AISI 304 STAINLESS STEEL IN 10% (w/w) HCl AT 30°C.

APPENDIX S

THE GEOMETRIC PROFILE PRODUCED BY GALVANOSTATIC ETCHING

This appendix contains all the surface trace results produced by the 'Talysurf 3' with the 120mm extenion arm. The latter reduced the magnification of the instrument sufficiently so that the surface profile could be measured in a similar manner to that of a peak-to-valley surface texture measurement.

The sweeps were carried out at right angles to the vertical orientation of etching. The measurement traverse was >12mm and the sample was levelled prior to the measurement such that the deflexion of the stylus produced the same readings at the beginning and end of run.

The 10 x 10mm apertures on the 3 x 3 matrix on the sample plates were measured individualy and a trace was produced for each. Dimensional measurements were then made from the traces at intervals of 10mm along the trace and therefore 20 readings per aperture were made. After compensating for the vertical magnifications, the measurement results were then tabulated and plotted.

Plotting was with the aid of the program 'DPLOT' where the scale was selected automatically and the maximum and minimum values of the scale correspond to those of the results. Hence maximum possible magnification was used.

Four traces corresponding to the etch durations of 10, 15, 20 & 25 minutes for each of the current densities investigated were recorded but only a sample is presented in the figure. The results for the current densities 10 A/dm^2 are illustrated in figures S1. A sample of the measured results are tabulated and plotted in figures S11,15,,20,23,27,31,35,39,43 and S45 corresponding to all current densities (10-90 A/dm^2). The range extends from 5 to 20 minutes in steps of 5 minutes but only the results for 10 minutes are presented.

Fig. S1

Horizontal scale 1 div. = 0.5 mm

$J = 10\ A/dm^2$

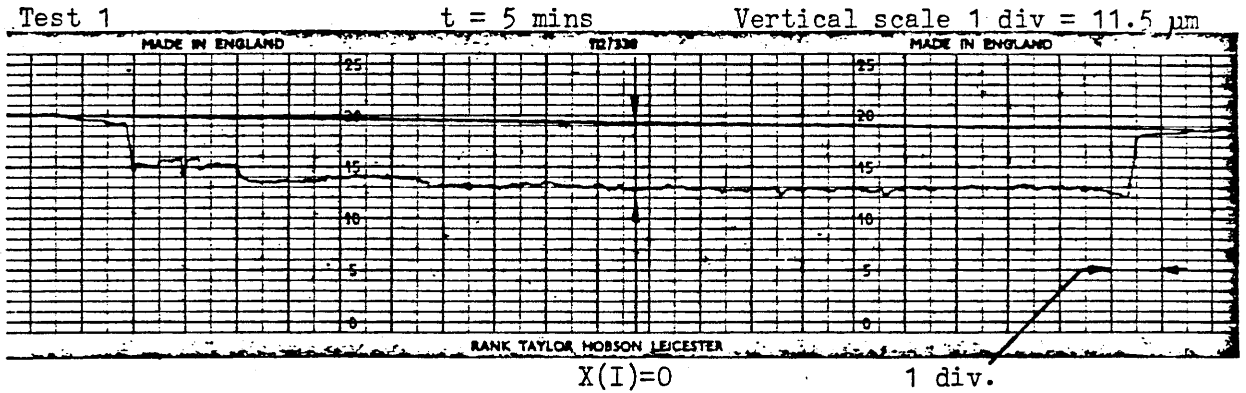

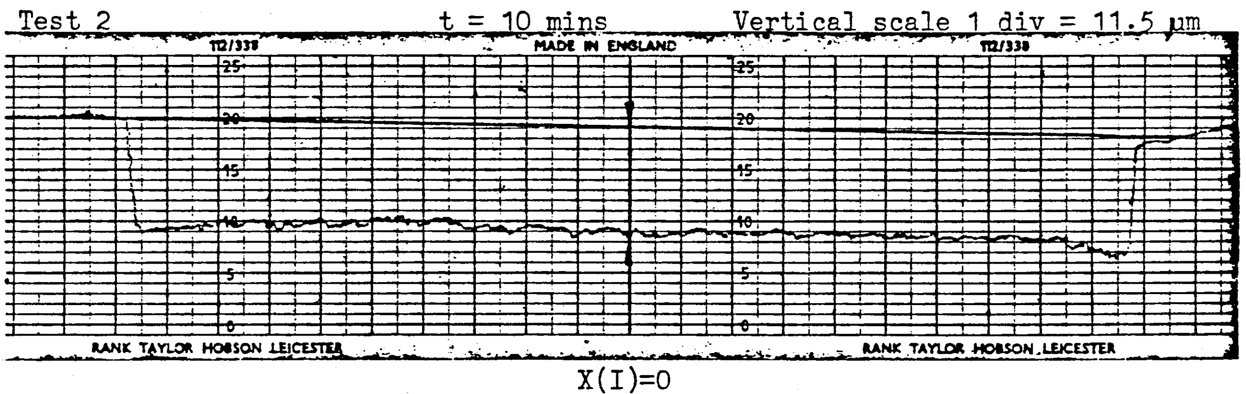

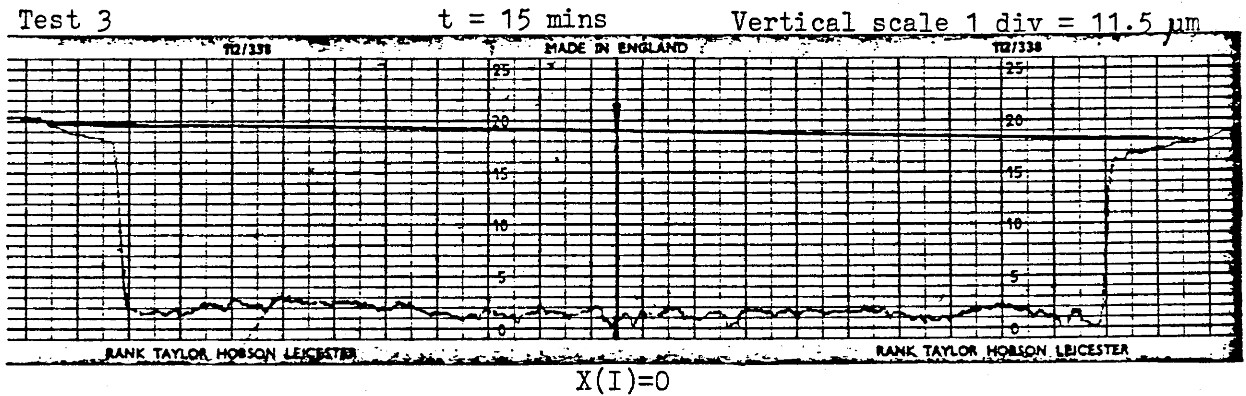

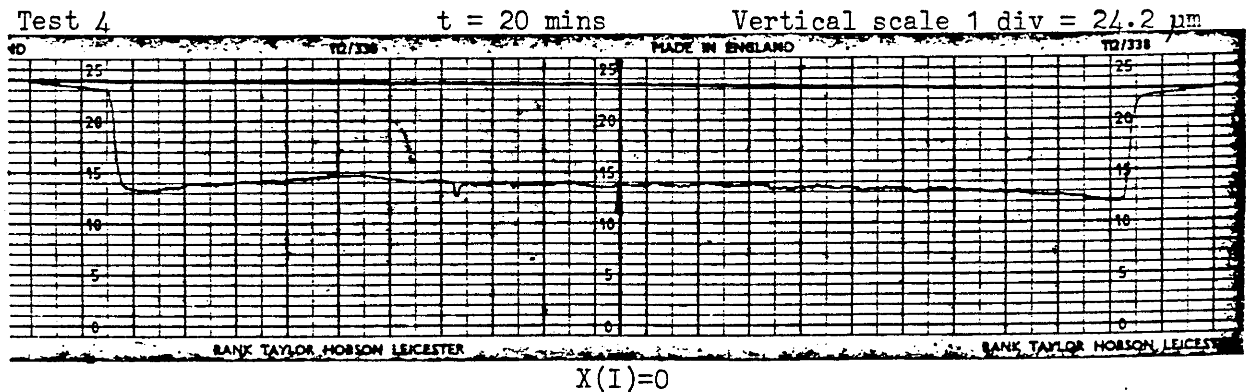

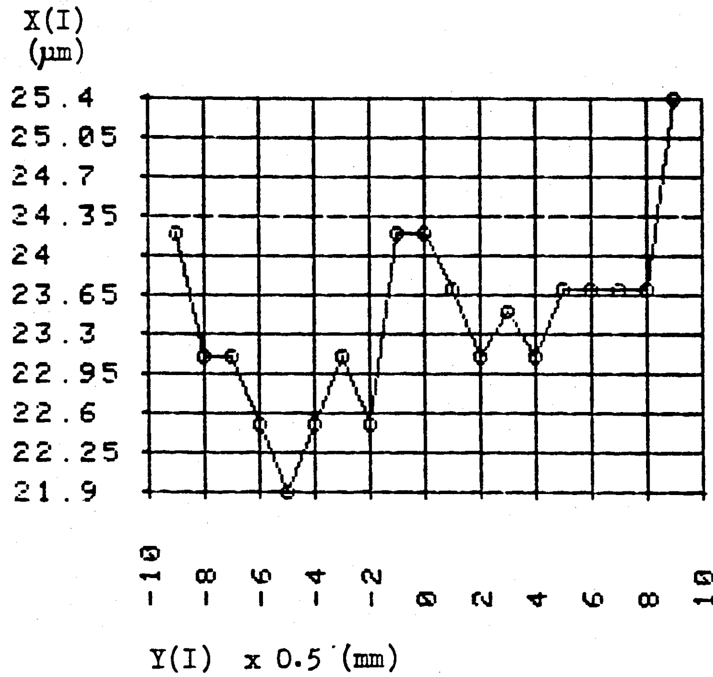

I	X(I)	Y(I)
1	-9.0000	24.2000
2	-8.0000	23.1000
3	-7.0000	23.1000
4	-6.0000	22.5000
5	-5.0000	21.9000
6	-4.0000	22.5000
7	-3.0000	23.1000
8	-2.0000	22.5000
9	-1.0000	24.2000
10	0.0000	24.2000
11	1.0000	23.7000
12	2.0000	23.1000
13	3.0000	23.5000
14	4.0000	23.1000
15	5.0000	23.7000
16	6.0000	23.7000
17	7.0000	23.7000
18	8.0000	23.7000
19	9.0000	25.4000

X(I) = Horizontal distance about the centre of the aperture at X(I) = 0

Y(I) = Depth of etch

Fig. S11 TABLE AND PLOT OF THE RESULTS OF THE GEOMETRIC PROFILE FOR J = 10 A/dm^2 AND t = 10 mins.

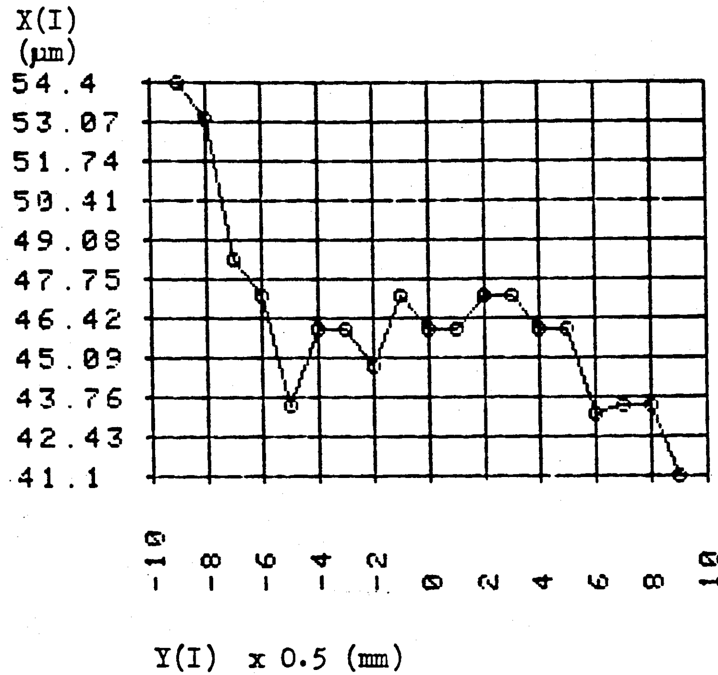

I	X(I)	Y(I)
1	-9.0000	54.4000
2	-8.0000	53.2000
3	-7.0000	48.4000
4	-6.0000	47.2000
5	-5.0000	43.5000
6	-4.0000	46.0000
7	-3.0000	46.0000
8	-2.0000	44.8000
9	-1.0000	47.2000
10	0.0000	46.0000
11	1.0000	46.0000
12	2.0000	47.2000
13	3.0000	47.2000
14	4.0000	46.0000
15	5.0000	46.0000
16	6.0000	43.2000
17	7.0000	43.5000
18	8.0000	43.5000
19	9.0000	41.1000

X(I) = Horizontal distance about the centre of the aperture at X(I) = 0

Y(I) = Depth of etch

Fig. S15 TABLE AND PLOT OF THE RESULTS OF THE GEOMETRIC PROFILE FOR J = 20 A/dm^2 AND t = 10 mins.

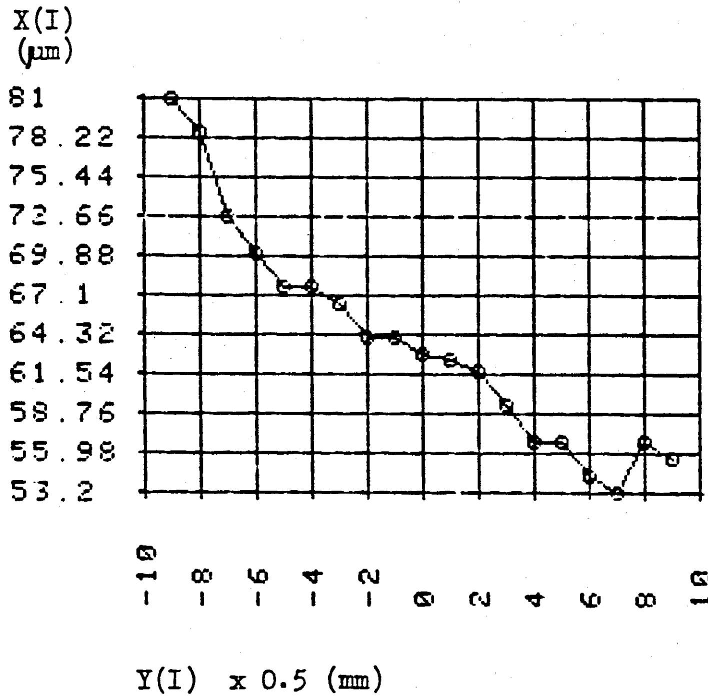

I	X(I)	Y(I)
1	-9.0000	81.0000
2	-8.0000	78.6000
3	-7.0000	72.6000
4	-6.0000	70.1000
5	-5.0000	67.7000
6	-4.0000	67.7000
7	-3.0000	66.5000
8	-2.0000	64.1000
9	-1.0000	64.1000
10	0.0000	62.9000
11	1.0000	62.6000
12	2.0000	61.7000
13	3.0000	59.3000
14	4.0000	56.8000
15	5.0000	56.8000
16	6.0000	54.4000
17	7.0000	53.2000
18	8.0000	56.8000
19	9.0000	55.6000

X(I) = Horizontal distance about the centre of the aperture at X(I) = 0

Y(I) = Depth of etch

Fig. S20 TABLE AND PLOT OF THE RESULTS OF THE GEOMETRIC PROFILE FOR J = 30 A/dm^2 AND t = 10 mins.

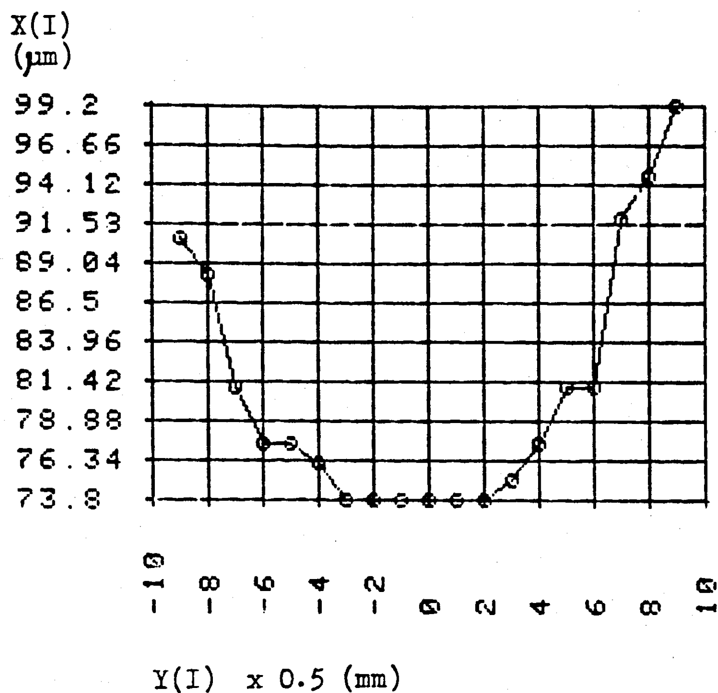

I	X(I)	Y(I)
1	-9.0000	90.7000
2	-8.0000	88.3000
3	-7.0000	81.0000
4	-6.0000	77.4000
5	-5.0000	77.4000
6	-4.0000	76.2000
7	-3.0000	73.8000
8	-2.0000	73.8000
9	-1.0000	73.8000
10	0.0000	73.8000
11	1.0000	73.8000
12	2.0000	73.8000
13	3.0000	75.0000
14	4.0000	77.4000
15	5.0000	81.0000
16	6.0000	81.0000
17	7.0000	91.9000
18	8.0000	94.6000
19	9.0000	99.2000

X(I) = Horizontal distance about the centre of the aperture at X(I) = 0

Y(I) = Depth of etch

Fig. S23 TABLE AND PLOT OF THE RESULTS OF THE GEOMETRIC PROFILE FOR J = 40 A/dm^2 AND t = 10 mins.

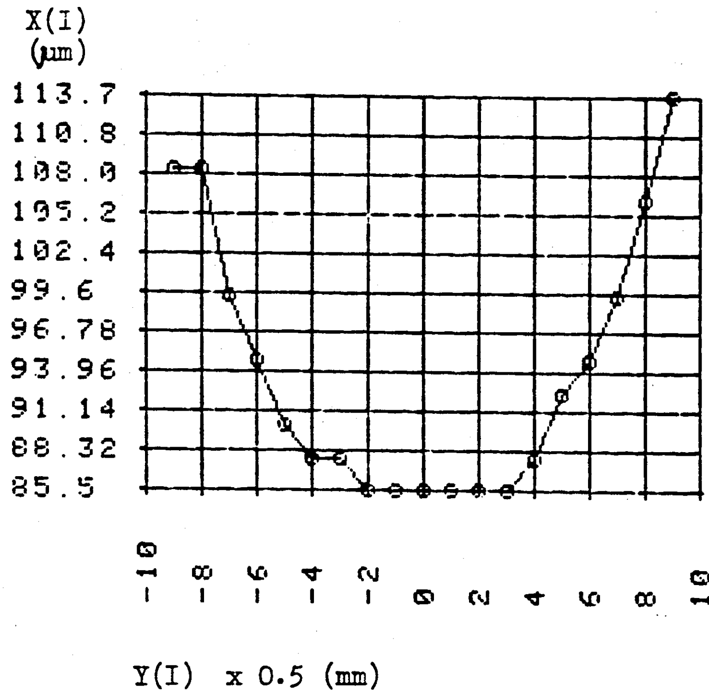

I	X(I)	Y(I)
1	-9.0000	108.5000
2	-8.0000	108.5000
3	-7.0000	99.3000
4	-6.0000	94.7000
5	-5.0000	90.1000
6	-4.0000	87.8000
7	-3.0000	87.8000
8	-2.0000	85.5000
9	-1.0000	85.6000
10	0.0000	85.5000
11	1.0000	85.5000
12	2.0000	85.5000
13	3.0000	85.5000
14	4.0000	87.8000
15	5.0000	92.4000
16	6.0000	94.7000
17	7.0000	99.3000
18	8.0000	106.2000
19	9.0000	113.7600

X(I) = Horizontal distance about the centre of the aperture at X(I) = 0

Y(I) = Depth of etch

Fig. S27 TABLE AND PLOT OF THE RESULTS OF THE GEOMETRIC PROFILE FOR J = 50 A/dm^2 AND t = 10 mins.

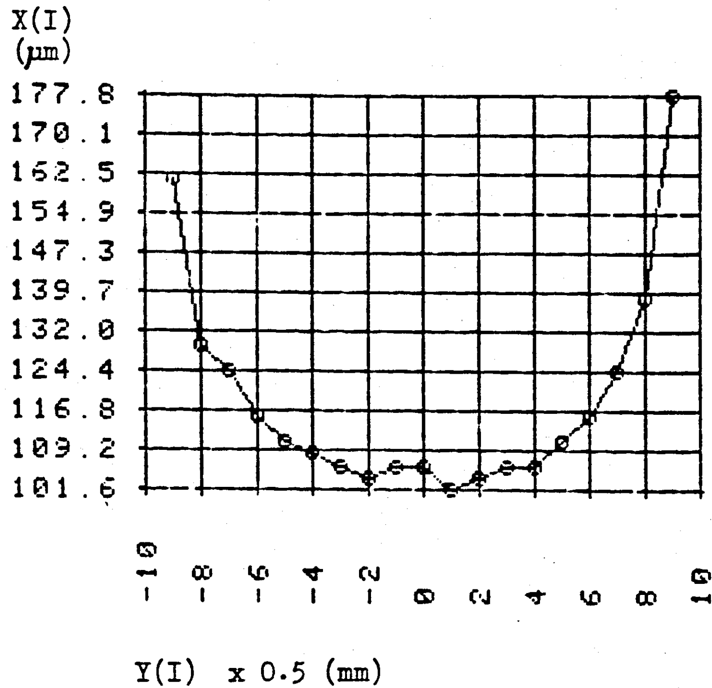

I	X(I)	Y(I)
1	-9.0000	161.7000
2	-8.0000	129.3000
3	-7.0000	124.7000
4	-6.0000	115.5000
5	-5.0000	110.9000
6	-4.0000	108.5000
7	-3.0000	106.2000
8	-2.0000	103.9000
9	-1.0000	106.2000
10	0.0000	106.2000
11	1.0000	101.6000
12	2.0000	103.9000
13	3.0000	106.2000
14	4.0000	106.2000
15	5.0000	110.9000
16	6.0000	115.5000
17	7.0000	124.7000
18	8.0000	138.6000
19	9.0000	177.8000

X(I) = Horizontal distance about the centre of the aperture at X(I) = 0

Y(I) = Depth of etch

Fig. S31 TABLE AND PLOT OF THE RESULTS OF THE GEOMETRIC PROFILE FOR J = 60 A/dm^2 AND t = 10 mins.

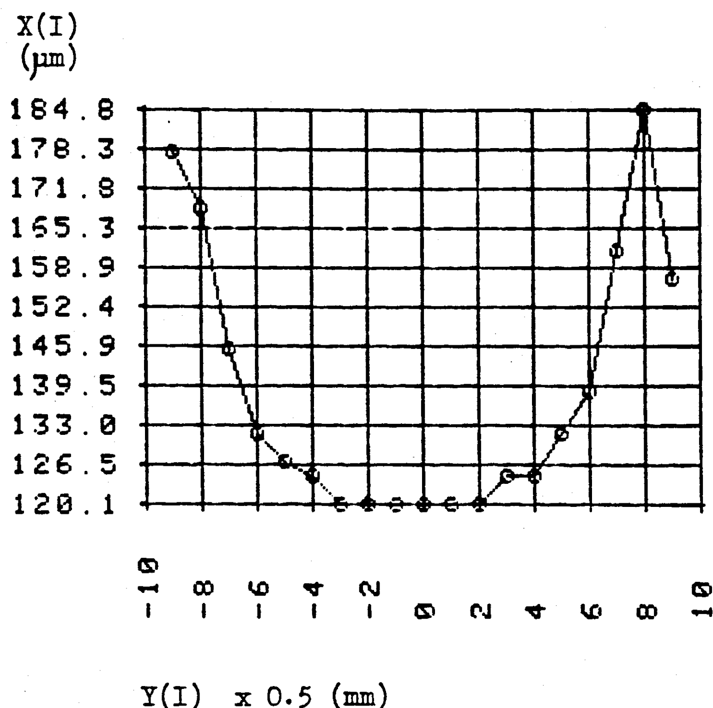

I	X(I)	Y(I)
1	-9.0000	177.8000
2	-8.0000	168.6000
3	-7.0000	145.5000
4	-6.0000	131.6000
5	-5.0000	127.0000
6	-4.0000	124.7000
7	-3.0000	120.1000
8	-2.0000	120.1000
9	-1.0000	120.1000
10	0.0000	120.1000
11	1.0000	120.1000
12	2.0000	120.1000
13	3.0000	124.7000
14	4.0000	124.7000
15	5.0000	131.6000
16	6.0000	138.6000
17	7.0000	161.7000
18	8.0000	184.8000
19	9.0000	157.0000

X(I) = Horizontal distance about the centre of the aperture at X(I) = 0

Y(I) = Depth of etch

Fig. S35 TABLE AND PLOT OF THE RESULTS OF THE GEOMETRIC PROFILE FOR J = 70 A/dm^2 AND t = 10 mins.

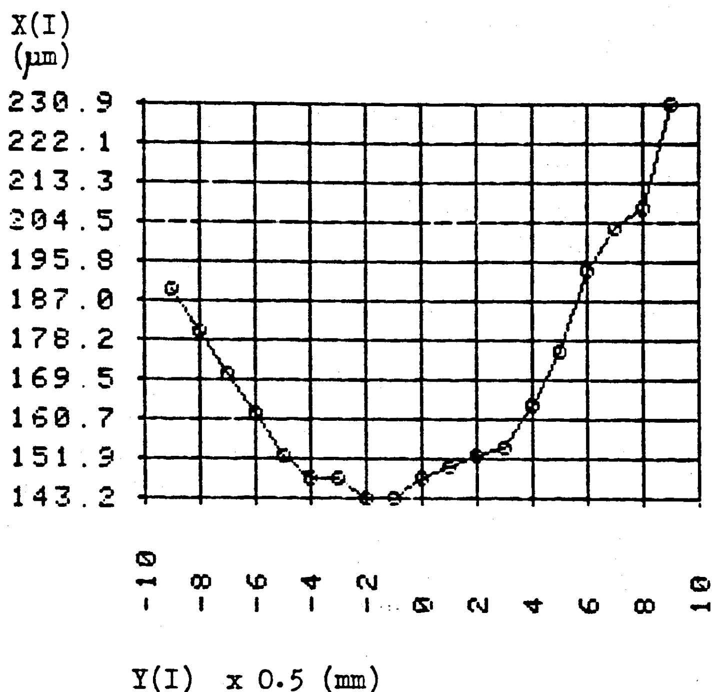

I	X(I)	Y(I)
1	-9.0000	189.4000
2	-8.0000	180.1000
3	-7.0000	170.9000
4	-6.0000	161.7000
5	-5.0000	152.4000
6	-4.0000	147.8000
7	-3.0000	147.8000
8	-2.0000	143.2000
9	-1.0000	143.2000
10	0.0000	147.8000
11	1.0000	150.1000
12	2.0000	152.4000
13	3.0000	154.7000
14	4.0000	164.0000
15	5.0000	175.5000
16	6.0000	194.0000
17	7.0000	203.2000
18	8.0000	207.9000
19	9.0000	230.9000

X(I) = Horizontal distance about the centre of the aperture at X(I) = 0

Y(I) = Depth of etch

Fig. S39 TABLE AND PLOT OF THE RESULTS OF THE GEOMETRIC PROFILE FOR J = 80 A/dm^2 AND t = 10 mins.

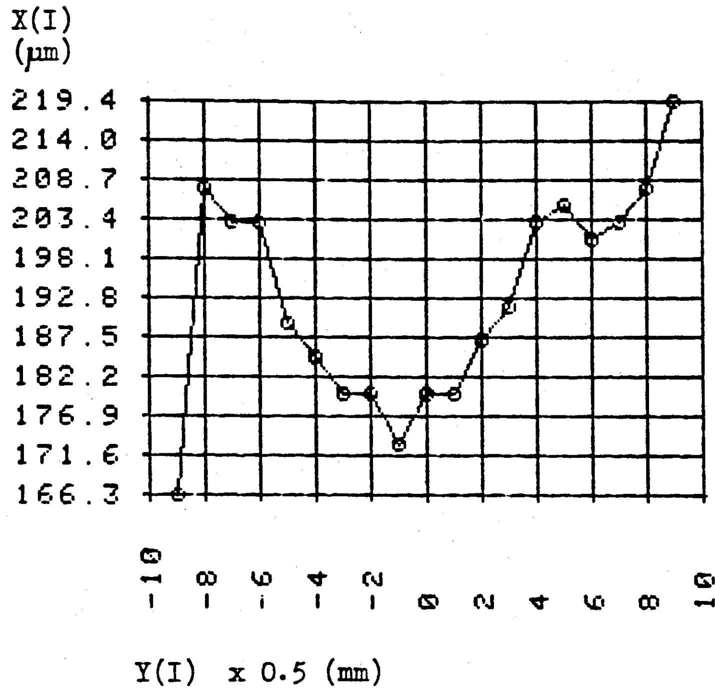

I	X(I)	Y(I)
1	-9.0000	166.3000
2	-8.0000	207.8000
3	-7.0000	203.2000
4	-6.0000	203.2000
5	-5.0000	189.4000
6	-4.0000	184.8000
7	-3.0000	180.1000
8	-2.0000	180.1000
9	-1.0000	173.2000
10	0.0000	180.1000
11	1.0000	180.1000
12	2.0000	187.1000
13	3.0000	191.7000
14	4.0000	203.2000
15	5.0000	205.5000
16	6.0000	200.9000
17	7.0000	203.2000
18	8.0000	207.8000
19	9.0000	219.4000

X(I) = Horizontal distance about the centre of the aperture at X(I) =0

Y(I) = Depth of etch

Fig. S43 TABLE AND PLOT OF THE RESULTS OF THE GEOMETRIC PROFILE FOR J = 90 A/dm^2 AND t = 10 mins.

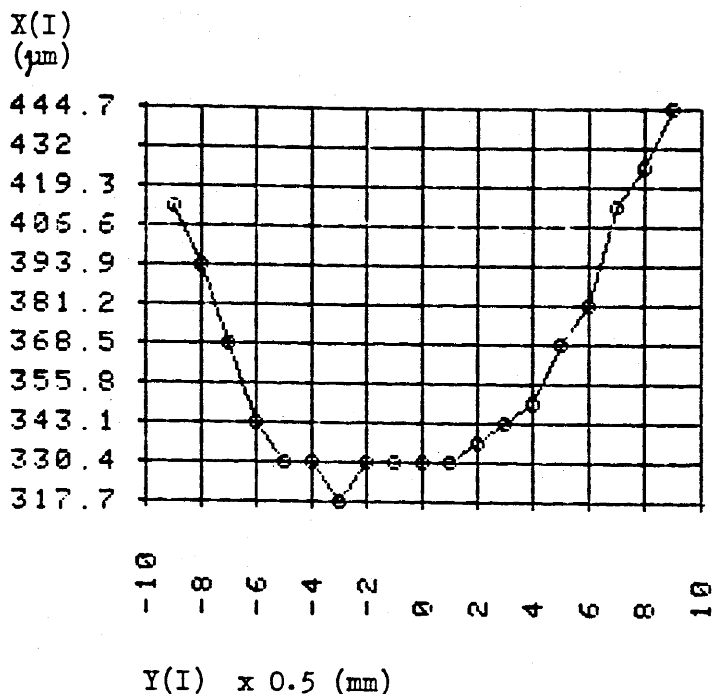

I	X(I)	Y(I)
1	-9.0000	413.0000
2	-8.0000	393.9000
3	-7.0000	368.5000
4	-6.0000	343.1000
5	-5.0000	330.4000
6	-4.0000	330.4000
7	-3.0000	317.7000
8	-2.0000	330.4000
9	-1.0000	330.4000
10	0.0000	330.4000
11	1.0000	330.4000
12	2.0000	336.7000
13	3.0000	343.1000
14	4.0000	349.4000
15	5.0000	368.5000
16	6.0000	381.2000
17	7.0000	413.0000
18	8.0000	425.7000
19	9.0000	444.7000

X(I) = Horizontal distance about the centre of the aperture at X(I) = 0

Y(I) = Depth of etch

Fig. S45 TABLE AND PLOT OF THE RESULTS OF THE GEOMETRIC PROFILE FOR J = 90 A/dm^2 AND t = 20 mins.

APPENDIX T

PHOTOMICROGRAPHS OF THE STAINLESS STEEL SECTIONS PRODUCED BY E.P.E.

The results presented in this appendix are of the electro photoetched AISI 304 stainless steel. The lines were produced with the aid of the phototool described in the main text figures 5.1a,b. Etching was in 10% HCl w/w at 25°C at 50 A/dm^2. The results are presented in the figures T1 to T10 as tabulated below:

Figure	stencil line width mm	etch duration mins.
T1	1.6	
	0.8	
T2	0.4	3
	0.2	
	0.1	
	0.05	
T3	1.6	
	0.8	
T4	0.4	6
	0.2	
	0.1	
	0.05	
T5	1.6	
	0.8	
T6	0.4	9
	0.2	
	0.1	
	0.05	
T7	1.6	
	0.8	
T8	0.4	12
	0.2	
	0.1	
	0.05	
T9	1.6	
	0.8	
T10	0.4	15
	0.2	
	0.1	
	0.05	

STENCIL WIDTH = 1.6 mm

STENCIL WIDTH = 0.8 mm

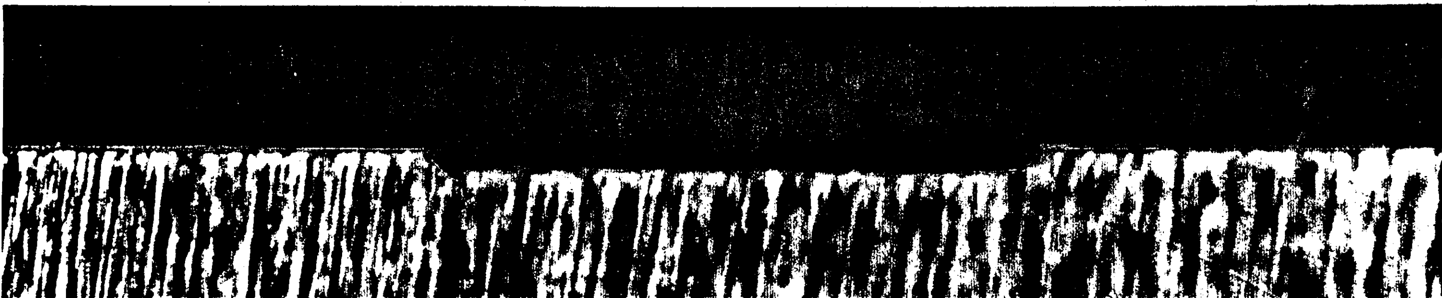

Fig. T1 PHOTOMICROGRAPH (X100) OF THE CROSS SECTION OF THE ETCHED LINES, t = 3 MINUTES.

STENCIL WIDTH = 0.2 mm 0.4 mm

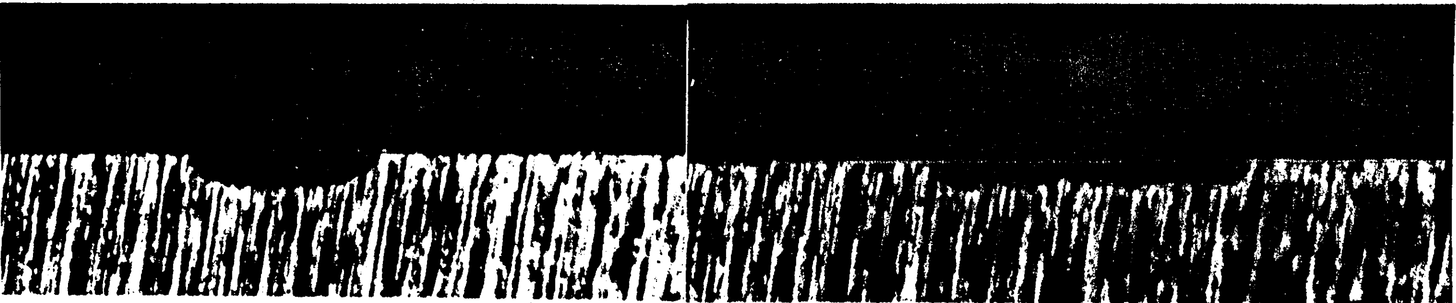

STENCIL WIDTH = 0.05 mm 0.1 mm

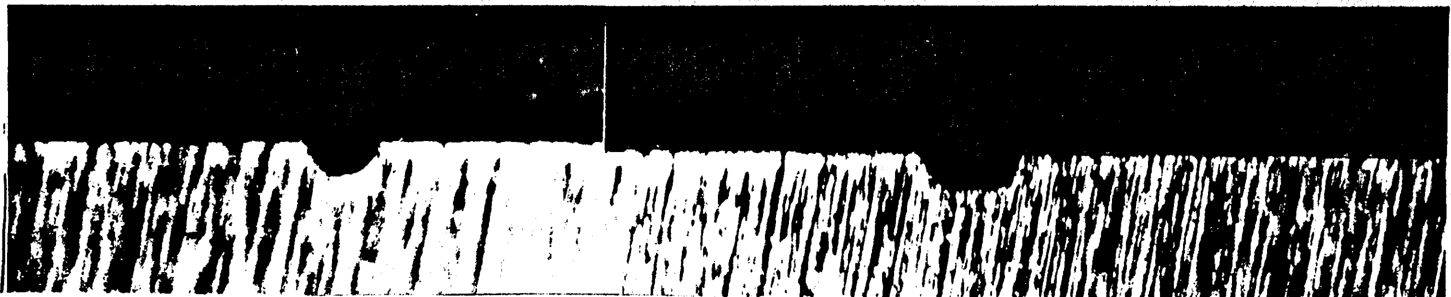

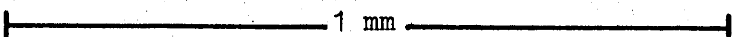

Fig. T2 PHOTOMICROGRAPH (X100) OF THE CROSS-SECTION OF THE ETCHED LINES, t = 3 MINUTES.

STENCIL WIDTH = 1.6 mm

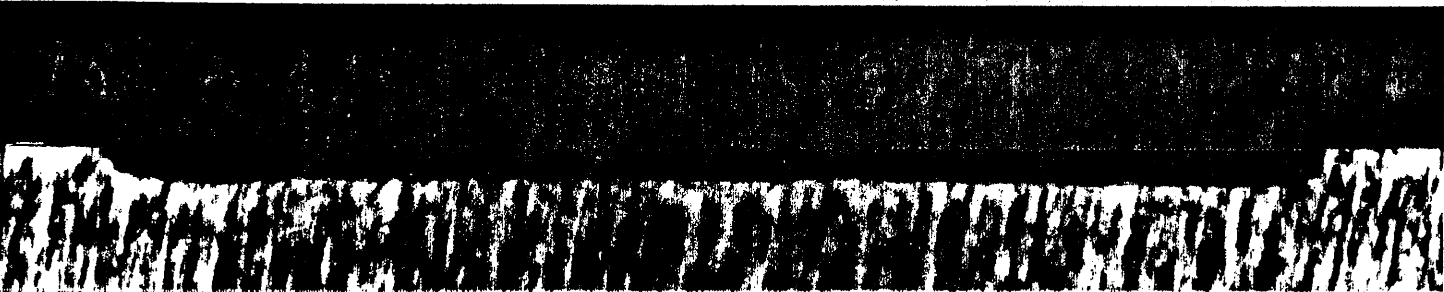

STENCIL WIDTH = 0.8 mm

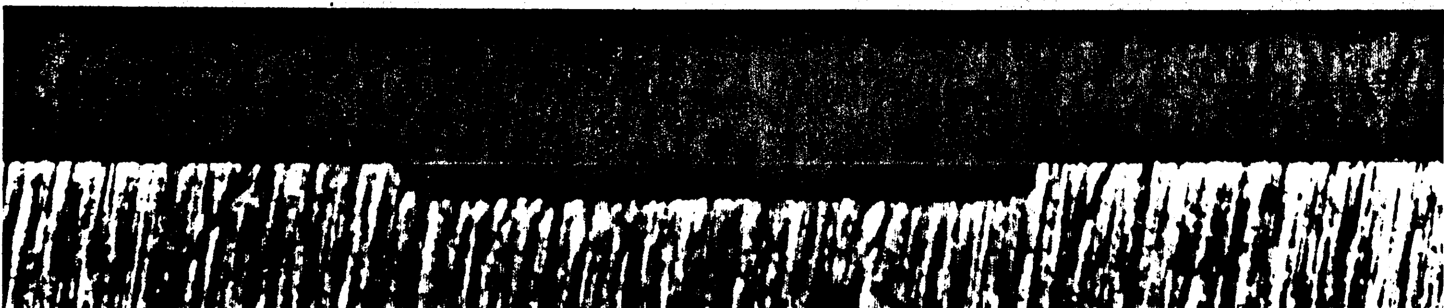

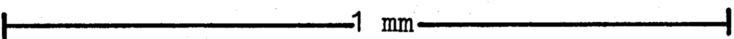

Fig. T3 PHOTOMICROGRAPH (X100) OF THE CROSS-SECTION OF THE ETCHED LINES, t = 6 MINUTES.

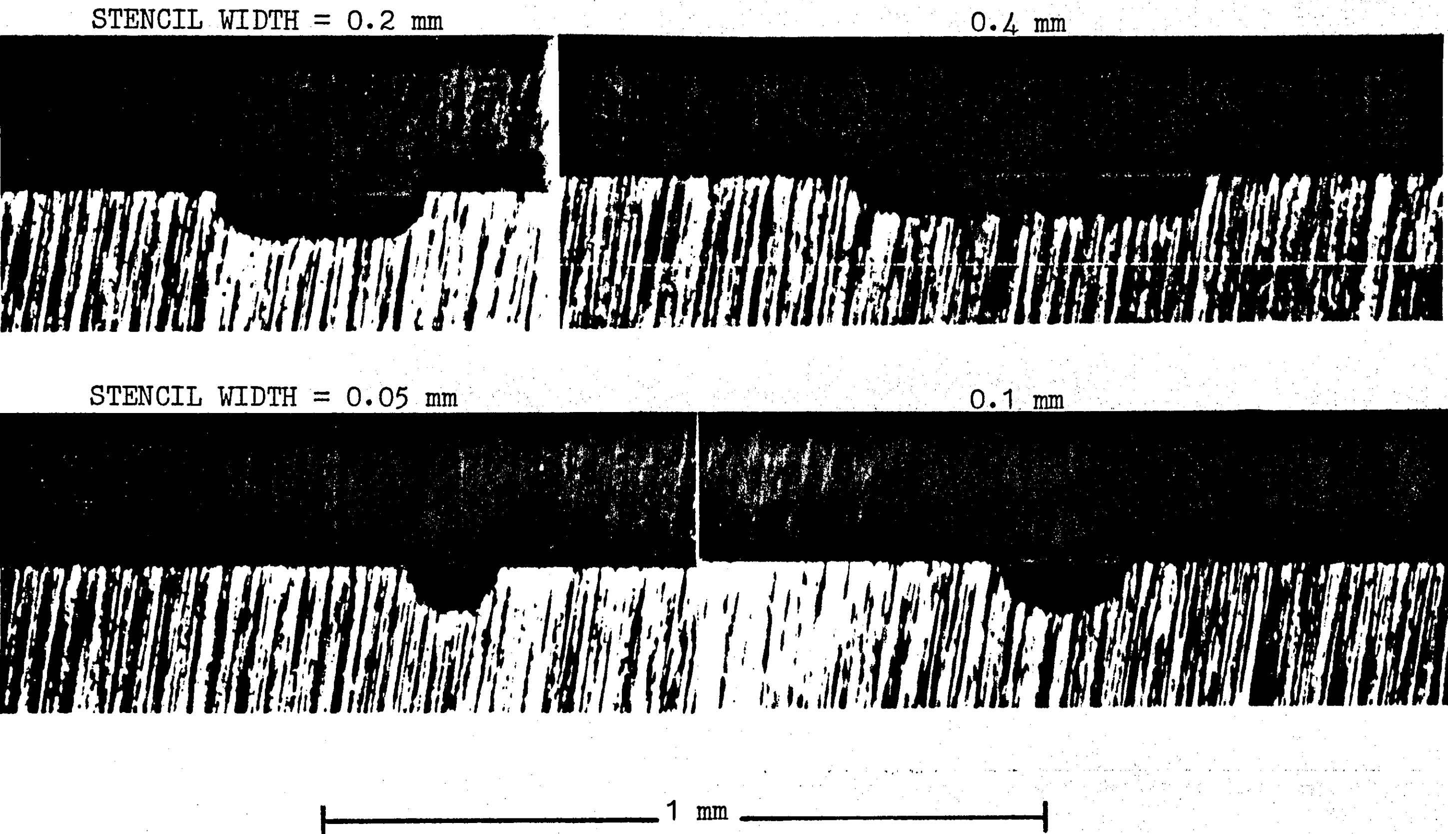

Fig. T4 PHOTOMICROGRAPH (X100) OF THE CROSS-SECTION OF THE ETCHED LINES, t = 6 MINUTES.

STENCIL WIDTH = 1.6 mm

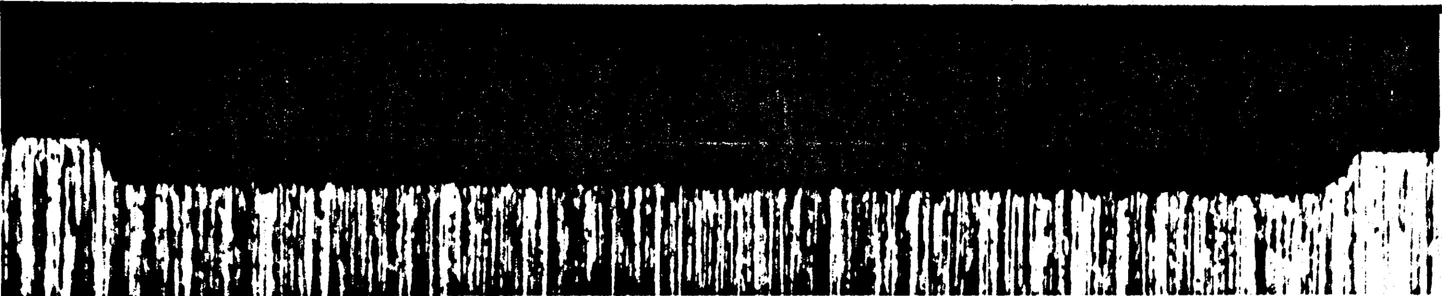

STENCIL WIDTH = 0.8 mm

Fig. T5 PHOTOMICROGRAPH (X100) OF THE CROSS-SECTION OF THE ETCHED LINES, t = 9 MINUTES

STENCIL WIDTH = 0.2mm

0.4 mm

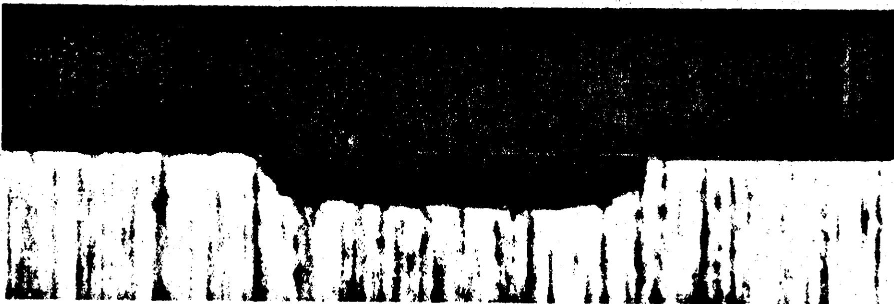

STENCIL WIDTH = 0.05 mm

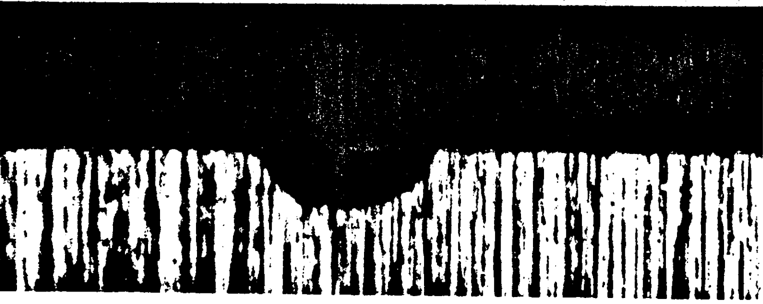

0.1 mm

Fig. T6 PHOTOMICROGRAPH (X100) OF THE CROSS-SECTION OF THE ETCHED LINES, $t = 9$ MINUTES.

STENCIL WIDTH = 1.6 mm

STENCIL WIDTH = 0.8 mm

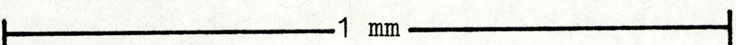

Fig. T7 PHOTOMICROGRAPH (X100) OF THE CROSS-SECTION OF THE ETCHED LINES, t = 12 MINUTES.

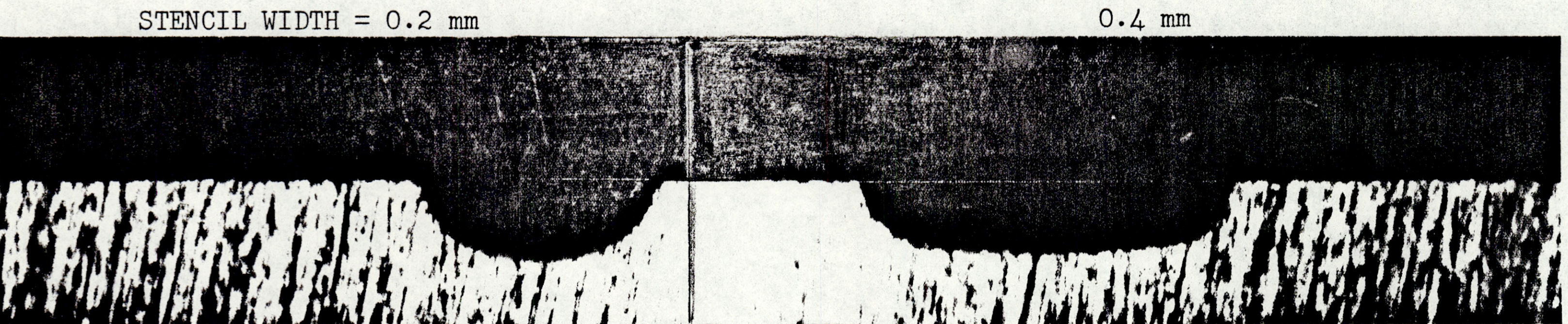

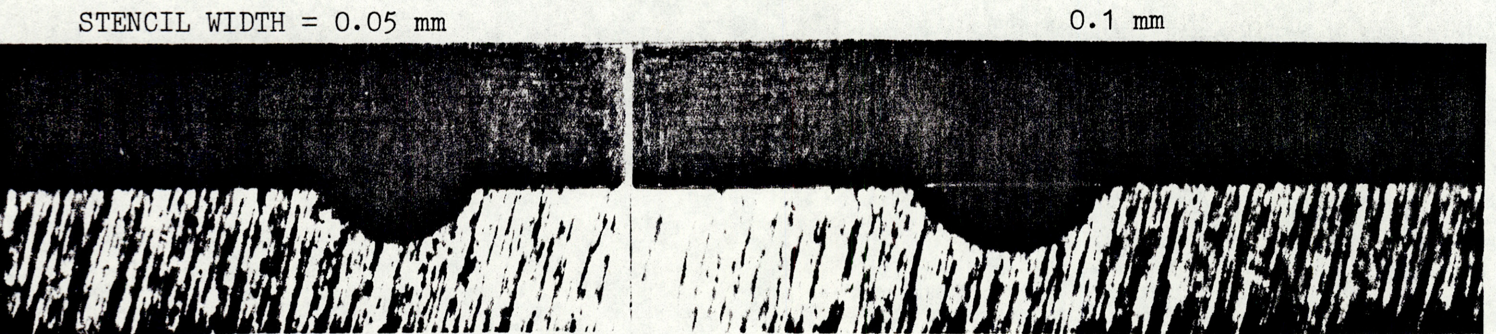

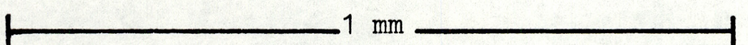

Fig. T8 PHOTOMICROGRAPH (X100) OF THE CROSS-SECTION OF THE ETHED LINES, t = 12 MINUTES.

STENCIL WIDTH = 1.6 mm

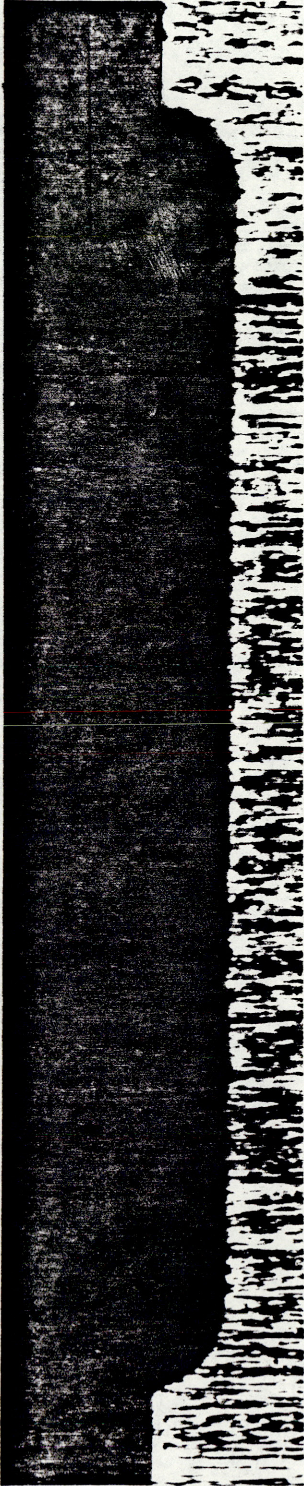

STENCIL WIDTH = 0.8 mm

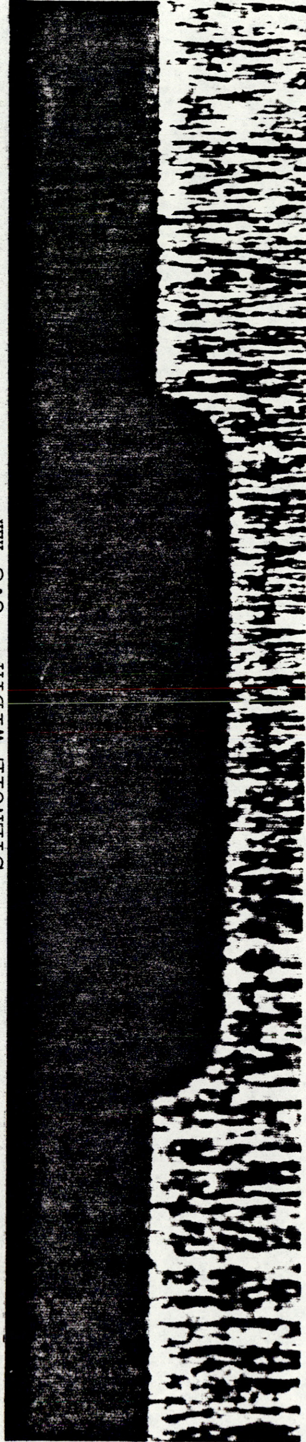

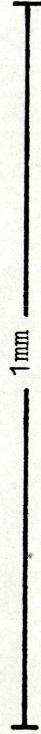

Fig. T9 PHOTOMICROGRAPH (X100) OF THE CROSS-SECTION OF THE ETCHED LINES, t = 15 MINUTES.

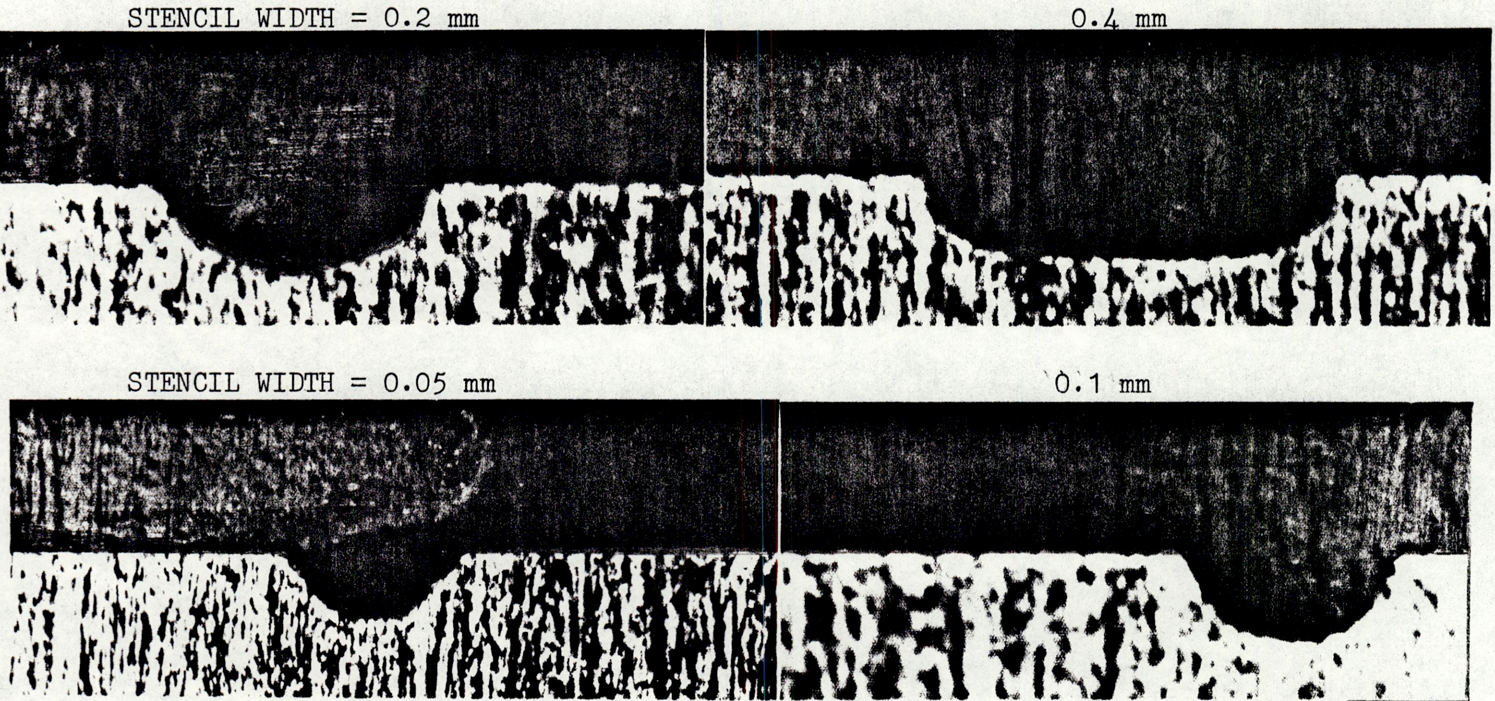

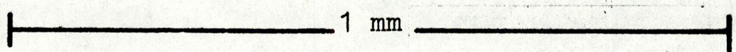

Fig. T10 PHOTOMICROGRAPH (X100) OF THE CROSS-SECTION OF THE ETCHED LINES, t = 15 MINUTES.

APPENDIX U

AN APPLICATION FOR E.P.E. IN THE PRODUCTION OF STEEL RULERS.

Industrial enquiries were made with two commercial concerns regarding the manufacture of precision steel rulers as used in the engineering field. These are at present produced by p.c.m. Many versions and qualities are produced. In general the cost of the ruler is determined by the type of substrate material, if it is chromium plated, the resolution of the scale and the quality of black filling of the markings.

It is known that one of the companies utilises an electrolytic method of stripping the plated chromium through the photoresist stencil prior to etching the steel by immersing in ferric chloride.

The blacking of the scales is produced manually using an unspecified filler. the cost of this operation on a high quality 300mm chromium plated ruler was 90 pence in the year 1983 [Ref.]. This was approximately 20% of the retail price.

It is believed that the production cost may be reduced if electro blacking is employed. This may be carried out in the same electro etching bath by changing the electrical parameters from high current densities initially to suitably low current densities for electro blacking. As previously described in chapter 4, blacking for AISI 304 occurred at anode potentials <-250mV (v. SCE) in a 10% w/w HCl solution. Therefore a limited experiment was setup to test its' suitability for application to the production of an adherent black film in the photoengraved surface of the steel.

The steel sample was prepared by the company mentioned above and was supplied with a resist stencil as produced by one of their phototools.

Due to the unknown area defined by the photo resist stencil on the sample supplied, potentiostatic etching was employed. This was carried out utilising the polarization measurement setup as described in chapter 4.

A total mean depth of 17μm was achieved in two stages as follows:

1- Electro photoetching at -130mV (v. SCE) produced a mean depth of etch of 10μm in one minute (@ 50 A/dm^2).

2- Electro photoblacking at -280mV (v. SCE) for two minutes produced a depth of etch of 7μm.

The above values were calculated from the metal removal equation (11) and using '7.9 g/cm^3 ' as the density of steel. These results

were not confirmed by measurement.

The resultant etching and blacking may be seen in the attached figure U1, a photomicrograph of part of a steel ruler where the figure '3' is electroblacked and the figure '0' is unetched.

Figure U2 is of a different ruler where a chromium layer is plated on the steel. This layer was stripped through the resist stencil prior to repeating the same electroetching procedure as described above. The lower part of the ruler was unetched, the middle and top parts were electro photoetched for 10 minutes and only the top part was electroblacked. The scale numbers represent millimeters. The blacking density was found to be comparable with those produced by manual filling.

REFERENCE

Private Communication with Moore & Wright Ltd, Sheffield, England.

Fig. U1 PHOTOMICROGRAPH OF FEATURES ON AN ELECTRO PHOTOETCHED/BLACKED STEEL RULER (Mag. x 40).

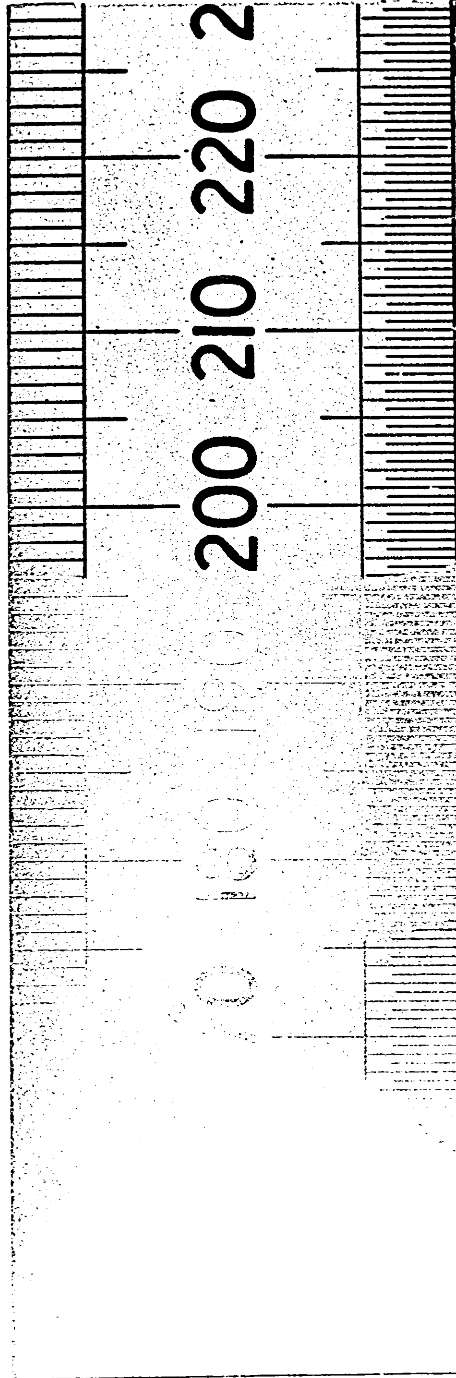

Fig. U2 PHOTOGRAPH OF THE ELECTRO PHOTOETCHED/BLACKED CHROMIUM ON STEEL RULER.

APPENDIX V

SPECIFICATIONS AND PROCESSING OF SHIPLEY AZ.340 PHOTORESIST

This is a positive working photoresist which may be applied in relatively thick layers. Coatings that have a dry film thickness of more than 12.5 μm have been claimed (Ref.). The resolution capabilities AZ-340 permit images as fine as 200 lines/mm to be reproduced with coatings of 6.25μm.

Applying the resist at full strength is recommended by the manufacturer and thicknesses of 5μm are recommended.

When dip-coating the withdrawal rate should be from 5 to 60 cm per minute. Coating uniformity of +10% from top to bottom of 30 cm is further claimed.

Drying the coatings should be carried out between 50 and 80°C and typically for 15-20 minutes at 65°C.

After imaging the resist is developed in an AZ-303 solution, this rapidly dissolves the exposed areas of the AZ-340 photoresist coatings. The substrate is immersed in 1 part of AZ-303 developer to 4 parts of distilled water for 1 to 2.5 minutes. It is then rinsed in clean running water, preferably by spraying. The developer solution should be used at 18° to 24°C and must not be used above 29°C.

Generally post-baking is not recommended by the manufacturer, but if resistance to severe etching or high current densities is required a post-bake at 65°C for 20-30 minutes may be used. Higher temperatures are said to be generally harmful. Stencil removal is by immersing in acetone for 5 to 30 seconds.

The stencils produced are resistant to both hydrochloride acid and phosphoric acid.

SUPPLIED BY: Shipley Chemicals Ltd., Coventry.
REFERENCE: Technical Data Sheet PI-340A (UK), August 1972, Shipley Chemicals.

APPENDIX W

PRELIMINARY TESTS FOR ETCHING VITROVAC AND RECOVAC WITH FERRIC CHLORIDE

The following tests were not intended to be thorough or rigorous investigations, but merely a rapid check to experience at first hand the reported problems in conventionally etching the two materials.

Preliminary etching tests were carried out on both 'Recovac' and 'Vitrovac', this by spray etching with aqueous ferric chloride. Attempts to etch Recovac with a commercially used concentration of 40 Baume [*] containing $<0.3\%$ w/w free HCl at $45^{\circ}C$ for 5 minutes yielded negative results and only slight staining of the surface was achieved.

Vitrovac 6025 was also spray etched under the same conditions as above and similar results were obtained with this material, where little effect was made on the surface. Nevertheless some etching took place when the temperature was increased, this at $>55^{\circ}C$. Etching was non-uniform and exhibited poor surface results and poor linearity at the resist edges.

It is possible that temperatures in the order of 60° C and higher would yield improved results but this was not investigated as softening of the plastic panels of the spray etching machine was noted. As most machines of this type are fabricated from PVC panels it is not practical to operate at these temperatures.

* The figures for the specific gravity of an etchant are converted to degrees Baume by means of a conversion factor.

$$\text{Baum}\bar{e} = 145 \times \frac{(\text{Specific Gravity} - 1)}{\text{Specific Gravity}}$$

APPENDIX X

FLUXGATE MAGNETOMETERS

This is an explenation of the principals of the fluxgate magnetometer based on the article by Pollock (Ref) in which he demonstrated the application of such a device in an electronic compass.

There are very few means of measuring absolute values of magnetic fields. The most popular one is the Hall effect sensor, but most commercial units are designed for relatively high values of field.

The fluxgate configuration can measure very low field magnitudes by using the chopper-amplifier principle. Briefly, it is based on the fact that all parts of an uniformly excited toroidal magnetic circuit would be equally magnetized in the absence of external magnetic fields and therefore no voltage would be induced into a coil encompassing the whole magnetic circuit.

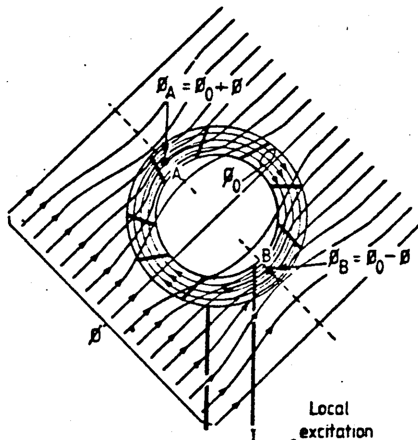

Flux interference pattern.

The introduction of external field in the plane of the toroid would result in a slight unbalance between the two halves of the magnetic circuit (Fig. above)

The flux at point A equals $\phi_A = \phi_o + \phi$

whereas point B, situated 180° away

would correspond to a flux $\phi_B = \phi_o - \phi$

Where ϕ_o is due to local toroid excitation and ϕ , to the external field.

Although the unbalance is very slight, it can be measured through one of its side effects: If we cyclically change the local excitation so as to switch the toroid between its two magnetic saturation points, we find that due to the unbalance, one half would be driven into saturation a short time before the opposite half and the toroid as a whole would, for a short period of time act as a small magnet. The net result is that a coil encompassing the complete magnetic circuit would pick up an induced voltage impulse, proportional to the external field.

By mounting two such coils perpendicularly to each other onto the same toroid, we can resolve any external field into its X and Y components in the toroid plane.

Ref. N. Pollock, Electronic Compass Using A Fluxgate Sensor, Wireless World, Oct. 1982.

APPENDIX Y

METHOD OF MEASURING THE RECORDING HEAD LAMINATIONS

A random sample of 10 frets were used for the measurement of total number of 60 frets produced. The highest specification on the drawing of the magnetic recording head lamination was that circled in the figure below:

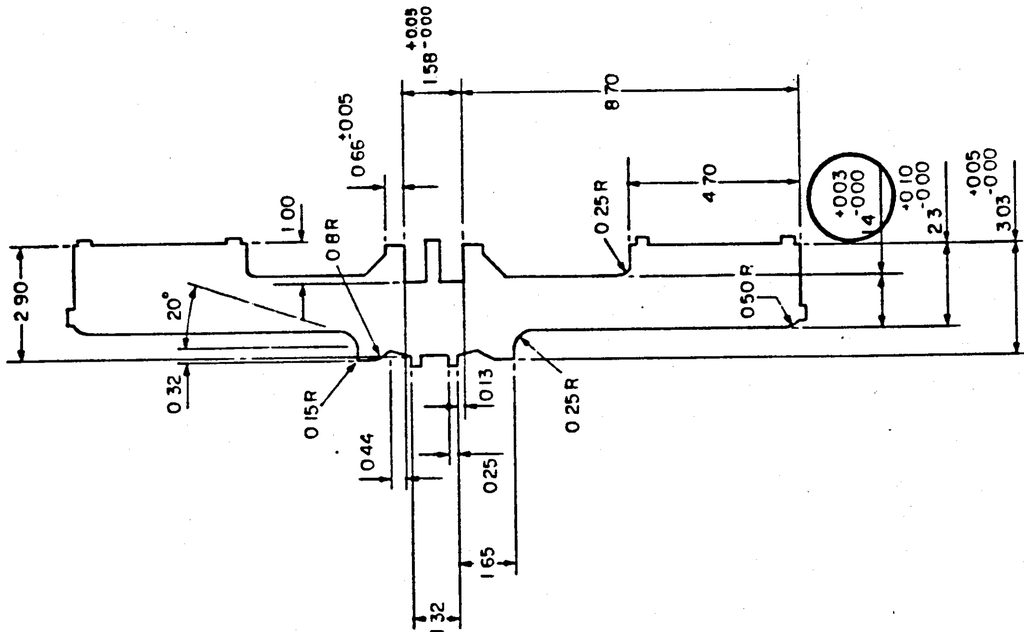

Hence it was the dimension used for assessing the repeatability and accuracy of the process. Further it is a method for checking the estimated etch factor of one as well as the effects of vertical etching. The laminations were measured and the mean of the rows was calculated as follows:

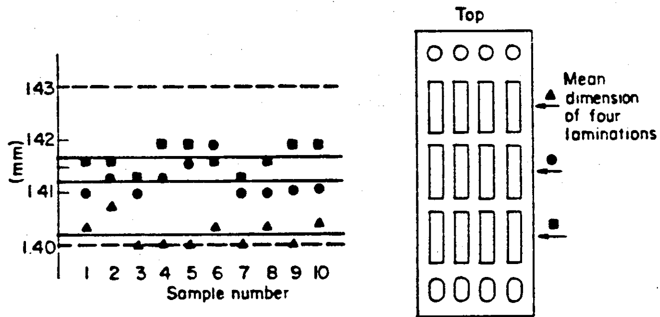

Measured distribution of the mean dimension.

Result table:

MEAN DIMENSION OF 4 LAMINATIONS (mm)

SAMPLE	BOTTOM ROW	MID. ROW	TOP ROW
1	1.416	1.410	1.403
2	1.416	1.413	1.407
3	1.413	1.410	1.410
4	1.419	1.413	1.400
5	1.419	1.416	1.400
6	1.416	1.419	1.403
7	1.413	1.410	1.400
8	1.416	1.410	1.403
9	1.419	1.403	1.400
10	1.419	1.410	1.403

APPENDIX Z

PROPOSED CONTINUOUS PHOTOCHEMICAL MACHINING OF AMORPHOUS ALLOYS

The production of precision components from amorphous metal alloys in general may be achieved by a number of manufacturing processes. The following is a proposed method for the continuous processing of such materials.

Amorphous metals, due to their availability in limited widths lend themselves to be processed continuously. This type of processing is not new to p.c.m., the shadow masks of colour television screens are manufactured by continuous and automatic processing as described by Harris (Ref.).

Vitrovac like other amorphous materials is supplied on reels. It is in an extremely clean state as supplied, it is rolled on to the reel immediately after casting. This has the advantage of minimal pre-coating preparation if any. Large volume production with high quality control may be achieved by continuous photochemical machining (CPCM), this is schematically illustrated in Figure Z1 where the ribbon may be coated with a photoresist by either a dipcoat or a hot roller laminating system or alternatively a printing method. The choice being dependent upon factors such as resolution, type of substrate, subsequent chemical operations and in certain conditions the final product requirements. In certain requirements, retaining the resist stencil in a modified form upon the substrate surface for further operations is necessary, as required for recording head laminating where the photoresist stencil acts as a bonding agent for the laminations.

The photographic imaging of the ribbon is an incremental operation, hence requiring ribbon pre and post buffering stages. Resist exposure is the delaying stage and hence a multi-exposure method may be employed to increase the throughput. Dynamic resist development may be employed by spray developing the exposed ribbon during its′ movement through the unit.

As some amorphous alloys may be readily etched using conventional chemical spray etching, hence one of two metal removal methods may be employed:

a. Conventional spray etching.
b. Electrolytic etching.

The process may be controlled using a central processing unit controlling the coating thickness (liquid resist) by adjusting the withdrawal rate of the ribbon through the resist container. Exposure, developing and etching may be similarly controlled, by controlling the ribbon feed rate through each individual process. Feedback elements using charged couple devices (CCD) line cameras measuring the stencil dimensions may be employed suitably positioned after the photoresist developing and the substrate

etching stages.

The dimensions received from the cameras can be analysed and compared with the entered data concerning product dimensions and process parameters and central processing device could then control each element of the process.
Amorphous materials in general are suitable for this and their advantages may be summerised as follows:

1. Material is supplied in a clean state.
2. It can be readily bent and hence not damaged by passing through the line.
3. Material available on reels and in long lengths.
4. Material handling in a reel form is suited for follow up operations featuring continuous processing.

The advantages of the process may be higher outputs, improved inspection by total quality control, and accuracy and repeatability.

A flow diagram illustrating the proposed system for the continuous production of precision components from ribbon is attached figure Z1.

REFERENCE

W. T. Harris, CHEMICAL MILLING, Oxford series on advanced manufacturing.

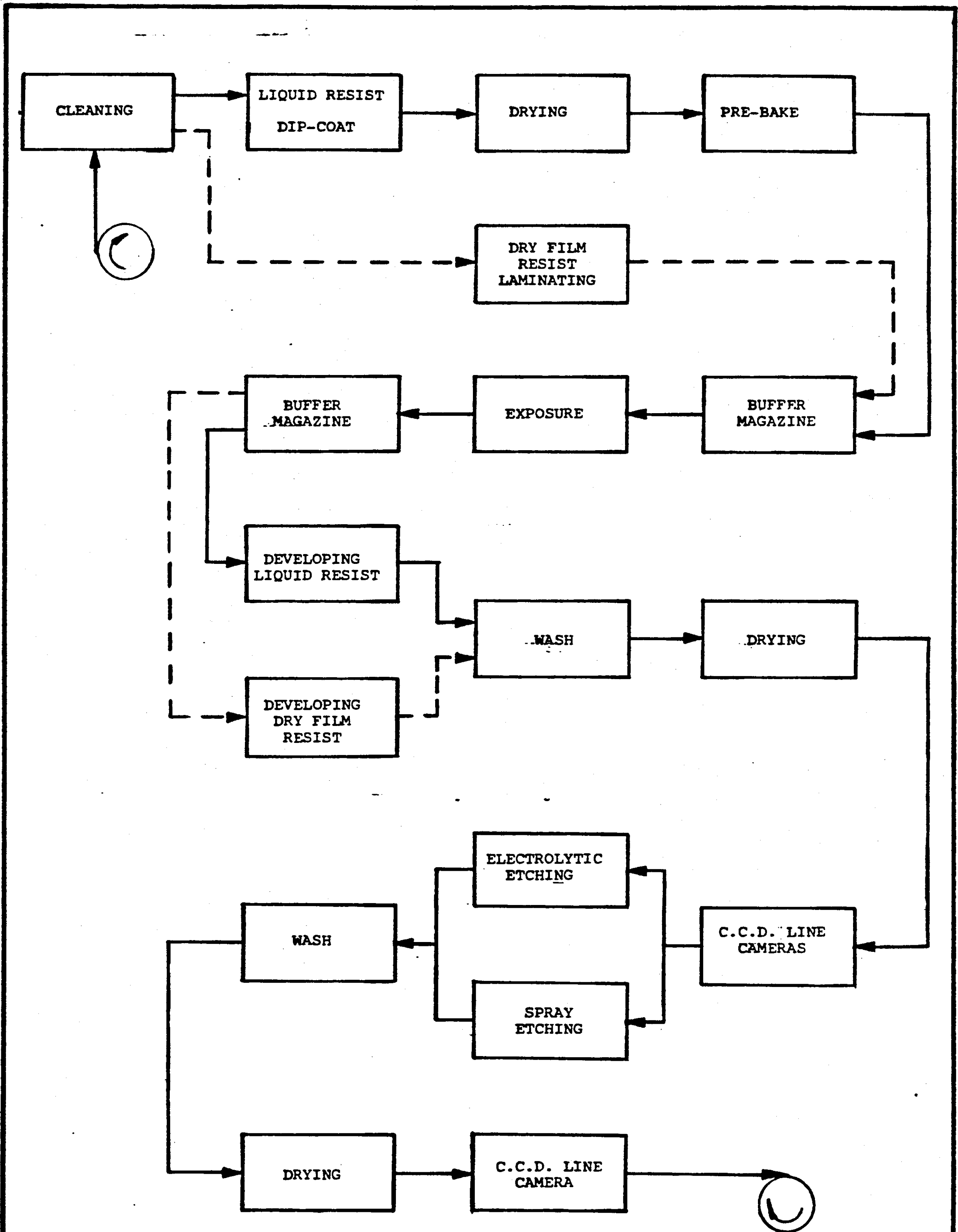

Fig. Z1 FLOW DIAGRAM ROR THE PROPOSED CONTINUOUS PROCESSING OF VITROVAC 6025.

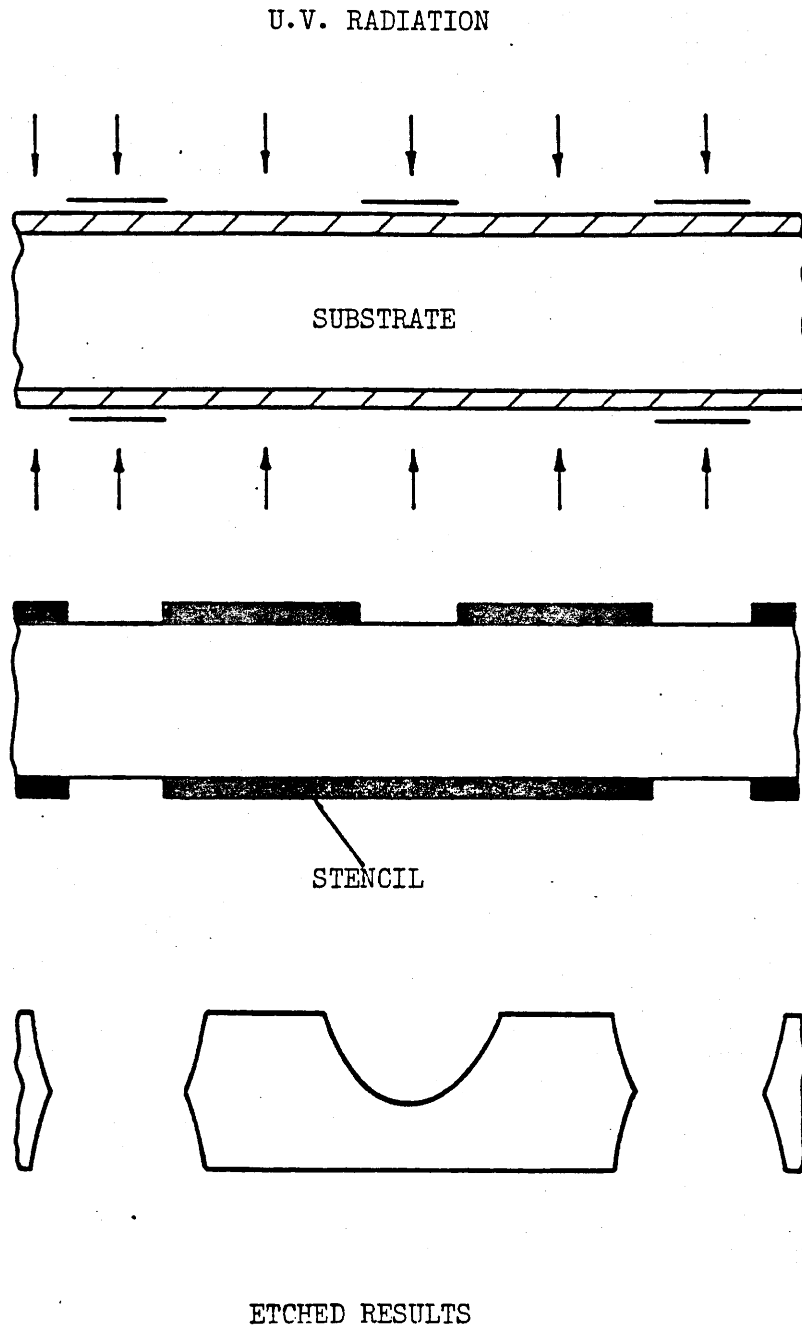

Fig. 1.1 SCHEMATIC ILLUSTRATING THE EXPOSURE AND DEVELOPMENT OF NEGATIVE WORKING PHOTORESIST; Fig. 1.2 FOR +ve WORKING RESISTS WHERE THE SAME TOOL IS USED.

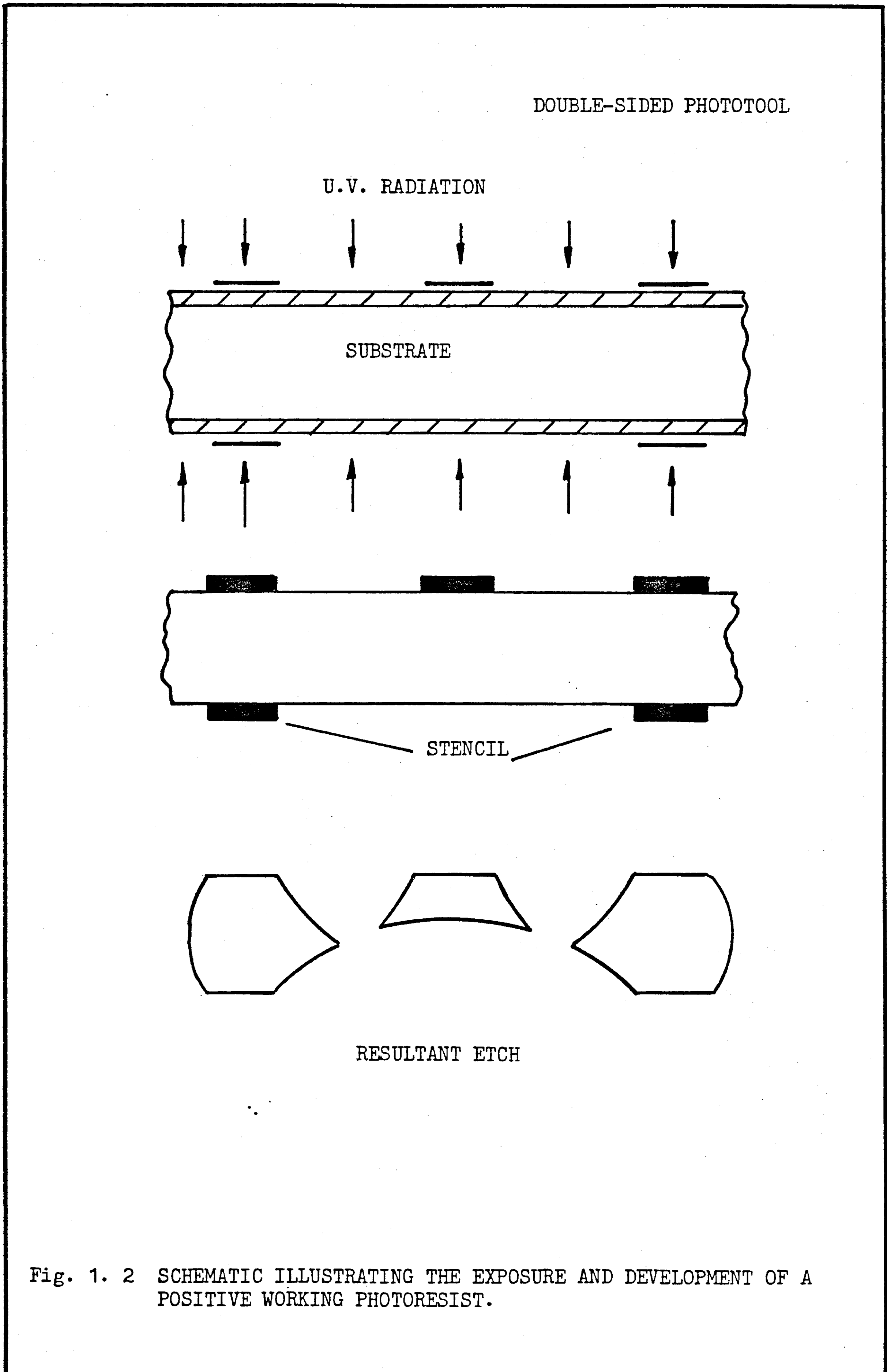

Fig. 1. 2 SCHEMATIC ILLUSTRATING THE EXPOSURE AND DEVELOPMENT OF A POSITIVE WORKING PHOTORESIST.

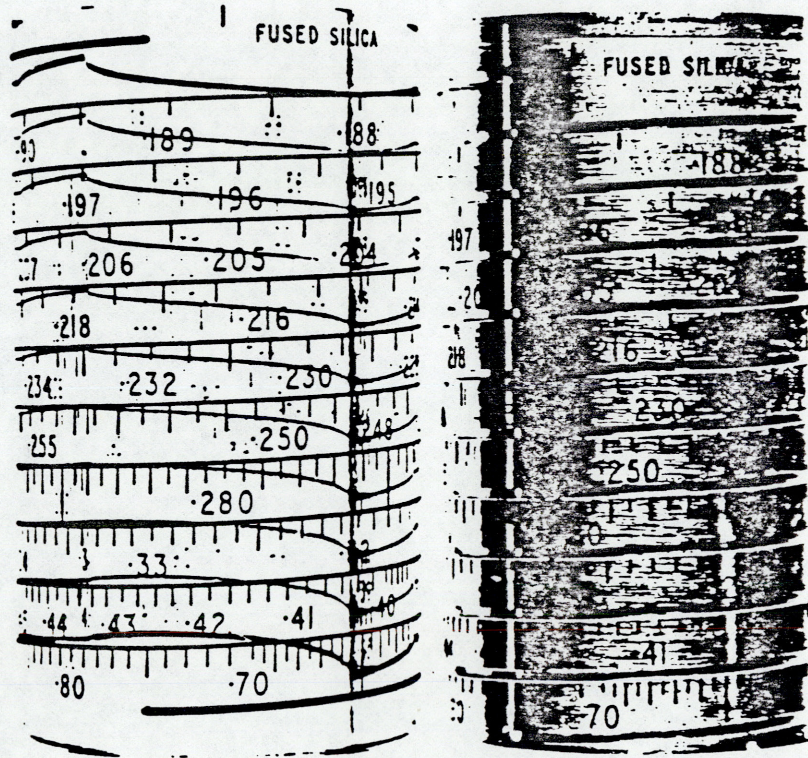

PHOTOTOOL　　　　ETCHED DRUM

Fig. 1.3 A PHOTOETCHED ALUMINIUM DRUM AND PHOTOTOOL.

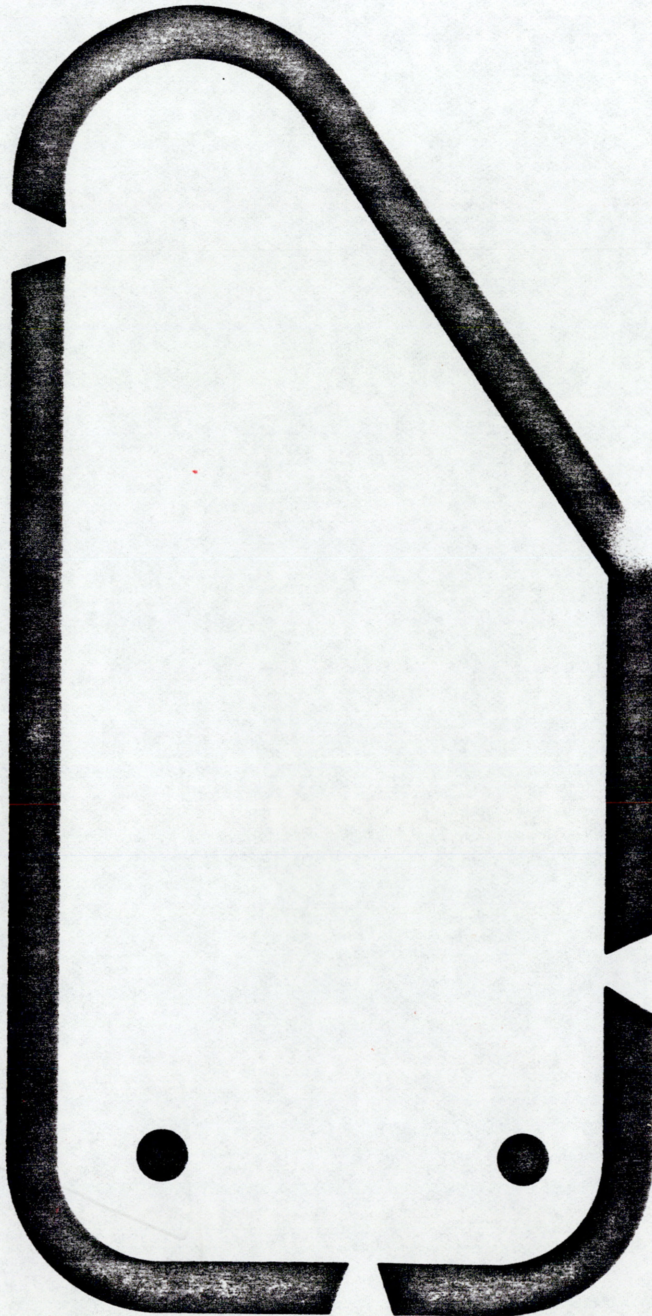

Fig. 1.4 MAGNIFICATION OF A PHOTOTOOL FOR THE PRODUCTION OF CAMERA SHUTTER BLADES MADE FROM SPRING STEEL, COURTESY OF ALLEN ET AL.

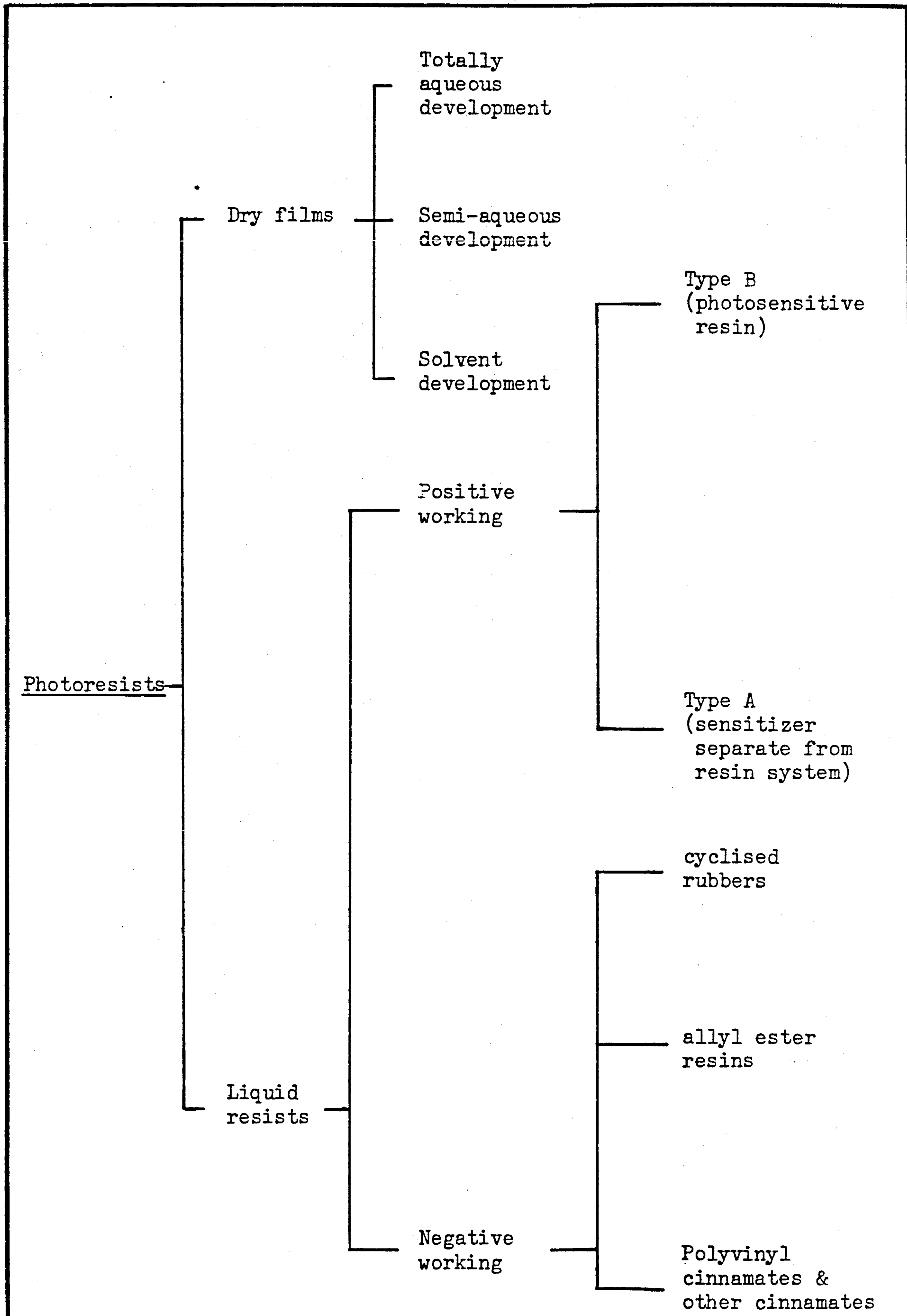

Fig. 1.5 A COMMERCIAL PHOTORESIST CLASSIFICATIONS; FROM LECTURE NOTES AT C.I.T.

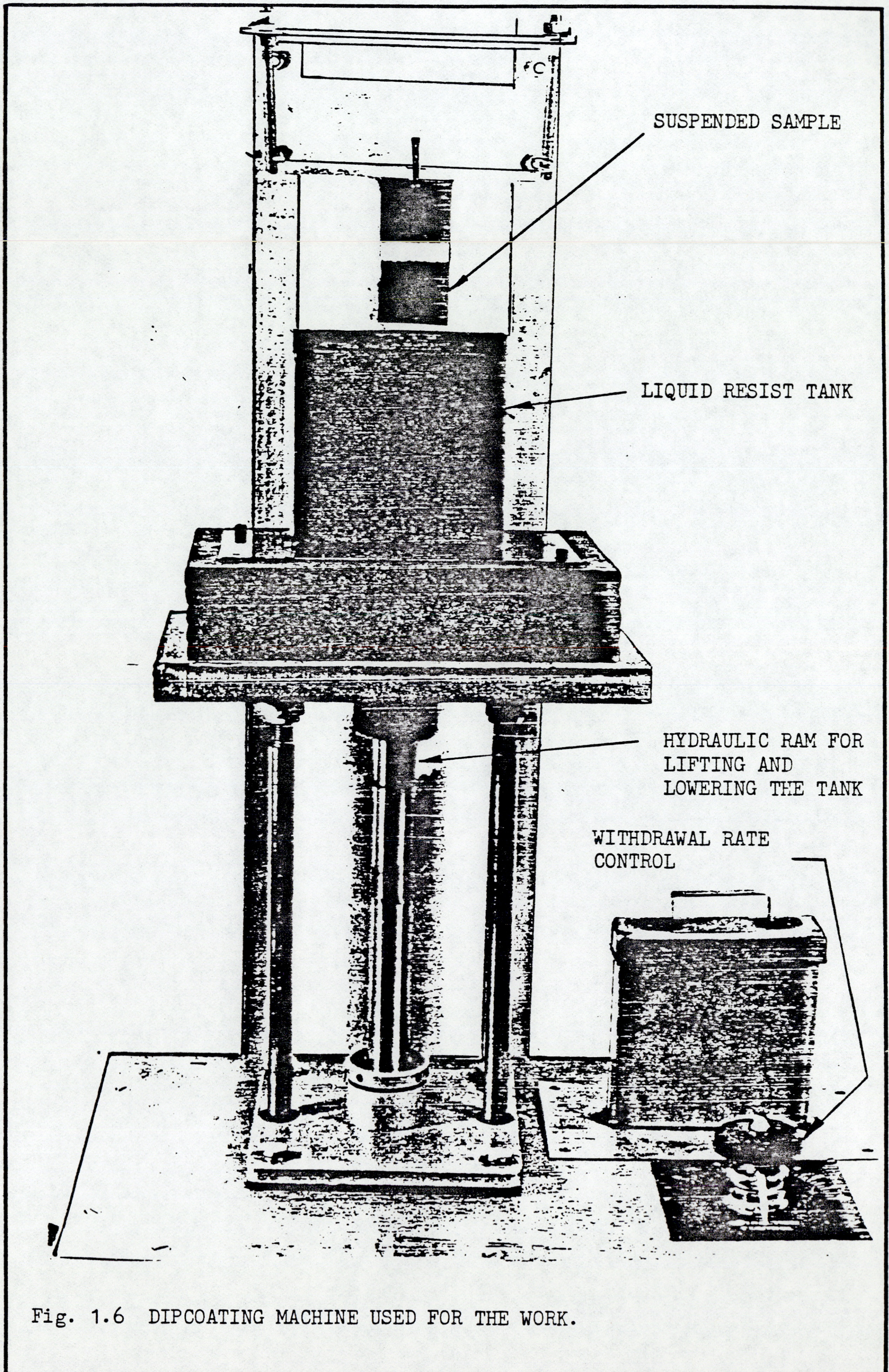

Fig. 1.6 DIPCOATING MACHINE USED FOR THE WORK.

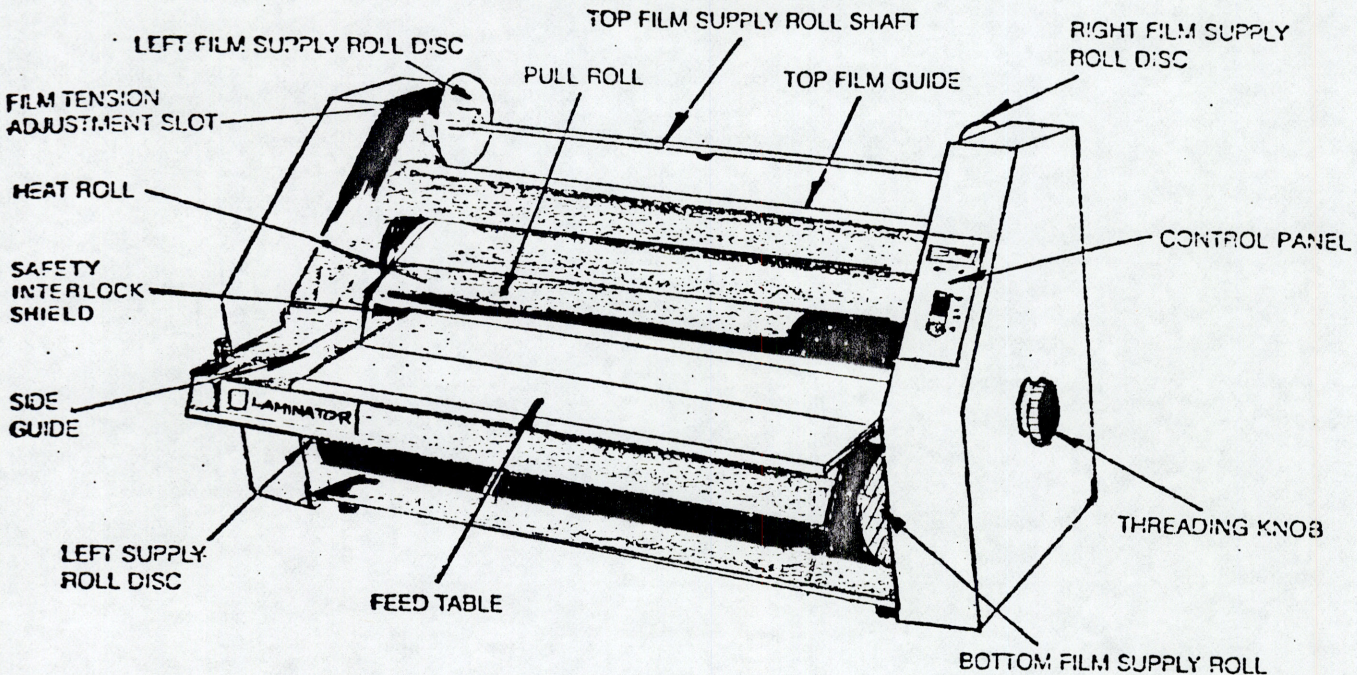

Fig. 1.7 DRY FILM PHOTORESIST LAMINATION MACHINE.

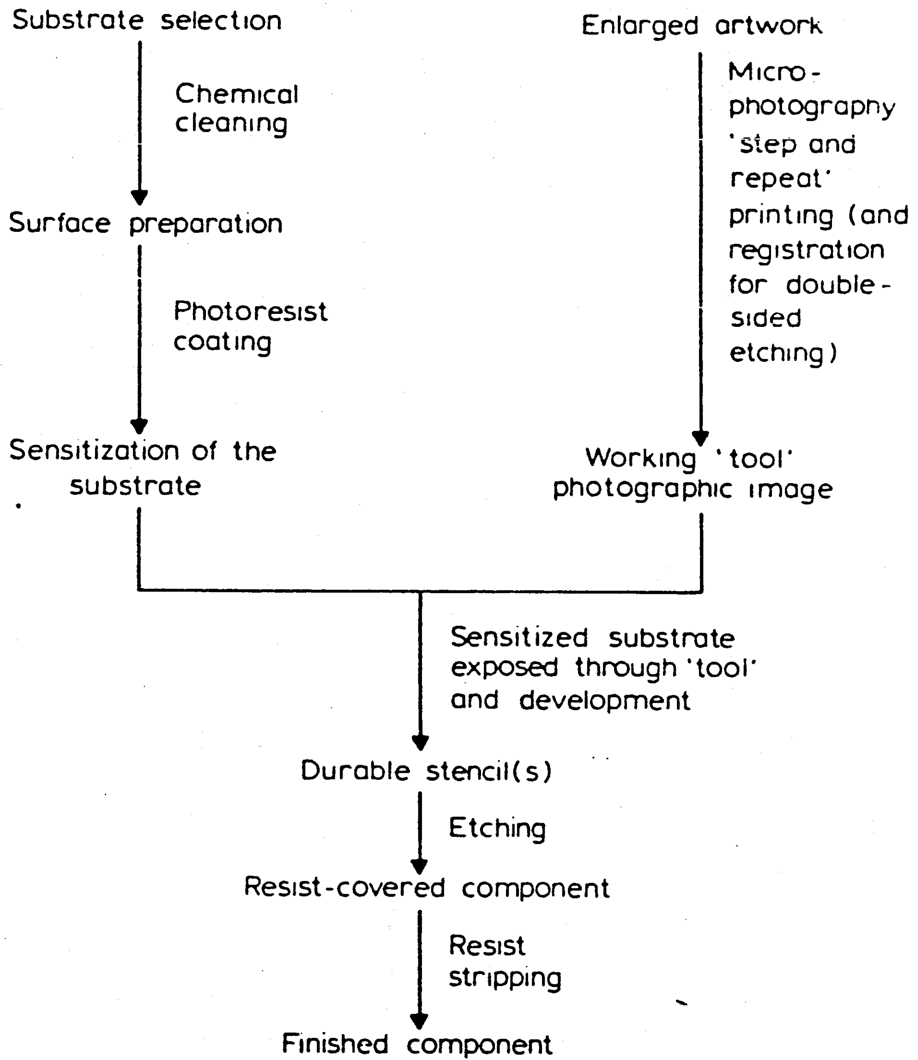

Fig. 1.8 A TYPICAL P.C.M. PROCESS FLOW CHART.

Reaction	Volts*
$Au = Au^{+++} + 3e$	+1.498
$O_2 + 4H^+ + 4e = 2H_2O$	+1.229
$Ag = Ag^+ + e$	+0.799
$Fe^{+++} + e = Fe^{++}$	+0.771
$O_2 + 2H_2O + 4e = 4OH-$	+0.401
$Cu = Cu^{++} + 2e$	+0.337
$2H^+ + 2e = H_2$	+0.000
$Ni = Ni^{++} + 2e$	-0.250
$Fe = Fe^{++} + 2e$	-0.440
$Cr = Cr^{+++} + 3e$	-0.744
$Zn = Zn^{++} + 2e$	-0.763
$Al = Al^{+++} + 3e$	-1.662
$Na = Na^+ + e$	-2.714

* Volts versus normal hydrogen electrode at 25 C.

Fig. 1.9 STANDARD OXIDATION-REDUCTION POTENTIALS

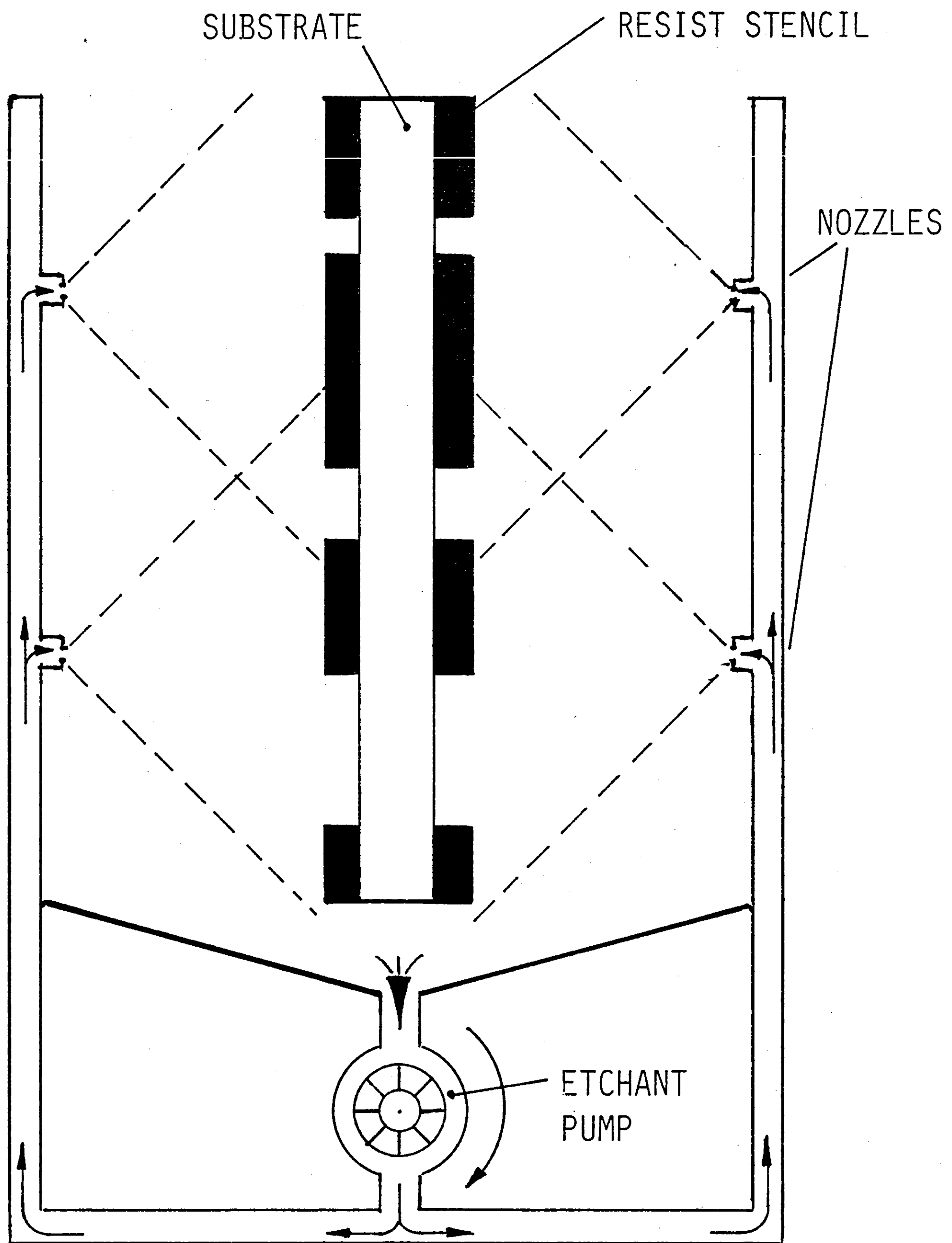

Fig. 1.10 SCHEMATIC DIAGRAM OF A CONVENTIONAL SPRAY ETCHING SYSTEM.

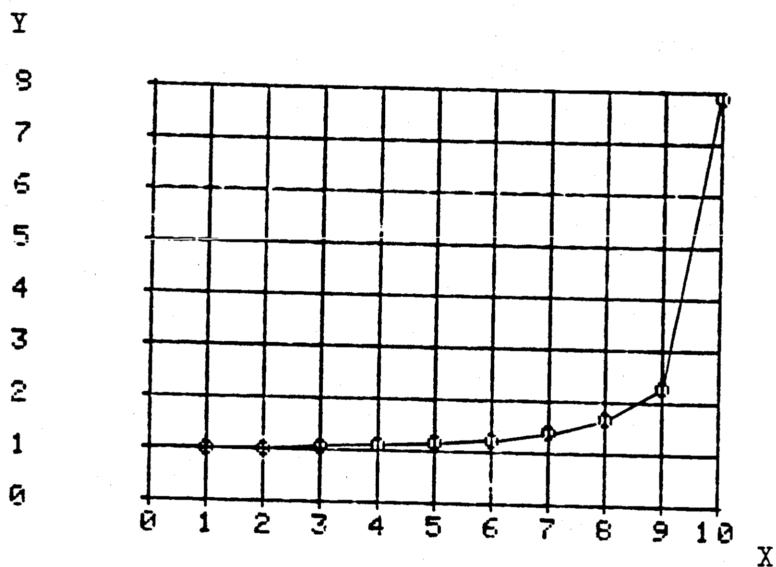

INDEX	X	Y
1	1.0000	1.0050
2	2.0000	1.0200
3	3.0000	1.0400
4	4.0000	1.0900
5	5.0000	1.1500
6	6.0000	1.2500
7	7.0000	1.4000
8	8.0000	1.6700
9	9.0000	2.2900
10	10.0000	7.9000

where,

X = The distance between the centre of the etched line (@ X = 0) and the resist edge (@ X = 10).

$$Y = \frac{1}{\sqrt{(L^2 - X^2)}}$$

where, $L = \frac{\text{line width}}{2} = 10$

Fig. 2.1 CALCULATED CURRENT DENSITY DISTRIBUTION RESULTS AND PLOT.

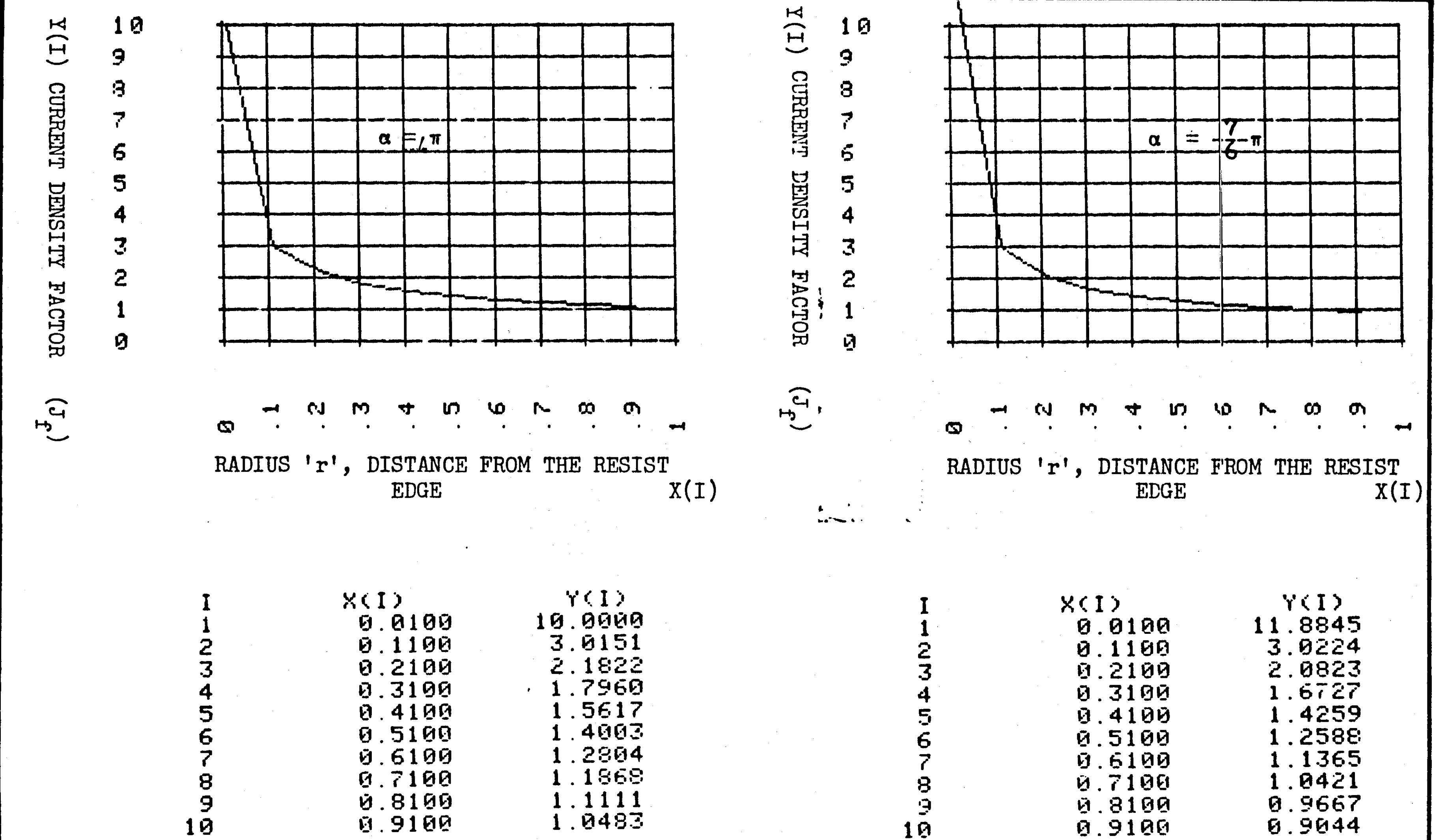

I	X(I)	Y(I)
1	0.0100	10.0000
2	0.1100	3.0151
3	0.2100	2.1822
4	0.3100	1.7960
5	0.4100	1.5617
6	0.5100	1.4003
7	0.6100	1.2804
8	0.7100	1.1868
9	0.8100	1.1111
10	0.9100	1.0483

I	X(I)	Y(I)
1	0.0100	11.8845
2	0.1100	3.0224
3	0.2100	2.0823
4	0.3100	1.6727
5	0.4100	1.4259
6	0.5100	1.2588
7	0.6100	1.1365
8	0.7100	1.0421
9	0.8100	0.9667
10	0.9100	0.9044

Fig. 2.2 THE EFFECT OF CHANGES IN THE VALUE OF THE ANGLE α ON THE EQUATION FOR CURRENT DENSITY DISTRIBUTION FOR THE SOLUTION OF CASE 2.

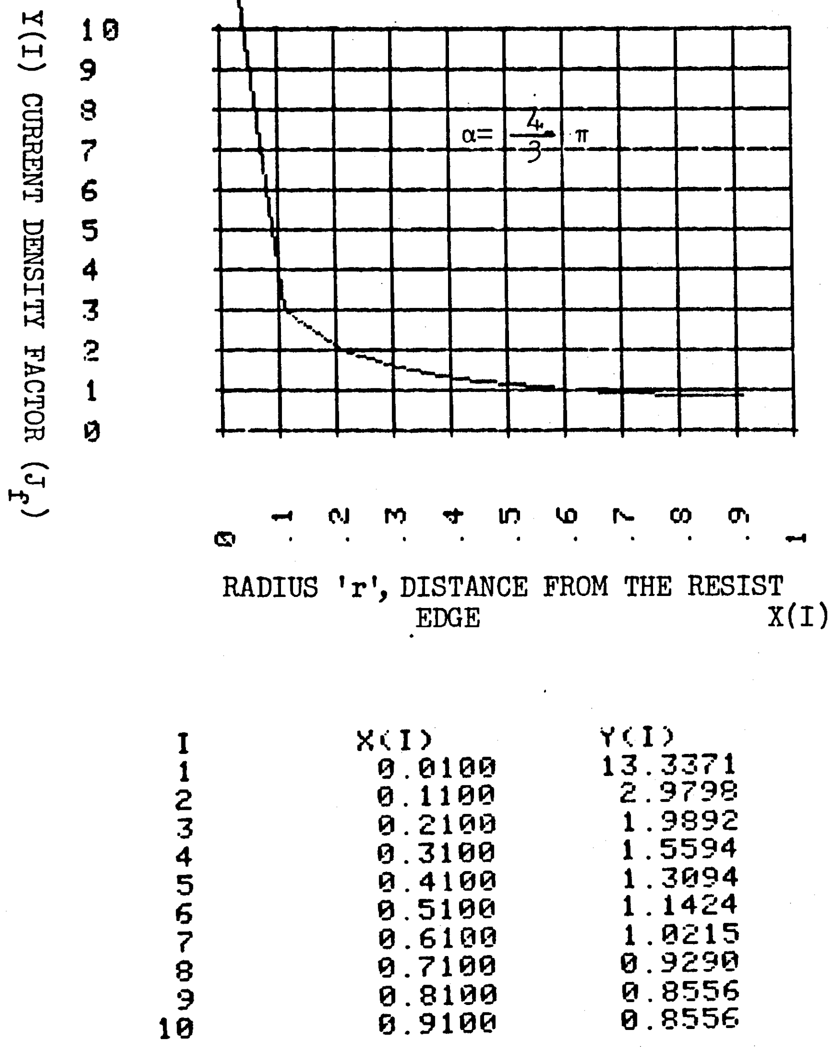

I	X(I)	Y(I)
1	0.0100	13.3371
2	0.1100	2.9798
3	0.2100	1.9892
4	0.3100	1.5594
5	0.4100	1.3094
6	0.5100	1.1424
7	0.6100	1.0215
8	0.7100	0.9290
9	0.8100	0.8556
10	0.9100	0.8556

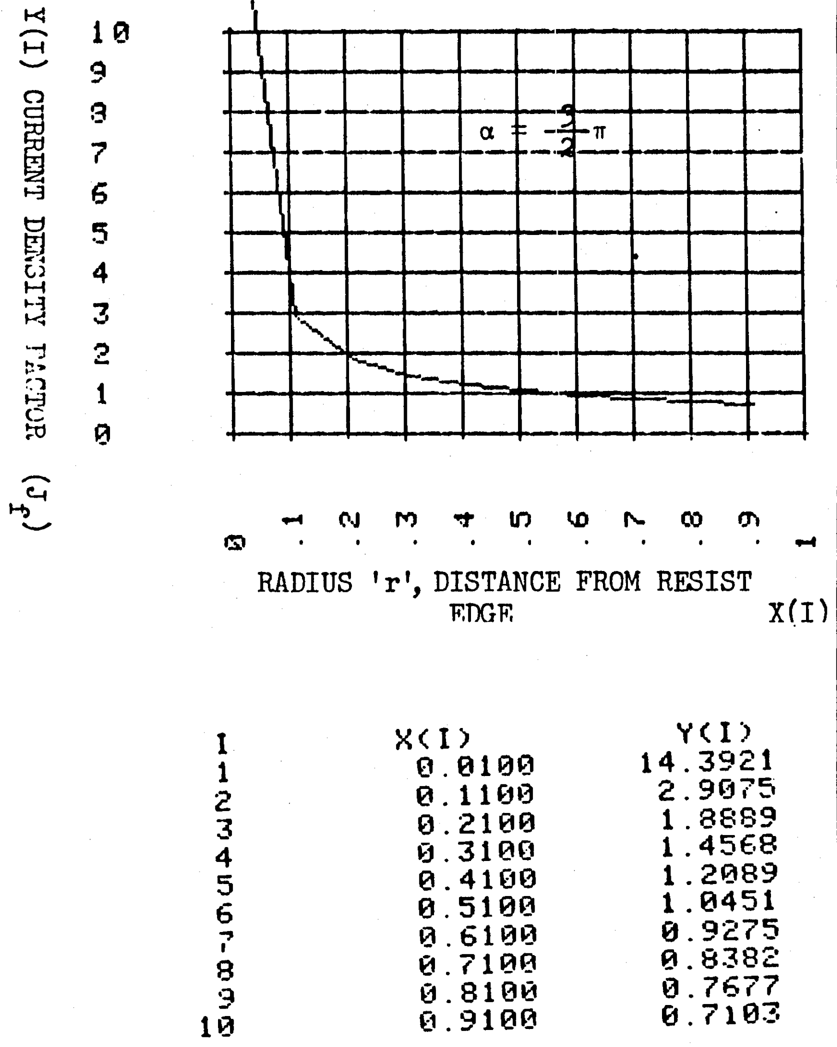

I	X(I)	Y(I)
1	0.0100	14.3921
2	0.1100	2.9075
3	0.2100	1.8889
4	0.3100	1.4568
5	0.4100	1.2089
6	0.5100	1.0451
7	0.6100	0.9275
8	0.7100	0.8382
9	0.8100	0.7677
10	0.9100	0.7103

Fig. 2.3 THE EFFECT OF CHANGES IN THE VALUE OF THE ANGLE α ON THE EQUATION FOR CURRENT DENSITY DISTRIBUTION FOR THE SOLUTION OF CASE 2.

EQUIPOTENTIAL LINES

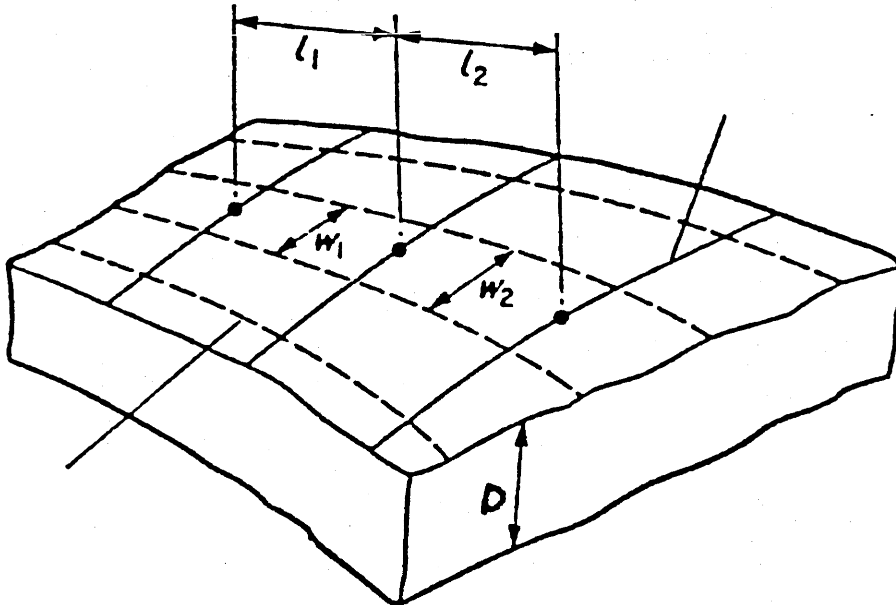

CURRENT LINES

l = Current tube element lengths

w = Current tube element widths

D = Current tube element Depth (Constant for 2-D)

Fig. 2.4 THE PRINCIPLE OF GRAPHICAL FIELD PLOTTING

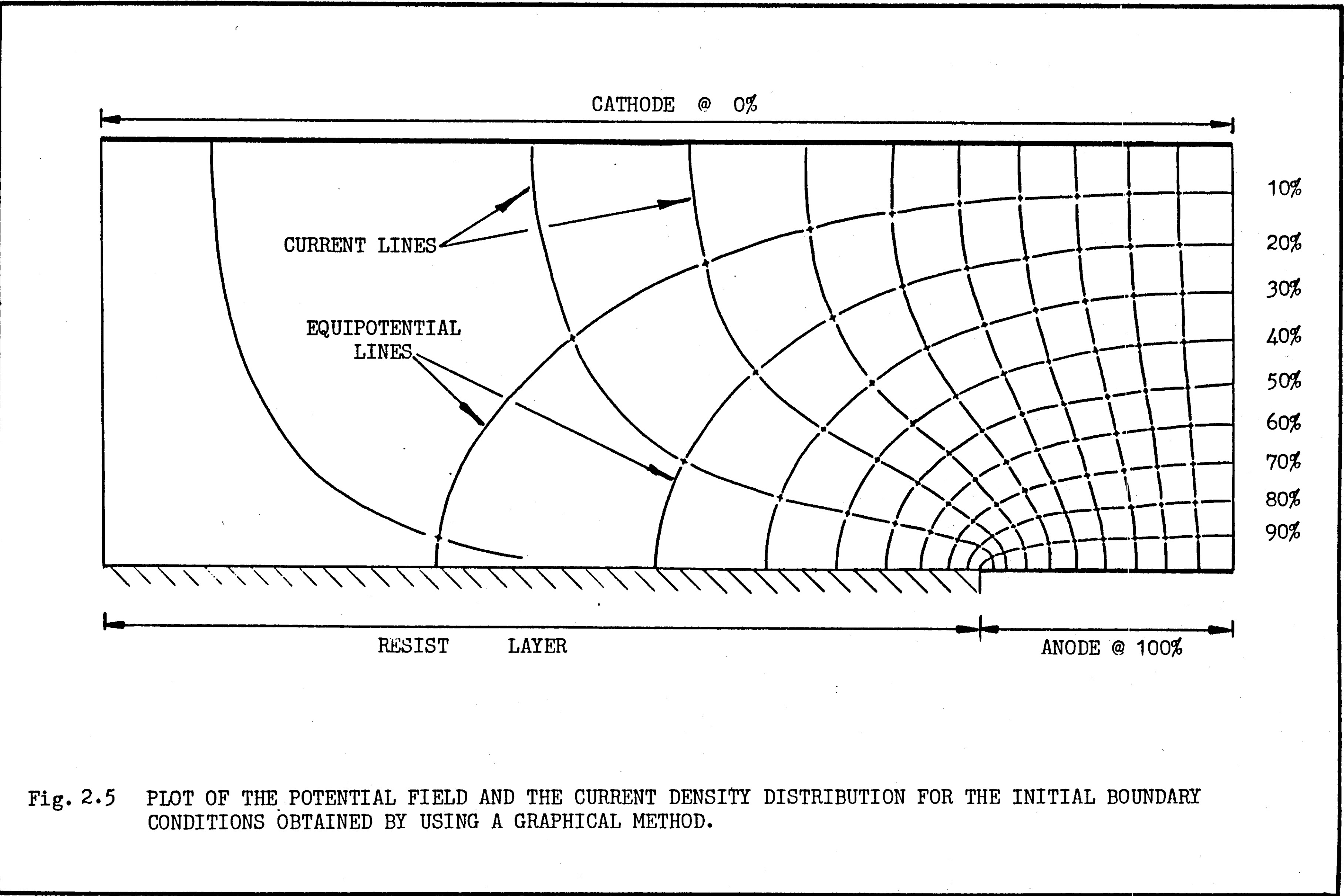

Fig. 2.5 PLOT OF THE POTENTIAL FIELD AND THE CURRENT DENSITY DISTRIBUTION FOR THE INITIAL BOUNDARY CONDITIONS OBTAINED BY USING A GRAPHICAL METHOD.

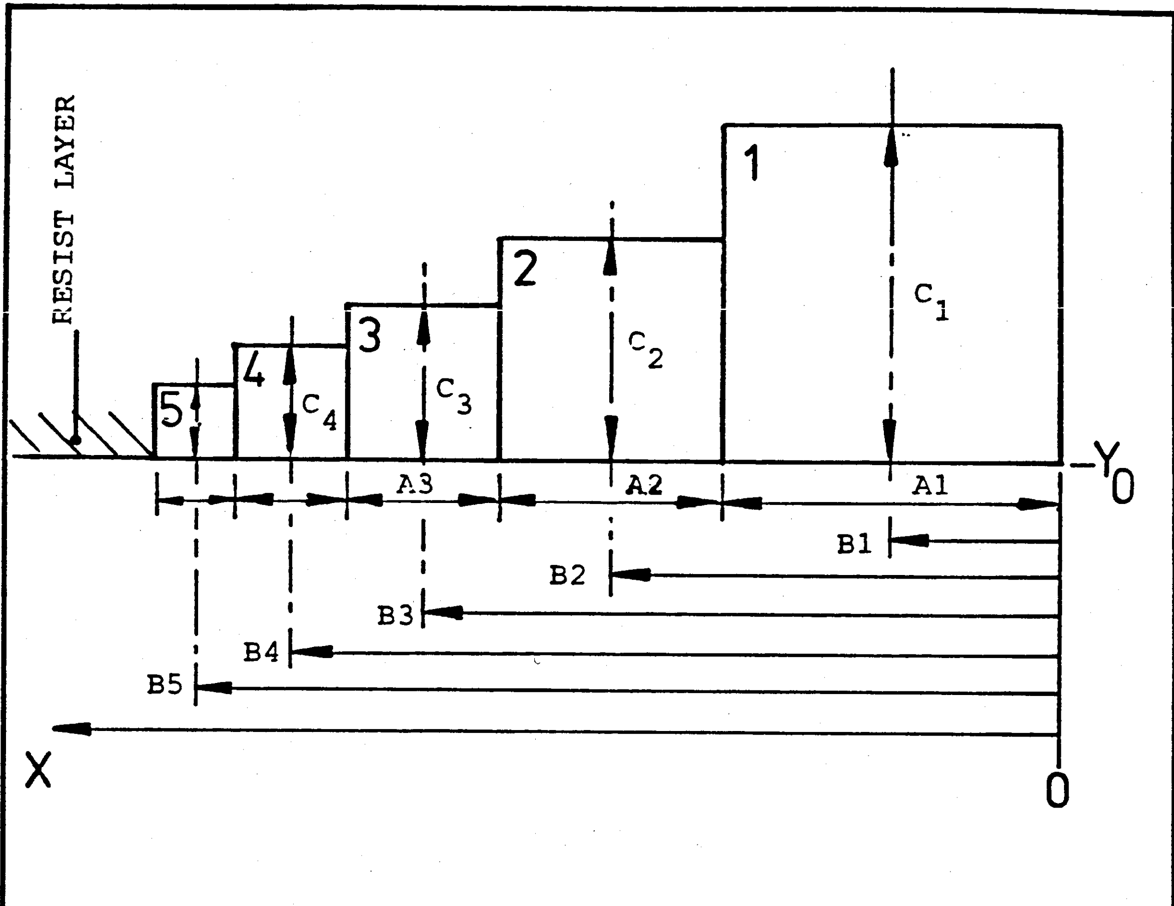

INDEX	A R/Linear Sq measured in X axis @ Y_o	B Dimension between centre of the R/linear Sq and X_o	C R/Linear Sq measured in Y axis @ centre	D $D = \frac{C_1}{C_{index}}$
1	27	13.5	27	1
2	24	39	26.5	1.02
3	24	63	26.5	1.02
4	25.5	87.75	26.5	1.02
5	23	112	25	1.08
6	22	134.5	22	1.23
7	18	154.5	19	1.42
8	14.5	170.75	15	1.8
9	11.5	183.75	11.5	2.35
10	9	194	8	3.38

Fig. 2.6 CALCULATIONS FOR THE INITIAL CURRENT DENSITY DISTRIBUTION BY THE GRAPHICAL METHOD.

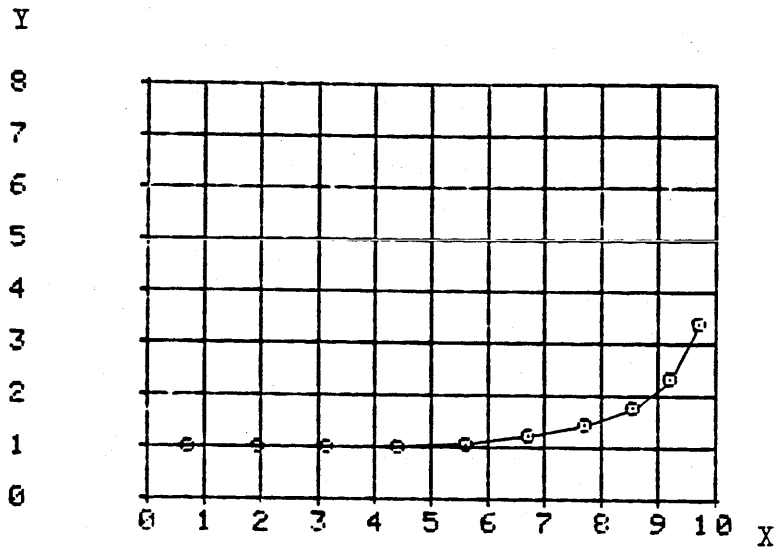

INDEX	X	Y
1	0.6800	1.0000
2	1.9500	1.0200
3	3.1500	1.0200
4	4.3900	1.0200
5	5.6600	1.0800
6	6.7000	1.2300
7	7.7000	1.4200
8	8.5300	1.8000
9	9.2000	2.3500
10	9.7000	3.3800

where,

X = The distance between the centre of the etched line (@ X = 0) and the resist edge (@ X = 10).

Y = The current density factor relative to the result at X_1.

Fig. 2.7 MEASUREMENTS AND PLOT OF THE CURRENT DENSITY DISTRIBUTION OBTAINED BY A GRAPHICAL METHOD.

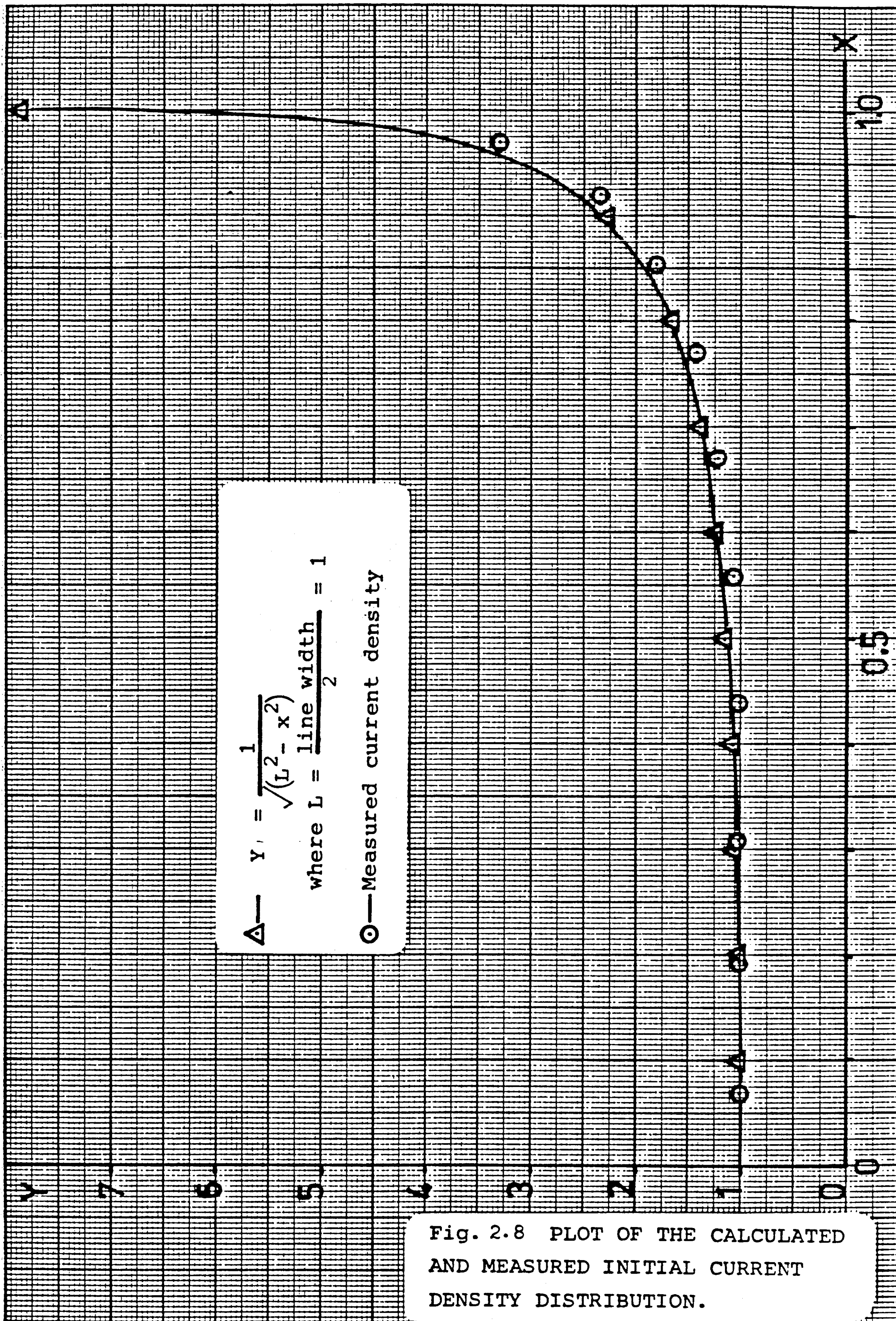

Fig. 2.8 PLOT OF THE CALCULATED AND MEASURED INITIAL CURRENT DENSITY DISTRIBUTION.

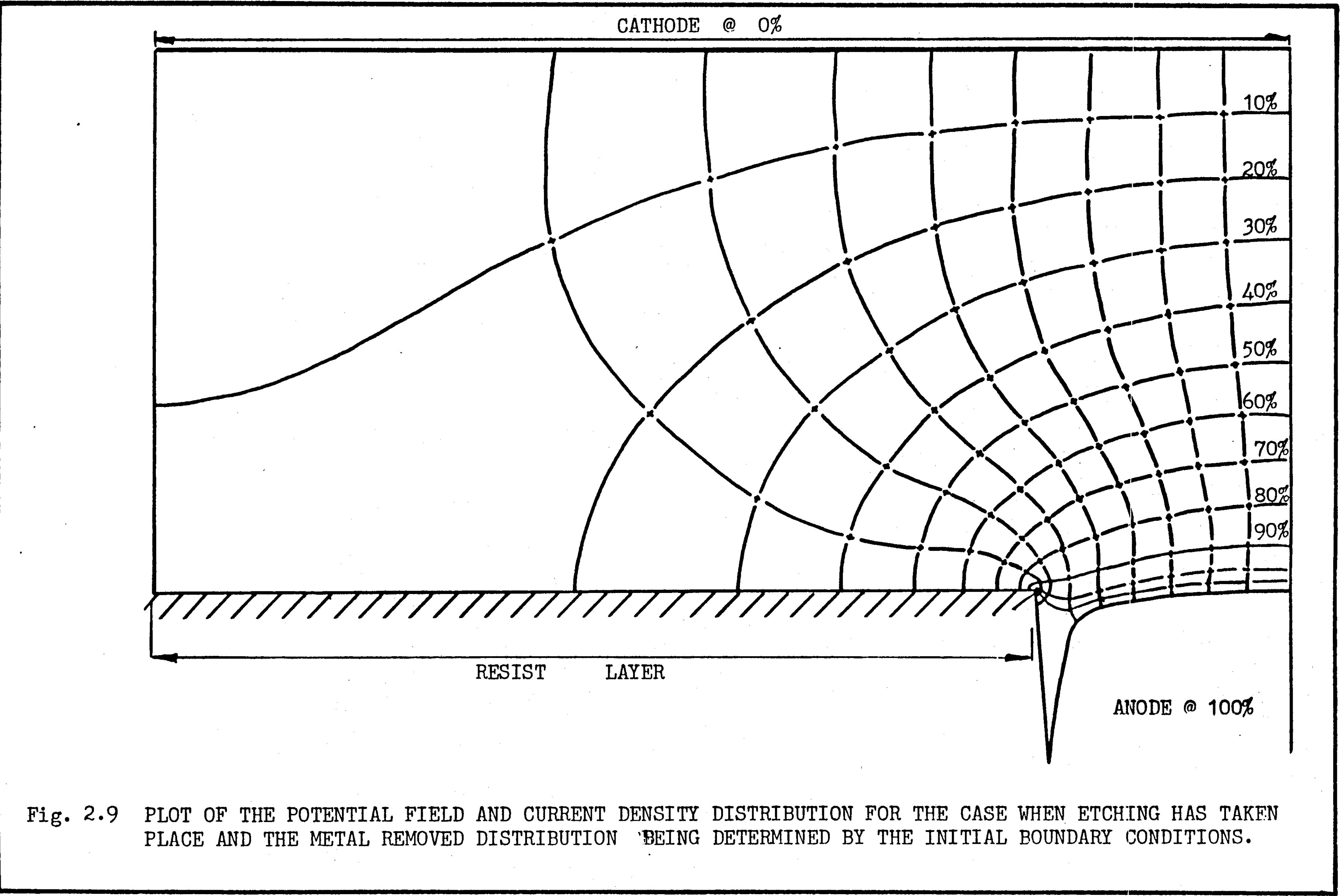

Fig. 2.9 PLOT OF THE POTENTIAL FIELD AND CURRENT DENSITY DISTRIBUTION FOR THE CASE WHEN ETCHING HAS TAKEN PLACE AND THE METAL REMOVED DISTRIBUTION BEING DETERMINED BY THE INITIAL BOUNDARY CONDITIONS.

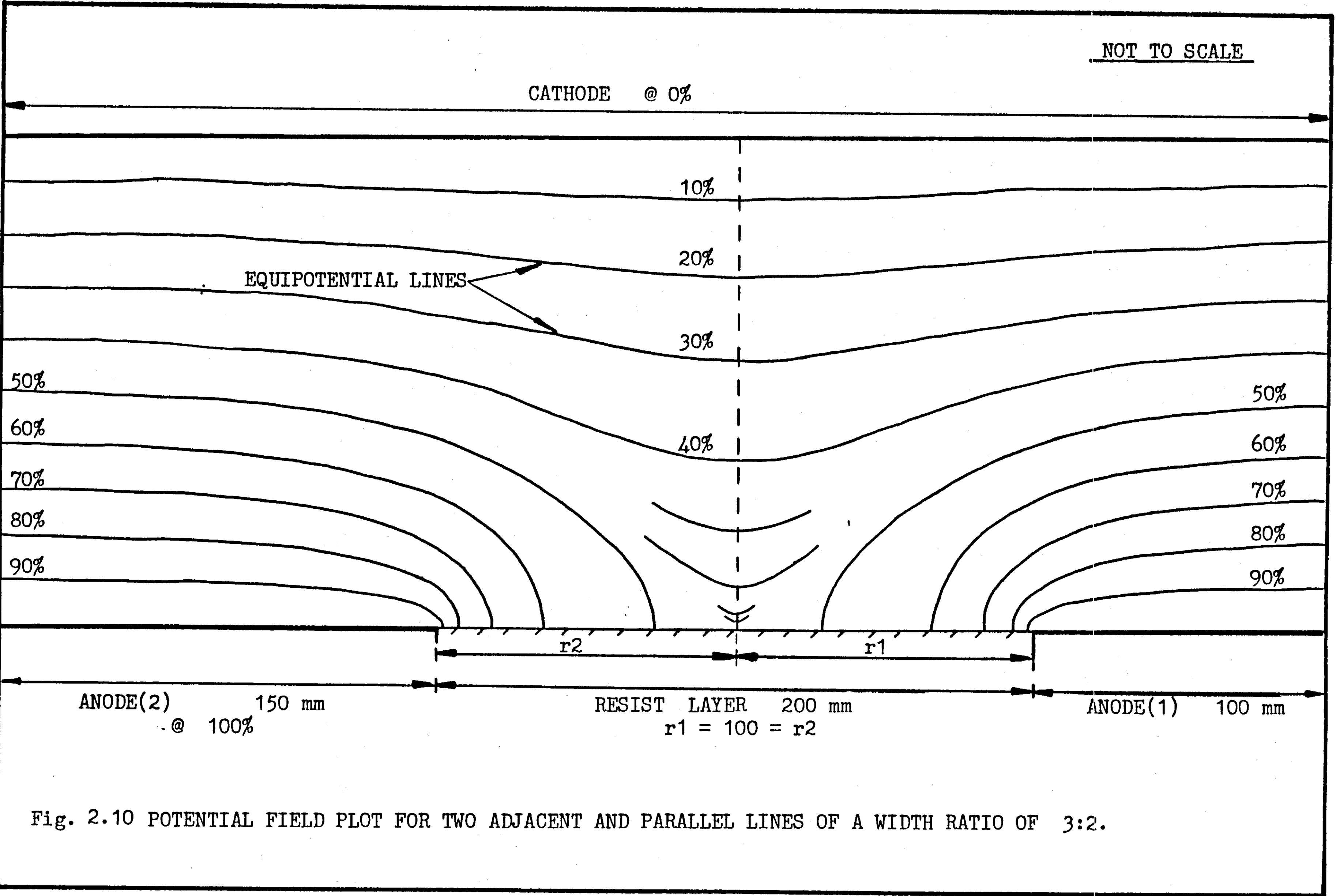

Fig. 2.10 POTENTIAL FIELD PLOT FOR TWO ADJACENT AND PARALLEL LINES OF A WIDTH RATIO OF 3:2.

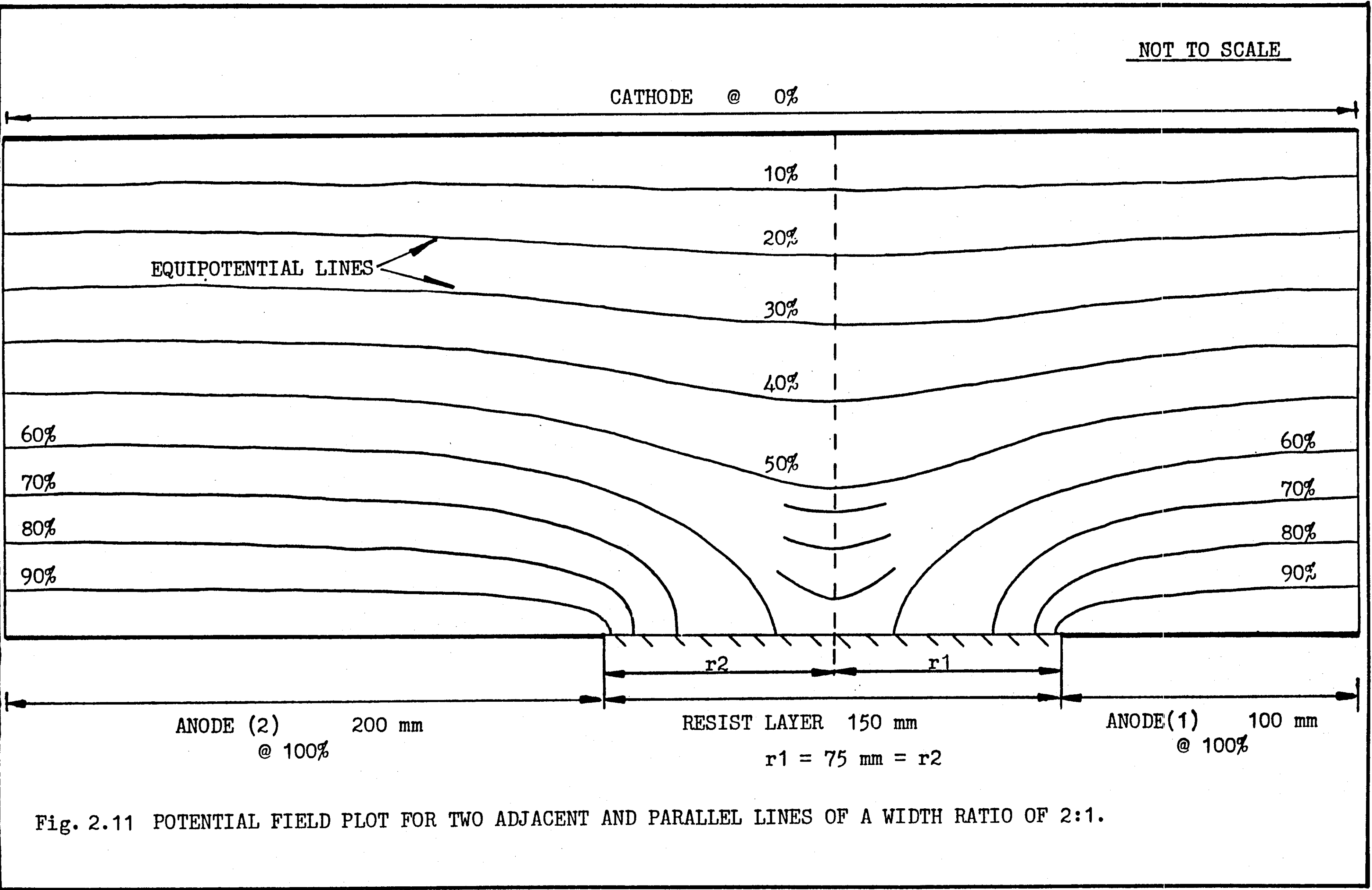

Fig. 2.11 POTENTIAL FIELD PLOT FOR TWO ADJACENT AND PARALLEL LINES OF A WIDTH RATIO OF 2:1.

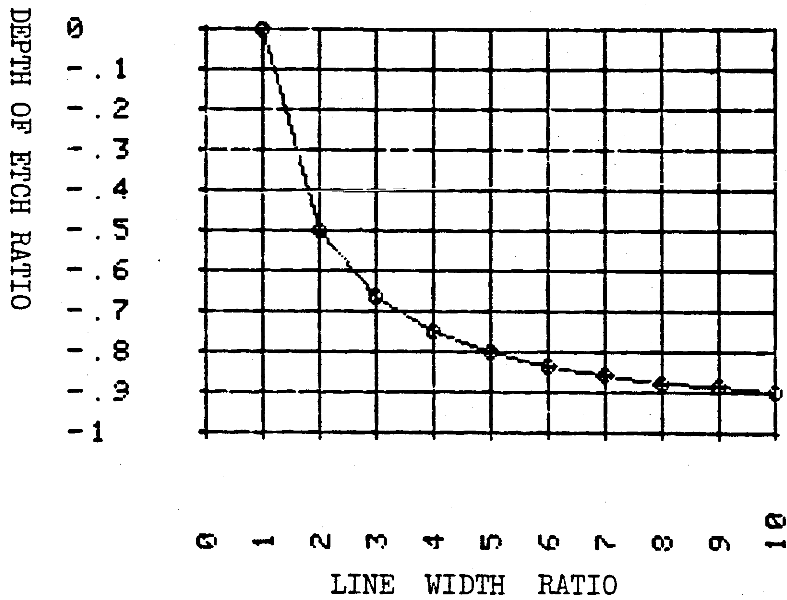

INDEX	LINE WIDTH RATIO	DEPTH OF ETCH RATIO
1	1.0000	0.0000
2	2.0000	-0.5000
3	3.0000	-0.6667
4	4.0000	-0.7500
5	5.0000	-0.8000
6	6.0000	-0.8333
7	7.0000	-0.8571
8	8.0000	-0.8750
9	9.0000	-0.8889
10	10.0000	-0.9000

$$\text{DEPTH OF ETCH} = 1 - \frac{1}{L2}$$

$$L2 = 1, 2, 3 \ldots\ldots 10 = \text{LINE WIDTH RATIO}$$

Fig. 2.12 PLOT OF THE RELATIONSHIP BETWEEN ETCHED LINE WIDTH AND DEPTH OF ETCH AT THE CENTRE OF THE ETCHED LINE FOR TWO ADJACENT AND PARALLEL LINES.

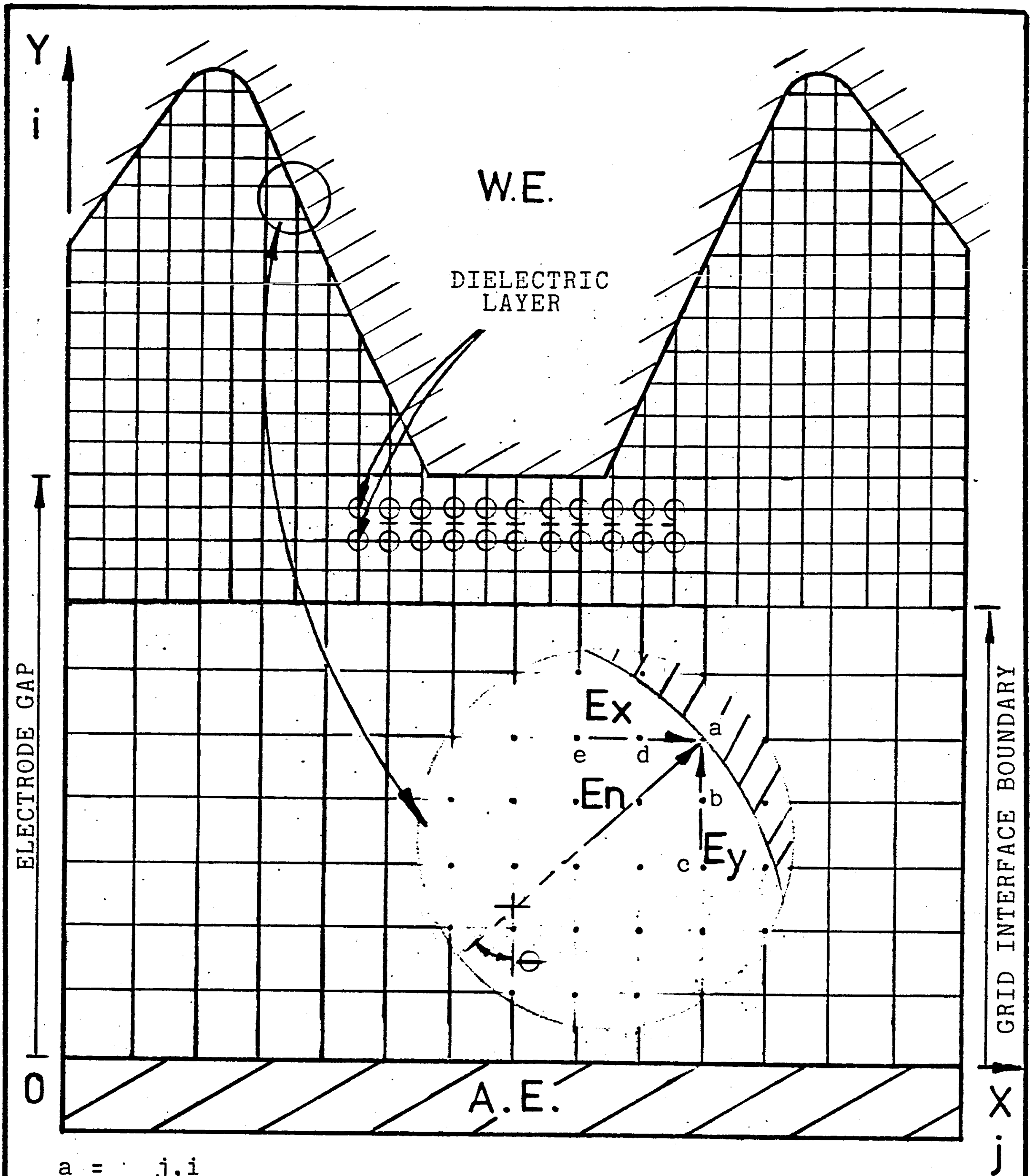

a = j,i
b = j,i-1
c = j,i-2

d = j-1,i
e = j-2,i

Fig. 2.13 SCHEMATIC OF THE NUMERICAL CELL

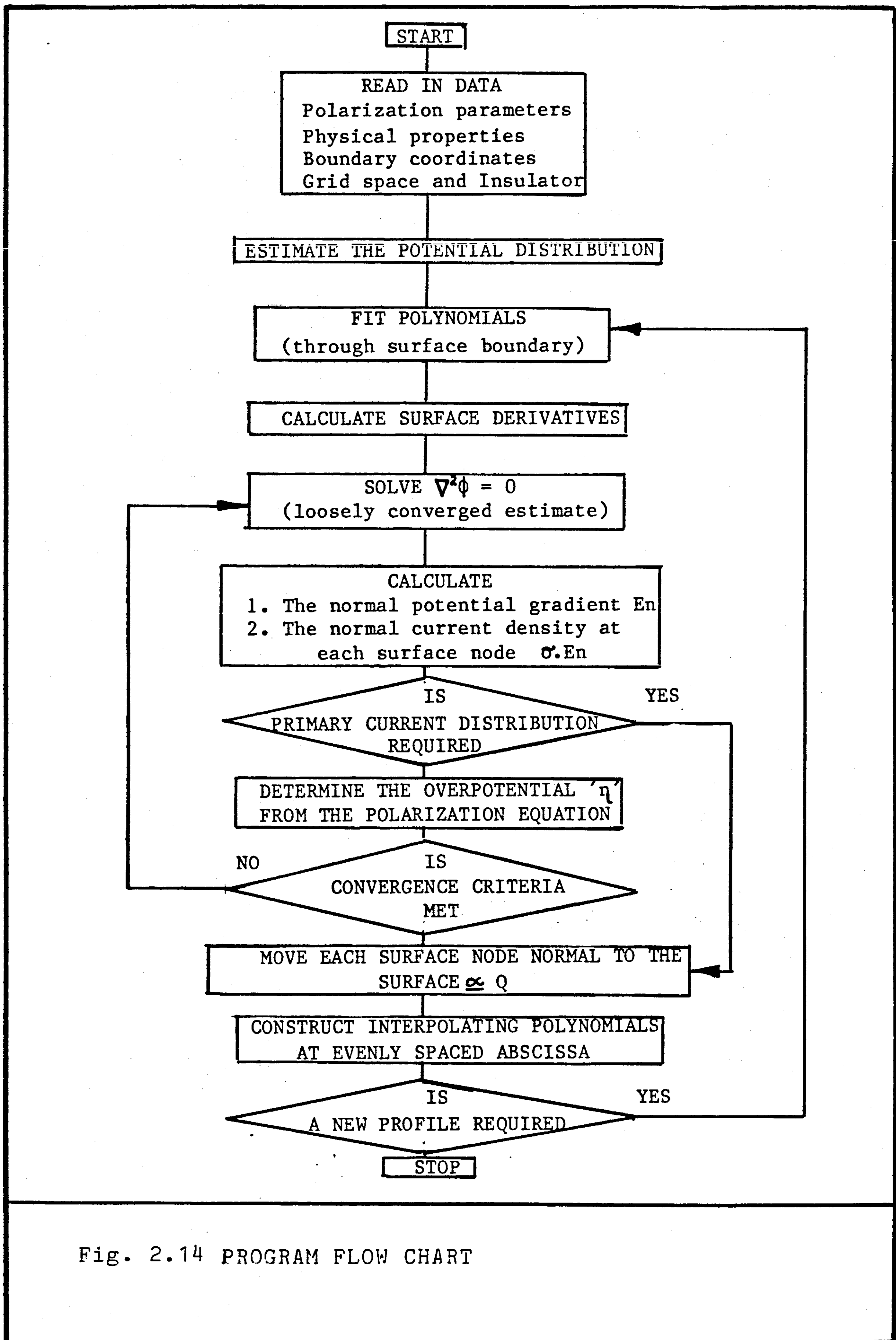

Fig. 2.14 PROGRAM FLOW CHART

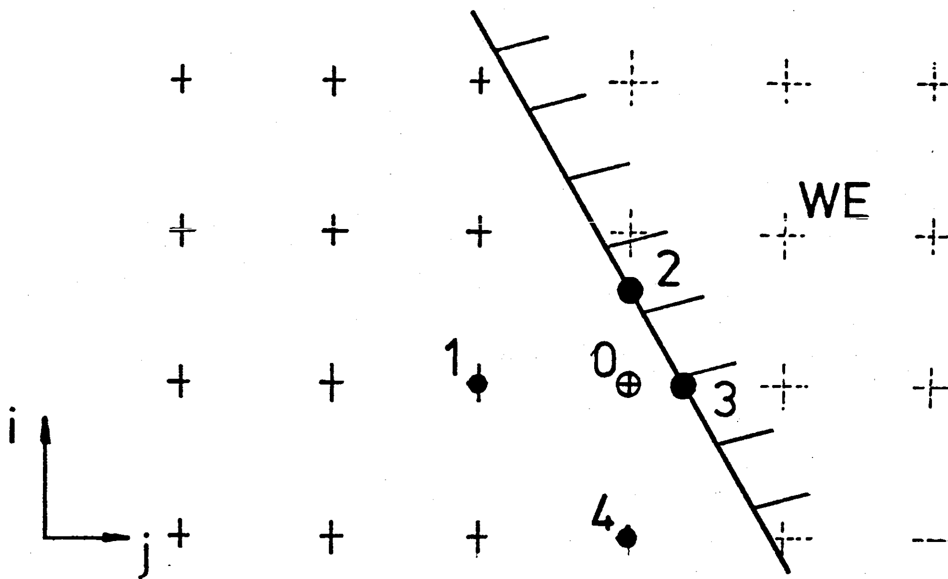

$$P0 = \frac{f(P,h)}{f(h)}$$

where,

$$f(P,h) = \frac{P1 + \frac{h1}{h3} P3}{h1^2 \left(1 + \frac{h3}{h1}\right)} + \frac{p2 + \frac{h2}{h4} P4}{h2 \left(1 + \frac{h4}{h2}\right)}$$

$$f(h) = \frac{1 + \frac{h1}{h3}}{h1^2 \left(1 + \frac{h3}{h1}\right)} + \frac{1 + \frac{h2}{h4}}{h2^2 \left(1 + \frac{h4}{h2}\right)}$$

Therefore if h1=h2=h3=h4 then,

$$4P0 = P1 + P2 + P3 + P4$$

Fig. 2.15 NODE POTENTIAL CALCULATIONS

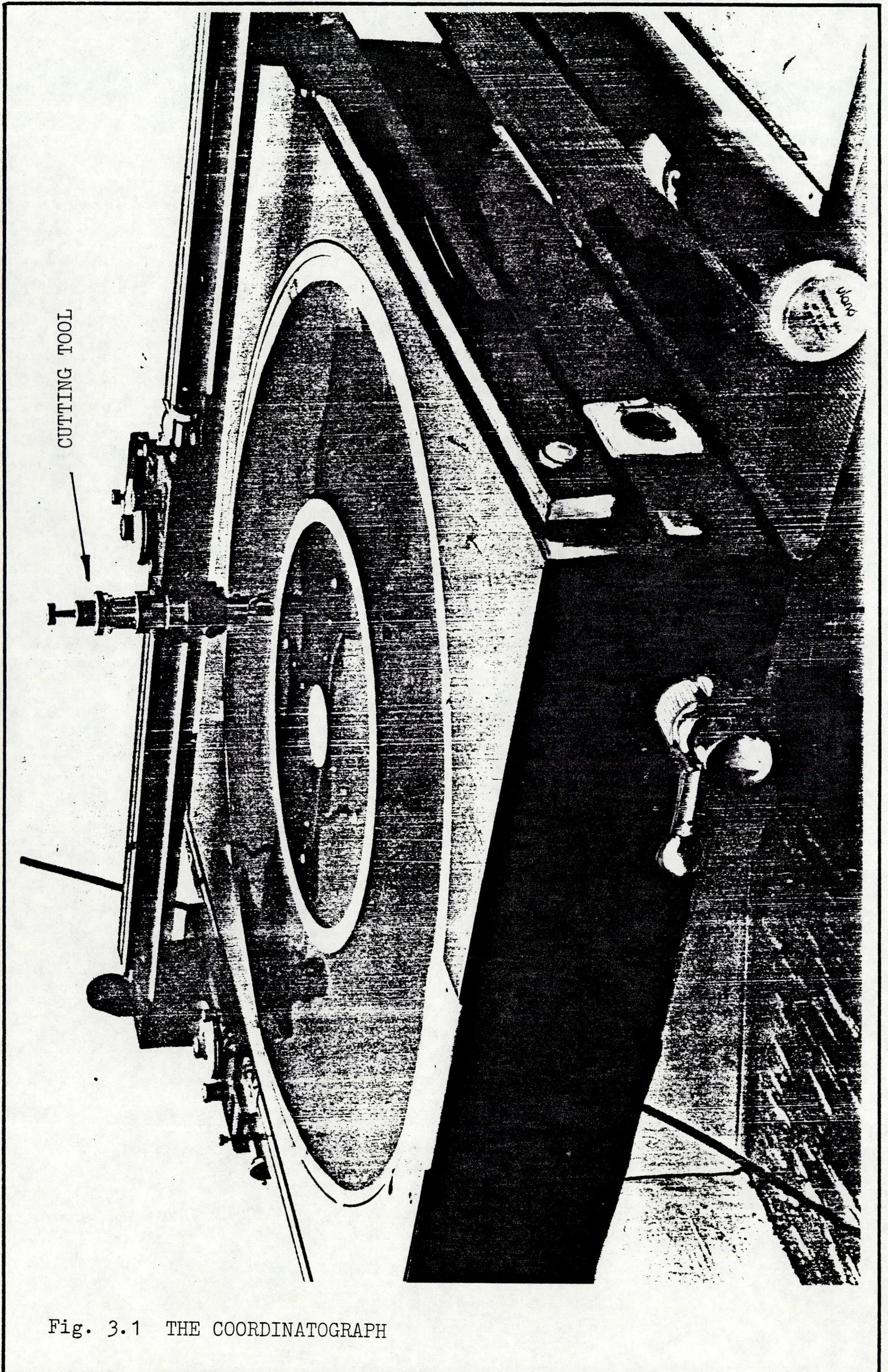

Fig. 3.1 THE COORDINATOGRAPH

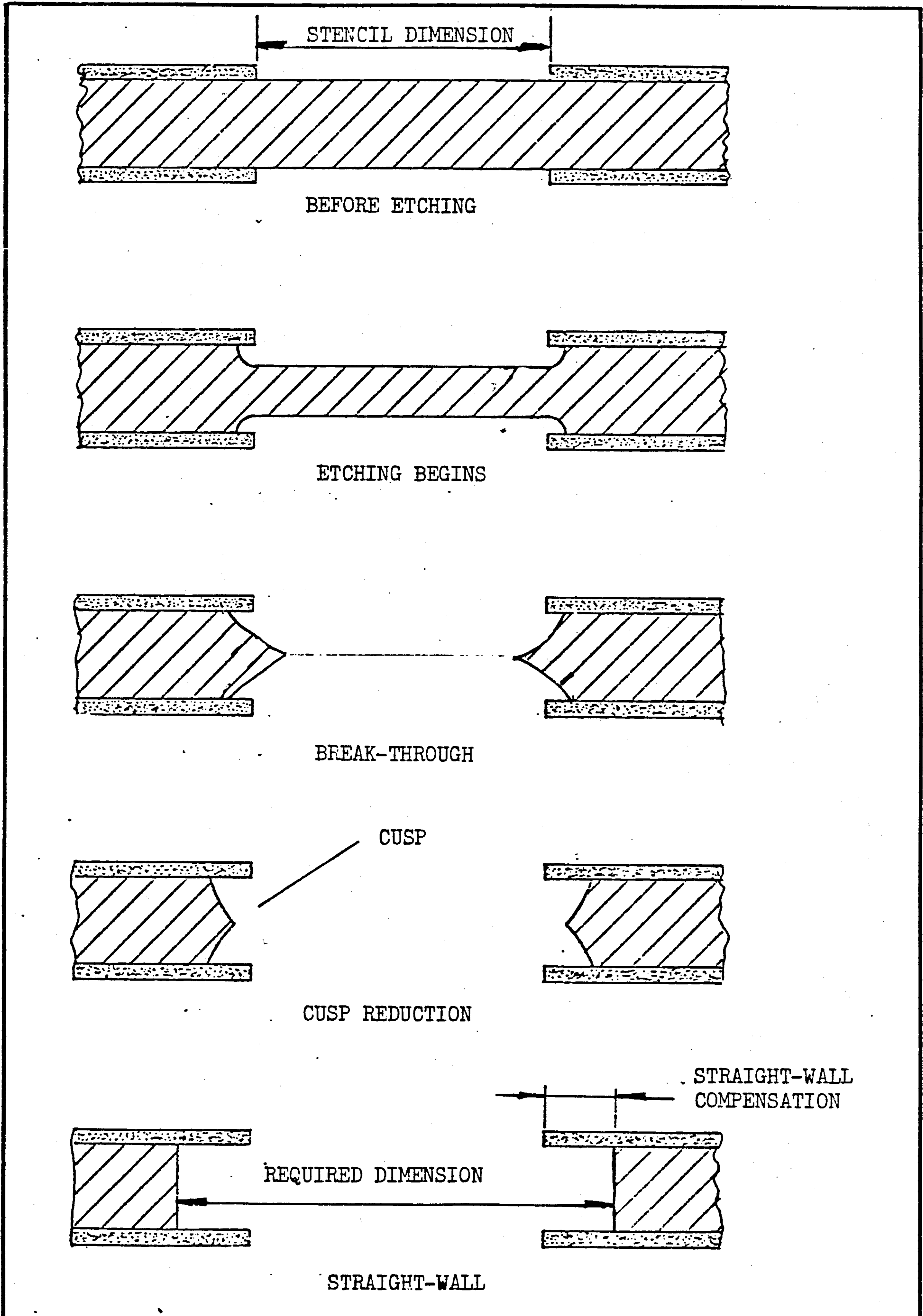

Fig. 3.2 SCHEMATIC ILLUSTRATING THE DIMENSION COMPENSATION FOR STRAIGHT EDGE RESULTS.

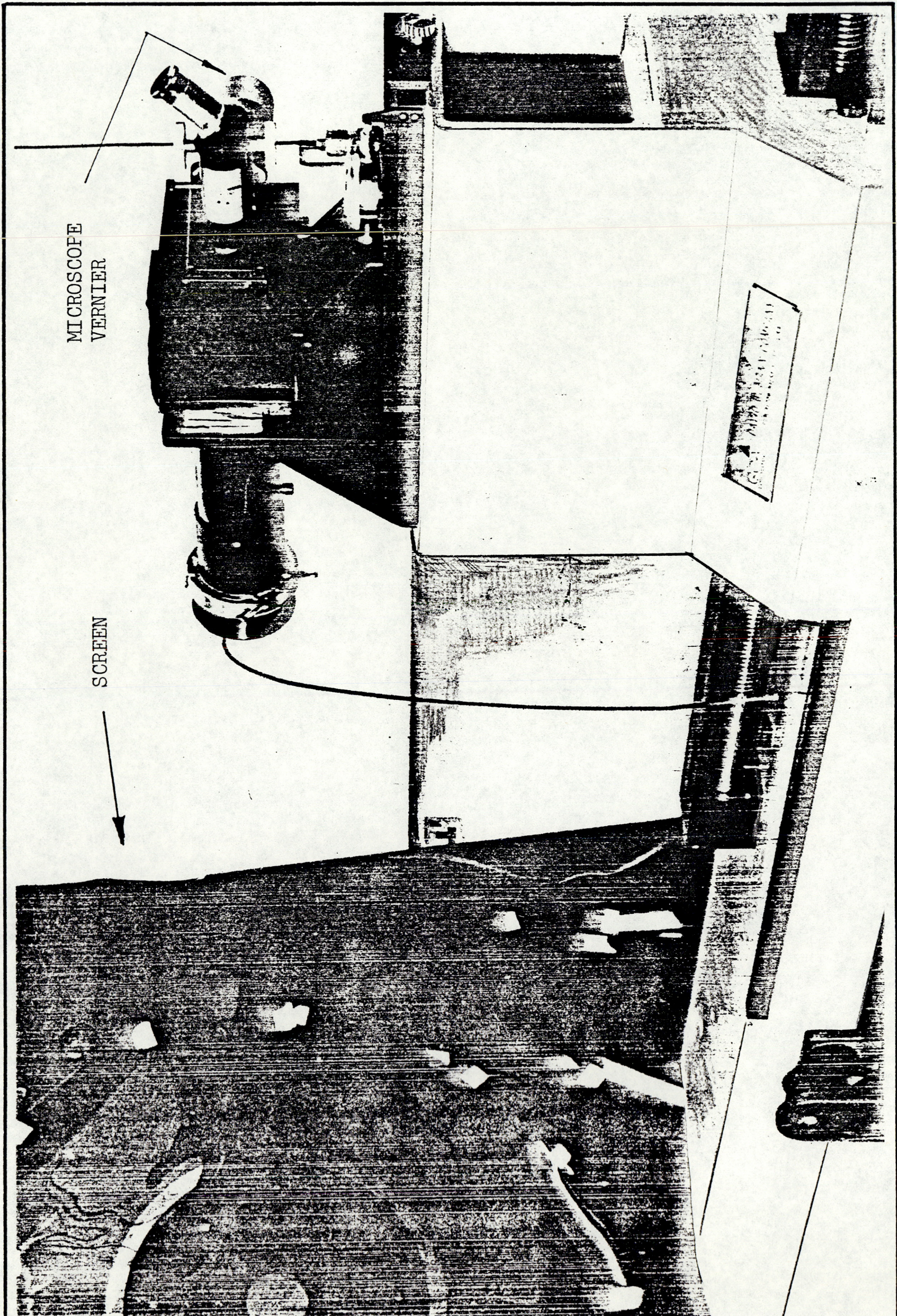

Fig. 3.3 THE PHOTOGRAPHIC REDUCTION CAMERA

Fig. 3.4 THE MERCURY VAPOUR UV EXPOSURE UNIT AND FRAME.

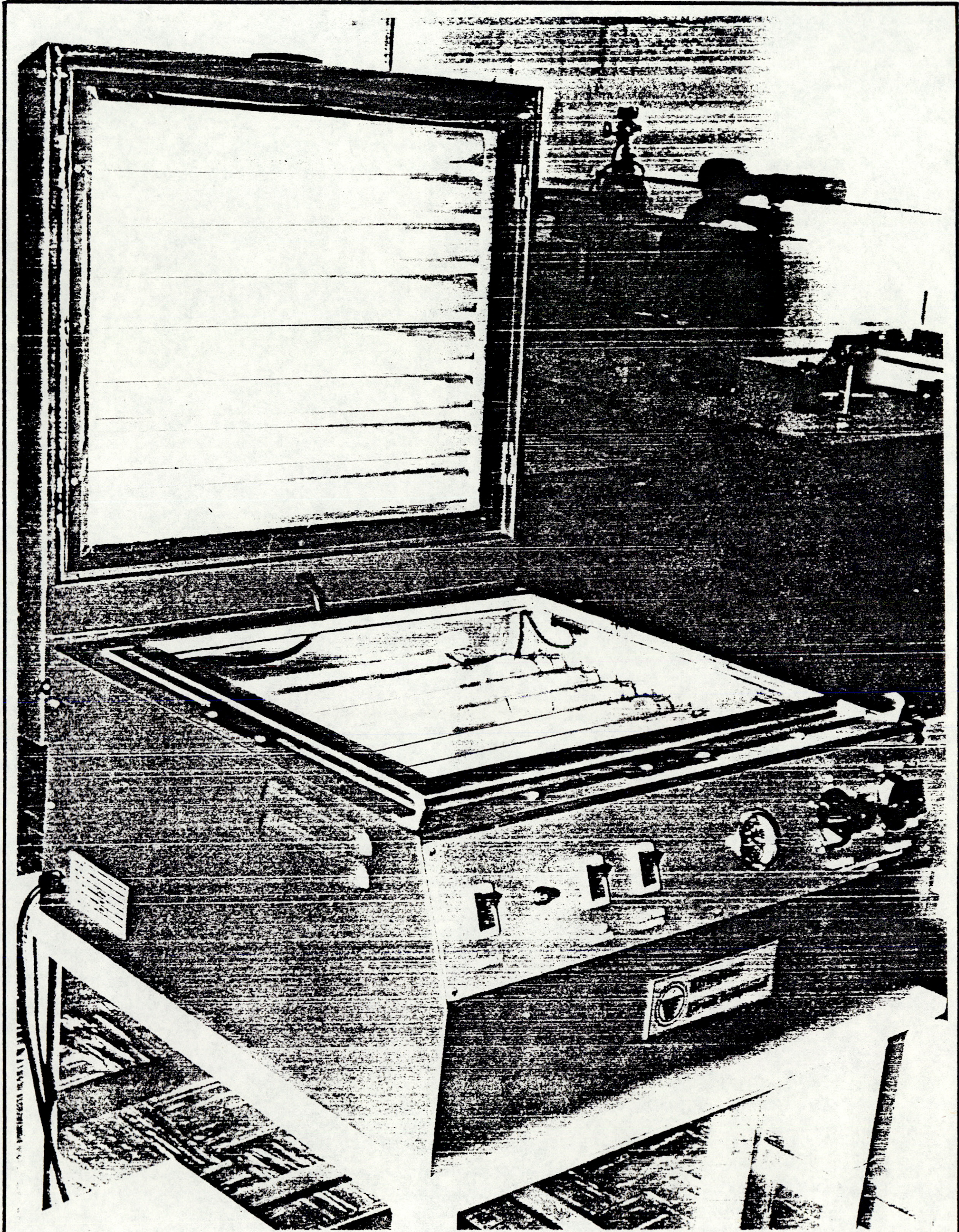

Fig. 3.5 THE 'LITTLEJOHN' DOUBLE SIDED EXPOSURE UNIT.

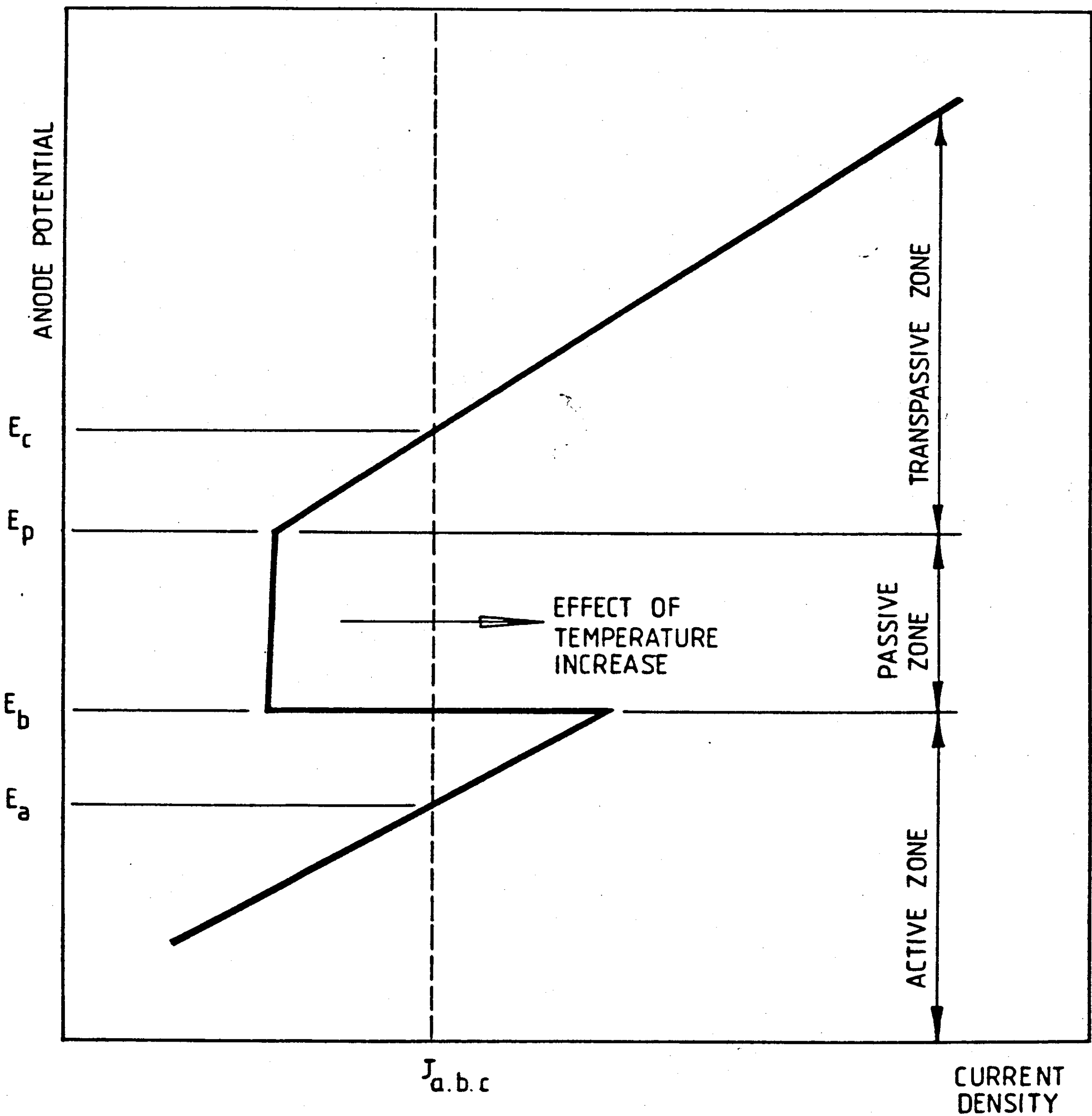

Fig. 4.1 SCHEMATIC POLARIZATION DIAGRAM OF A PASSIVATING SYSTEM.

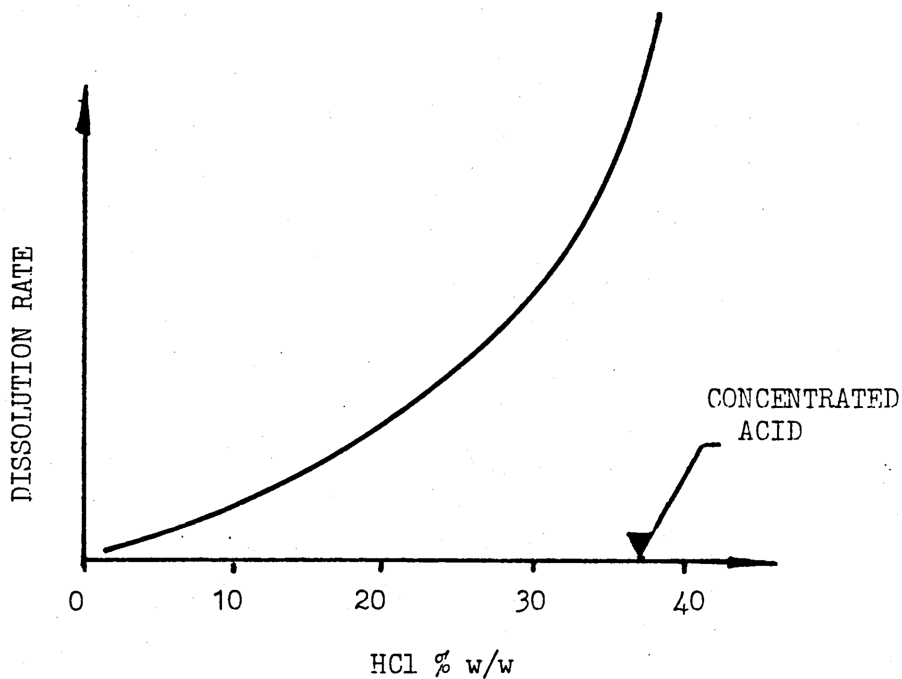

Fig. a

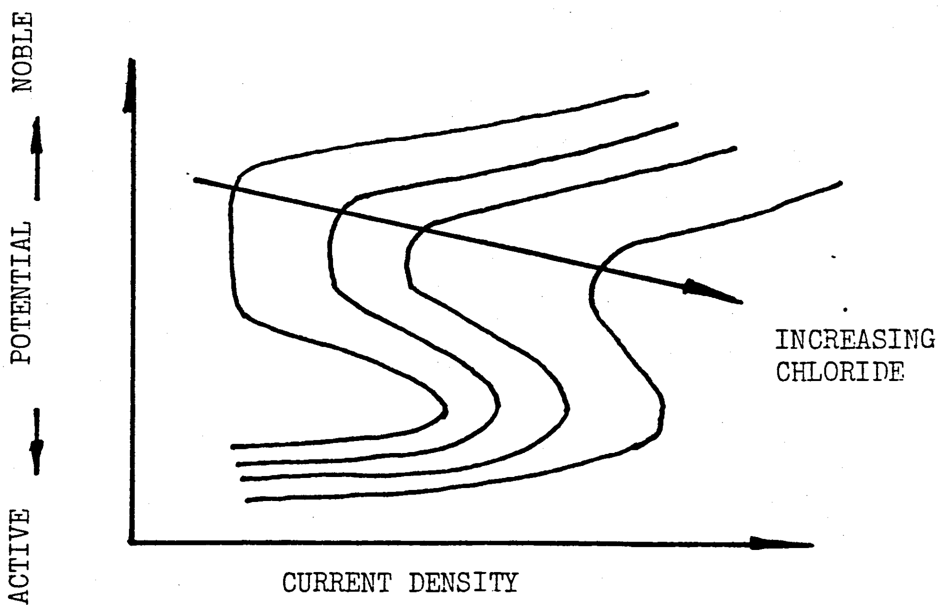

Fig. b

Figs. 4.2 a & b. Figure a THE EFFECT OF CONCENTRATION ON THE CORROSION OF IRON IN HCl.
Figure b THE INFLUENCE OF CHLORIDES ON ANODIC POLARIZATION.

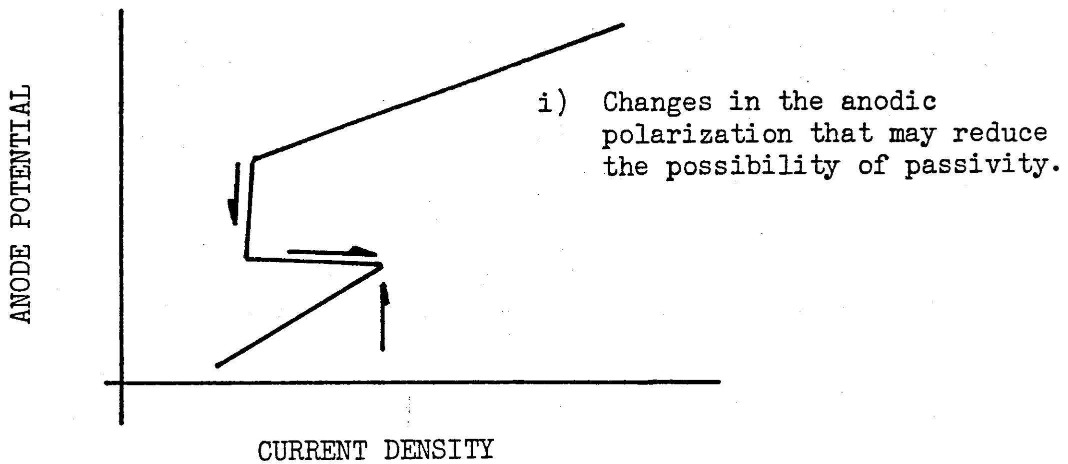

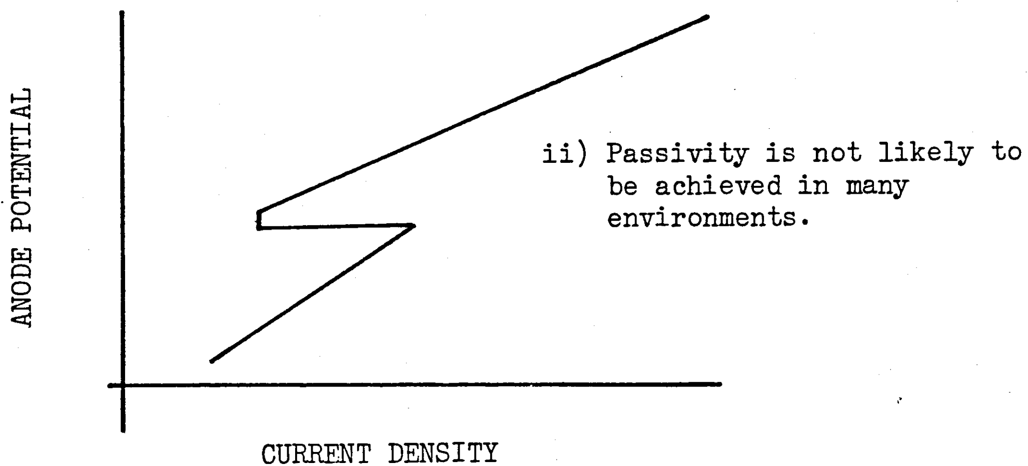

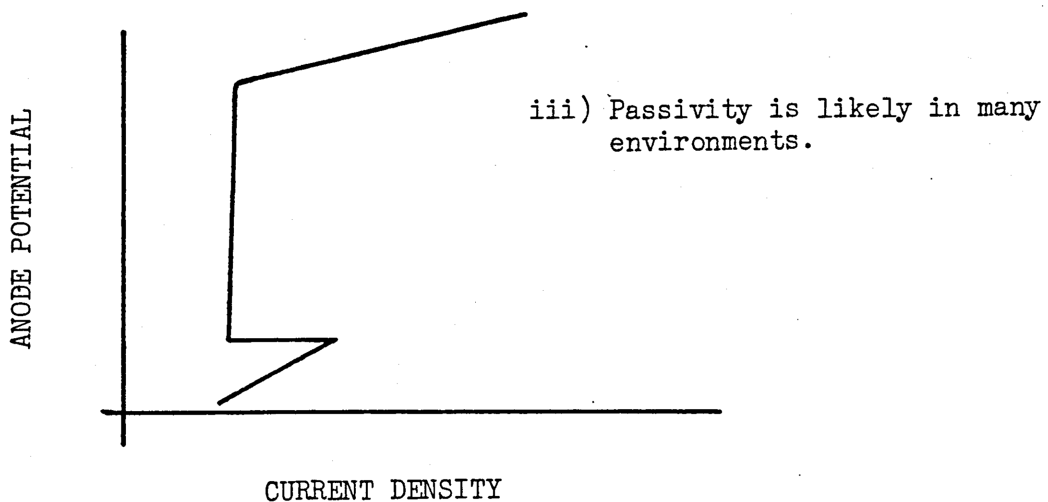

Fig. 4.3 SCHEMATIC POLARIZATION PLOTS FOR PASSIVATING SYSTEMS.

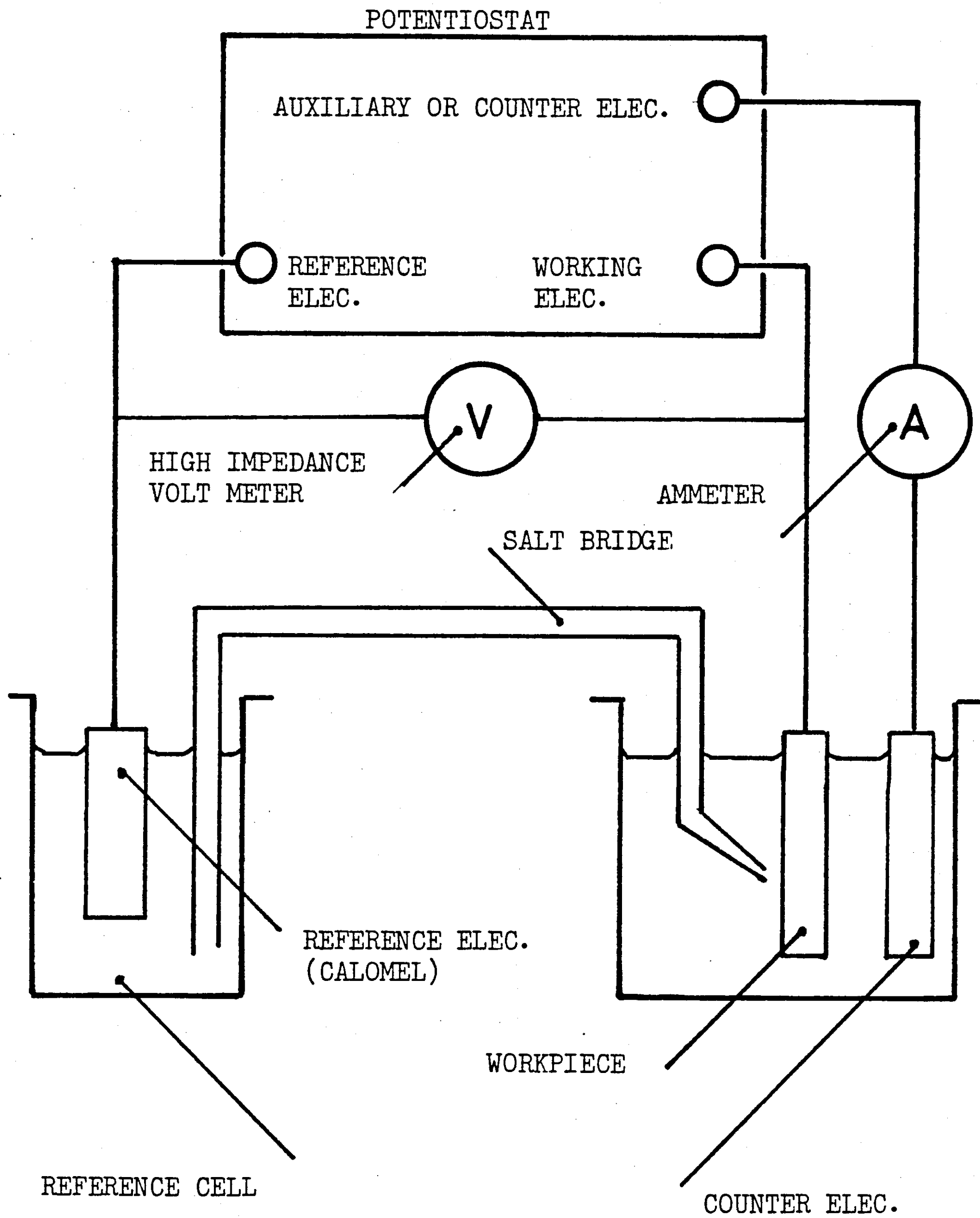

Fig. 4.4 SCHEMATIC OF A POLARIZATION MEASUREMENT CELL.

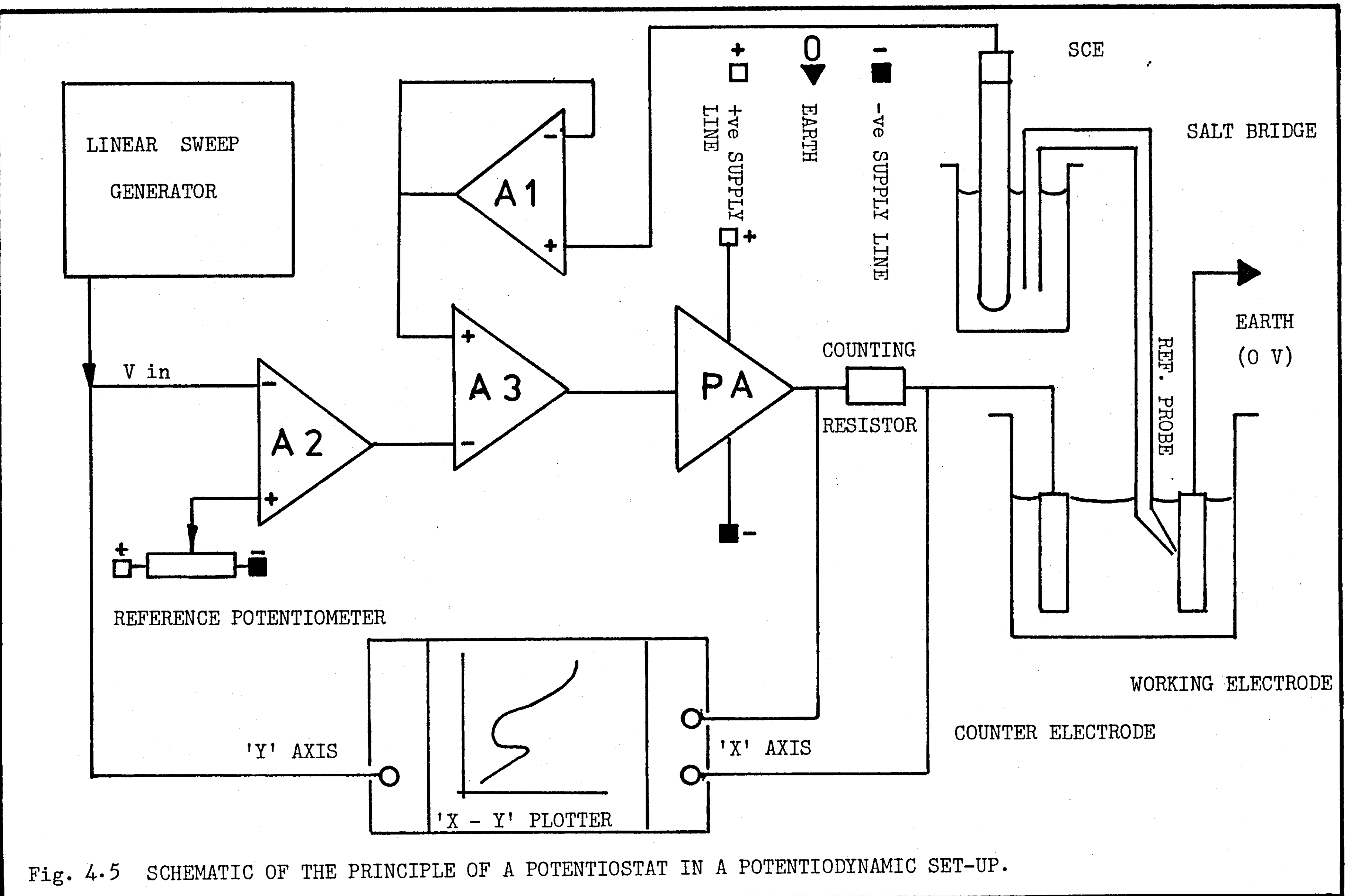

Fig. 4.5 SCHEMATIC OF THE PRINCIPLE OF A POTENTIOSTAT IN A POTENTIODYNAMIC SET-UP.

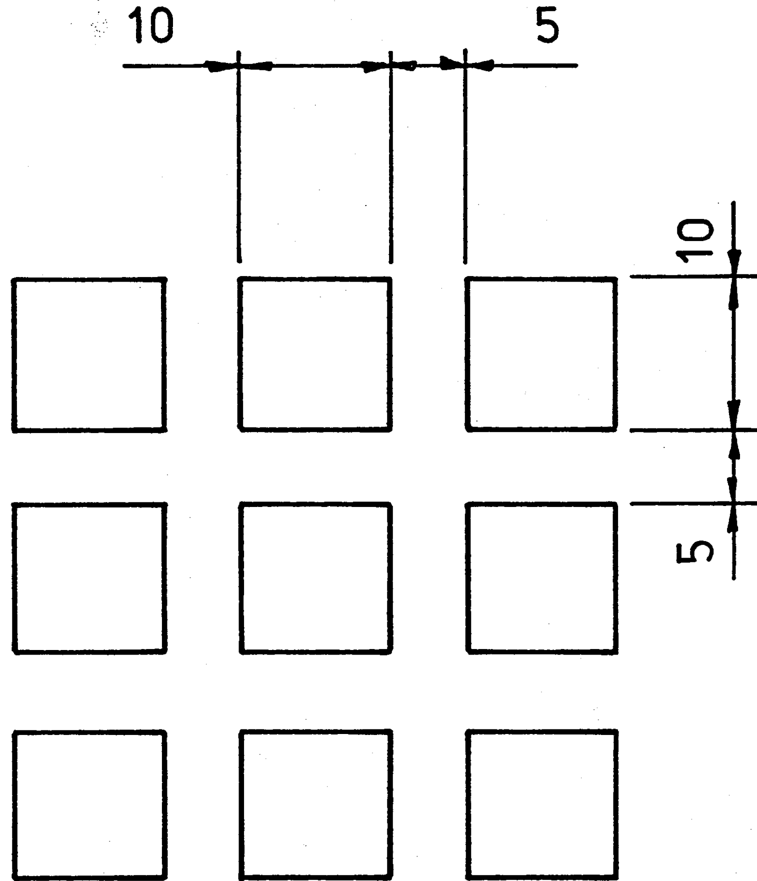

ALL DIMENSIONS IN mm

SCALE X 2

Fig. 4.6 DIMENSIONS MATRIX FOR THE TOOL USED FOR THE POLARIZATION MEASUREMENTS AND THE PRELIMINARY ETCHING TESTS.

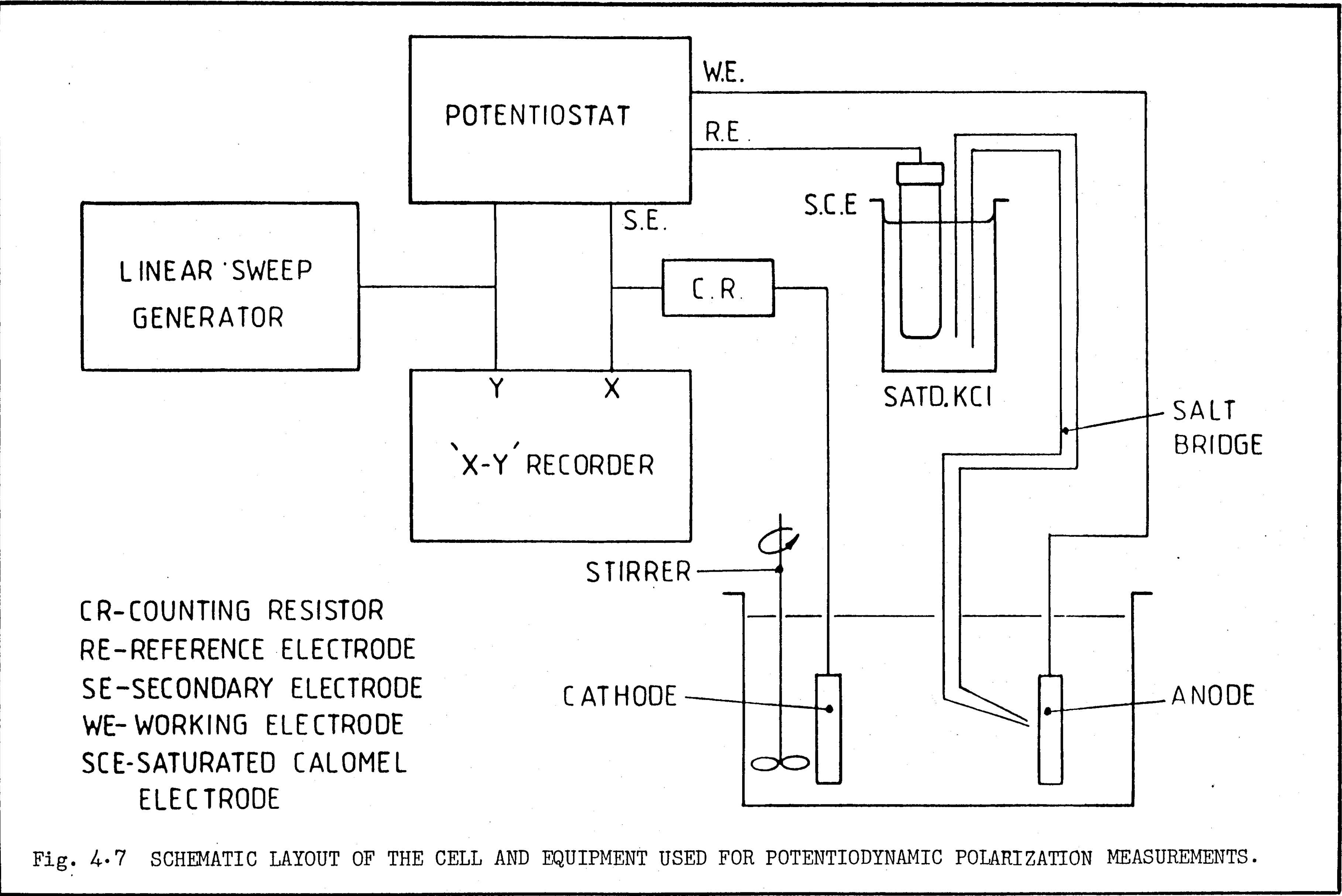

Fig. 4.7 SCHEMATIC LAYOUT OF THE CELL AND EQUIPMENT USED FOR POTENTIODYNAMIC POLARIZATION MEASUREMENTS.

Fig. 4.8 PHOTOGRAPH ILLUSTRATING THE CELL COMPONENT PARTS.

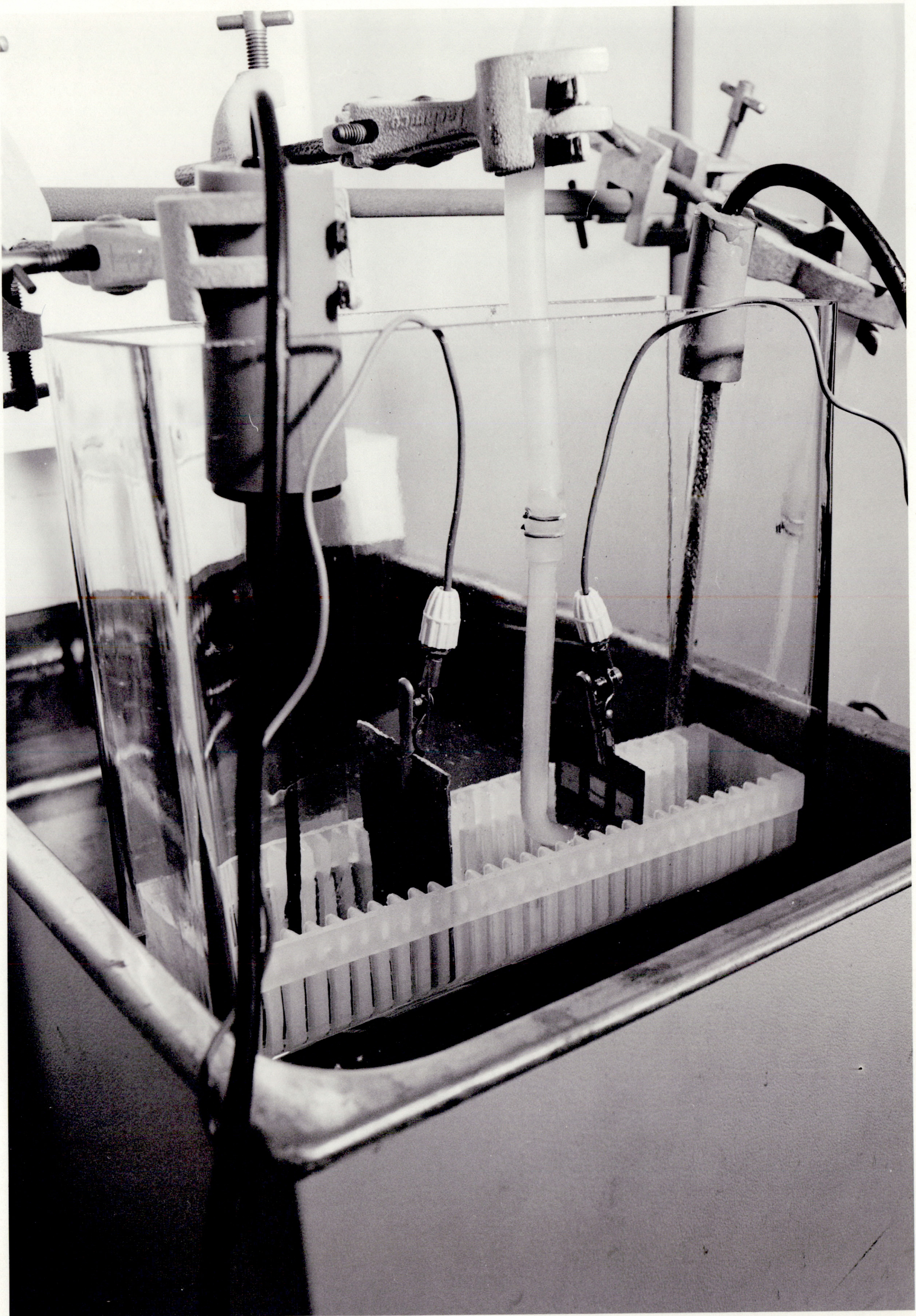

Fig. 4.9 PHOTOGRAPH ILLUSTRATING THE COMPONENT PARTS OF THE MEASURING CELL IN POSITION.

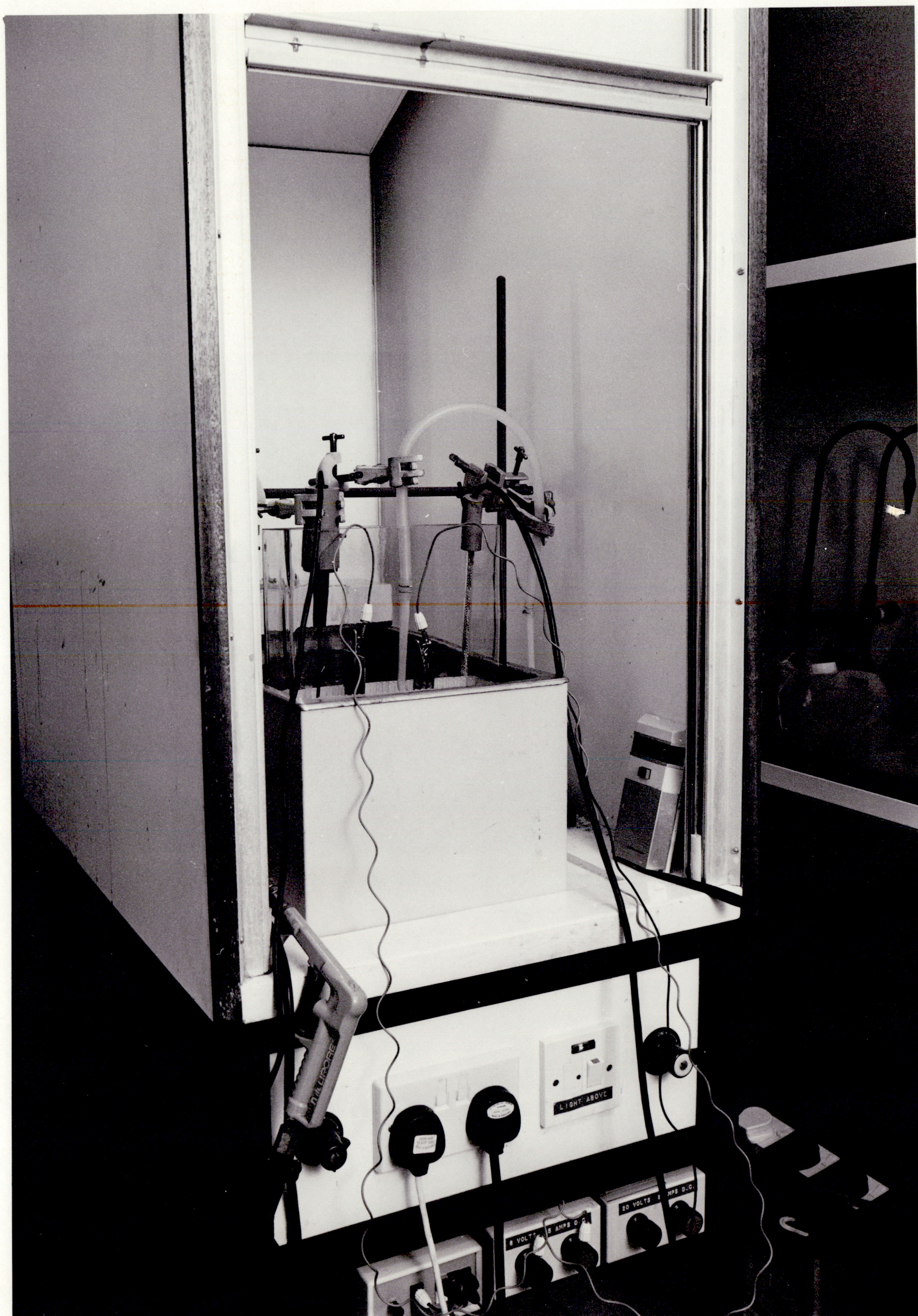

Fig. 4.10 PHOTOGRAPH ILLUSTRATING THE CELL IN POSITION IN THE WATER BATH AND FUME CABINET.

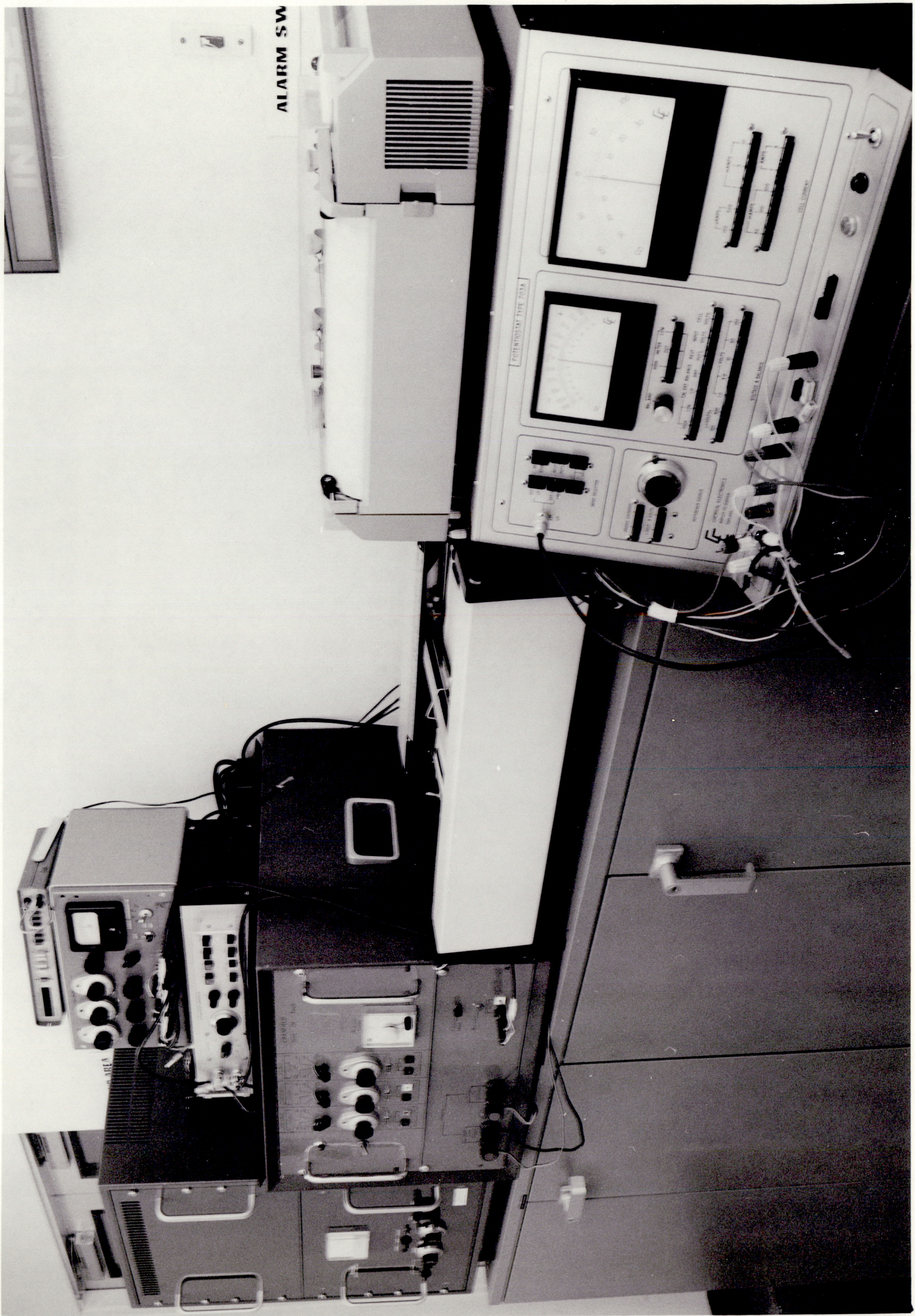

Fig. 4.11 THE INSTRUMENTATION UTILISED FOR CARRYING OUT THE POTENTIODYNAMIC MEASUREMENTS.

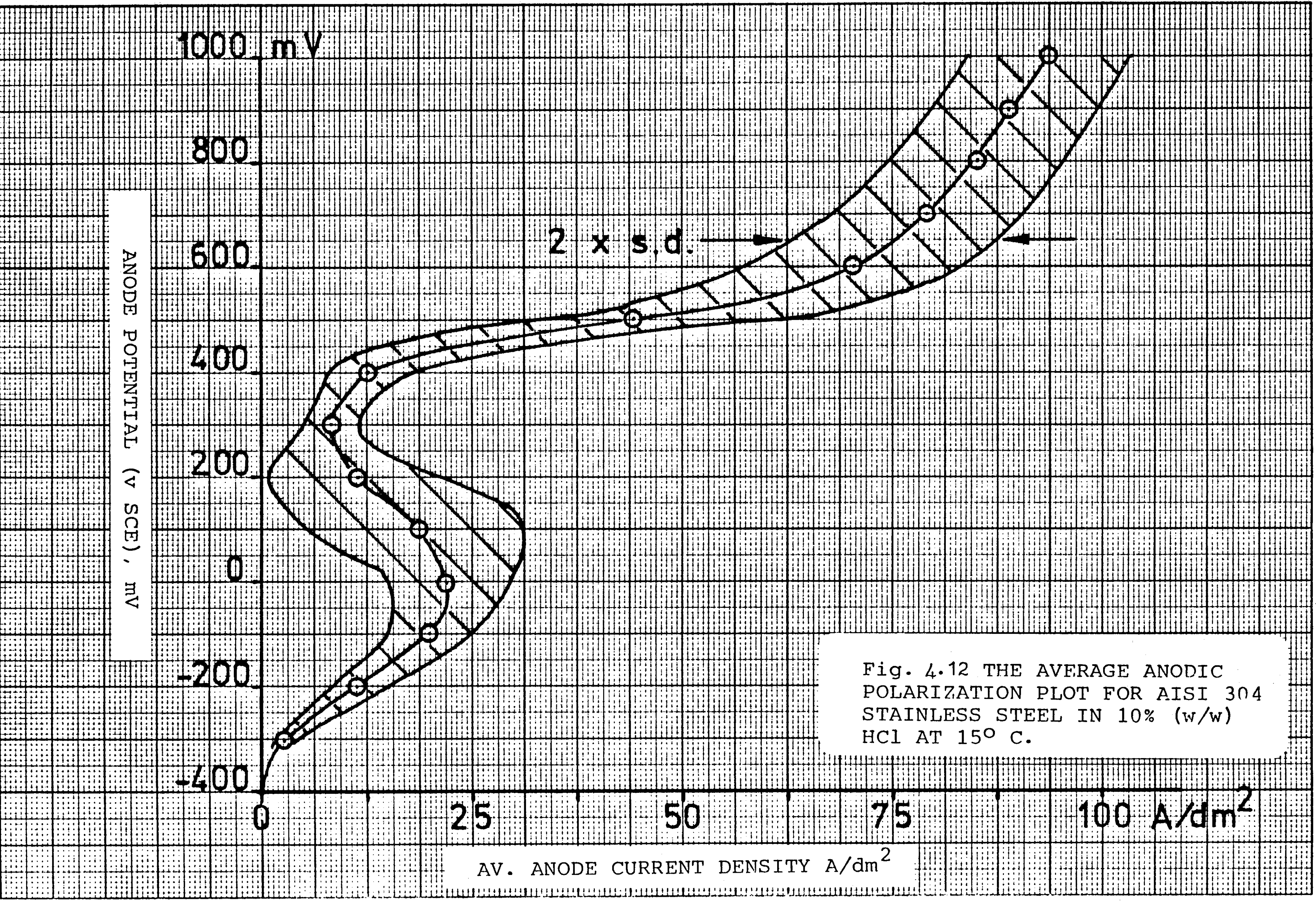

Fig. 4.12 THE AVERAGE ANODIC POLARIZATION PLOT FOR AISI 304 STAINLESS STEEL IN 10% (w/w) HCl AT 15° C.

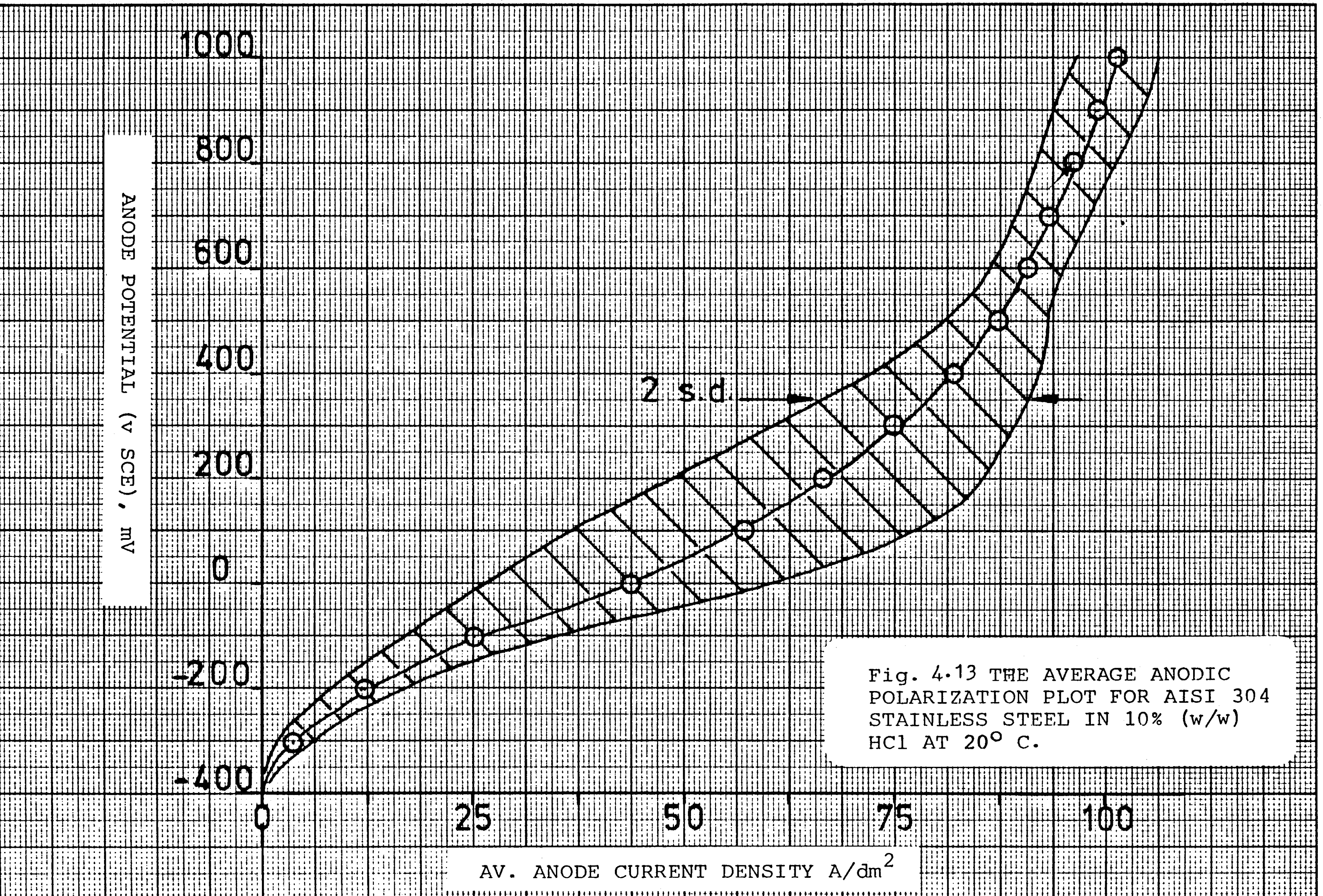

Fig. 4·13 THE AVERAGE ANODIC POLARIZATION PLOT FOR AISI 304 STAINLESS STEEL IN 10% (w/w) HCl AT 20° C.

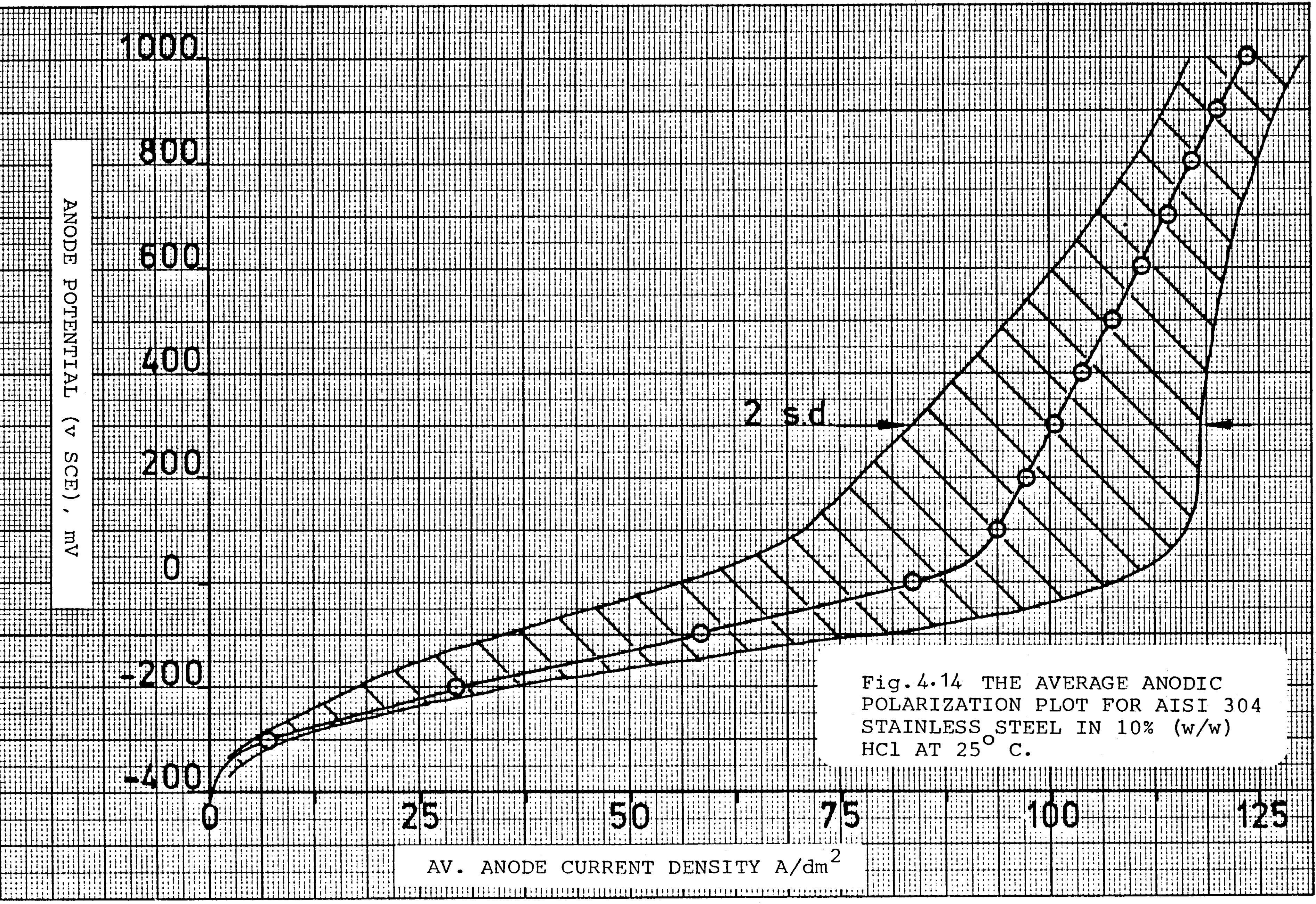

Fig.4.14 THE AVERAGE ANODIC POLARIZATION PLOT FOR AISI 304 STAINLESS STEEL IN 10% (w/w) HCl AT 25° C.

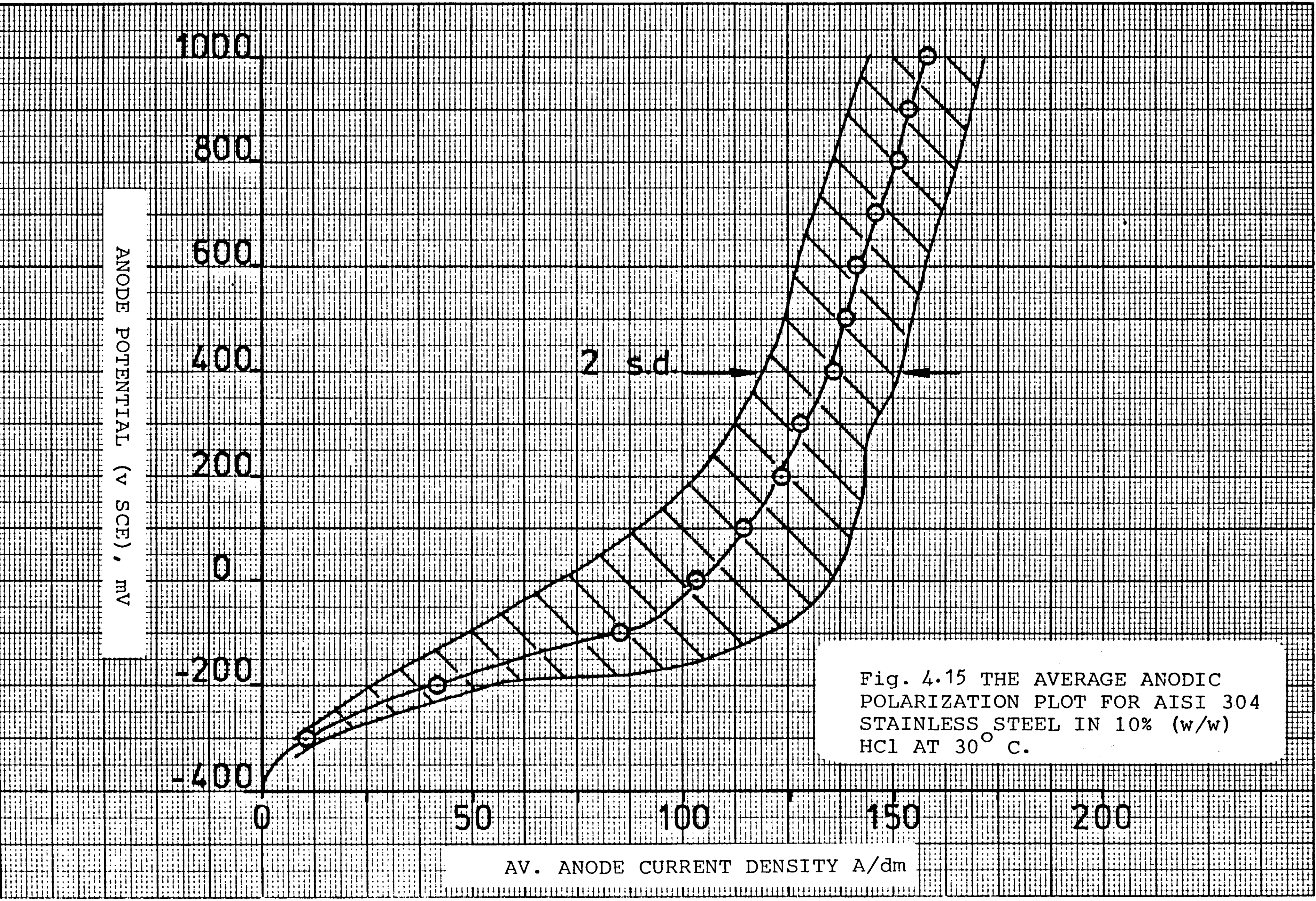

Fig. 4.15 THE AVERAGE ANODIC POLARIZATION PLOT FOR AISI 304 STAINLESS STEEL IN 10% (w/w) HCl AT 30° C.

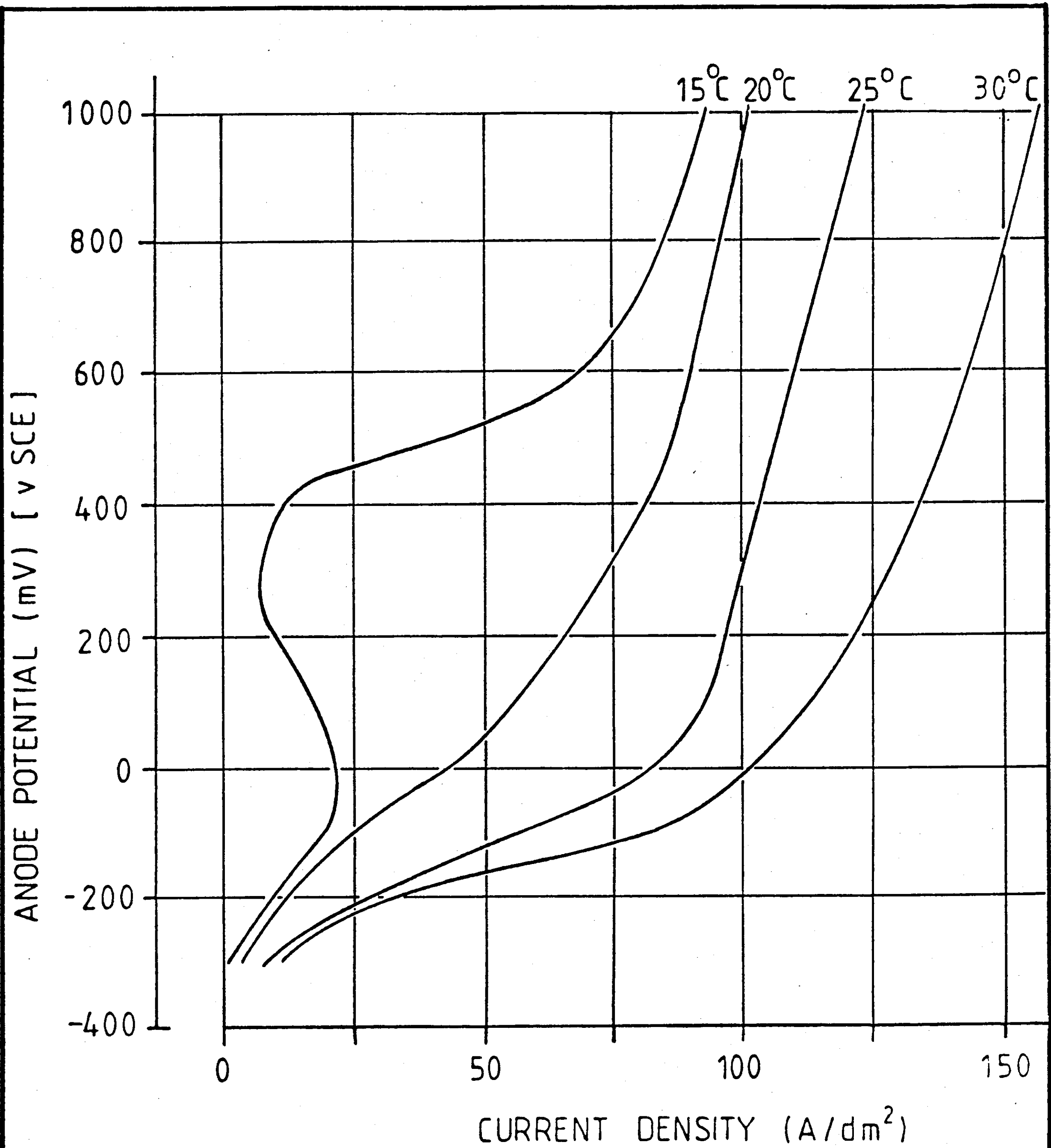

Fig.4.16 ANODIC POLARIZATION DIAGRAMS FOR AISI STAINLESS STEEL IN 10% (w/w) HCl.

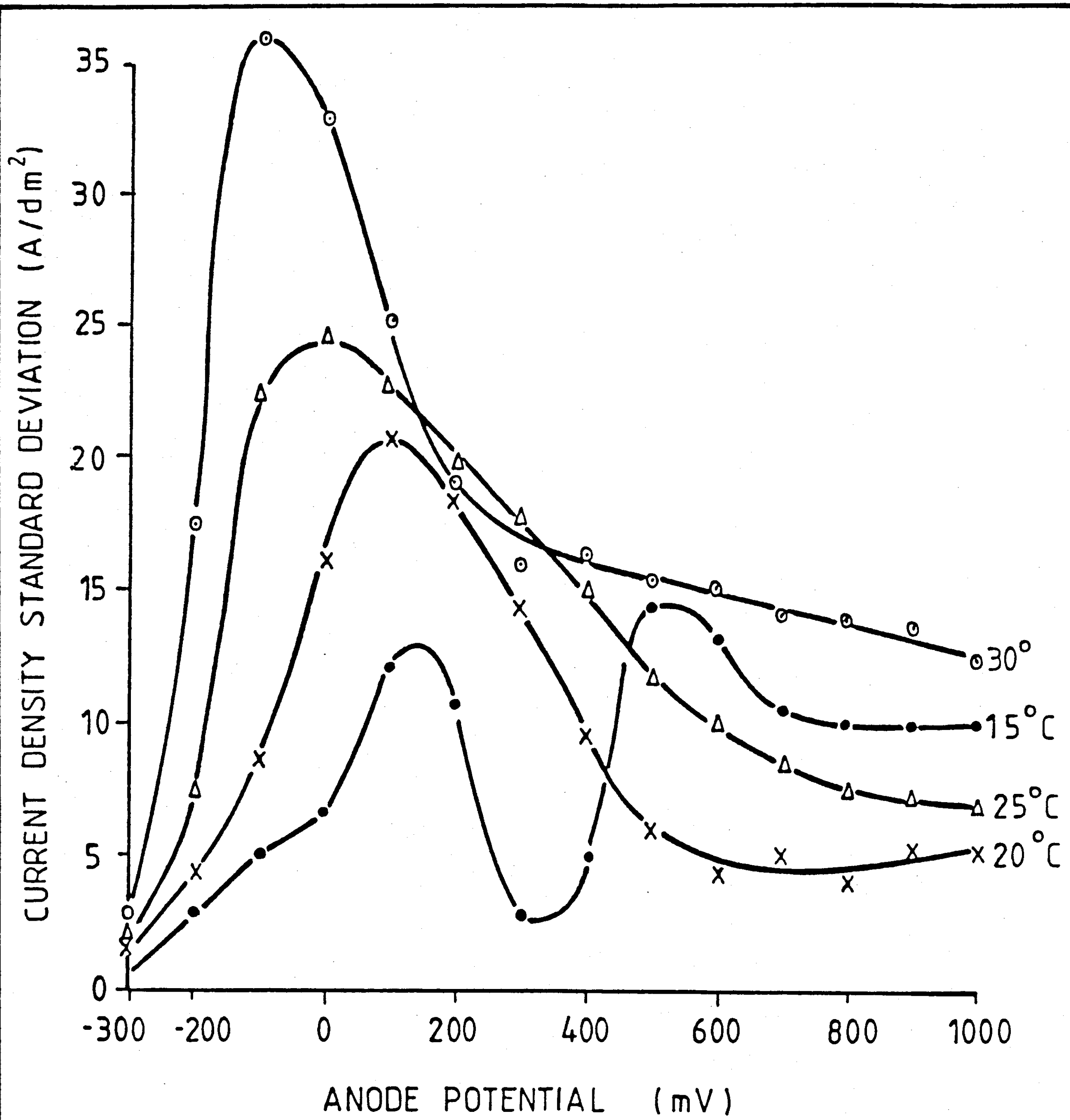

Fig. 4.17 CURRENT DENSITY STANDARD DEVIATION VERSUS ANODE POTENTIAL.

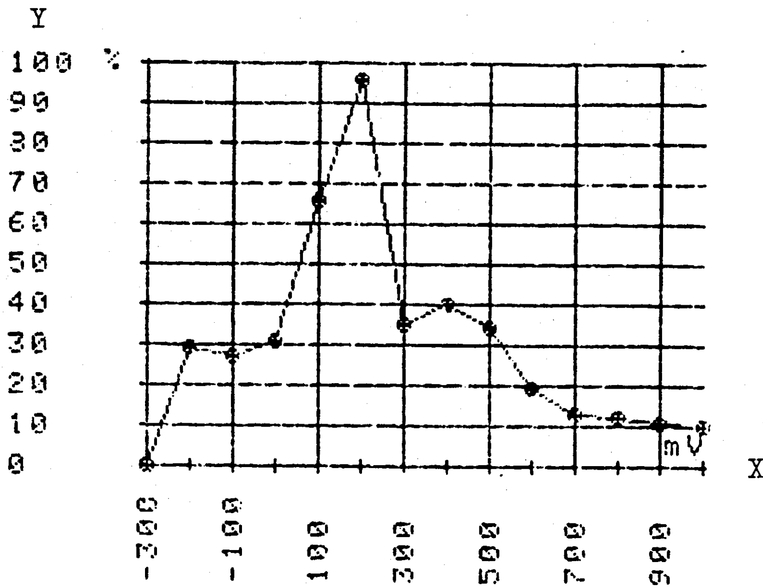

Index	X	Y
1	-300.0000	0.0000
2	-200.0000	25.0000
3	-100.0000	27.0000
4	0.0000	31.0000
5	100.0000	66.0000
6	200.0000	96.0000
7	300.0000	35.0000
8	400.0000	40.0000
9	500.0000	34.0000
10	600.0000	19.0000
11	700.0000	13.0000
12	800.0000	12.0000
13	900.0000	11.0000
14	1000.0000	10.0000

$$Y = \frac{s.d.}{\bar{J}} \times 100 \ (\%)$$

X = Anode potential (mV) v. SCE

Fig. 4.18 THE PERCENTAGE STANDARD DEVIATION OF CURRENT DENSITY VERSUS ANODE POTENTIAL AT 15°C.

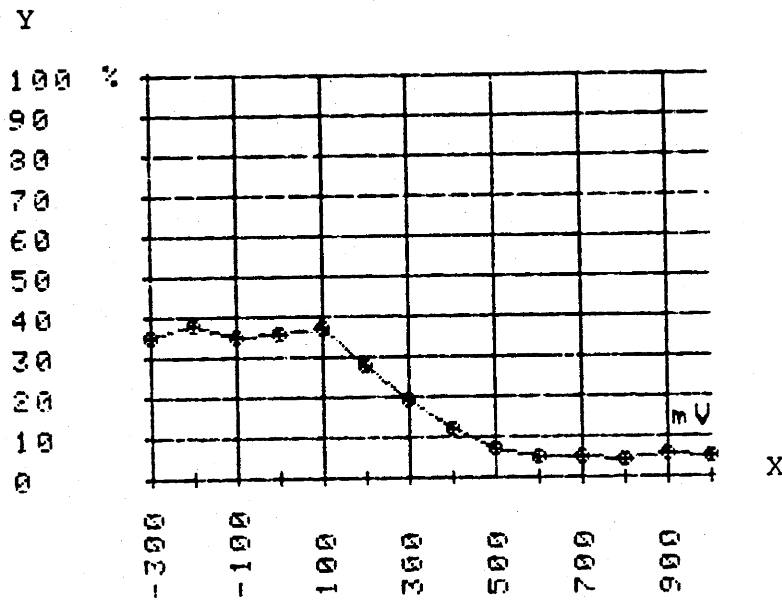

Index	X	Y
1	-300.0000	35.0000
2	-200.0000	38.0000
3	-100.0000	35.0000
4	0.0000	36.0000
5	100.0000	37.0000
6	200.0000	28.0000
7	300.0000	19.0000
8	400.0000	12.0000
9	500.0000	7.0000
10	600.0000	5.0000
11	700.0000	5.0000
12	800.0000	4.0000
13	900.0000	6.0000
14	1000.0000	5.0000

$$Y = \frac{s.d.}{\bar{J}} \times 100\ (\%)$$

X = Anode potential (mV) v. SCE

Fig. 4.19 THE PERCENTAGE STANDARD DEVIATION OF CURRENT DENSITY VERSUS ANODE POTENTIAL AT 20°C.

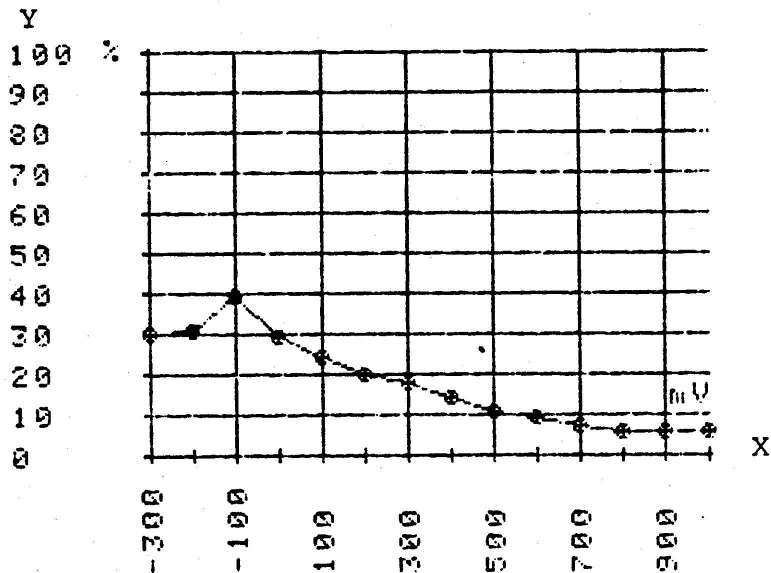

Index	X	Y
1	-300.0000	30.0000
2	-200.0000	31.0000
3	-100.0000	39.0000
4	0.0000	29.0000
5	100.0000	24.0000
6	200.0000	20.0000
7	300.0000	18.0000
8	400.0000	14.0000
9	500.0000	11.0000
10	600.0000	9.0000
11	700.0000	7.0000
12	800.0000	6.0000
13	900.0000	6.0000
14	1000.0000	6.0000

$$Y = \frac{s.d.}{\bar{J}} \times 100\ (\%)$$

X = Anode potential (mV) v. SCE

Fig. 4.20 THE PERCENTAGE STANDARD DEVIATION OF CURRENT DENSITY VERSUS ANODE POTENTIAL AT 25°C.

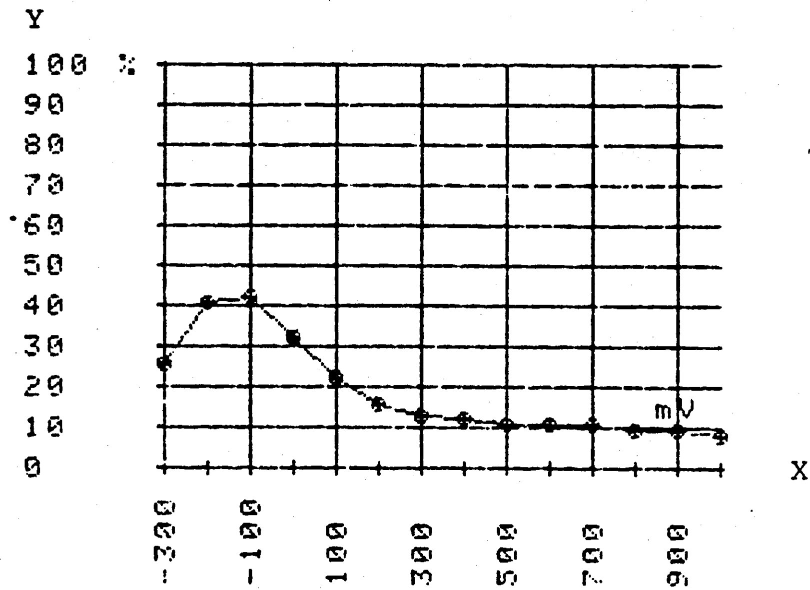

Index	X	Y
1	-300.0000	26.0000
2	-200.0000	41.0000
3	-100.0000	42.0000
4	0.0000	32.0000
5	100.0000	22.0000
6	200.0000	16.0000
7	300.0000	13.0000
8	400.0000	12.0000
9	500.0000	11.0000
10	600.0000	11.0000
11	700.0000	11.0000
12	800.0000	9.0000
13	900.0000	9.0000
14	1000.0000	8.0000

$$Y = \frac{s.d.}{\bar{J}} \times 100 \ (\%)$$

X = Anode potential (mV) v. SCE

Fig. 4.21 THE PERCENTAGE STANDARD DEVIATION OF CURRENT DENSITY VERSUS ANODE POTENTIAL AT 30°C.

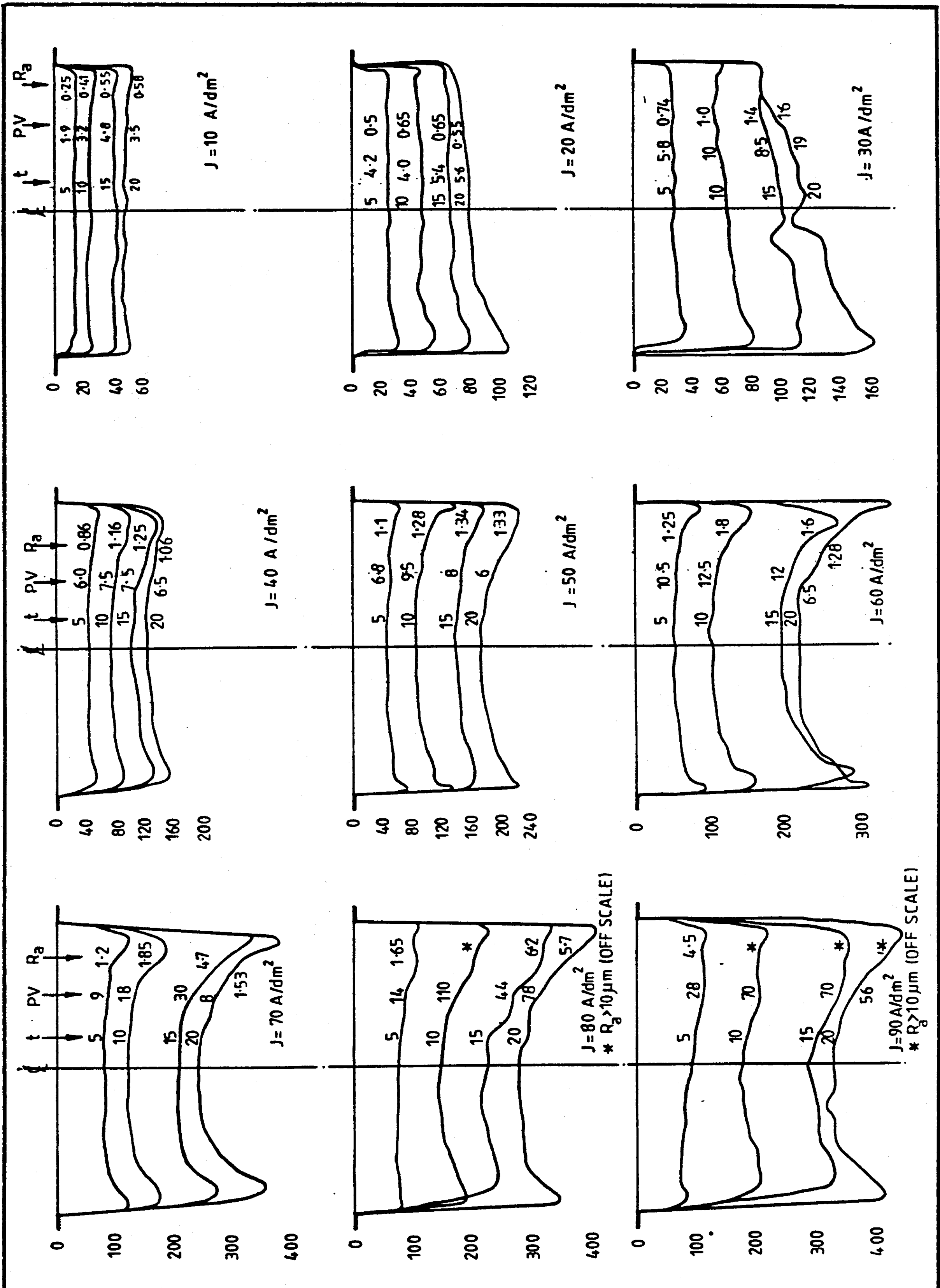

Fig. 4.22 Profiles produced by e.p.e. at a range of current densities together with time of etch (t, min.), peak-to-valley measurement (PV, µm) and surface texture (R_a, µm). The matrix corresponds to the position of the apertures in the resist stencil on the stainless steel anode.

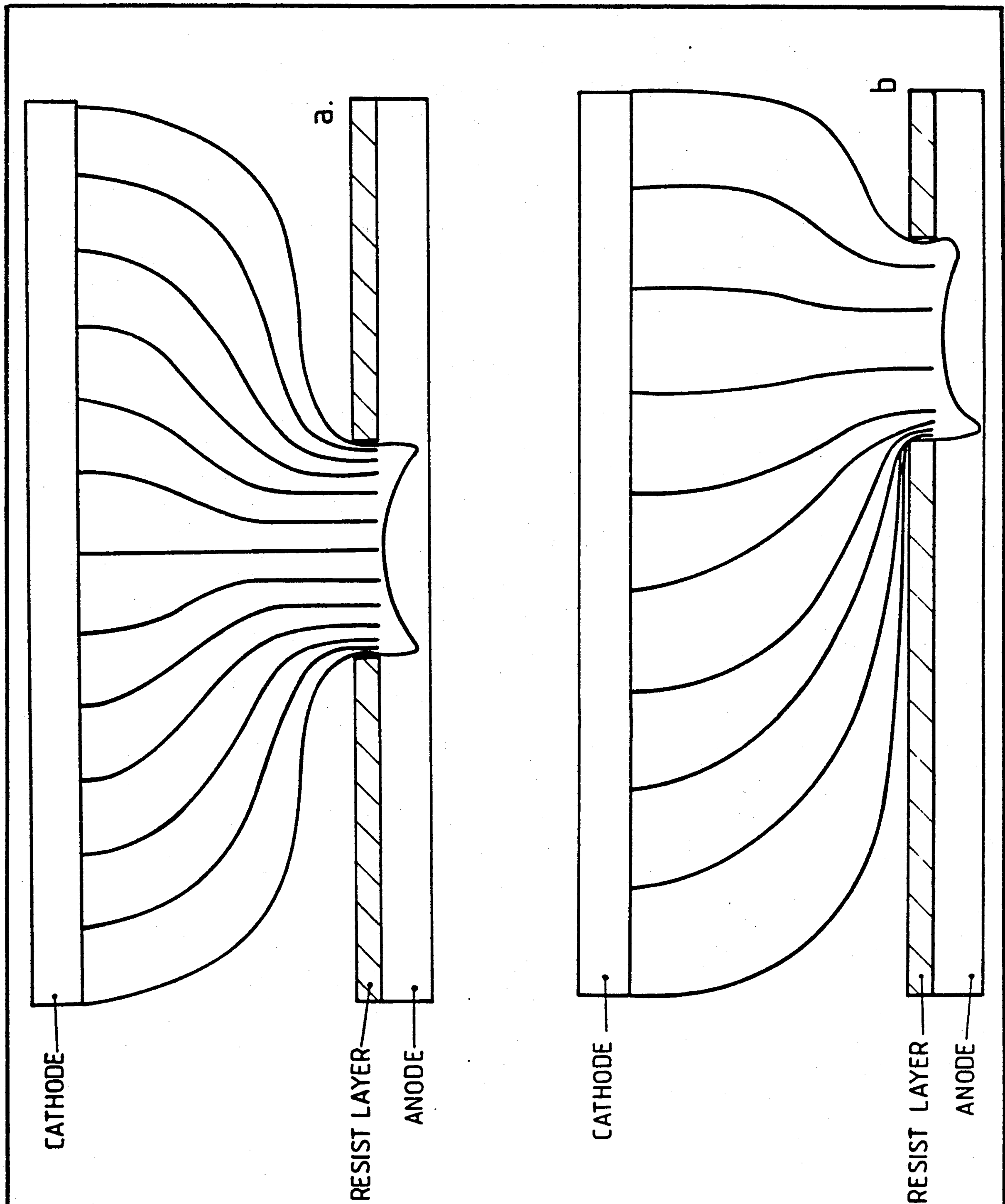

a. WHEN THE RESIST APERTURE IS SYMMETRICAL WITH RESPECT TO THE CATHODE AREA.
b. WHEN THE RESIST APERTURE IS ASYMMETRIC WITH RESPECT TO THE CATHODE AREA.

Fig.4.23 STYLISED CURRENT DENSITY DISTRIBUTION OBTAINED IN ELECTROLYTIC PHOTOETCHING.

```
   AOV: LINEAR REG:CODE 1
SOURCE/DF      SS       MS      F
TOTAL   8    4877.6
REG     1    4793.6   4793.6 399.5
RESID   7      84.0     12.0
R SQUARE =            0.983

YHAT =     -2.069 +       0.894 X
```

X(I)	Y(I)	YHAT	RESIDUALS
10.00	5.20	6.87	-1.67
20.00	16.80	15.81	0.99
30.00	27.00	24.75	2.25
40.00	32.80	33.68	-0.88
50.00	41.30	42.62	-1.32
60.00	47.70	51.56	-3.86
70.00	66.00	60.50	5.50
80.00	72.60	69.44	3.16
90.00	74.20	78.36	-4.18

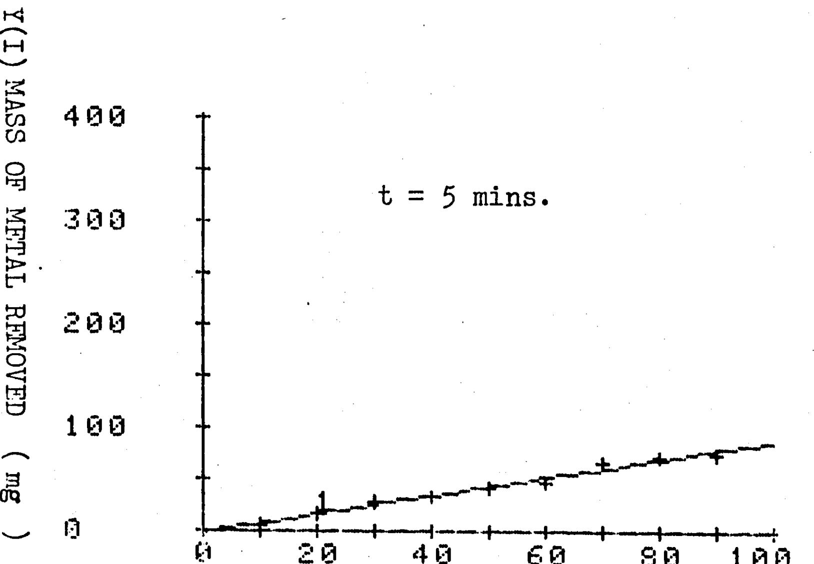

$Y_{HAT} = m_{t=5} = 0.894J - 2.069$ (mg)

X(I) = CURRENT DENSITY J (A/dm^2)

Y(I) = MASS OF METAL REMOVED (mg)

Fig. 4.24 THE MASS OF AISI 304 STAINLESS STEEL REMOVED UNDER GALVANOSTATIC ETCHING IN 5 MINUTES.

AOV: LINEAR REG:CODE 1

SOURCE/DF		SS	MS	F
TOTAL	8	16468.5		
REG	1	16374.6	16374.6	999.9
RESID	7	93.9	13.4	
R SQUARE =			0.994	

YHAT = -0.789 + 1.652 X

X(I)	Y(I)	YHAT	RESIDUALS
10.00	13.00	15.73	-2.73
20.00	36.00	32.25	3.75
30.00	54.20	48.77	5.43
40.00	60.60	65.29	-4.69
50.00	80.60	81.81	-1.21
60.00	94.40	98.33	-3.93
70.00	116.00	114.85	1.15
80.00	132.20	131.37	0.83
90.00	149.30	147.89	1.41

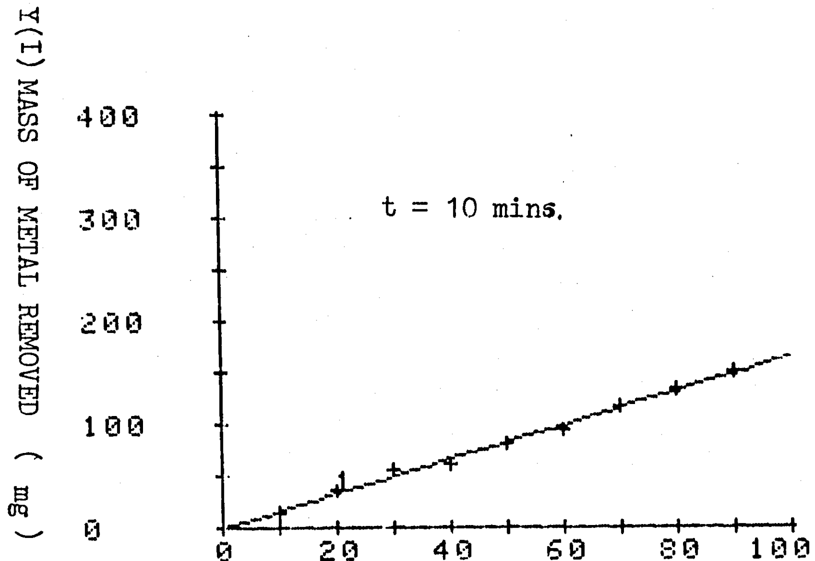

$Y_{HAT} = m_{t=10} = 1.652J - 0.789$ (mg)

X(I) = CURRENT DENSITY J (A/dm^2)

Y(I) = MASS OF METAL REMOVED (mg)

Fig.4.25 THE MASS OF AISI 304 STAINLESS STEEL REMOVED UNDER GALVANOSTATIC ETCHING IN 10 MINUTES.

AOV: LINEAR REG:CODE 1

SOURCE/DF		SS	MS	F
TOTAL	8	36664.5		
REG	1	36521.5	36521.5	999.9
RESID	7	143.0	20.4	
R SQUARE =			0.996	

YHAT = -1.203 + 2.467 X

X(I)	Y(I)	YHAT	RESIDUALS
10.00	27.60	23.47	4.13
20.00	50.20	48.14	2.06
30.00	63.60	72.81	-9.21
40.00	98.60	97.48	1.12
50.00	119.60	122.16	-2.56
60.00	150.80	146.83	3.97
70.00	170.20	171.50	-1.30
80.00	199.30	196.17	3.13
90.00	219.50	220.84	-1.34

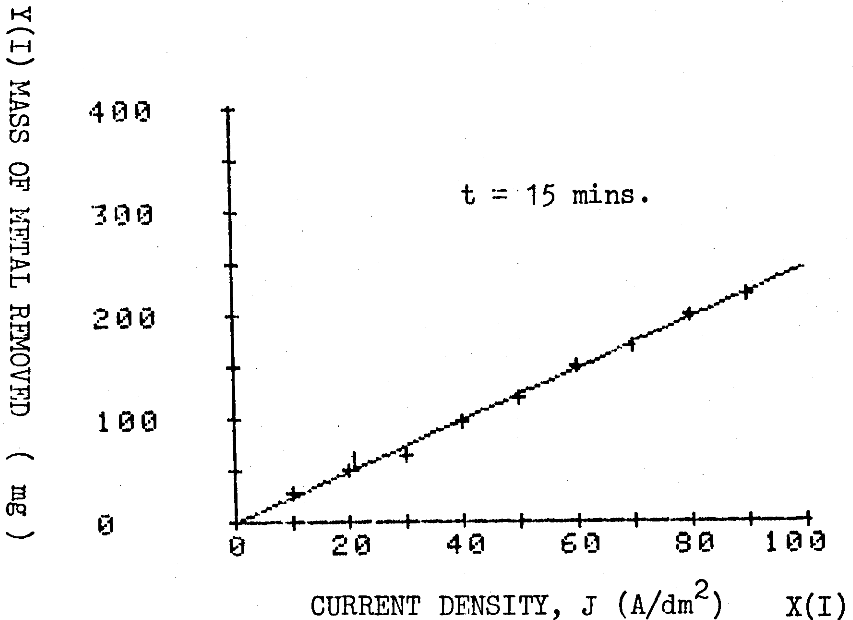

$Y_{HAT} = m_{t=15} = 2.647J - 1.203$ (mg)

X(I) = CURRENT DENSITY J (A/dm^2)

Y(I) = MASS OF METAL REMOVED (mg)

Fig.4.26 THE MASS OF AISI 304 STAINLESS STEEL REMOVED UNDER GALVANOSTATIC ETCHING IN 15 MINUTES.

AOV: LINEAR REG:CODE 1

SOURCE/DF		SS	MS	F
TOTAL	8	58957.9		
REG	1	58456.3	58456.3	815.8
RESID	7	501.6	71.7	
R SQUARE =			0.991	

YHAT = 1.789 + 3.121 X

X(I)	Y(I)	YHAT	RESIDUALS
10.00	36.00	33.00	3.00
20.00	64.40	64.22	0.18
30.00	97.80	95.43	2.37
40.00	114.60	126.64	-12.04
50.00	165.00	157.86	7.14
60.00	177.80	189.07	-11.27
70.00	232.70	220.28	12.42
80.00	252.60	251.50	1.10
90.00	279.80	282.71	-2.91

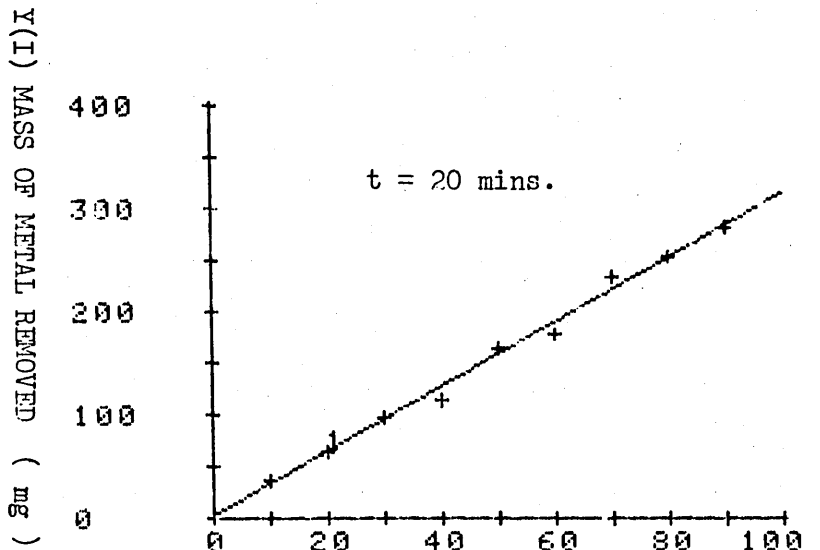

$Y_{HAT} = m_{t=20} = 3.121J + 1.789$ (mg)

X(I) = CURRENT DENSITY J (A/dm^2)

Y(I) = MASS OF METAL REMOVED (mg)

Fig.4.27 THE MASS OF AISI 304 STAINLESS STEEL REMOVED UNDER GALVANOSTATIC ETCHING IN 20 MINUTES.

AOV: LINEAR REG:CODE 1

SOURCE/DF		SS	MS	F
TOTAL	3	2.6		
REG	1	2.6	2.8	999.9
RESID	2	0.0	0.0	

R SQUARE = 0.998

YHAT = 0.160 + 0.150 X

X(I)	Y(I)	YHAT	RESIDUALS
5.00	0.89	0.91	-0.02
10.00	1.65	1.66	-0.01
15.00	2.47	2.41	0.06
20.00	3.12	3.16	-0.04

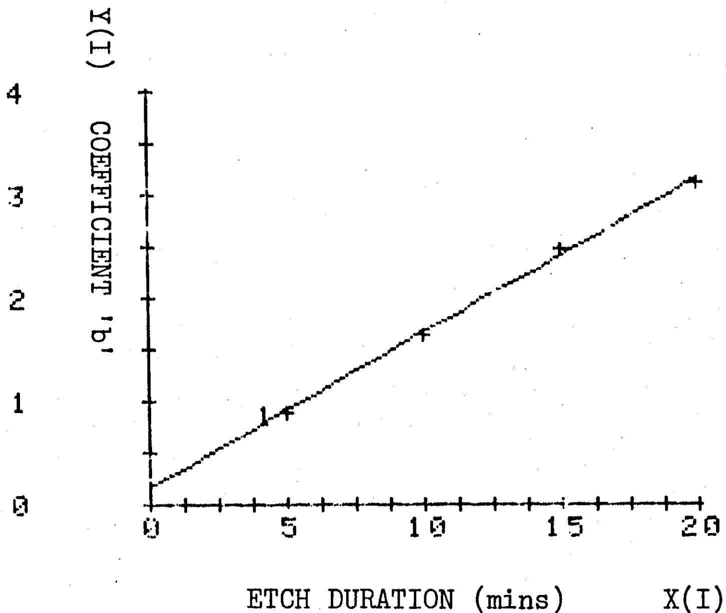

Y_{HAT} = Coefficient for t = 0.150t + 0.16

where t is the etching duration in minutes

X(I) = ETCH DURATION (mins)

Y(I) = COEFFICIENT 'b'

Fig. 4.28 CALCULATION OF THE COEFFICIENT OF THE VARIABLE (TIME) FOR THE GENERAL EQUATION OF MASS OF METAL REMOVED.

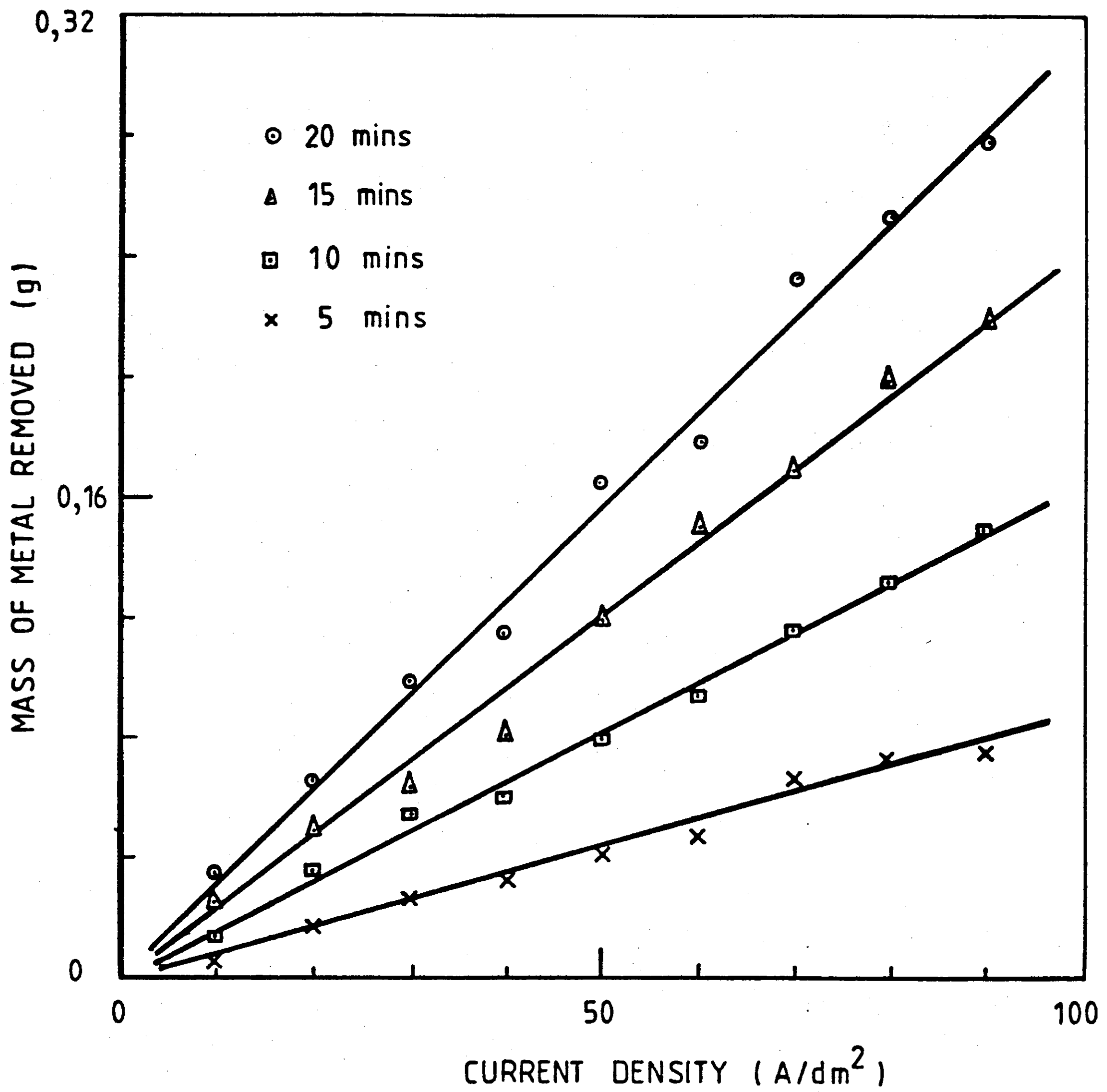

Fig. 4.29 THE MASS OF METAL REMOVED VERSUS CURRENT DENSITY FOR AISI 304 STAINLESS STEEL IN 10% (w/w) HCl AT 25°C.

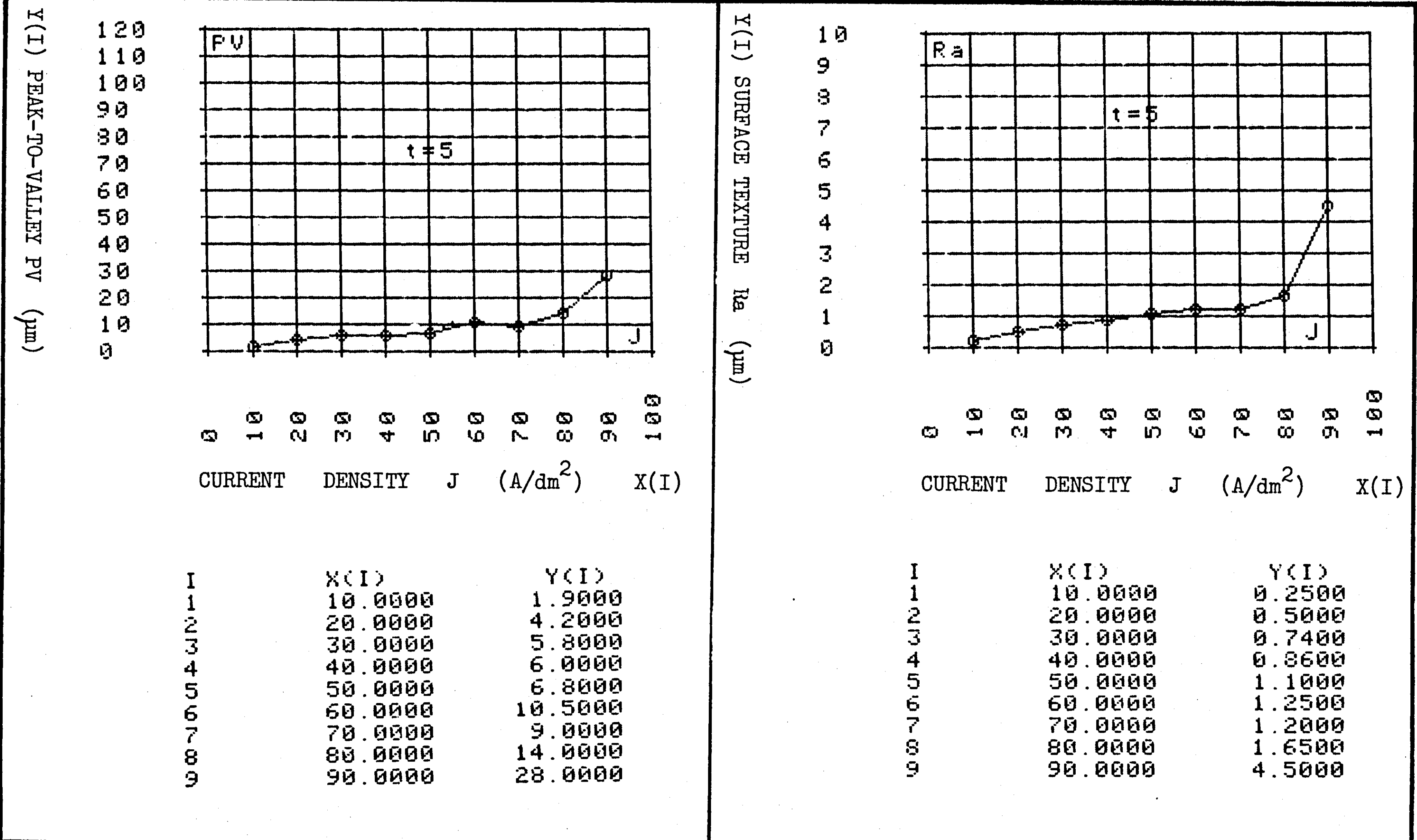

Fig. 4.30 THE SURFACE TEXTURE AND PEAK-TO-VALLEY VERSUS CURRENT DENSITY RESULTS FOR E.P.E. AISI 304 STAINLESS STEEL FOR 5 MINUTES IN 10% (w/w) HCl.

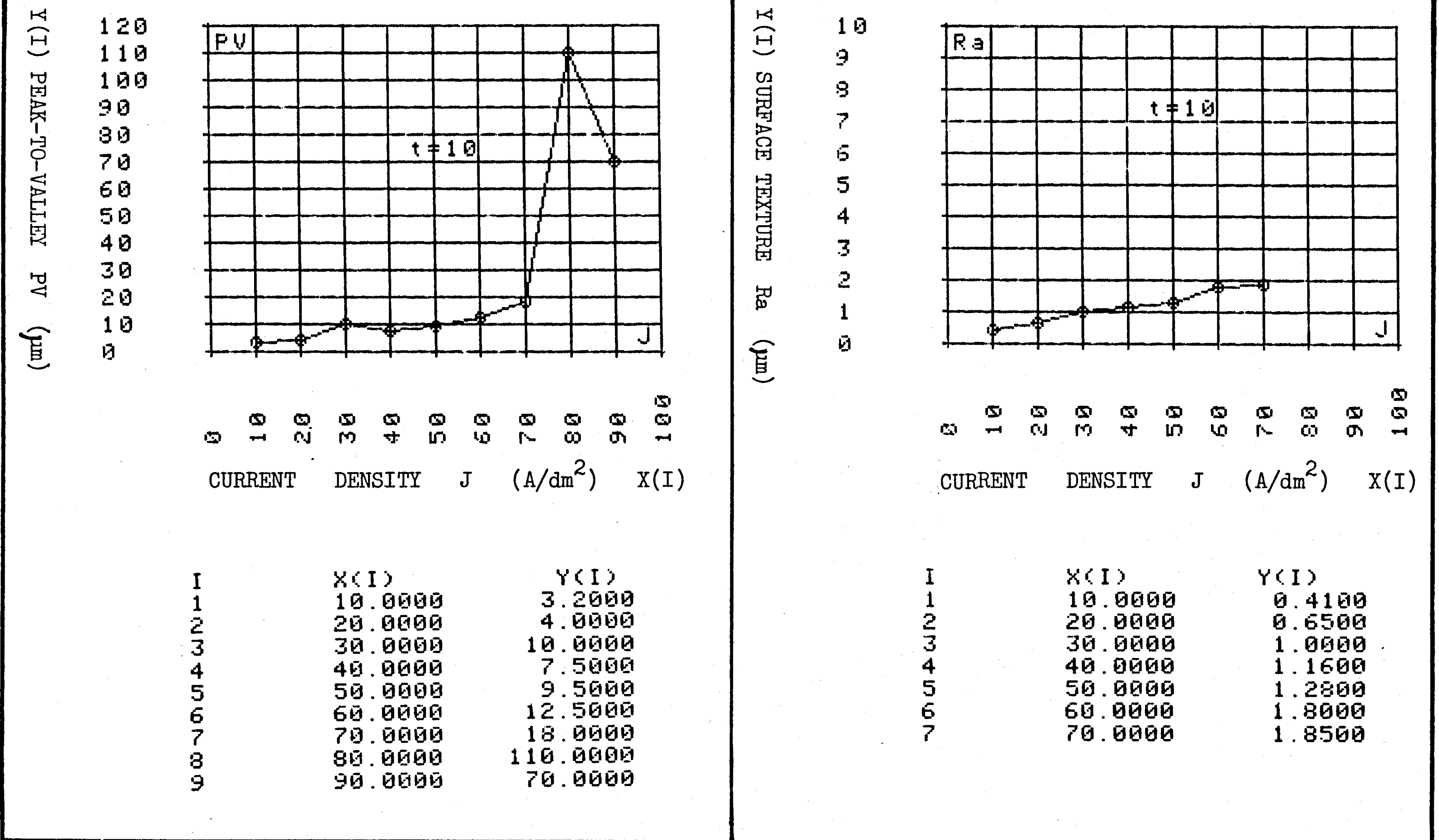

I	X(I)	Y(I)
1	10.0000	3.2000
2	20.0000	4.0000
3	30.0000	10.0000
4	40.0000	7.5000
5	50.0000	9.5000
6	60.0000	12.5000
7	70.0000	18.0000
8	80.0000	110.0000
9	90.0000	70.0000

I	X(I)	Y(I)
1	10.0000	0.4100
2	20.0000	0.6500
3	30.0000	1.0000
4	40.0000	1.1600
5	50.0000	1.2800
6	60.0000	1.8000
7	70.0000	1.8500

Fig. 4.31 THE SURFACE TEXTURE AND PEAK-TO-VALLEY VERSUS CURRENT DENSITY RESULTS FOR E.P.E. AISI 304 STAINLESS STEEL FOR 10MINUTES IN 10% (w/w) HCl.

Y(I) PEAK-TO-VALLEY PV (µm)

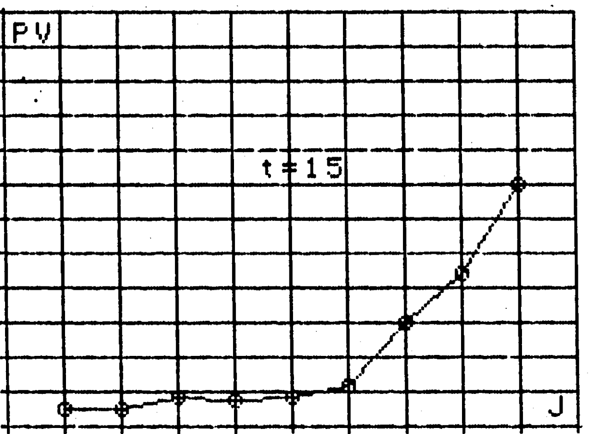

CURRENT DENSITY J (A/dm^2) X(I)

I	X(I)	Y(I)
1	10.0000	4.8000
2	20.0000	5.4000
3	30.0000	8.5000
4	40.0000	7.5000
5	50.0000	8.0000
6	60.0000	12.0000
7	70.0000	30.0000
8	80.0000	44.0000
9	90.0000	70.0000

Y(I) SURFACE TEXTURE Ra (µm)

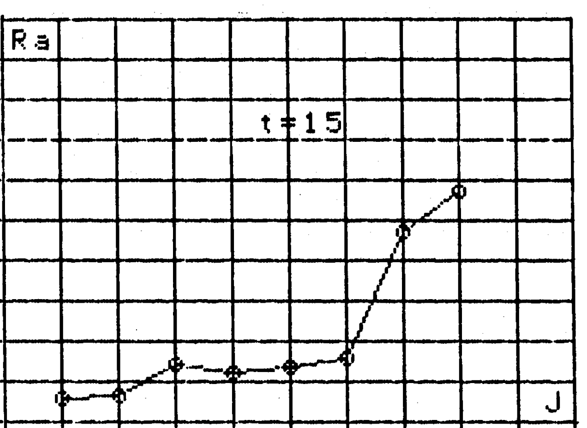

CURRENT DENSITY J (A/dm^2) X(T)

I	X(I)	Y(I)
1	10.0000	0.5500
2	20.0000	0.6500
3	30.0000	1.4000
4	40.0000	1.2500
5	50.0000	1.3400
6	60.0000	1.6000
7	70.0000	4.7000
8	80.0000	5.7000

Fig. 4.32 THE SURFACE TEXTURE AND PEAK-TO-VALLEY VERSUS CURRENT DENSITY RESULTS FOR E.P.E. AISI 304 STAINLESS STEEL FOR 15 MINUTES IN 10% (w/w) HCl.

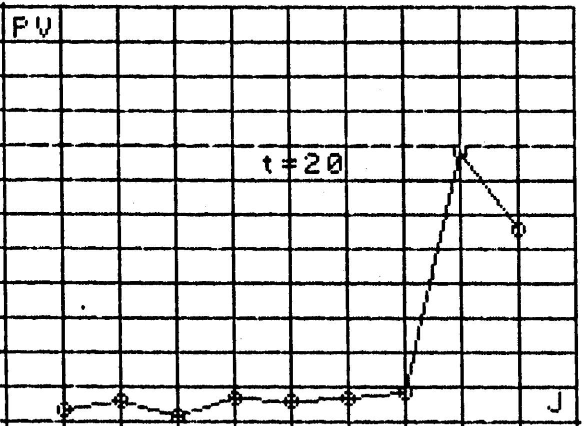

I	X(I)	Y(I)
1	10.0000	3.5000
2	20.0000	5.6000
3	30.0000	1.9000
4	40.0000	6.5000
5	50.0000	6.0000
6	60.0000	6.5000
7	70.0000	8.0000
8	80.0000	78.0000
9	90.0000	56.0000

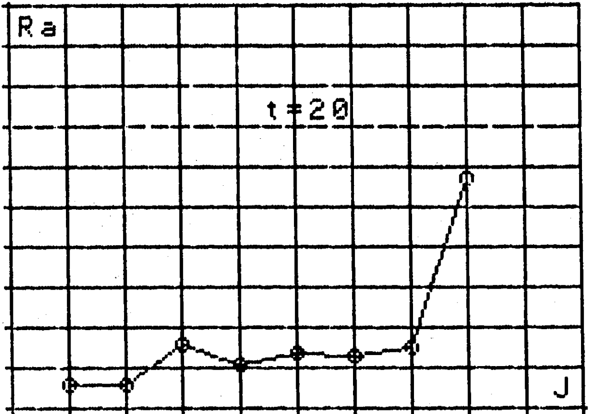

I	X(I)	Y(I)
1	10.0000	0.5800
2	20.0000	0.5500
3	30.0000	1.6000
4	40.0600	1.0600
5	50.0000	1.3300
6	60.0000	1.2800
7	70.0000	1.5300
8	80.0000	5.7000

Fig. 4.33 THE SURFACE TEXTURE AND PEAK-TO-VALLEY VERSUS CURRENT DENSITY RESULTS FOR E.P.E. AISI 304 STAINLESS STEEL FOR 20 MINUTES IN 10% (w/w) HCl.

RESIST TOP EDGE

MAG x 40

MAG x 400

Fig. 4.34 PHOTOMICROGRAPH OF A POTENTIOSTATIC ETCHING OF A 10 X 10 mm APERTURE AT -250 mV (v. SCE) IN 10% (w/w) HCl ACID SOLUTION.

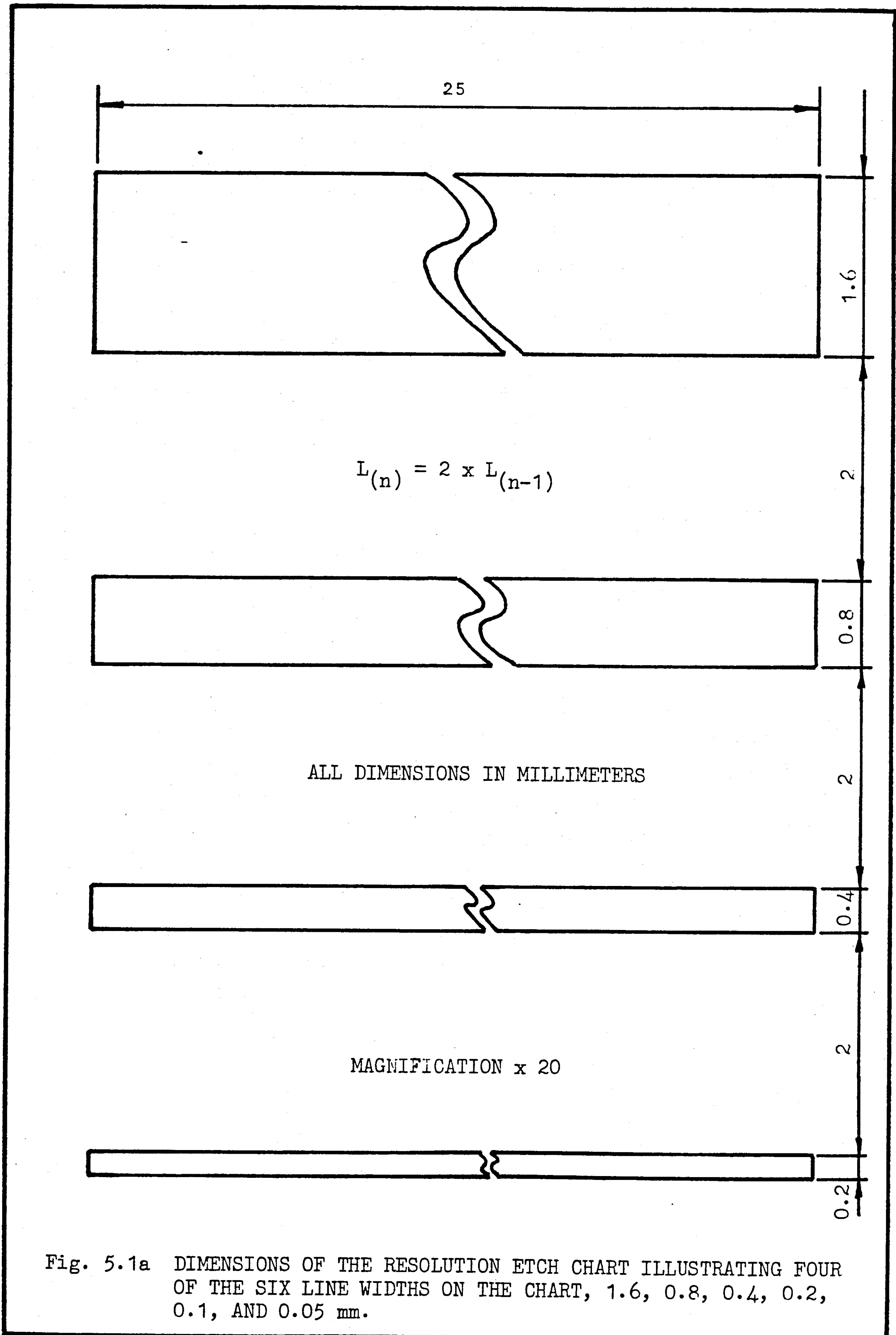

Fig. 5.1a DIMENSIONS OF THE RESOLUTION ETCH CHART ILLUSTRATING FOUR OF THE SIX LINE WIDTHS ON THE CHART, 1.6, 0.8, 0.4, 0.2, 0.1, AND 0.05 mm.

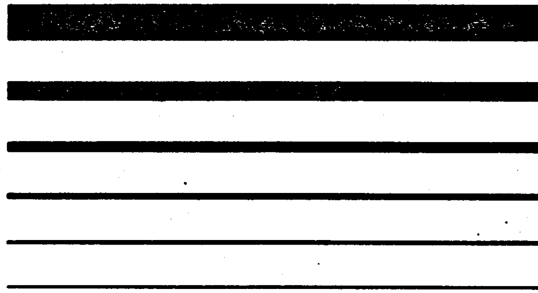

MAGNIFICATION x 2.8 APPROX.

Fig. 5.1b PHOTOGRAPH OF THE RESOLUTION ETCH CHART (NOT TO SCALE).

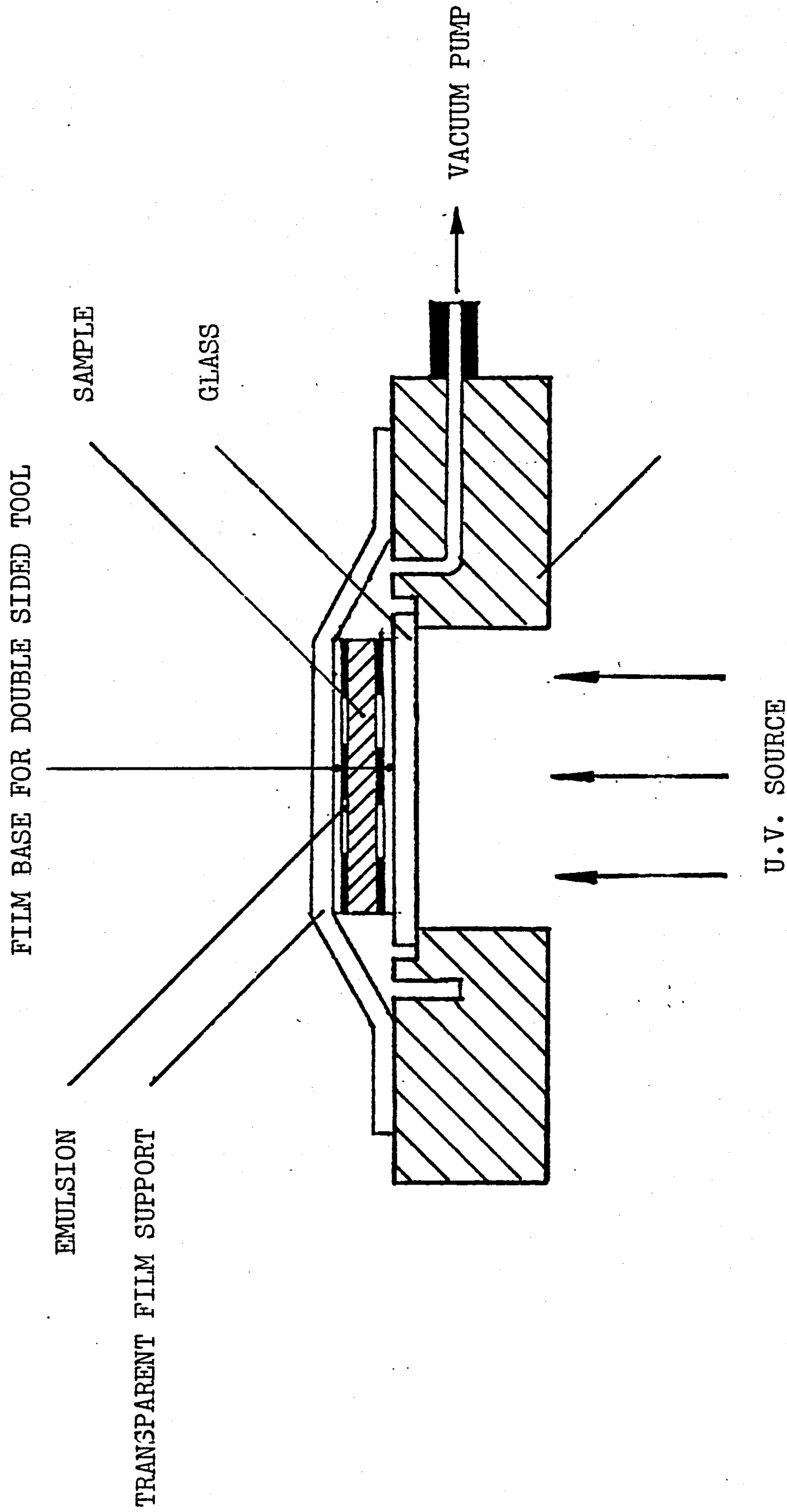

Fig. 5.2 DOUBLE SIDED EXPOSURE FRAME

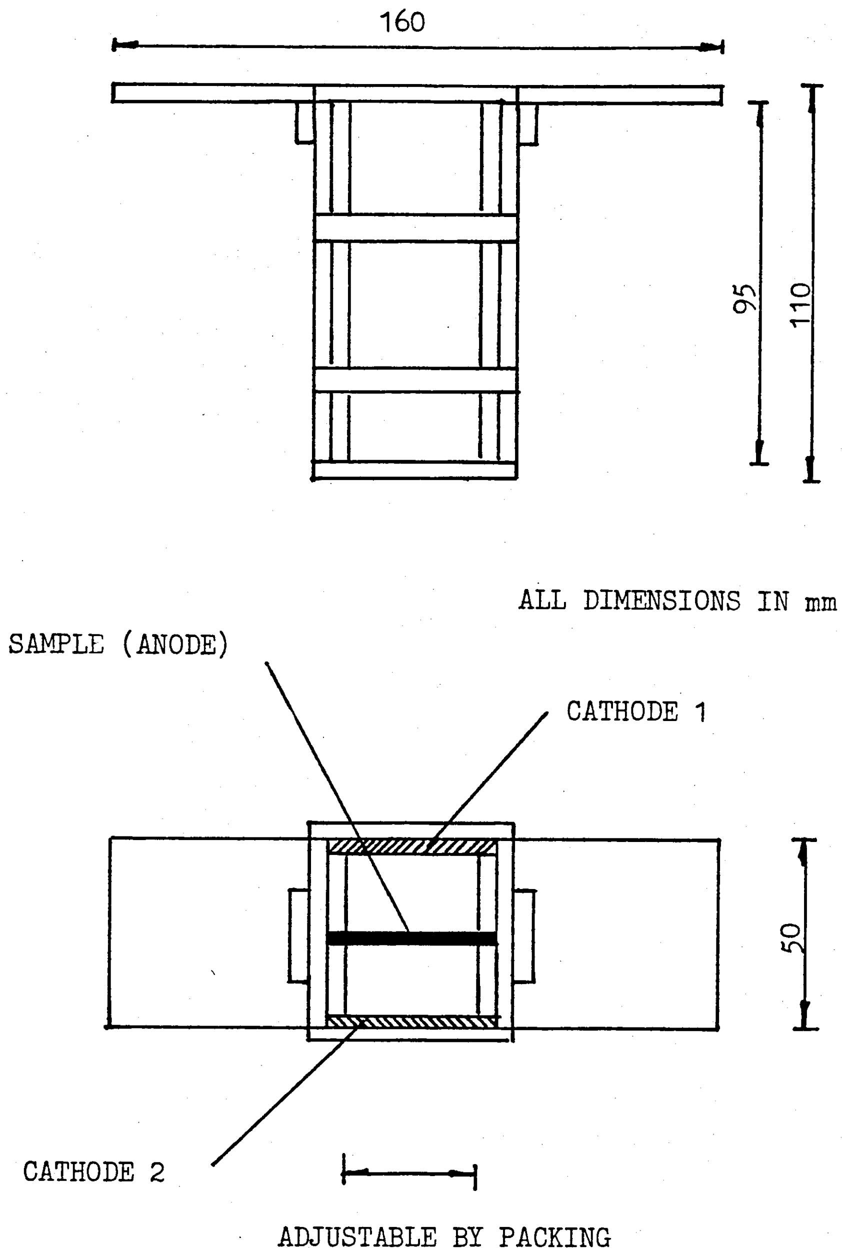

Fig. 5.3 SCHEMATIC DIAGRAM OF THE ETCHING JIG MADE FROM ACRYLIC.

I	X(I)	Y(I)
1	50.0000	57.0000
2	100.0000	52.0000
3	200.0000	52.0000
4	400.0000	49.0000
5	800.0000	41.0000
6	1600.0000	36.0000

AOV: POWER: CODE 4

SOURCE/DF		SS	MS	F
TOTAL	5	0.1		
REG	1	0.1	0.1	37.7
RESID	4	0.0	0.0	

R SQUARE = 0.904

YHAT= 96.554X ^ -0.127

X(I)	Y(I)	YHAT	RESIDUALS
50.00	57.00	58.85	-1.85
100.00	52.00	53.91	-1.91
200.00	52.00	49.38	2.62
400.00	49.00	45.24	3.76
800.00	41.00	41.44	-0.44
1600.00	36.00	37.96	-1.96

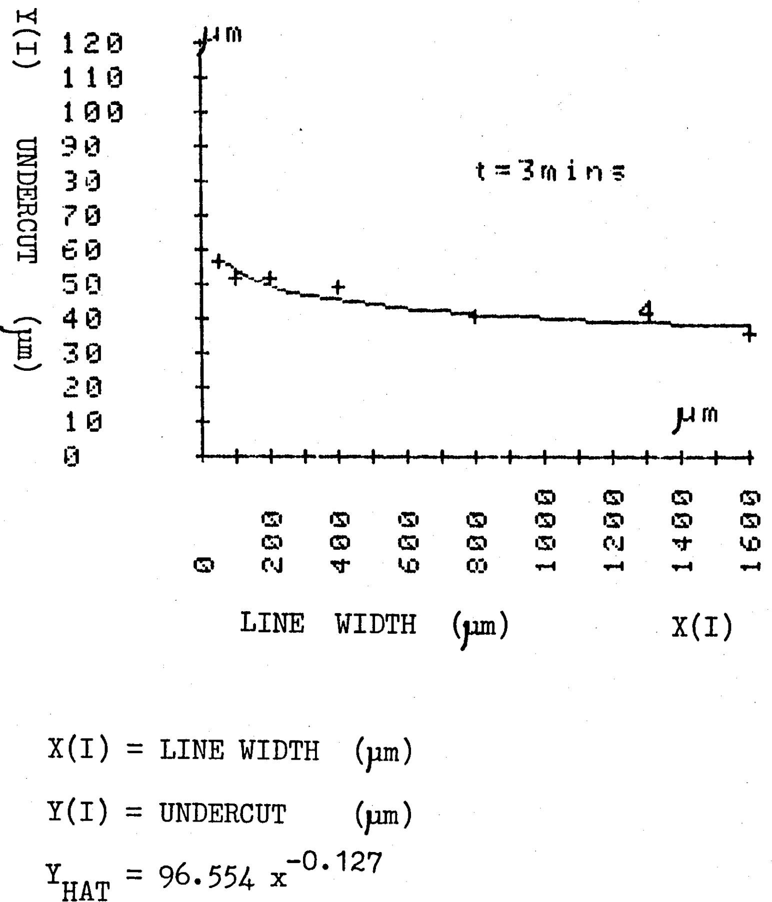

X(I) = LINE WIDTH (µm)

Y(I) = UNDERCUT (µm)

$Y_{HAT} = 96.554\ x^{-0.127}$

Fig. 5.4 RESULTS AND PLOT OF THE UNDERCUT OF THE RESIST LAYER VERSUS ETCHED LINE WIDTH FOR AISI 304 STAINLESS STEEL IN 10% (w/w) HCl AT 25°C IN 3 MINUTES.

I	X(I)	Y(I)
1	50.0000	81.8000
2	100.0000	76.1000
3	200.0000	78.0000
4	400.0000	69.5000
5	800.0000	64.5000
6	1600.0000	59.6000

AOV: POWER: CODE 4

SOURCE/DF		SS	MS	F
TOTAL	5	0.1		
REG	1	0.1	0.1	53.1
RESID	4	0.0	0.0	

R SQUARE = 0.930

YHAT= 118.562X ^ -0.090

X(I)	Y(I)	YHAT	RESIDUALS
50.00	81.80	83.22	-1.42
100.00	76.10	78.17	-2.07
200.00	78.00	73.42	4.58
400.00	69.50	68.95	0.55
800.00	64.50	64.76	-0.26
1600.00	59.60	60.83	-1.23

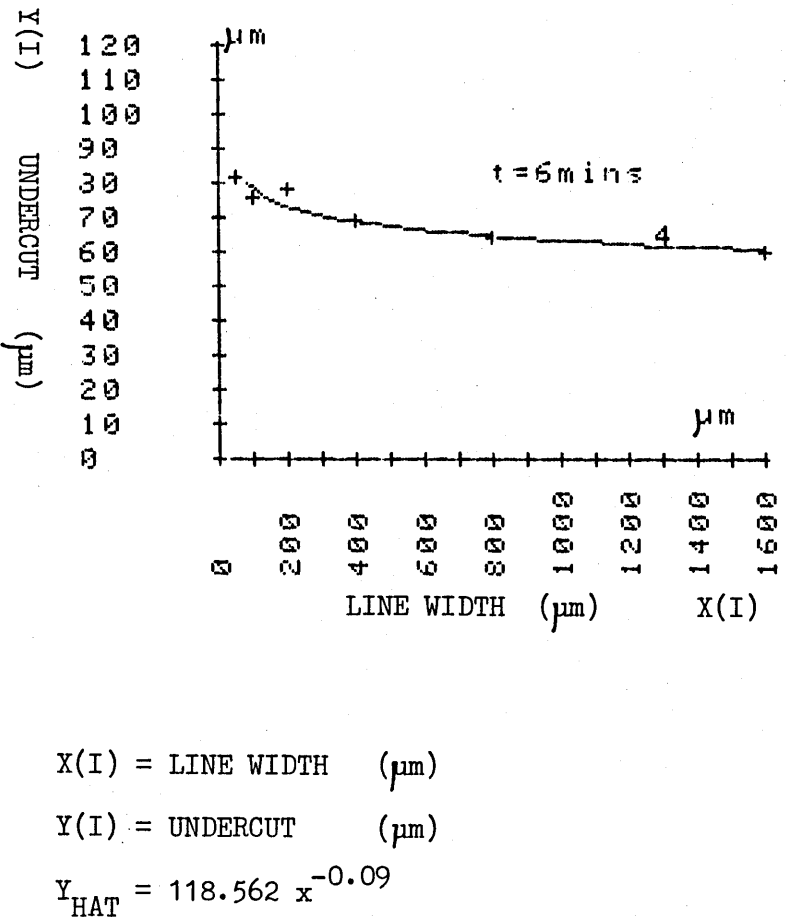

X(I) = LINE WIDTH (μm)

Y(I) = UNDERCUT (μm)

$Y_{HAT} = 118.562\ x^{-0.09}$

Fig. 5.5 RESULTS AND PLOT OF THE UNDERCUT OF THE RESIST LAYER VERSUS ETCHED LINE WIDTH FOR AISI 304 STAINLESS STEEL IN 10% (w/w) HCl AT 25°C IN 6 MINUTES.

I	X(I)	Y(I)
1	50.0000	92.0000
2	100.0000	88.1000
3	200.0000	84.1000
4	400.0000	84.9000
5	800.0000	79.3000
6	1600.0000	80.9000

AOV: POWER: CODE 4

SOURCE/DF		SS	MS	F
TOTAL	5	0.0		
REG	1	0.0	0.0	25.6
RESID	4	0.0	0.0	

R SQUARE = 0.865

YHAT= 105.728X ^ -0.039

X(I)	Y(I)	YHAT	RESIDUALS
50.00	92.00	90.72	1.28
100.00	88.10	88.30	-0.20
200.00	84.10	85.93	-1.83
400.00	84.90	83.64	1.26
800.00	79.30	81.40	-2.10
1600.00	80.90	79.22	1.68

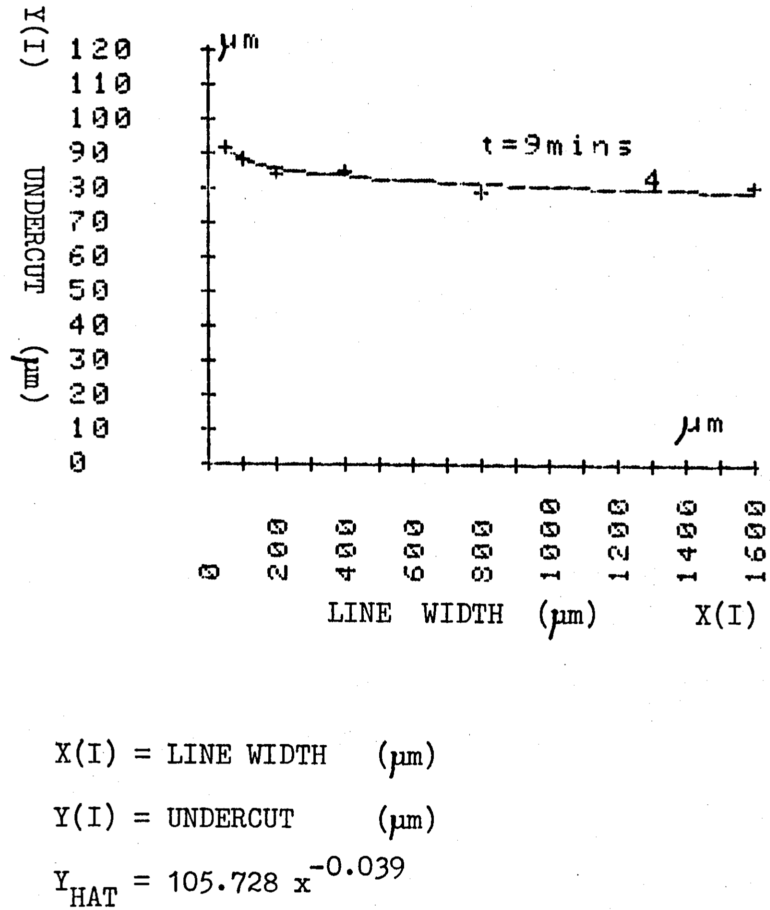

X(I) = LINE WIDTH (μm)

Y(I) = UNDERCUT (μm)

$Y_{HAT} = 105.728\ x^{-0.039}$

Fig. 5.6 RESULTS AND PLOT OF THE UNDERCUT OF THE RESIST LAYER VERSUS ETCHED LINE WIDTH FOR AISI 304 STAINLESS STEEL IN 10% (w/w) HCl AT 25°C IN 9 MINUTES.

I	X(I)	Y(I)
1	50.0000	104.7000
2	100.0000	100.0000
3	200.0000	96.0000
4	400.0000	94.4000
5	800.0000	87.6000
6	1600.0000	85.3000

AOV: POWER: CODE 4

SOURCE/DF		SS	MS	F
TOTAL	5	0.0		
REG	1	9.0	0.0	188.8
RESID	4	0.0	0.0	

R SQUARE = 0.979

YHAT= 131.972X ^ -0.059

X(I)	Y(I)	YHAT	RESIDUALS
50.00	104.70	104.65	0.05
100.00	100.00	100.43	-0.43
200.00	96.00	96.39	-0.39
400.00	94.40	92.51	1.89
800.00	87.60	88.78	-1.18
1600.00	85.30	85.21	0.09

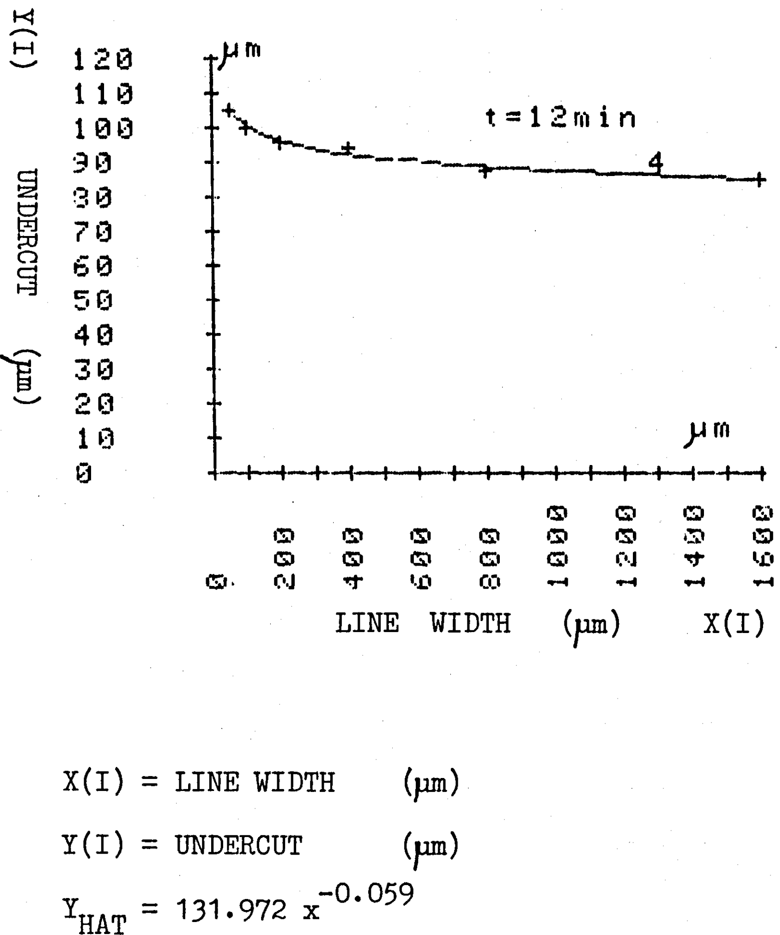

X(I) = LINE WIDTH (µm)

Y(I) = UNDERCUT (µm)

$Y_{HAT} = 131.972\ x^{-0.059}$

Fig. 5.7 RESULTS AND PLOT OF THE UNDERCUT OF THE RESIST LAYER VERSUS ETCHED LINE WIDTH FOR AISI 304 STAINLESS STEEL IN 10% (w/w) HCl AT 25°C IN 12 MINUTES.

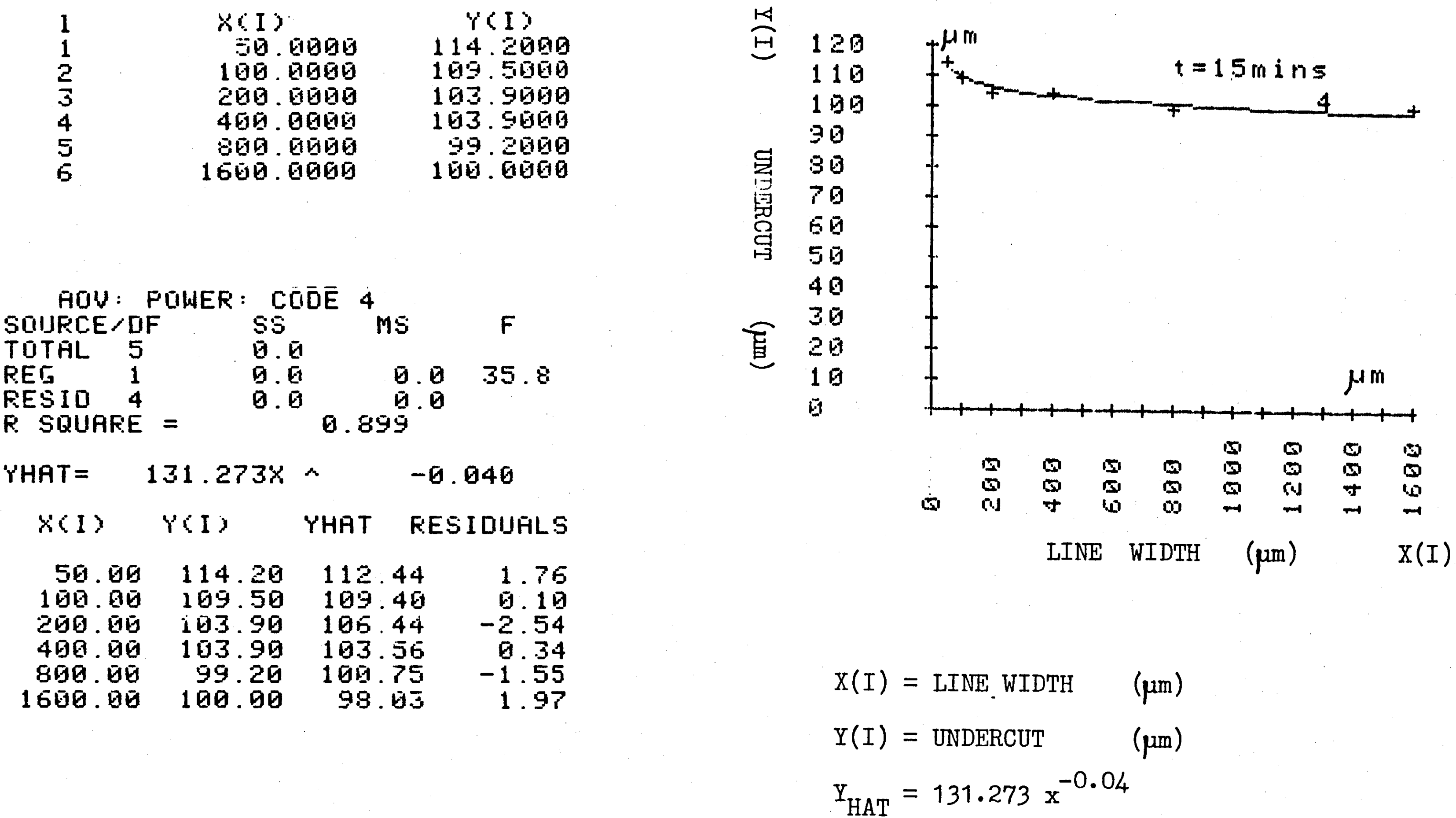

I	X(I)	Y(I)
1	50.0000	114.2000
2	100.0000	109.5000
3	200.0000	103.9000
4	400.0000	103.9000
5	800.0000	99.2000
6	1600.0000	100.0000

AOV: POWER: CODE 4

SOURCE/DF		SS	MS	F
TOTAL	5	0.0		
REG	1	0.0	0.0	35.8
RESID	4	0.0	0.0	

R SQUARE = 0.899

YHAT= 131.273X ^ -0.040

X(I)	Y(I)	YHAT	RESIDUALS
50.00	114.20	112.44	1.76
100.00	109.50	109.40	0.10
200.00	103.90	106.44	-2.54
400.00	103.90	103.56	0.34
800.00	99.20	100.75	-1.55
1600.00	100.00	98.03	1.97

X(I) = LINE WIDTH (μm)

Y(I) = UNDERCUT (μm)

$Y_{HAT} = 131.273\ x^{-0.04}$

Fig. 5.8 RESULTS AND PLOT OF THE UNDERCUT OF THE RESIST LAYER VERSUS ETCHED LINE WIDTH FOR AISI 304 STAINLESS STEEL IN 10% (w/w) HCl AT 25°C IN 15 MINUTES.

I	X(I)	Y(I)
1	3.0000	96.5540
2	6.0000	118.5620
3	9.0000	105.7280
4	12.0000	131.9720
5	15.0000	131.2730

AOV: POWER: CODE 4

SOURCE/DF		SS	MS	F
TOTAL	4	0.1		
REG	1	0.1	0.1	7.4
RESID	3	0.0	0.0	

R SQUARE = 0.711

YHAT= 79.887t ^ 0.181

X(I)	Y(I)	YHAT	RESIDUALS
3.00	96.55	97.49	-0.93
6.00	118.56	110.54	8.03
9.00	105.73	118.97	-13.24
12.00	131.97	125.33	6.64
15.00	131.27	130.50	0.77

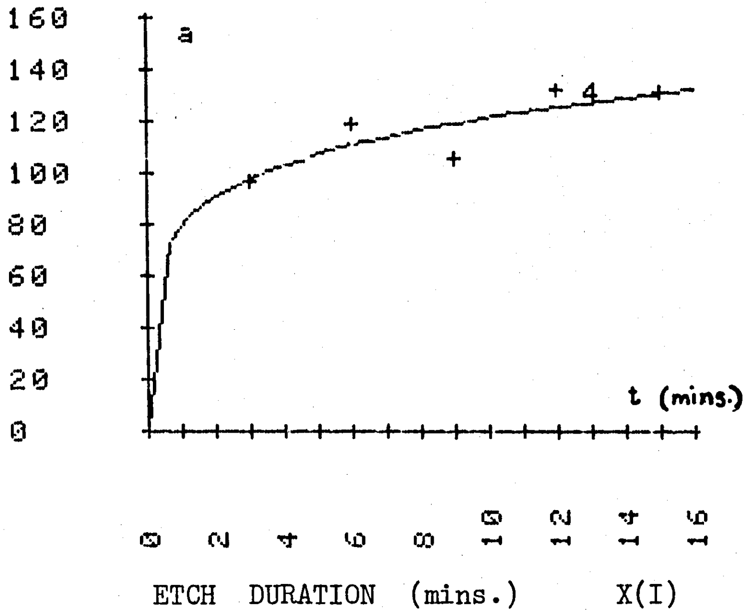

FOR A GENERAL EQUATION FOR UNDERCUT:

$$Y = a\,x^{b}$$

WHERE $Y_{HAT} = a = 79.887\ t^{0.181}$

AND $X(I) = t =$ ETCH DURATION (mins.)

$Y(I) = a =$ REGRESSION COEFFICIENT

Fig. 5.9 CALCULATION FOR THE REGRESSION COEFFICIENT 'a' OF THE GENERAL EQUATION FOR UNDERCUT.

I	X(I)	Y(I)
1	3.0000	-0.1270
2	6.0000	-0.0900
3	9.0000	-0.0390
4	12.0000	-0.0590
5	15.0000	-0.0400

AOV: LINEAR REG:CODE 1

SOURCE/DF		SS	MS	F
TOTAL	4	0.0		
REG	1	0.0	0.0	8.9
RESID	3	0.0	0.0	

R SQUARE = 0.747

YHAT = -0.133 + 0.007t

X(I)	Y(I)	YHAT	RESIDUALS
3.00	-0.13	-0.11	-0.02
6.00	-0.09	-0.09	0.00
9.00	-0.04	-0.07	0.03
12.00	-0.06	-0.05	-0.01
15.00	-0.04	-0.03	-0.01

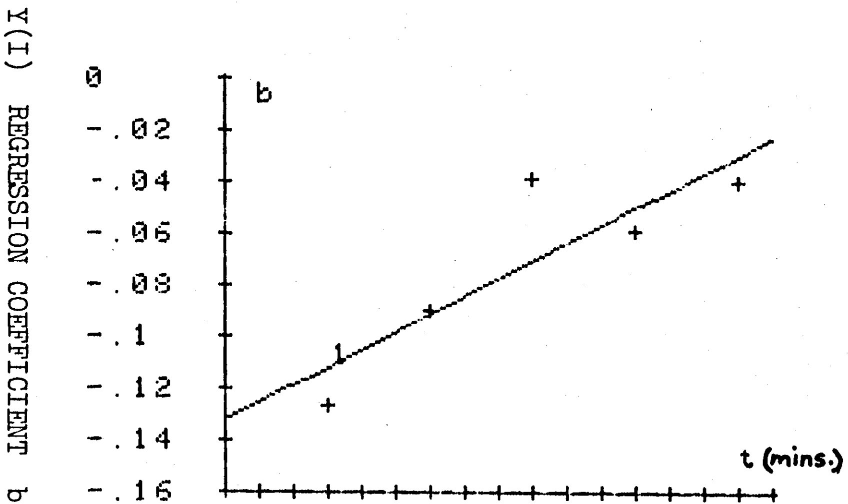

FOR A GENERAL EQUATION FOR UNDERCUT:

$$Y_{UC} = a\,x^{b}$$

WHERE $Y_{HAT} = b = 0.007\,t - 0.133$

AND $X(I) = t =$ ETCH DURATION (mins.)
$Y(I) = b =$ REGRESSION COEFFICIENT

Fig. 5.10 CALCULATION FOR THE REGRESSION COEFFICIENT 'b' OF THE GENERAL EQUATION FOR UNDERCUT.

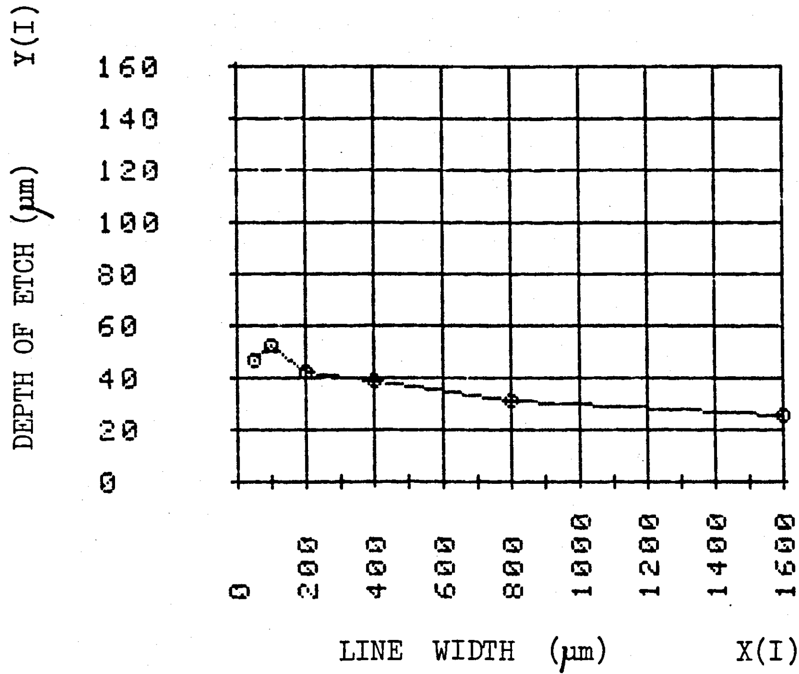

I	X(I)	Y(I)
1	50.0000	47.0000
2	100.0000	52.0000
3	200.0000	42.0000
4	400.0000	39.0000
5	800.0000	31.0000
6	1600.0000	26.0000

X(I) = LINE WIDTH (STENCIL) (μm)

Y(I) = DEPTH OF ETCH (μm)

Fig.5.11 THE DEPTH OF ETCH VERSUS ETCHED LINE WIDTH IN 3 MINUTES.

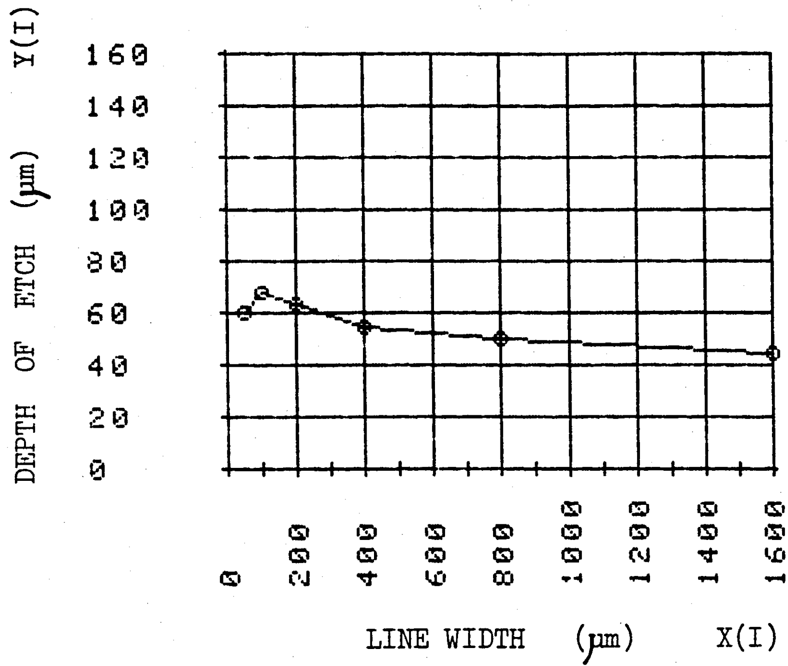

I	X(I)	Y(I)
1	50.0000	60.0000
2	100.0000	68.0000
3	200.0000	63.0000
4	400.0000	54.5000
5	800.0000	49.5000
6	1600.0000	44.5000

X(I) = LINE WIDTH (STENCIL) (µm)

Y(I) = DEPTH OF ETCH (µm)

Fig. 5.12 THE DEPTH OF ETCH VERSUS ETCHED LINE WIDTH IN 6 MINUTES.

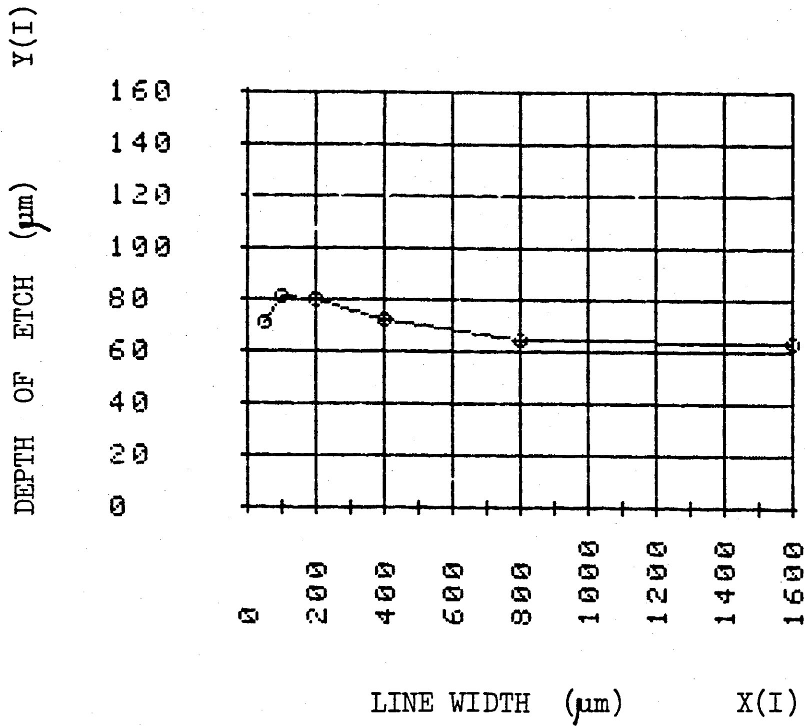

I	X(I)	Y(I)
1	50.0000	71.0000
2	100.0000	81.0000
3	200.0000	80.5000
4	400.0000	72.0000
5	800.0000	64.0000
6	1600.0000	63.0000

X(I) = LINE WIDTH (STENCIL) (μm)

Y(I) = DEPTH OF ETCH (μm)

Fig. 5.13 THE DEPTH OF ETCH VERSUS ETCHED LINE WIDTH IN 9 MINUTES.

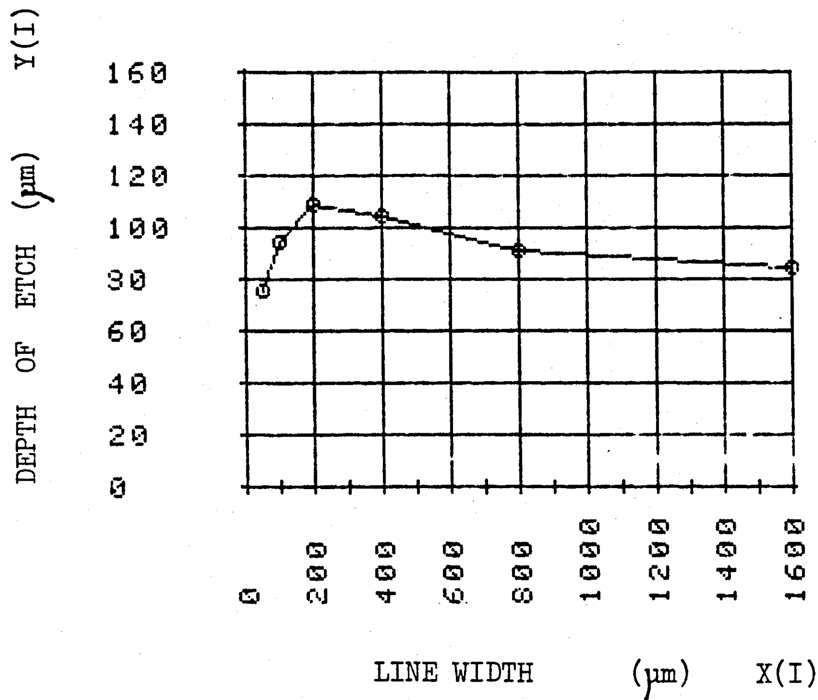

I	X(I)	Y(I)
1	50.0000	76.0000
2	100.0000	94.0000
3	200.0000	109.0000
4	400.0000	104.0000
5	800.0000	91.5000
6	1600.0000	84.6000

X(I) = LINE WIDTH (STENCIL) (μm)

Y(I) = DEPTH OF ETCH (μm)

Fig. 5.14 THE DEPTH OF ETCH VERSUS ETCHED LINE WIDTH IN 12 MINUTES.

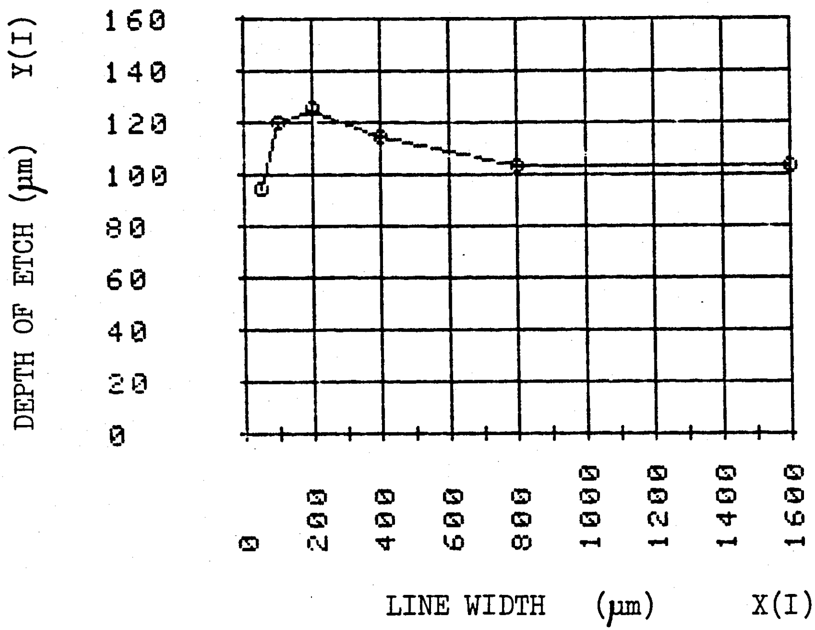

I	X(I)	Y(I)
1	50.0000	94.0000
2	100.0000	120.0000
3	200.0000	125.0000
4	400.0000	115.0000
5	800.0000	103.0000
6	1600.0000	103.0000

X(I) = LINE WIDTH (STENCIL) (μm)

Y(I) = DEPTH OF ETCH (μm)

Fig. 5.15 THE DEPH OF ETCH VERSUS ETCHED LINE WIDTH IN 15 MINUTES.

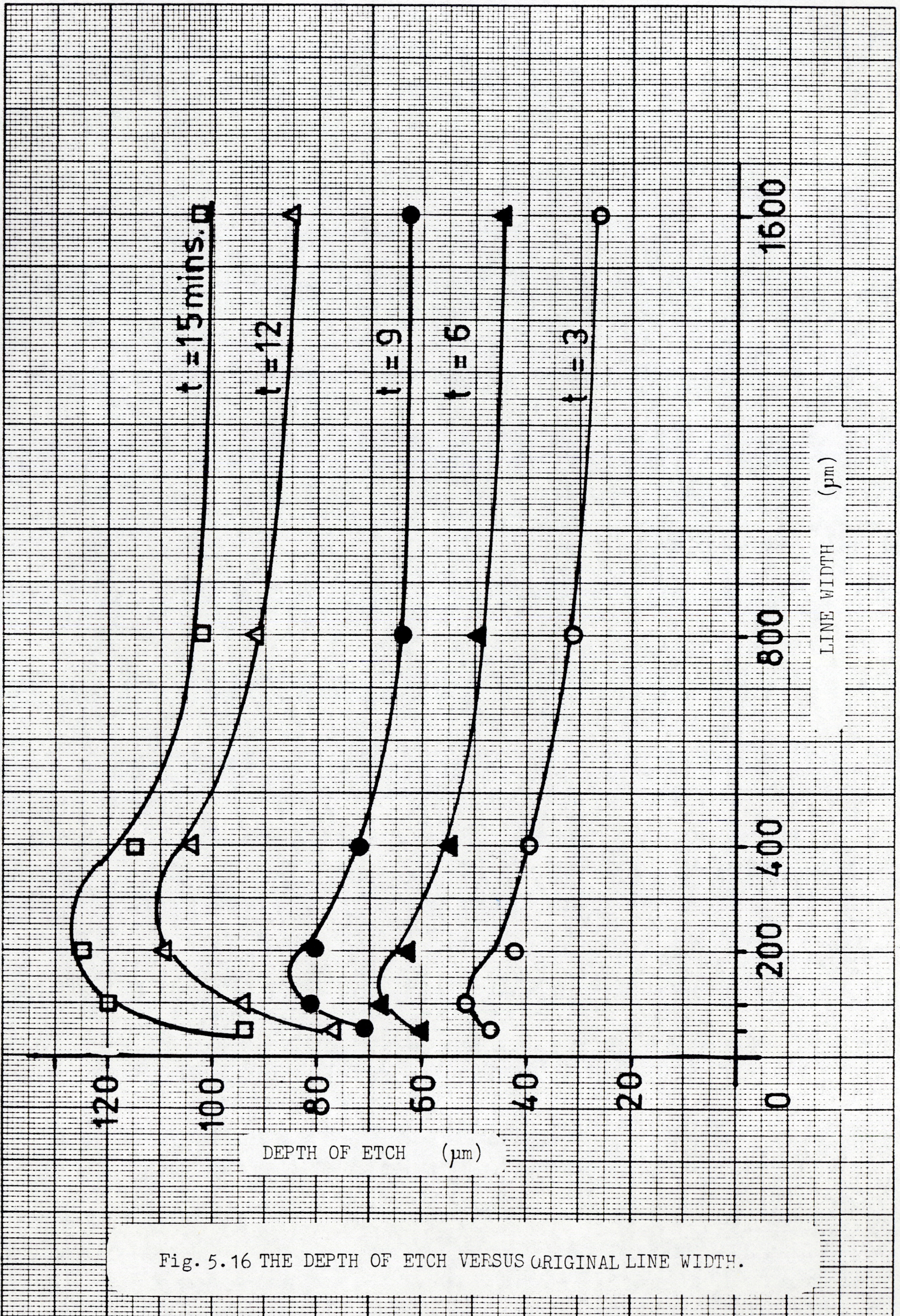

Fig. 5.16 THE DEPTH OF ETCH VERSUS ORIGINAL LINE WIDTH.

AOV: POWER: CODE 4

SOURCE/DF		SS	MS	F
TOTAL	4	0.3		
REG	1	0.3	0.3	95.3
RESID	3	0.0	0.0	

R SQUARE = 0.969

YHAT= 29.574X ^ 0.403

X(I)	Y(I)	YHAT	RESIDUALS
3.00	47.00	46.06	0.94
6.00	60.00	60.92	-0.92
9.00	71.00	71.75	-0.75
12.00	76.00	80.58	-4.58
15.00	94.00	88.16	5.84

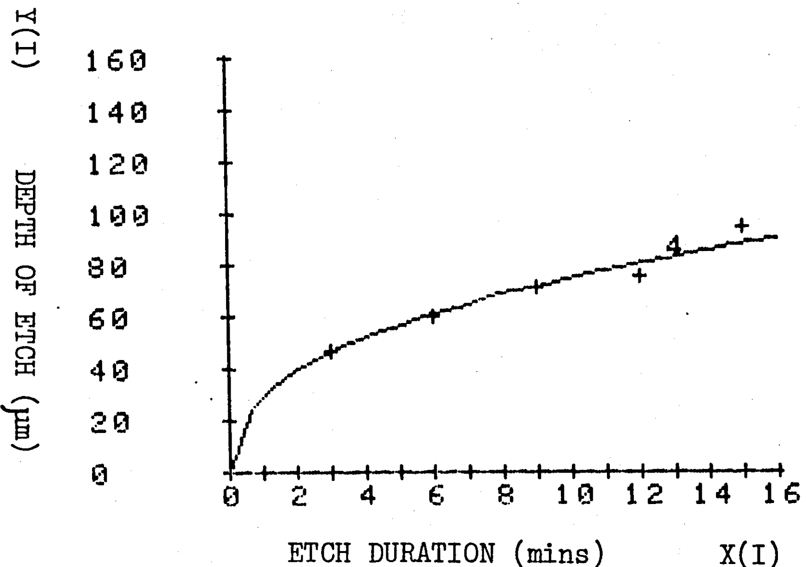

$$Y_{HAT} = 29.574t^{0.403}$$

Fig. 5.17 RESULTS AND PLOT OF THE DEPTH OF ETCH VERSUS ETCH DURATION FOR AN ORIGINAL LINE WIDTH OF 50 µm.

AOV: POWER: CODE 4

SOURCE/DF		SS	MS	F
TOTAL	4	0.4		
REG	1	0.4	0.4	74.8
RESID	3	0.0	0.0	

R SQUARE = 0.961

YHAT= 29.162X ^ 0.489

X(I)	Y(I)	YHAT	RESIDUALS
3.00	52.00	49.93	2.07
6.00	68.00	70.09	-2.09
9.00	81.00	85.48	-4.48
12.00	94.00	98.40	-4.40
15.00	120.00	109.76	10.24

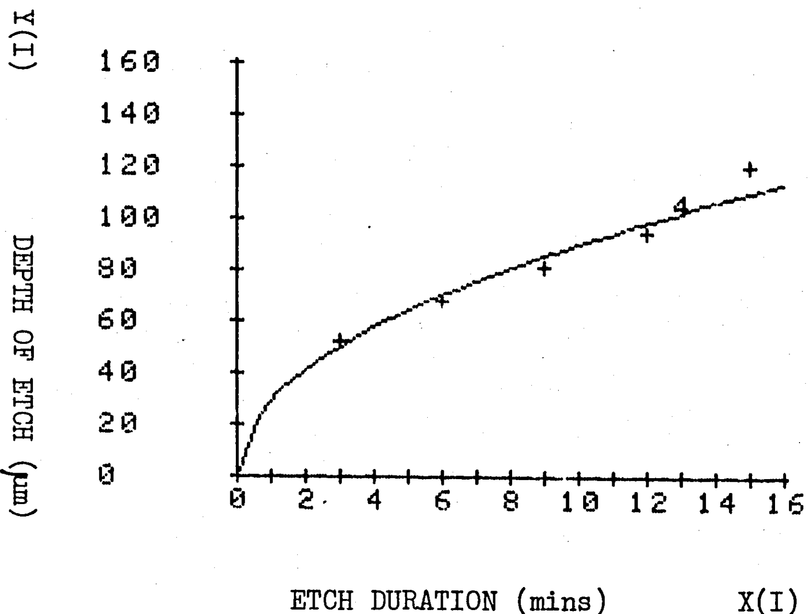

$Y_{HAT} = 29.162t^{0.489}$

Fig. 5.18 RESULTS AND PLOT OF THE DEPTH OF ETCH VERSUS ETCH DURATION FOR AN ORIGINAL LINE WIDTH OF 100 μm.

```
   AOV: POWER: CODE 4
SOURCE/DF       SS       MS       F
TOTAL   4       0.8
REG     1       0.8      0.8  253.3
RESID   3       0.0      0.0
R SQUARE =           0.988

YHAT=      19.142X ^         0.684
```

X(I)	Y(I)	YHAT	RESIDUALS
3.00	42.00	40.57	1.43
6.00	63.00	65.17	-2.17
9.00	80.50	85.99	-5.49
12.00	109.00	104.68	4.32
15.00	125.00	121.94	3.06

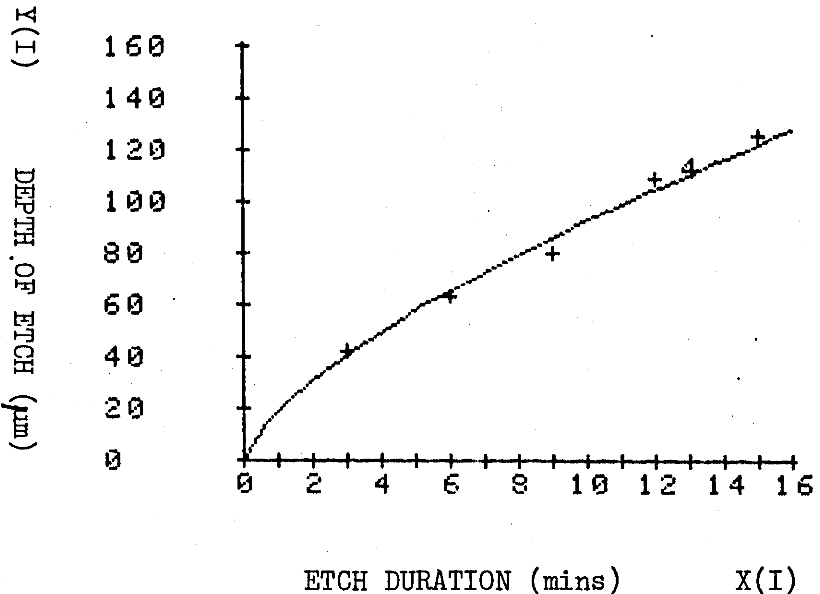

$$Y_{HAT} = 19.142t^{0.684}$$

Fig. 5.19 RESULTS AND PLOT OF THE DEPTH OF ETCH VERSUS ETCH DURATION FOR AN ORIGINAL LINE WIDTH OF 200 μm.

AOV: POWER: CODE 4

SOURCE/DF		SS	MS	F
TOTAL	4	0.8		
REG	1	0.8	0.8	90.8
RESID	3	0.0	0.0	

R SQUARE = 0.968

YHAT= 17.038X ^ 0.696

X(I)	Y(I)	YHAT	RESIDUALS
3.00	39.00	36.58	2.42
6.00	54.50	59.25	-4.75
9.00	72.00	78.55	-6.55
12.00	104.00	95.95	8.05
15.00	115.00	112.06	2.94

$$Y_{HAT} = 17.038t^{0.696}$$

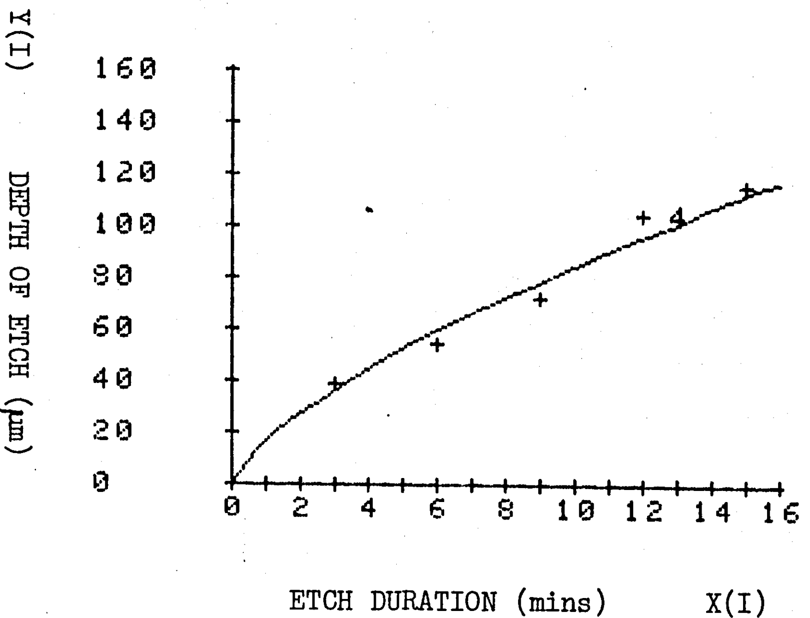

Fig. 5.20 RESULTS AND PLOT OF THE DEPTH OF ETCH VERSUS ETCH DURATION FOR AN ORIGINAL LINE WIDTH OF 400 μm.

AOV: POWER: CODE 4

SOURCE/DF		SS	MS	F
TOTAL	4	0.9		
REG	1	0.9	0.9	240.1
RESID	3	0.0	0.0	

R SQUARE = 0.988

YHAT= 13.058X ^ 0.759

X(I)	Y(I)	YHAT	RESIDUALS
3.00	31.00	30.05	0.95
6.00	49.50	50.84	-1.34
9.00	64.00	69.15	-5.15
12.00	91.50	86.01	5.49
15.00	103.00	101.87	1.13

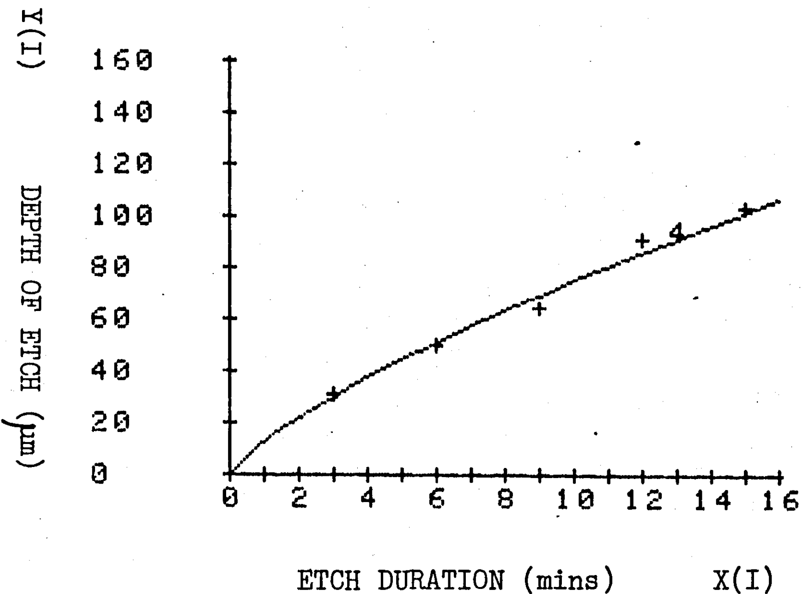

$$Y_{HAT} = 13.058t^{0.759}$$

Fig. 5.21 RESULTS AND PLOT OF THE DEPTH OF ETCH VERSUS ETCH DURATION FOR AN ORIGINAL LINE WIDTH OF 800 µm.

AOV: POWER: CODE 4

SOURCE/DF		SS	MS	F
TOTAL	4	1.2		
REG	1	1.2	1.2	999.9
RESID	3	0.0	0.0	

R SQUARE = 0.997

YHAT= 9.871X ^ 0.858

X(I)	Y(I)	YHAT	RESIDUALS
3.00	26.00	25.34	0.66
6.00	44.50	45.93	-1.43
9.00	63.00	65.04	-2.04
12.00	84.60	83.25	1.35
15.00	103.00	100.82	2.18

$$Y_{HAT} = 9.871t^{0.858}$$

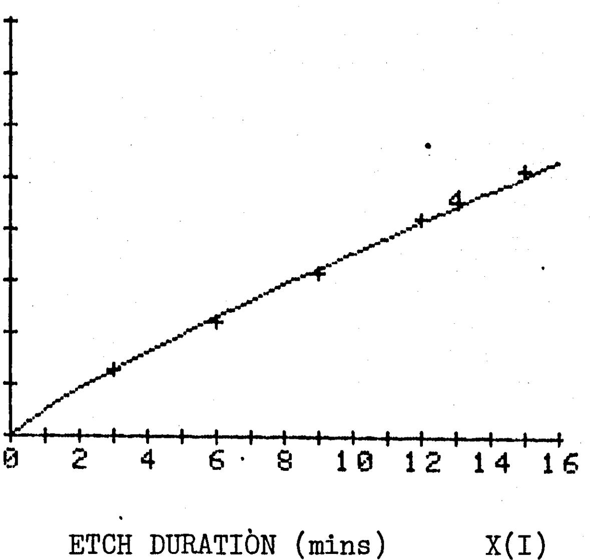

Fig. 5.22 RESULTS AND PLOT OF THE DEPTH OF ETCH VERSUS ETCH DURATION FOR AN ORIGINAL LINE WIDTH OF 1600 μm.

A=Original line width

A=50 µm

50

AOV: LINEAR REG:CODE 1

SOURCE/DF		SS	MS	F
TOTAL	4	1241.2		
REG	1	1210.0	1210.0	116.3
RESID	3	31.2	10.4	
R SQUARE =			0.975	

YHAT = 36.600 + 3.667 X

100

AOV: LINEAR REG:CODE 1

SOURCE/DF		SS	MS	F
TOTAL	4	2680.0		
REG	1	2624.4	2624.4	141.6
RESID	3	55.6	18.5	
R SQUARE =			0.979	

YHAT = 34.400 + 5.400 X

200

AOV: LINEAR REG:CODE 1

SOURCE/DF		SS	MS	F
TOTAL	4	4523.2		
REG	1	4494.4	4494.4	468.2
RESID	3	28.8	9.6	
R SQUARE =			0.994	

YHAT = 20.300 + 7.067 X

400

AOV: LINEAR REG:CODE 1

SOURCE/DF		SS	MS	F
TOTAL	4	4148.2		
REG	1	4060.2	4060.2	138.5
RESID	3	88.0	29.3	
R SQUARE =			0.979	

YHAT = 16.450 + 6.717 X

800

AOV: LINEAR REG:CODE 1

SOURCE/DF		SS	MS	F
TOTAL	4	3504.3		
REG	1	3459.6	3459.6	232.2
RESID	3	44.7	14.9	
R SQUARE =			0.987	

YHAT = 12.000 + 6.200 X

1600

AOV: LINEAR REG:CODE 1

SOURCE/DF		SS	MS	F
TOTAL	4	3770.4		
REG	1	3767.5	3767.5	999.9
RESID	3	2.9	1.0	
R SQUARE =			0.999	

YHAT = 5.990 + 6.470 X

Fig. 5.23 ANALYSIS OF VARIANCE FOR LINEAR REGRESSION APPLIED TO THE DEPTH OF ETCH EXPERIMENTAL DATA.

AOV: POWER: CODE 4

SOURCE/DF		SS	MS	F
TOTAL	5	0.9		
REG	1	0.9	0.9	114.4
RESID	4	0.0	0.0	

R SQUARE = 0.966

YHAT= 117.397X ^ -0.330

X(I)	Y(I)	YHAT	RESIDUALS
50.00	29.57	32.25	-2.67
100.00	29.16	25.65	3.51
200.00	19.14	20.40	-1.26
400.00	17.04	16.22	0.81
800.00	13.06	12.90	0.15
1600.00	9.87	10.26	-0.39

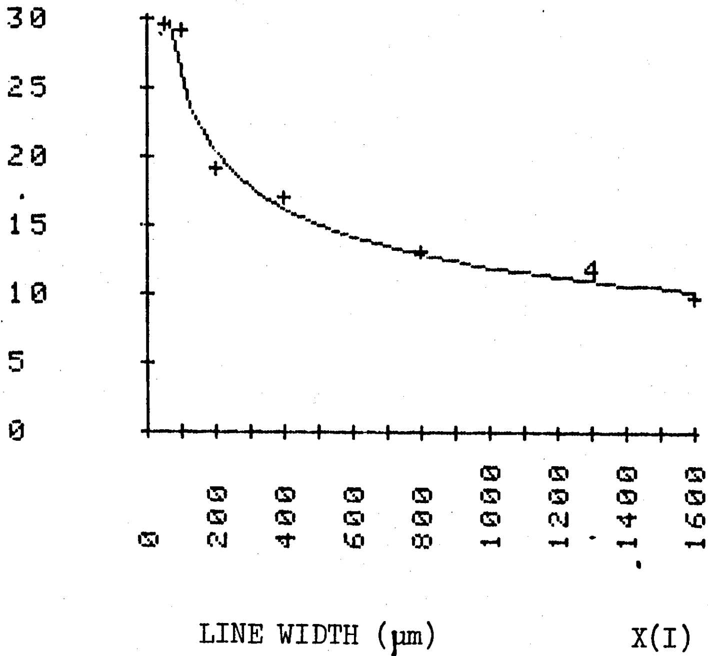

$$Y_{HAT} = a_{general} = 117.397A^{-0.33}$$

X(I) = CORRELATION COEFFICIENT 'a'

Y(I) = ORIGINAL LINE WIDTH (μm)

Fig. 5.24 THE CORRELATION COEFFICIENT 'a' FROM THE EQUATIONS FOR DEPTH OF ETCH VERSUS ETCH DURATIONS PLOTTED VERSUS ORIGINAL LINE WIDTH.

AOV: LOG REG:CODE 2

SOURCE/DF		SS	MS	F
TOTAL	5	0.1		
REG	1	0.1	0.1	66.0
RESID	4	0.0	0.0	

R SQUARE = 0.943

YHAT= -0.072+ 0.128LOG X

X(I)	Y(I)	YHAT	RESIDUALS
50.00	0.40	0.43	-0.02
100.00	0.49	0.52	-0.03
200.00	0.68	0.60	0.08
400.00	0.70	0.69	0.00
800.00	0.76	0.78	-0.02
1600.00	0.86	0.87	-0.01

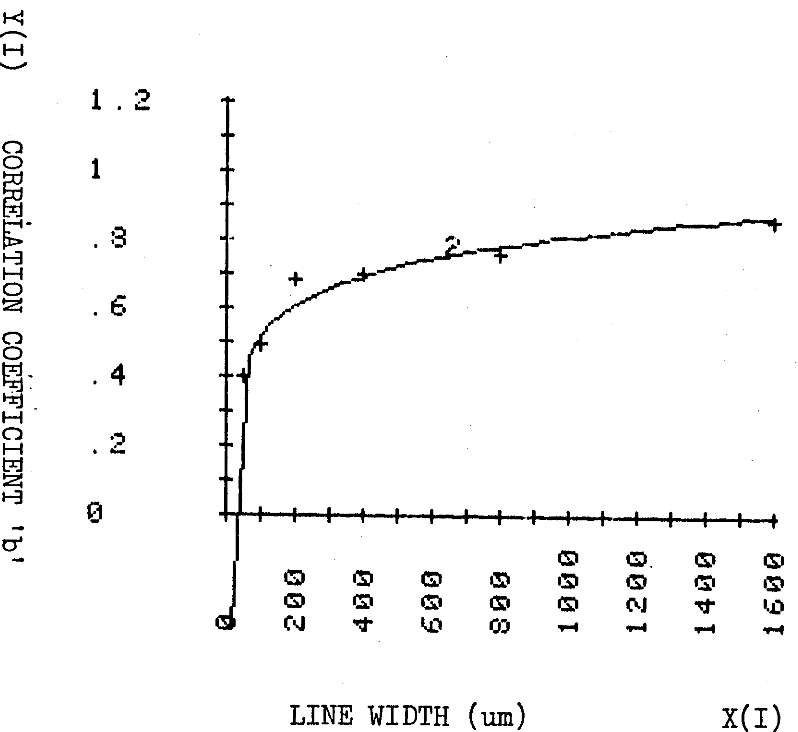

$$Y_{HAT} = b_{general} = -0.072 + 0.128 \ln A$$

X(I) = CORRELATION COEFFICIENT 'b'

Y(I) = ORIGINAL LINE WIDTH (um)

Fig. 5.25 THE CORRELATION COEFFICIENT 'b' FROM THE EQUATIONS FOR DEPTH OF ETCH VERSUS ETCH DURATIONS PLOTTED VERSUS ORIGINAL LINE WIDTH.

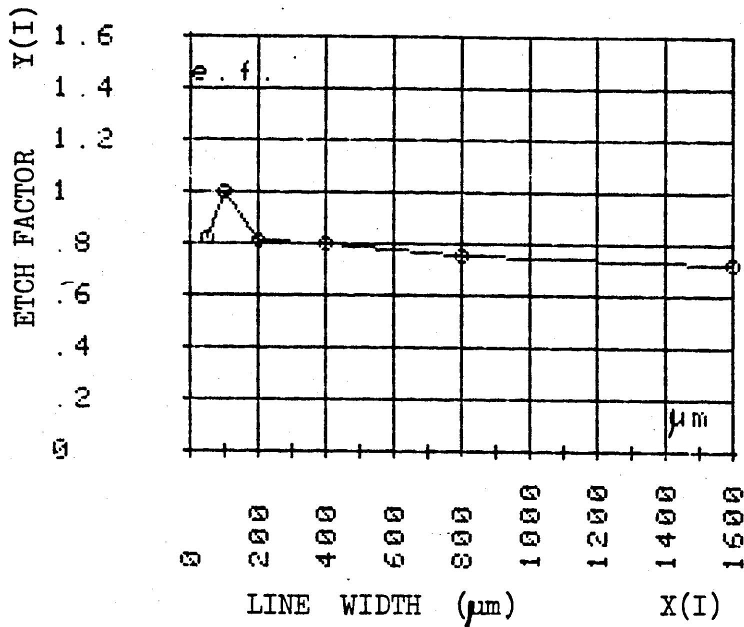

I	X(I)	Y(I)
1	50.0000	0.8250
2	100.0000	1.0000
3	200.0000	0.8080
4	400.0000	0.7960
5	800.0000	0.7560
6	1600.0000	0.7220

X(I) = ETCHED LINE STENCIL WIDTH (um)

Y(I) = ETCH FACTOR (e.f.)

t = 3 MINUTES

Fig. 5.26 THE ETCH FACTOR VERSUS ETCHED LINE WIDTH FOR AN ETCH DURATION OF 3 MINUTES.

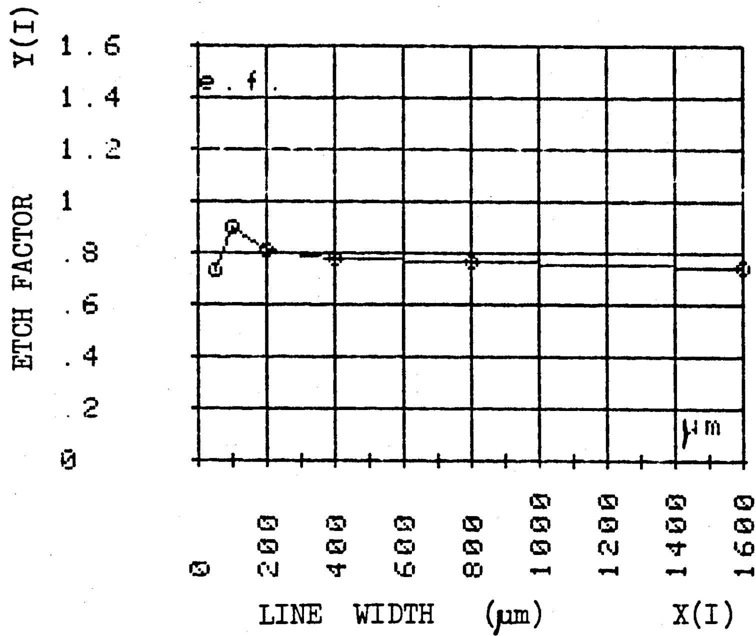

I	X(I)	Y(I)
1	50.0000	0.7330
2	100.0000	0.8950
3	200.0000	0.8080
4	400.0000	0.7830
5	800.0000	0.7670
6	1600.0000	0.7470

X(I) = ETCHED LINE STENCIL WIDTH (µm)

Y(I) = ETCH FACTOR (e.f.)

t = 6 MINUTES

Fig. 5.27 THE ETCH FACTOR VERSUS ETCHED LINE WIDTH FOR AN ETCH DURATION OF 6 MINUTES.

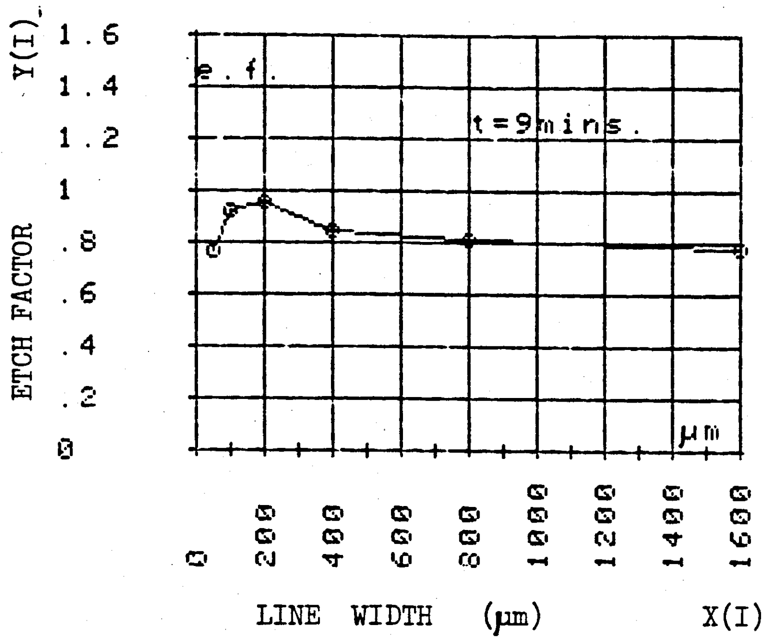

I	X(I)	Y(I)
1	50.0000	0.7720
2	100.0000	0.9190
3	200.0000	0.9570
4	400.0000	0.8480
5	800.0000	0.8070
6	1600.0000	0.7790

X(I) = ETCHED LINE STENCIL WIDTH (μm)

Y(I) = ETCH FACTOR (e.f.)

t = 9 MINUTES

Fig. 5.28 THE ETCH FACTOR VERSUS ETCHED LINE WIDTH FOR AN ETCH DURATION OF 9 MINUTES.

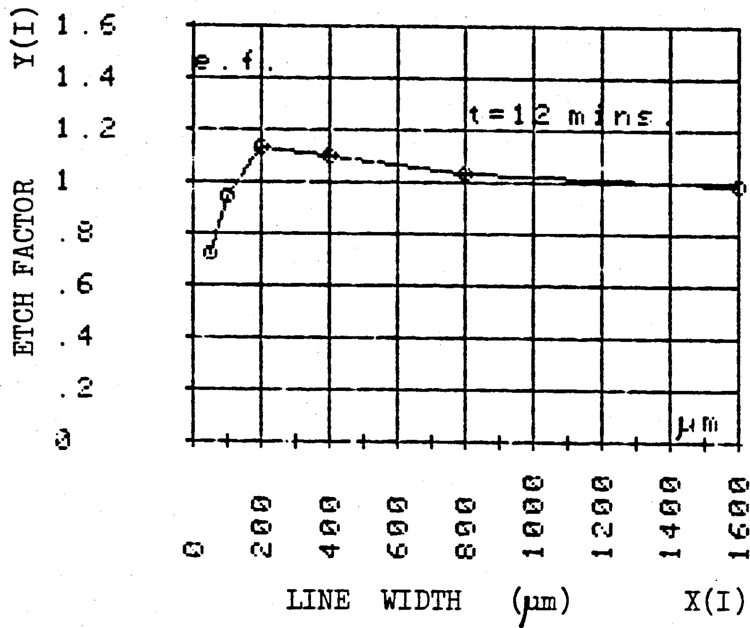

I	X(I)	Y(I)
1	50.0000	0.7260
2	100.0000	0.9400
3	200.0000	1.1350
4	400.0000	1.1020
5	800.0000	1.0320
6	1600.0000	0.9910

X(I) = ETCHED LINE STENCIL WIDTH (µm)

Y(I) = ETCH FACTOR (e.f.)

t = 12 MINUTES

Fig.5. 29 THE ETCH FACTOR VERSUS ETCHED LINE WIDTH FOR AN ETCH DURATION OF 12 MINUTES.

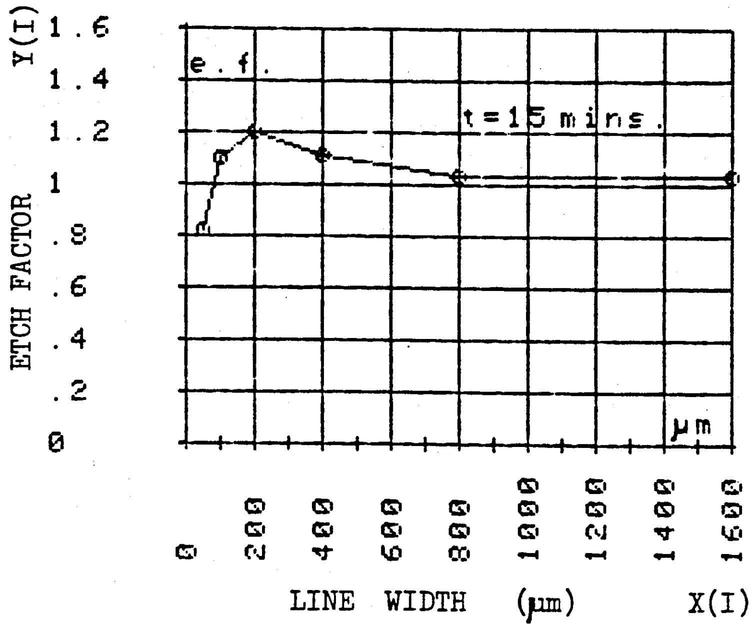

I	X(I)	Y(I)
1	50.0000	0.8230
2	100.0000	1.0960
3	200.0000	1.2030
4	400.0000	1.1070
5	800.0000	1.0280
6	1600.0000	1.0300

X(I) = ETCHED LINE STENCIL WIDTH (μm)

Y(I) = ETCH FACTOR (e.f.)

t = 15 MINUTES

Fig.5.30 THE ETCH FACTOR VERSUS ETCHED LINE WIDTH FOR AN ETCH DURATION OF 15 MINUTES.

$$\text{ETCH FACTOR e.f.} = \frac{DE}{UC} = \frac{117.4A^{-0.33} \cdot t^{(0.128\ \ln.\ A\ -\ 0.072)}}{79.9\ A^{(0.007t\ -\ 0.133)}\ t^{0.181}}$$

$$= 1.47\ A^{-(0.007\ t\ +\ 0.197)} \cdot t^{(0.128\ \ln.A\ -\ 0.2)}$$

WHERE A = ORIGINAL LINE WIDTH (μm)
t = ETCH DURATION IN (mins)

Note the above equation is only used for detecting the general trend for etch factor by pooling all the results.

ORIGINAL LINE WIDTH (μm) / ETCH DURATION (mins)	3	6	9	12	15
50	0.872 */	0.99 *	1.03 +	1.035 + $	1.019 +
100	0.826 /	0.982	1.044	1.06 $	1.049
200	0.783 /	0.976	1.06	1.088 $	1.083
400	0.742 /	0.970	1.076	1.117	1.118 $
800	0.704 /	0.964	1.093	1.155 $	1.154
1600	0.666 +/	0.956 +	1.107 *	1.175 *	1.188 * $

* highest e.f. in columns + lowest e.f. in columns

$ highest e.f. in rows / lowest e.f. in rows

Fig. 5.31 THE GENERAL ETCH FACTOR TREND IN TERMS OF LINE WIDTH AND ETCH DURATION.

EQUATION FOR THE e.f. TREND =

$$1.47\ A^{-(0.007\ t\ +\ 0.197)}\ .\ t^{(0.128\ \ln.A\ -\ 0.2)}$$

WHERE A = ORIGINAL LINE WIDTH (μm)

t = ETCH DURATION IN (mins)

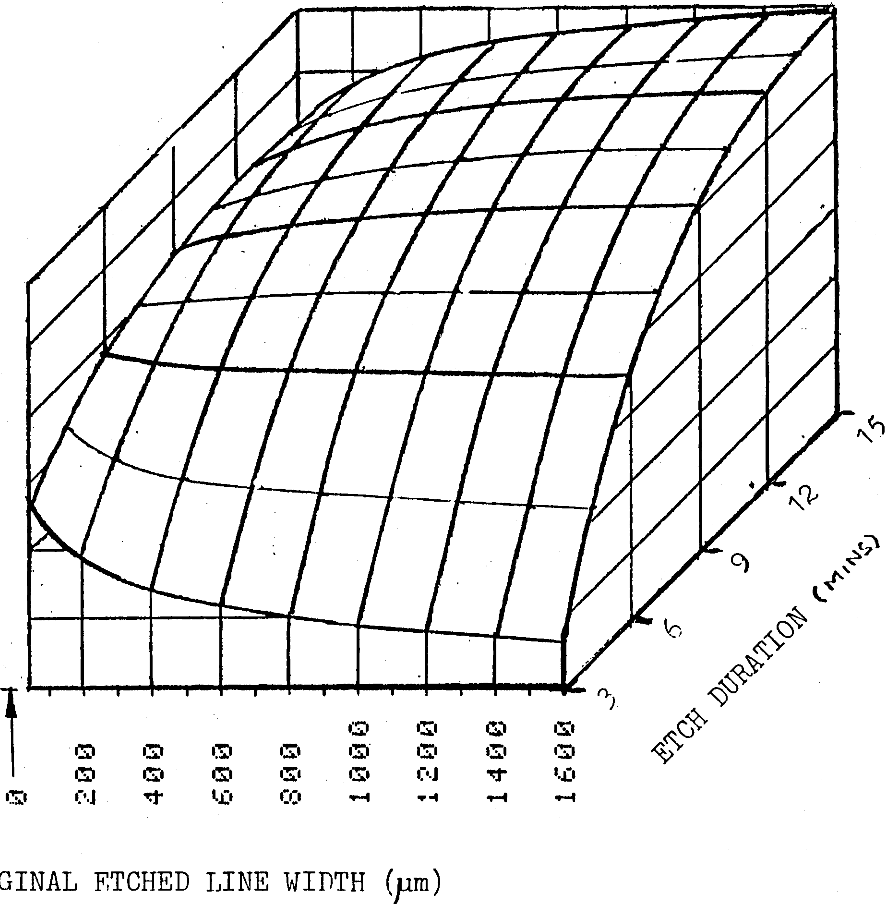

Fig. 5.3 2 THREE DIMENSIONAL PLOT OF THE POOLED EXPERIMENTAL DATA ILLUSTRATING ETCH FACTOR IN TERMS OF ETCH DURATION AND ORIGINAL LINE WIDTH.

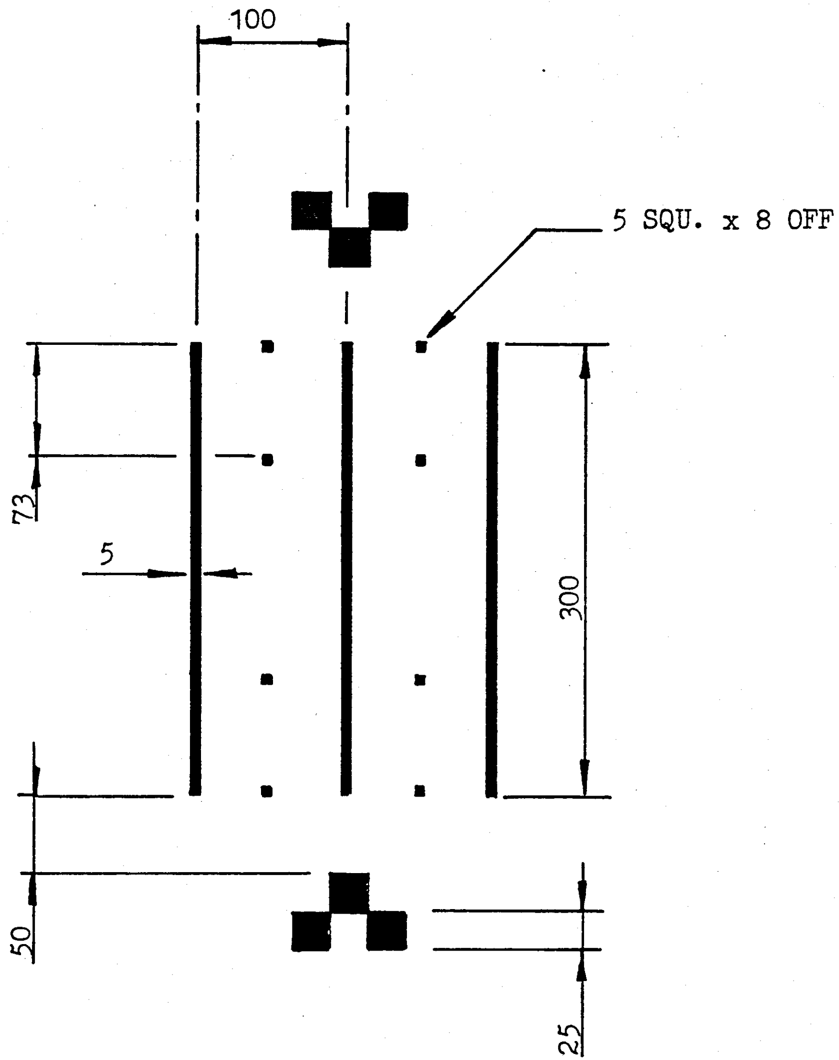

ALL DIMENSIONS IN mm

Fig. 5.33 DIMENSIONS FOR THE DOUBLE SIDED TOOL ARTWORK.

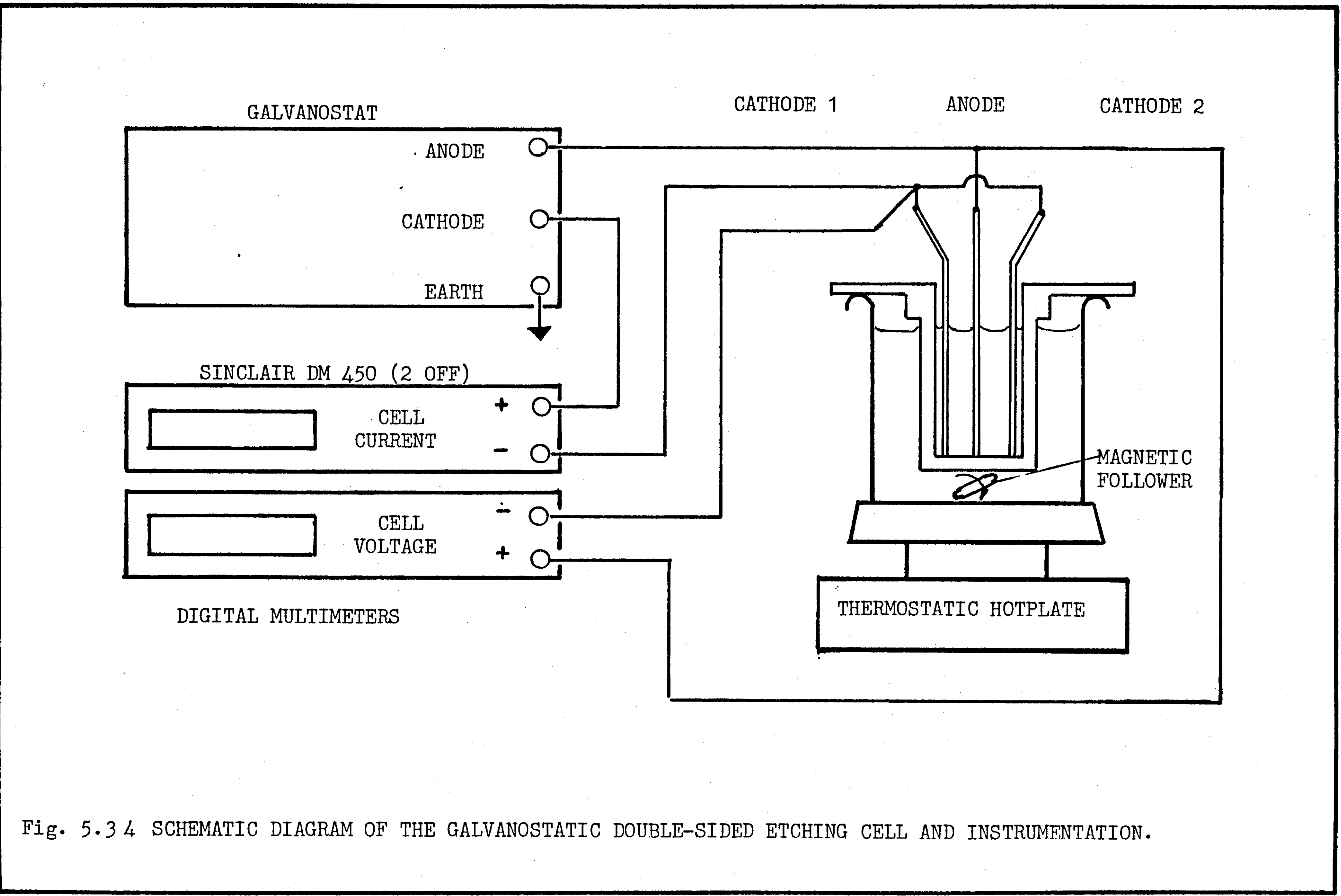

Fig. 5.3 4 SCHEMATIC DIAGRAM OF THE GALVANOSTATIC DOUBLE-SIDED ETCHING CELL AND INSTRUMENTATION.

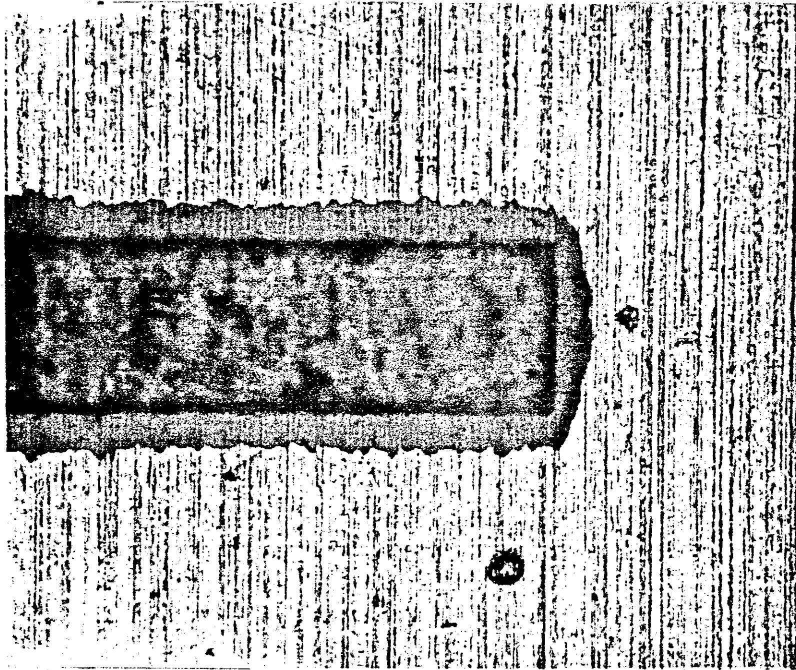

a)

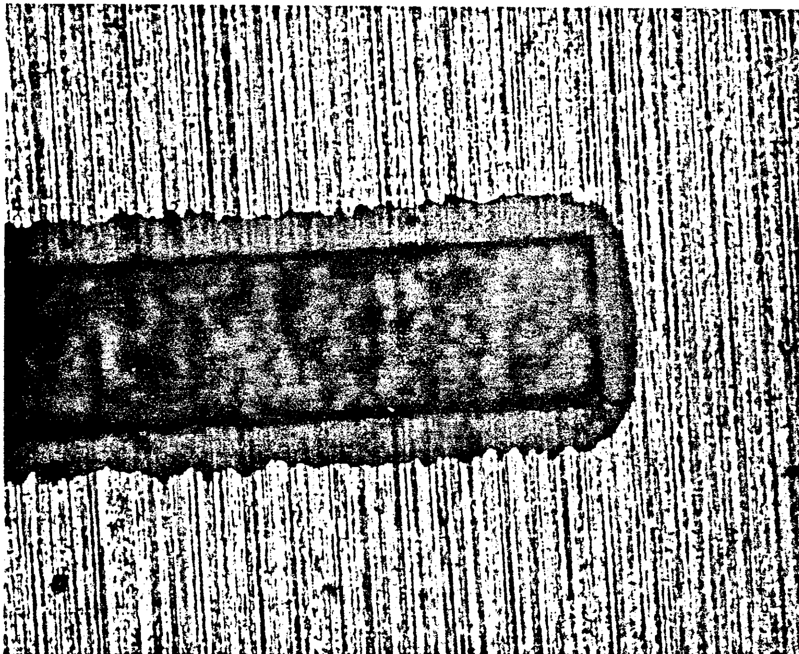

b)

Fig. 5.35 PHOTOMICROGRAPH (X100) OF THE SURFACE OF THE RESIST WHEN DOUBLE-SIDED ETCHING.

a) t = 6 minutes

b) t = 8 minutes

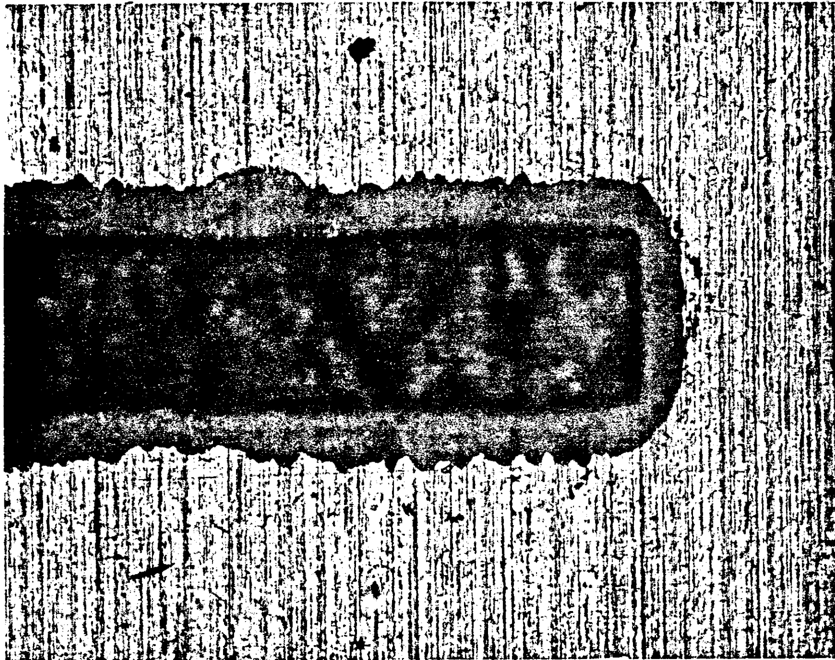

c)

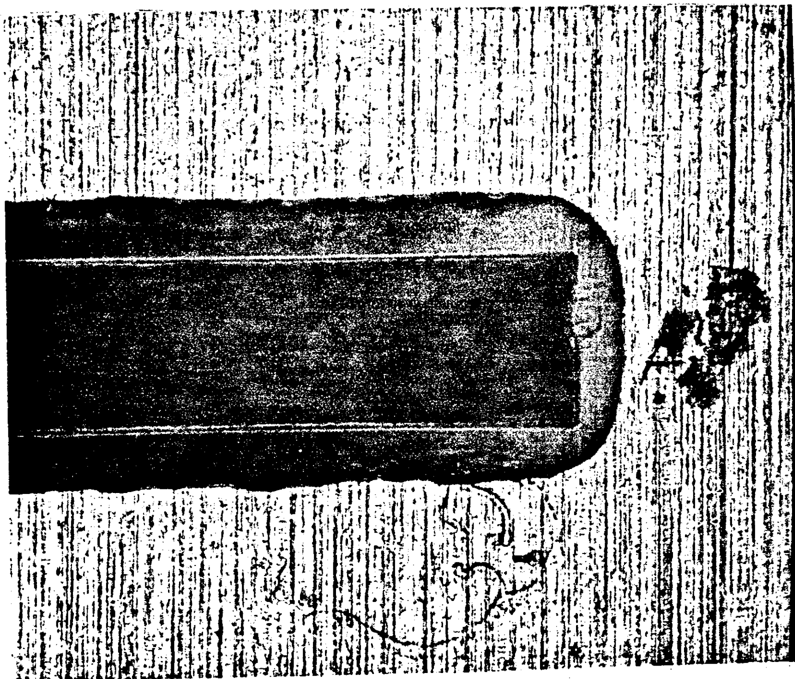

d)

Fig. 5.36 PHOTOMICROGRAPH (X100) OF THE SURFACE OF THE RESIST WHEN DOUBLE-SIDED ETCHING.

c) t = 10 minutes

d) t = 12 minutes

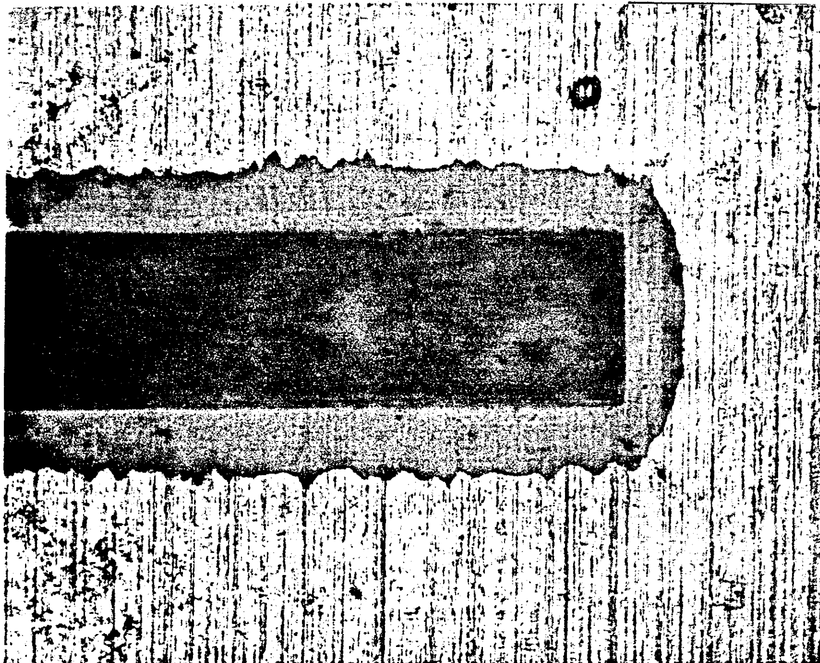

Fig. 5.37 PHOTOMICROGRAPH (X100) OF THE SURFACE OF THE RESIST WHEN DOUBLE-SIDED ETCHING.

e) t = 14 minutes

I	X(I)	Y(I)
1	6.0000	46.2500
2	8.0000	63.7500
3	10.0000	75.2500
4	12.0000	82.5000
5	14.0000	88.8000

AOV: POWER: CODE 4

SOURCE/DF		SS	MS	F
TOTAL	4	0.3		
REG	1	0.3	0.3	83.8
RESID	3	0.0	0.0	

R SQUARE = 0.965

YHAT= 12.441X ^ 0.762

X(I)	Y(I)	YHAT	RESIDUALS
6.00	46.25	48.69	-2.44
8.00	63.75	60.62	3.13
10.00	75.25	71.85	3.40
12.00	82.50	82.55	-0.05
14.00	88.80	92.84	-4.04

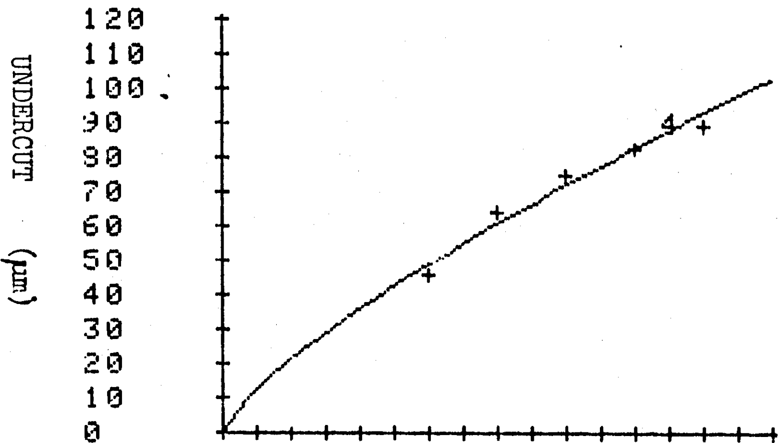

X(I) = THE ETCH DURATION (mins.)

Y(I) = THE UNDERCUT (µm)

$$U_d = Y_{HAT} = 12.441\, t^{0.762} \quad \text{(um)}$$

Fig. 5.38 THE UNDERCUT VERSUS ETCH DURATION FOR DOUBLE-SIDED ETCHING.

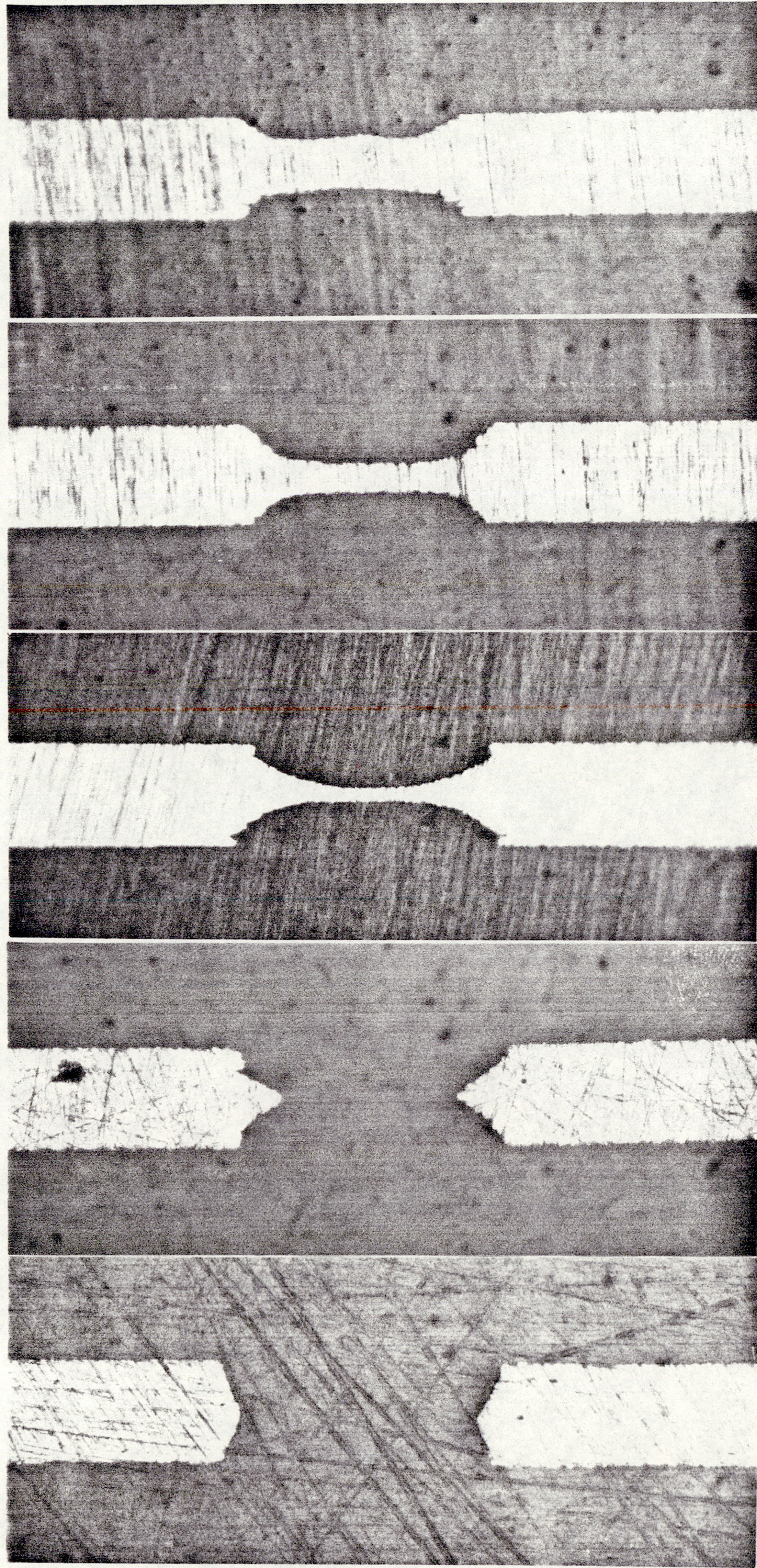

Fig. 5.39 PHOTOMICROGRAPHS (X100) OF THE CROSS-SECTIONS OF THE DOUBLE-SIDED RESULTS; PRINT MAG. = X96.7 .

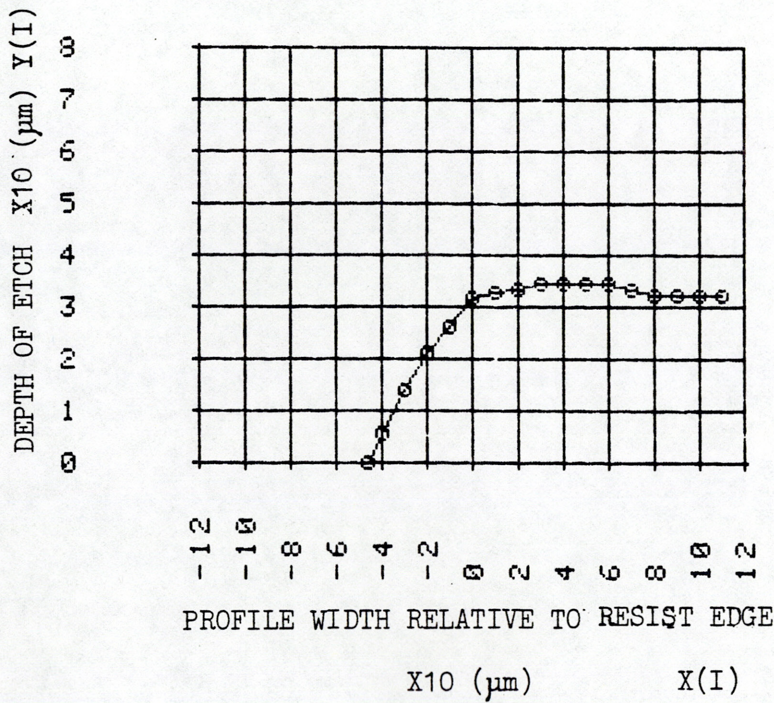

I	X(I) X10	Y(I) X10
1	-4.6250	0.0000
2	-4.0000	0.5500
3	-3.0000	1.4130
4	-2.0000	2.1380
5	-1.0000	2.6380
6	0.0000	3.1750
7	1.0000	3.2880
8	2.0000	3.3500
9	3.0000	3.4250
10	4.0000	3.4370
11	5.0000	3.4500
12	6.0000	3.4500
13	7.0000	3.3500
14	8.0000	3.2130
15	9.0000	3.2000
16	10.0000	3.2150
17	11.0000	3.2200

X(I) = THE PROFILE WIDTH RELATIVE TO THE RESIST EDGE X10 (µm).

Y(I) = THE DEPTH OF ETCH X10 (µm).

t = 6 MINUTES

Fig. 5.40 THE AVERAGE CROSS-SECTIONAL PROFILE FOR DOUBLE-SIDED ETCHING; t = 6 mins.

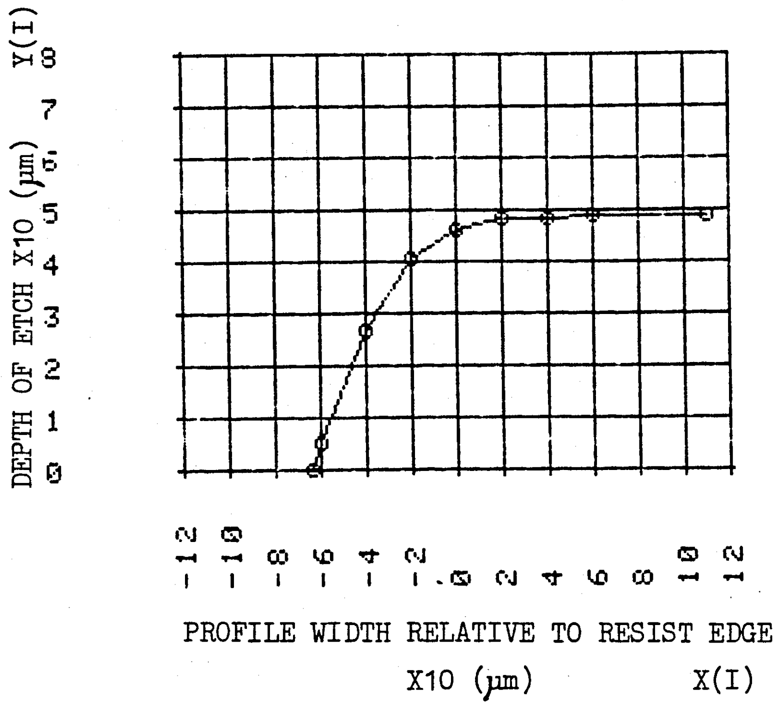

I	X(I) X 10	Y(I) X 10
1	-6.3750	0.0000
2	-6.0000	0.5130
3	-4.0000	2.6900
4	-2.0000	4.0500
5	0.0000	4.6250
6	2.0000	4.8130
7	4.0000	4.8130
8	6.0000	4.8750
9	11.0000	4.8750

X(I) = THE PROFILE WIDTH RELATIVE TO THE RESIST EDGE X10 (µm).

Y(I) = THE DEPTH OF ETCH X10 (µm).

t = 8 MINUTES

Fig.5.41 THE AVERAGE CROSS-SECTIONAL PROFILE FOR DOUBLE-SIDED ETCHING ; t = 8 mins.

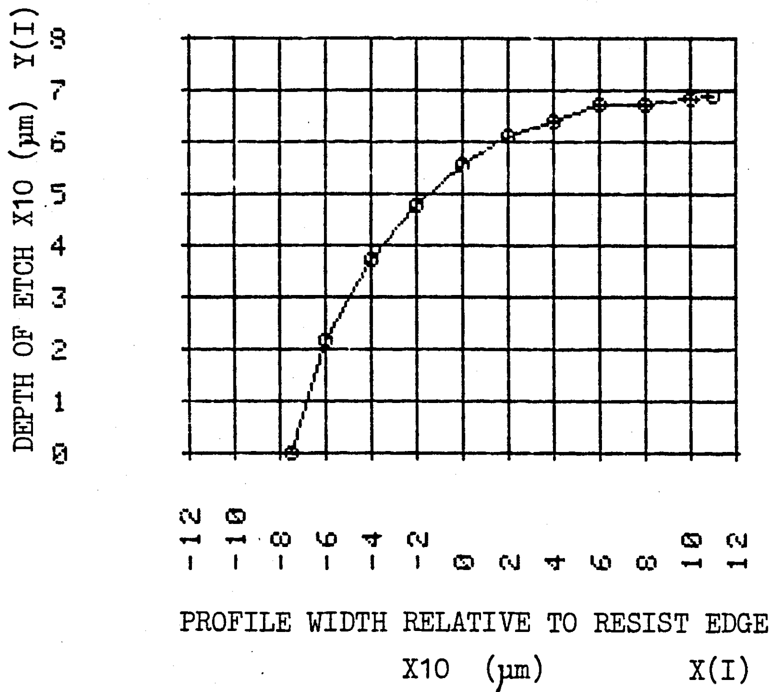

I	X(I) X10	Y(I)X10
1	-7.5250	0.0000
2	-6.0000	2.1600
3	-4.0000	3.7500
4	-2.0000	4.8000
5	0.0000	5.5800
6	2.0000	6.1000
7	4.0000	6.3900
8	6.0000	6.7100
9	8.0000	6.7500
10	10.0000	6.8500
11	11.0000	6.9000

X(I) = THE PROFILE WIDTH RELATIVE TO THE RESIST EDGE X10 (μm).

Y(I) = THE DEPTH OF ETCH X10 (μm).

t = 10 MINUTES

Fig. 5.42 THE AVERAGE CROSS-SECTIONAL PROFILE FOR DOUBLE-SIDED ETCHING ; t = 10 mins.

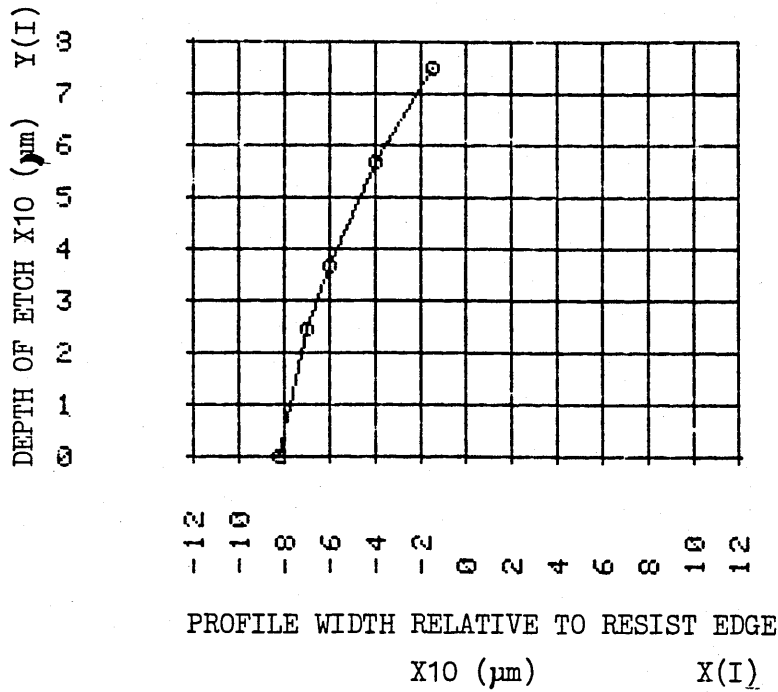

I	X(I) X10	Y(I) X10
1	-1.5000	7.5000
2	-4.0000	5.6750
3	-6.0000	3.6900
4	-7.0000	2.4250
5	-8.2500	0.0000

X(I) = THE PROFILE WIDTH RELATIVE TO THE RESIST EDGE X10 (μm).

Y(I) = THE DEPTH OF RTCH X10 (μm).

t = 12 MINUTES

Fig.5.43 THE AVERAGE CROSS-SECTIONAL PROFILE FOR DOUBLE-SIDED ETCHING ; t = 12 mins.

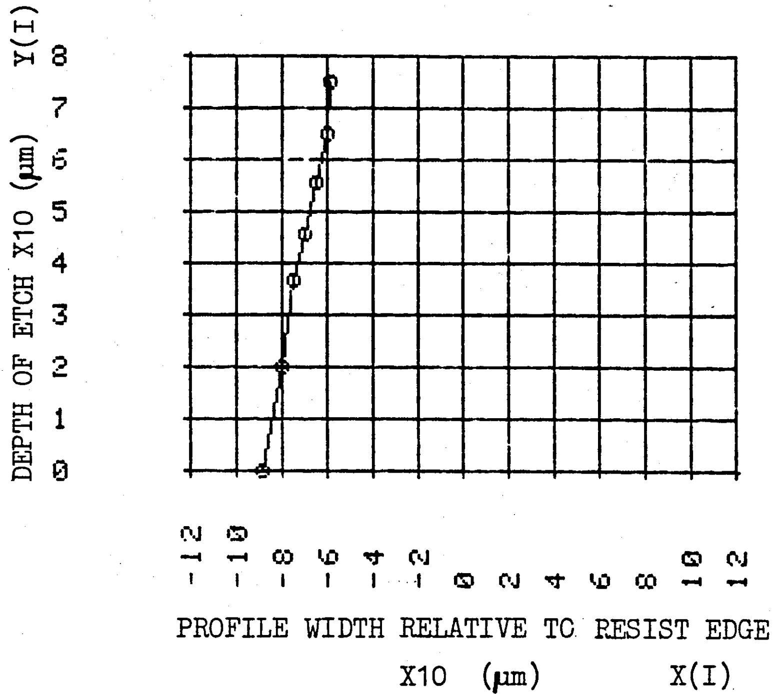

I	X(I) X10	Y(I) X10
1	-8.8800	0.0000
2	-8.0000	2.0000
3	-7.5000	3.6500
4	-7.0000	4.5300
5	-6.5000	5 5500
6	-6.0000	6.5000
7	-5.9000	7.5000

X(I) = THE PROFILE WIDTH RELATIVE TO THE RESIST EDGE X10 (µm).

Y(I) = THE DEPTH OF THE ETCH X10 (µm).

t = 14 MINUTES

Fig. 5.44 THE AVERAGE CROSS-SECTIONAL PROFILE FOR DOUBLE-SIDED ETCHING ; t = 14 mins.

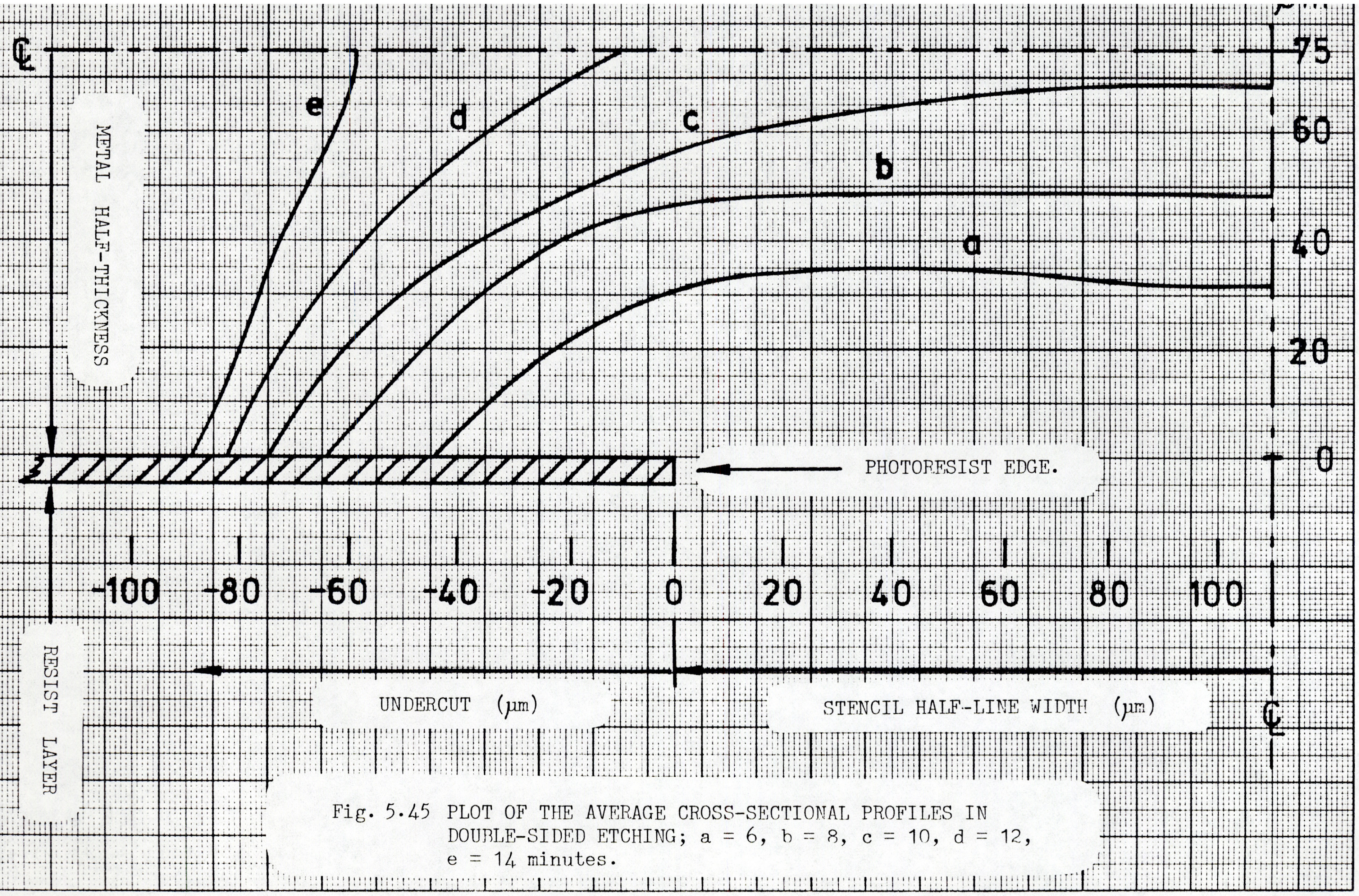

Fig. 5.45 PLOT OF THE AVERAGE CROSS-SECTIONAL PROFILES IN DOUBLE-SIDED ETCHING; a = 6, b = 8, c = 10, d = 12, e = 14 minutes.

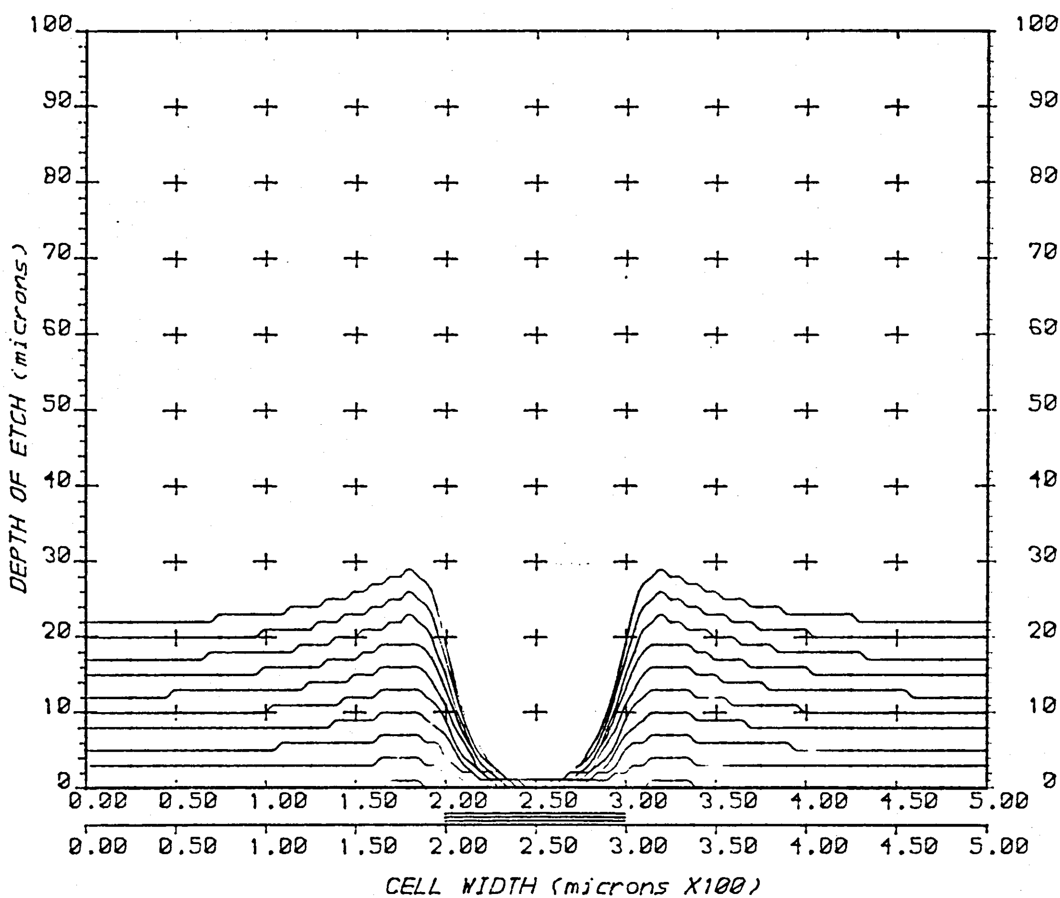

Temperature	25°C
Electrolyte conductivity	0.035 Ω^{-1}
Constant polarization (A)	130 mV
Interelectrode gap	5 mm
Overrelaxation parameter (w)	1.85
convergence criterion	10^{-5} to 10^{-4}
calculated atomic weight	55.14 (Alloy)
Density	7.913 gms/cm^3
Calculated valency	1.97 (Alloy)
Efficiency	100%
coulombs per time step	1.5
Anode potential	5 volts
Cathode potential	0 volts
Max. field iterations	2000
Feature 'a'	200 μm
Insulator	100 μm
feature 'b'	200 μm

Fig. 5.46 NUMERICAL SIMULATION OF A CENTRALLY POSITIONED INSULATOR (DIMENSION 100 μm)

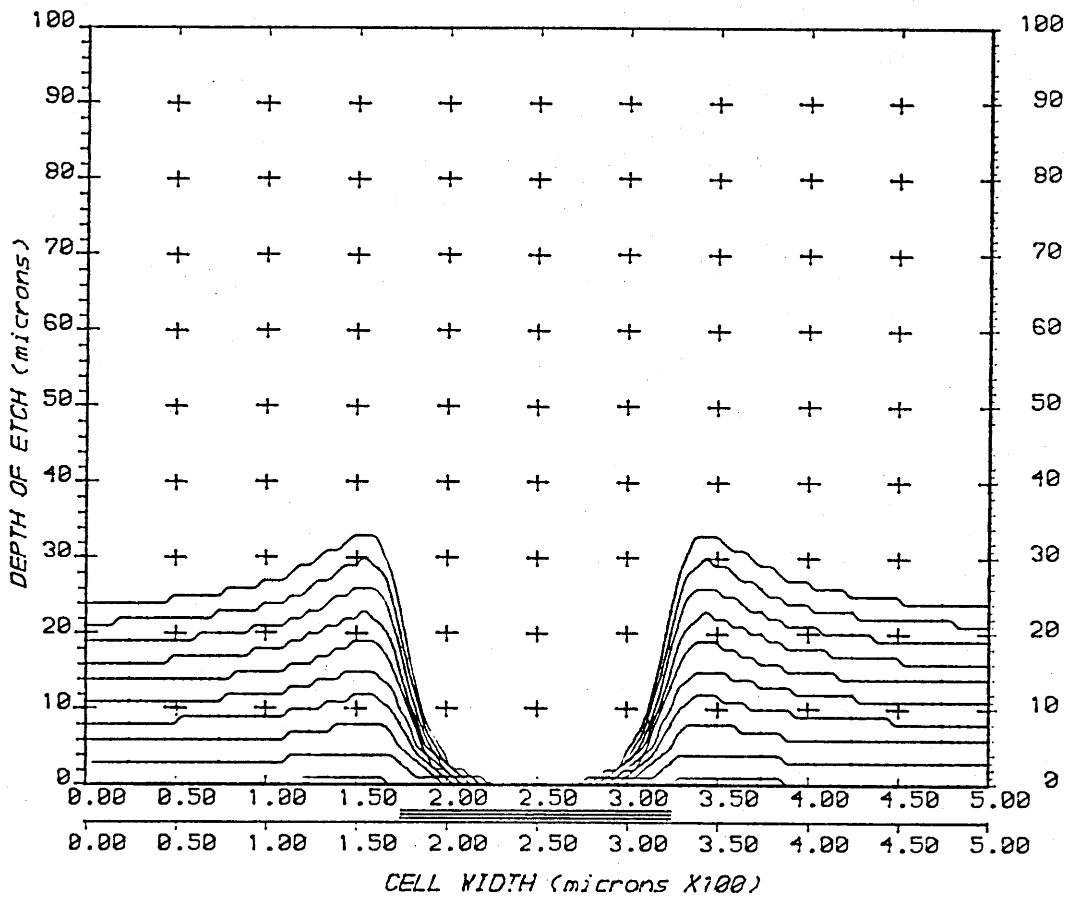

Temperature	25°C
Electrolyte conductivity	0.035 Ω^{-1}
Constant polarization (A)	130 mV
Interelectrode gap	5 mm
Overrelaxation parameter (w)	1.85
convergence criterion	10^{-5} to 10^{-4}
calculated atomic weight	55.14 (Alloy)
Density	7.913 gms/cm^3
Calculated valency	1.97 (Alloy)
Efficiency	100%
coulombs per time step	1.5
Anode potential	5 volts
Cathode potential	0 volts
Max. field iterations	2000
Feature 'a'	175 µm
Insulator	150 µm
feature 'b'	175 µm

Fig. 5.47 NUMERICAL SIMULATION OF A CENTRALLY POSITIONED INSULATOR (DIMENSION 150 µm)

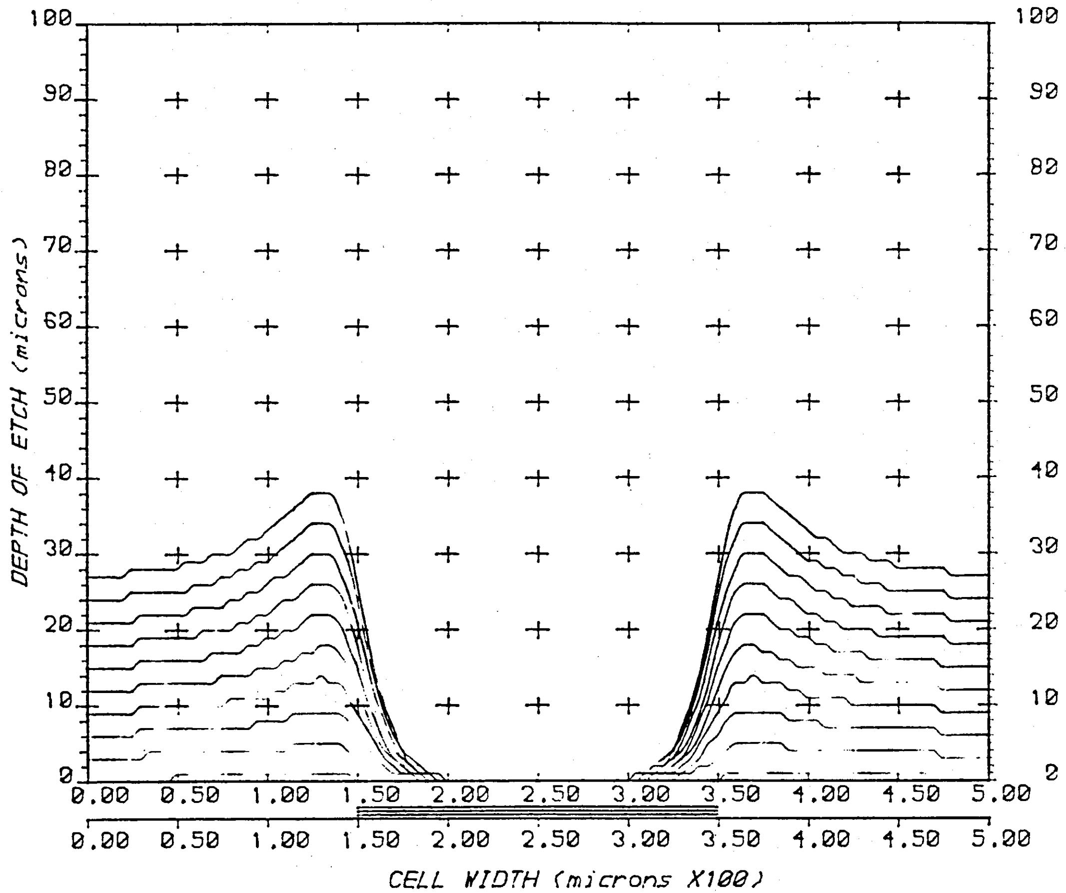

Temperature	25°C
Electrolyte conductivity	0.035 Ω^{-1}
Constant polarization (A)	130 mV
Interelectrode gap	5 mm
Overrelaxation parameter (w)	1.85
convergence criterion	10^{-5} to 10^{-4}
calculated atomic weight	55.14 (Alloy)
Density	7.913 gms/cm^3
Calculated valency	1.97 (Alloy)
Efficiency	100%
coulombs per time step	1.5
Anode potential	5 volts
Cathode potential	0 volts
Max. field iterations	2000
Feature 'a'	150 µm
Insulator	200 µm
feature 'b'	150 µm

Fig. 5.48 NUMERICAL SIMULATION OF A CENTRALLY POSITIONED INSULATOR (DIMENSION 200 µm)

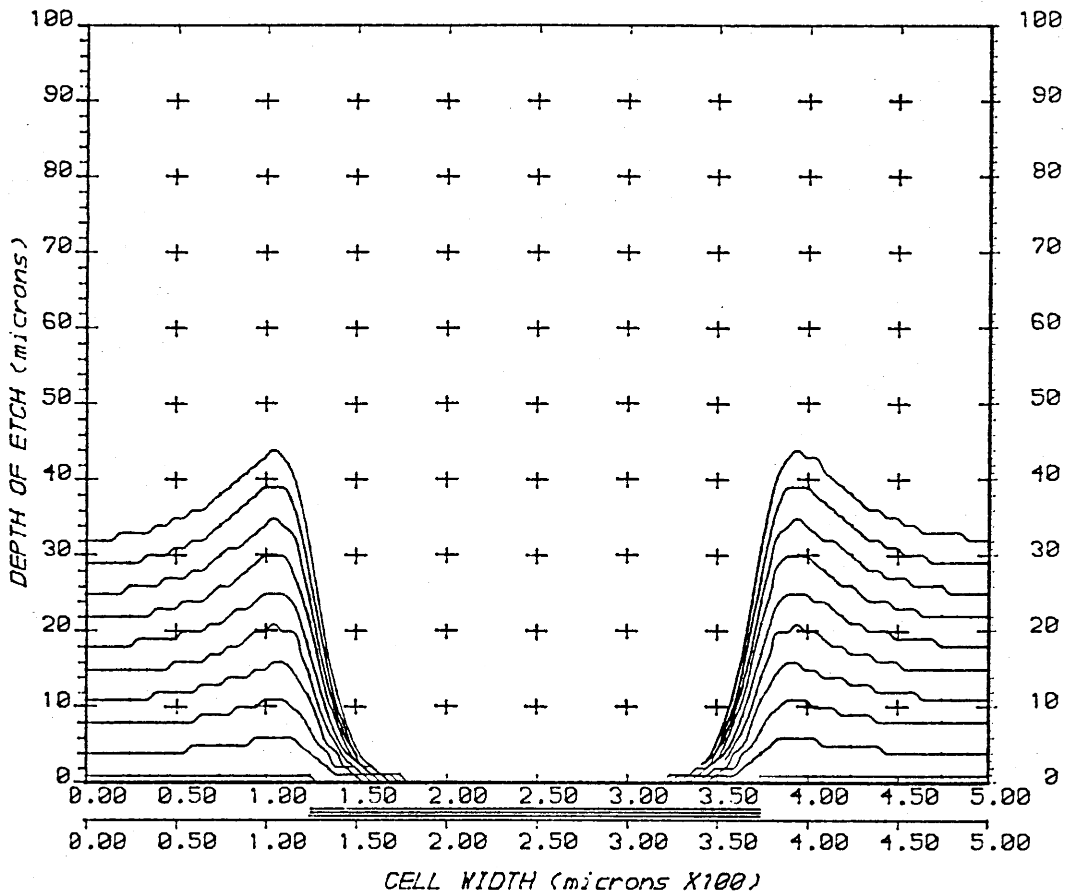

Temperature	25°C
Electrolyte conductivity	0.035 Ω^{-1}
Constant polarization (A)	130 mV
Interelectrode gap	5 mm
Overrelaxation parameter (w)	1.85
convergence criterion	10^{-5} to 10^{-4}
calculated atomic weight	55.14 (Alloy)
Density	7.913 gms/cm^3
Calculated valency	1.97 (Alloy)
Efficiency	100%
coulombs per time step	1.5
Anode potential	5 volts
Cathode potential	0 volts
Max. field iterations	2000
Feature 'a'	125 µm
Insulator	250 µm
feature 'b'	125 µm

Fig. 5.49 NUMERICAL SIMULATION OF A CENTRALLY POSITIONED INSULATOR (DIMENSION 250 µm)

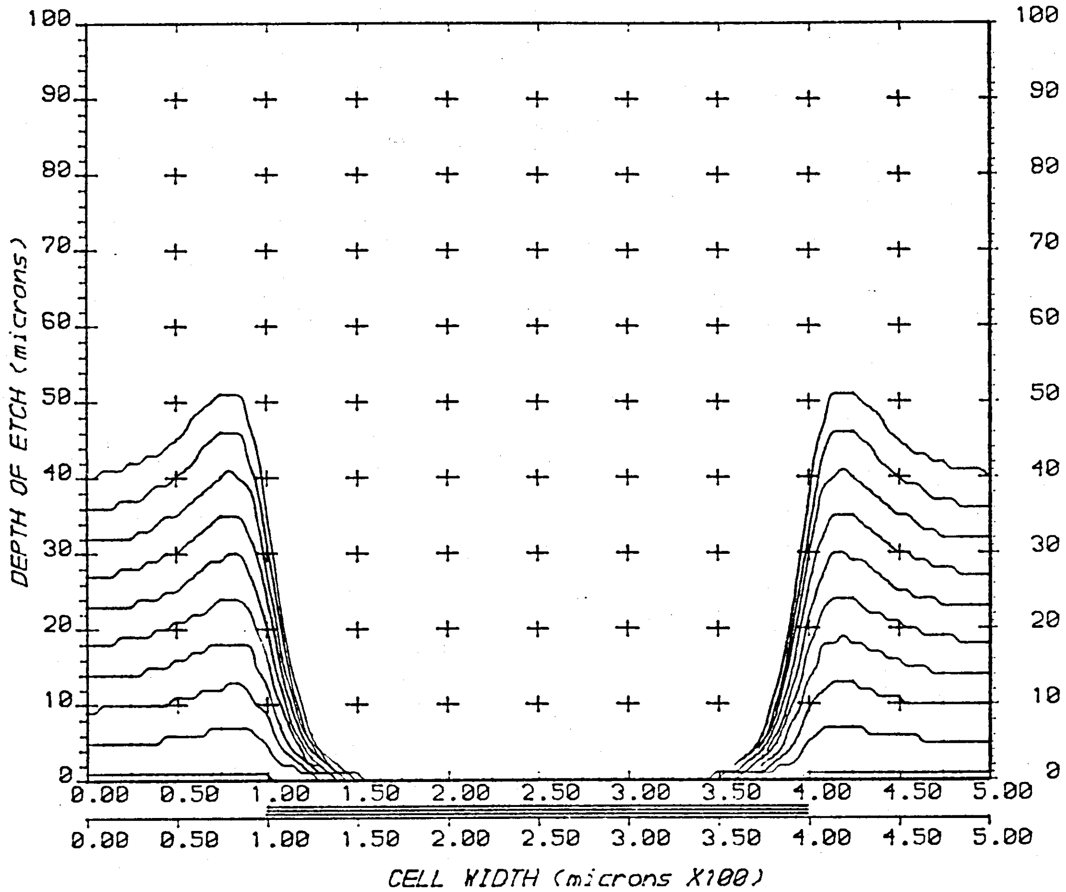

Temperature	25° C
Electrolyte conductivity	0.035 Ω^{-1}
Constant polarization (A)	130 mV
Interelectrode gap	5 mm
Overrelaxation parameter (w)	1.85
convergence criterion	10^{-5} to 10^{-4}
calculated atomic weight	55.14 (Alloy)
Density	7.913 gms/cm^3
Calculated valency	1.97 (Alloy)
Efficiency	100%
coulombs per time step	1.5
Anode potential	5 volts
Cathode potential	0 volts
Max. field iterations	2000
Feature 'a'	100 µm
Insulator	300 µm
feature 'b'	100 µm

Fig. 5.50 NUMERICAL SIMULATION OF A CENTRALLY POSITIONED INSULATOR (DIMENSION 300 µm)

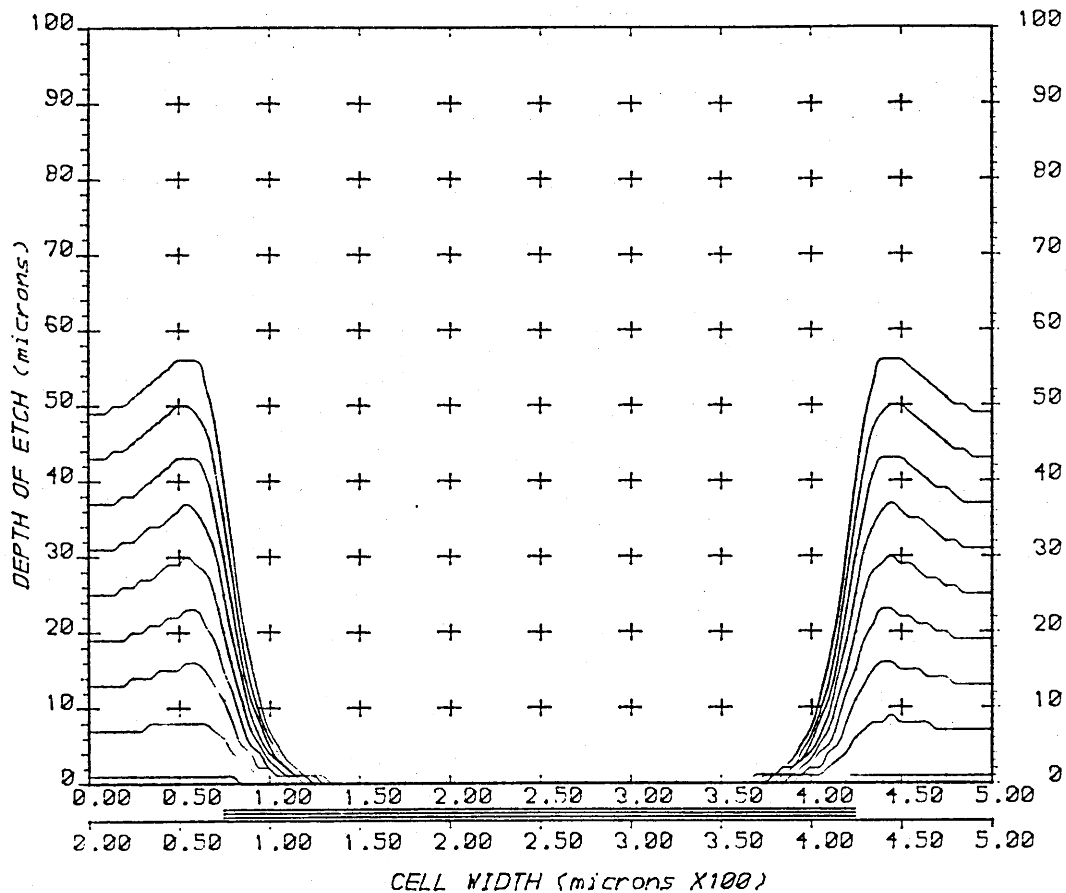

Temperature	25°C
Electrolyte conductivity	0.035 Ω^{-1}
Constant polarization (A)	130 mV
Interelectrode gap	5 mm
Overrelaxation parameter (w)	1.85
convergence criterion	10^{-5} to 10^{-4}
calculated atomic weight	55.14 (Alloy)
Density	7.913 gms/cm^3
Calculated valency	1.97 (Alloy)
Efficiency	100%
coulombs per time step	1.5
Anode potential	5 volts
Cathode potential	0 volts
Max. field iterations	2000
Feature 'a'	75 μm
Insulator	350 μm
feature 'b'	75 μm

Fig. 5.51 NUMERICAL SIMULATION OF A CENTRALLY POSITIONED INSULATOR (DIMENSION 350 μm)

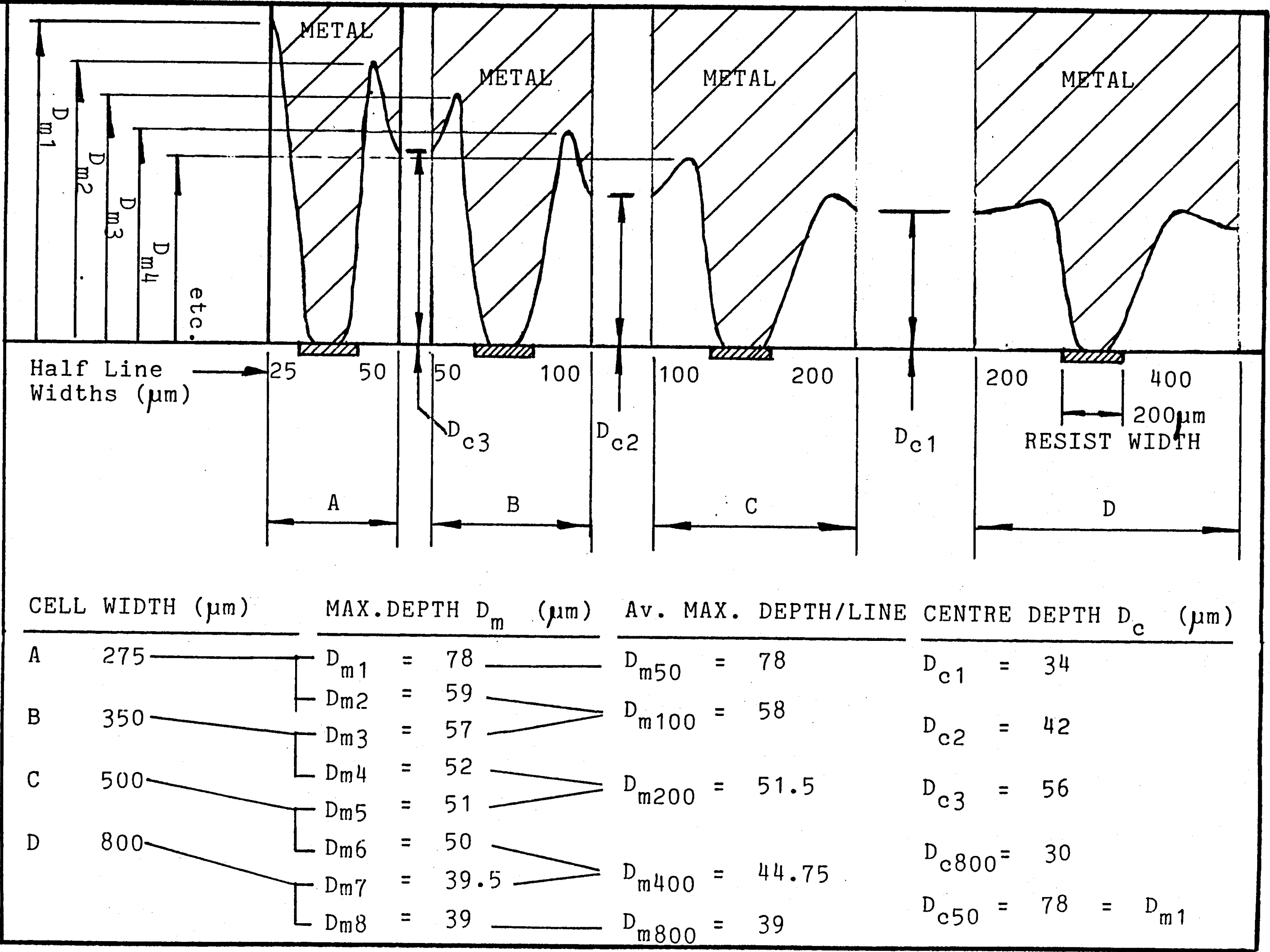

Fig.5.52 KEY AND RESULTS OF THE SPLICING IN MODELING THE ETCHED CHART.

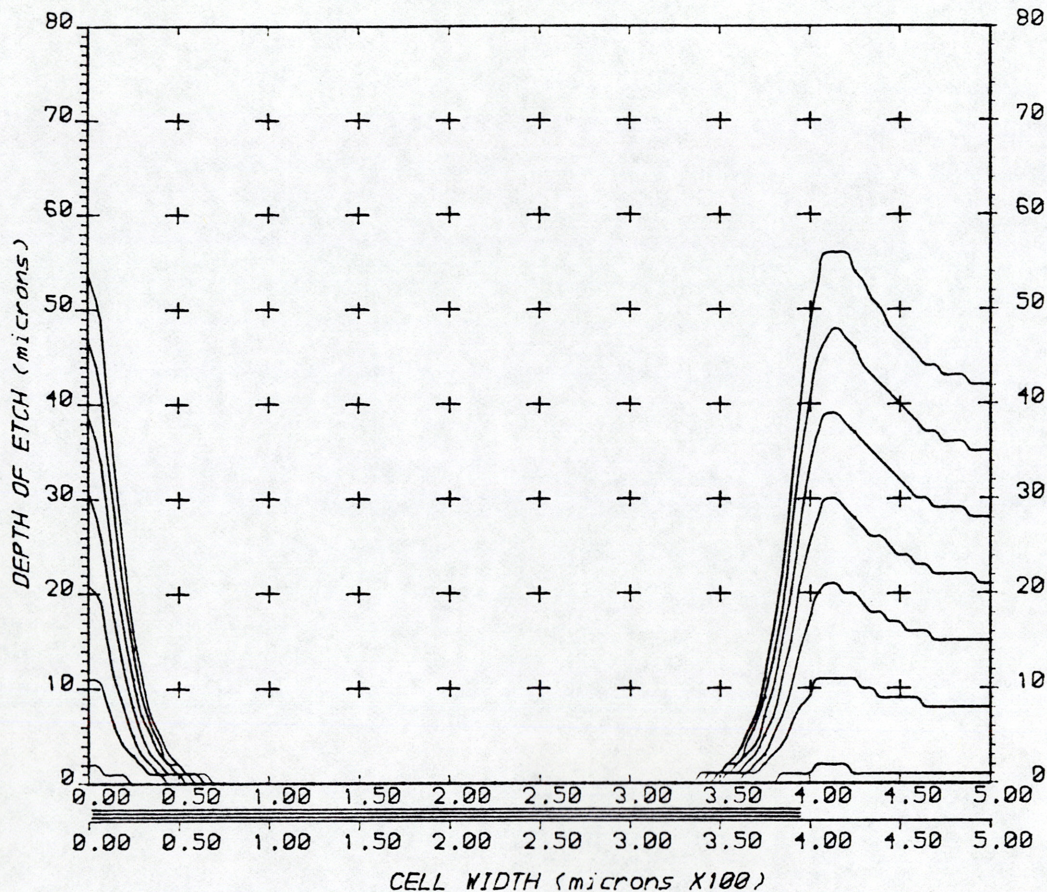

Temperature	25°C
Electrolyte conductivity	0.035 Ω^{-1}
Constant polarization (A)	130 mV
Interelectrode gap	5 mm
Overrelaxation parameter (w)	1.85
convergence criterion	10^{-5} to 10^{-4}
calculated atomic weight	55.14 (Alloy)
Density	7.913 gms/cm^3
Calculated valency	1.97 (Alloy)
Efficiency	100%
coulombs per time step	1.0
Anode potential	5 volts
Cathode potential	0 volts
Max. field iterations	2000
Feature 'a'	10 µm
Insulator	380 µm
feature 'b'	220 µm

Fig. 5.53 NUMERICAL SIMULATION OF RESIST FAILURE (PIN HOLE).

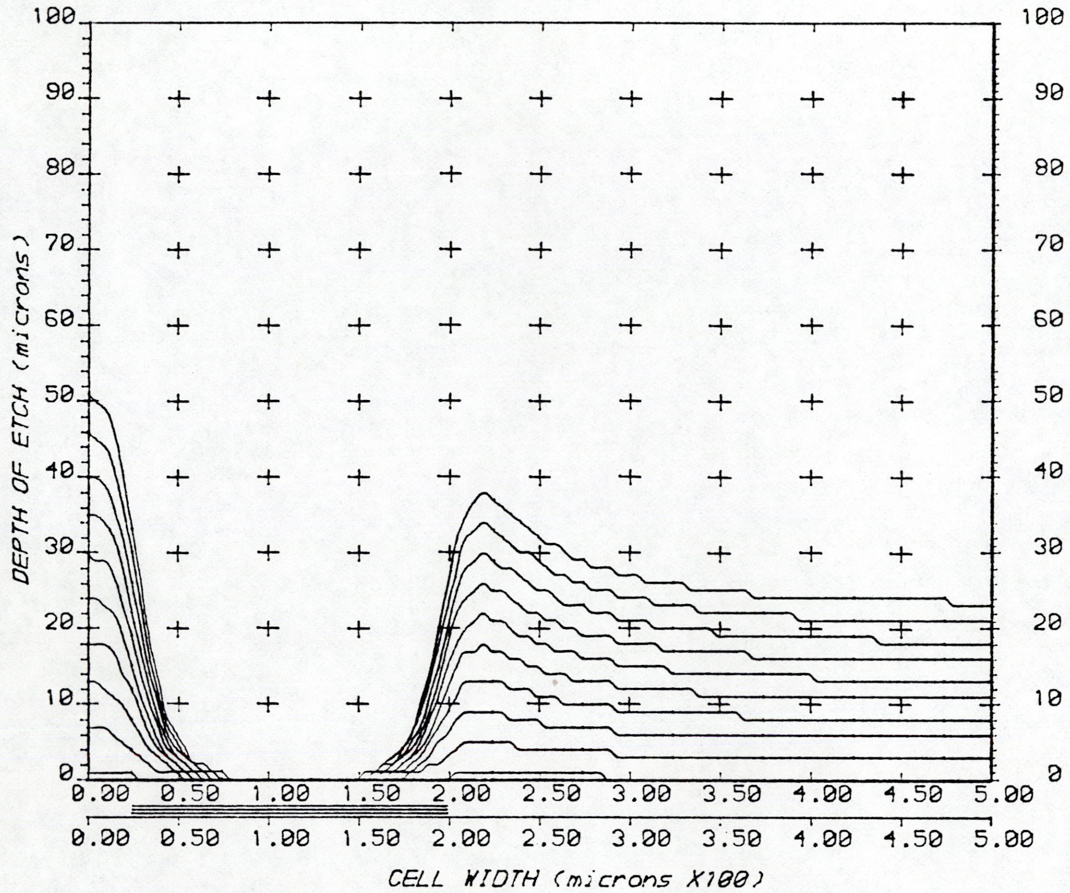

Temperature	25°C
Electrolyte conductivity	0.035 Ω^{-1}
Constant polarization (A)	130 mV
Interelectrode gap	5 mm
Overrelaxation parameter (w)	1.85
convergence criterion	10^{-5} to 10^{-4}
calculated atomic weight	55.14 (Alloy)
Density	7.913 gms/cm^3
Calculated valency	1.97 (Alloy)
Efficiency	100%
coulombs per time step	1.0
Anode potential	5 volts
Cathode potential	0 volts
Max. field iterations	2000
Feature 'a'	50 um
Insulator	175 um
feature 'b'	600 um

Fig. 5.54 NUMERICAL SIMULATION OF DISSOLUTION OF DISSIMILAR FEATURES 50, 600 μm WIDE.

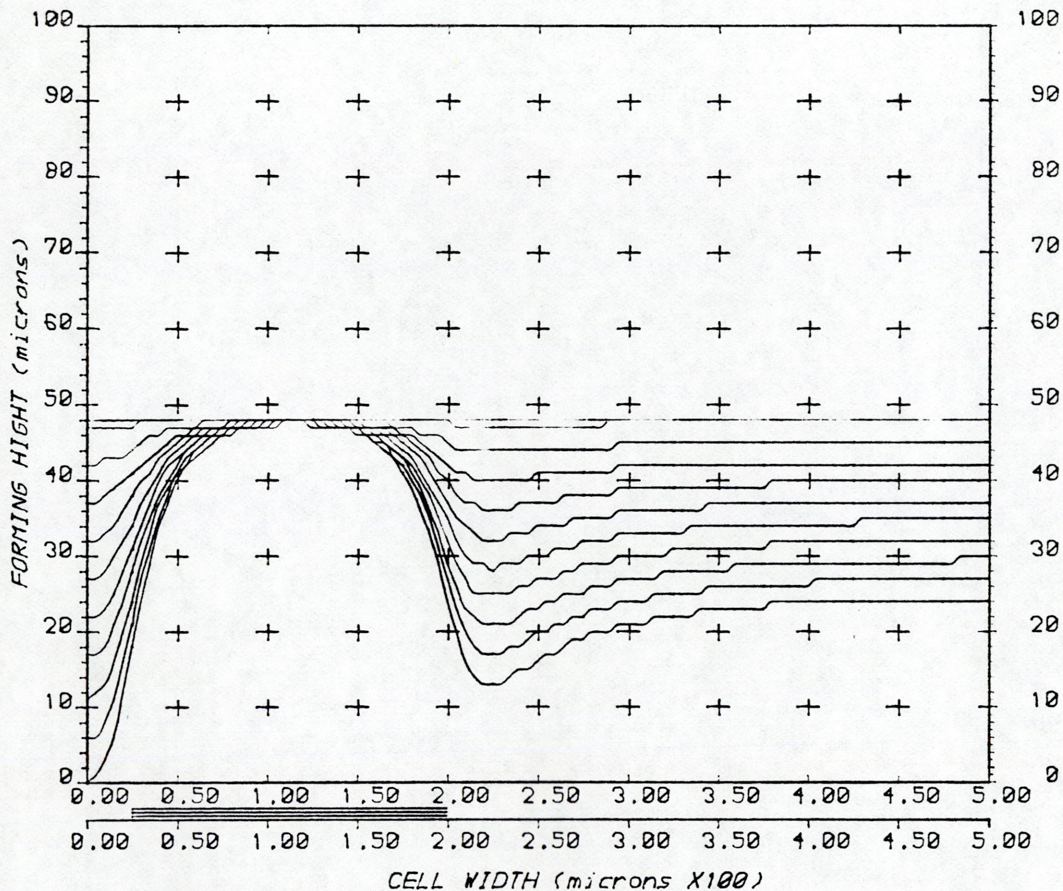

Temperature	25°C
Electrolyte conductivity	0.035 Ω^{-1}
Constant polarization (A)	130 mV
Interelectrode gap	5 mm
Overrelaxation parameter (w)	1.85
convergence criterion	10^{-5} to 10^{-4}
calculated atomic weight	55.14 (Alloy)
Density	7.913 gms/cm^3
Calculated valency	1.97 (Alloy)
Efficiency	100%
coulombs per time step	1.0
Anode potential	5 volts
Cathode potential	0 volts
Max. field iterations	2000
Feature 'a'	50 μm
Insulator	175 μm
feature 'b'	600 μm

Fig. 5.55 NUMERICAL SIMULATION ILLUSTRATING ELECTRO-FORMING OF DISSIMILAR FEATURES 50, 600 μm WIDE.

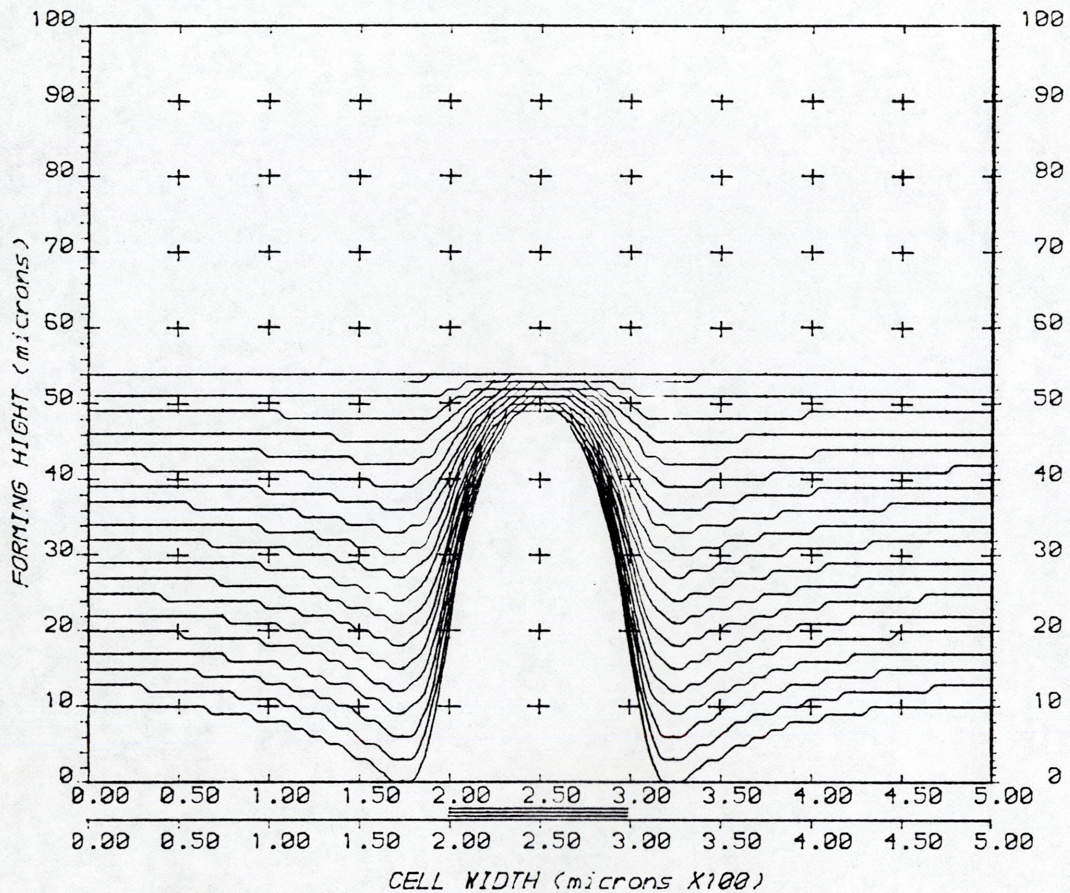

Temperature	25°C
Electrolyte conductivity	0.035 Ω^{-1}
Constant polarization (A)	130 mV
Interelectrode gap	5 mm
Overrelaxation parameter (w)	1.85
convergence criterion	10^{-5} to 10^{-4}
calculated atomic weight	55.14 (Alloy)
Density	7.913 gms/cm^3
Calculated valency	1.97 (Alloy)
Efficiency	100%
coulombs per time step	0.75
Anode potential	5 volts
Cathode potential	0 volts
Max. field iterations	2000
Feature 'a'	400 µm
Insulator	100 µm
feature 'b'	400 µm

Fig. 5.56 NUMERICAL SIMULATION OF ELECTRO-FORMING ILLUSTRATING RESIST OVER-PLATING.

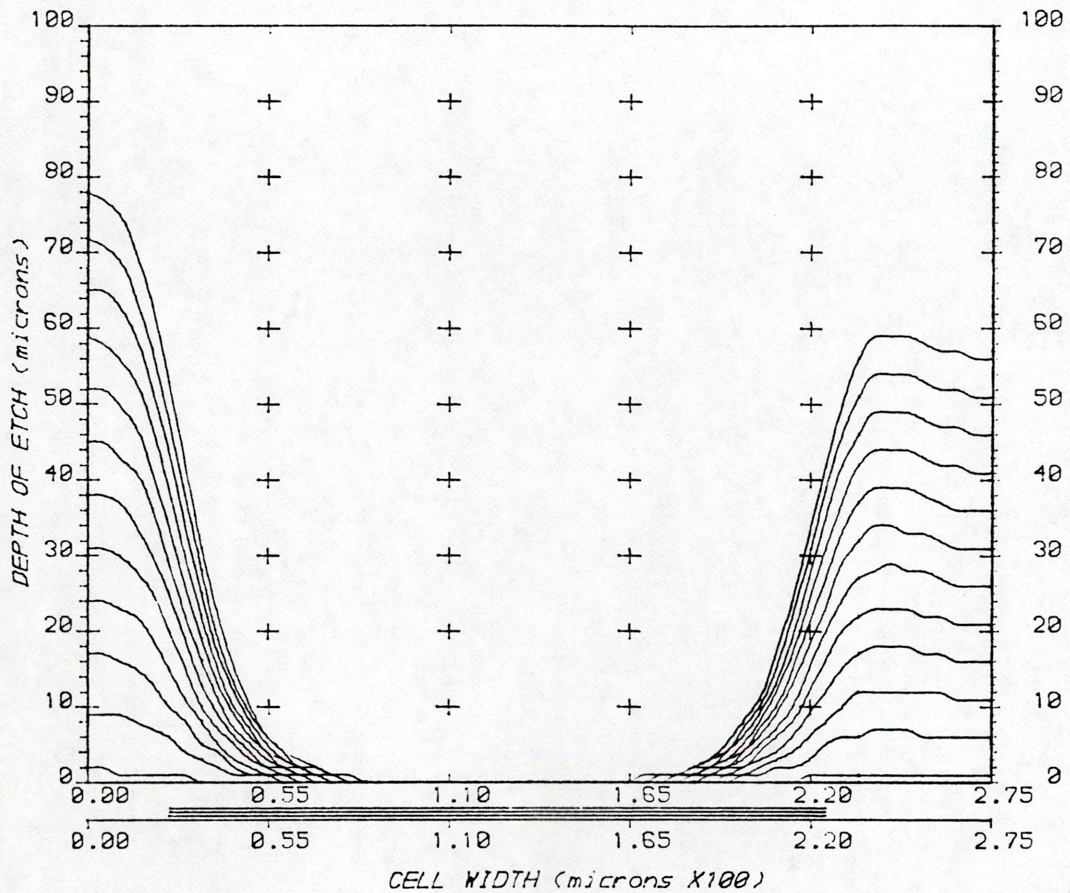

Temperature	25°C
Electrolyte conductivity	0.035 Ω^{-1}
Constant polarization (A)	130 mV
Interelectrode gap	5 mm
Overrelaxation parameter (w)	1.85
convergence criterion	10^{-5} to 10^{-4}
calculated atomic weight	55.14 (Alloy)
Density	7.913 gms/cm^3
Calculated valency	1.97 (Alloy)
Efficiency	100%
coulombs per time step	variable
Anode potential	5 volts
Cathode potential	0 volts
Max. field iterations	2000
Feature 'a'	50 μm
Insulator	200 μm
feature 'b'	100 μm

Fig. 5.58 NUMERICAL SIMULATION OF RESOLUTION CHART (MINOR CELL'A').

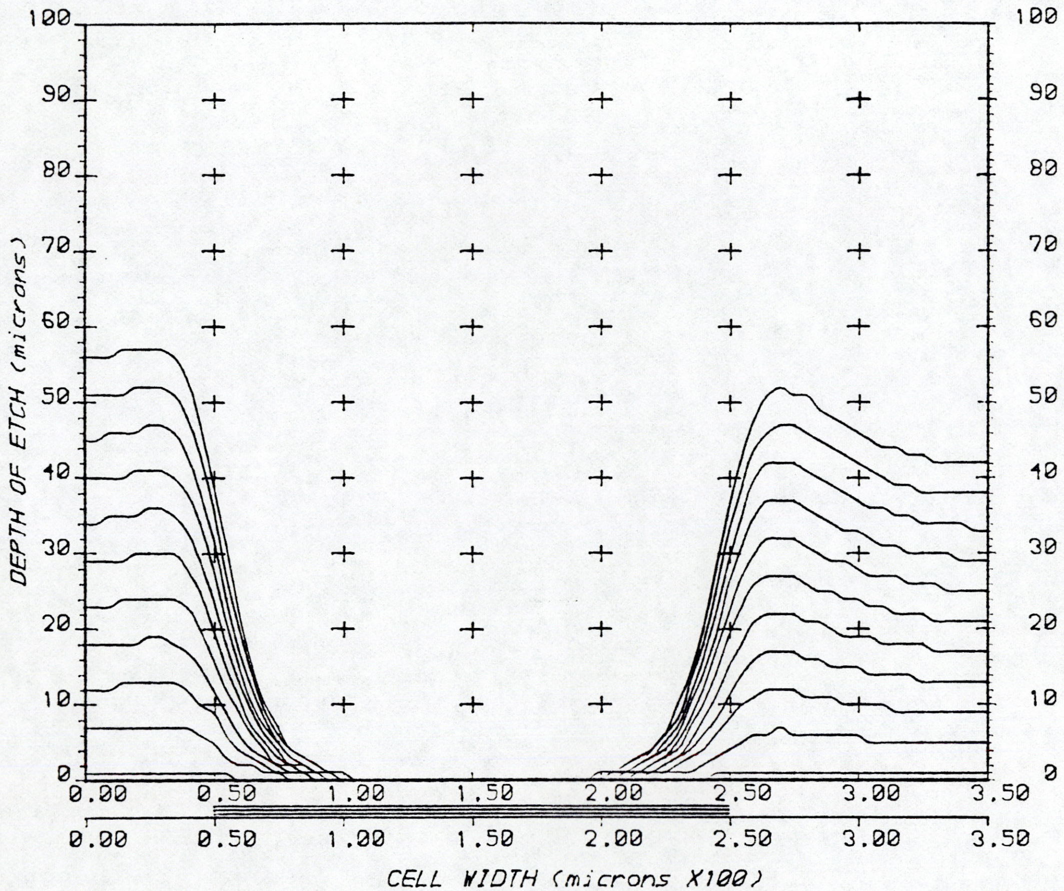

Temperature	25°C
Electrolyte conductivity	0.035 Ω^{-1}
Constant polarization (A)	130 mV
Interelectrode gap	5 mm
Overrelaxation parameter (w)	1.85
convergence criterion	10^{-5} to 10^{-4}
calculated atomic weight	55.14 (Alloy)
Density	7.913 gms/cm^3
Calculated valency	1.97 (Alloy)
Efficiency	100%
coulombs per time step	variable
Anode potential	5 volts
Cathode potential	0 volts
Max. field iterations	2000
Feature 'a'	100 µm
Insulator	200 µm
feature 'b'	200 µm

Fig. 5.59 NUMERICAL SIMULATION OF RESOLUTION CHART (MINOR CELL'B').

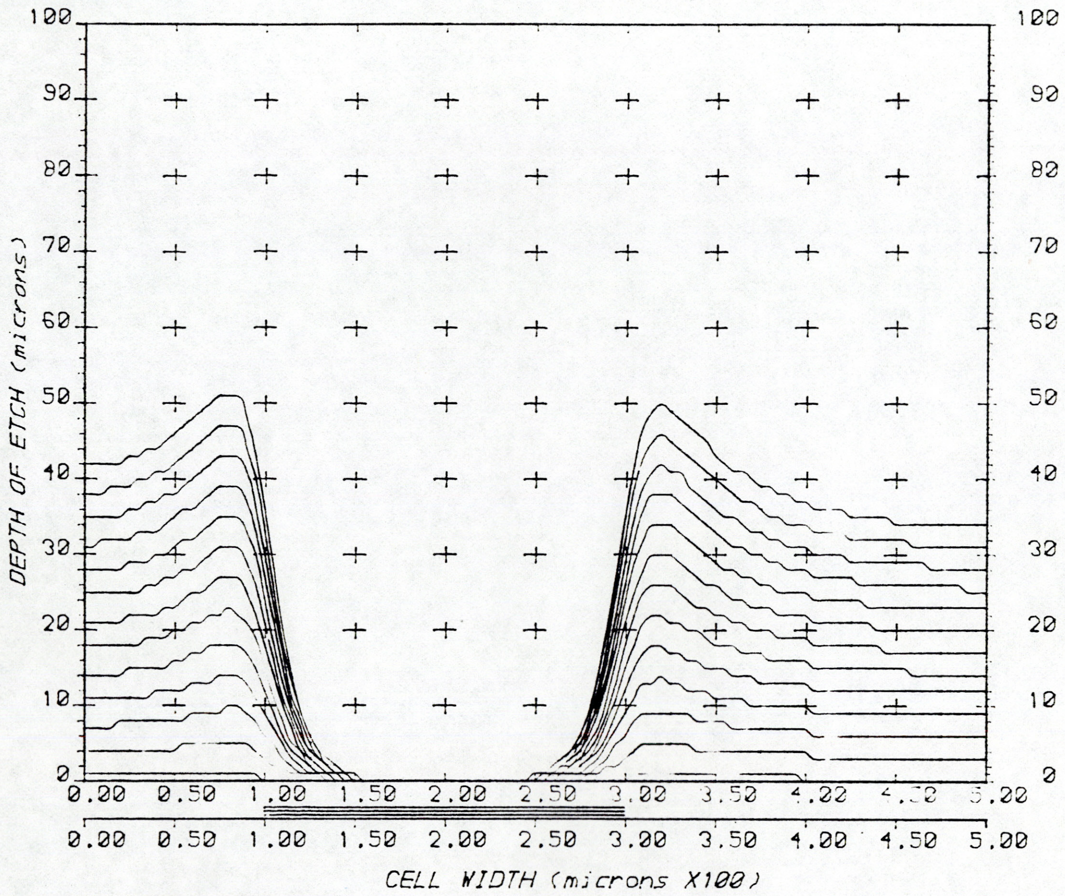

Temperature	25°C
Electrolyte conductivity	0.035 Ω^{-1}
Constant polarization (A)	130 mV
Interelectrode gap	5 mm
Overrelaxation parameter (w)	1.85
convergence criterion	10^{-5} to 10^{-4}
calculated atomic weight	55.14 (Alloy)
Density	7.913 gms/cm^3
Calculated valency	1.97 (Alloy)
Efficiency	100%
coulombs per time step	variable
Anode potential	5 volts
Cathode potential	0 volts
Max. field iterations	2000
Feature 'a'	200 µm
Insulator	200 µm
feature 'b'	400 µm

Fig. 5.60 NUMERICAL SIMULATION OF RESOLUTION CHART (MINOR CELL'C').

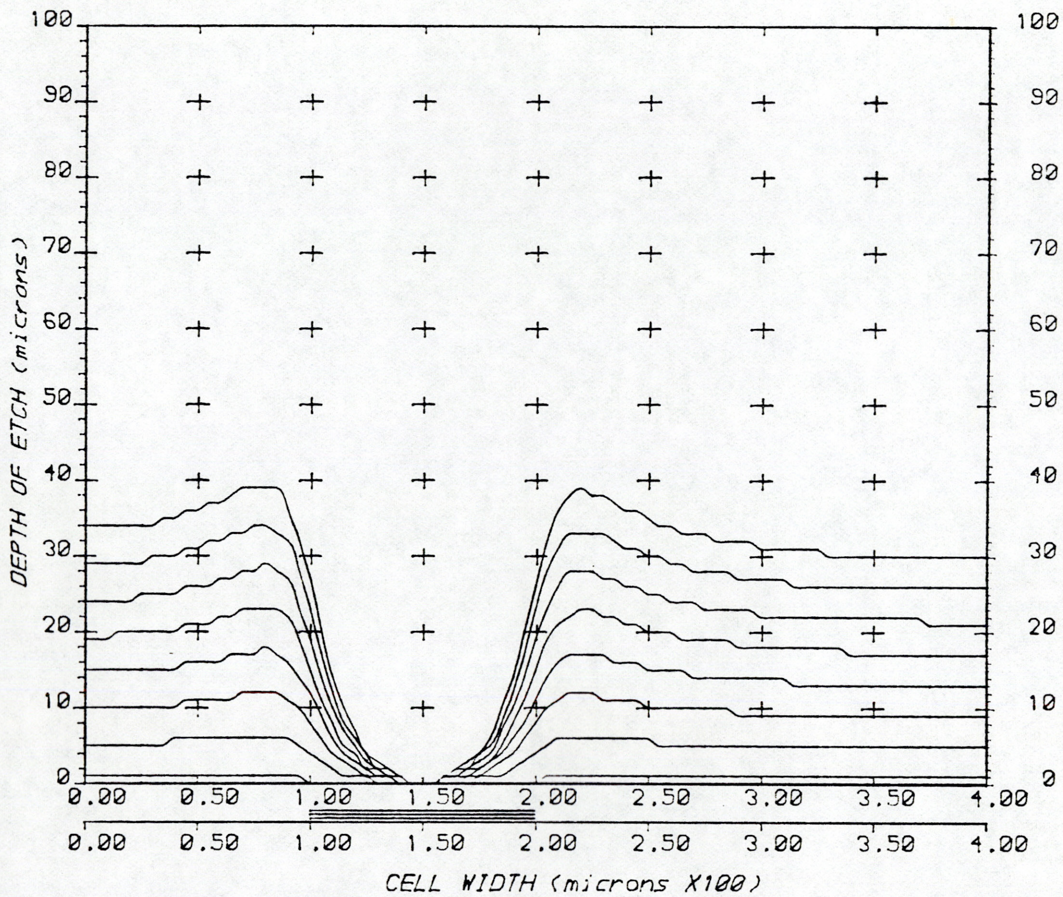

Temperature	25°C
Electrolyte conductivity	0.035 Ω^{-1}
Constant polarization (A)	130 mV
Interelectrode gap	5 mm
Overrelaxation parameter (w)	1.85
convergence criterion	10^{-5} to 10^{-4}
calculated atomic weight	55.14 (Alloy)
Density	7.913 gms/cm^3
Calculated valency	1.97 (Alloy)
Efficiency	100%
coulombs per time step	variable
Anode potential	5 volts
Cathode potential	0 volts
Max. field iterations	2000
Feature 'a'	400 μm
Insulator	200 μm
feature 'b'	800 μm

Fig. 5.61 NUMERICAL SIMULATION OF RESOLUTION CHART (MINOR CELL'D').

CURVE TYPE: $Y=a+b*X+c*X^2+d*X^3$ DATA FILE: 1A50

REGRESSION COEFFICIENTS

a=58.2037729 b=-2.99639227

c=5.28915194E-2 d=-3.15370894E-4

Coefficient of determination=0.99866591

X1=0	XINT=5	X2=70	Undercut	(µm)
Y1=0	YINT=5	Y2=50	Depth	(µm)

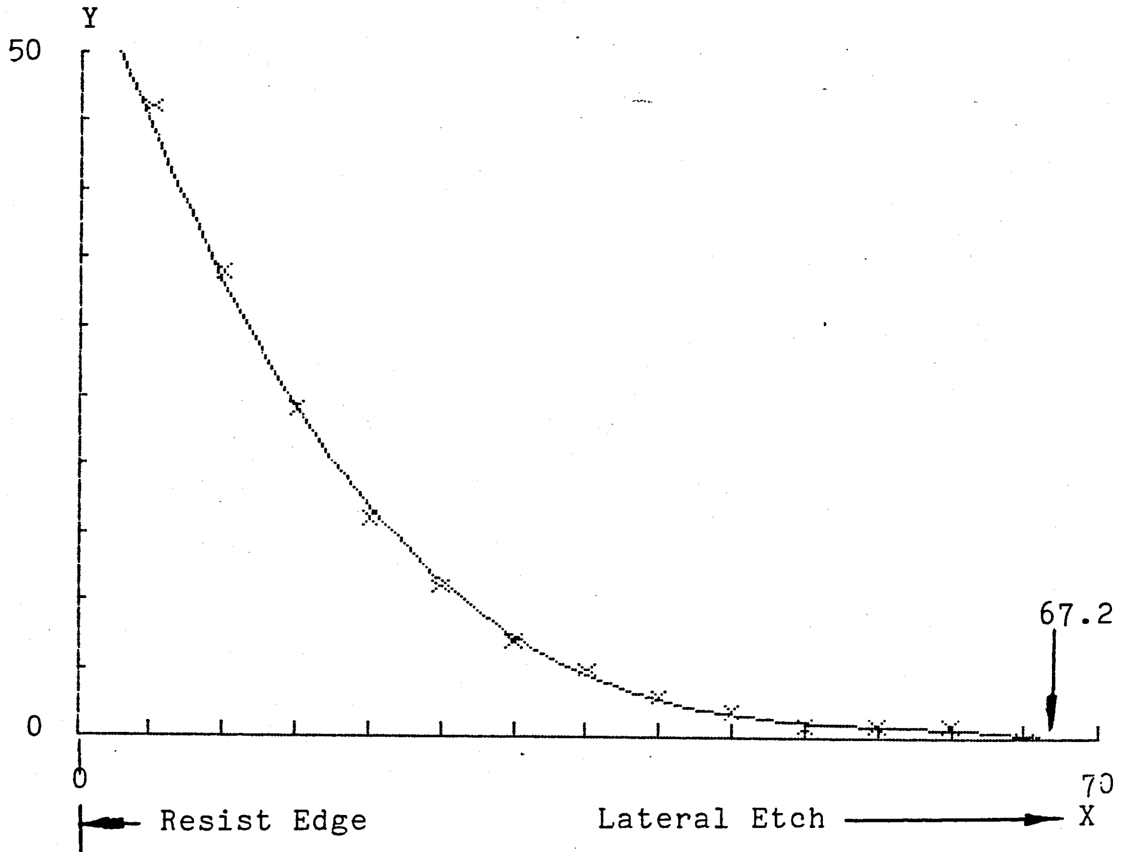

Fig. 5.62 UNDERCUT FOR 50 µm LINE IN CELL 'A'.

CURVE TYPE: Y=a+b*X+c*X^2+d*X^3 DATA FILE: UC100A

REGRESSION COEFFICIENTS

a=46.5082549 b=-2.46419425

c=4.48851169E-2 d=-2.77389298E-4

Coefficient of determination=0.999164221

X1=0	XINT=5	X2=70	Undercut	(µm)
Y1=0	YINT=5	Y2=50	Depth	(µm)

Cell 'A' Line 100 µm

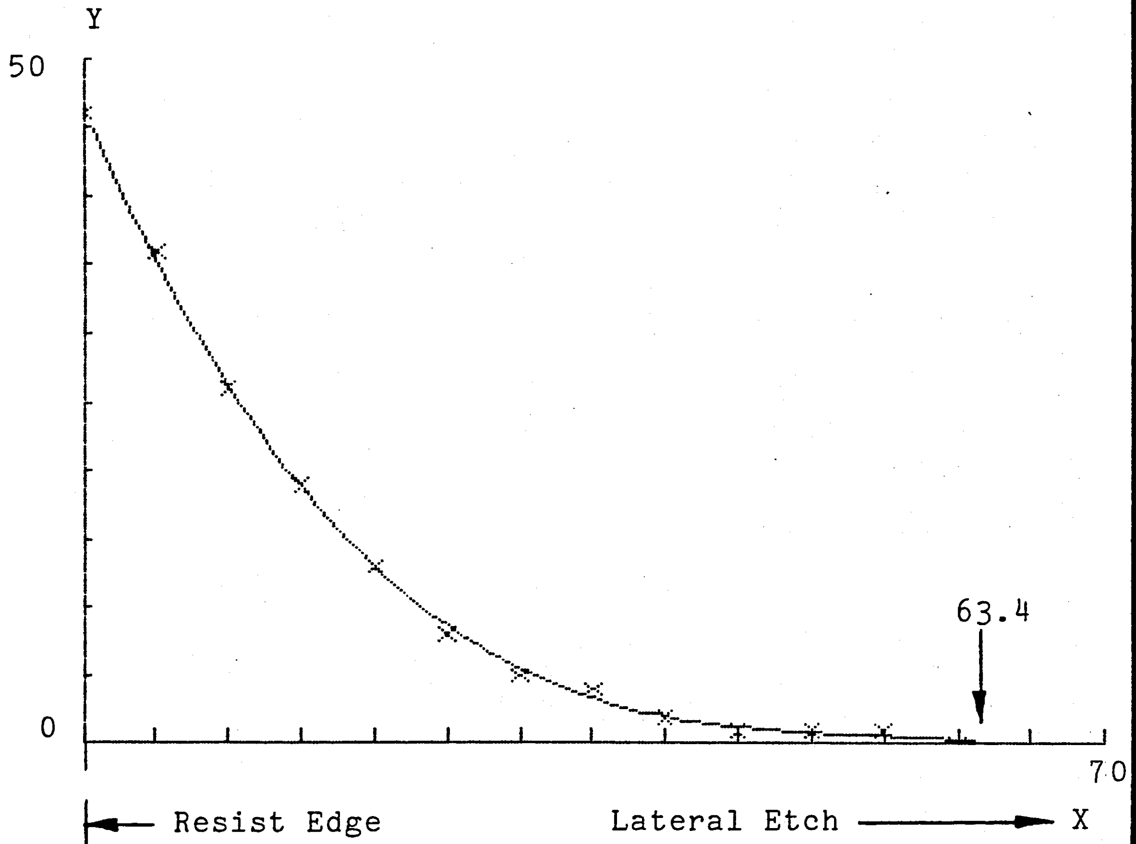

Fig. 5.63 UNDERCUT FOR 100 µm LINE IN CELL'A'.

CURVE TYPE:Y=a+b*X+c*X^2+d*X^3 DATA FILE: 1B100

REGRESSION COEFFICIENTS

a=39.7838781 b=-2.20575705

c=4.2826062E-2 d=-2.86972278E-4

Coefficient of determination=0.998355726

X1=0	XINT=5	X2=70	Undercut	(µm)
Y1=0	YINT=5	Y2=50	Depth	(µm)

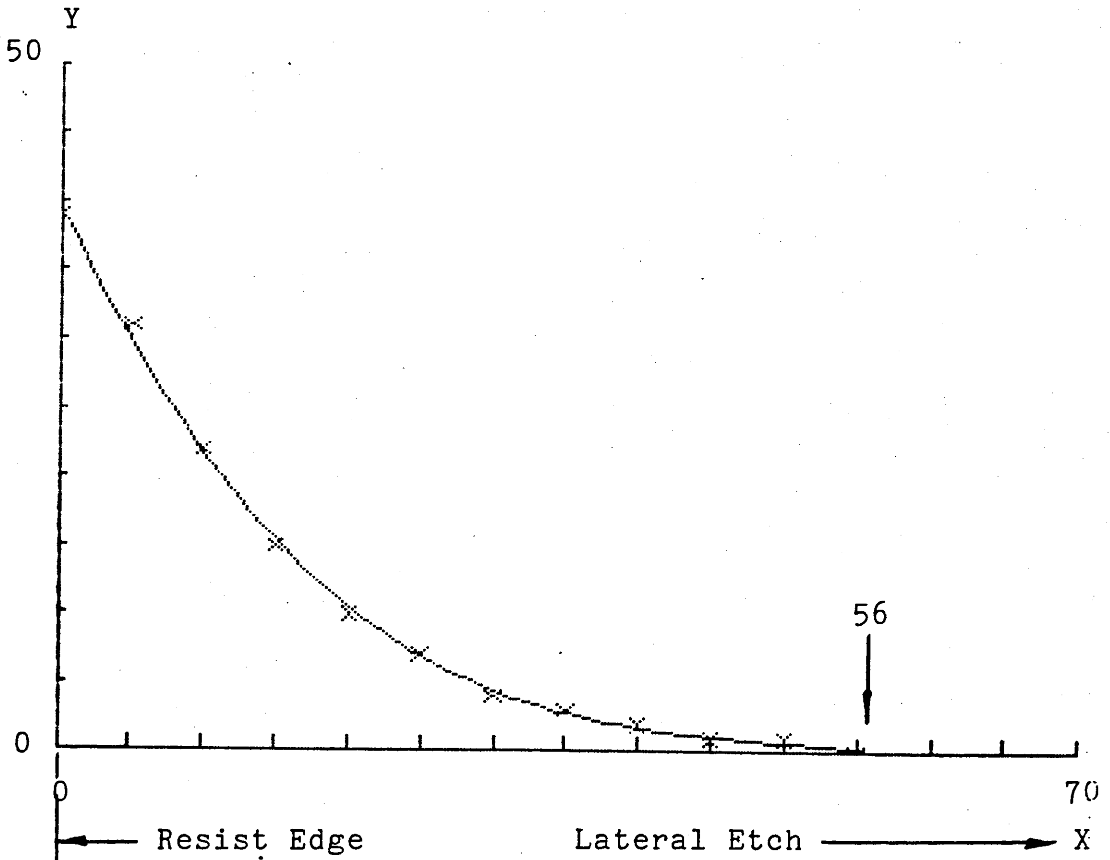

Fig. 5.64 UNDERCUT FOR 100 µm LINE IN CELL 'B'

CURVE TYPE: $Y=a+b*X+c*X^2+d*X^3$ DATA FILE: 1C200

REGRESSION COEFFICIENTS

a=36.5531129 b=-2.0646539

c=4.14740812E-2 d=-2.90080286E-4

Coefficient of determination=0.998917445

X1=0	XINT=5	X2=70	Undercut	(µm)
Y1=0	YINT=5	Y2=50	Depth	(µm)

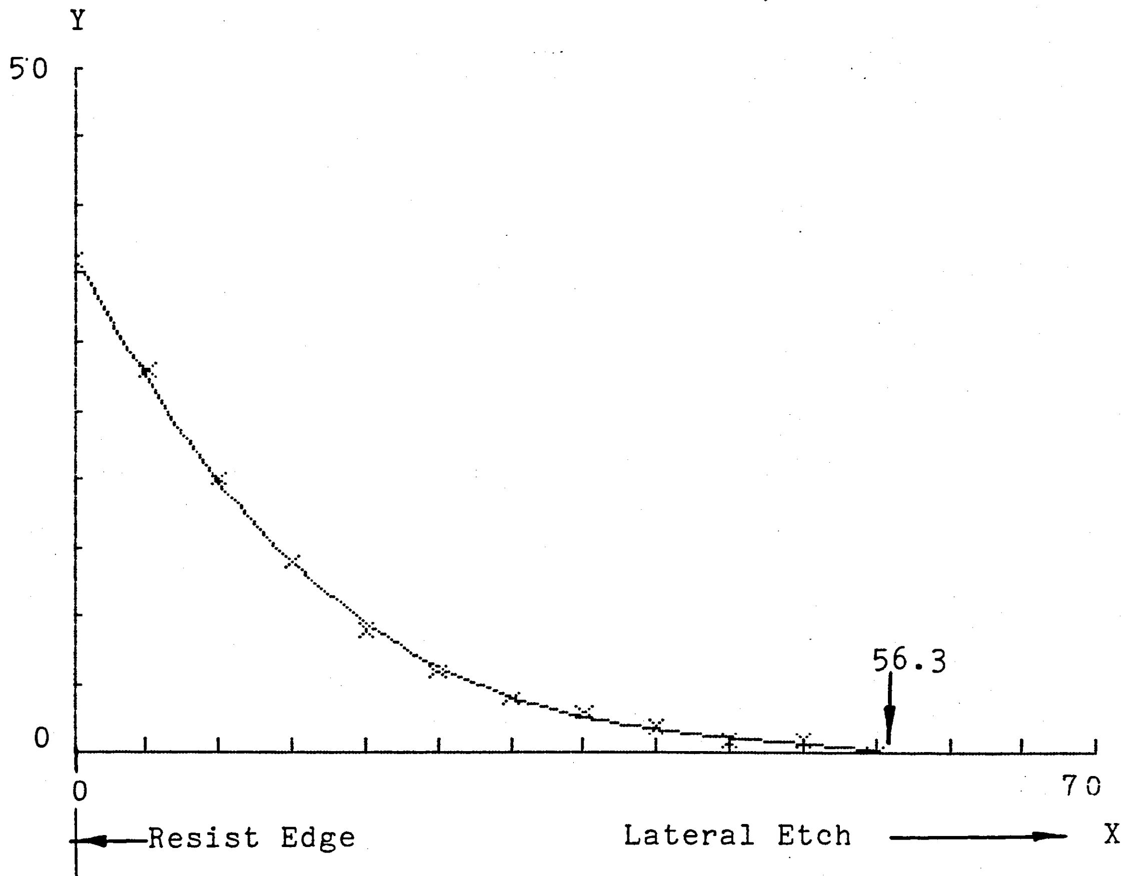

Fig. 5.65 UNDERCUT FOR 200 µm LINE IN CELL 'C'.

CURVE TYPE: Y=a+b*X+c*X^2+d*X^3   DATA FILE: 1B200

REGRESSION COEFFICIENTS

a=36.4395549   b=-2.01661669

c=3.95604395E-2   d=-2.70396272E-4

Coefficient of determination=0.999108781

X1=0	XINT=5	X2=70	Undercut	(µm)
Y1=0	YINT=5	Y2=50	Depth	(µm)

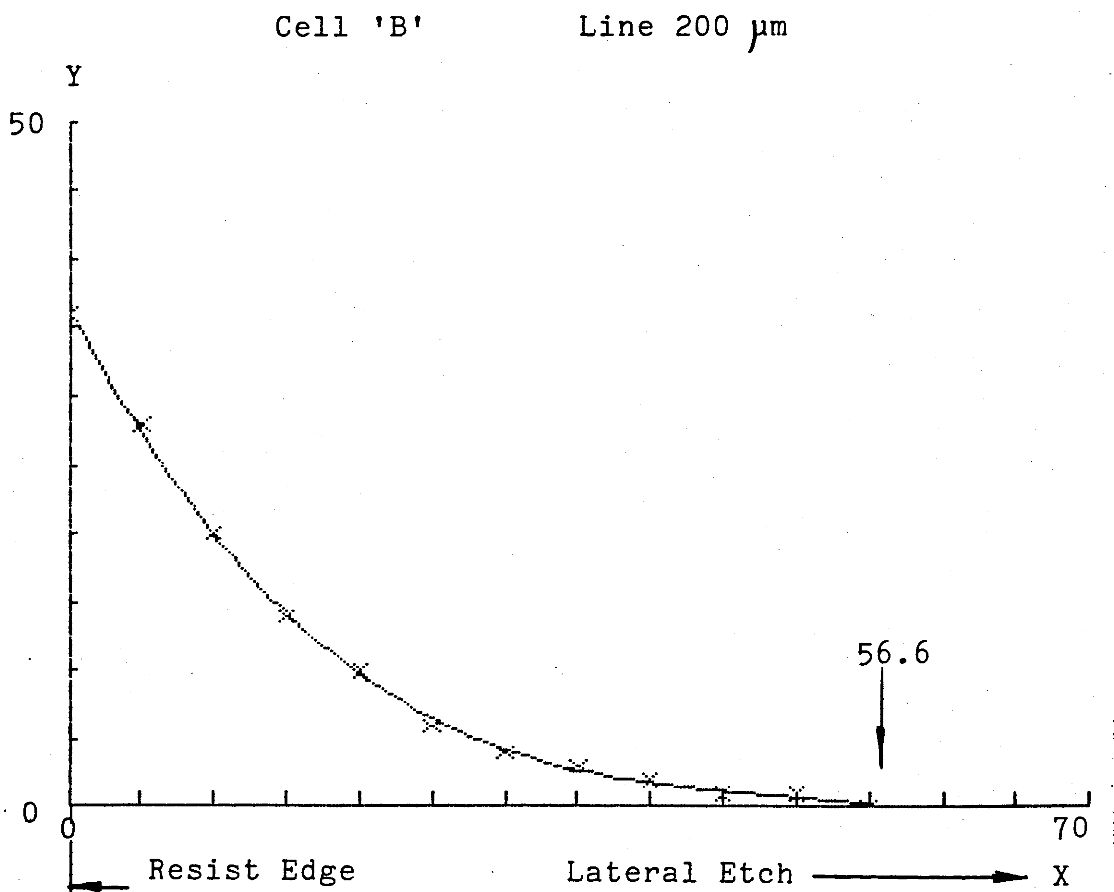

Fig. 5.66 UNDERCUT FOR 200 µm LINE IN CELL 'B'

CURVE TYPE: Y=a+b*X+c*X^2+d*X^3   DATA FILE: 1C400

REGRESSION COEFFICIENTS

a=35.443217   b=-1.95271029

c=3.81107782E-2   d=-2.5900026E-4

Coefficient of determination=0.998972631

X1=0	XINT=5	X2=70	Undercut	(µm)
Y1=0	YINT=5	Y2=50	Depth	(µm)

Cell 'C'   Line 400 µm

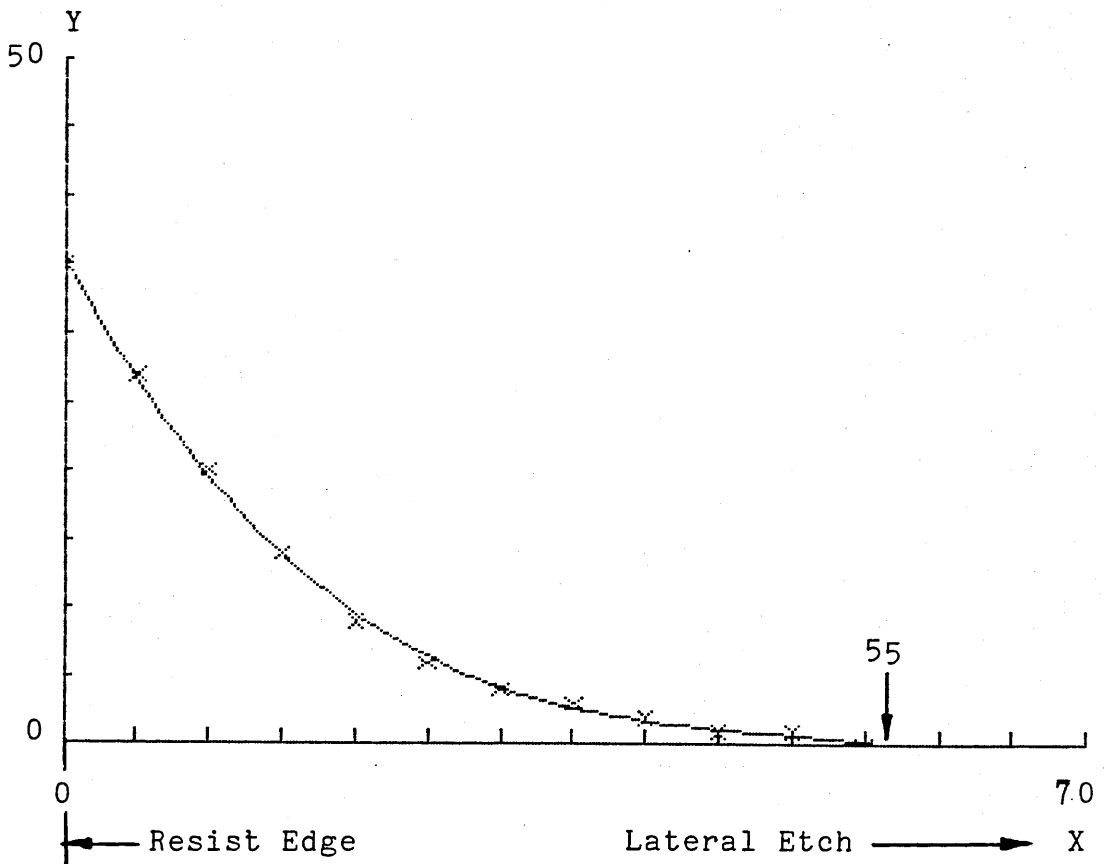

Fig. 5.67 UNDERCUT FOR 400 µm LINE IN CELL 'C'.

CURVE TYPE: Y=a*X^b　　　DATA FILE: UC50A

REGRESSION COEFFICIENTS

a=19.6975014　　　b=0.273207406

c=0　　　d=0

Coefficient of determination=0.980324213

X1=0	XINT=10	X2=100	Max/Centre Depth(µm)
Y1=0	YINT=10	Y2=100	Undercut (µm)

Cell 'A'　　　Line 50 µm

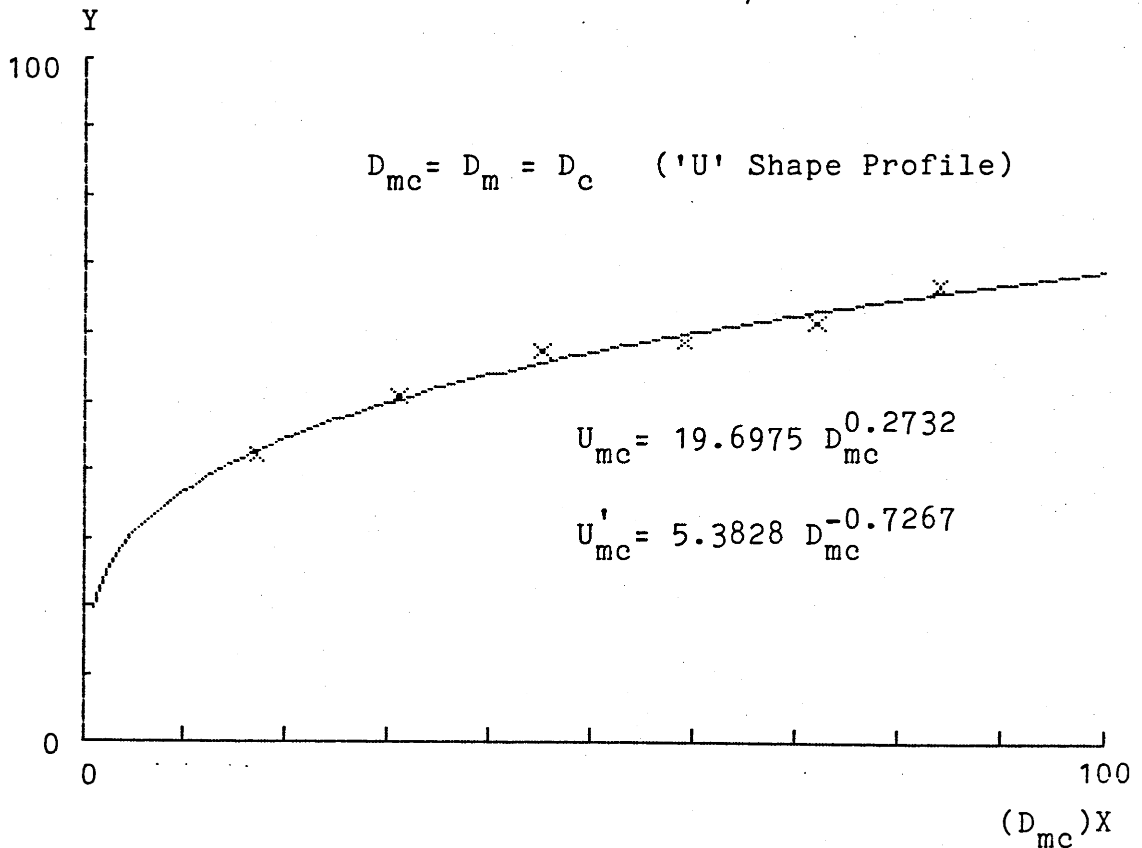

Fig.5.68 UNDERCUT vs. MAX./CENTRE DEPTH FOR 50 µm LINE IN CELL 'A'.

CURVE TYPE:Y=a*X^b DATA FILE: UCM10A

REGRESSION COEFFICIENTS

a=15.416597 b=0.351159637

c=0 d=0

Coefficient of determination=0.967694287

X1=0	XINT=10	X2=100	Max. Depth	(μm)
Y1=0	YINT=10	Y2=100	Undercut	(μm)

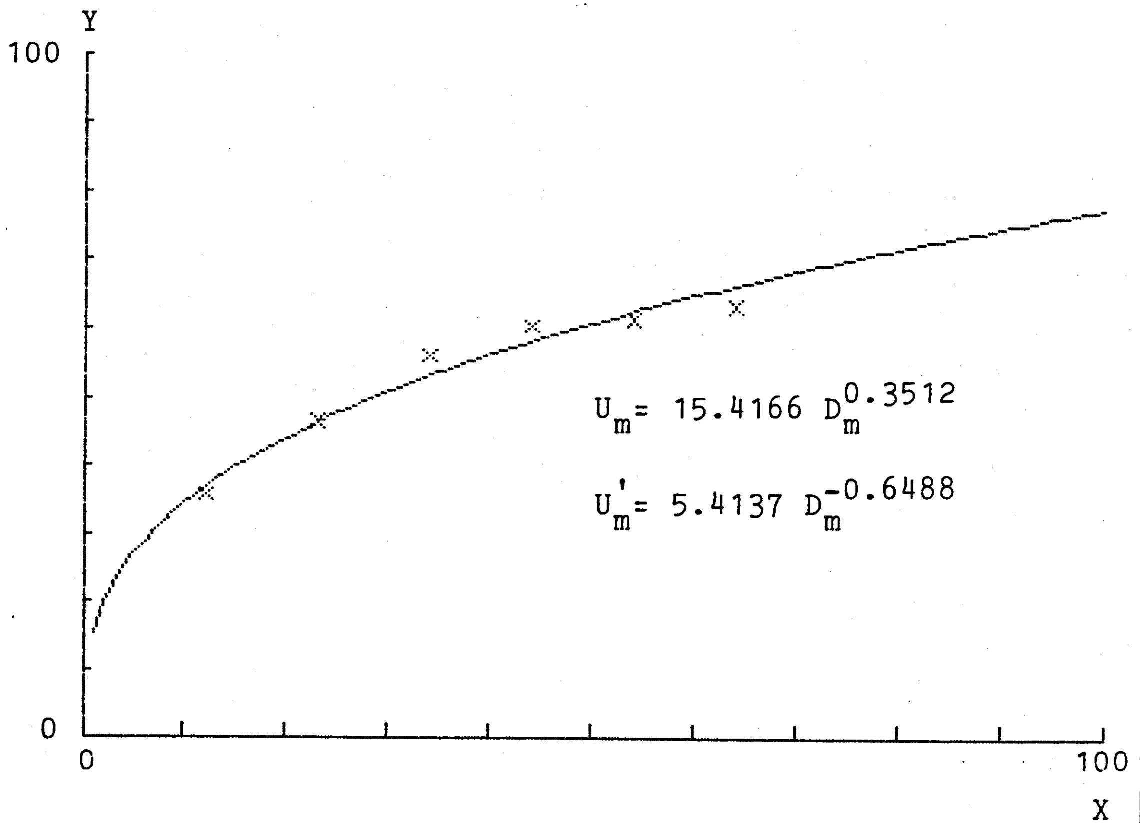

Fig.5.69 UNDERCUT vs. MAX. DEPTH FOR 100 μm LINE IN CELL 'A'.

CURVE TYPE:Y=a*X^b

DATA FILE: UCM100B

REGRESSION COEFFICIENTS

a=21.8374447

b=0.243915224

c=0

d=0

Coefficient of determination=0.966993788

X1=0	XINT=10	X2=100	Max. Depth	(µm)
Y1=0	YINT=10	Y2=100	Undercut	(µm)

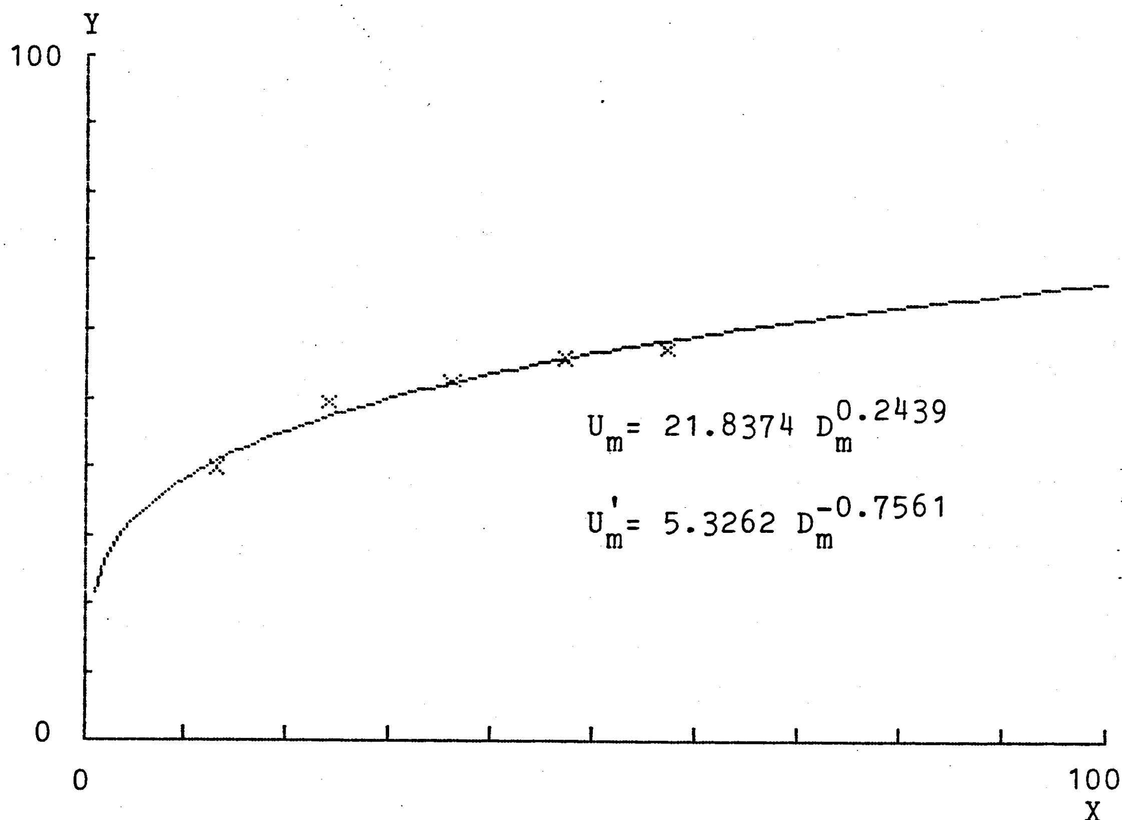

Fig.5.70 UNDERCUT vs. MAX. DEPTH FOR 100 µm LINE IN CELL 'B'.

CURVE TYPE: Y=a*X^b

DATA FILE: UCM200B

REGRESSION COEFFICIENTS

a=18.2027289

b=0.300355562

c=0

d=0

Coefficient of determination=0.932420798

X1=0	XINT=10	X2=100	Max. Depth	(μm)
Y1=0	YINT=10	Y2=100	Undercut	(μm)

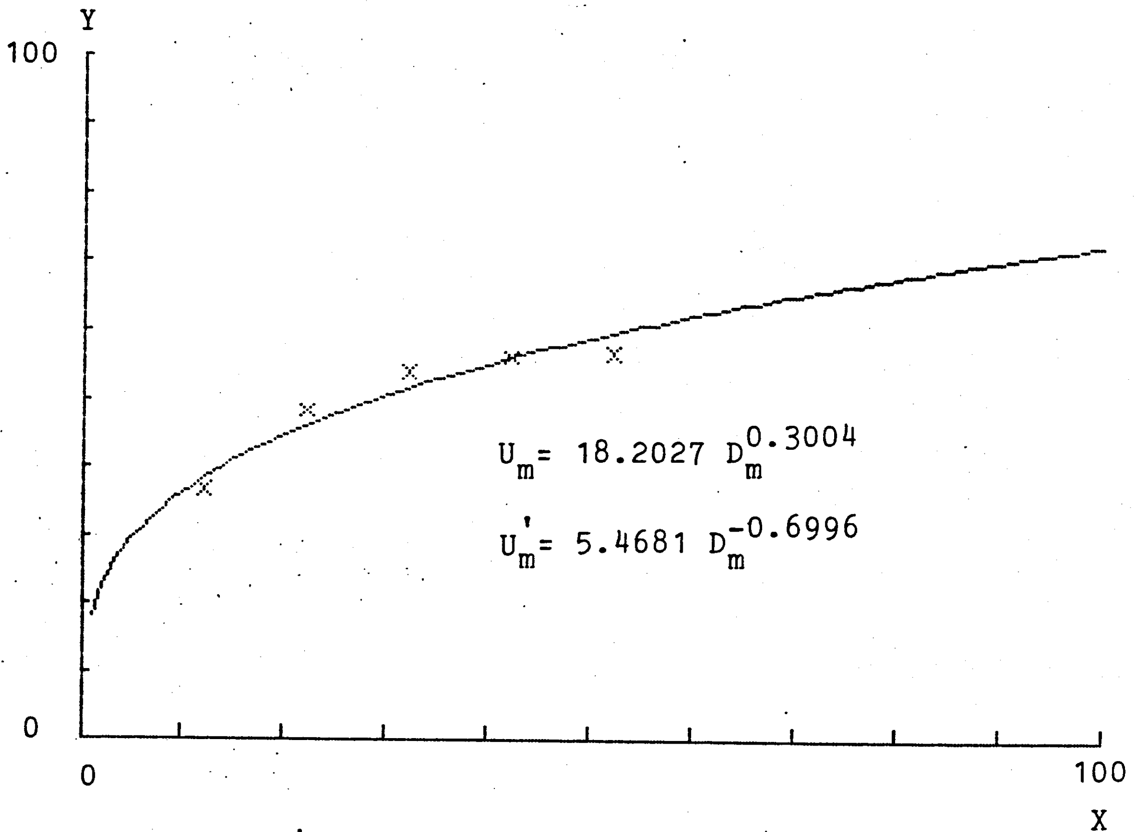

Fig. 5.71 UNDERCUT vs. MAX. DEPTH FOR 200 μm LINE IN CELL 'B'.

CURVE TYPE:Y=a*X^b DATA FILE: UCM200C

REGRESSION COEFFICIENTS

a=17.7353705 b=0.293500181

c=0 d=0

Coefficient of determination=0.989041761

X1=0	XINT=10	X2=100	Max. Depth	(μm)
Y1=0	YINT=10	Y2=100	Undercut	(μm)

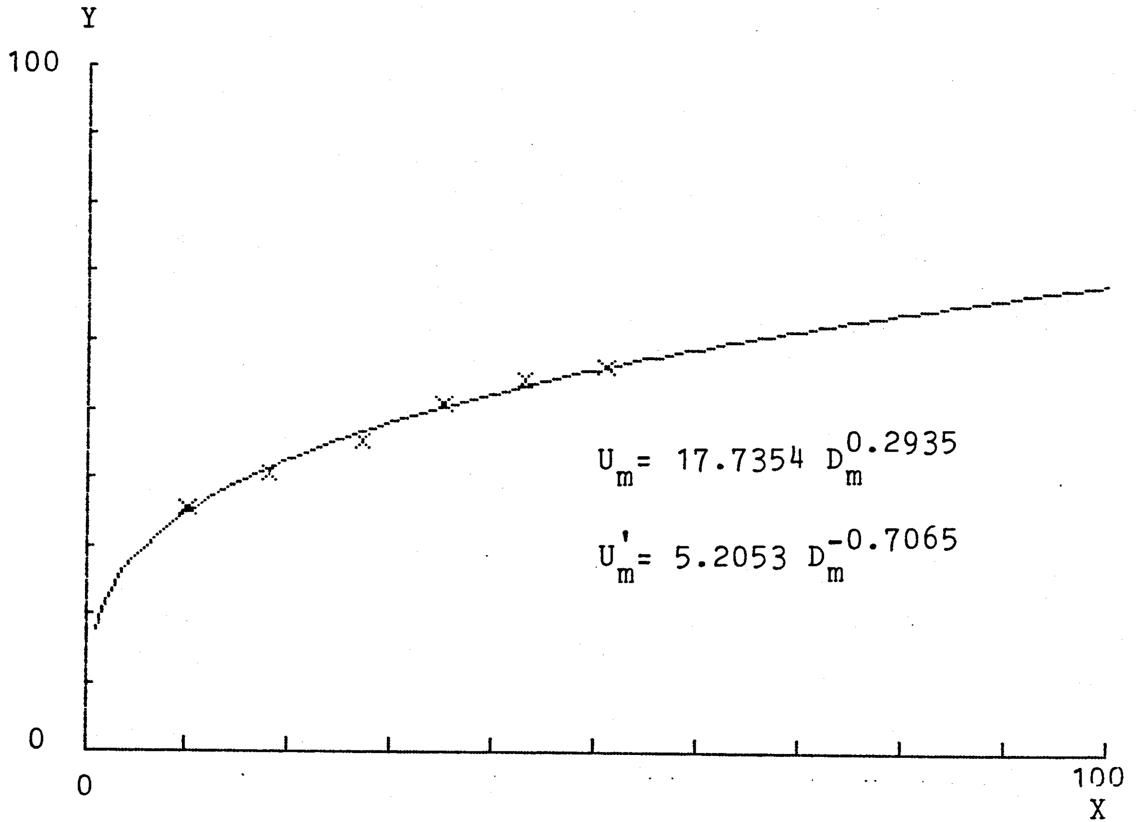

Fig.5.72 UNDERCUT vs. MAX. DEPTH FOR 200μm LINE IN CELL 'C'

CURVE TYPE:Y=a*X^b			DATA FILE: UCM400C	
	REGRESSION COEFFICIENTS			
a=18.4822547			b=0.284603752	
c=0			d=0	
Coefficient of determination=0.981148904				

X1=0	XINT=10	X2=100	Max. Depth	(μm)
Y1=0	YINT=10	Y2=100	Undercut	(μm)

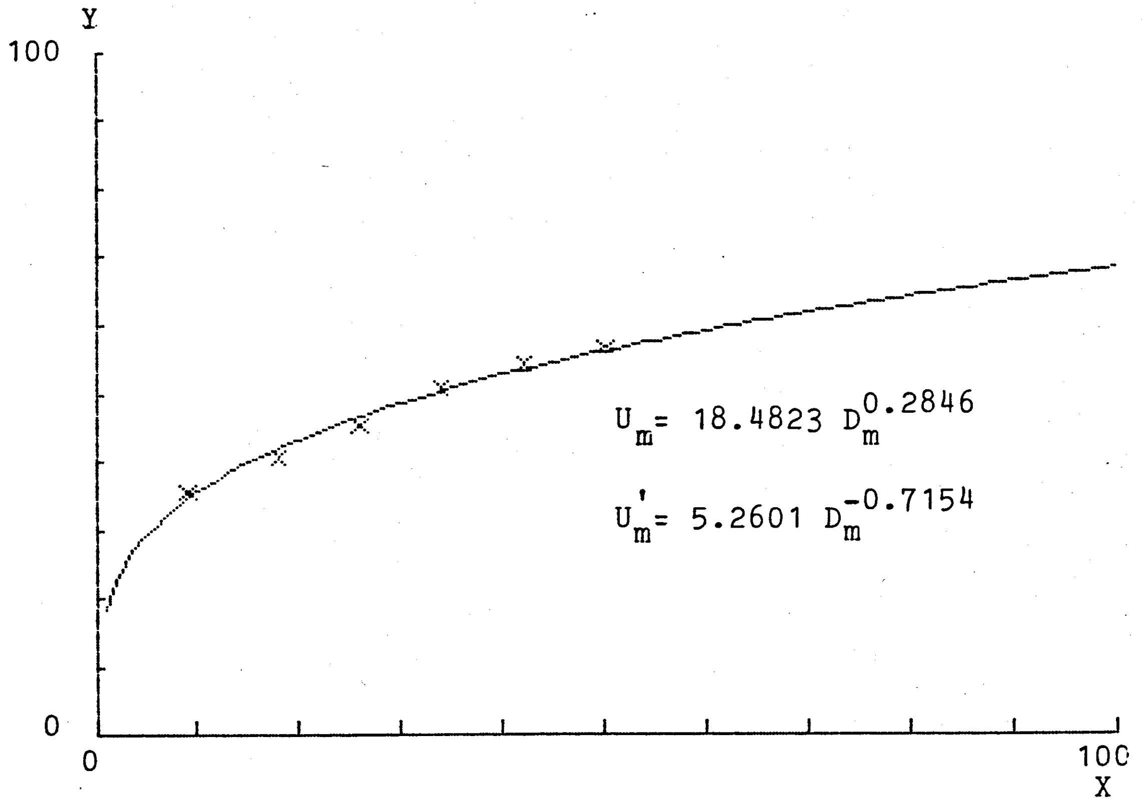

Fig.5.73 UNDERCUT vs. MAX. DEPTH FOR 400 μm LINE IN CELL 'C'

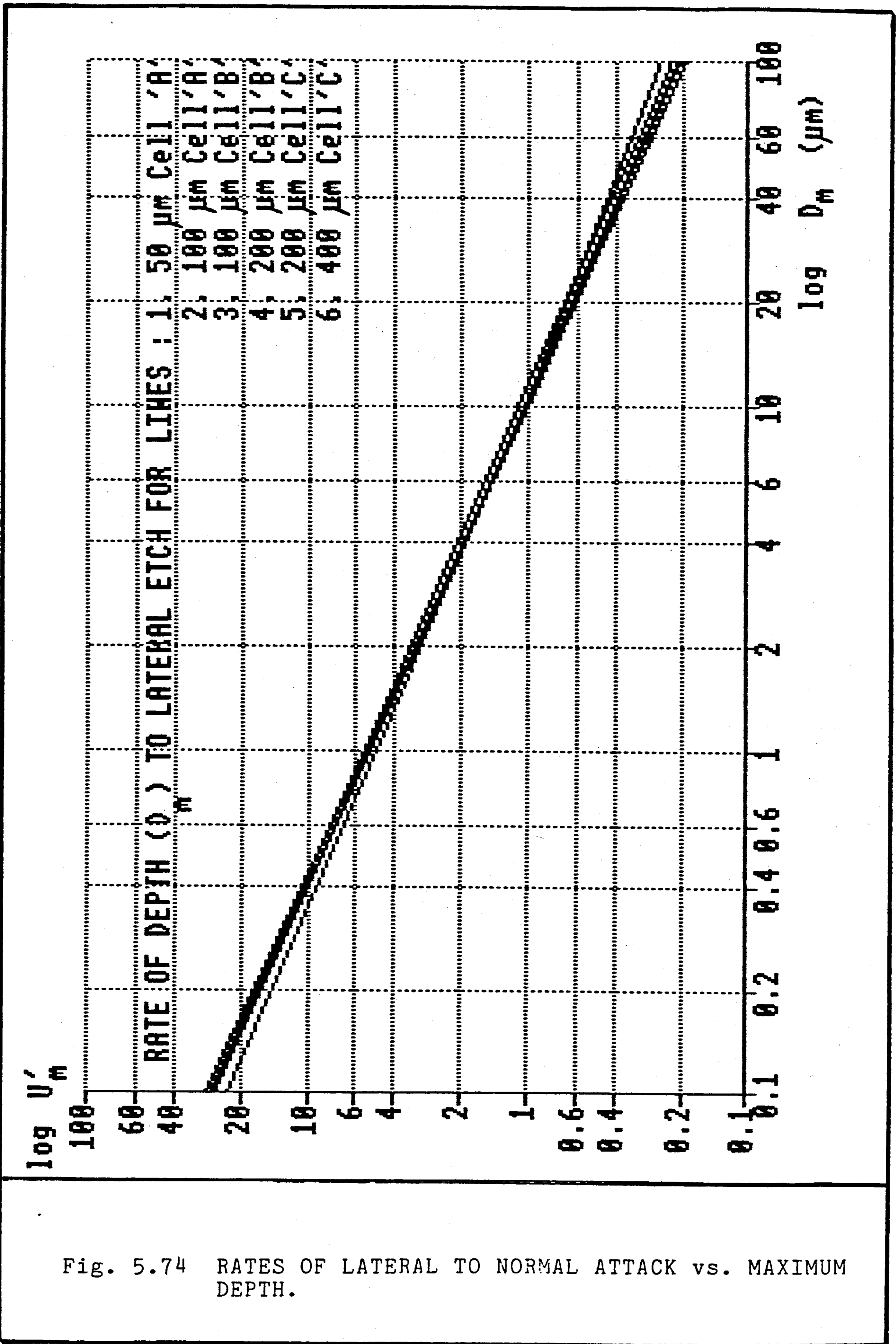

Fig. 5.74 RATES OF LATERAL TO NORMAL ATTACK vs. MAXIMUM DEPTH.

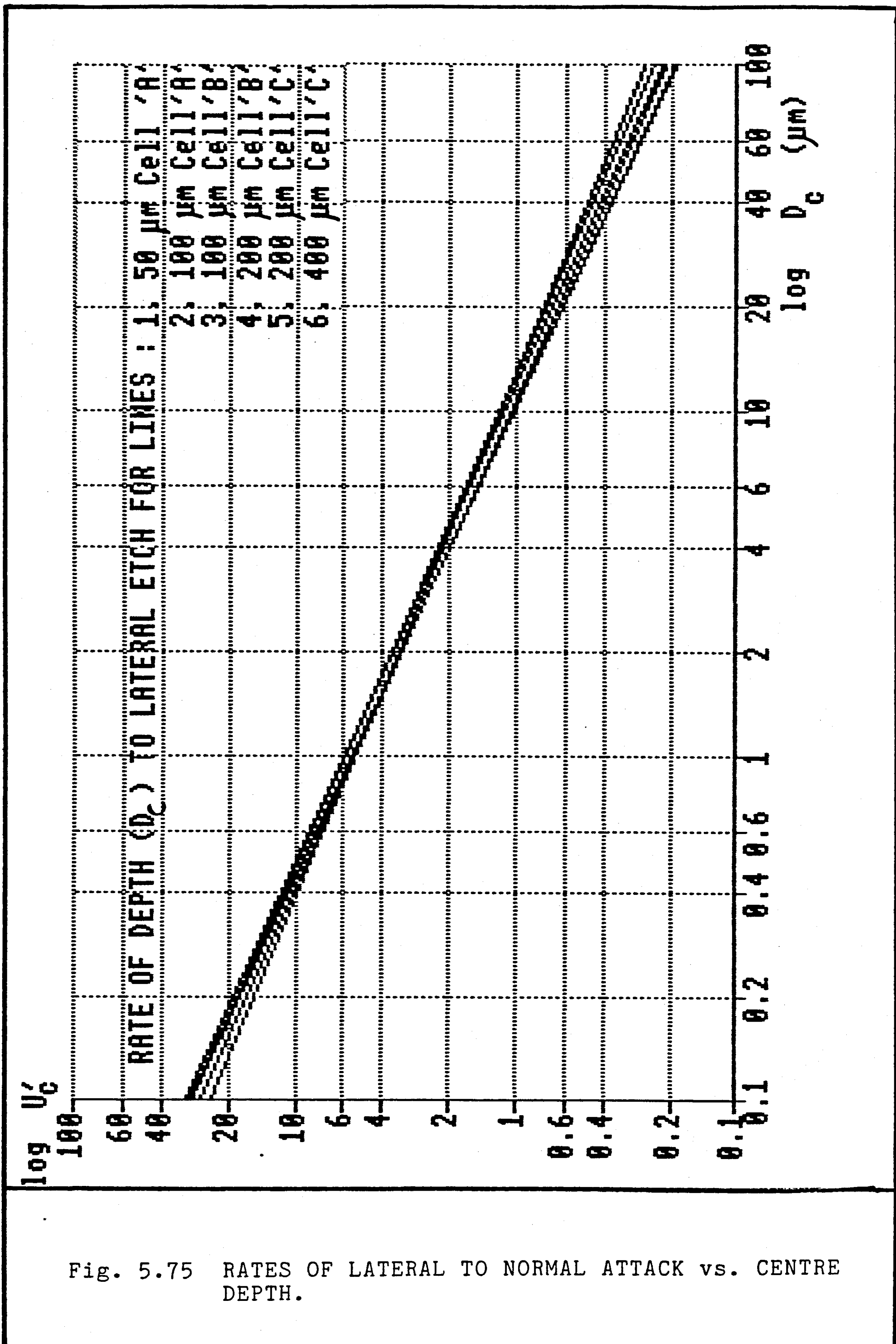

Fig. 5.75 RATES OF LATERAL TO NORMAL ATTACK vs. CENTRE DEPTH.

CURVE TYPE: Y=a*X^b DATA FILE: DMav/LW

REGRESSION COEFFICIENTS

a=186.000114 b=-0.238224754

c=0 d=0

Coefficient of determination=0.964556195

X1=0	XINT=50	X2=1600	Line Width (µm)
Y1=0	YINT=10	Y2=80	Av. Max. Depth (µm)

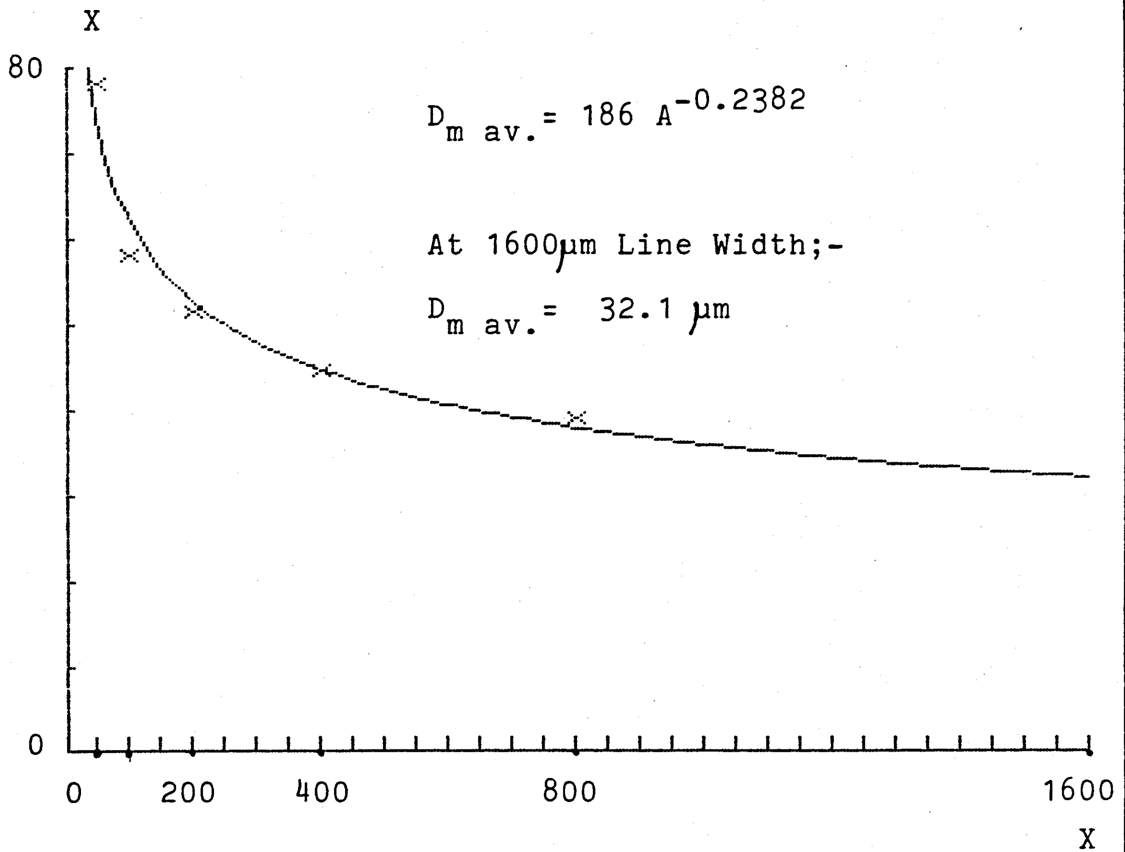

Fig. 5.76 PREDICTED AVERAGE MAXIMUM DEPTH OF ETCH OF CHART.

CURVE TYPE: Y=a*X^b   DATA FILE: DC/LW

REGRESSION COEFFICIENTS

a=284.757424   b=-0.347691536

c=0   d=0

Coefficient of determination=0.971153786

X1=0	XINT=50	X2=1600	Line Width (µm)
Y1=0	YINT=10	Y2=80	Centre Depth (µm)

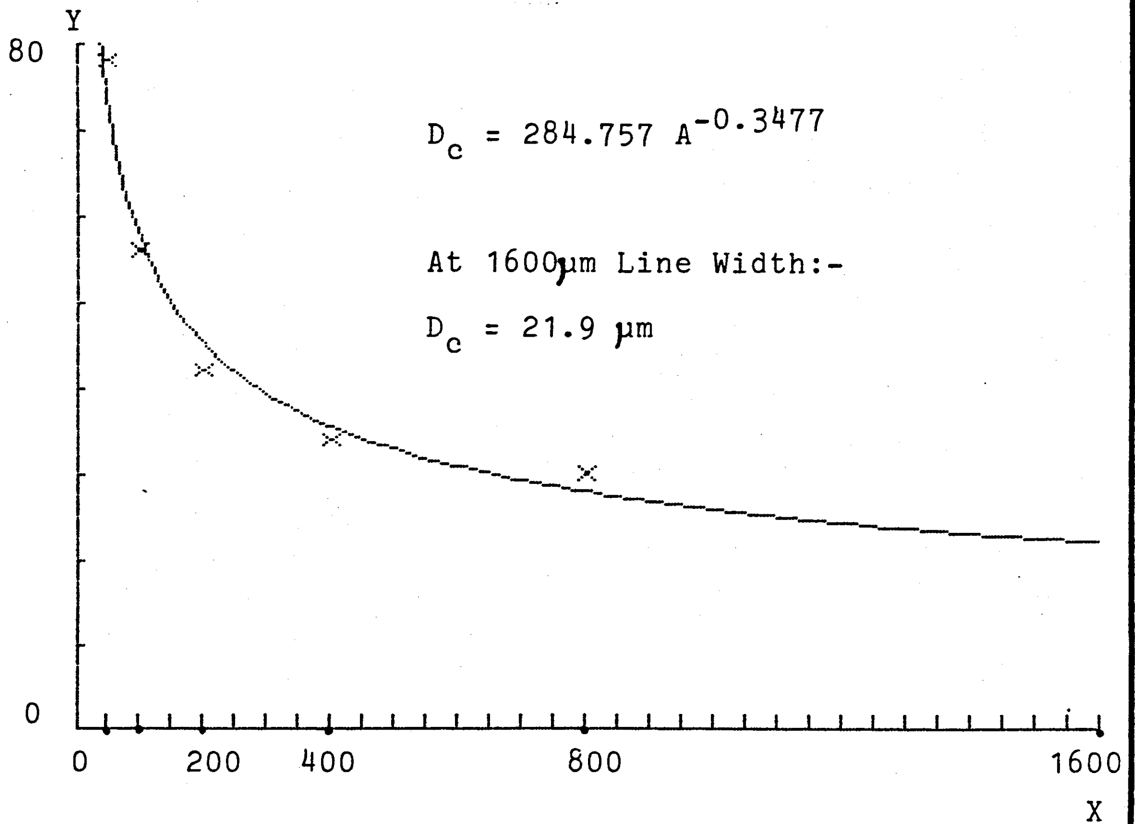

Fig. 5.77 PREDICTED FEATURE CENTRE DEPTH OF ETCH OF CHART.

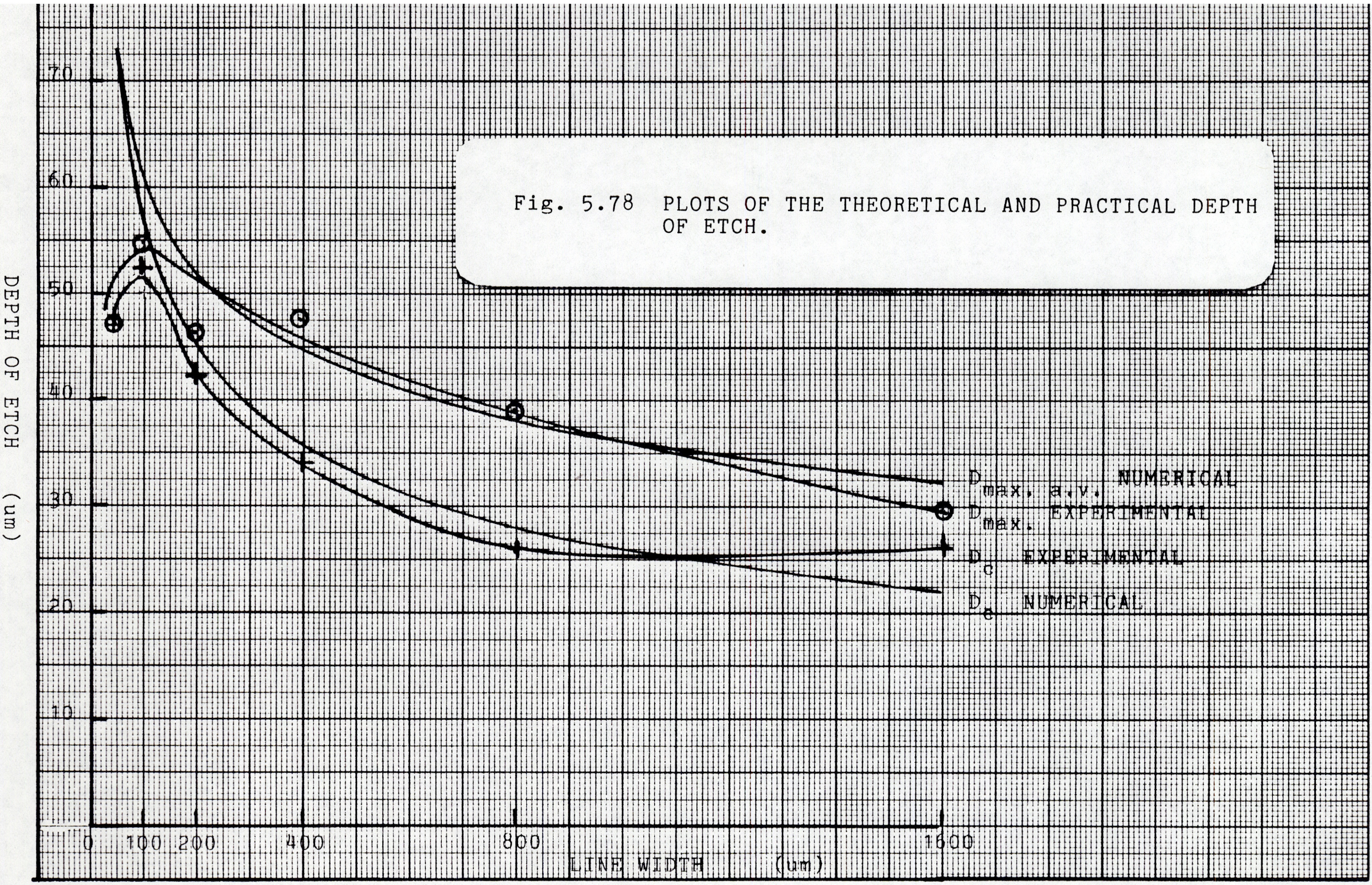

Fig. 5.78 PLOTS OF THE THEORETICAL AND PRACTICAL DEPTH OF ETCH.

CURVE TYPE:Y=a*X^b

DATA FILE: UCVLINE

REGRESSION COEFFICIENTS

a=94.3149222

b=-9.34945794E-2

c=0

d=0

Coefficient of determination=0.911465226

X1=0	XINT=50	X2=800
Y1=0	YINT=10	Y2=70

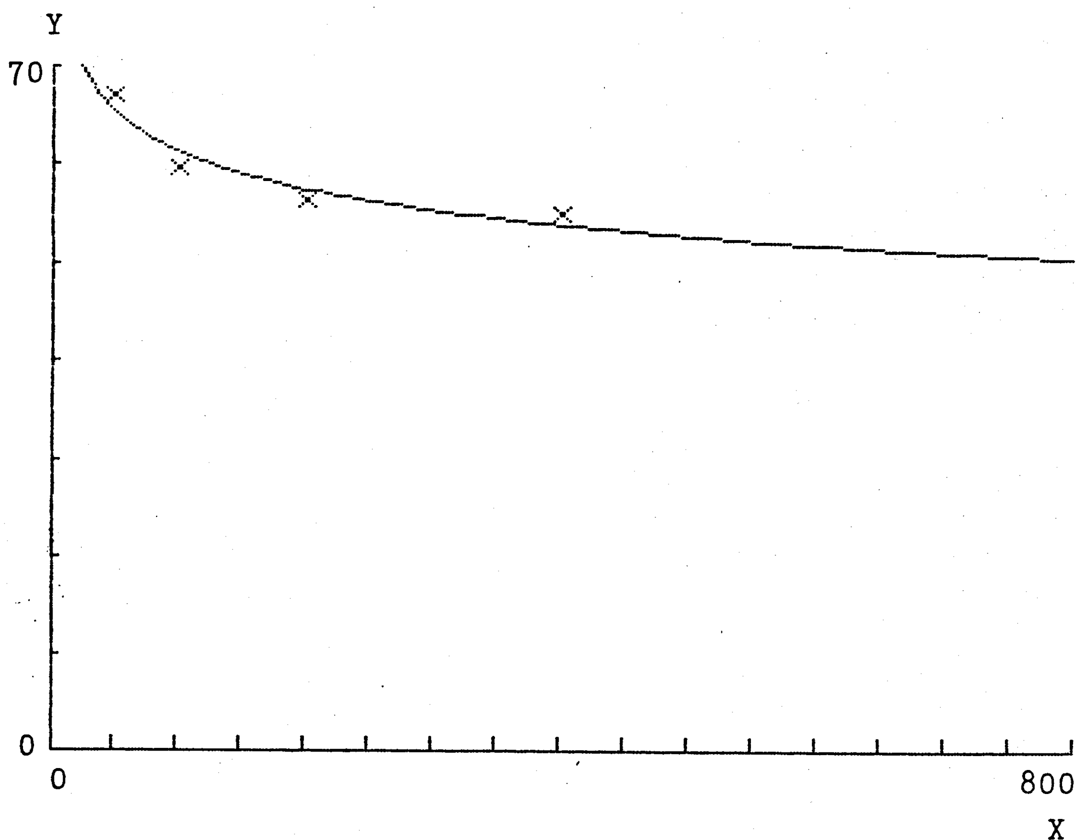

Fig. 5.79 PREDICTED UNDERCUT vs. LINE WIDTH.

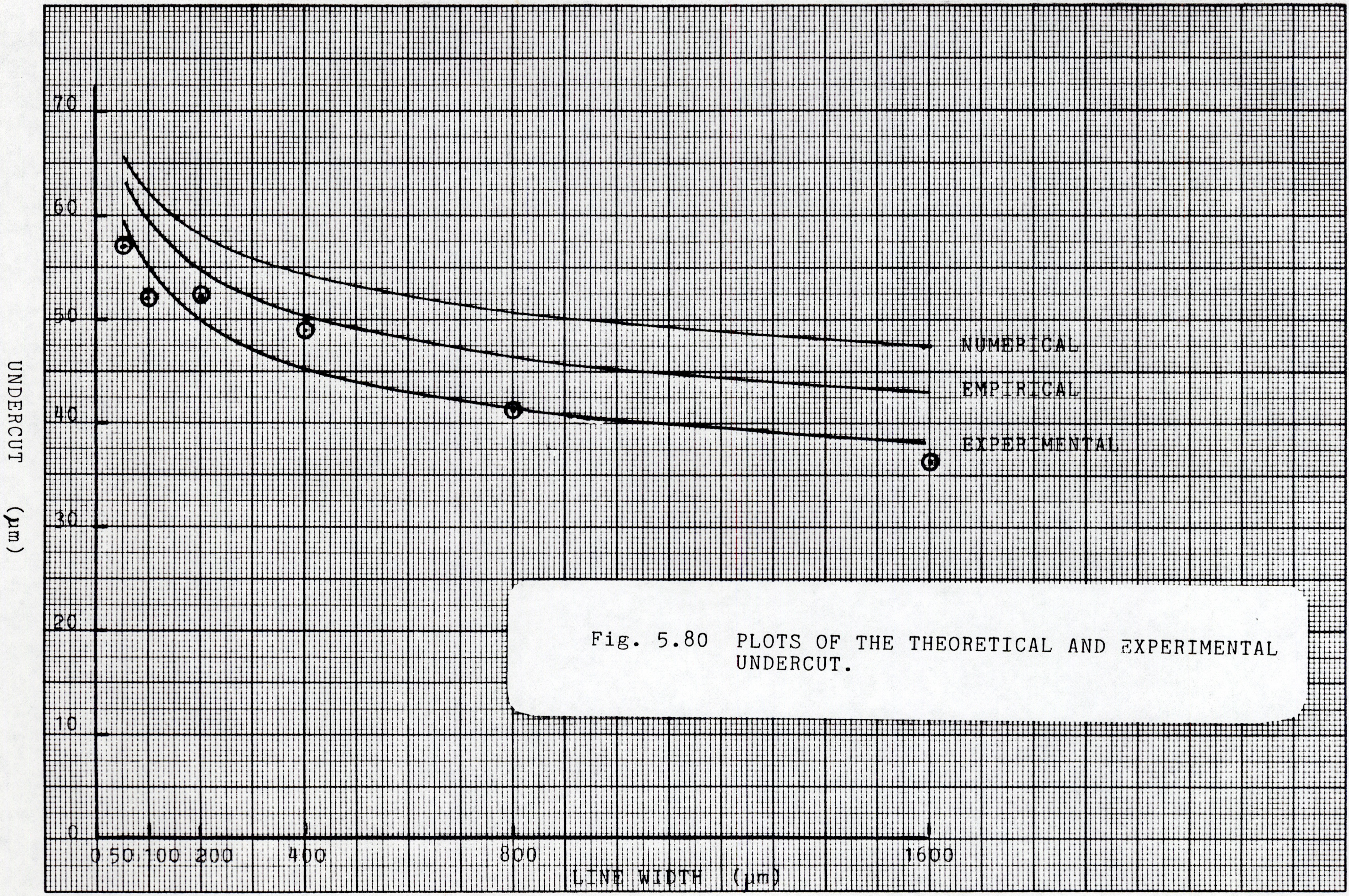

Fig. 5.80 PLOTS OF THE THEORETICAL AND EXPERIMENTAL UNDERCUT.

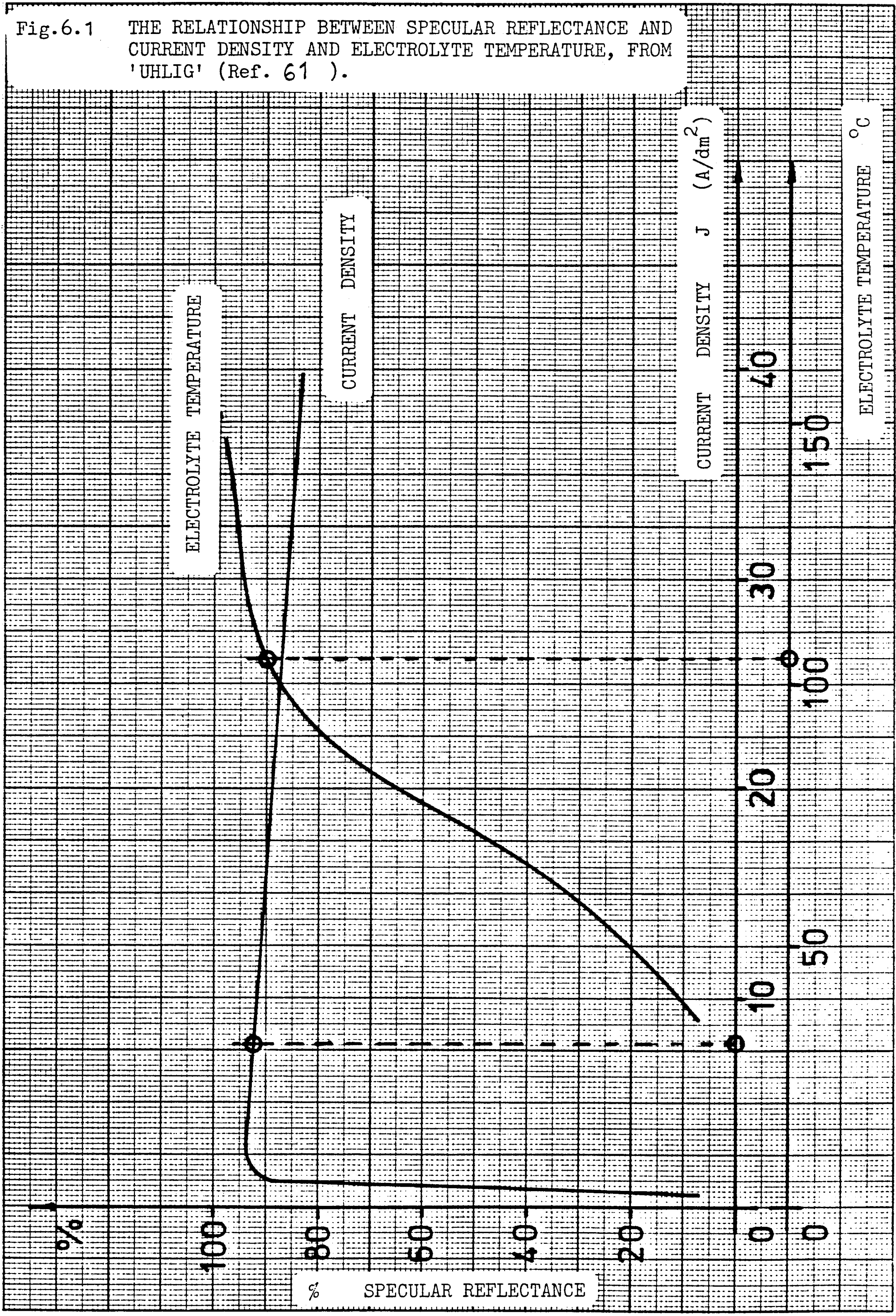

Fig.6.1 THE RELATIONSHIP BETWEEN SPECULAR REFLECTANCE AND CURRENT DENSITY AND ELECTROLYTE TEMPERATURE, FROM 'UHLIG' (Ref. 61).

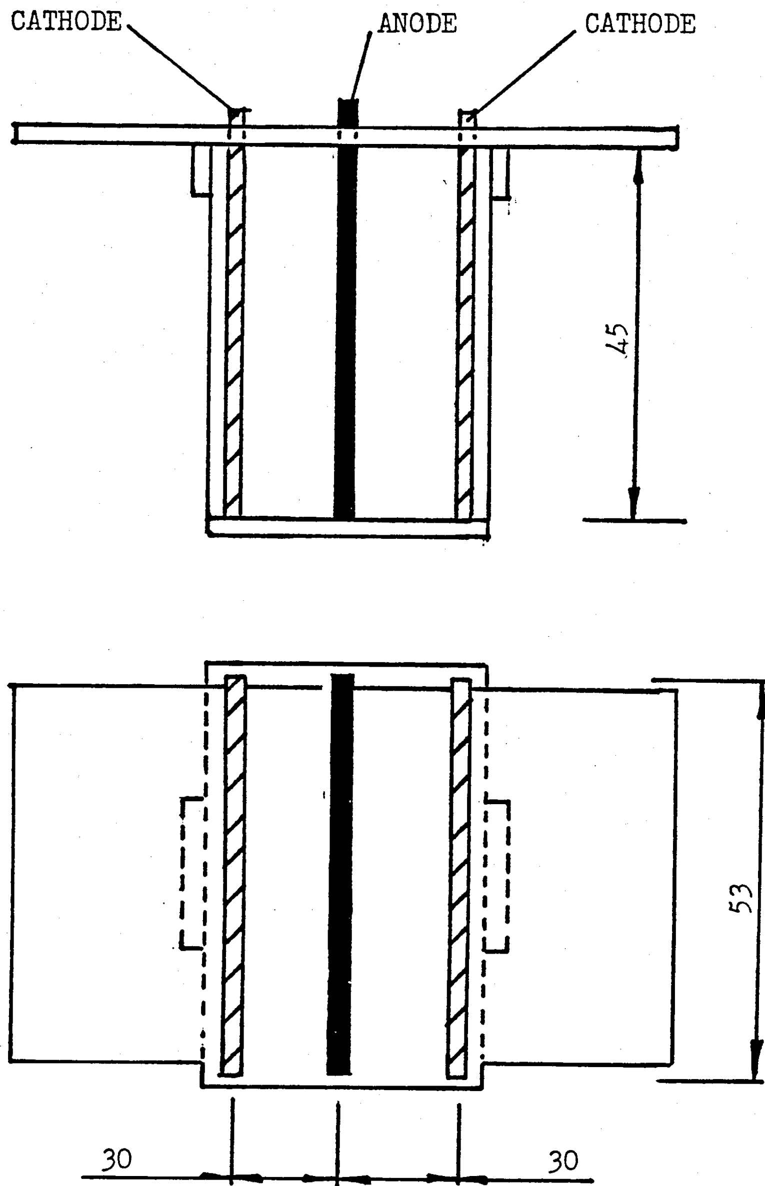

Fig. 6.2 SCHEMATIC DIAGRAM OF THE POLISHING JIG FABRICATED FROM ACRYLIC SHEET 6.35 mm THICK.

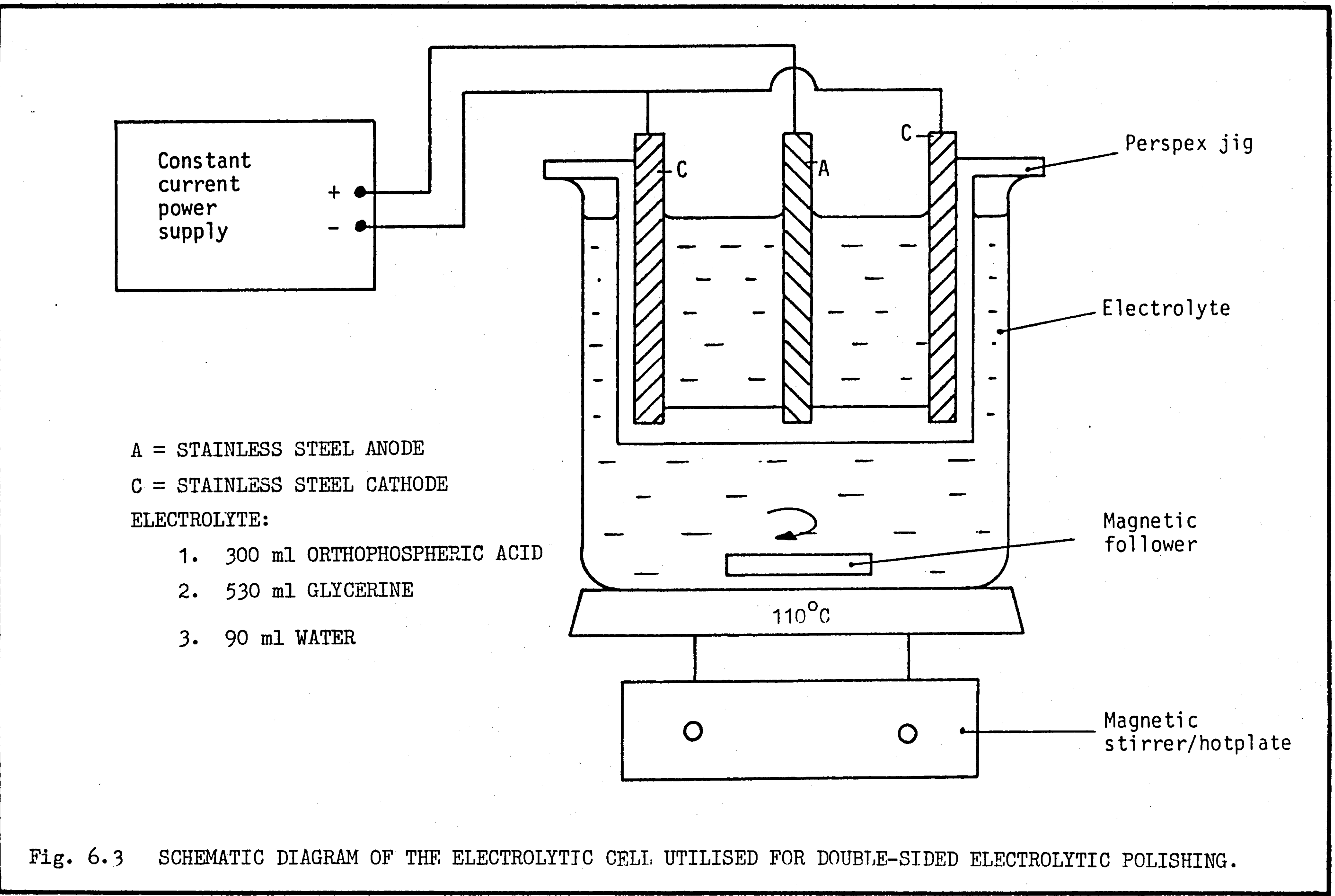

Fig. 6.3 SCHEMATIC DIAGRAM OF THE ELECTROLYTIC CELL UTILISED FOR DOUBLE-SIDED ELECTROLYTIC POLISHING.

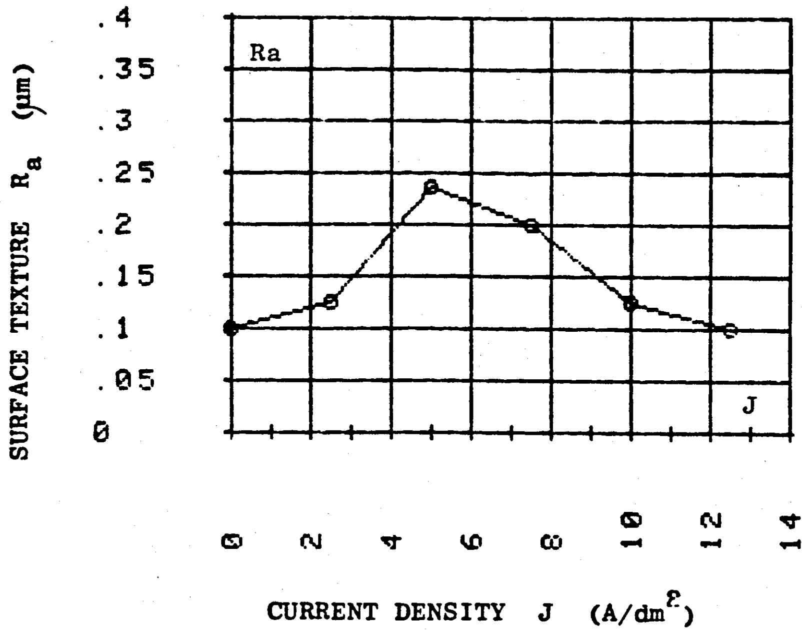

I	X(I)	Y(I)
1	0.0000	0.1000
2	2.5000	0.1250
3	5.0000	0.2350
4	7.5000	0.2000
5	10.0000	0.1250
6	12.5000	0.1000

I = Index of pair

X(I) = The current density J (A/dm^2)

Y(I) = The surface texture Ra (μm)

Fig. 6.4 PLOT OF THE SURFACE TEXTURE OF THE ELECTRO-POLISHED AISI 304 STAINLESS STEEL VERSUS CURRENT DENSITY IN 5 MINUTES.

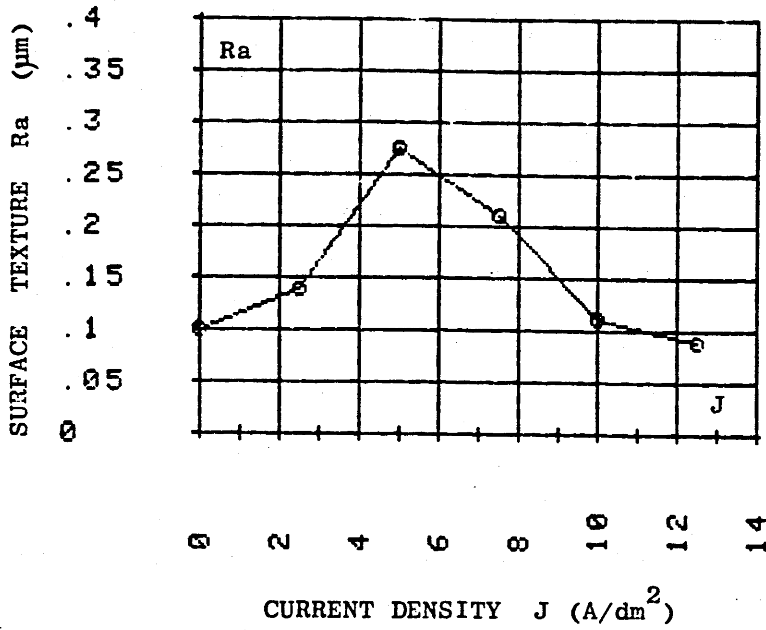

I	X(I)	Y(I)
1	0.0000	0.1000
2	2.5000	0.1400
3	5.0000	0.2750
4	7.5000	0.2100
5	10.0000	0.1100
6	12.5000	0.0900

I = Index of pair

X(I) = The current density J (A/dm^2)

Y(I) = The surface texture Ra (μm)

Fig. 6.5 PLOT OF THE SURFACE TEXTURE OF THE ELECTRO-POLISHED AISI 304 STAINLESS STEEL VERSUS CURRENT DENSITY IN 10 MINUTES.

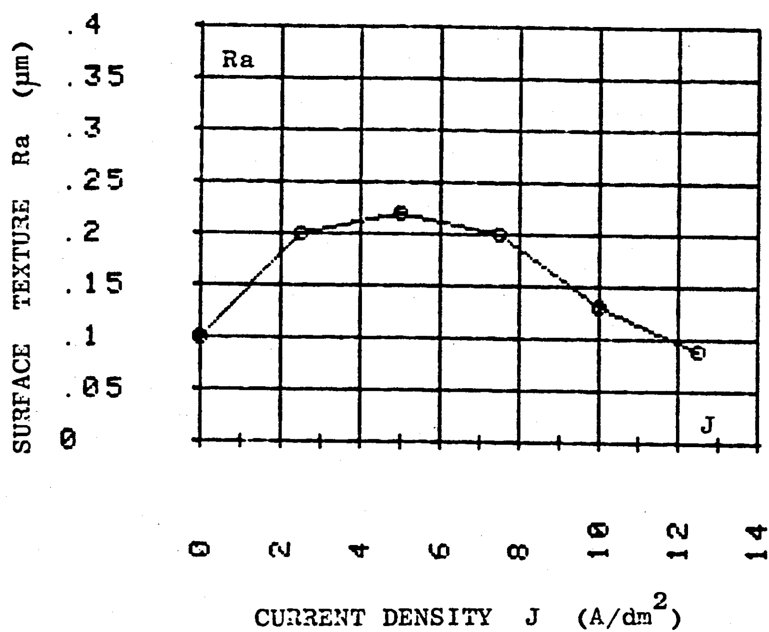

I	X(I)	Y(I)
1	0.0000	0.1000
2	2.5000	0.2000
3	5.0000	0.2200
4	7.5000	0.2000
5	10.0000	0.1300
6	12.5000	0.0900

I = Inex of pair

X(I) = The current density J (A/dm^2)

Y(I) = The surface texture Ra (μm)

Fig. 6.6 PLOT OF THE SURFACE TEXTURE OF THE ELECTRO-POLISHED AISI304 STAINLESS STEEL VERSUS CURRENT DENSITY IN 15 MINUTES.

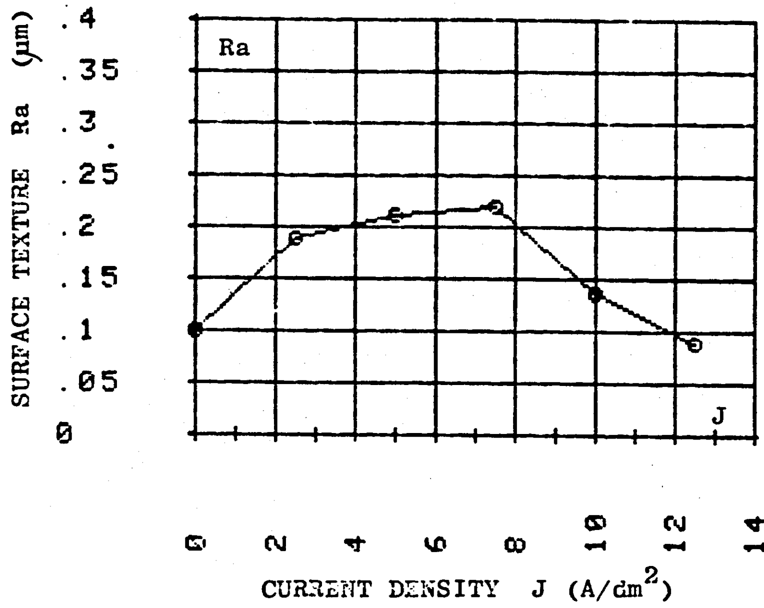

I	X(I)	Y(I)
1	0.0000	0.1000
2	2.5000	0.1900
3	5.0000	0.2100
4	7.5000	0.2200
5	10.0000	0.1350
6	12.5000	0.0900

I = Index of pair

X(I) = The current density J (A/dm^2)

Y(I) = The surface texture Ra (μm)

Fig. 6.7 PLOT OF THE SURFACE TEXTURE OF THE ELECTRO-POLISHED AISI 304 STAINLESS STEEL VERSUS CURRENT DENSITY IN 20 MINUTES.

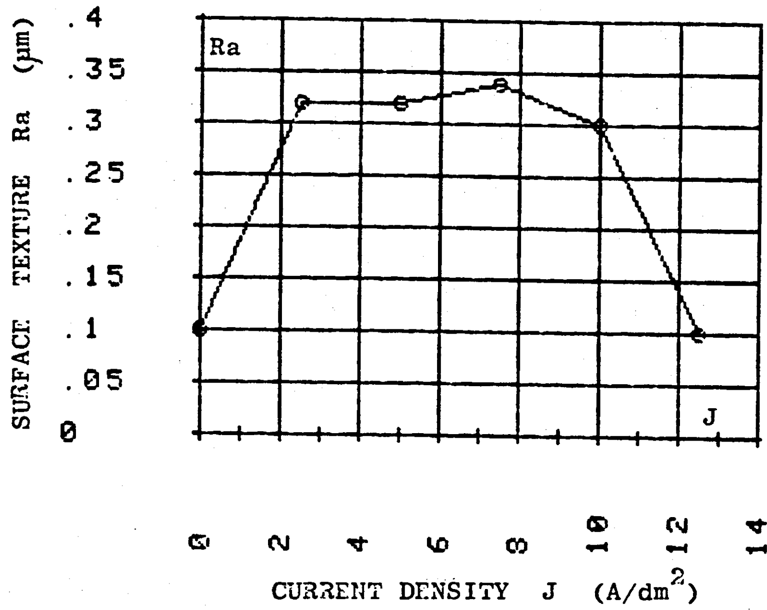

I	X(I)	Y(I)
1	0.0000	0.1000
2	2.5000	0.3200
3	5.0000	0.3200
4	7.5000	0.3400
5	10.0000	0.3000
6	12.5000	0.1000

I = Index of pair

X(I) = The current density J (A/dm^2)

Y(I) = The surface texture Ra (μm)

Fig. 6.8 PLOT OF THE SURFACE TEXTURE OF THE ELECTRO-POLISHED AISI 304 STAINLESS STEEL VERSUS CURRENT DENSITY IN 25MINUTES.

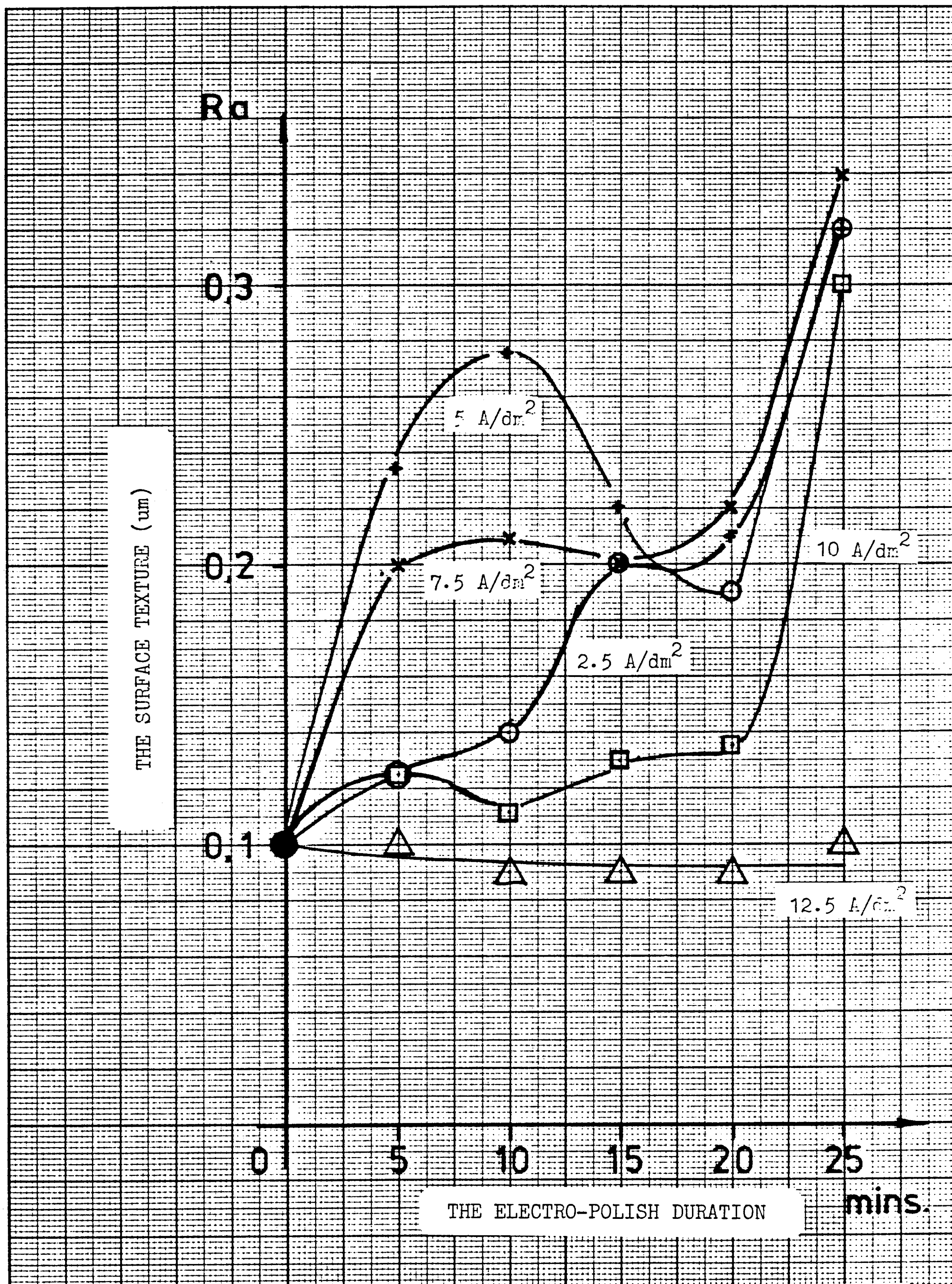

Fig. 6.9 THE SURFACE TEXTURE OF ELECTRO POLISHED AISI 304 STAINLESS STEEL FOR CURRENT DENSITIES OF 2.5, 5, 7.5, 10 AND 12.5 A/dm^2.

AOV: LOG REG:CODE 2

SOURCE/DF		SS	MS	F
TOTAL	6	984.9		
REG	1	884.5	884.5	44.1
RESID	5	100.4	20.1	

R SQUARE = 0.898

YHAT= 76.361+ -3.284LOG X

X(I)	Y(I)	YHAT	RESIDUALS
0.00	100.00	99.04	0.96
5.43	65.00	70.81	-5.81
12.94	73.00	67.95	5.05
14.20	65.00	67.65	-2.65
16.50	65.00	67.16	-2.16
25.75	65.00	65.69	-0.69
34.90	70.00	64.70	5.30

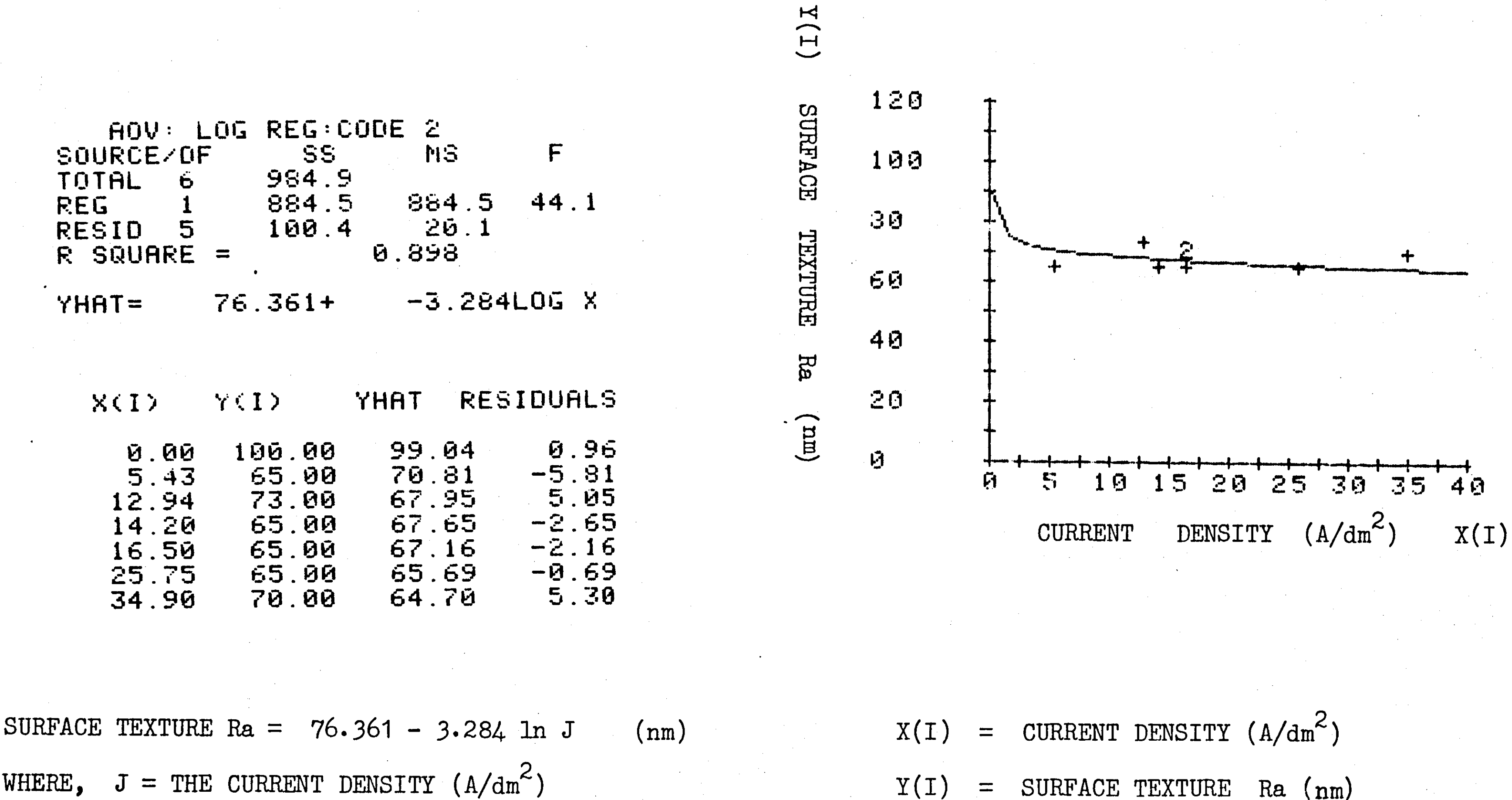

SURFACE TEXTURE Ra = 76.361 - 3.284 ln J (nm)

WHERE, J = THE CURRENT DENSITY (A/dm^2)

X(I) = CURRENT DENSITY (A/dm^2)

Y(I) = SURFACE TEXTURE Ra (nm)

Fig. 6.10 AOV OF THE RESULTS FOR THE SURFACE TEXTURE VERSUS CURRENT DENSITY FOR THE MODIFIED ELECTROPOLISHING SOLUTION, ETCH DURATION WAS 15 MINUTES.

AOV: LINEAR REG:CODE 1

SOURCE/DF		SS	MS	F
TOTAL	6	0.8		
REG	1	0.8	0.8	177.2
RESID	5	0.0	0.0	

R SQUARE = 0.973

YHAT = -0.035 + 0.032 X

X(I)	Y(I)	YHAT	RESIDUALS
0.00	0.00	-0.03	0.03
5.43	0.13	0.14	-0.01
12.94	0.30	0.37	-0.07
14.20	0.40	0.41	-0.01
16.50	0.57	0.49	0.08
25.75	0.70	0.78	-0.08
34.29	1.10	1.05	0.05

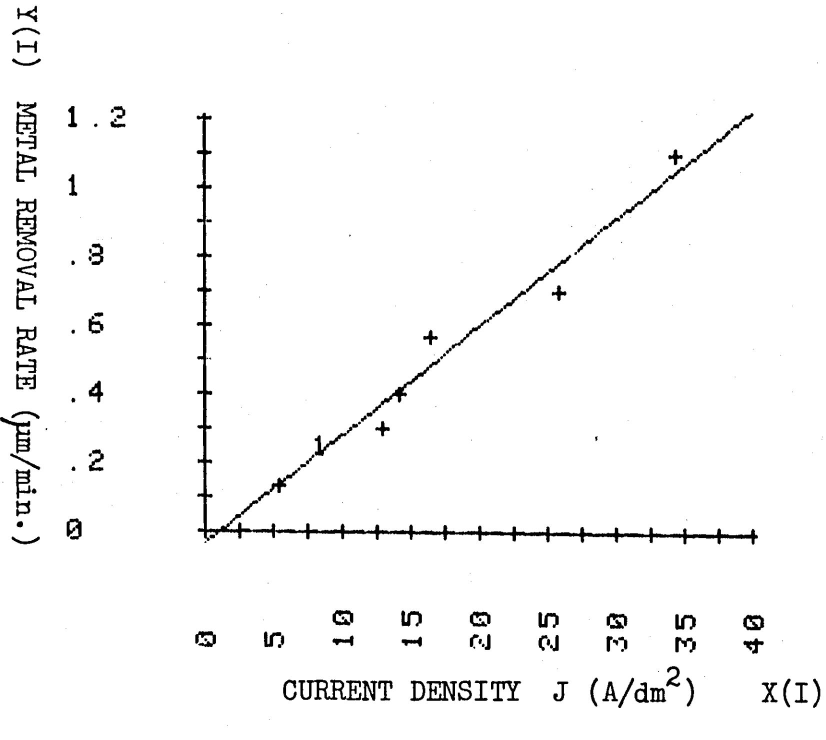

X(I) = THE CURRENT DENSITY J (A/dm^2)

Y(I) = THE METAL REMOVAL RATE (µm/min.)

Y_{HAT} = METAL REMOVAL RATE = 0.032 J - 0.035 (µm/min)

WHERE, J = THE CURRENT DENSITY (A/dm^2)

Fig. 6.11 AOV OF THE RESULTS FOR THE METAL REMOVAL RATE VERSUS THE CURRENT DENSITY WHEN ELECTROPOLISHING AISI 304 STAINLESS STEEL WITH THE MODIFIED ELECTROLYTE.

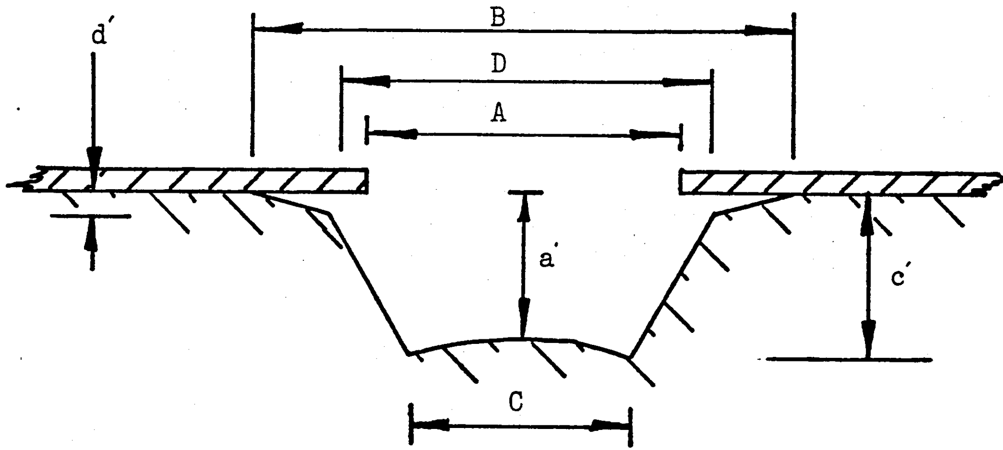

Line number (n)

		1	2	3	4	5	6
A	µm	60	130	240	470	870	1740
A/2	µm	30	65	120	235	435	870
B	µm	350	390	500	690.	1090	1880
B/2	µm	175	195	250	345	545	940
C	µm	θ	θ	80	320	730	1450
C/2	µm	-	-	40	160	365	725
D	µm	180	220	360	570	980	1750
D/2	µm	90	110	180	285	490	875
Slope		.176	.212	.314	.417	.510	.508
Undercut	µm	145	130	130	110	110	70
a′	µm	29	36	46	47	43	40
c′	µm	29	36	47	55	61	72
d′	µm	15	18	22	25	28	33
e.f. @ centre		0.20	.277	.357	.427	.391	.571
Max e.f.		.2	.277	.362	0.5	.555	1.029

Where,

$$\text{e.f. @ Centre} = \frac{a'}{\text{undercut}}$$

$$\text{e.f. max.} = \frac{c'}{\text{undercut}}$$

$$\text{Slope} = \frac{d'_n}{0.5(B-D)_n}$$

Fig. 6.12 METHOD AND RESULTS FOR THE PROFILE MEASUREMENT OF THE ELECTRO PHOTOPOLISHED RESULTS.

AOV: LINEAR REG:CODE 1

SOURCE/DF		SS	MS	F
TOTAL	5	3420.8		
REG	1	3198.0	3198.0	57.4
RESID	4	222.9	55.7	
R SQUARE =			0.935	

YHAT = 139.052 + -0.040 X

X(I)	Y(I)	YHAT	RESIDUALS
60.00	145.00	136.67	8.33
130.00	130.00	133.89	-3.89
240.00	130.00	129.53	0.47
470.00	110.00	120.40	-10.40
870.00	110.00	104.52	5.48
1740.00	70.00	69.99	0.01

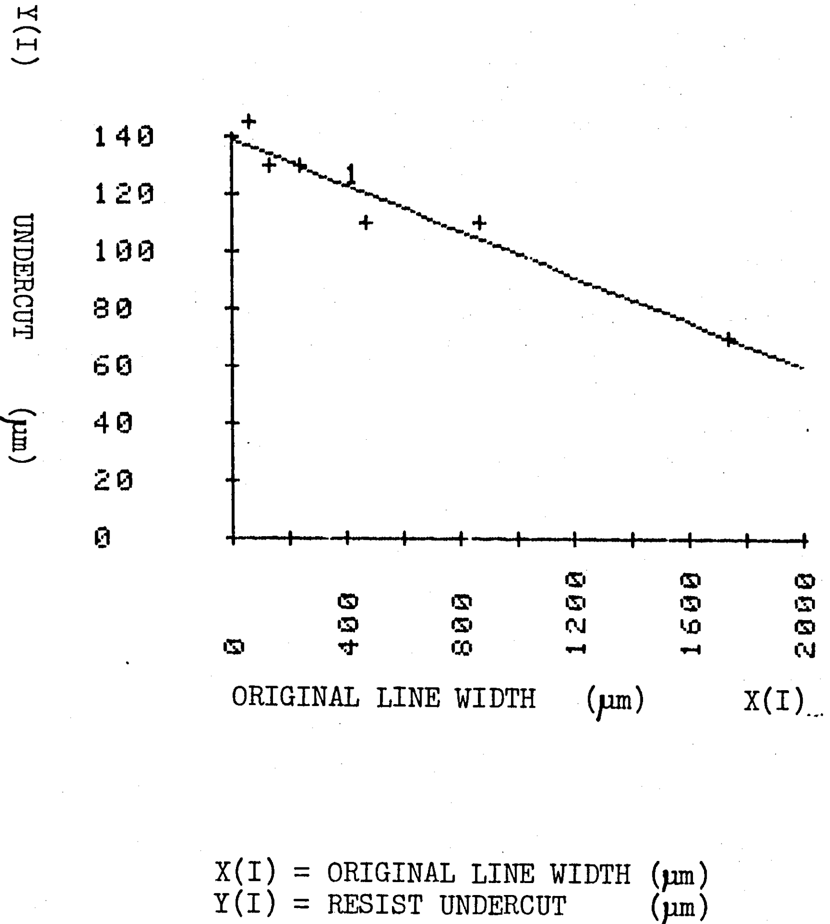

RESIST UNDERCUT = Y_{HAT} = 139.025 - 0.04 A (µm)

WHERE, A = ORIGINAL LINE WIDTH (µm)

X(I) = ORIGINAL LINE WIDTH (µm)
Y(I) = RESIST UNDERCUT (µm)

Fig. 6.13 AOV OF THE RESULTS FOR THE RESIST UNDERCUT VERSUS THE ORIGINAL LINE WIDTH IN E.P.P. AISI 304 STAINLESS STEEL.

ORIGINAL LINE WIDTH = 470 μm

n 4

ORIGINAL LINE WIDTH = 240 μm

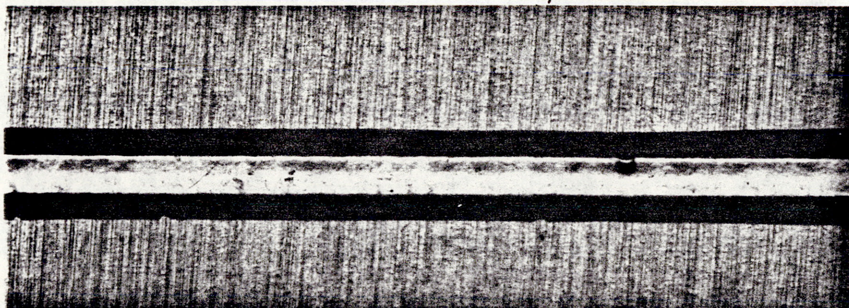

n 3

ORIGINAL LINE WIDTH = 130 μm

n 2

ORIGINAL LINE WIDTH = 60 μm

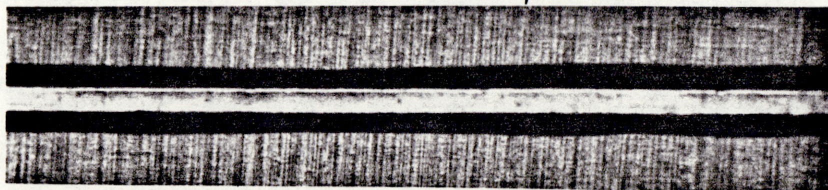

n 1

Fig. 6.14 PHOTOMICROGRAPH OF THE ELECTRO PHOTOPOLISHED CHART, MAGNIFICATION = x 23.2

ORIGINAL LINE WIDTH = 1740 μm

n 6

ORIGINAL LINE WIDTH = 870 μm

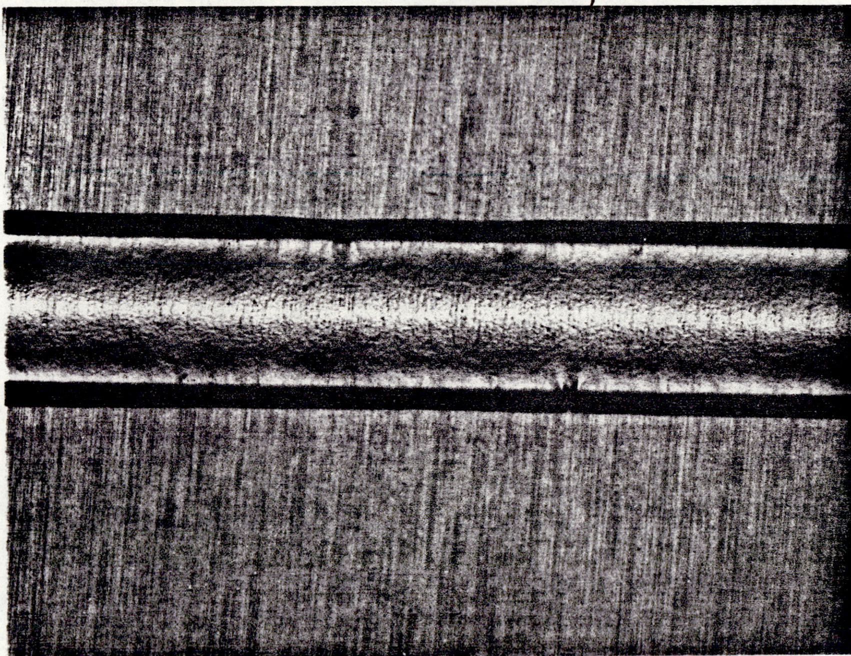

n 5

Fig. 6.15 PHOTOMICROGRAPH OF THE ELECTRO PHOTOPOLISHED CHART, MAGNIFICATION = x 23.2

ORIGINAL LINE WIDTH = 130 µm (Mag x 91.2)

n 2

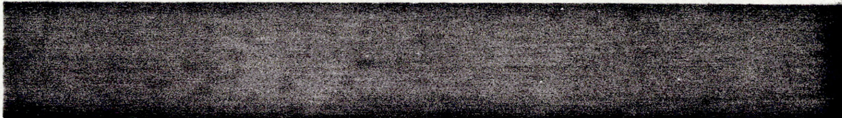

ORIGINAL LINE WIDTH = 60 µm (Mag x 91.2)

n 1

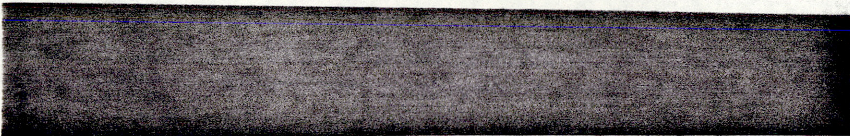

GRATICULE SCALE 1 DIVISION = 0.01 mm

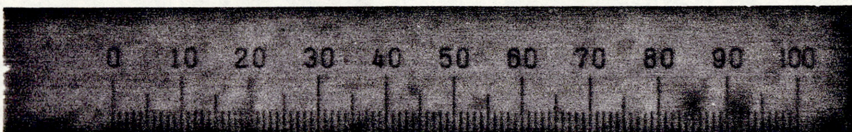

Fig. 6.16 PHOTOMICROGRAPHS OF THE SECTIONS OF THE ELECTRO PHOTOPOLISHED RESOLUTION CHART.

ORIGINAL LINE WIDTH = 470 µm (Mag x 91.2)

n 4

ORIGINAL LINE WIDTH = 240 µm (Mag x 91.2)

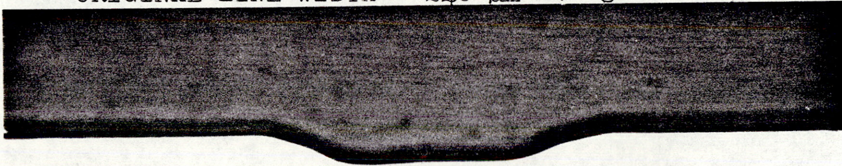

n 3

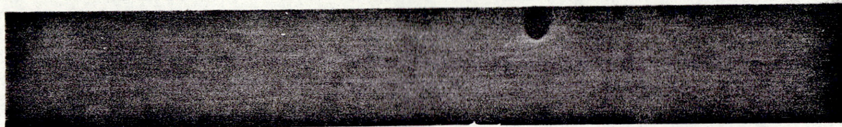

GRATICULE SCALE 1 DIVISION = .01 mm

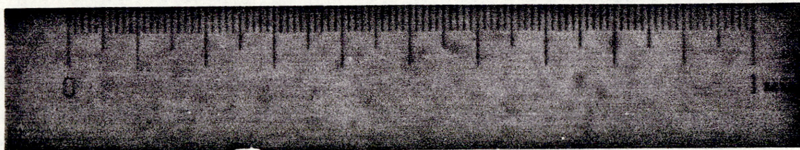

Fig. 6.17 PHOTOMICROGRAPHS OF THE SECTIONS OF THE ELECTRO PHOTOPOLISHED RESOLUTION CHART.

ORIGINAL LINE WIDTH = 1740 um (Mag = x 45.3)

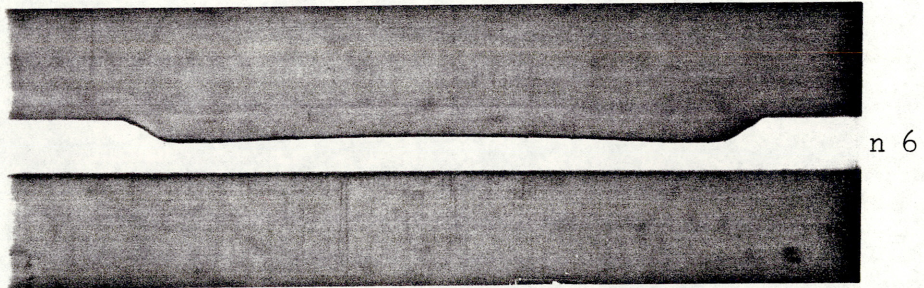

n 6

ORIGINAL LINE WIDTH = 870 um (Mag = x 45.83)

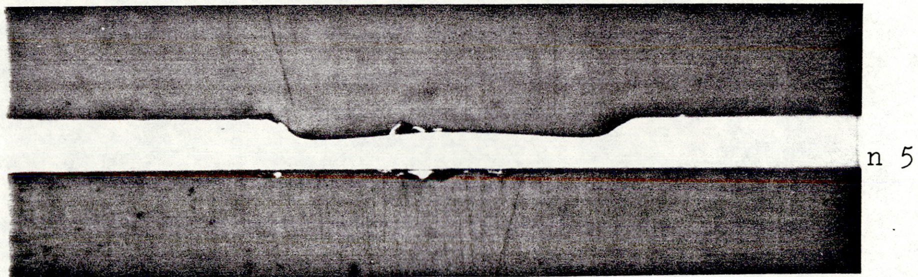

n 5

GRATICULE SCALE 1 DIVISION = 0.1 mm

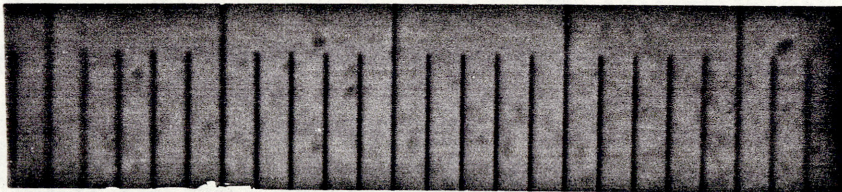

Fig. 6.18 PHOTOMICROGRAPHS OF THE SECTIONS OF THE ELECTRO PHOTOPOLISHED RESOLUTION CHART.

AOV: POWER: CODE 4

SOURCE/DF		SS	MS	F
TOTAL	5	0.6		
REG	1	0.6	0.6	269.3
RESID	4	0.0	0.0	

R SQUARE = 0.985

YHAT= 9.813X ^ 0.272

X(I)	Y(I)	YHAT	RESIDUALS
60.00	29.00	29.88	-0.88
130.00	36.00	36.88	-0.88
240.00	46.00	43.57	2.43
470.00	55.00	52.31	2.69
870.00	61.00	61.85	-0.85
1740.00	72.00	74.68	-2.68

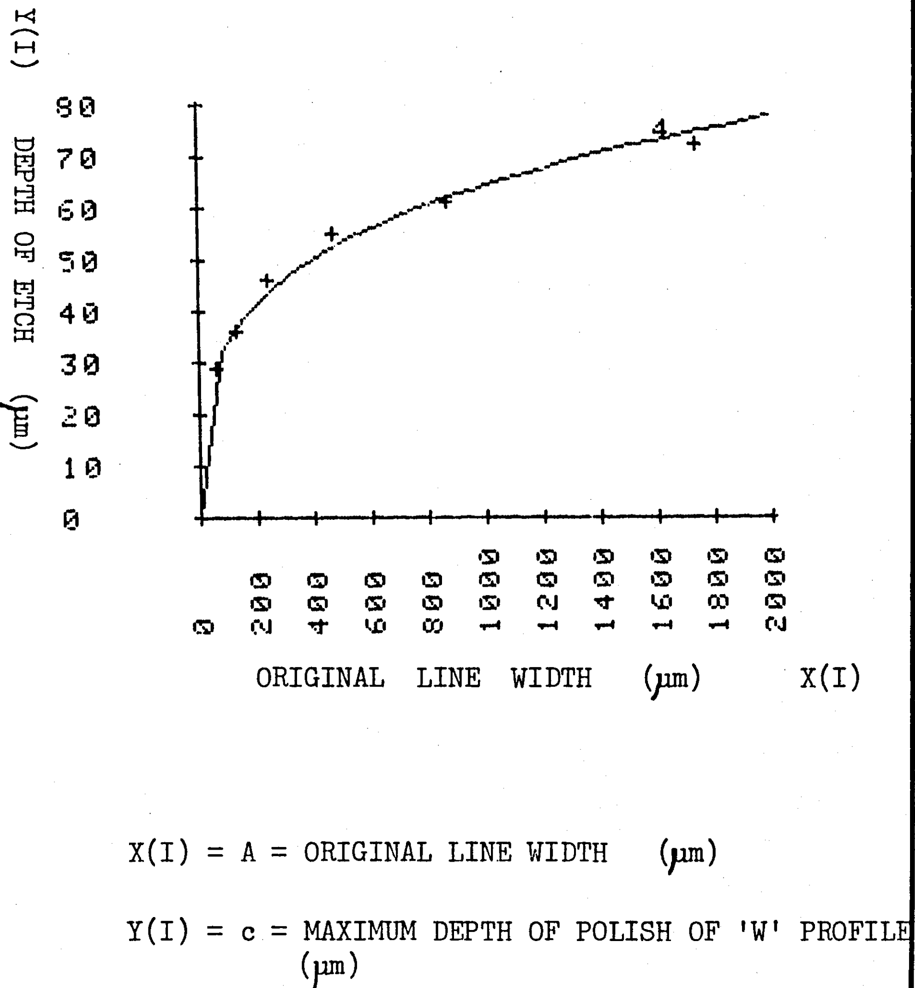

X(I) = A = ORIGINAL LINE WIDTH (μm)

Y(I) = c = MAXIMUM DEPTH OF POLISH OF 'W' PROFILE (μm)

MAX. DEPTH OF POLISH = $Y_{HAT} = 9.813\ A^{0.272}$ (μm)

Fig. 6.19 AOV OF THE RESULTS FOR THE MAXIMUM DEPTH OF POLISH (c) OF THE 'W' PROFILE VERSUS THE ORIGINAL LINE WIDTH.

```
   AOV: POWER: CODE 4
SOURCE/DF      SS       MS      F
TOTAL   2      0.0
REG     1      0.0       0.0 113.5
RESID   1      0.0       0.0
R SQUARE =          0.991

YHAT=     99.602X ^       -0.123


  X(I)     Y(I)      YHAT   RESIDUALS

  470.00   47.00    46.78      0.22
  970.00   43.00    43.38     -0.38
 1740.00   40.00    39.84      0.16

   X(I)        YHAT

  240.00     50.81
```

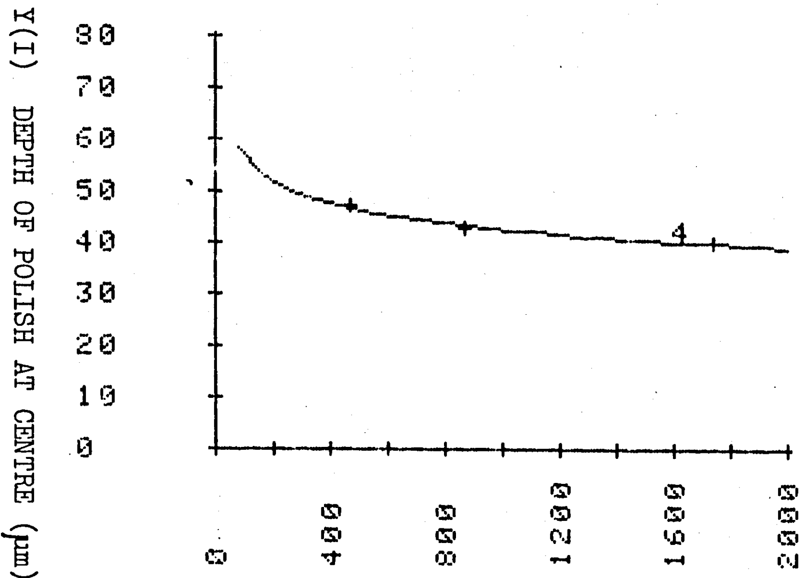

DEPTH OF POLISH AT CENTRE = Y_{HAT} = 99.602 $A^{-0.123}$ (µm)

X(I) = ORIGINAL LINE WIDTH (µm)
Y(I) = DEPTH OF POLISH AT CENTRE (µm)

Fig. 6.20 THE DEPTH OF POLISH MEASURED AT THE CENTRE VERSUS ORIGINAL LINE WIDTH FOR LINE NUMBERS 4, 5 & 6.

AOV: POWER: CODE 4

SOURCE/DF		SS	MS	F
TOTAL	5	1.7		
REG	1	1.6	1.6	136.7
RESID	4	0.0	0.0	

R SQUARE = 0.972

YHAT= 0.030X ^ 0.457

X(I)	Y(I)	YHAT	RESIDUALS
60.00	0.20	0.19	0.01
130.00	0.28	0.28	0.00
240.00	0.36	0.36	-0.00
470.00	0.50	0.50	0.00
870.00	0.56	0.66	-0.10
1740.00	1.03	0.90	0.13

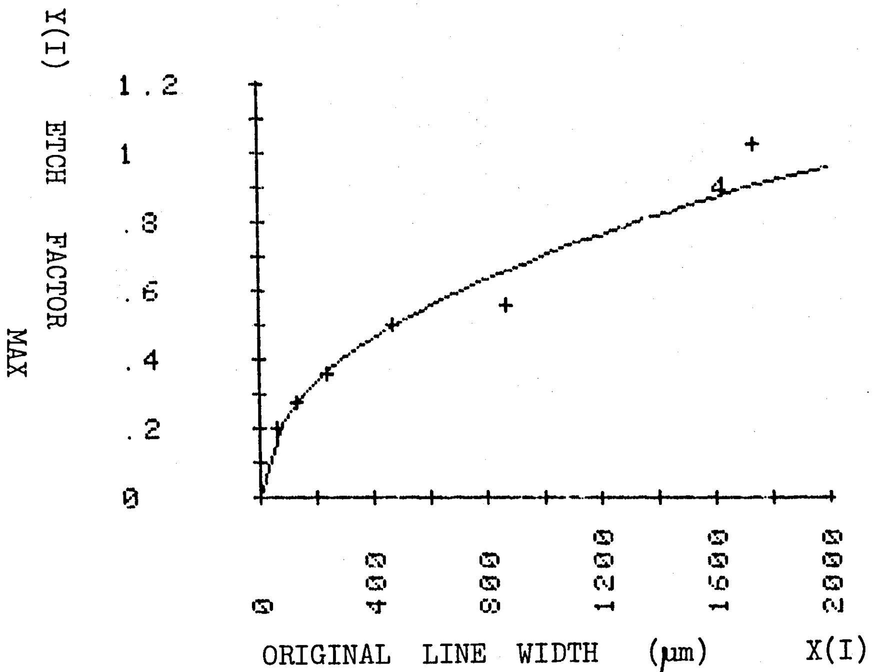

$Y_{HAT} = e.f._{max.} = 0.03\ A^{0.457}$

X(I) = A = ORIGINAL LINE WIDTH (µm)

Y(I) = $\text{ETCH FACTOR}_{\text{MAX}}$

Fig. 6.21 AOV OF THE RESULTS FOR THE ETCH FACTOR VERSUS ORIGINAL LINE WIDTH IN E.P.P., WHERE THE ETCH FACTOR WAS CALCULATED USING THE MAXIMUM DEPTH OF POLISH.

AOV: POWER: CODE 4

SOURCE/DF		SS	MS	F
TOTAL	5	0.7		
REG	1	0.6	0.6	44.9
RESID	4	0.1	0.0	

R SQUARE = 0.918

YHAT= 0.069X ^ 0.280

X(I)	Y(I)	YHAT	RESIDUALS
60.00	0.20	0.22	-0.02
130.00	0.28	0.27	0.01
240.00	0.35	0.32	0.03
470.00	0.43	0.39	0.04
870.00	0.39	0.46	-0.07
1740.00	0.57	0.56	0.01

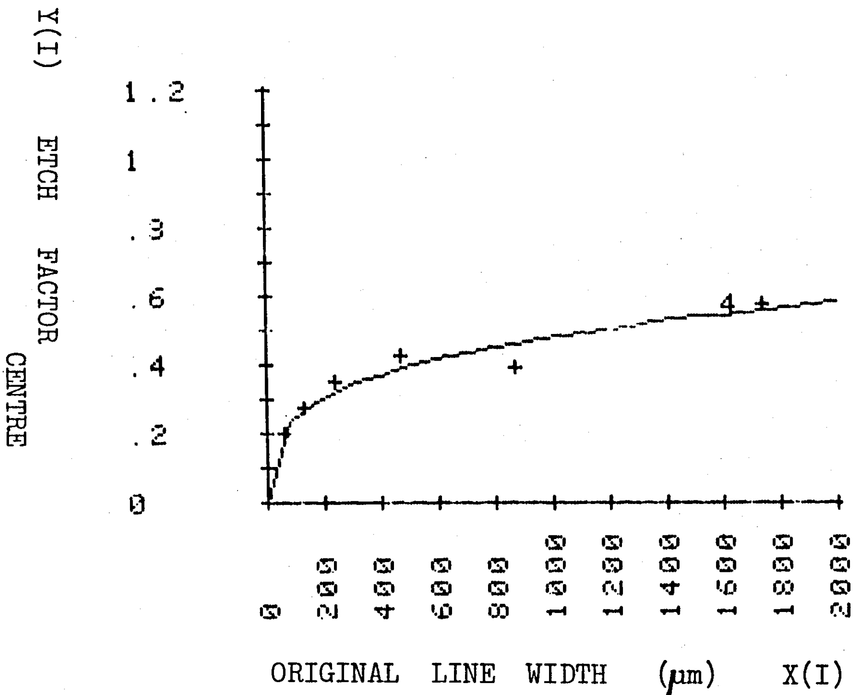

$Y_{HAT} = e.f._{CENTRE} = 0.069\, A^{0.28}$

X(I) = A = ORIGINAL LINE WIDTH (µm)

Y(I) = ETCH FACTOR $_{CENTRE}$

Fig. 6.22 AOV OF THE RESULTS FOR THE ETCH FACTOR VERSUS ORIGINAL LINE WIDTH IN E.P.P. WHERE THE ETCH FACTOR WAS CALCULATED USING THE DEPTH OF POLISH AT THE CENTRE OF THE LINE.

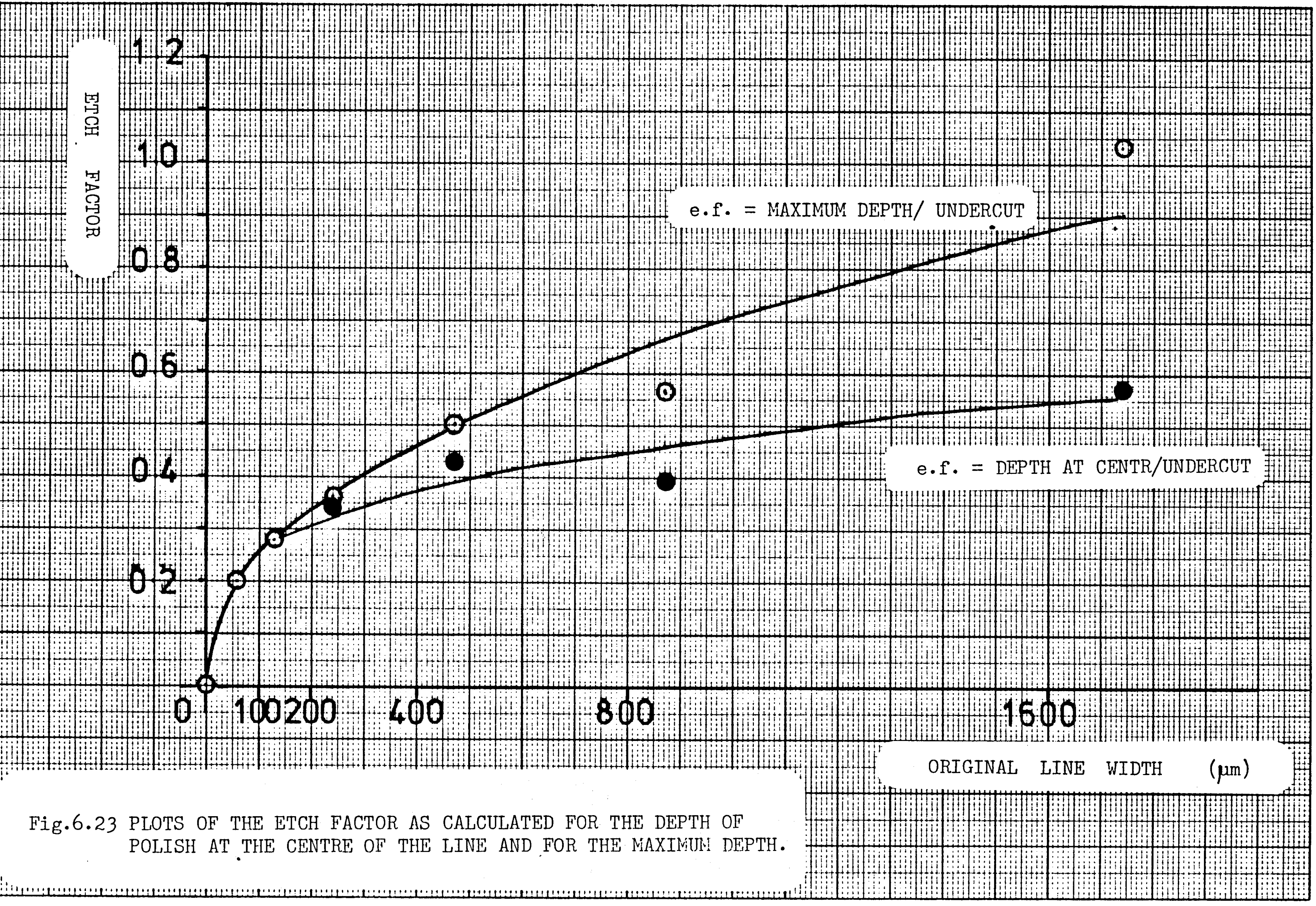

Fig.6.23 PLOTS OF THE ETCH FACTOR AS CALCULATED FOR THE DEPTH OF POLISH AT THE CENTRE OF THE LINE AND FOR THE MAXIMUM DEPTH.

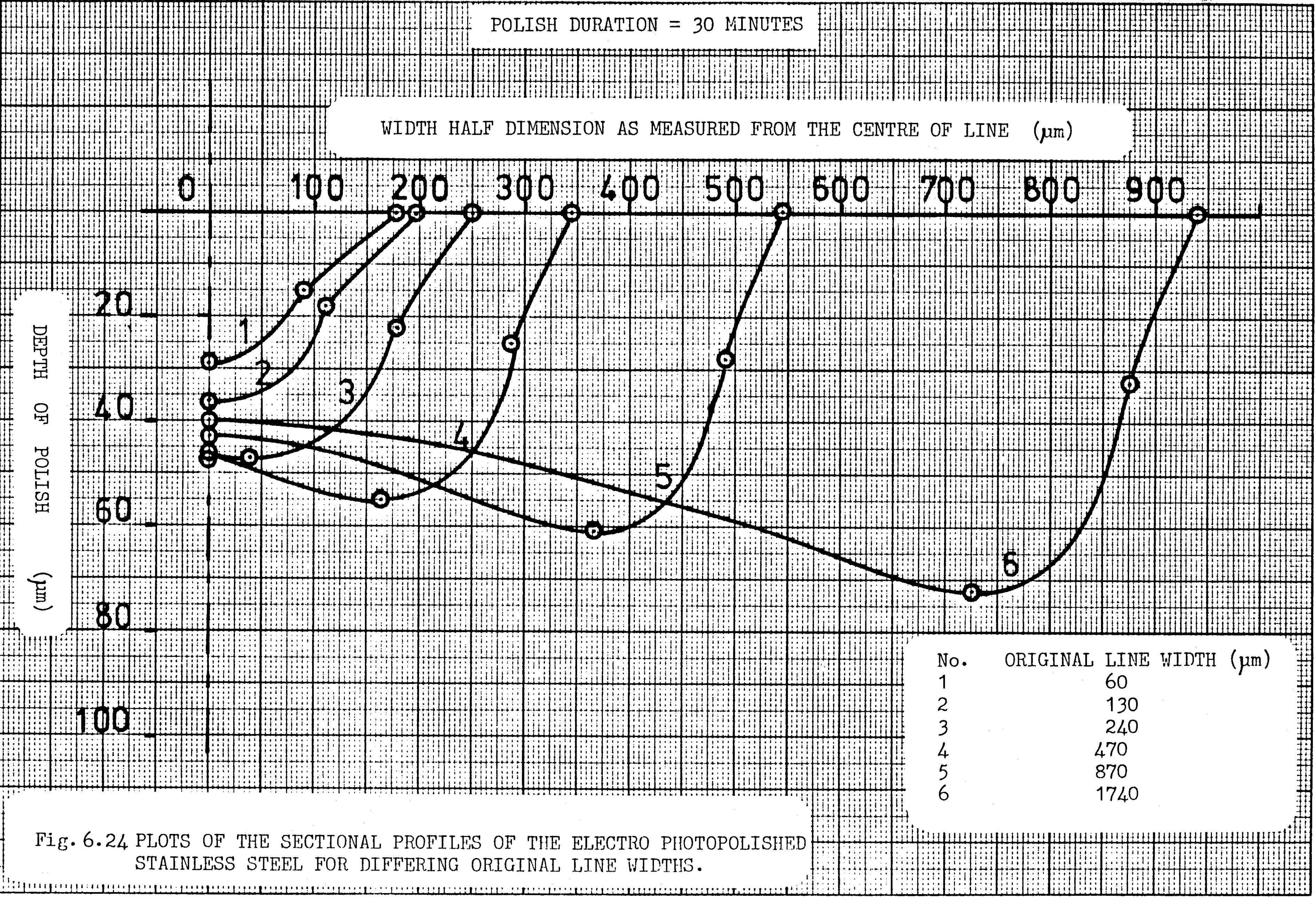

Fig. 6.24 PLOTS OF THE SECTIONAL PROFILES OF THE ELECTRO PHOTOPOLISHED STAINLESS STEEL FOR DIFFERING ORIGINAL LINE WIDTHS.

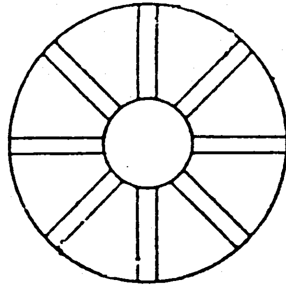

PLAN VIEW

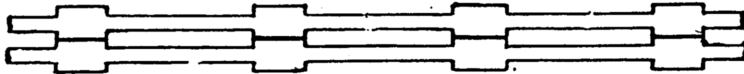

STACK OF TWO ANNULAE

Fig. 6.25 EDGE FILTER PATENTED BY THE SWEDISH COMPANY AKTIEBOLAGET SEPARATOR IN 1927.

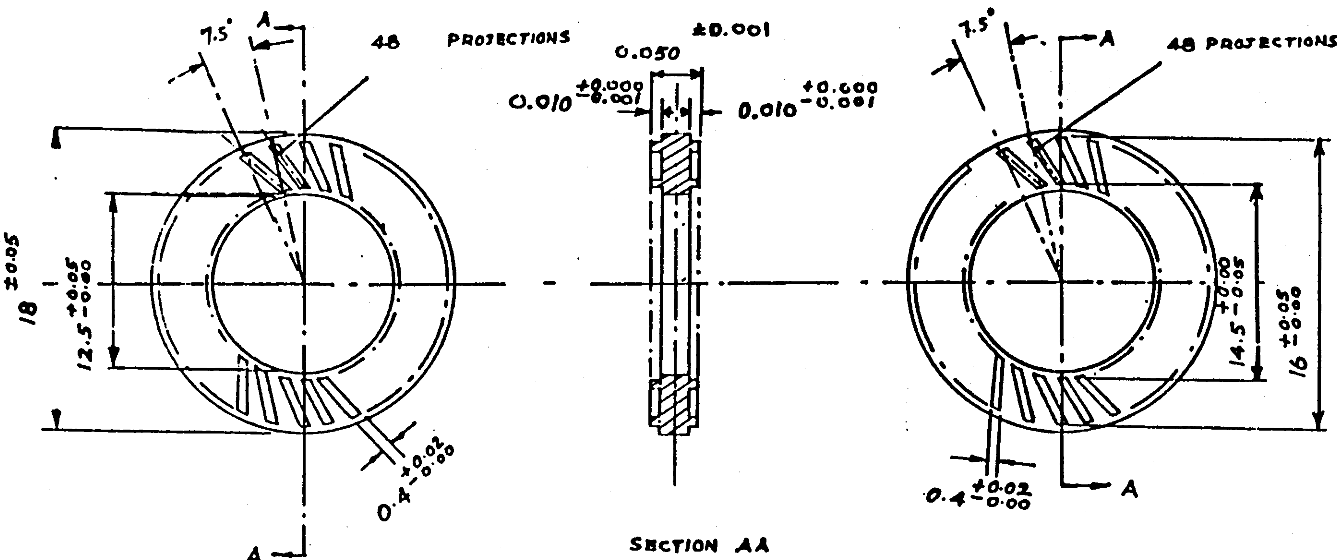

Fig. 6.26 DIMENSIONS OF THE EDGE FILTER PRODUCED BY E.P.E.

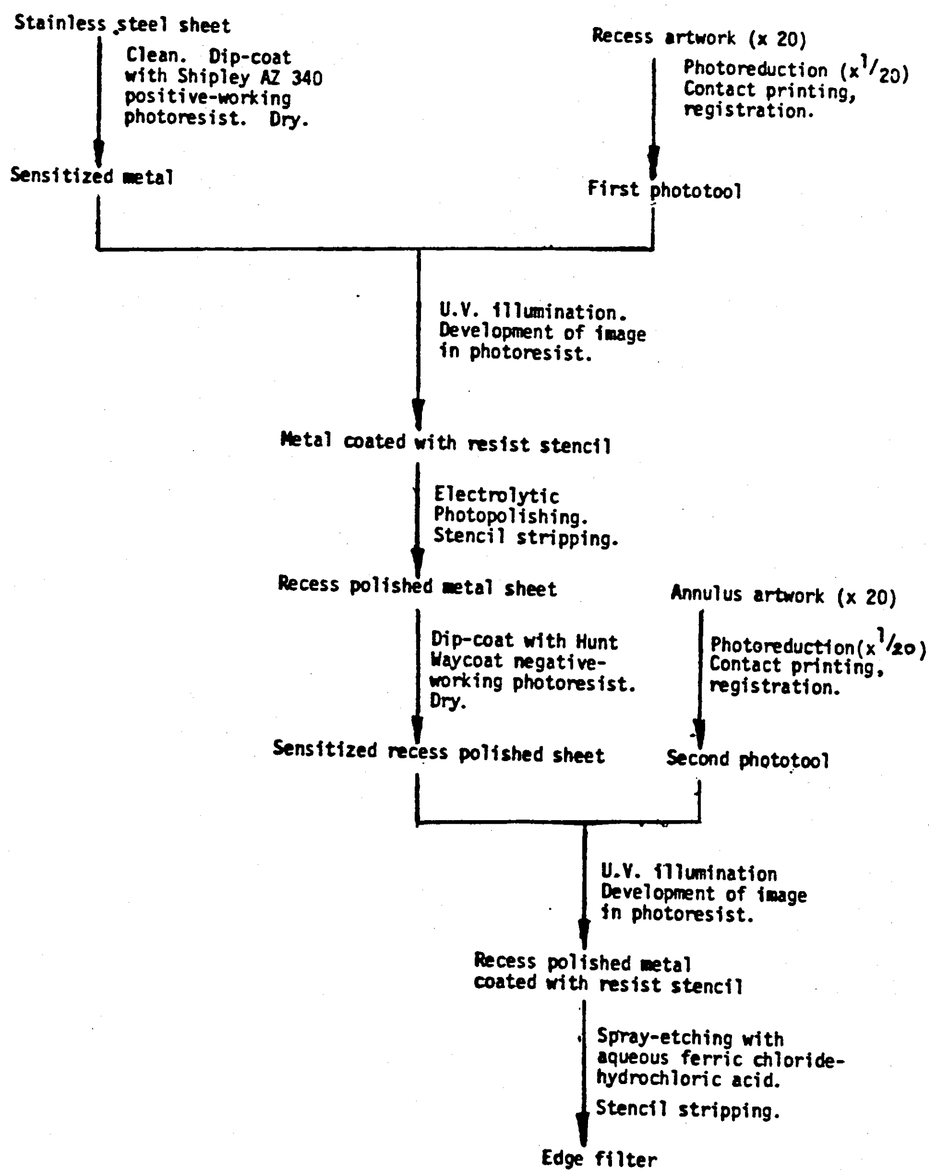

Fig. 6.27 STRATEGY OF EDGE FILTER PRODUCTION.

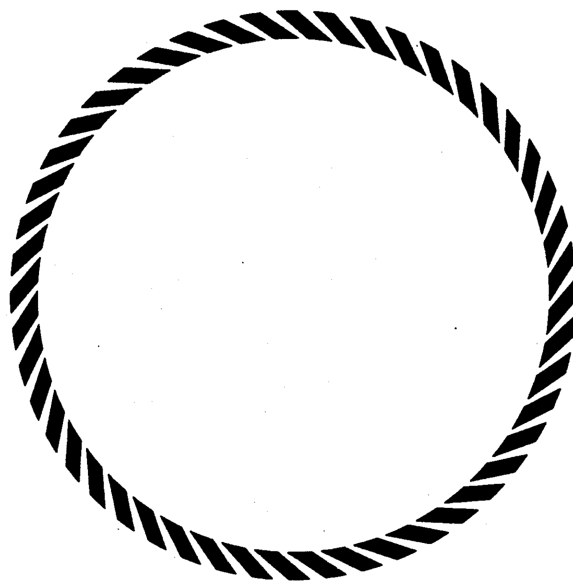

Fig. 6.28 THE E.P.P. TOOL FOR PRODUCING THE EDGE FILTER (MAGNIFICATION x 4.7).

Fig. 6.29 PHOTOMICROGRAPH OF A SECTION OF THE ELECTRO PHOTOPOLISHED EDGE FILTER. (MAGNIFICATION = x 25).

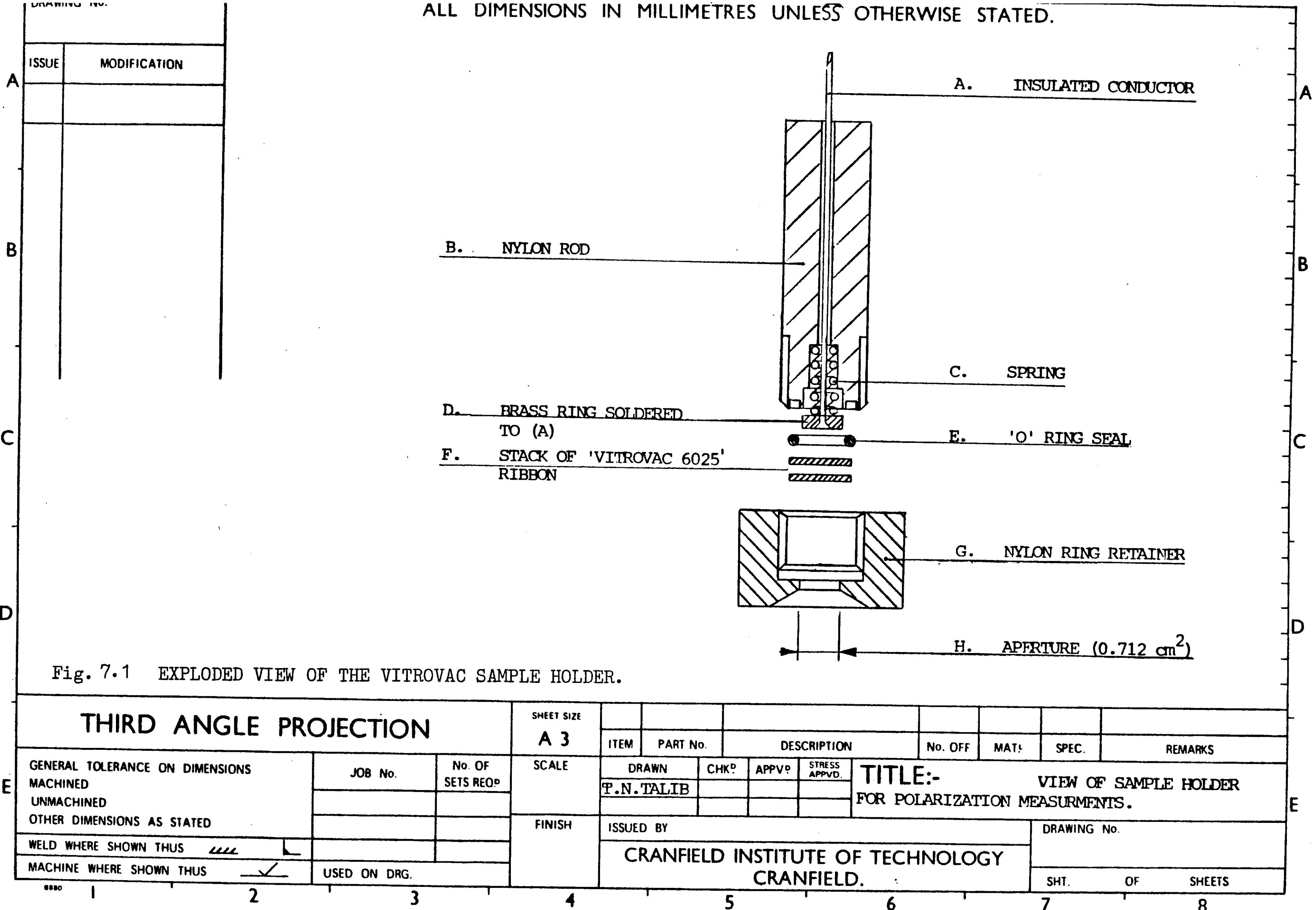

Fig. 7.1 EXPLODED VIEW OF THE VITROVAC SAMPLE HOLDER.

ALL DIMENSIONS IN MILLIMETRES UNLESS OTHERWISE STATED.

DRAWING No.	
ISSUE	MODIFICATION

A. Analogue ammeter.
B&C. Digital multimeters measuring current & potential respectively. Type Sinclair DM 450.
D. Linear sweep generator. Type Thompson DRG 16.
E. Potentiostat. Type Thompson Ministat 7 AMP.
F. 'X-Y' recorder. Type J.J.Loyde P 50
G. Thermostatic hot plate / Magnetic stirrer. Type Gallen kamp.
H. Follower.
I. Sample holder.
J. Glass salt bridge (KCl + Agar).
K. 'Calomel' Ref. electrode. (Kent Inds.1370)

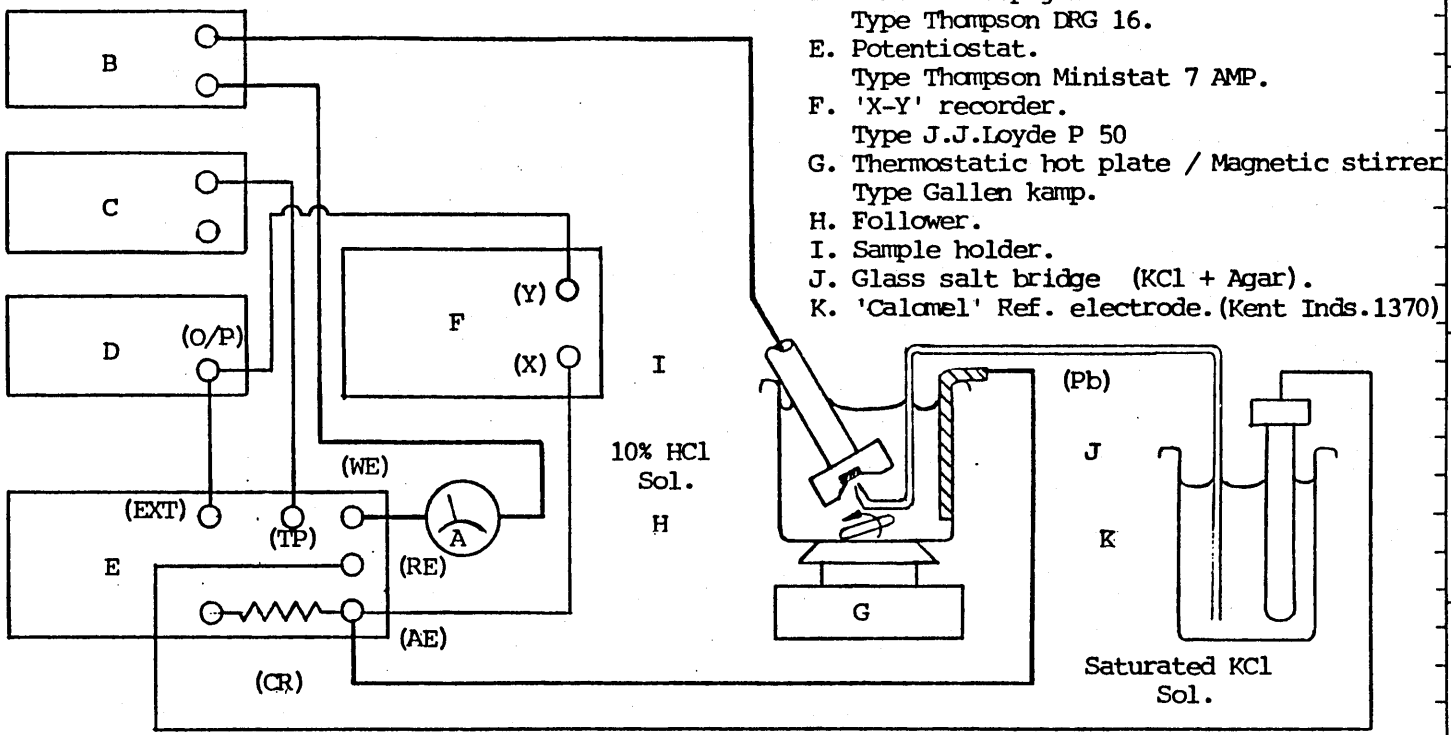

(CR). Counting resistor
(EXT). External input
(AE). Auxiliary electrode
(RE). Reference electrode
(WE). Working electrode
(Pb). Lead cathode
(TP). Total potential

Fig.7.2 SCHEMATIC DIAGRAM OF THE EQUIPMENT AND INSTRUMENTATION USED IN THE POTENTIODYNAMIC POLARIZATION MEASUREMENT FOR VITROVAC 6025.

THIRD ANGLE PROJECTION

SHEET SIZE A 3

ITEM	PART No.	DESCRIPTION	No. OFF	MAT'L	SPEC.	REMARKS

GENERAL TOLERANCE ON DIMENSIONS
MACHINED
UNMACHINED
OTHER DIMENSIONS AS STATED
WELD WHERE SHOWN THUS
MACHINE WHERE SHOWN THUS

JOB No. | No. OF SETS REQ'D | USED ON DRG. | SCALE | FINISH

DRAWN	CHK'D	APPV'D	STRESS APPV'D
T.N.TALIB			

TITLE:- DIAGRAM OF EQUIPMENT & INSTREMENTS USED IN POTENTIODYNAMIC MEASURMENTS.

ISSUED BY
CRANFIELD INSTITUTE OF TECHNOLOGY
CRANFIELD.

DRAWING No.

SHT. OF SHEETS

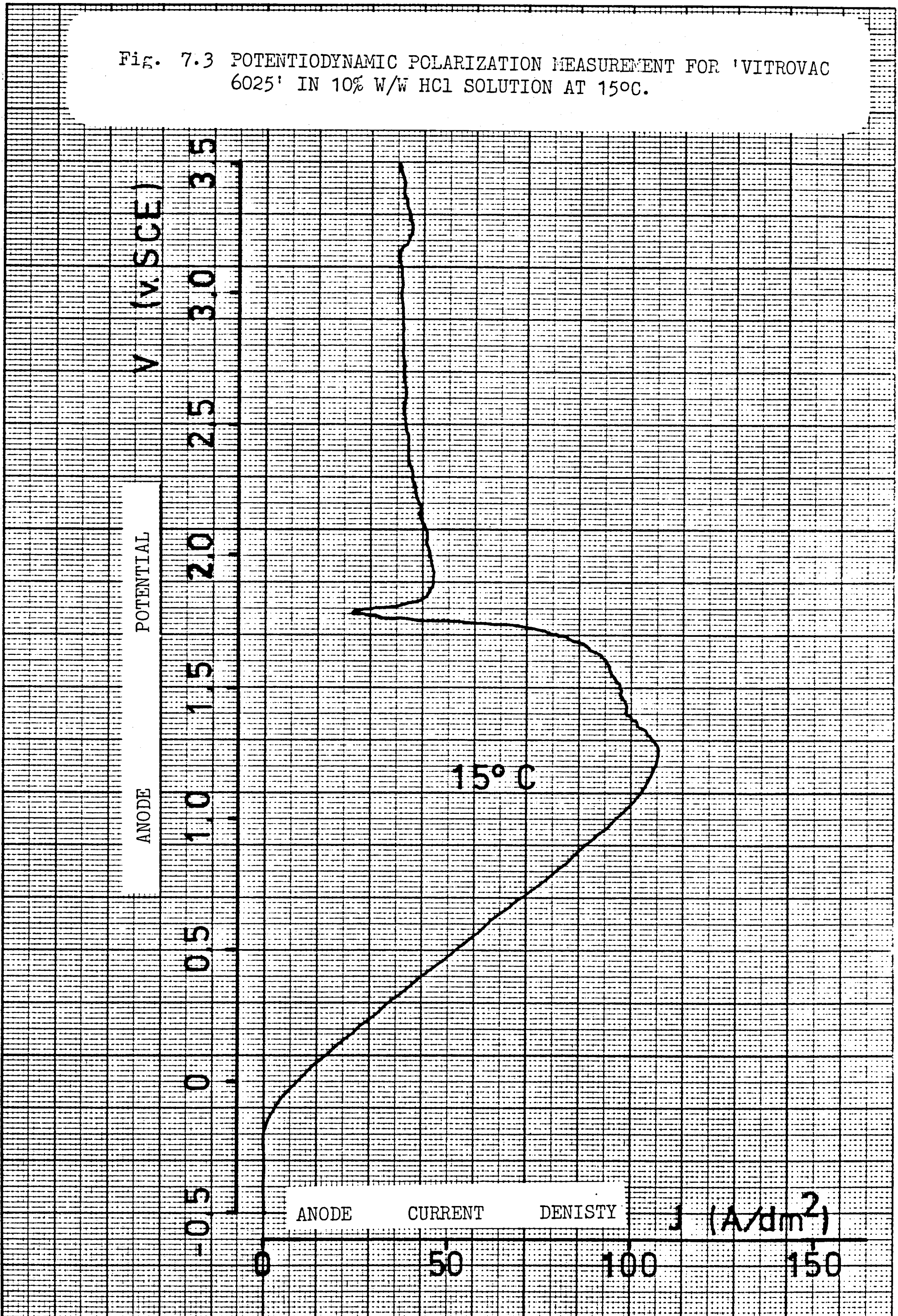

Fig. 7.3 POTENTIODYNAMIC POLARIZATION MEASUREMENT FOR 'VITROVAC 6025' IN 10% W/W HCl SOLUTION AT 15°C.

Fig. 7.4 POTENTIODYNAMIC POLARIZATION MEASUREMENT FOR 'VITROVAC 6025' IN 10% W/W HCl SOLUTION AT 20°C.

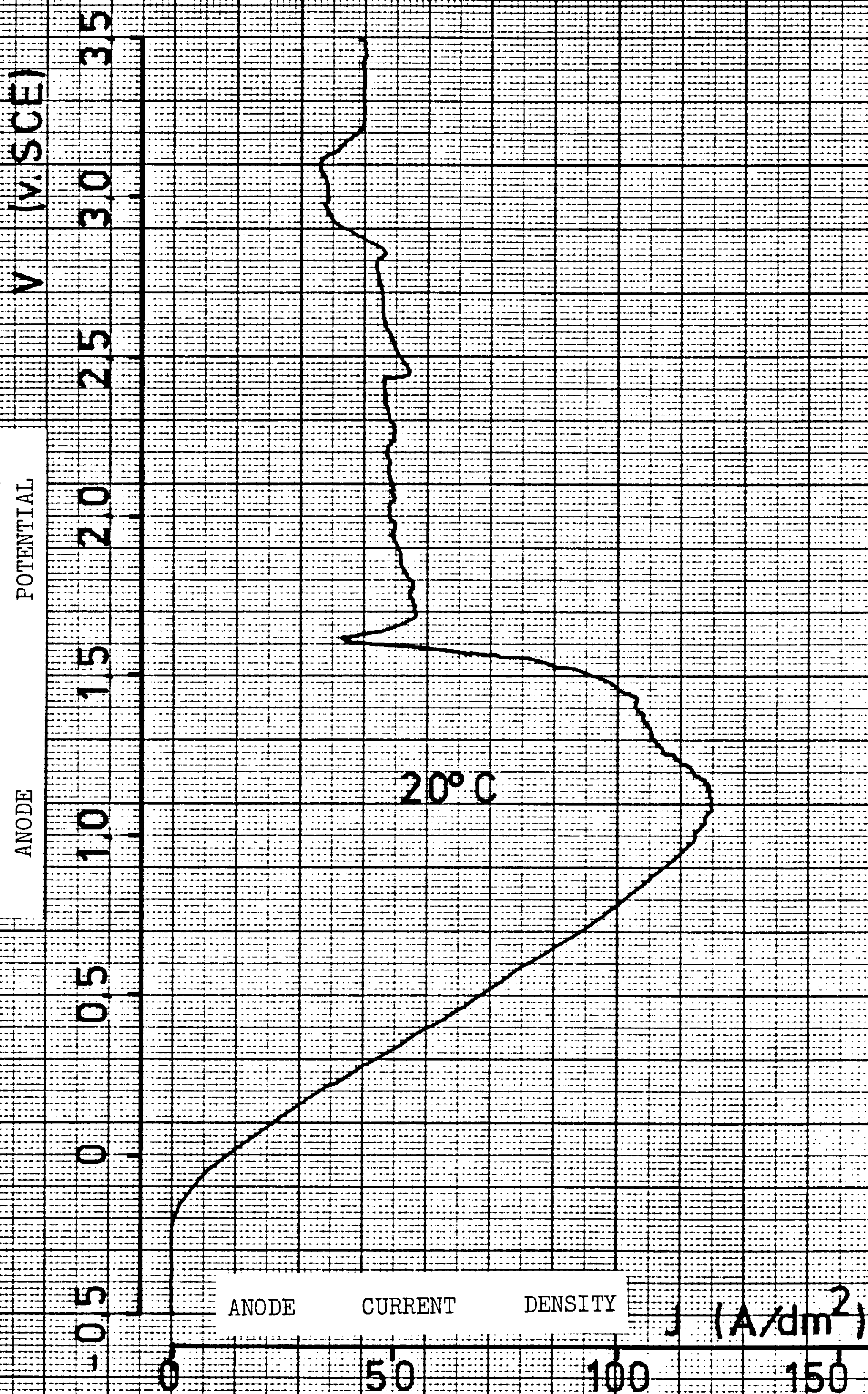

Fig. 7.5 POTENTIODYNAMIC POLARIZATION MEASUREMENT FOR 'VITROVAC 6025' IN 10% W/W HCl SOLUTION AT 25°C.

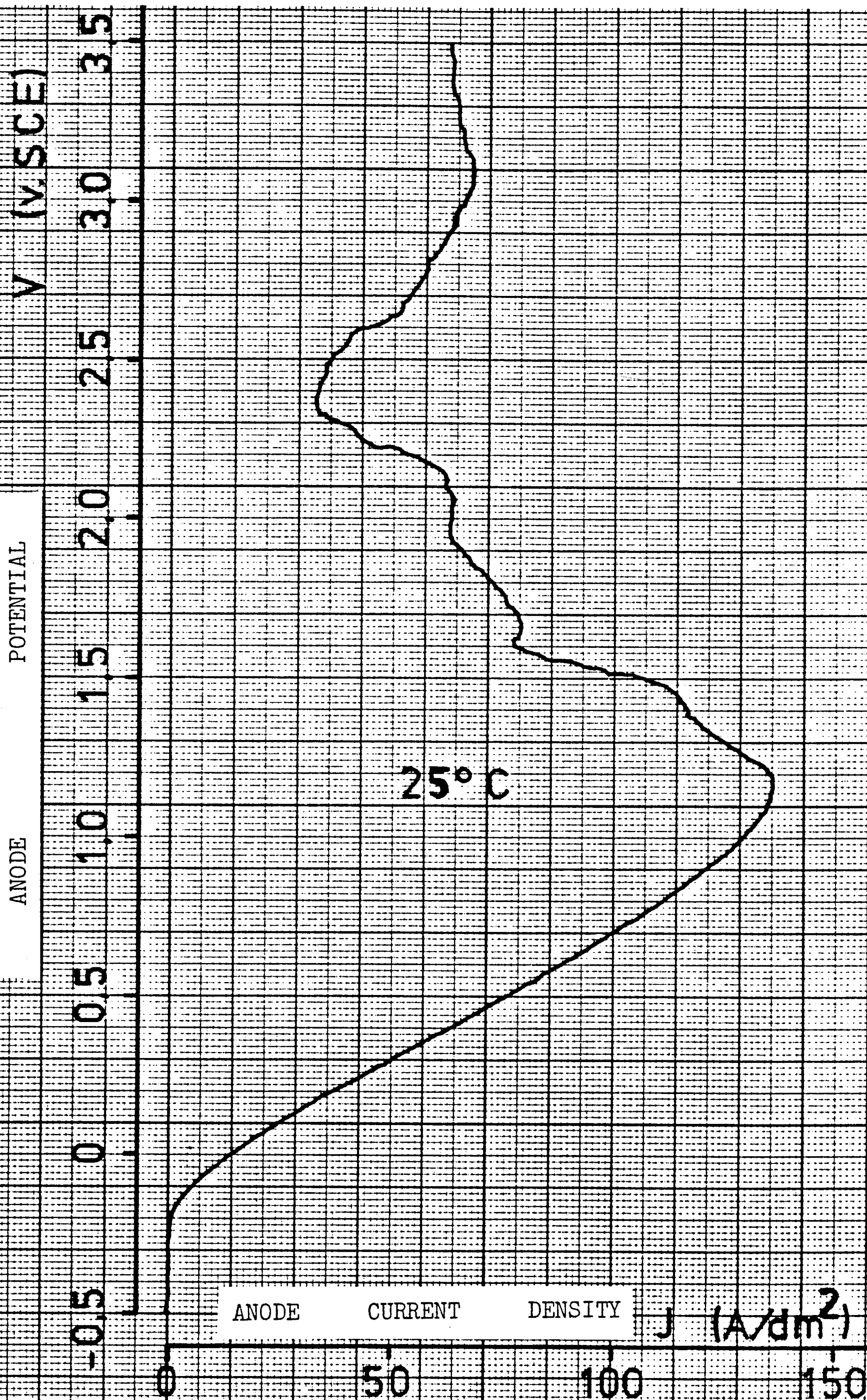

Fig. 7.6 POTENTIODYNAMIC POLARIZATION MEASUREMENT FOR 'VITROVAC 6025' in 10% W/W HCl SOLUTION AT 30°C.

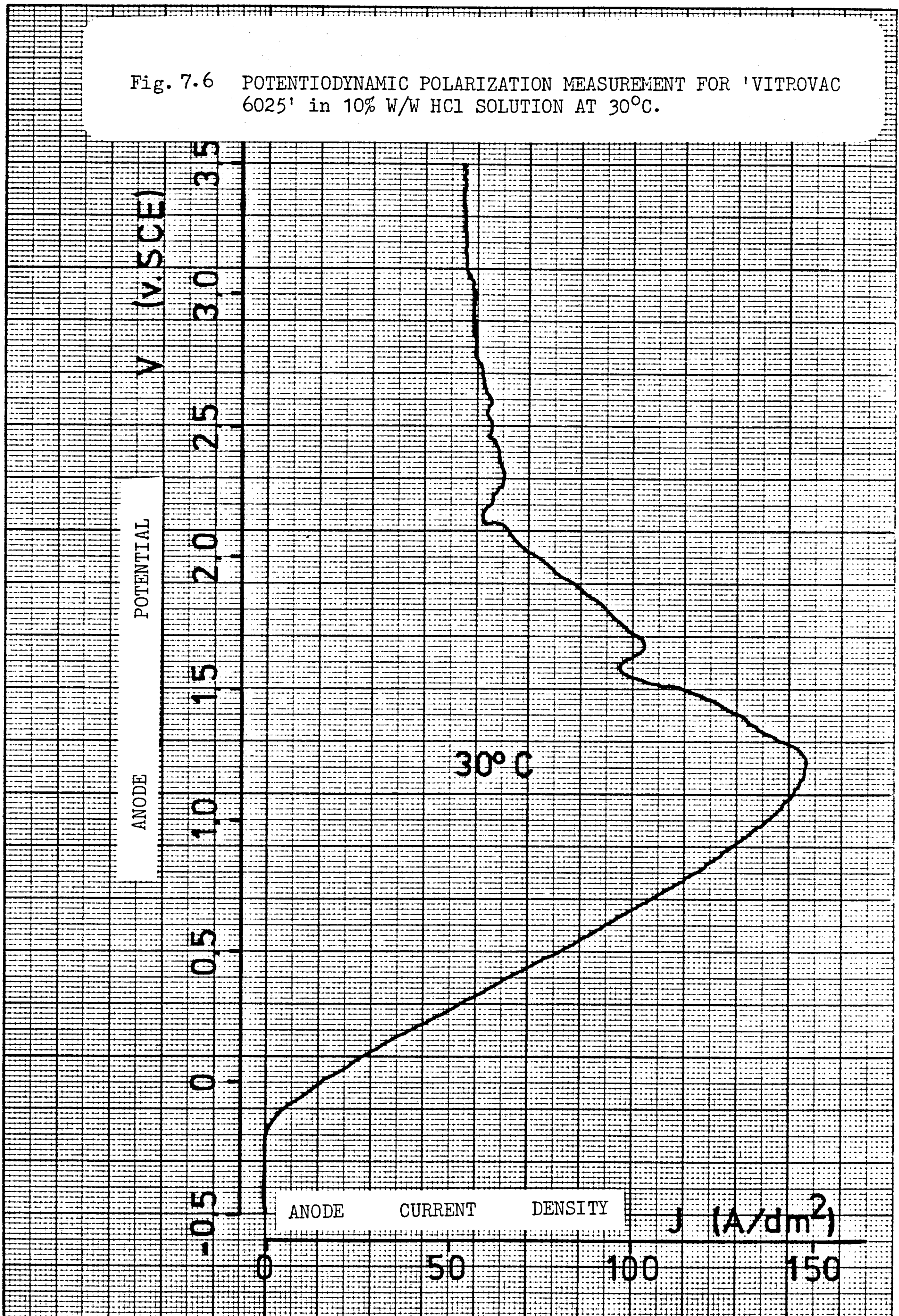

AOV: LOG REG:CODE 2

SOURCE/DF		SS	MS	F
TOTAL	3	962.8		
REG	1	961.4	961.4	999.9
RESID	2	1.4	0.7	

R SQUARE = 0.999

YHAT= -58.867+ 59.906LOG X

X(I)	Y(I)	YHAT	RESIDUALS
15.00	102.80	103.36	-0.56
20.00	121.40	120.59	0.81
25.00	134.30	133.96	0.34
30.00	144.30	144.88	-0.58

X(I)	YHAT
0.00	-472.68

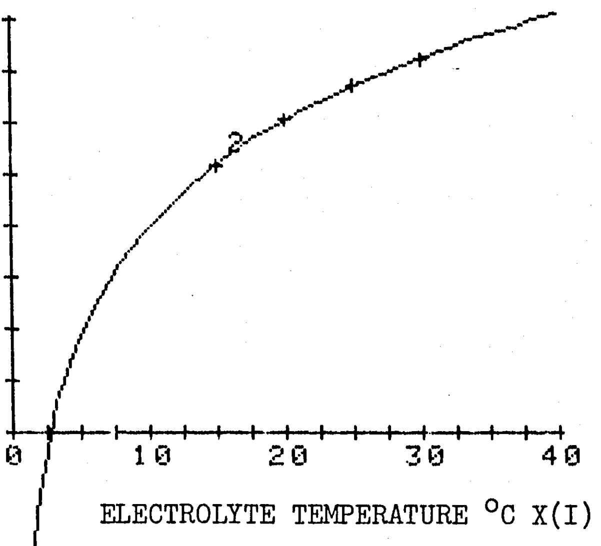

X(I) = ELECTROLYTE TEMPERATURE °C

Y(I) = MAXIMUM ACTIVE ZONE CURRENT DENSITY A/dm^2

The maximum useable current density =

$J_{max} = Y_{HAT} = 59.906 \ln. T - 58.867$ (A/dm^2)

where, T = the electrolyte temperature °C

Fig. 7.7 PLOT OF THE MAXIMUM ACTIVE ZONE CURRENT DENSITY VERSUS ELECTROLYTE TEMPERATURE FOR VITROVAC 6025 IN 10% w/w HCl.

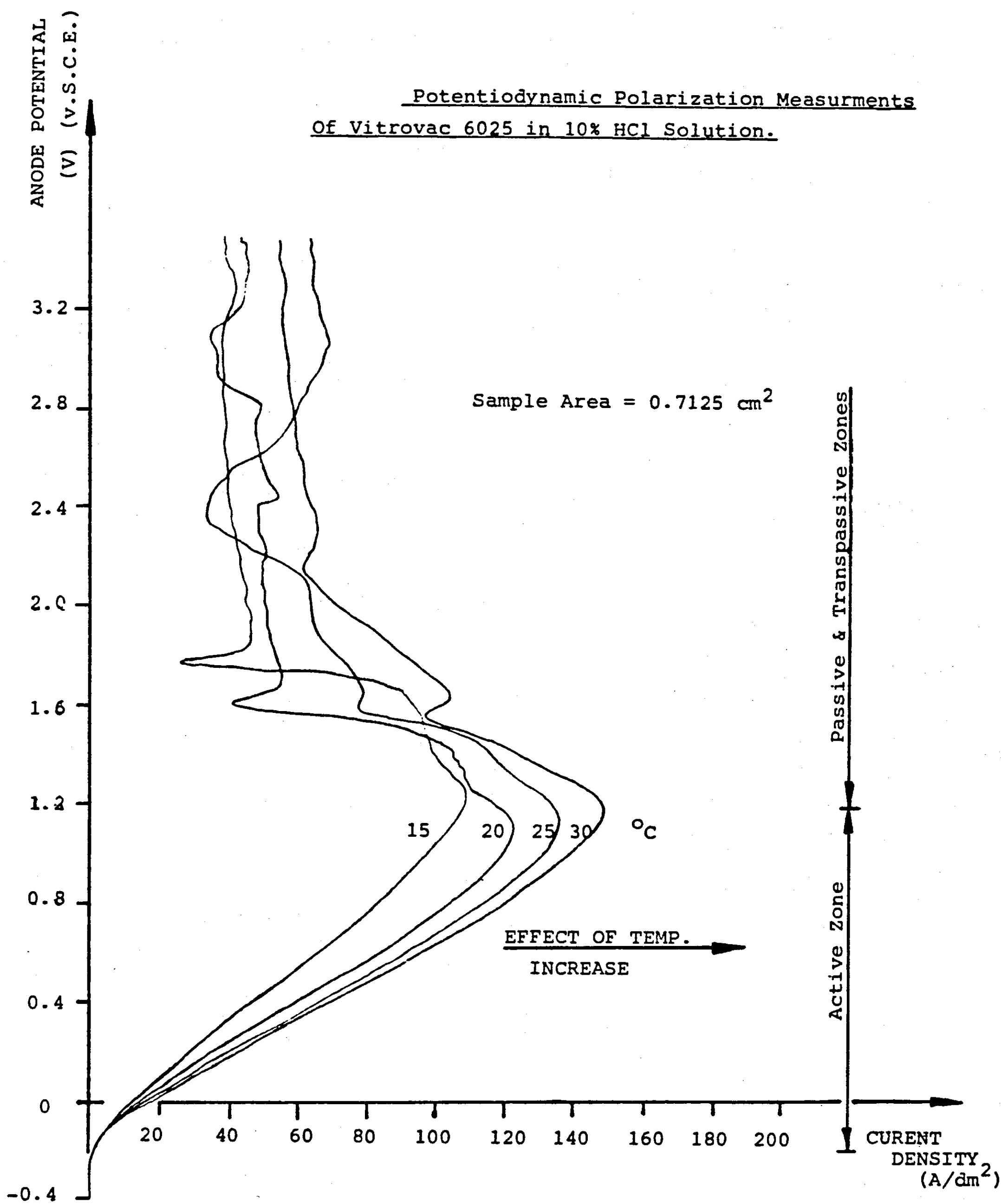

Fig. 7.8 POTENTIODYNAMIC POLARIZATION MEASUREMENTS OF VITROVAC 6025 IN 10% (w/w) HCl SOLUTION.

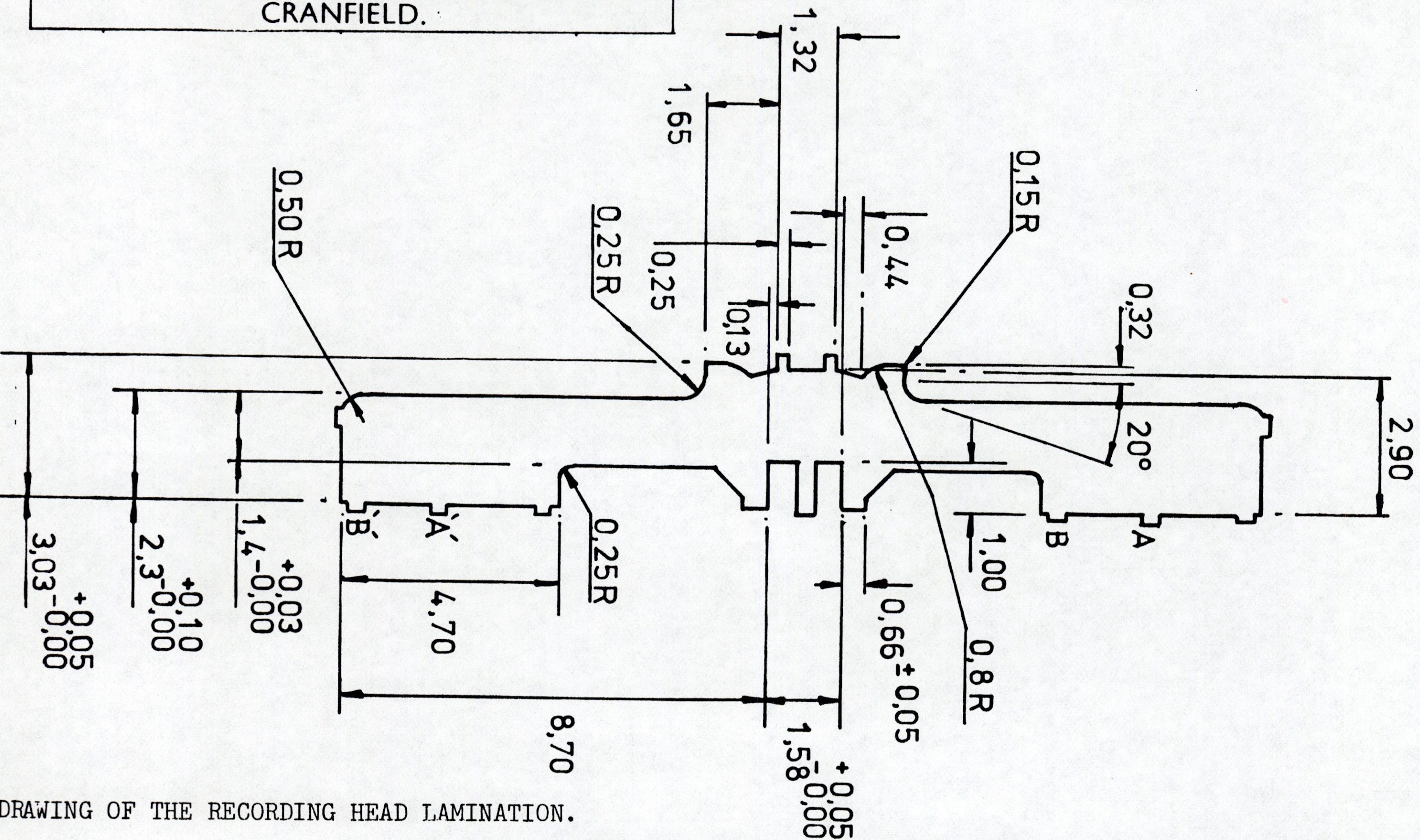

Fig. 7.9 DRAWING OF THE RECORDING HEAD LAMINATION.

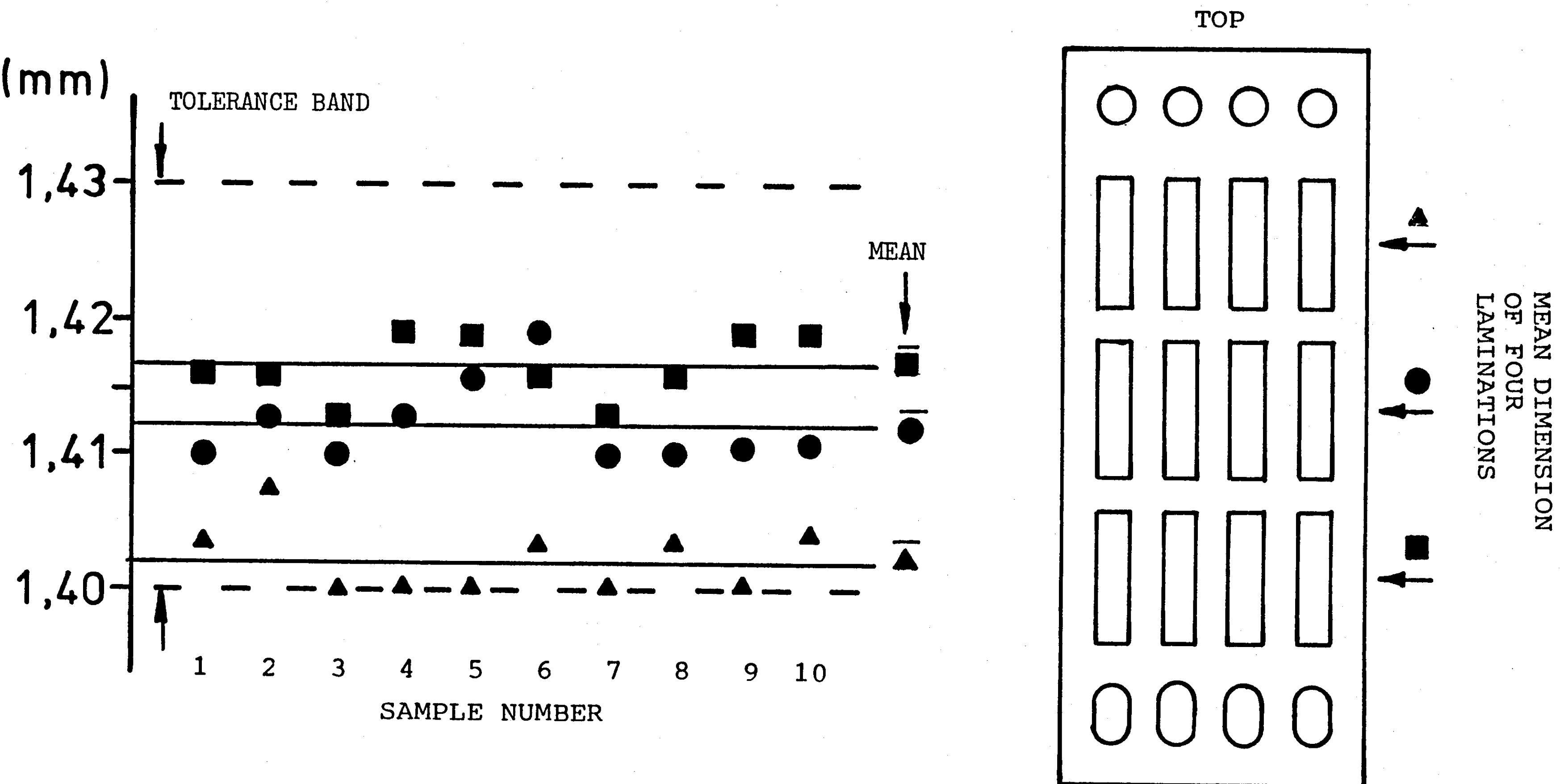

FIG.7.10 The measured distribution of the dimension ($1.4^{+0.03}_{-0.00}$ mm) of a sample of ten etched frets. The mean of each row of four is plotted.

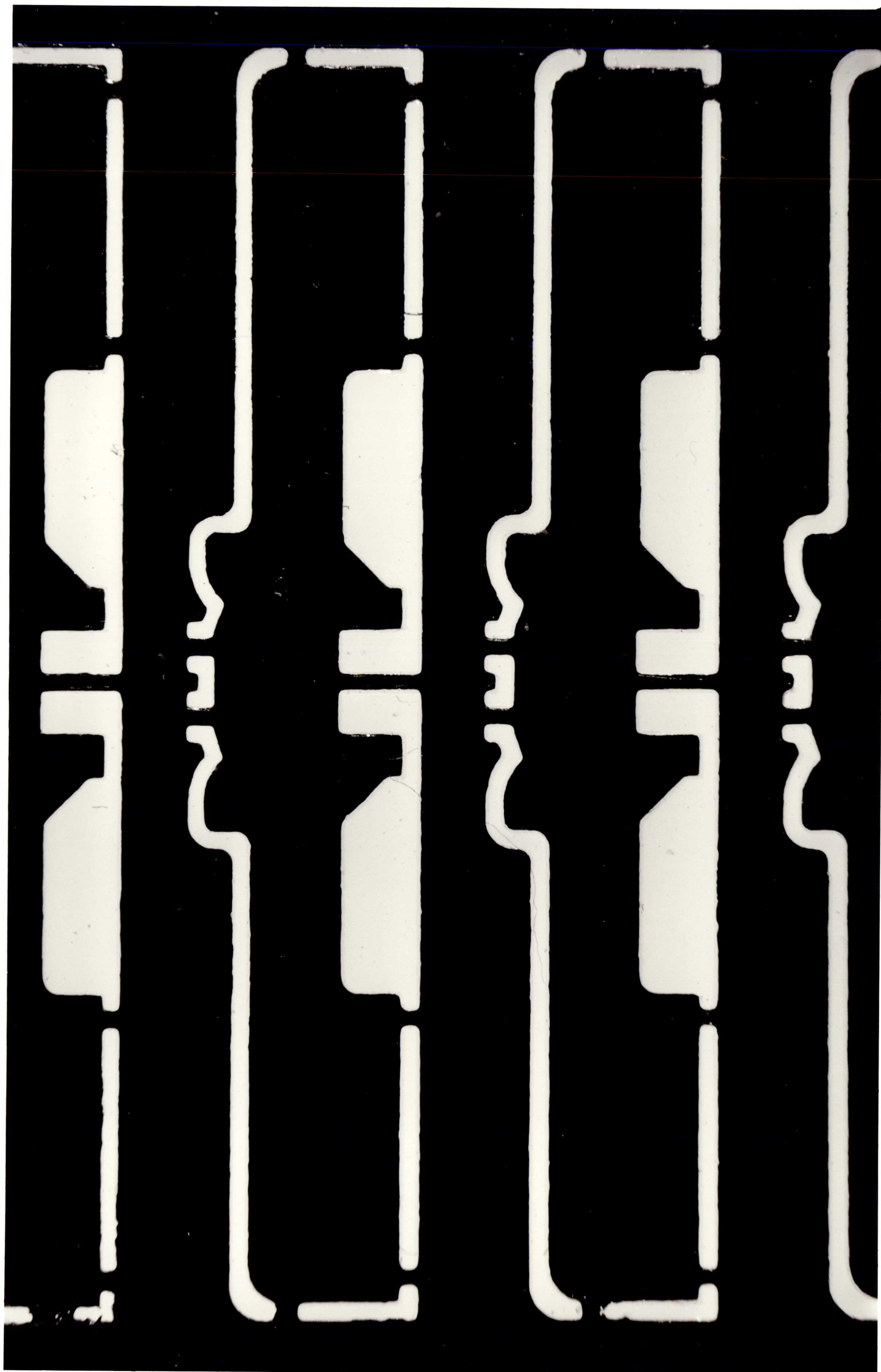

MAG. X 12

Fig. 7.11 PHOTOGRAPH ILLUSTRATING PART OF A FRET PRODUCED BY E.P.E.

Mag x 100

Dark area is unetched

Grey area is residue (Metalloid)

Light areas are where the metalloid has shrunk and cracked.

Fig. 7.12 PHOTOMICROGRAPH OF PARTLY ELECTROETCHED VITROVAC 6025.

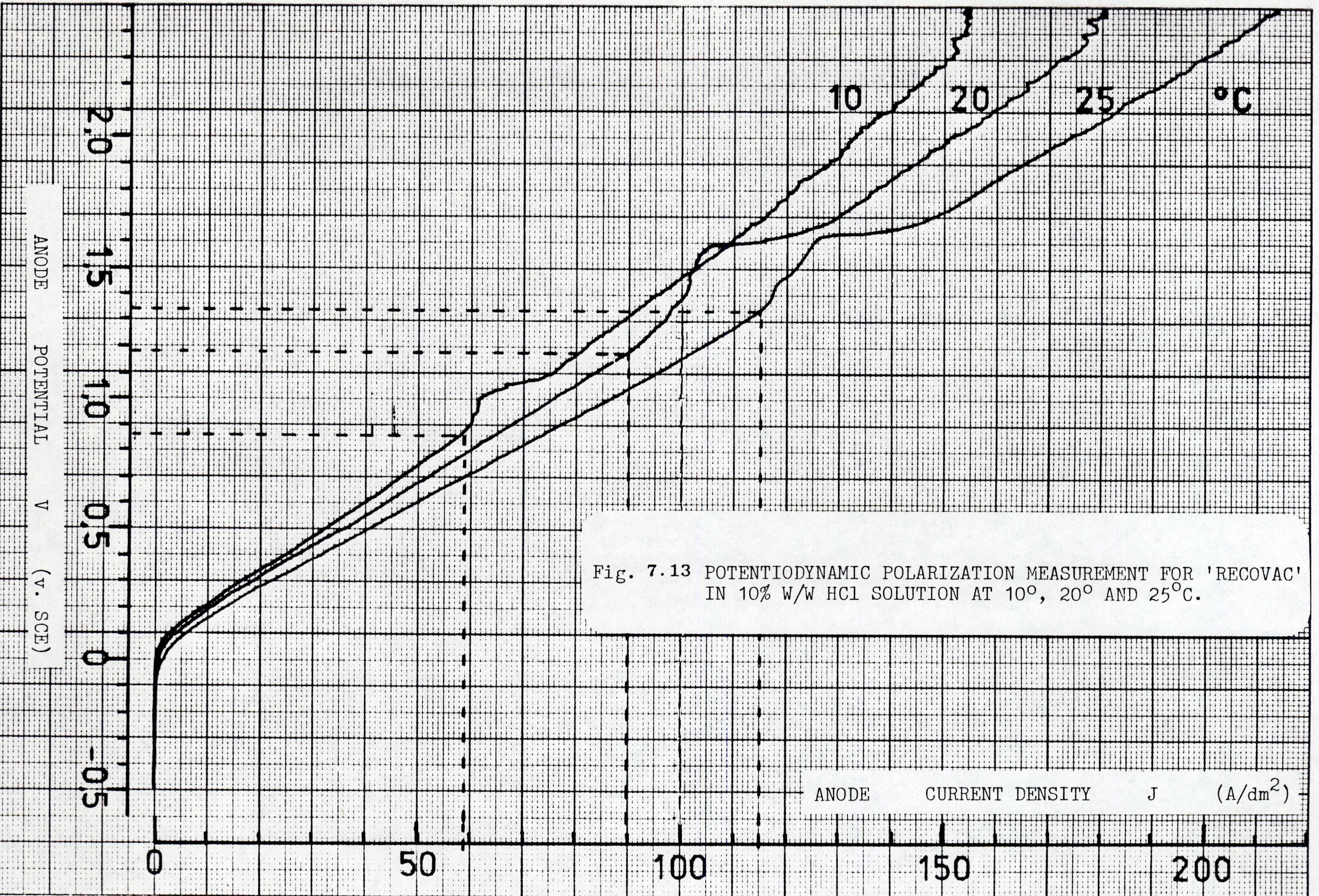

Fig. 7.13 POTENTIODYNAMIC POLARIZATION MEASUREMENT FOR 'RECOVAC' IN 10% W/W HCl SOLUTION AT 10°, 20° AND 25°C.

AOV: LINEAR REG:CODE 1

SOURCE/DF		SS	MS	F
TOTAL	3	534.8		
REG	1	530.5	530.5	246.7
RESID	2	4.3	2.2	

R SQUARE = 0.992

YHAT = -1.000 + 4.120 X

X(I)	Y(I)	YHAT	RESIDUALS
2.50	10.00	9.30	0.70
5.00	18.00	19.60	-1.60
7.50	31.00	29.90	1.10
10.00	40.00	40.20	-0.20

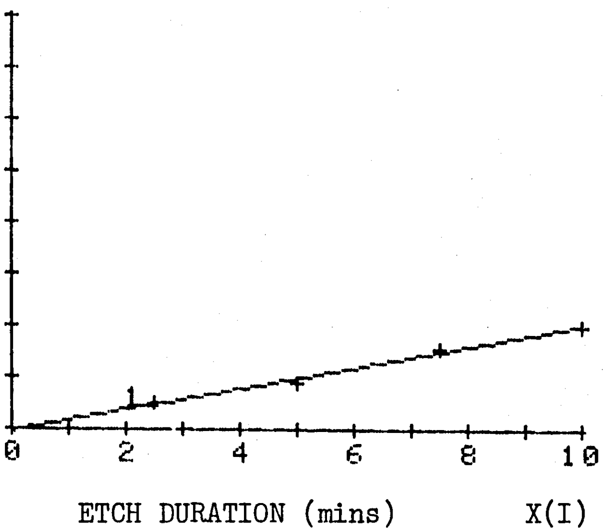

Y_{HAT} = Depth of etch = 4.12 t -1 (µm)

where t is etch duration in mins.

X(I) = ETCH DURATION (mins)

Y(I) = DEPTH OF ETCH (µm)

Fig.7.14 THE DEPTH OF ETCH OF 'RECOVAC' VERSUS ETCH DURATION AT J = 25 A/dm^2

AOV: LINEAR REG:CODE 1

SOURCE/DF		SS	MS	F
TOTAL	3	2398.8		
REG	1	2398.1	2398.1	999.9
RESID	2	0.7	0.4	

R SQUARE = 1.000

YHAT = -1.000 + 8.760 X

X(I)	Y(I)	YHAT	RESIDUALS
2.50	21.00	20.90	0.10
5.00	43.00	42.80	0.20
7.50	64.00	64.70	-0.70
10.00	87.00	86.60	0.40

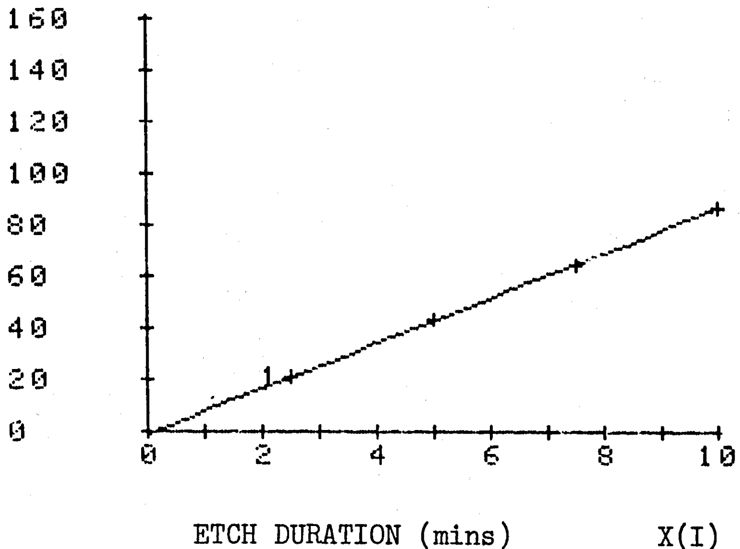

Y_{HAT} = Depth of etch = 8.76 t-1 (μm)

where t is the etch duration in mins.

X(I) = ETCH DURATION (mins)

Y(I) = DEPTH OF ETCH (μm)

Fig. 7.15 THE DEPTH OF ETCH OF 'RECOVAC' VERSUS ETCH DURATION AT J = 50 A/dm^2.

AOV: LINEAR REG:CODE 1

SOURCE/DF		SS	MS	F
TOTAL	3	8642.8		
REG	1	8611.3	8611.3	546.7
RESID	2	31.5	15.8	

R SQUARE = 0.996

YHAT = -5.500 + 16.600 X

X(I)	Y(I)	YHAT	RESIDUALS
2.50	37.00	36.00	1.00
5.00	74.00	77.50	-3.50
7.50	123.00	119.00	4.00
10.00	159.00	160.50	-1.50

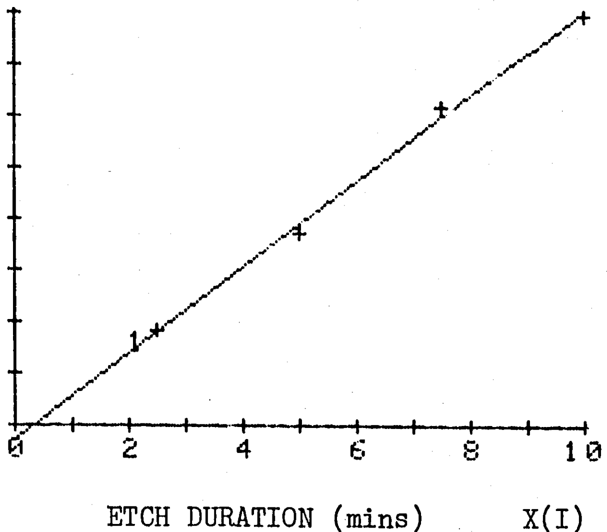

Y_{HAT} = Depth of etch = 16.6 t−5.5 (µm)

where t is etch duration in mins.

X(I) = ETCH DURATION (mins)

Y(I) = DEPTH OF ETCH (µm)

Fig. 7.16 THE DEPTH OF ETCH OF 'RECOVAC' VERSUS ETCH DURATION AT J = 100 A/dm^2.